Reconstructing the Quaternary denudation history of the Orange River basin, southern Africa using cosmogenic ^{10}Be and ^{26}Al analysis

Jonathan J Butler

Volume 1: Thesis

PhD

The University of Edinburgh

2007

This thesis has been composed entirely by myself and is my own work. This work has not been submitted for any other degree or professional qualification

Jonathan J Butler

Acknowledgements

There too many people who have been involved with this project to thank individually. However, there are a few who deserve special mention: thanks must go first and foremost to Mike Summerfield, my supervisor, for his ideas, help, support, and attention to detail, both geomorphological and political. Thanks also to both Christoph Schnabel, my co-supervisor, and Bill Phillips, my initial co-supervisor, for their technical expertise. Special thanks to Steve Binnie for his invaluable lab support and support with many other aspects of the project. Thanks to Tibor Dunai for his help with calculations and interpretation, and to Rachel Walcott for her DEM and GIS expertise. Thanks also to Stewart Freeman and Colin Maden at SUERC for their patience and hard work in ensuring that this project ended up with decent AMS data.

Thanks to Joe Hägg, Tom Hartley and Bex Seymour for good times and good humour in the field. Thanks also to John Boardman, Ian Foster, Mike Meadows, and Peter Holmes for help and advice in the field and support throughout the project. Thanks to Bruce King for the extremely detailed topographic and lithological summary maps of South Africa. Thanks also to Hugo Bezuidenhout at SANParks for permission to work in the National Parks of South Africa, and to Stephen Smith, Park Manager at the Augrabies Falls and Johan Taljaard, Park Manager at the Golden Gate Highlands National Park. Thanks to Stephen Tooth for interesting discussions and the use of photographs.

Special thanks to friends and colleagues in Edinburgh for making my time here so memorable. Thanks to Lis for patience and encouragement. Thanks most of all to my parents for their constant support.

This work was funded by the Natural Environment Research Council (Studentship NER/S/A/2003/11231)

Nomenclature

Various studies use different terminology for aspects of geomorphology, cosmogenic nuclide analysis and when quoting rates of erosion. In the interests of clarity, a brief note is given here on the nomenclature conventions used in this thesis. Whilst this study deals with denudation, i.e. the removal of earth surface material both as solid particles and dissolved material (Summerfield, 1991b), erosion (*sensu stricto* the removal of solid particles) is at times used as a shorthand for denudation in this study.

The word isotope conventionally refers to a chemical variation of an element with a different number of neutrons. Therefore, a cosmogenic isotope is one element formed by interaction with cosmic rays, e.g. ^{10}Be. The word nuclide refers to more than one isotope, and therefore the term cosmogenic nuclide refers to more than one cosmogenic isotope, e.g. both ^{10}Be and ^{26}Al. In this study the term cosmogenic nuclide analysis is referred to throughout, as this study involves both cosmogenic isotopes ^{10}Be and ^{26}Al.

Studies that involve measuring the cosmogenic nuclide component in river sediment have, variously, been referred to as the basin wide technique, or the catchment-averaged approach. The author makes no distinction between these terms, however for consistency, the term catchment-averaged is used when referring to this technique. When quoting rates of erosion, different authors have referred to different rates (e.g. meters per year (m a^{-1}), millimetres per thousand years (mm ka^{-1}), and meters per million years (m Ma^{-1}). The latter two are interchangeable and are both used in this study, depending on the context of the sample: basin wide rates of erosion are quoted in millimetres per thousand years, appropriate to the averaging time of the samples. Full details are given in this study of how erosion rates were calculated. Full sample details, together with erosion rates calculated using the Stone (2000) and Dunai (2000) conventions are also given. Unless otherwise stated, erosion rates quoted in this study are calculated using the Stone (2000) scaling factors for spallation and muons. For a full discussion of the reasons for this, refer to Chapters 2 and 3.

Abstract

Break-up of the Gondwana supercontinent ~ 130 Ma ago resulted in the formation of new base levels for erosion around the coastline of southern Africa. Although the post–break-up denudational history has been quantified using low-temperature thermochronology, the more recent Quaternary record is currently poorly constrained. Cosmogenic-nuclide based estimates of denudation rates applicable over time scales of $10^4 - 10^6$ years exist for some localities in southern Africa, but there have been no equivalent catchment-wide studies in the Orange basin, the primary drainage basin of the subcontinent. In this study a regional-scale picture of catchment-wide denudation based on ^{10}Be and ^{26}Al is presented that shows rates varying from ~ 2 to ~ 50 mm ka^{-1}. These rates are consistent with existing cosmogenic-derived site-specific estimates, and are also compatible with the much longer term denudation record derived from low-temperature thermochronology. This record indicates generally low rates of denudation across southern Africa after a phase of locally high rates in the period after continental break-up. Despite the low rates reported here, it is evident that low-relief erosion surfaces in the Orange basin could not have survived unmodified over geological time scales, as implied in traditional denudation chronology approaches to landscape history. The cosmogenic-derived denudation rates presented here, which provide mean rates over time scales of $10^3 - 10^5$ years, also provide a benchmark against which rates estimated by other methods for the past few decades in catchments in the central Orange Basin can be compared. Such comparisons reveal that short-term denudation rates, which in some cases at least have been influenced by anthropogenic factors, have been up to two orders of magnitude higher than the longer term cosmogenic-derived rates. The major knickpoint on the Orange River, the Augrabies Falls, exerts a fundamental control on landscape evolution across the two-thirds of the basin area upstream, but the rates of channel incision above and below the Falls have not previously been constrained. Site-specific cosmogenic nuclide concentrations of ^{10}Be and ^{26}Al from channel bed and interfluve samples from a range of sites across the complex anabranching channel system of the Augrabies Falls region indicate that channel incision rates in the higher gradient zone above the main falls average ~ 70 mm ka^{-1},

whereas rates in the gorge section below the main falls are typically ~10 mm ka^{-1}. Rates of denudation on interfluves of ~ 6 mm ka^{-1} show that local relief is increasing, albeit very slowly. Together, the cosmogenic-derived catchment-wide and site-specific denudation rates presented here significantly improve our knowledge of Quaternary-scale denudation rates across the Orange Basin in general, and the key Augrabies Falls knickpoint of the Orange River, in particular.

List of Colour Plates

List of Figures

List of Tables

Chapter 1 – Introduction

1.1 The physical and intellectual geomorphic setting of southern Africa

The discipline of geomorphology is at the interface between the lithosphere, atmosphere, hydrosphere and biosphere. An increasing recognition that these different 'spheres' are interdependent has given rise to the 'Earth system science' approach to studying geomorphology, an approach which emphasises the interconnectivity of external (exogenic) and internal (endogenic) processes operating at the surface of the Earth (Summerfield, 1988). Understanding the morphology of the Earth is predicated on understating rates of geomorphic processes on a variety of timescales. The accretion and breakup of continents as part of Wilson cycles has driven global climatic changes and influences the earth's morphology today. What happens to continents after accretion or breakup can be understood by the rate, timescale and extent of how the landscape subsequently erodes. Regional tectonic movements have created vast mountain ranges over tens of millions of years, yet their evolution can only be understood with reference to denudation and climate, which ultimately regulates their height (Whipple & Tucker, 1999). Local hotspots of contemporary denudation appear to largely be caused by anthropogenic activity or climatic change, yet their importance can only really be understood if benchmark pre-anthropogenic denudation rates are known. Understanding rates of denudation (the removal of weathered material) is therefore also key to understanding long-term global climatic changes. On a global scale over hundreds of millions of years, Earth's climate has been forced externally by orbital changes. Initial external forcing has led to increased temperature, precipitation and vegetation. This in turn increases the rates of chemical weathering of silicate rocks, which causes drawdown of CO_2 which reduces the warming effect (Raymo *et al.*, 1988). This internal feedback mechanism may also operate in reverse to reduce an initial cooling effect. Crucial in understanding both Earth's tectonic and climatic history is therefore knowledge of denudation rates on various timescales. A range of new techniques are becoming available that link the study of landscape evolution over hundreds of millions of years with processes that operate over decades to centuries.

Low-temperature thermochronological methods have revolutionised our understanding of landscape evolution over millions to hundreds of millions of years. Apatite fission track thermochronology (AFTT) measures the products of radioactive decay (fission tracks) in a mineral system. The number and length of the tracks is dependent on the temperature at which the material was held at various times. From measurements of the degree of annealing (shortening) of the fission tracks, it is possible to reconstruct the thermal history experienced by a mineral sample over geological time (Gleadow & Brown, 2000). AFTT is useful over a temperature range up to 110 °C which characterises temperatures in the upper part of the Earth's crust. The mineral's proximity to the surface is likely to be the dominant influence on palaeotemperature. Denudation at the Earth's surface exerts the major control on the cooling patterns obtained (Summerfield & Brown, 1998). Therefore, fission track thermochronology provides a readily accessible framework for quantifying the previously un-measurable, i.e. the timing and magnitude of long term denudation for a large part of the geological record (Kohn *et al.*, 2002). This data offers enormous potential for developing models of long-term landscape evolution, in particular the formation and subsequent long-term development of passive margins. Passive margins in various locations on the former Gondwana supercontinent have been the focus of several recent AFTT studies; for example in southeastern Brazil (Harman *et al.*, 1998); southeastern Australia (Gleadow *et al.*, 2002; Kohn *et al.*, 2002); and southern Africa (Brown *et al.*, 1990; Gallagher *et al.*, 1998; Gallagher & Brown, 1999a; Gallagher & Brown, 1999b; Gallagher *et al.*, 1999; Brown *et al.*, 2000).

These data on long term denudation rates build on earlier estimates of denudation rates from offshore sedimentary sequences (e.g. Rust & Summerfield, 1990), although uncertainties in former basin extents limited the usefulness of denudation rates derived from these sedimentary sequences. What has been uncertain until recently is how these long-term rates of denudation (tens of millions of years) compare with rates spanning thousands to hundreds of thousands years and whether these denudation rates and their dependence on various controlling factors can be extrapolated back to understand the denudational response to tectonic processes (Gleadow & Brown, 2000). AFTT data can only be understood properly with respect

to geomorphic mechanisms, i.e. crustal denudation, as well as tectonic factors. This reflects the need for the community of 'geographical' as well as 'geophysical' geomorphologists in the discipline of geomorphology, as discussed by Church (2005) and Summerfield (2005a).

AFTT and offshore sedimentary sequences provide data on very long term rates of denudation whilst recent denudation rates (over tens to hundreds of years) can be measured directly or from instrumental and proxy sedimentary records. What has been missing until recently is a reliable technique for measuring denudation rates over thousands to hundreds of thousands of years. Cosmogenic nuclide analysis is now spanning this gap, and allowing denudational processes on short and medium timescales to be extrapolated to long timescales. AFTT and cosmogenic nuclide analysis are complementary techniques, although AFTT data must be integrated with other sources of information, especially on characteristic rates of denudation over shorter timescales (which cosmogenic techniques can now provide) in order to be understood (Gleadow & Brown, 2000). Thus the linking of spatial and temporal scales, perhaps the holy grail of geomorphology for many decades (since at least the seminal work of Schumm & Lichty, 1965), is now possible by a combination of these different techniques.

Southern Africa (Figure 1.1.1) has been the inspiration and natural laboratory for several key theories of landscape evolution. As well as being the location for seminal work on the origin of pediments, inselbergs, escarpments and gorges, southern Africa and particularly the Orange River basin, which drains over two thirds of the southern African landmass, has become the type locality for the study for large scale denudational geomorphology. Davis, du Toit, King and Wellington, titans of geomorphology all, carried out definitive works on the denudational history of southern Africa since the breakup of Gondwana. Since supercontinental breakup ~ 130 Ma ago, Gondwana's constituent continents have had very different histories. Put simply, Australia drifted into the subtropical zone of descending air, became arid and geomorphically stable. Antarctica drifted away to the south and effectively became refrigerated as the Antarctic circumpolar current was set up ~ 35 Ma ago. South America formed the Andes on its western flank after collision with the Pacific

plate, and the massive Amazon basin on its eastern flank developed in response to the uplift on the Andes. India drifted to the north, collided with Eurasia and formed the Himalayas. Perhaps most interestingly of all, southern Africa, a passive margin, uplifted after continental breakup. The potential energy generated from this uplift, together with an east-west climatic gradient, helped erode a large volume of sediment. Thermochronologic methods reveal between 1 and 5 km of denudation since rifting (Brown *et al.*, 1990; Gallagher *et al.*, 1998). This led to the exposure of progressively older rocks to the north and west of the subcontinent, a feature that was the inspiration for King's (1951) and subsequent authors' (e.g. Partridge & Maud, 1987) theory of pediplanation and scarp retreat, discussed in detail below. Wellington's (1955) alternative explanation – that structure and lithology control passive margin evolution and that southern Africa is undergoing a single, sustained and still incomplete cycle of denudation in contrast with King's multiple cycles of denudation – is increasingly supported by offshore sedimentary, thermochronological and now cosmogenic evidence, and King's erosion cycles are increasingly discredited.

Figure 1.1.1 Composite DEM and satellite image of southern Africa (Bowen, 2005). The principal features of the southern African landscape can be identified: the Great Escarpment which bounds the subcontinent to the south, east and west, the Orange River, which can be seen deeply incised

on the west side of the subcontinent, the Cape Fold Belt in the south, the Augrabies Falls region, the Fish River tributary and other points of interest such as the Okavango delta in Botswana.

The post-breakup denudation history of the subcontinent over millions of years has been quantified using thermochronological methods (Brown *et al.*, 2002; van der Beek, 2002), which support Wellington's ideas of a sustained cycle of denudation. More recent rates of denudation, particularly for the Quaternary, remain unknown for large parts of the interior of southern Africa. Rates of denudation over these timescales are crucial for understanding 'benchmark' pre-anthropogenic denudation rates and also denudation over glacial – interglacial timescales. Initial cosmogenic derived denudation rates covering tens of thousands of years already exist for some parts of southern Africa (e.g. Cockburn *et al.*, 1999; Fleming *et al.*, 1999; Bierman & Caffee, 2001) but there are no catchment-scale studies of denudation over these timescales for the Orange River basin, the principal westward-draining catchment on the southern African passive margin. Such data would link the long-timescale denudation rates already published from thermochronological methods with records of denudation over hundreds to thousands of years derived from sedimentary deposits (e.g. Lewis *et al.*, 2005). Here, a regional scale picture of cosmogenic-derived catchment-scale denudation trends over tens of thousands of years for the Orange River basin is presented for the first time

Over 80 % of the area drained by the Orange River lies upstream of a large knickpoint, the Augrabies Falls, which is approximately 600 km upstream of the mouth of the Orange at Alexander Bay. The Augrabies region is a bedrock dominated stretch of the Orange River that effectively controls all geomorphic activity upstream by acting as a base level down to which the entire upstream region is incising. There is a very complex set of anabranching bedrock channels above the main knickpoint in the Augrabies region. Numerous anabranches are seen in this area which end in various knickpoints including the Augrabies main Falls. Below the main Falls, the trunk channel of the river is restricted to a deeply incised, structurally controlled bedrock gorge which some of the anabranches rejoin downstream of the main Falls, and numerous tributaries drain into. The fact that the Augrabies region is

the most important element of the Orange River system necessitates a detailed regional study of how this landscape has evolved. The first direct, long term bedrock incision rates derived from *in-situ* cosmogenic nuclides are presented for the main channel and anabranch channels of the Orange River and its tributaries. In addition, 'benchmark' background denudation rates are presented for the interfluves in the Augrabies region, and are amongst the lowest denudation rates measured for southern Africa.

In addition to the rates presented for ~50 samples that were processed and measured as part of this PhD project, a number of additional samples taken from similar locations in the Augrabies region are presented in Appendix 5. These were collected at the same time as many of the samples presented in this PhD (November-December 2004) but were processed and measured as part a project awarded to M.A. Summerfield (Project 9007/1004 at the NERC Cosmogenic Isotope Analysis Facility (CIAF), Scottish Universities Environmental Research Centre (SUERC)). The denudation rates derived from the CIAF samples are in good agreement with the rates derived as part of the PhD project. The CIAF samples were processed independently and at different laboratories, which serves as a useful check on sources of uncertainty in sample processing. A short discussion of the CIAF samples follows each section of results in Chapters 7 and 8. Due to the late stage at which this data became available, it was not possible to integrate the data more fully into the thesis.

The denudation rates presented here suggest that landscape development maintains the imprint of continental breakup long after passive margin rifting has occurred. Low to moderate rates of denudation have been experienced by large parts of the Orange River for at least hundreds of thousands, and possibly millions, of years. This emphasises the great antiquity of the southern African landmass and the essential stability of the landscape since at least continental breakup. The rates previously determined from thermochronological methods give great insights into denudation rates during continental breakup, but give little indication of rates during the Quaternary, the period of time that has seen large fluctuations in global climate and sea level, and the development of humans. This new cosmogenic data helps to

answer some long standing problematic questions in the development of southern Africa, arguably the passive continental margin type locality. It shows that traditional explanations of southern African landscape development (e.g. King, 1951; Partridge & Maud, 1987) are wrong and that the landscape has eroded slowly and continuously rather than episodically with the formation of characteristic erosion surfaces. It also opens up the possibility of comparing long term 'benchmark' rates of denudation with modern rates in order to better inform land management practices in a highly sensitive landscape and denudation 'hotspot'. The data presented here also provide regional denudation rates with which models of weathering, climate and uplift can be tuned and tested.

1.2 Denudation chronologies in southern Africa: progress, problems and potential

Landscape history in southern Africa has traditionally been studied by the denudation chronology approach. This involves identifying, correlating and extrapolating landforms themselves to provide information on the timing and style of landscape development (Summerfield, 2005b). Central to this view is that landscapes experience a succession of formative events which are then preserved in the landscape. Indeed, Partridge & Maud (1987) identify denudation surfaces representative of the Cretaceous phase of denudation (the 'African' surface) as well as denudation surfaces from the Miocene and Pliocene periods of high denudation (the post African-I and post African-II surfaces, respectively). This approach has its flaws: denudation is likely to have occurred at some point after the landscape has formed (Summerfield, 2005a) thus disrupting the morphological evidence of previous landscape-forming events (Chorley, 1965).

As is argued below, a lack of distinction between what is thought to have occurred in the landscape and what is merely observed in the landscape has been one of the chief weaknesses of many attempts to construct denudation chronologies for southern Africa. This has been compounded by a lack of precise dating, and the idea, espoused by King (1951) and repeatedly reported by King and his students, that planation surfaces representing a discrete event are preserved unmodified in the landscape over

time. The lack of knowledge of processes and process rates at relevant temporal and spatial scales led to an abandonment of focus on regional scale landscape evolution in the 1950s and 1960s by many geomorphologists in favour of quantitative small-scale process studies (Summerfield, 2005a). This effectively excluded tectonic geomorphology from the discipline just at the time when the plate tectonic paradigm was being developed in other areas of the Earth sciences (Summerfield, 2000). In the last two or three decades, it has been increasingly acknowledged that the focus on small scale stochastic processes (Church, 1996) is inadequate to understand long-term landscape development due to the significance of tectonics and the role of contingency at large temporal and spatial scales (Summerfield, 2005b). As increasingly high resolution long term data on large scale denudation has become available, long standing questions on denudation chronology in southern Africa have come to be addressed. Offshore sediment volumes first allowed very long-term records of subcontinental scale denudation to be reconstructed (Rust & Summerfield, 1990, albeit with the caveat that it is difficult to reconstruct former basin extents). In the 1980s and 1990s, thermochronological techniques allowed denudation histories over tens to hundreds of millions of years to be reconstructed (e.g. Brown *et al.*, 1990; Brown *et al.*, 2002; van der Beek *et al.*, 2002); and more recently, cosmogenic nuclide techniques have allowed the gap between long term denudation rates (millions to hundreds of millions of years) and denudation rates in the Quaternary to be spanned (e.g. Fleming and *et al.*, 1999). In some ways, geomorphology is now going back to its pre-1960s, regionalist roots with a focus on regional-scale processes and rates. The difference is that now the tools and models are available to adequately quantify regional scale rates and processes. This study represents one of the first attempts to answer long standing questions on the denudation history of southern Africa and link very long term landscape development with Quaternary landscape development derived from cosmogenic nuclide analysis.

1.2.1 The intellectual background to denudation chronology

Denudation chronology is the reconstruction of landscape history that documents a sequence of erosional events (Summerfield, 1991a). It is one of the central, founding

themes of geomorphology and aims to use denudational remnants in the landscape to reconstruct Earth history where the stratigraphic record is unclear (Wooldridge, 1957). Much of the early work on denudation chronology came out of North America, where denudation surfaces were recognised and the key concepts of base level, the lower limit of weathering processes; and the peneplain, a flat denudational remnant, were defined by Powell (1875, cited in Summerfield, 1991b) and Davis (1899), respectively. In Europe, Suess (1904, cited in Summerfield, 1991b) built on the idea of planation surfaces by postulating that it may be possible to correlate denudation surfaces globally, on the basis that they may once have been connected, but are now isolated as a result of eustatic sea level change. By the 1930s, the universal applicability of planation surface correlation on a simple height basis began to be questioned as the reality of isostasy in many parts of the world was acknowledged (Chorley, 1963). Different regions have undergone different degrees of apparent eustatic sea level change owing to local uplift, and therefore two surfaces cannot be correlated simply on the basis of their common height.

Davis (1899) envisaged a systematized sequence of landforms through an ideal cycle that emphasised the critical importance of time in landscape evolution. According to Davis, landscapes progress through a series of evolutionary stages following a rapid single uplift event, termed youth, maturity and old age, as they are subject to 'peneplanation' (declining surface gradients through time) with the final stage resulting in the formation of a peneplain (Summerfield, 1991c). Uplift of the peneplain may 'rejuvenate' the landscape and initiate a further period of downwearing. This 'geographical cycle' and subsequent modifications of it became the dominant ruling paradigm in Anglo-American geomorphology until the 1960s, and emphasised the time-dependent nature of landscape evolution. Identification of peneplains and base levels was crucial in elucidating denudation chronologies. An example of this is Wooldridge and Linton's (1955) reconstruction of the Plio-Pleistocene evolution of drainage in south-east England based on what they identified as denudational remnants of planation surfaces and local base levels.

While Davis' idealised cycle was useful in establishing denudation chronologies for landscapes with a single base level in a humid temperate climate undergoing a single initial uplift event, in truth very few landscapes conform to this ideal state. Davis' cycle also assumed that after uplift, a prolonged period of stability ensues, during which time peneplanation will occur. This both precludes the potential for rejuvenation mid-cycle, and also the formation of a palimpsest of young and older landforms in the same landscape, a common occurrence as a cursory study of many humid temperate environments will attest. Davis was also vague about surface denudation processes and lithology and failed to consider the influence of climatic change. Penck's (1953) modification of Davis' cycle considered that uplift was continued throughout time, which could lead to a situation of steady state between uplift and denudation. As attractive as Penck's ideas were, at least to continental European workers, he still paid scant attention to the nature of weathering, the role of lithology and the landscape's response to climatic change.

1.2.2 Lester King and denudation chronology

By the 1950s, Davisian concepts were still firmly established in geomorphology, despite an increasing tide of criticism from the equilibrium school, of whom amongst others Chorley and Strahler were leading proponents, which was to become a deluge by the next decade. In 1953, King published his 'Canons of Landscape Evolution' (King, 1953), a 50-point challenge to the established paradigm of Davisian landscape evolution. Despite containing many subjective statements and examples only relevant to the Southern African context, it was a major refutation of Davis' approach (Ollier, 1995). King substantially revised the nature of denudation as proposed by Davis, arguing that parallel retreat of slopes, rather than downwearing, was the principal mechanism of change in the landscape; that slope retreat created footslopes (pediments) that eventually united to form pediplains. Pediplains were described as cyclic landforms, and adhere to Davis' time-dependent strategy. Remnants of old pediplains are preserved as plateaus and can be fitted into the overall denudation chronology. Therefore, King's approach to denudation chronology is still essentially a Davisian one that involves identifying characteristic

forms in a cyclical landscape that is rejuvenated by periodic uplift. Furthermore, King apportioned no important role to climate in changing the physical controls of slope development, a Davisian assumption that was disproved for slopes in a North American context by Frye (1958).

King's 'Canons' became basic articles of faith for him and his followers and have resulted in much misinterpretation of southern African denudation chronology, as discussed below. Whilst King invoked, and in some ways anticipated, the plate tectonics paradigm which was to revolutionise the Earth sciences in the 1960s, he became sidelined by that same revolution, studying as he was, the passive margin of Southern Africa (Ollier, 1995). Due to the lack of accurate time- and process-constraints on denudation chronologies, in the 1960s geomorphologists began to move away from historical landscape narratives and towards short-term, small scale processes that could be readily quantified (Chorley, 1965). As a result, King became a somewhat marginalised figure, notwithstanding his classic textbook 'Morphology of the Earth' (1962, 1967). Studies of denudation chronology fell out of fashion, although King *et al.*'s perhaps spurious Southern African chronology was repeatedly published, at least in that country. It was the 1980s before wider interest returned to African denudation chronologies, spurred on by a renewed attention to global-scale geomorphology in general and, interest in the evolution of passive margins in particular. New methodological advances were by that time allowing better quantification of denudation chronologies (Summerfield, 1988).

1.2.3 Progress: King *et al.*'s Southern African denudation chronology

Early models of landscape evolution in southern Africa drew on ideas of deep weathering and denudation to explain landforms such as plains and inselbergs, which characterise the geomorphology of southern Africa (Goudie, 1997). Büdel's model of etchplanation to explain landscape lowering in terms of a 'double surface' of deep chemical weathering and denudation by sheetwash (Büdel, published 1982). None of this early work was a systematic attempt at establishing a denudation chronology for Southern Africa. King's was the first systematic chronology and was deeply rooted

in his cycles of pediplanation – scarp retreat and pedimentation. Pediplanation is a simple and elegant theory of subaerial denudation: after a short period of initial uplift, river incision occurs, leading to the development of denudational scarps, which undergo parallel retreat to leave denudational pediments (King, 1967). Determining the age of these pediments allows the timing of denudation to be constrained, and where successive pediments occur, a long-term denudation chronology can be established.

By assigning an age to these remnants, King was able to construct initially three major cycles of denudation (King, 1962). These were, in order of height, a 'Gondwana' surface, believed to have formed before the Cretaceous and the breakup of the Gondwana supercontinent. Next was a 'post-Gondwana' landsurface believed to reflect an early-mid Cretaceous cycle of denudation, initiated from the rapid fall in baselevel as Gondwana broke up. Finally an 'African' Highveld landsurface, believed to reflect a denudation cycle between the Late Cretaceous and mid-Cenozoic (King, 1962) was proposed. The nomenclature and timing of these events have been subject to considerable revision over time, significantly by Partridge & Maud (1987, 2000). Thus the Cretaceous denudation cycle prior to rifting of Gondwana generated the African surface, and the Miocene and Pliocene cycles generated the Post-African I and the Post-African II surfaces, respectively.

1.2.4 The problems with Southern African chronologies – spurious theory?

Before entering a discussion on the limitations to the techniques used by King, Partridge & Maud and others in proving their respective chronologies, the fact that the chronology fails on a theoretical level must be addressed. Most critically, they assumed that denudation only occurred in response to base level fall, and then in the form of cycles of denudation. They did not acknowledge that denudation of a surface could go on after the surface was formed and thus disrupt the record of the formative event. The mechanism for initiating each cycle was a vague notion defined as 'cymatogeny' (King, 1967), which involved the upwarping and flexure of the continental margin by subcrustal processes. It is not the mechanism of cymatogeny

as such that is at fault (the concept is understandably spurious as it dated from a time before the mechanism of continental rifting was properly understood), but rather the assumption that denudation is limited to the period immediately following uplift. It seems likely that a remnant denudation surface will be still subject to the same denudation processes that operate on a later surface, therefore it is meaningless to date a denudation surface as belonging to a particular denudation cycle. One of the major problems with Davis' scheme was its failure to account for continuous uplift and denudation. King makes the same mistake – he diagnoses landsurfaces as dating from a particular denudation cycle (using spurious dating methods – see below) and precludes the possibility that any modification of the surface has gone on since the end of that cycle.

Another principal theoretical limitation of the cyclic chronology of King *et al.* is their consistent confusion of observation and interpretation. The 'stepped' planation surfaces that they based much of their chronology on are often resistant layers of bedrock (de Swardt and Bennet, 1974). The persistence of these features in the landscape can be explained by the simple fact that they are more resistant to denudation than the surrounding rocks and are not necessarily the end products of a denudation cycle (Gilchrist *et al.*, 1994). In refuting de Swardt and Bennet's assertion regarding the resistance of so-called planation surfaces, King merely re-states his view on cyclic denudation and appears to suggest that the planation surfaces are obvious in the landscape to anyone who chooses to see them (King, 1976). Indeed, the surfaces may with the eye of faith be seen as planation surfaces, but a rational examination of the theories for their origin can only lead one to interpret them as resistant residuals in a landscape that has undergone prolonged (non-cyclic) denudation (de Swardt and Bennet, 1974).

Similar exchanges went on throughout the 1970s between the denudation chronologists of the classical King school and (mostly) foreign researchers. Butzer *et al.* (1973) indicate the difficulty that they have reconstructing King's 'African' Highveld Cretaceous denudation surface and question whether this surface is contemporaneous everywhere and attributable to a single set of geomorphic forces.

The authors conclude that the 'African land surface' is far from established in fact, either in age or functional origin (Butzer *et al.*, 1973). Partridge and Brink (1974) reply that the African land surface is a better established entity than Butzer *et al.* (1973) give credit for, although they concede that in some areas the African surface has become obliterated by the very process of pediplanation. It is Partridge and Brink's repeated assertion, supported by nothing more than field study of undated material, that the Highveld landsurface can be attributed to a single Late Tertiary denudation cycle that denuded the whole of Southern Africa. Contrary to this, Helgren and Butzer (1974) remain to be convinced of the 'African' landsurface and attest that no amount of geomorphic mapping can categorically prove its existence. Once again, this points to the difference between observing and interpreting the landscape and the way that observed denudation remnant phenomena are subjectively interpreted to fit the idealised theory of King and others.

1.2.5 Problems and potential: techniques used to establish chronologies

Moving beyond the theory- and observation-based aspects of denudation chronologies to consider the techniques and data involved in quantifying denudation, it becomes apparent how much the 'classical' school of King *et al.* relied on qualitative information to support their ideas of cyclic denudation. There is very little absolute dating control on the denudation cycles proposed by King and others. King (1967) describes the techniques used for dating landsurfaces: a combination of fossil and archaeological evidence; elevation above sea level; offshore sedimentary evidence; correlation with previously dated surfaces; and assessment of the stage of development within the denudation cycle. As illustrated above, the utility of correlating landsurfaces at all must be questioned given the low likelihood that an denudation surface is preserved unmodified. It is also notoriously difficult to constrain ages using fossil evidence, due to the potential for selective preservation, stratigraphic disturbance and the lack of an agreed chronology of fossil evolution in many parts of the world (Watchman and Twidale, 2002). Archaeological evidence is similarly difficult to draw conclusions from, especially since King and co-workers did not use radiocarbon-dated material, and in any case archaeological evidence is

extremely limited in its temporal range. King's use of height above sea level as a proxy for the age of a landsurface is of equally dubious value, especially since the existence of local base levels precludes a simple time/height model of landscape evolution, a point made by otherwise uncritical followers of King (Partridge and Maud, 1987). Whilst offshore sedimentary evidence has the potential to be a useful proxy for continental denudation, the record has been shown by subsequent workers to be inconsistent with King's chronology (Summerfield, 1985, Brown *et al.*, 1990). Perhaps the least reliable dating control comes from correlations with previously dated surfaces, a method that involves making a subjective judgement on the basis of height or morphological evidence as to whether a surface in one area is contemporaneous with another. Given that local base levels exert strong controls on denudation, this is a difficult task. Finally, King's use of stage of development in the denudation cycle as a proxy for landsurface age is a classic tautology. It is hard to imagine how the age of a landsurface can be determined on the basis of stage of development when deciding that surface's stage of development necessarily means knowing its age. Even so, King maintains that 'certainly no great error induced by this practice has yet come to my notice' (King, 1967).

Partridge and Maud (1987) acknowledge the difficulties in dating approaches used until then, and note the lack of reliable age control particularly with respect to initial and terminal ages of landscape cycles. Yet they proceed to construct a revised chronology based partly on offshore sediment data, however it is uncertain what the former extent of the basin would have been, therefore what the denudation rate would have been. This is shown to still conform to the entrenched ideas of cycles of denudation, which they correlate with the 'African I' and 'African II' surfaces. This chronology does not relate to the tectonic history of Southern Africa, nor does it redress King's incorrect assumption that pediments do not erode once created, when in fact they will continue to erode along with the rest of the landscape regardless of the 'cycle' the landscape is undergoing (Summerfield, 1991b). In this sense Partridge and Maud's (1987) chronology is not relevant. It is based on an oversimplified model of systematic landscape evolution that does not account for the reality of different lithological and morphoclimatic regimes. The classical denudation chronologies of

King *et al.* still appear in the contemporary literature (e.g. Partridge and Maud, 2000), although they are now losing ground to ideas of non-cyclic denudation thanks to advances in technology that has brought thermochronological and cosmogenic data which have allowed proper quantification of continental denudation. The remarkable staying power of the classical ideas can be seen as less a function of their scientific merit as the lack of any proper data to refute them, and relentless re-statement by their principal proponents.

1.2.6 The potential: new models and techniques

In the last fifteen years or so, new techniques have been developed that have started to provide a more accurate picture of denudation chronology for southern Africa. Two principal ideas to emerge from the new chronology are that landsurfaces continue to erode as long as they are exposed (although rates of denudation may change), and that marginal tectonics, particularly the formation of marginal upwarps by rifting, have been crucial in the geomorphic evolution of southern Africa (Gilchrist and Summerfield, 1990; 1991). By correlating long-term (10^6 a) data from offshore sediments with denudation rates gained from apatite fission track thermochronology (AFTT), recent researchers have been able to suggest that an initial post-rifting phase of denudation is promoted by the establishment of new base levels and is followed by slower rates of denudation and escarpment retreat at the end of the Eocene. These data do not rely on correlation or inference, rather they provide independent estimates of denudation.

Based on continental outcrop and borehole AFTT and offshore sedimentary data, Brown *et al.* (1990) present a chronology of accelerated denudation on the southwestern margin of Southern Africa in the early Cretaceous. The AFTT data are gained by measuring the number and length of etched fission tracks (the products of radioactive decay of ^{238}U, tracks are usually of the order of several μm in length) in apatite separates. The number of tracks in the apatite is an indication of the time elapsed since closure of the apatite (at a temperature of 110 ± 10 °C), with more fission tracks indicating a greater age. The length of the tracks also reveals

considerable information about the denudation history of the sample. As a sample is heated, the fission tracks shorten (anneal) to a length characteristic of the temperature to which it has been exposed. Thermal history models can be reconstructed which best match the observed fission-track data in any individual rock sample. This technique can also be used to model the thermal history of large numbers of samples in broad regional arrays to establish the pattern of cooling which has prevailed over an extensive area (Gleadow & Brown, 2000). Surface denudation primarily controls the cooling history of a sample (rather than tectonic uplift, discussed in Summerfield, 1991a). Mean track lengths suggest that there was an accelerated phase of denudation and uplift of the rock column in the early Cretaceous in southern Africa, which is synchronous with the breakup of Gondwana, and also correlates well with the offshore sedimentary record (Brown *et al.*, 1990). Reconstruction of age-elevation profiles reveals a distinct break in slope, which when compared with the present day elevation at which this break occurs, suggests that there has been regional denudation (and associated uplift) of around 3 km since the early Cretaceous.

More recently, a combination of AFTT and numerical modelling has been used to show that there has been a minimum of 4.5 km of denudation since formation of the southeast African margin ~ 130 Ma ago. This includes a marked period of Early Cretaceous accelerated denudation and subsequent lower denudation episode in the Late Cretaceous (Brown *et al.*, 2002; van der Beek *et al.*, 2002). The authors show that this data is incompatible with a model of landscape development involving constant retreat of an escarpment originally formed at the coast at the time of breakup (c.f. King, 1967). Van der Beek *et al.*'s (2002) data are, however, consistent with an escarpment which was initiated at the coast at the time of continental breakup and subsequently rapidly destroyed by rivers draining from an interior divide formed at a local high (van der Beek *et al.*, 2002). The authors also propose that the escarpment became pinned at this divide and subsequently retreated inland at a rate of only ~ 100–200 m Ma^{-1}. Thus the utility of thermochronological methods for quantitatively unravelling long-term denudation history is demonstrated.

1.2.7 Linking long term and Quaternary-scale denudation rates

Traditional approaches to establishing long-term denudational histories for passive margins involved the landward extrapolation of offshore sedimentary sequences and the use of dated inland sedimentary deposits where they were present (King, 1967). As described above, sediment volumes deposited offshore within known time sequences have been used to derive denudation histories (Rust & Summerfield, 1990) although uncertainties in former sediment source areas limit this method. Thermochronological techniques provide a location-specific measure of crustal stripping and denudation. They have been used to evaluate conceptual models of long term landscape development – for example, post-breakup denudation models of southern Africa. These interpretations can now be fully evaluated when supplemented by cosmogenic nuclide techniques (Brown *et al.*, 2002). Since thermochronological techniques cover millions to hundreds of millions of year timescales, cosmogenic nuclides, covering thousands to hundreds of thousands of year timescales, provide a crucial link between long-term contingent processes and short term stochastic processes.

By quantifying the concentration of *in-situ* produced cosmogenic nuclides in bedrock outcrops or fluvial sediments, geomorphologists can calculate the time-integrated denudation rate of features from bedrock interfluves to entire river basins (see Chapter 2). Cosmogenic nuclide analysis has been used to quantify denudation rates on the Drakensberg Escarpment (Fleming, *et al.*, 1999). The rate of retreat (~ 50-90 m Ma^{-1} over the past 10^4-10^6 a) is an order of magnitude lower than the 667 m Ma^{-1} of some estimates (Gilchrist and Summerfield, 1990) and too low for King's model of parallel retreat from the coast to hold true (Fleming *et al.*, 1999). This further supports the theory that the Great Escarpment formed by post-rifting flexural isostasy rather than constant retreat of an escarpment from the coast (Fleming *et al.*, 1999). It also further undermines King's model of cyclic denudation as the rate of retreat is too rapid for so-called cyclic denudation surfaces to have survived in the landscape (Fleming *et al.*, 1999). Cosmogenic nuclide and AFTT data from elsewhere in Southern Africa show a similar trend – Cockburn and Summerfield (2000) have

demonstrated that retreat rates in the Gamsberg in Namibia are consistently low compared with retreat rates in models of passive margins, thus indicating a need to revise traditional conceptual models of landscape development. Comparison of thermochronologic- and cosmogenic nuclide- derived denudation rates seem to show that extremely low rates of denudation have been maintained at least over hundreds of thousands of years and possibly for millions of years.

The suite of recently-developed techniques described above are revolutionising our understanding of denudation chronology. For the first time, they allow quantification of rates of denudation of particular elements in the landscape. The techniques offer enormous potential to further our understanding of the rates, timing and style of landscape evolution and answer long-standing questions of southern African landscape evolution. As well as facilitating quantification of denudation rates of particular landforms, from escarpments to individual interfluves, cosmogenic nuclide analysis also has the potential to determine catchment-averaged denudation rates for entire drainage basins and small tributary catchments. By anlaysing the cosmogenic nuclide concentration from a well-mixed fluvial sediment it has been shown that it is possible to obtain a long-term time integrated denudation rate for an entire catchment (Schaller, *et al.,* 2001, Kirchner *et al.,* 2001) (see Chapter 2).

1.2.8 Future developments and the focus of this study

What has been missing from studies of denudation in southern Africa has been a regional scale denudation history for the Quaternary. This would help to answer questions of long term landscape evolution, in particular to establish whether the long term denudation rates established by thermochronologic techniques and offshore sediment studies are comparable with rates over tens of thousands of years derived from cosmogenic nuclide analysis. Furthermore, cosmogenic derived denudation rates would help bridge the crucial timescale between deep, geologic time (millions of years) and modern, anthropogenic time (decades to centuries). Cosmogenic nuclide analysis would also help to better understand geomorphic processes by putting time and rate- constraints on various established mechanisms of landscape evolution, in particular how bedrock channels evolve. The challenge

remains to quantify how various processes operate over different timescales and generate landforms. This is attempted by quantifying denudation rates over various spatial scales in the Orange River basin. By quantifying rates of evolution over thousands to hundreds of thousands of years, it may be possible to elucidate any additional or alternative controlling factors which operate on different timescales and the validity of extrapolating short- or long-term process relationships to different timescales can be evaluated. This is tested in this study by comparing denudation rates on long- and short- timescales with medium- timescale denudation rates.

This study also attempts to use medium- timescale denudation rates to evaluate different theories of landscape evolution in southern Africa. As discussed above, substantial denudation across the southern African margin has occurred since the breakup of Gondwana. The thermochronologic and offshore sedimentary data previously published argues strongly against previous ideas of the long term survival of denudation surfaces and undermines the method of reconstructing landscape history on the basis of tectonic uplift being reflected in denudation surfaces that remain today (Gleadow & Brown, 2000). The question remains whether the medium term cosmogenic derived denudation rate data also supports the long term preservation of ancient landsurfaces. As Gleadow & Brown have written, attention is likely to be more beneficially paid to establishing variations in rates across landscapes rather than trying to diagnose the amount and timing of uplift based on denudational remnants. It is the aim of this study to establish those variations in denudation rates across the southern African landscape over thousands to tens of thousands of years.

Thermochronologic data have proved ideal for testing the predictions and scaling the input parameters of complex numerical models (Gallagher *et al.*, 1999). It is likely that shorter timescale cosmogenic derived data may also play a similar role. The data presented here also link to wider questions in Earth systems science - of our understanding of climate-tectonic interactions, and the role of weathering in CO_2 drawdown and global climate regulation. Two theories have been put forward to explain the onset on the Quaternary, each of which have rock weathering as a key

process, but neither of which can be properly tested in the absence of data on long term weathering. Berner *et al.* (1983), in what has become known as the BLAG hypothesis, postulated that global climate has cooled over the last few million years in response to a changing of the rate of sea floor spreading. As sea floor spreads more rapidly, CO_2 is rapidly input into the atmosphere. This increases global temperature, precipitation and vegetation and therefore increases rates of chemical weathering. CO_2 is then drawn from the atmosphere by the weathering of silicate rocks, and the warming effect is decreased. However, given that there has been a slowing in the sea floor spreading rate in the last 15 Ma there should have in fact been an observed warming (Ruddiman, 2001).

An alternative hypothesis by Raymo *et al.* (1988), the uplift-weathering hypothesis, implies weathering is the active driver of climate change, as it determines the amount of fresh rock exposed at the surface. In this theory, tectonic uplift increases the amount of fresh rock available for weathering, and generates steep slopes, mass wasting, and earthquakes, all of which promote further exposure of fresh rock (Raymo *et al.*, 1988). Where uplift is very large, glaciation and heavy precipitation may further increase rock weathering rates. This promotes CO_2 drawdown from the atmosphere, as silicate rocks are chemically weathered. Reduced CO_2 in the atmosphere causes a cooling effect which will serve to reduce weathering rates as part of a negative feedback (Ruddiman, 2001). However, this neglects the fact that uplift is largely driven by denudation – as material is removed from a column of rock, the rock will isostatically uplift in response – thus driving further denudation (Summerfield & Brown, 1998).

Whatever the cause of the onset of the Quaternary, it is currently difficult to verify the competing theories in the absence of actual long term rates of denudation. The proxies that have previously been relied upon, such as terrestrial sediment in ocean basins, are relatively short in timescale and there are uncertainties in former basin extents. The problem with the above theories has traditionally been that past weathering rates are difficult to determine. Cosmogenic nuclide studies are now overcoming that problem and providing regional time-integrated rates of denudation

over tens to hundreds of thousands of years. This may help to understand what drove rapid global climate changes and what might happen in the long term future. Long term cosmogenic derived weathering rates may also help test a related theory; that of climatic regulation by weathering in response to an external perturbation. An initial perturbation in climate (such as by orbital forcing or by anthropogenic greenhouse gas emissions) may lead to changes in temperature, precipitation or vegetation which causes changes in weathering rates of silicate rocks and consequent changes to the rate of CO_2 drawdown, therefore reducing either the initial warming or cooling effect and regulating climate (Ruddiman, 2001). By understanding a key component of the earth system – i.e. weathering of the lithosphere – the role of feedbacks and interdependencies of other parts of the system may be better understood.

As discussed by Church (2005) and Summerfield (2005a), geophysicists have been responsible for producing sophisticated models of landscape evolution. However, some of their work has borne striking similarity to work previously done in geomorphology (e.g. Allen 2005 vs. Brunsden & Thornes, 1979, as cited in Summerfield, 2005b) and there are some tendencies to accept uncritically older ideas of denudation chronology. Nonetheless, for the first time, geomorphologists have sophisticated models of landscape evolution but lack empirical data with which to fine-tune them (Molnar, 2003). This is beginning to be addressed by both thermochronology and cosmogenic nuclide data, and is achieving a high profile - witness the three geomorphology papers in the same issue of Nature (Burbank *et al.*, 2003; Dadson *et al.*, 2003; Wobus *et al.*, 2003). This study is an attempt to allow the data to catch up to the models by providing Quaternary-timescale denudation rates for large parts of southern Africa, which can be linked to both long term and contemporary denudation rates. This data should help add to the sum of geomorphological knowledge and help geomorphologists fulfil their twin role – as Earth system scientists looking at the relative roles of climate and tectonics in passive margin evolution and as environmental stewards in a sensitive landscape prone to denudation, in which long term 'benchmark' rates of denudation can be compared with more modern rates.

Geomorphologists now have an unprecedented range of tools – from satellite images (Plate 1.2.2) and digital elevation models to cosmogenic nuclide derived denudation rates Tooth (2006) - to tackle long-standing questions, and play a crucial role both in the emerging discipline of Earth system science and as environmental managers. Cosmogenic nuclide analysis is the missing link uniting long term, large scale, contingent aspects of geomorphology, and the small time and spatial scale, stochastic aspects of the discipline that have been so dominant for several decades. Geomorphologists have the theory (models), the visual tools (e.g. DEMs and 'virtual globes' Tooth (2006)); and increasingly the empirical data on denudation – surely the three ingredients required to achieve the re-enchantment of geomorphology called for by Baker & Twidale (1991). The difficulty in extrapolating processes across different scales has artificially divided geomorphologists into the 'small scale/process-orientated' and 'large scale/landscape-orientated' camps. Cosmogenic nuclide analysis, in conjunction with other techniques now allows those sometimes opposing camps to be reconciled and work co-operatively (Summerfield, 2005a). The difficulty for geomorphologists has always been in extrapolating processes across wide temporal and spatial scales - processes acting today are not necessarily representative of long term processes (Baker & Twidale, 1991). This study is an attempt to reconcile those scales and provide an updated study on long-term landscape development in southern Africa backed up by denudation rate data, focusing on key areas of the Orange River basin, including the crucial Augrabies Falls knickpoint region.

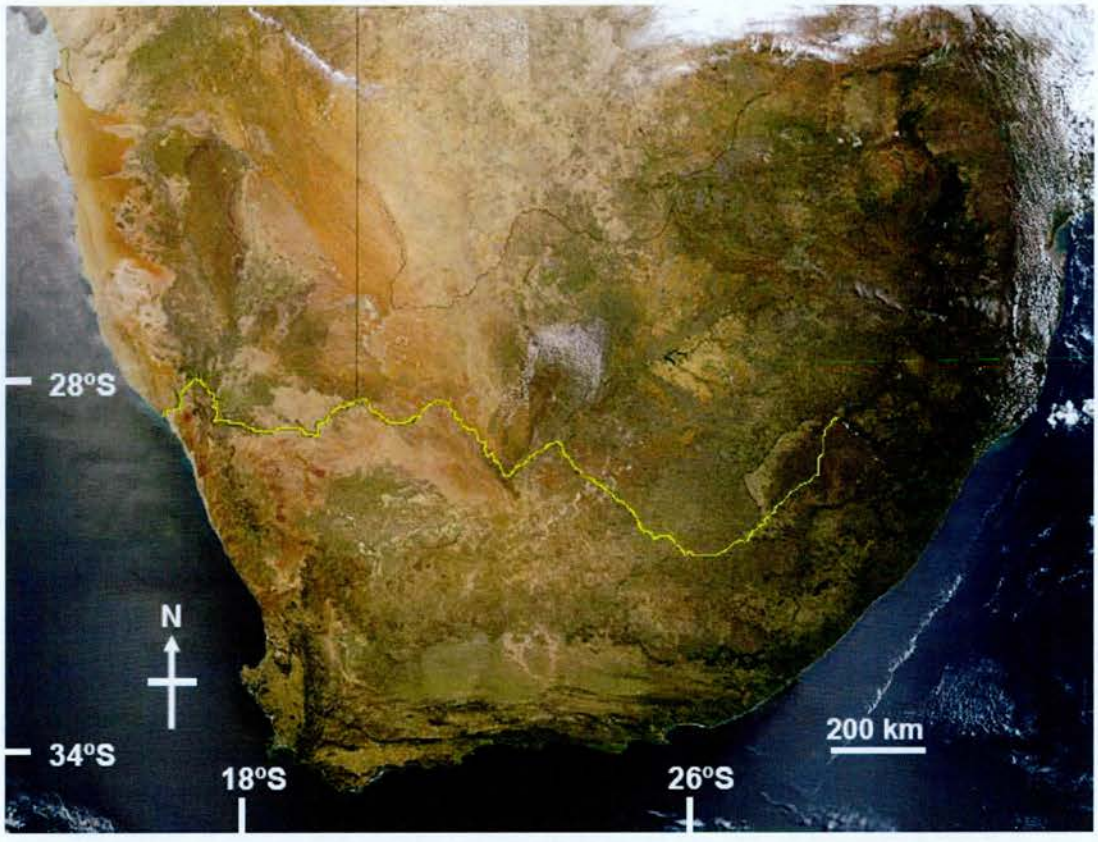

Plate 1.2.1 Composite satellite image of southern Africa taken by the Aqua (left half) and Terra (right half) satellites. The trunk channel of the Orange River is traced in yellow [1].

1 http://Earthobservatory.nasa.gov/Newsroom/NewImages/images.php3?imgd=10823

As described in the next section, the Orange is the principal westward-draining river basin in southern Africa (Plate 1.2.1) and has been responsible for the evolution of much of the southern African landscape in the Quaternary. The rates of denudation presented in this study are the first systematic attempt to quantify the evolution of the Orange River over thousands to hundreds of thousands of years. The rates presented here may be extrapolated back over millions of years to better understand the imprint of continental breakup on rates of landscape denudation long after breakup. The Augrabies Falls region is a key element of the southern African landscape and controls the evolution of a large part of the Orange basin upstream of the Augrabies main Falls knickpoint. This region is described in detail in section 1.4. Denudation rates from actively incising bedrock channel and bedrock interfluves are presented in this study and for the first time models of the evolution of the region (Springer *et al.*, 2006; Tooth & McCarthy, 2004) can be constrained with actual incision rate data. This helps to answer long-standing questions of rates of small scale bedrock incision processes. Rates of basin-wide denudation are also quantified for the first time in the Orange basin on spatial scales from a few tens of square kilometres to hundreds of thousands of square kilometres. This data helps to test long term theories of landscape evolution in southern Africa and build up a regional-scale picture of denudation history on timescales that span from the recent past to those covered by thermochronological techniques.

1.3 Introduction to the Orange River basin

1.3.1 Morphotectonic setting

The principal large scale tectonic events prior to the Early Cretaceous when southern Africa began to rift from Gondwana are the stabilisation of the Kaapvaal Craton around 2600 Ma ago (de Wit & Ransome, 1992), the ending of the Pan African tectonic cycle that resulted in basin and swell structures (Burke *et al.*, 1996), and the formation of the Cape Fold Mountain belt at the end of the Permian (240-250 Ma ago). Karoo sedimentation began around 183 Ma ago as the southern African landmass began to rift from Gondwana (Partridge & Maud, 2000). Evidence for uplift of the flanks of the landmass can still be seen in the landscape today as the

Great Escarpment that bounds southern Africa to the east, south and west and it has been postulated that this uplift preceded continental separation (Partridge & Maud, 2000). Numerical modelling results suggest that the Escarpment formed by rapid incision seaward of a pre-existing drainage divide after continental breakup (van der Beek *et al.*, 2002). Mozambique began rifting from India and Antarctica around 140 Ma ago, the Kwa-Zulu Natal region of the present-day Republic of South Africa began rifting around 130 Ma ago (de Wit & Ransome, 1992). On the west coast of southern Africa, separation from South America began around 129-121 Ma ago (Dingle *et al.*, 1983).

Extensive denudation of Karoo sediments is believed to have gone on in the Early and Late Cretaceous (Brown *et al.*, 2002). Following continental breakup, several kilometres of material have been shown to have been denuded from south and central southern Africa (Brown *et al.*, 1998) partly due to the humid contemporary climate. Denudation rates declined during the Cenozoic (after 65 Ma) as a result of global climatic cooling (evidence for this is from silcrete deposits in southern Africa reflecting a drier, cooler climate (Summerfield, 1981)) possibly related to a large meterorite impact, large scale volcanism originating in the Deccan Traps or a combination of the two. These different theories are still hotly debated (Partridge & Maud, 2000). In the Miocene (~ 23 Ma ago), uplift occurred in the east of the subcontinent whilst incision occurred in the west, as inferred from sedimentary deposits. By 15 Ma ago, arid conditions had returned to the subcontinent, caused by the growth of the East Antarctic ice sheet, and later (around 10-12 Ma ago), the establishment of the cold Benguela current on the western margin of southern Africa (Partridge & Maud, 1987; de Wit & Ransome, 1992; Partridge, 1997a). There is much debate on subsequent landscape evolution in the Pliocene, and a definitive chronology of morphotectonic evolution has not yet been settled upon. Further uplift may have occurred in the Pliocene, mainly concentrated in the south east of the subcontinent which would have resulted in an increase in local relief of the Great Escarpment in the south east and produced a pronounced rain shadow effect over the western part of southern Africa, and enhanced the east-west rainfall gradient (Partridge & Maud, 2000). Pliocene uplift of the eastern part of southern Africa

coincided with global aridification and the growth of large high latitude ice sheets around 3-2 Ma ago (Ruddiman, 2001).

1.3.2 Geomorphology and Hydrology

The Orange is the largest westward-draining river basin in southern Africa draining some 45% of the land area of the Republic of South Africa (RSA) (Figure 1.3.1) and covering an area of 891,780 km^2 with a length of 2173 km (Zawada *et al.*, 1996). Runoff volumes have been estimated at 11 900 x10^6 m^3, representing 22% of total runoff in the RSA (Zawada, 2000). Since it covers such a large area, and has evolved over hundreds of millions of years, its evolution is key to understanding the geomorphic history of a large part of southern Africa.

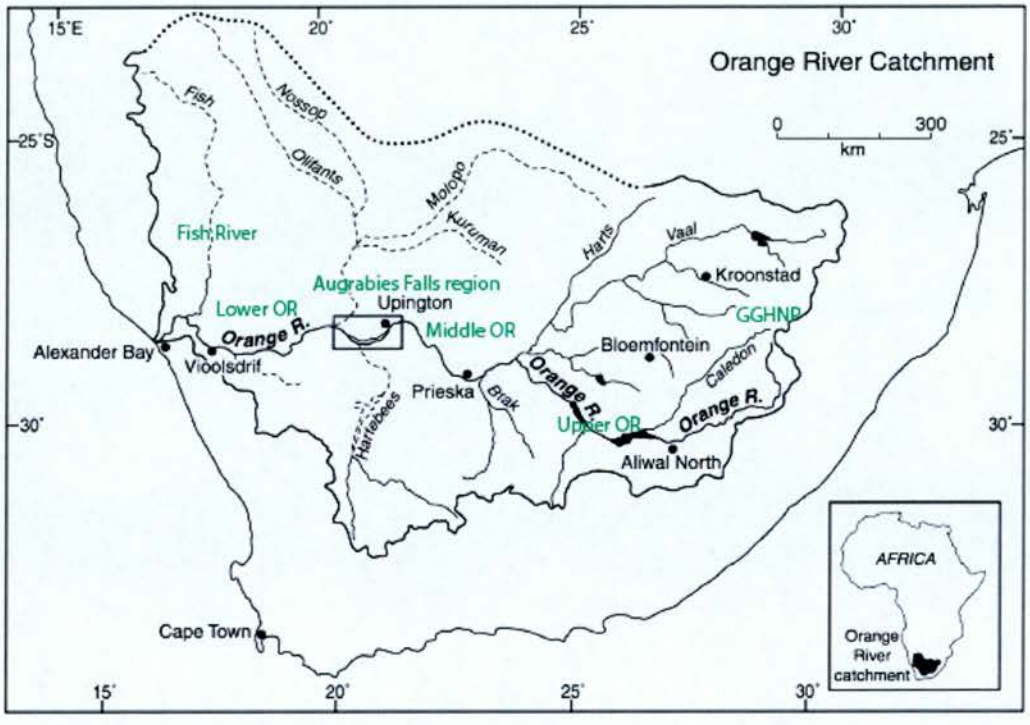

Figure 1.3.1 The Orange River basin. Lighter text shows principal sample locations (*after* Tooth & McCarthy, 2004, and Bremner *et al.*,1990). The most upstream sample is taken at the Golden Gate Highlands National Park (GGHNP) whilst the most downstream sample is taken at Vioolsdrif.

The Orange River has an unusual morphology compared with other African rivers. A relatively small proportion of the Orange River lies at high elevation, and a very small proportion of the river lies at low elevation. Most of the basin lies inland of the

Great Escarpment, at an elevation of ~ 500 – 1000 m with a low gradient (~ 1.7 m km^{-1}) (Figure 1.3.2)

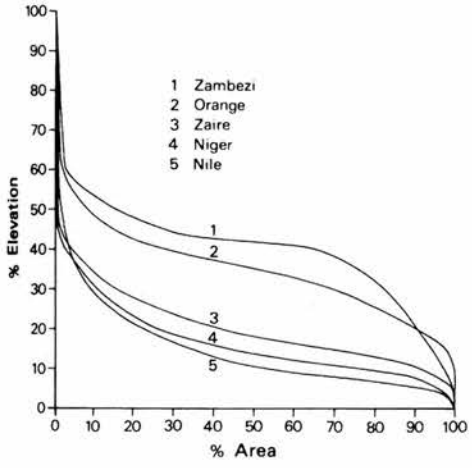

Figure 1.3.2 Hypsometry of the Orange River compared with other African rivers (Summerfield, 1991b).

An abrupt change in the Orange River's gradient occurs at the Augrabies Falls region, which are located approximately 630 km inland from the mouth of the Orange River (Summerfield *et al.*, unpublished data) on the Atlantic coast (at 28°35' S 20°25'E) (Wellington, 1955). The gradients of different stretches of the Orange River are summarised in Table 1.3.1 and general characteristics are summarised in Table 1.3.2.

Locations	Distance from Aliwal North (km)	Surface elevation at low flow (m)	Gradient (m km^{-1})
Aliwal North	0.0	1290.5	0.0
Average Aliwal North to Orange Vaal confluence	264.9	1136.7	7.7
Average Orange-Vaal confluence to Prieska	539.7	938.6	1.8
Average Prieska to Upington	824.8	842.8	1.0
Kakamas	1007.4	644.0	0.6
5 km below Kakamas	1020.3	638.6	0.6
Head of Augrabies Falls	1041.2	606.2	0.6
Foot of Augrabies Falls	1043.7	460.2	0.4
Average Upington to foot of Augrabies Falls	983.1	678.9	0.7

Table 1.3.1 Gradients in the Orange River (from Wellington, 1955).

The Orange River has its headwaters in the Lesotho Highlands at Mont Aux Sources (Wellington, 1955) with an altitude of 3282 m ASL (Osmaston & Harrison, 2005). Numerous tributaries such as the Caledon River of the upper Orange flow alongside the high relief terrain of the Lesotho Highlands. The middle course of the Orange River is characterised by the lower relief topography of the Karoo Basin. The Orange River basin, together the major tributaries the Vaal and Oliphants basins, originated during the Cretaceous (see Section 1.3.3). Through its middle course, the Orange River flows from an elevation of ~ 1200 m at Aliwal North to a little over 600 m at the head of the Augrabies Falls (Wellington, 1955), with a mean channel gradient between Aliwal North and the Orange-Vaal confluence of 1.70 m km^{-1} (Summerfield & Hulton, 1994). The low relief environment of the middle Orange catchment is mirrored by that of the Vaal catchment. The lower part of the Orange River, below the Augrabies Falls (~ 640 m from the mouth), is deeply incised into bedrock, in contrast with the wide, mixed bedrock-alluvial channel in much of the river's middle course. The Vaal, one of the principal tributaries of the Orange, is longer from its source to the Orange/Vaal confluence than the Orange is from its source to the confluence. Since it flows primarily over shale and tillite lithologies, it is not believed to contribute significant volumes of quartz grains to the middle and lower parts of the Orange, and thus in a sense cosmogenic nuclide analysis of riverborne quartz from the Orange catchment does not capture the denudation signal from the Vaal catchment. This is discussed further in Chapters 2 and 6. The other major tributaries of the Orange include the Molopo/Kuruman/Nossop/Oliphants system (here termed the Molopo system) which drains the Kalahari desert. Owing to the hydrologically discontinuous nature of the Molopo system (Goudie, 2005) it is not believed to be a significant source of sediment to the Orange River. The Fish River is the most downstream tributary and drains a large area of Namibia. This also is hydrologically discontinuous upstream therefore it is uncertain just how much sediment is being contributed by the Fish catchment into the Orange catchment, and hence what denudation signal the sediment clasts represent.

The mean annual discharge at Alexander Bay has been estimated at 11 $km^3 a^{-1}$ (equivalent to ~ 349 $m^3 s^{-1}$) (Milliman & Meade, 1983) although this is highly

dependent on flow regulation by large dams upstream. Under natural (i.e. non-anthropogenically modified) conditions, the mean annual sediment load of the Orange River has been estimated at $58x10^6$ t a^{-1} whilst the mean annual solute load has been estimated as $17x10^6$ t a^{-1} (Summerfield & Hulton, 1994), emphasising the predominant role of mechanical denudation over chemical denudation for the Orange catchment. Milliman and Meade (1983) estimate that the Orange's sediment discharge is ~ 17 $x10^6$ t a^{-1}, however this incorporates the effects on sediment yield of the anthropogenic modification of the Orange basin, something Summerfield and Hulton attempted to exclude. In common with other African rivers such as the Zambezi, present day sediment loads have decreased compared with the recent past. The solid load of the Orange is believed to have decreased by 50% between the 1950s and the 1980s. This is believed to have been due to a change in the available material being trapped behind dam structures built between the 1950s and 1970s rather than land use (Rooseboom and Harmse, 1979). This has significant bearing on catchment-averaged denudation rates, discussed in Chapter 6.

Zawada (2000) has attempted to reconstruct former discharges of the Orange based on dated slackwater deposits in the middle course of the River. Based on these reconstructions, the lower Orange has experienced 13 major floods with discharges over 10,000 m^3 s^{-1} in the last 5.5 ka. Four periods of distinct discharges are identified: the period 1.8 to 5.5 ka ago when discharges did not exceed 12,800 m^3 s^{-1}; a second period between 1.1 ka and 0.5 ka ago when discharges were around 14,000 m^3 s^{-1} ; a period of high discharges between AD 1452 and AD 1785 when discharges were as high as 27,000 m^3 s^{-1}; and finally a period between AD 1785 and the present when the lower Orange did not experience discharges greater than 9500 m^3 s^{-1} (Zawada, 2000). Two events of particularly high magnitude are identified from the instrumental record gauged at Vioolsdrif in the lower Orange River: 8330 m^3 s^{-1} in 1974 and 7700 m^3 s^{-1} in 1988 (Zawada, 2000). Periods of high discharge have been linked to climate (which is discussed in Section 1.5); in particular a strengthening of tropical easterly winds causes a disturbance of topical circulation, leading to summer rainfall in some regions of southern Africa (primarily the east), and increased winter rainfall in others (primarily the west) (Tyson, 1986). High discharges for the Orange

in the Middle Ages have been related to the Little Ice Age where disruption to tropical easterlies may have resulted in higher summer rainfall in the east of the Orange basin with a dramatic effect on river discharges (Zawada, 2000). The return period of catastrophic floods (i.e. greater than 10,000 $m^3 s^{-1}$ has been estimated as 200-1000 years (Zawada *et al.*, 1996; Zawada, 2000).

Characteristic	Value
Area[1]	890,000 km^2
Mean trunk channel gradient[2]	1.77 m km^{-1}
Relief[3]	3048 m
Relief ratio[4]	0.00222
Mean modal elevation[5]	1242 m
Mean local relief[6]	190 m
Hypsometric integral[7]	41%
Mean annual runoff[8]	103 mm
Runoff variability[9]	53%
Mean annual temperature[10]	15 ° C
Mean annual precipitation[10]	380 mm
Mean annual solid load[11]	58 Mt a^{-1}
Mean annual specific load[12]	65 t $km^{-2} a^{-1}$
Mechanical denudation rate[13]	24 mm ka^{-1}
Mean annual solute load[12]	17 Mt a^{-1}
Mean annual specific denudational solute load[14]	11t $km^{-2} a^{-1}$
Chemical denudation rate[13]	4 mm ka^{-1}
Total denudation rate[15]	28 mm ka^{-1}
Chemical denudation as a proportion of total[16]	14.50%

Table 1.3.2 Summary of characteristics of the Orange River (from Summerfield & Hulton, 1994 and Summerfield, personal communication, 2006). [1] Calculated from National Geophysical Data Centre 10-minute topographic database; [2] Calculated from channel lengths and estimates of source elevations; [3] Maximum minus minimum basin elevation; [4] Basin relief divided by basin length; [5] Calculated from 10 minute modal elevation data weighted in proportion to variation of area with latitude for each 10 minute grid unit; [6] Defined as the maximum elevation difference within a specified unit area; [7] Calculated from modal elevation and area estimates; [8] Calculated from Meybeck (1976); [9] Proportion of total mean annual runoff during the three months of maximum runoff; [10] From Pinet & Souriau (1988); [11] Derived from Rooseboom & Harmse (1979) – 2100 Mt between 1932-1969 at Upington and Prieska. Meybeck (1976) uses a higher value of 153 Mt a^{-1} [12] from Meybeck (1987); [12] Mean annual solid load divided by basin area; [13] Calculated assuming a mean rock density of 2700 kg^{-3} assuming steady state regolith thickness (Summerfield, personal communication, 2006);

[14] Mean annual solute load divided by basin area; [15] Solid load plus solute load; [16] Chemical denudation rate as a percentage of total denudation rate.

1.3.3 Geology and geomorphology

On the west coast of the Republic of South Africa (RSA), a narrow (~ 100 km) coastal plain gives way to the Cape Fold Belt, consisting of folded and faulted Palaeozoic Cape Supergroup rocks (Figure 1.3.3). Further inland, the Great Escarpment consisting largely of the Table Mountain sandstone group rocks (Smith, 1990) divides the coastal region from the Karoo province. This area contains rocks of the Karoo Supergroup, a sequence of Carboniferous to early Jurassic sedimentary rocks capped with a resistant layer of dolerite rock (Table 1.3.3). Further east, the Karoo Supergroup is revealed; starting with the Carboniferous Dwyka glacial deposits, then the early Permian Ecca shales, and on through the Adelaide then Tarkastad subgroups of the Beaufort series, a sequence of mainly fine-grained sandstones and mudstones. Further east still, the Molteno, Elliot and Clarens formations appear, consisting of increasingly coarse-grained material. Finally, at the eastern end of the subcontinent, in the vicinity of the Lesotho Highlands, are found the flood basalts of the Drakensberg volcanic group, which mark the upper limit of the Karoo sequence (Cox, 1988), the highest point of which also marks the eastern limit of the Great Escarpment. Southern Africa's geological history has been extremely long and complex, and indeed some of the oldest rocks on Earth have been found in the Barbeton Greenstone belt in the RSA (de Wit, 1999). Much work has been carried out on the geological history of southern Africa – e.g. the development of the Kaapvaal craton, which was part of a stable continent with a cool, thick mantle of over 150 km by 2.7 Ga (Tinker & De Wit, 2004). However, this study is primarily concerned with the Quaternary denudation history of the Orange River basin derived from cosmogenic nuclide analysis, and therefore the focus is largely on the Karoo Supergroup which makes up a large part of the Orange basin.

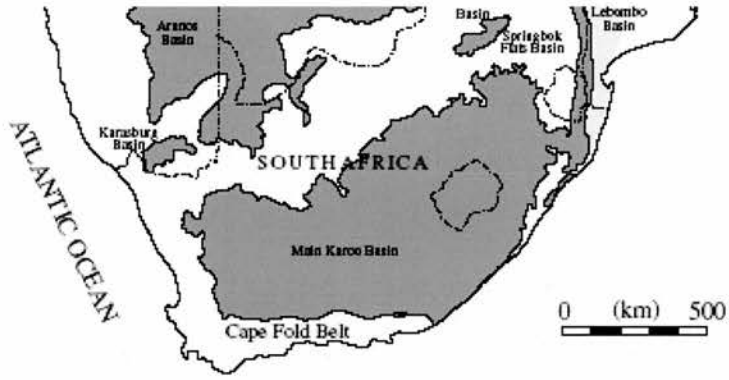

Figure 1.3.3 Generalised geological map of southern Africa showing Cape Fold Belt and Karoo Basin (Catuneanu *et al.*, 2005).

Age	Period	Group	Subgroup	Formation
180 Ma	Jurassic	Drakensberg (volcanics)		
	Stormberg			Clarens
				Elliot
				Molteno
208 Ma	Triassic	Beaufort	Tarkastad	Burgersdorp
245 Ma	Permian			Katberg
			Adelaide	Balfour
				Middleton
				Koonap
290 Ma		Ecca		
	Caboniferous			Dwyka

Table 1.3.3 The Karoo Supergroup (Cox, 1988, Smith, 1990) and others.

a. The Cape Fold Belt

To the general picture above must be added some detail. The Cape Basin contains the Palaeozoic Cape Supergroup sedimentary rocks that were deposited on a passive continental margin in a variety of terrestrial and shallow marine environments from the early Ordovician until the mid-Carboniferous (Shone & Booth, 2005). Tectonism affected the Cape Supergroup between 278 and 230 Ma and resulted in the formation of the Cape Fold Belt, although did not affect the syn-depositional Natal Group in the east. Deformation of the Cape Fold Belt began at around 278 Ma ago and ended during the mid-Triassic (230 Ma) during the deposition of the Molteno Formation of the Karoo Supergroup (Shone & Booth, 2005). The intense crustal shortening

associated with the Cape Fold deformation included thrusting and folding of the lowermost Karoo Supergroup as well as folding of the Cape Supergroup (Shone & Booth, 2005).

b. The Great Escarpment

The Great Escarpment lies ~ 100-200 km inland of the coast (Fleming *et al.*, 1999). It separates a dissected coastal plain from the elevated terrain of the Karoo basin to the south and west and the Lesotho Highlands in the east. In the east, the Great Escarpment attains a relief of over 1000 m and is locally known as the Drakensberg Escarpment. The high relief terrain of the Drakensberg Escarpment marks the major remnant of the Early Jurassic Karoo flood basalt province (Cox, 1988). Traditional models of landscape evolution (e.g. Partridge & Maud, 1987) have suggested that the Escarpment originated at the Indian ocean continental margin at the time of passive margin rifting from the Falkland Plateau (~ 130 Ma) and subsequent retreat of the Drakensberg Escarpment has occurred, with an implied retreat rate of 1-1.5 km Ma^{-1} since then (Fleming *et al.*, 1999). Cosmogenic nuclide studies on the Drakensberg Escarpment (Fleming *et al.*, 1999) indicate that escarpment retreat rate has been 15-20x smaller than this (50-95 m Ma^{-1}), suggesting that a re-interpretation is needed of how the Drakensberg, and indeed the wider Great Escarpment, has developed. Conceptual models (Kooi & Beaumont *et al.*, 1996) suggest that the formation of an escarpment such as this could be the direct consequence of continental breakup. The present escarpment would have grown vertically through differential denudation of the area above and below the escarpment as the feature remained pinned at the seaward flank of the drainage divide. Subsequent inland retreat of the escarpment of only a few kilometres would then have occurred (Fleming *et al.*, 1999). Kooi & Beaumont's (1996) modelling work suggests that escarpment retreat is favoured where an escarpment coincides with a drainage divide (as in the case of the Great Escarpment) and continuous back-tilting of the escarpment in response to denudational unloading helps maintain the escarpment summit as a drainage divide (Beaumont *et al.*, 2000) due to the focus of flexural isostatic rebound in a zone seaward of the escarpment (Summerfield, 2005b).

c. The Karoo Basin

Catuneanu *et al.* (2005) have suggested that orogenic cycles of loading and unloading related to the Cape Orogeny led to the deposition of overlying sediments of the Karoo Supergroup in a retro-arc foreland basin immediately to the north of the Cape Basin. The Karoo Basin underlies a large part of the Orange River basin, and is bounded by the Cape Fold Belt to the west and south, the Great Escarpment to the east and the Kalahari desert to the north. The southern limit of the Karoo basin coincides with the southern limit of the Stormberg basin. The northern limits of the basin have probably been removed by post-Karoo denudation (Bordy *et al.*, 2004a; 2004b). It evolved during the cycle of supercontinent assembly and subsequent breakup of Pangaea under the influence of two tectonic regimes. Syn-depositional 'Karoo basins' have been identified in Namibia, Botswana, Zimbabwe, Mozambique, Madagascar, Zambia, Angola, Tanzania and the Democratic Republic of Congo in addition to the main Karoo basin in South Africa and Lesotho (Catuneanu *et al.*, 2005 – Figure 1.3.4).

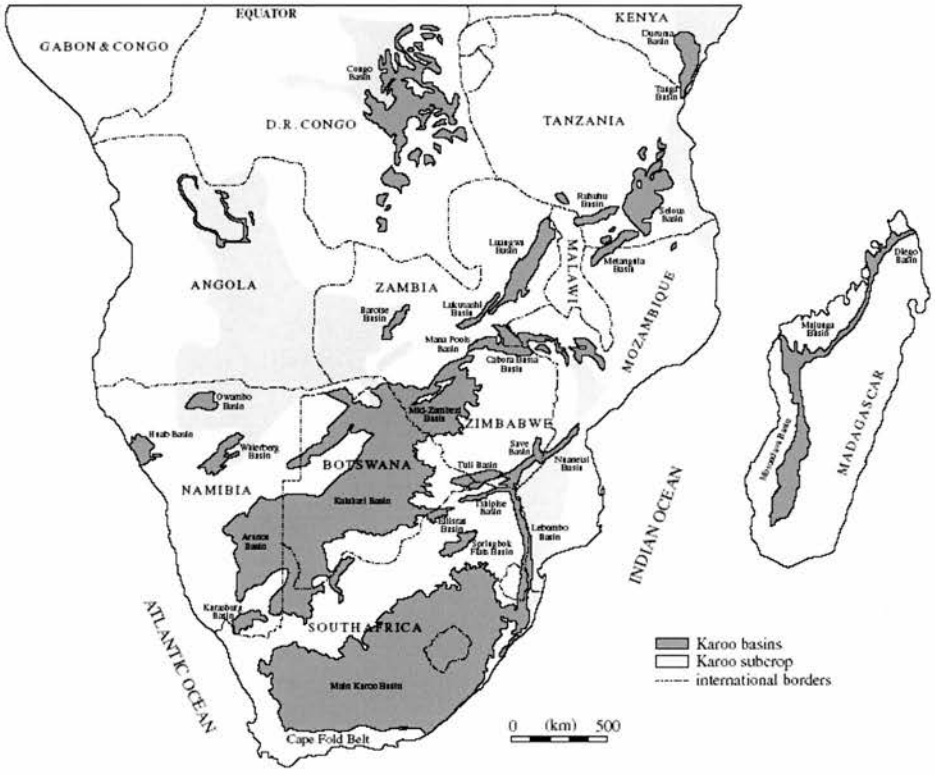

Figure 1.3.4 Syn-depositional 'Karoo' basins in southern Africa (Catuneanu *et al.*, 2005).

The Karoo basin formed as a retro-arc foreland system on the palaeo-Indian Ocean margin of Gondwana. The primary subsidence mechanisms were flexural and dynamic loading (Catuneanu *et al.*, 2005). It evolved structurally from the Triassic to Jurassic (Table 1.3.1). The main Karoo basin preserves the reference stratigraphy of the Late Carboniferous to Mid Jurassic Karoo time, including the Dwyka, Ecca, Beaufort and Stormberg lithostratigraphic units (Catuneanu *et al.*, 2005). During this time, climate changed from cold and semi arid to warm and eventually hot. This climatic change accounts for the change in lithostratigraphic character of the Karoo Supergroup towards finer grained lithology laid down by aeolian deposition (e.g. the Clarens unit). The Stormberg series covers the Molteno, Elliot and Clarens sedimentary Formations as well as the Drakensberg Group basalts and spans the Late Jurassic to Late Triassic. The base-Molteno (Plate 1.3.1) angular conformity represents a significant tectonic event across the region that ushered in a period of Stormberg sedimentation. (Catuneanu *et al.* (2005). The Molteno Formation is a northerly thinning intra-cratonic, bedload-dominated fluvial wedge deposit scoured from the tectonically active Cape Fold Belt (Smith, 1990).

The Elliot Formation lies between the Molteno Formation and the overlying Clarens Formation. The Elliot formation has been studied most extensively (Bordy *et al.*, 2004), and these studies reveal a northward-thinning and -fining wedge shaped deposit dominated by upward fining cycles of various sandstone grades and mudrocks, suggesting a semiarid meandering river style at formation. The overlying Clarens sandstones (Plate 1.3.2) are pale yellow and locally red quartz rich feldspathic wackes reflecting their desert channel, wadi and aeolian derivation – as revealed by the extremely fine grain size (Eriksson *et al.*, 1994). There is a gradual grain-size reduction and a thickness decrease from south to north in the Stormberg Series (Catuneanu *et al.*, 2005). This study looks at the variation in cosmogenic nuclide concentration between these lithologies and deals with some of the issues surrounding this in Chapters 5 and 6.

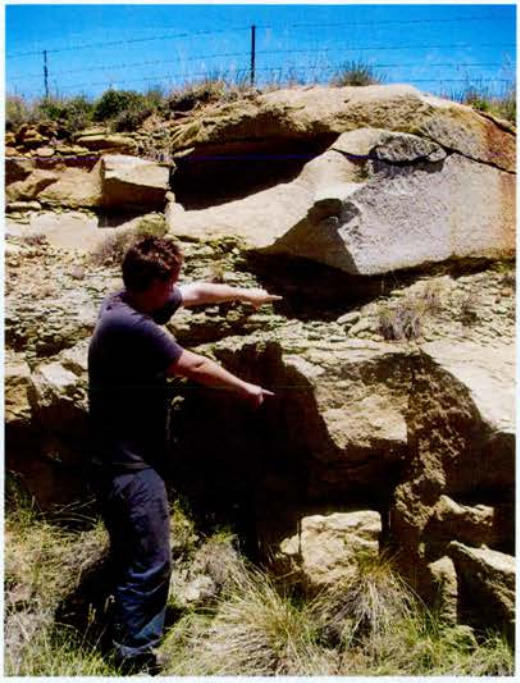

Plate 1.3.1 Molteno Formation: mudstone unit can be seen between the two sandstone units.

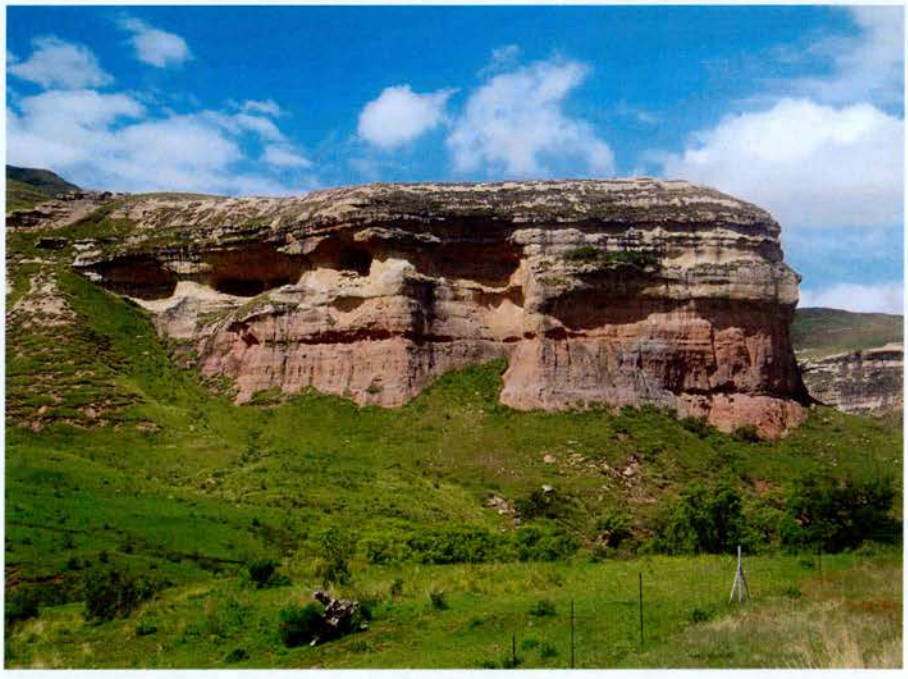

Plate 1.3.2 Clarens Formation. Note the erodible Clarens sandstone creates caves in the cliff, hence the former name 'Cave Sandstone'. Sandstone is capped by a resistant layer of Drakensberg basalt.

Within the Karoo basin, the 1370 m thick Drakensberg Group reflects initial magmatic volcanism in the south and south-east followed by fissure type eruptions building up thick sequences of evenly superposed lavas (10-20 m and associated with numerous dolerite dykes and skills (Catuneanu *et al.*, 2004)). As well as the thick sequence of Drakensberg basalts evident in the eastern part of the Orange basin, and particularly in Lesotho, evidence for the Jurassic Drakensberg volcanism is present in the many dolerite sills and dykes found in southern Africa which were intruded into the Karoo sedimentary sequence. These often form spectacular residual 'koppie' landforms where the overlying resistant dolerite capping preserves sequences of Karoo sandstones, and are undergoing lateral retreat where the less resistant Karoo sandstone units are exposed (Plate 1.3.3).

1.3.4 Evolution of the Orange River

Two major controls were exerted on the evolution of the Orange River: denudation, which exposed resistant pre-Karoo topography; and continental uplift in the hinterland of the Orange (de Wit *et al.*, 2000). The Orange River has developed since the Late Cretaceous (Figure 1.3.5), first as two main rivers that drained central southern Africa: the Karoo river in the south and the Kalahari River in the north (Goudie, 2005). The Karoo had its source in the present Orange River basin and its outlet at the mouth of the present Oliphants River (de Wit, 1999). The Kalahari River drained Namibia and southern Botswana and met the Atlantic via the lower Orange River (de Wit *et al.*, 2000). By the early Cenozoic, the lower Kalahari River had captured the upper part of the Karoo River after uplift of the southern and eastern subcontinental margins ~ 100–80 million years ago (Goudie, 2005), leaving the drainage pattern around Prieska that is still seen today. The drainage pattern may have been affected by doming of large mantle plumes that emerged post continental breakup. In some areas drainage radiates away from the centre of the plumes (Cox, 1989), possibly including the Fish and Molopo rivers, but the precise location and number of the plumes is uncertain (Cox, 1988). During the Oligocene the Orange River may have met the Atlantic through the Cape Canyon, some 300–500 km south of its present position.

Plate 1.3.3 Two koppies (Teebus, left, Kaffiebus, right) formed by denudation of a formerly continuous dolerite sill.

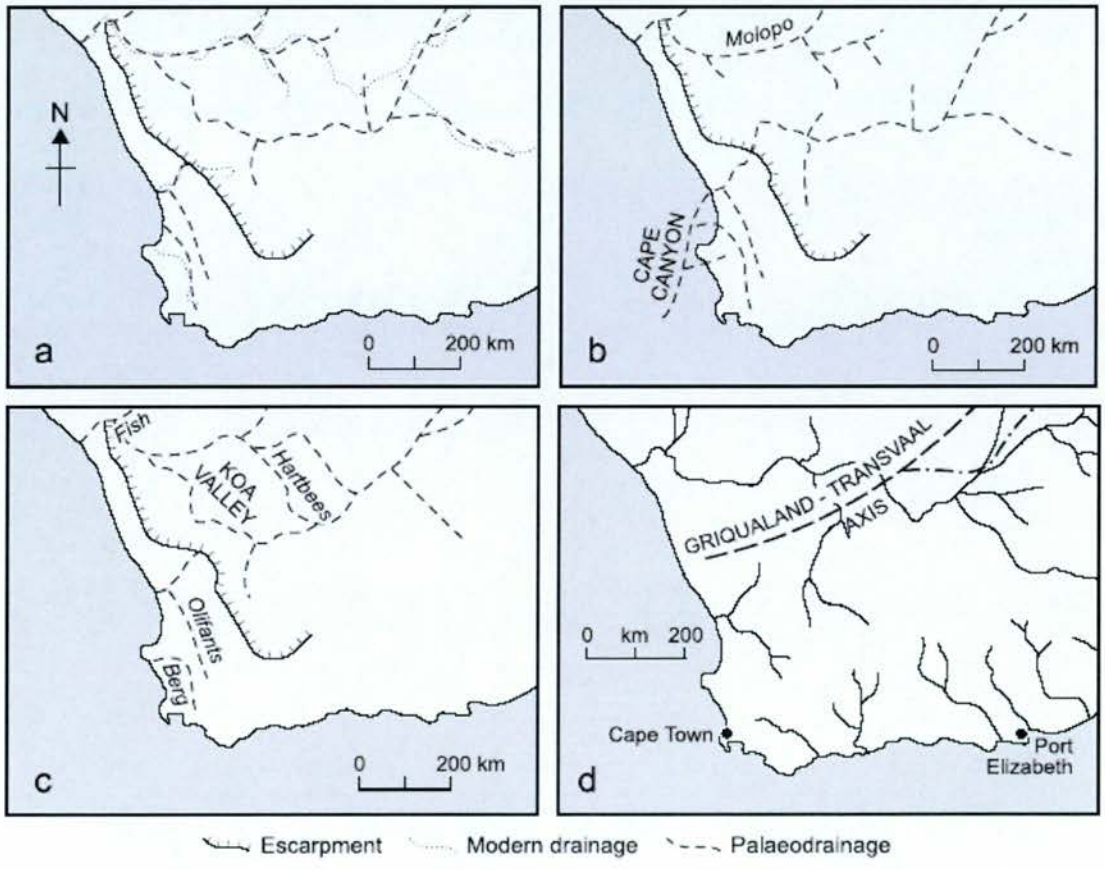

Figure 1.3.5 (previous page) Development of the Orange River: (a) Late Cretaceous ~ 90 Ma, (b) Palaeogene ~ 40 Ma (c) Neogene ~ 10 Ma (d) Present (modified after Dingle and Hendey, 1984, in Goudie, 2005).

Subsequent drainage capture in the Miocene diverted the Orange River to its present course. De Wit (1999) has postulated that towards the end of the Miocene, river capture by the Koa River and its tributary headwaters resulted in the diversion of the upper Orange to its present course. The lower part of the Orange River has been in the deeply incised river channel between Alexander Bay and the Augrabies Falls for at least 19 Ma, since middle Orange River was captured by the lower Orange (de Wit *et al.*, 2000). Later tectonic activity and aridification caused abandonment of the flow through the Koa (Dingle and Hendey, 1984).

1.3.5 Climate of the Orange River basin

The present climate of southern Africa varies from arid (<250 mm a^{-1} precipitation) in the far north and west of the region, to semi-arid (<500 mm) in much of the central part of the subcontinent, which covers a large part of the Orange River basin to high seasonal precipitation in the eastern edge of the Orange River basin, a region affected by the winter rainfall that comes from the Indian ocean (up to 2000 mm a^{-1} in the Lesotho Highlands, close to the source of the Orange River). The mean annual average precipitation for the Orange River basin is around 380 mm a^{-1} (Summerfield & Hulton, 1994). Mean annual temperatures are 15 degrees Celsius, although there are considerable local variations in this. There is a distinct climatic gradient from east to west in southern Africa – the eastern shores of the subcontinent lie on the warm Agulhas current, which flows southwards from the tropics. The western shores lie on the cool Benguela current, which flows northwards from the Southern Ocean. The far north east of southern Africa is humid and tropical (as a result of tropical to subtropical easterly winds delivering rainfall from the Indian Ocean) and the eastern half of the subcontinent generally receives summer rainfall from the Indian Ocean (the 'summer rainfall zone'). Amounts of annual rainfall decline progressively to the west, further away from the influence of the Indian Ocean (Plate 1.3.4). The far north west of southern Africa is warm and arid owing to the cold Benguela current suppressing rainfall generation. The south west of southern Africa experiences

atmospheric disturbances emanating from the Southern Ocean and bringing rainfall primarily in the winter (the 'winter rainfall zone') (Tyson & Partridge, 2000).

1.3.6 Soils and vegetation

With increasing aridity and higher summer temperatures in the west of the Orange River basin, the vegetation changes from tall-grass savanna to short-grass steppe with scattered deciduous or drought resistant trees and shrubs (Mountjoy & Embleton, 1965). This characteristic 'bushveld' vegetation becomes sparser revealing bare ground over large parts of the Karoo geological province (Plate 1.3.5), where low karroid bushes and succulent palatable and non-palatable grasses are the principal vegetation, there are large parts of bare ground, and the few trees there grow primarily in watercourses (Keay-Bright & Boardman, 2006). The western half of the Orange River basin is covered by what is termed desert soil (Mountjoy & Embleton, 1965) containing little organic matter, and with a large degree of control exerted by the parent rock. There is widespread evidence of chemical weathering in the western portion of the Orange River basin, causing silicates to weather and become mobile, eventually forming surface crusts of silcrete (Summerfield, 1981). In the eastern half of the Orange River, in the seasonal rainfall zone, the more abundant vegetation is underlain by more organic-rich soils primarily derived from weathered dolerite and shale (Kent, 1980). In large parts of the middle and upper Orange River basin, soil denudation has become a significant problem, leading to the deposition of colluvial material which have incised to form colluvial 'badlands' (Plate 1.3.6).

1.4 The Augrabies Falls region

1.4.1 Morphology

The Augrabies Falls region forms a major part of this study (Plate 1.4.1). It is an area of complex bedrock-dominated river channels that includes the 90 m high main Augrabies main Falls together with a number of anabranch links which bypass the main Falls and flow over smaller knickpoints – these knickpoints are collectively termed the Augrabies Falls system (Tooth & McCarthy, 2004).

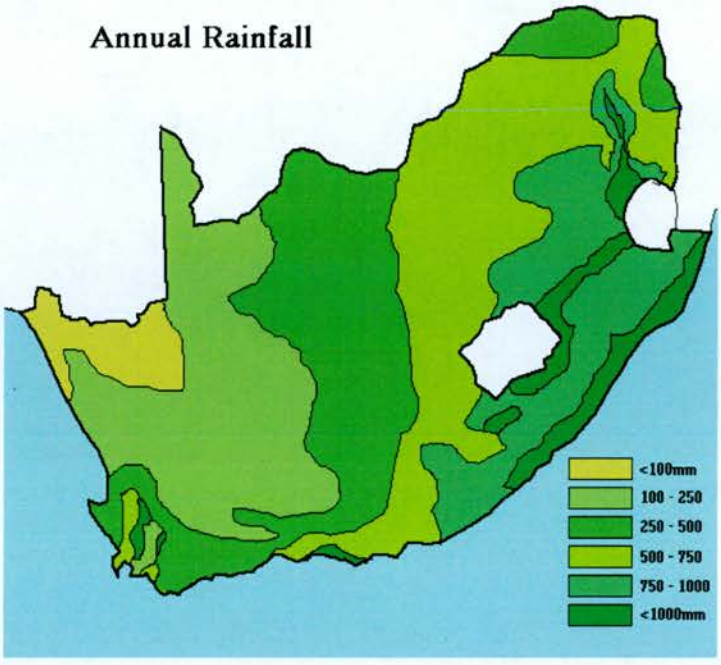

Plate 1.3.4 Rainfall map of southern Africa[1].

Plate 1.3.5 Typical Karoo vegetation, near Middelburg, central South Africa.

[1] (www.aabtourism.com/english%20climate.htm)

Plate 1.3.6 Colluvial 'badlands' in Lesotho.

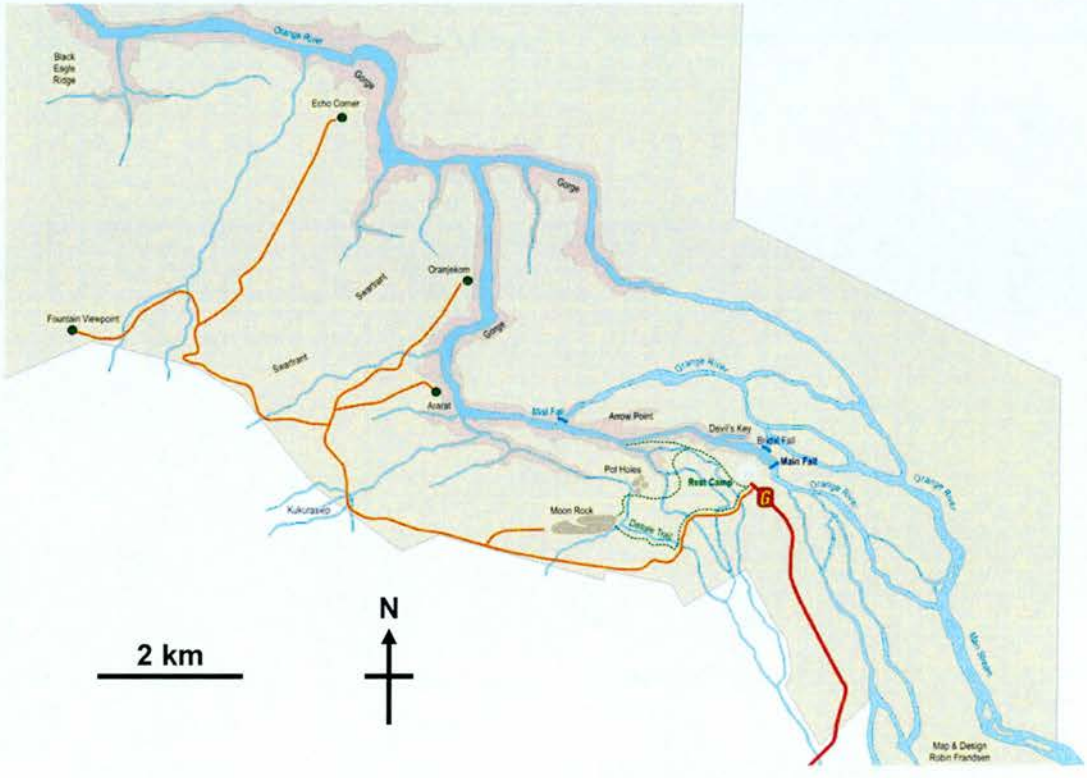

Plate 1.4.1 Map of the Augrabies Falls National Park, Northern Cape, Republic of South Africa (Courtesy of SANParks).

The area upstream of the Main Falls is a complex mixed bedrock-alluvial anabranching river channel which extends for approximately 150 km upstream (Tooth & McCarthy, 2004). The area a few hundred metres immediately above the main Falls consists of a complex series of bedrock anabranches which merge and flow over the main Falls (Plate 1.4.2, Figure 1.4.1). The area above and below the main Falls is strongly controlled by master joints orientated at ~ 10° and ~ 100°. These joints are most apparent below the main Falls and there are a number of inferior joints which radiate in all directions. Incision of the trunk channel and its tributaries along these joints has resulted in a series of spectacular 90 ° bends and switchbacks in the deeply incised main channel (~ 100 m), as well as a number of 'hanging' anabranch channels, some parallel and some perpendicular to the trunk channel, which appear to have been left at the former level of the trunk channel after the knickpoint has receded leaving the main channel in a deeply incised gorge.

For approximately 20 km below the main Falls, the trunk channel is constrained within a deeply incised (~ 100 m deep) bedrock channel with steep, potholed sides. A number of anabranch links re-join the trunk channel downstream of the main Falls, often at spectacular 90-degree intersections (Plate 1.4.2). Unpublished data by Summerfield *et al.* derived from 1:50,000 topographic maps of the region shows the long profile of the river in the Augrabies Falls region (Figure 1.4.2). This reveals that over 20 km stretches, the gradient upstream of the main Falls is lower than that downstream of the main Falls, although there is a locally steep knickpoint drawdown zone immediately above the main Falls.

Plate 1.4.2 (a) Picture of 'hanging' anabranch channel and (b) series of 90 degree switchbacks in the river.

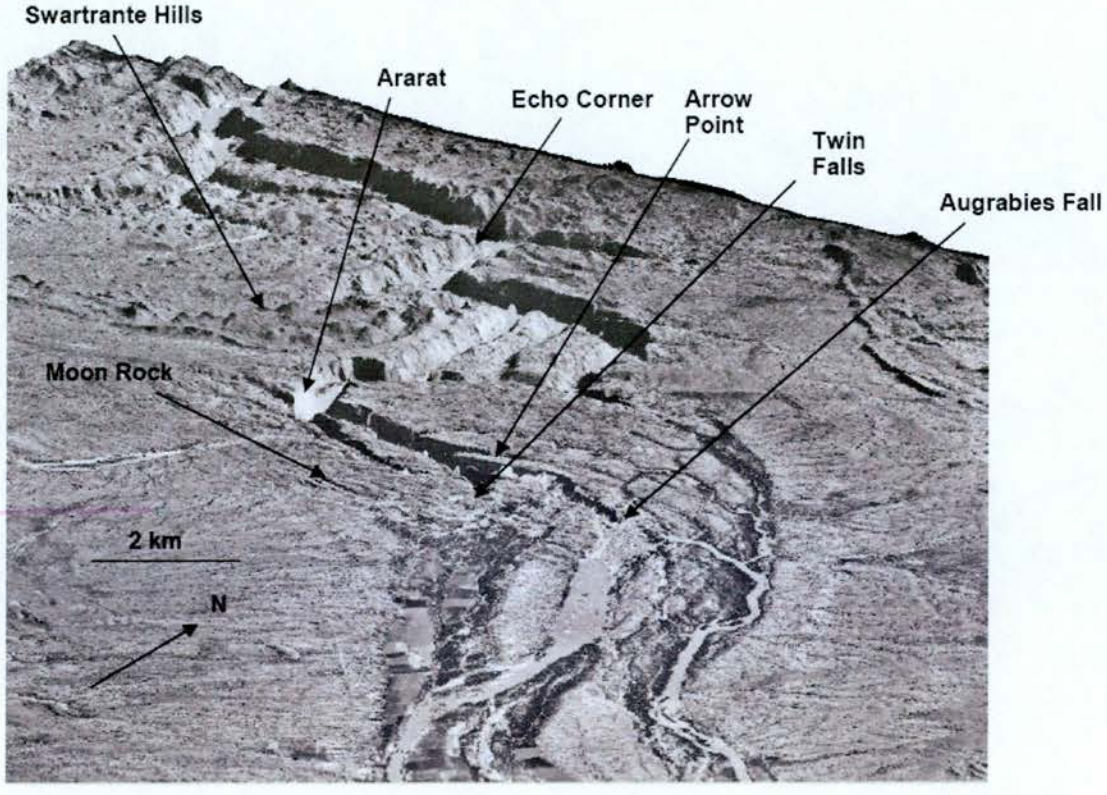

Figure 1.4.1 Digital Elevation Model (DEM) of the Augrabies region based on 10 m resolution aerial photographs with notable locations labelled (based on Walcott *et al.*, unpublished data). Note that flow goes from east to west (bottom to top of DEM) from the anabranching zone above the main Falls, to a bedrock gorge dominated zone.

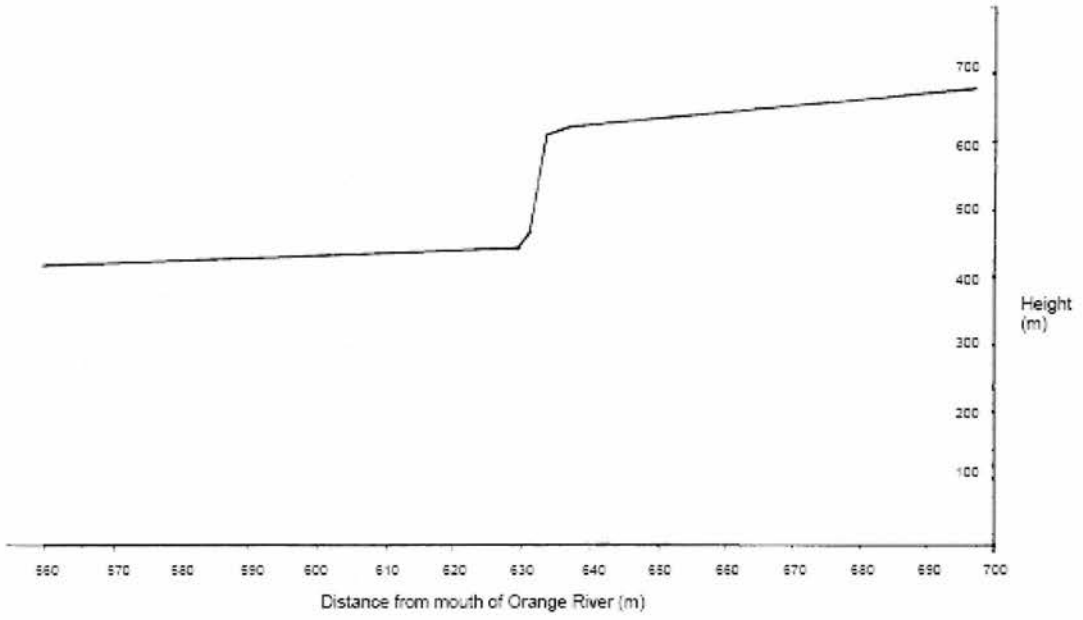

Figure 1.4.2 Long profile of the trunk channel of the Orange River in the Augrabies Falls region (taken from Summerfield *et al.*, unpublished data) (left of diagram is west, right is east).

1.4.2 Vegetation and soils

The vegetation of the region, although sparse in its cover, is part of the Nama-Karoo biome, and is characterised by grassy dwarf shrubland (van der Walt, 2000). Vegetation cover is limited by sparse soils in the region, although shallow sandy soils (a few centimetres thick) are found on the lower slopes of some hills and in many rock crevices. These soils give rise to a number of perennial tufted grasses (van der Walt, 2000). The vegetation and soils of the Augrabies has been characterised as hilltop veld (ranteveld), undulating veld (bulteveld) and drainage channels (Bezuidenhout, 1996). Hilltop veld vegetation is found on domes, ridges and rock outcrops with undulating topography. Runoff from the slopes keeps the shallow soils occasionally moist and has led to a sparse woodland cover that includes the well-known Quiver tree (*Aloe dichotoma*). Undulating veld is the most common vegetation type in Augrabies. Soils around 1 m deep and associated grasses have formed at some foothills (Bezuidenhout, 1996). and sparse plant cover with ~ 80% rock outcrops is found on the dominant shallow, stony soils. Vegetation is most abundant in drainage channels (Plate 1.4.3) where riparian bush, with up to 12.4% canopy cover, dominates (Bezuidenhout, 1996). The relatively large vegetation (up

to 7 m high tree stands) grow in fertile sediment deposited by high magnitude Orange River floods (van der Walt, 2000). Riparian vegetation is relatively resistant to floods, forming dense thickets with roots that are deeply stuck in the joints of the granite-gneiss bedrock (van der Walt, 2000).

1.4.3 Geology

The local lithology is predominantly granite-gneiss. There is a large degree of variation in this general lithology (Plate 1.4.4) from the pink coloured Augrabies granite to the more grey Riemsvasmaak gneiss. There are also marked differences between weathered and unweathered forms of granite gneiss (discussed further in Chapter 5). Many locations have veins of quartz and pegmatite running through them (Figure 1.4.4). The anabranch links of the river contain fluted and sculpted bedforms, as well as a wide range of sizes of potholes. Springer et al. (2006) found the relative Schmidt hammer rebound value of the granite gneiss on sculpted bedforms to be 69 ± 2, whereas non sculpted forms had a value of 43 ± 15.

The Falls are believed to have been initiated where the Orange River crossed the Great Escarpment after shifting its palaeo-course with its mouth close to the present day Oliphants River (de Wit, 1999). From there it may have retreated inland by pothole incision (described as the preferred method of development by Tooth *et al.* (2004), Springer et al., 2006, and in general terms by Dury (1976)), and of which there is much evidence around the Augrabies Falls region (Plate 1.4.5). Potholes begin as a shallow depression which subsequently deepen faster than they widen (Lourenc *et al.*, 1994), and ultimately coalesce to form a longitudinally continuous channel (Springer et al., 2006). A full discussion of how the Falls has developed by potholing is given in Chapter 5.

1.4.4 Hydrology and climate

Hydrologically, there is little reliable data on flows in the Augrabies region as the nearest gauging station is several tens of kilometres upstream and the anabranching nature of the region means that discharge is subdivided among many different channels (Tooth & McCarthy, 2004). Base flows at Augrabies are around 50 $m^3 s^{-1}$,

due to the constrained nature of discharge from upstream dams (Figure 1.4.3). Peak flows as high as 11,000 $m^3 s^{-1}$ were recorded in a 1988 flood (van der Walt, 2000) although past floods have been estimated as high as 30,000 $m^3 s^{-1}$ (Plate 1.4.6). This is perhaps closer to the 'natural' pre- large dam construction flow value (particularly before the construction of the large H. Verwoerddam and the P.K. Le Rouxdam in the middle course of the River). The Orange River basin has for the last few hundred years been subject to some form of flow regulation, even in the form of small earth dams constructed for cattle watering. The climate of the Augrabies region is arid with a mean annual rainfall of 211 mm, with the main season for rainfall being between December and April (van der Walt, 2000).

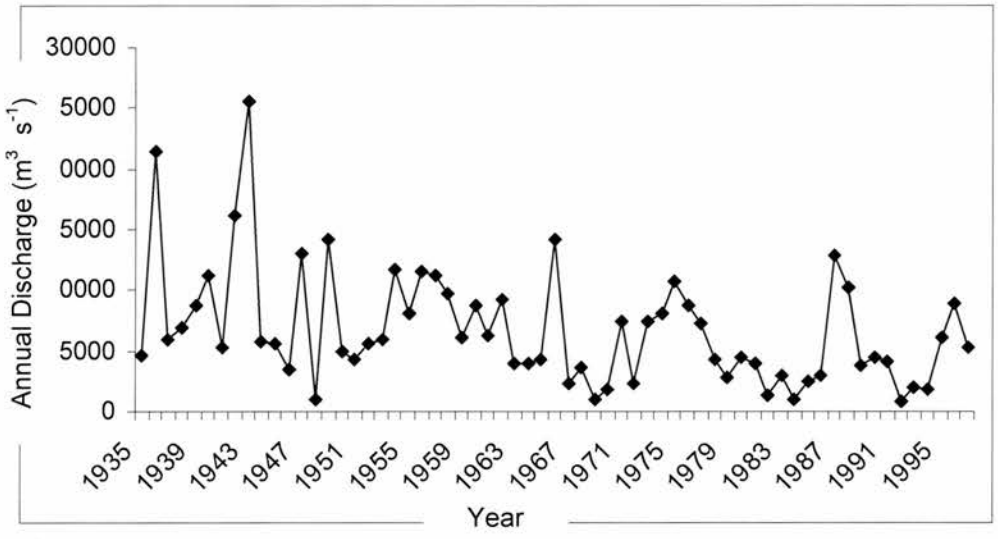

Figure 1.4.3 Orange River flows at Upington 1935-1998 (SA Department of Forestry and Water Resources).

Plate 1.4.3 Typical vegetation in the Augrabies region: (left) Sparse Nama/Karoo vegetation in an undulating veld environment (right) relatively abundant vegetation.

Plate 1.4.4 Geology of Augrabies region: (Left to right, top to bottom): Pegmatite vein running through granite gneiss bedrock; grey Riemasvasmaak gneiss (left of picture), pink Augrabies granite (right of picture); weathered (top right) and unweathered (bottom left) granite, Ararat area; mega-pothole just above the main Falls.

Plate 1.4.5 Potholed and fluted bedrock close to channel.

Plate 1.4.6 Augrabies Falls in low flow, 2004, and high flow, 2005 (SANPArks[1], 2006).

[1] http://www.sanparks.org/parks/augrabies/tourism/activities.php

1.5 Climatic history of southern Africa

1.5.1 Long term climatic history

The climatic history of southern Africa, like its geological history, is long and complicated. Over the last 65 million years, orbital forcing and changes in the subcontinent's location due to continental drift have driven large-scale climatic changes (Partridge, 1997b; Tyson & Partridge, 2000). Superimposed on these large scale influences have been regional influences in the form of topography, tectonics, the opening of ocean basins, and sea surface temperatures. A paucity of long term terrestrial records of climatic change in southern Africa makes the reconstruction of pre-Pleistocene climatic history in the region difficult. Nonetheless, from geological evidence, the climate of southern Africa has fluctuated from cold and semi-arid during the Late Carboniferous to earliest Permian interval to warmer and eventually hot with fluctuating precipitation during the Jurassic when Karoo sediments were deposited (Catuneanu *et al.*, 2005). In the Jurassic and Cretaceous, alternating periods of humid and arid climate in Africa are believed to have been driven by orbital precession. From sedimentary evidence, Dingle *et al.* (1983) have postulated that warm humid climate conditions prevailed during the Cretaceous and was followed by cooling at the Cretaceous/Tertiary boundary around 65 Ma ago. This coincided with global cooling and mass faunal extinctions, the cause of which is still much debated (Ruddiman, 2001). The northward drift of southern Africa and the establishment of a South Atlantic and Indian Ocean coastal margin after continental breakup c. 130 Ma led to the development of a climatic gradient in southern Africa (a dry west, caused by the Benguela current; and a moist east, driven by the warm Agulhas current) which persists to this day. Uplift of the eastern portion of the subcontinent in the Miocene and Pliocene accentuated the climatic gradient across the subcontinent. The cold upwelling of the Bengeula current on the western margin in the Neogene resulted in the development of the hyperarid Namib and Kalahari deserts and coincided with global cooling and aridification, particularly after ~ 3 Ma ago as the Earth slid into the cold period of the Quaternary (Tyson & Partridge, 2000).

1.5.2 Quaternary climatic history

The Quaternary period covering the last 2.6 Ma is most relevant for this study as this is the timescale over which denudation rates estimated from cosmogenic nuclide analysis can be applied. The plethora of available Quaternary environmental reconstruction techniques is now allowing a more detailed understanding of the precise nature and timing of climatic and environmental change in southern Africa. A Uranium-Potassium dated record from ODP Site 1087 (south east Atlantic) contains a sea surface temperature signal that documents the emergence of the 100 ka cycles that characterise Quaternary climatic changes. This is preceded by a cooling event that occurs 250 ka earlier at around 1 Ma ago (McClymont *et al.*, 2005). There is a predicted onshore increase in aridity as a result of this cooling, and is identified in a number of published records from southern Africa – particularly increased aeolian activity in arid parts of South Africa and Namibia as identified by e.g. Thomas and Shaw (1990). These records show that climatic-driven landscape changes are strongly controlled by external controls operating on Milankovitch timescales. Munyikwa (2005) reconstructed landscape responses to Quaternary climatic change south of the equator using optically stimulated luminescence of sand dune deposits and recorded how contemporaneous regional arid aeolian activity occurred in Australia and South Africa ~ 54-41 and ~ 36-9 ka. This indicates extensive aridity and associated landscape instability in the low to mid latitudes, particularly during the last glacial period. It also emphasises the cycles of aridity and humidity experienced during the Pleistocene, particularly in the west of southern Africa, which have been ascribed to the western displacement of the tropical easterly wave leading to higher magnitude summer rainfall events and periods of aridity when the tropical easterly wave was in its normal position (Tyson & Partridge, 2000).

1.5.3 The Last Glacial Maximum (LGM) and Holocene in southern Africa

The warming trend in southern Africa following the LGM (~ 18 ka) is mirrored in many other parts of the southern hemisphere, and indeed elsewhere. This has been associated with a shrinking of the circumpolar vortex and a southward advance of tropical circulation systems (Tyson & Partridge, 2000). A reconstruction of climatic change from the Late Glacial to the present based on fluvial, archaeological and

playnological evidence is summarised in Table 1.5.1. Much recent work in palaeoclimatic reconstruction has focused on the synchronicity of global climatic change, particularly the LGM and the Younger Dryas cooling event, ~ 12.5 ka ago (Lowe & Walker, 1997). Data from offshore sedimentary records near Namibia and Angola (Dupont & Behling, 2006) suggest that dry and cold conditions prevailed in southern Africa around the LGM followed by warming until the Younger Dryas. The applicability of these records over large parts of southern Africa must be questioned, however, as the authors point out that 5 degrees further south of their sampling location, marine and terrestrial developments during the Younger Dryas diverge. An important question for southern Africa has been whether, in common with all other continents, it was glaciated at the LGM. Lewis & Illger (2001) have studied features resembling moraines and protalus ramparts with striated clasts from the Drakensberg region, South Africa. Organic material on one ridge yielded an age of 44,000 radiocarbon years probably excavated and reworked by a glacier. Osmaston & Harrison (2005) note that it is still unclear whether these features can be attributed to the LGM. However, inferences can be drawn that indicate a temperature lowering of 5-6 degrees Celcius during the LGM in southern Africa, though uncertainties remain (Osmaston & Harrison, 2005). Mills and Grab (2005) demonstrate the presence of cirque or small valley glaciers in some high altitude south facing slopes of the Drakensberg. Using radiocarbon dating on the soil organic matter and debris ridges, they estimate that small, short lived cirque or small valley glaciers existed during the period 21–18 ka. These debris ridges were deposited during a period which was cold throughout southern Africa. Glacial or periglacial conditions are not thought to have had a significant impact on the denudation history of southern Africa.

Speleothem data from the Makapansgat Valley, South Africa (reconstructed using stable oxygen and carbon isotopes) suggest postglacial warming was initiated at 17 ka and was interrupted by cooling associated with the Antarctic Cold Reversal, followed by warming post 13.5 ka, a possibly Younger Dryas synchronous event (Holmgren *et al.*, 2003). Both terrestrial and marine records indicate warming and drying conditions in the Holocene (last ~ 10 ka), leading to changes in the landscape such as increased frequency and magnitude of aeolian deposition in the form of sand

dunes in the Kalahari, Namibia, northern and eastern South Africa (Thomas *et al.*, 2005). The Holocene climatic optimum around 6-7 ka was the culmination of the warming that went on from the end of the LGM and coincided with increased humidity in the western portion of southern Africa, whilst the eastern and southern parts experienced drier conditions (Tyson & Partridge, 2000). This is believed to have happened as a result of the tropical easterly wave over Botswana being displaced westwards during the summer months, as happens on an interannual scale at present (Tyson & Partridge, 2000). Wetter conditions in the previously arid north west region of southern Africa could have been responsible for mobilisation and stripping of aeolian sediment whilst drier conditions prevailing in previously moist areas could have resulted in the formation of colluvial deposits which are subsequently incised during moister periods. Cycles of wetting and drying could have been responsible for a great deal of weathering and sediment mobilisation in the Orange basin in the Holocene (Boardman, personal communication, 2004).

A detailed speleothem study from Cold Air Cave in the Makapansgat Valley has revealed a detailed climate record for the last ~ 6 ka. This record seems to accord well with other records of climatic change both from other proxy records from locations in southern Africa and elsewhere, including Greenland ice cores. In particular, the Holocene climatic optimum and the Little Ice Age show up in these records. Overall, in southern Africa the early Holocene has been reconstructed as warm with evaporative conditions prevailing. Cooling is evident from 6 to 2.5 ka followed by warming between 1.5 and 2.5 ka, and briefly at 1200AD. Maximum Holocene cooling occurred at 1700AD, which coincides with the apparently globally synchronous Little Ice Age (Holmgren *et al.*, 2003).

Approximate calibrated dates (a)	Inferred climate	Geomorphic evidence
900- Present	Relatively moist	Gully denudation on valley sides, flood plain, deposition on valley floors
2000-900	Relatively wet	Incision into flood plains
2500-2000	Relatively moist	Flood plain deposition
3200-2500	Relatively wet	Denudation off fans and valley sides
7000-3200	Semi-arid and cool	Limited valley floor infilling adjacent to valley head
7500-7000	Increasingly dry	Alluvial fan deposition terminates
10,000-7500	Relatively moist and cool	Flood plain and alluvial fan deposition
11,500-10,000	Dry and warm	(No evidence of fluvial events has been identified and dated from this time period. The events below are based on palynological and archaeological evidence) Decline in human occupation of the area and existence of Karroid vegetation
12,000-11,500	Relatively moist	Grassveld (grasslands) with some bushy areas, initial occupation by Later Stone Age hunter-gatherers
14,000-12,000	Relatively dry	Karoo-type vegetation
15,000-14,000	Relatively moist and cool	Grassveld (grasslands)
?- 15,000	Warming	A Start of organic sedimentation at Aliwal North and at other sites in the Eastern Cape and Lesotho (Meadows , 1988)

Table 1.5.1 Climatic history in the upper Orange River region from fluvial, archaeological and palynological evidence (based on Lewis, 2005).

Changes to precipitation regimes, and potentially to runoff and denudation regimes, are ultimately governed by changes in global and regional atmospheric circulation, which themselves may be governed by external forcing factors (Tyson & Partridge, 2000). One of the key locations in terms of wet-dry cycles is the winter rainfall zone of the southern margin of the subcontinent. This area is highly sensitive to the boundary between temperate and sub-tropical elements of the global atmospheric circulation; it is at the southern tip of Africa on two major ocean currents, the warm Agulhas and cold Benguela currents. Changes in their strengths and conditions have

considerable effects on the supply of moisture to terrestrial environments, and therefore the potential for denudation. Its evolution has been reconstructed from proxy records of coastal dune activity by Carr *et al.* (2006) and Lewis (2005), who dated numerous wet-dry fluctuations during the Last Glacial and the Holocene in the Eastern Cape Drakensberg. Changes to the Earth's orbital parameters have been invoked to ultimately explain the cycles of wet and dry periods. Changes in Earth's orbital parameters may have increased the amplitude of the seasonal cycle of solar radiation. This may have enhanced the land-ocean temperature contrast, and therefore strengthened the African summer monsoon Kutzbach *et al.* (1996; 1997). The enhanced land-sea temperatures and east-west precipitation contrasts may have been responsible for periods of apparently high denudation in the Holocene, a possibility that is discussed in later Chapters.

Southern Africa contains some of the oldest and most archaeologically important fossil hominids found in the world, and indeed southern Africa has been a crucial region for the development of anatomically modern humans (Bamford & Grab, 2005). This development has taken place against a backdrop of Quaternary climatic and environmental change revealed from various proxy records (Bamford & Grab, 2005). The role of humans in the landscape, particularly from the Late Holocene onwards cannot be discounted as a potentially major geomorphic effect. Although denudation has primarily been driven by climatic changes in the Holocene, human impact on denudation has become especially marked in the last two millennia. Where regional changes in climate have coincided with major human disturbance of the landscape (as has happened in the last few decades) extremely high denudation rates and desertification has resulted (Holmes *et al.*, 2004). This is discussed in Chapter 6 in detail in the context of how long term cosmogenic derived denudation rates can provide 'benchmark' denudation rates against which modern changes in the landscape can be compared. As Tyson & Partridge (2000) have written, one of the biggest challenges of the 21st Century is meeting the needs of a growing, and resource hungry, population in the world's poorest continent whilst managing an extremely sensitive landscape and mitigating the effects on the landscape of anthropogenic climate change.

Chapter 2 – Cosmogenic nuclide theory and applications

2.1 Applications of terrestrial cosmogenic nuclides

2.1.1 Cosmogenic nuclides in geoscience

Several different cosmogenic nuclides are produced from interactions of cosmic rays and target atoms in rock (Table 2.1.1). However, only a few of these have so far been used in geoscience applications: ^{3}He, ^{10}Be, ^{14}C, ^{21}Ne, ^{26}Al, and ^{36}Cl (Lal, 1991). Of these, ^{3}He and ^{21}Ne are stable nuclides, whereas the rest are radionuclides. The unstable nuclides have half-lives that are useful on geological timescales (e.g. ^{10}Be has a half life of ~ 1.5 million years, compared with ^{24}Na, a cosmogenic radionuclide with a half life of 15 hours (Gosse & Phillips, 2001)). Cosmogenic ^{3}He and ^{21}Ne are found in abundances that usually exceed the primordial or radiogenic ^{3}He and ^{21}Ne concentrations. This is not the case for in-situ cosmogenic ^{7}Li, for which the radiogenic component cannot be readily separated (Gosse & Phillips, 2001). The utility of long-lived cosmogenic radionuclides in geoscience applications is largely determined by the ability to measure them by accelerator mass spectrometry (AMS). The nuclides listed above have in common the characteristics that their production rate in rock is high enough for measurable quantities of the nuclides to accumulate, and also the fact that other isotopes of the same nuclide do not occur in sufficient abundance to make measurement difficult. The nuclides used in this study are ^{10}Be and ^{26}Al, discussed in more detail below.

Cosmogenic nuclide	Half life (a)	Target minerals	Advantages	Disadvantages	Recent examples
^{3}He	stable	Olivine, pyroxene, hornblende, garnet	High production rate and low detection limit allows quantification of both long and short exposure histories. Stability allows millions of years exposure/very low denudation rates to be determined	Not all lithologies retain ^{3}He, including quartz: limits to the possible useful lithologies, possible inheritance problems	Margerison *et al.* (2005); Williams *et al.* (2005)
^{10}Be	$1.51x10^{6}$	Quartz, olivine, carbonates	Quartz is globally ubiquitous: exposure histories and denudation rates can be determined for a wide range of lithologies. ^{26}Al is also produced in the target minerals, allowing quantification of exposure/burial history from paired nuclide analysis	Atmospheric ^{10}Be is a possible contaminant and rigorous treatment is required. Low production rate limits usefulness to fairly old exposed lithologies	Stock *et al.* (2005a); Schaller *et al.* (2004)
^{14}C	$5.73x10^{3}$	Quartz	Ubiquitous target minerals, paired analysis with stable and unstable nuclides is possible	Possible contamination by atmospheric ^{14}C, target chemistry is currently not well developed	Lifton *et al.* (2001) Yokoyama (2004)
^{21}Ne	stable	Quartz, olivine, garnet, clinopyroxene	Stability and retention in quartz gives it the potential to record some of the longest exposure histories on Earth	Inheritance is possible, correction for nucleogenic ^{21}Ne required	Dunai *et al.* (2005)
^{26}Al	$7.20x10^{5}$	Quartz	Ubiquitous target mineral, paired analysis is possible	Difficulty in measuring low $^{26}Al/^{27}Al$ by AMS	Stock *et al.* (2005a)
^{36}Cl	$3.01x10^{5}$	K-feldspar, plagioclase, calcite, 35Cl in quartz fluid inclusions	High production rates allow whole rock samples to be analysed	Multiple production pathways - many potential contaminants; limited usefulness on many lithologies	Lal *et al.* (2005)

Table 2.1.1 (previous page) Commonly used cosmogenic nuclides (*after* Cockburn & Summerfield, 2004, Gosse & Phillips, 2001, Lal, 1988).

a. Beryllium-10

Beryllium-10 (^{10}Be) is mostly produced by spallation of ^{16}O in quartz and, as such, has simple stoichiometric chemistry in a mineral that is near-ubiquitous in many different lithologies and is also resistant to chemical weathering (Gosse & Phillips, 2001). ^{10}Be has the advantage that it can be chemically isolated alongside ^{26}Al and the concentration of the two radionuclides (which have half lives of 1.5 Ma and 0.7 Ma, respectively) can be compared in order to quantify shielding effects (see Section 2.2). The long half life of ^{10}Be makes it suitable for quantifying long denudation histories, which is particularly relevant for southern Africa. However, terrestrial cosmogenic ^{10}Be has the drawbacks that it can be potentially contaminated by atmospheric ^{10}Be, and the isobar ^{10}B can be a problem during AMS measurement. ^{10}Be also has the lowest production rate of all the commonly used terrestrial cosmogenic nuclides (~ 5 atoms g^{-1} a^{-1} in quartz (Stone, 2000)), however this is only a problem in very young or very rapidly eroding surfaces, neither of which is a significant problem in southern Africa.

b. Aluminium-26

Like ^{10}Be, Aluminium-26 (^{26}Al) has simple stoichiometric chemistry and is relatively easily separated in the lab. Unlike ^{10}Be, ^{26}Al experiences little meteoric contamination due to the lack of target elements in the atmosphere. It is primarily formed from spallation of ^{28}Si in quartz and has a production rate of ~ 30 atoms g^{-1} a^{-1} (Stone, 2000). It can be paired with ^{10}Be to quantify shielding in bedrock surfaces. The stable isotope ^{27}Al occurs naturally in quartz and also acts as a carrier during AMS analysis, however this can only be done where the ^{26}Al/^{27}Al ratio is sufficiently high. Stable ^{27}Al concentrations can often swamp the cosmogenic ^{26}Al component. Also, ^{26}Mg as an isobar of ^{26}Al can potentially lead to problems in AMS analysis.

2.1.2 Applications of terrestrial cosmogenic nuclides

The development of accelerator mass spectrometry (AMS) in the 1980s allowed routine measurement of rare terrestrial cosmogenic nuclides such as ^{10}Be and ^{26}Al for the first time (Tuniz *et al.*, 1998) although there are hundreds of ^{26}Al determinations in meteorites with gamma-gamma techniques. As described in Chapter 3, measurement of these cosmogenic nuclides allows geomorphologists both to date landsurfaces and also to measure denudation rates. Some of the earliest applications of cosmogenic nuclides was in calculating exposure ages of bedrock surfaces, which allowed calculation of the timing of deglaciation, volcanic events and fault slip rates amongst others. Cosmogenic- derived denudation rates have for the first time allowed the quantification of some of the oldest continually exposed landscapes in the world, as Dunai *et al.* (2005) demonstrated for the Atacama Desert where ^{21}Ne was used to date sediment surfaces barely affected by denudation since 25 Ma. Extremely long-term denudation rates (10^3-10^5 years) have also been quantified and allowed questions of climate-tectonic interactions to be addressed. Some of the principal achievements of ^{10}Be and ^{26}Al applications in the earth and environmental sciences, with selected examples, are given below.

a. Ice sheet and global climate reconstruction

One of the most widely used applications of cosmogenic nuclides has been in determining former global ice extent by exposure dating of moraines and bedrock surfaces. This is important in elucidating regional and global Quaternary climate changes and inferring geomorphic responses. Some of the oldest ice on earth from Antarctica has been dated in this way and interpretations of the controls by Antarctica on southern hemisphere climates have been made. Schäfer, *et al.* (2000) presented minimum exposure ages of 2.3 Ma from Beacon Valley, Antarctica. There are many other examples of using novel cosmogenic techniques to quantify landscape development in Antarctica – e.g. Sugden, *et al.*, (1999) which provided evidence for the long term landscape stability of Royal Society Range, since the mid-Miocene. Stone *et al.* (2003) have provided evidence from cosmogenic ^{10}Be exposure ages that the West Antarctic ice sheet has been on a long-term trajectory of decline throughout the Holocene. Inferred climatic instability in Antarctica and the

Southern Ocean partly explains the cycles of aridity and humidity that the western margin of southern Africa experienced in the Holocene (see Chapter 1).

An interesting debate on the synchronicity of Quaternary global climate change, reconstructed from cosmogenic dated moraines in different parts of the world, has gone on for the past decade or so. Evidence from cosmogenic-dated moraines in North America has been presented to advance the argument that the Younger Dryas cooling event was a global phenomenon (Gosse *et al.*, 1995). This has been backed up by Ivy-Ochs *et al.* (1999) whose moraine exposure dates imply synchronous Younger Dryas cooling in the European Alps and the Southern Alps of New Zealand. A syn-Younger Dryas cooling event around 13.5 ka has been identified in southern Africa based on independently dated speleothem evidence (Holmgren *et al.*, 2003) showing that what have previously been thought of as northern hemisphere Quaternary climate changes extend to southern Africa. In southern South America, Kaplan *et al.* (2005) give ^{10}Be and Ar/Ar ages of 190-109 ka for two moraines deposited prior to the last glaciation, indicating that during the last two glacial cycles, major glaciations in the southern Andes were in phase with the growth and decay of Northern Hemisphere ice sheets, especially at the 100 ka periodicity. This supports the theory that glacial maxima are global in nature and ultimately paced by small changes in Northern Hemisphere insolation (Kaplan *et al.*, 2005). Other, independent, evidence from the global ^{18}O record suggests that there is in-phase behaviour of northern and southern hemisphere ice masses (Raymo *et al.*, 2006). However, interpretation has been challenged by other cosmogenic work in the southern hemisphere, notably Schulmeister *et al.* (2005) who from work in New Zealand argue for Southern Hemisphere climate forcing during the last deglaciation. Cosmogenic nuclides have been applied to the question of what role the Himalaya and Tibetan plateau have played in Quaternary climate change. Schäfer *et al.* (2002) present data that imply glacial advances in this region were limited to a few tens of kilometres in the period since 170 ka. Schäfer *et al.* use this evidence to suggest there was no Tibetan ice dome during the last two glacial cycles, and that northern hemisphere ice changes were not forced from the Himalaya-Tibet region.

Glacial and periglacial reconstructions have been carried out using cosmogenic nuclides on every continent. Paired Be-Al studies in the area of the Fennoscandian ice sheet allowed Fabel *et al.* (2006) to identify old moraines which were preserved during ice overriding by later expansion of the cold-based Fennoscandian ice sheet. This is backed up by Fjellanger *et al.* (in press) who present evidence of glacially derived blockfields in northern Sweden being preserved under at least one thick cold-based ice sheet. Barrows *et al.* (2001) have presented evidence for glaciation on the Australian mainland in the late Pleistocene. Osmaston & Harrison (2005) have used combined radiocarbon and cosmogenic techniques to date major Quaternary glaciations in Africa and have identified geomorphic features resembling moraines and protalus ramparts in the Drakensberg Mountains of southern Africa, although it is still unclear whether these features indicate glaciation and can be attributed to the LGM. The precision and accuracy of cosmogenic surface exposure dating is not good enough at present to test the synchronicity of glacial events on sub-millennial scales for the Holocene and Late glacial or sub-Milankovitch scales (Owen *et al.*, 2005).

b. Tectonics, climate and weathering

Some of the biggest questions in contemporary geomorphology and the emerging discipline of earth system science are now being answered by cosmogenic nuclide techniques. Questions on the role of erosion in regulating global climate, through the weathering of silicate rocks and CO_2 drawdown (Millot *et al.*, 2002) and the 'chicken or egg' hypothesis regarding tectonic uplift and erosion (Molnar and England, 1990) can now be answered better with actual rates of erosion derived from cosmogenic nuclides. Riebe *et al.* (2001a; 2001b) describe how climate only weakly regulates nonglacial denudation rates in mountainous granitic terrain. Chemical weathering rates for landscapes are generally difficult to quantify because the timescales over which weathering occurs are often unknown. Green *et al.* (2006) use timescales defined by cosmogenic nuclide analysis to calculate how chemical weathering rates vary across an eroding hillslope using a chemical depletion factor developed by Riebe *et al.* (2003). Kirchner *et al.* (2006) describe from cosmogenic nuclide methods that the strength of climate change feedbacks between temperature and silicate weathering rates may be weaker than previously thought, in actively eroding

unglaciated terrain. They propose that chemical weathering rates may often be limited by the rates that fresh minerals are supplied to soils by denudation, and imply that tectonic uplift may be an important regulator of long term chemical weathering rates in mountainous granitic landscapes. Schaller & Ehlers (in press) note how climate change significantly modifies the denudation history of an orogen. They test this using catchment-wide denudation rates and quantify how geomorphic processes, e.g. landsliding, respond to climate change and influence catchment-wide denudation rates. High denudation rates (0.5 mm ka^{-1}) and high amplification of the input denudation signal allow detection of an increase in denudation rates due to periodicity changes in the climate record.

Another important contribution to questions of weathering, climate and tectonics has been made by Owen *et al.* (2005) who quantified climatic and topographic controls on the style and timing of Late Quaternary glaciation in Tibet and the Himalaya defined by ^{10}Be cosmogenic radionuclide surface exposure dating. They present evidence that the regional patterns and timing of glaciation reflect temporal and spatial variability in the south Asian monsoon and regional precipitation gradients. Lal *et al.* (2003) use ^{10}Be to quantify variable rates of denudation across the Tibetan Plateau since the last interglacial. Cosmogenic techniques allow stratigraphic frameworks over the last few glacial interglacial frameworks to be reconstructed – something which Anders *et al.* (2005) report for the Colorado River for the last 400 ka. They report a disconnect between deposition and incision along the Colorado River and explain this as being due to the weathering limited nature of hillslope sediment supply. Thus cosmogenic nuclide analysis can help answer long-standing questions of how large parts of the earth have evolved over long timescales and contribute to the re-enchantment of large scale geomorphology (Summerfield, 2005a).

c. Fault slip and bedrock incision rates

On a smaller spatial scale, cosmogenic nuclide analysis can complement short-term process studies by quantifying small scale, stochastic process rates over tens of

thousands of years. A considerable amount of work has been done on quantifying fault slip rates and small scale incision rates using cosmogenic nuclides. Chevalier *et al.* (2005) have described secular variations in fault motion on the Karakoram Fault derived from ^{10}Be surface exposure dating of offset moraines over the past 140-20 ka. These findings have been disputed by Brown, *et al.* (2002, 2005) who argue that post depositional processes such as burial, denudation, and shifting position will reduce the cosmogenic nuclide concentration in the clasts of moraines and thus reduce apparent exposure age. This emphasises one of the principal problems with using cosmogenic nuclides for surface exposure age dating – one needs to have a very detailed understanding of what has happened to the surface since exposure – i.e. how much denudation (and therefore loss of cosmogenic nuclides) has gone on, whether burial and re-exposure has occurred (though this can on longer timescales be quantified using paired ^{10}Be-^{26}Al analysis). Variations in fault slip rates have also been described by Kirby *et al.* (in press) who determine temporal variations in fault slip by dating displaced alluvial deposits preserved along the White Mountains, California. This fault has experienced considerable temporal variations in slip rate over the past 760 ka. Jackson *et al.* (2002) have studied tectonic processes over the past 450 ka and quantified associated landscape development in Otago, New Zealand using in situ cosmogenic ^{10}Be. Cosmogenic nuclide studies have allowed the quantification of escarpment retreat rates (Cockburn *et al.*, 2000; Fleming *et al.* 1999); bedrock channel incision rates (Seidl *et al.*, 1994); knickpoint retreat rates (Seidl *et al.*, 1997) and the quantification of long-term fluvial incision rates and landscape responses (Brocard *et al.*, 2003).

d. Basin – wide denudation rates

As well as being able to help answer 'global' questions on uplift-weathering and climatic change, and small-scale processes integrated over thousands to hundreds of thousands of years, cosmogenic nuclides can also help address questions of regional landscape evolution at the scale of an individual river basin. This has been facilitated by the development of the basin-wide technique (Granger *et al.*, 1996) and a wide range of geomorphic questions can now be answered (Table 2.1.2).

Application	Examples
Physical denudation rate determination	Brown, *et al.* (1995); Bierman *et al.* (1996); Clapp *et al.* (2001); Kirchner *et al.* (2001); Schaller *et al.* (2001)
Chemical denudation rate determination and CO_2 drawdown	Riebe *et al.* (2001a, 2001b, 2003, 2004) Von Blanckenburg *et al.* (2004)
Sediment transport and sediment generation	Clapp *et al.* (2000); Clapp *et al.* (2002), Nichols (2002)
Sediment mixing	Nichols *et al.* (2005)
Escarpment retreat	Bierman & Caffee (2001); Heimsath *et al.* (2000)
Erosion-tectonic interaction	Wobus *et al.* (2003)
Controls on denudation	Riebe *et al.* (2000); Riebe *et al.* (2001a, 2001b); Matmon *et al.* (2003); Morel *et al.* (2003)
Soil production rate	Heimsath *et al.* (2001)
Soil denudation and land use change	Brown, *et al.* (2003); Hewawasam *et al.* (2003); Gellis *et al.* (2004)
Soil mixing and denudation	Small *et al.* (1999); Schaller *et al.* (2002)
Landsurface denudation and sediment burial	Granger *et al.* (1997, 2001), Hancock *et al.* (1999); Schaller *et al.* (2001)

Table 2.1.2 Applications of catchment-averaged technique (*after* von Blanckenburg, 2006).

Clapp *et al.* (2000) describe sediment yield exceeding sediment production in arid region drainage basins in Israel by comparing short term sediment yields with long-term cosmogenic derived sediment production rates. Clapp *et al.* (2001, 2002) have also determined rates of sediment supply to arroyos in the south western United States and identified several arroyo cycles occurring. Questions of anthropogenic impacts on sensitive landscapes have been addressed by comparing long-term, pre-anthropogenic 'benchmark' rates of denudation with those derived from modern sediment yield data (von Blanckenburg, 2006). Brown *et al.* (1995, 1998) describe a high recent rate of denudation (750 mm ka^{-1}) compared with long term cosmogenic-derived rates (40 mm ka^{-1}) for an agricultural basin in Puerto Rico. Kirchner *et al.* (2001) compare modern rates with Holocene rates of denudation in the United States and find that Holocene rates are as much as seventeen times higher than modern rates. This contrasts with cosmogenic derived denudation rates from Sri Lanka,

described by Hewawasam *et al.* (2003), where modern rates far exceed natural long term rates. This application of cosmogenic nuclides has a practical aspect in informing land-management decisions in sensitive landscapes. Cosmogenic nuclides have also been used to estimate soil accumulation rates (Phillips, 2000) and the dynamics of laterite development (Braucher *et al.,* 1998, 2000).

2.1.3 New and novel applications

A number of novel, experimental uses of cosmogenic nuclides in the future have been proposed (Jull & Burr, 2006). Recently, novel work involving exposure dating of underwater rocks to study land bridges during ice ages, focusing on underwater rock samples in Japan, has been carried out by Kim & Imamura (2004). Boaretto *et al.* (2000) apply the method of burial dating to prehistoric cave sediment using ^{10}Be and ^{26}Al, and Ivy-Ochs *et al.,* (2001) have proposed using cosmogenic nuclides to date archaeological stone artefacts. Stock *et al.* (2005a) conclude that cosmogenic techniques are the most reliable compared with U-Th and palaeomagnetism for cave burial dating. Lal *et al.* (2005) have recently dated corals using a multi-nuclide approach. Future uses of *in-situ* cosmogenic nuclides seem certain to include quantifying landscape evolution on planets other than our own (Jull & Burr, 2006).

2.2 Cosmogenic radionuclide production systematics

2.2.1 Cosmogenic nuclides

Terrestrial cosmogenic nuclides are produced in the earth's atmosphere and *in-situ* at the Earth's surface by the interaction of cosmic rays with surface materials. Cosmic rays are energetic nucleons (generally in the order of ~ 10^8 to ~ 10^{10} eV, with an average energy of ~ 3 x10^9 eV (GeV)) which originate mostly in the Milky Way galaxy, and were discovered in 1912 by Austrian physicist and Nobel Laureate Victor Hess. Galactic Cosmic Rays (GCRs) are composed of ~ 87% protons, ~ 12% alpha particles and ~ 1% heavy nuclei (Masarik and Reedy, 1995). There are also some lower energy particles originating from the sun (solar cosmic rays) with energies generally <10^9 eV. A small component of ultra-high energy particles

originate from extra-galactic sources and have energies of $>10^{20}$eV (Falcke *et al.*, 2005). These particles have sufficient energy to produce nuclear disintegrations in earth's upper atmosphere (Table 2.2.1).

Source	Typical energy (GeV)
Galactic cosmic radiation (Milky Way and Solar System)	$1\text{-}10^{10}$
Extra galactic cosmic radiation	Up to 10^{20}

Table 2.2.1 Range of cosmic ray sources and energies (Gosse &Phillips, 2001).

2.2.2 Attenuation

Cosmic rays are effectively filtered by the heliosphere, an area of plasma diffusing from the sun, and also by the earth's geomagnetic field and atmosphere. Temporal variations in the plasma flux of the heliosphere have the ability to modulate the incident GCR flux. During solar flares, the sun's magnetic field (heliomagnetic field) is strong leading to better shielding of the GCR. When the heliomagnetic field is strong, GCR flux is low with a correspondingly low terrestrial cosmogenic production rate. When the heliomagnetic field is weak, GCR flux is high and terrestrial cosmogenic production rates are high. During sunspot cycles, there is a strong heliomagnetic field, and GCR flux is low, as is cosmogenic production. The solar cosmic ray (SCR) flux is higher when the heliomagnetic field is strong, however solar cosmic rays do not normally contribute to radionuclide production on earth.

The majority of incoming cosmic ray particles are positively charged (Gosse and Phillips, 2001) and are thus influenced by both the geomagnetic and the heliomagnetic field. Whether or not a particle will pass through the atmosphere is determined by the cutoff rigidity, which is the momentum to charge ratio of the particle. It is therefore the minimum energy incoming particles must have to avoid deflection by the geomagnetic field (Figure 2.2.1). The higher the angle of incidence

between the magnetic field and incoming radiation, the higher the cutoff rigidity will be.

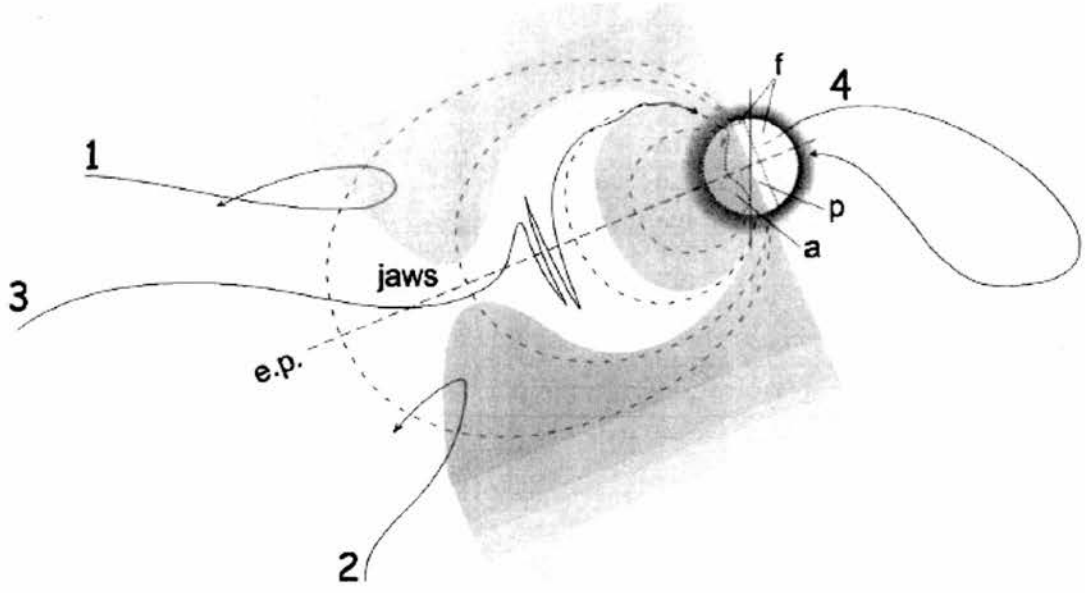

Figure 2.2.1 Diagram of cutoff rigidity (*from* Gosse & Phillips, 2001) where (a) is the allowed zone, (f) is the forbidden zone and (p) is the earth's penumbra. Trajectories 1, and 2 have insufficiently high cutoff rigidities for their angle of incidence and are deflected by the earth's magnetic field. Trajectory 3 is of rigidity equal to the vertical threshold rigidity and so the particle passes through the 'jaws' close to the equatorial plane (e.p.). Trajectory 4 is impossible due to the opaque nature of the Earth.

The Earth's magnetic field varies with latitude, hence the greatest effect on incident radiation is at equatorial latitudes, where the magnetic field is perpendicular to the average incident angle of cosmic radiation. The cosmic radiation that reaches the atmosphere will therefore tend to be composed of higher energy particles (higher cutoff rigidity) than at latitudes above 60° where the magnetic field will permit passage of radiation of lower energy, including solar cosmic rays (Dunai, 2000). Geomagnetic shielding effects are quantified when modelling cosmogenic nuclide production and due consideration must also be given to changes in geomagnetic intensity and dipole movement over timescales of thousands to hundreds of thousands of years (see Section 2.3).

Upon reaching the top of the earth's atmosphere, cosmic rays undergo a number of interactions which generate a secondary hadronic cascade (Masarik & Reedy, 1995), a 'shower' of secondary cosmic ray particles such as protons (p), neutrons (n),

electrons (e^-) positrons (e^+), pions (π) and muons (μ) (Figure 2.2.2). Neutrons make up the majority of the cascade with ~ 10% made up by protons (Nishiizumi *et al*, 1991). These secondary cosmic rays reach the surface of the earth and interact with earth surface materials to generate *in-situ* cosmogenic nuclides such as ^{10}Be in bedrock. It should be noted that ^{10}Be and ^{26}Al are also produced in the atmosphere (and termed meteoric or 'garden-variety' ^{10}Be) and while meteoric ^{10}Be has uses as a tracer in e.g. soil processes, it is not considered here. Care needs to be exercised in the laboratory preparation of cosmogenic ^{10}Be targets to avoid contamination from ubiquitous atmospheric ^{10}Be.

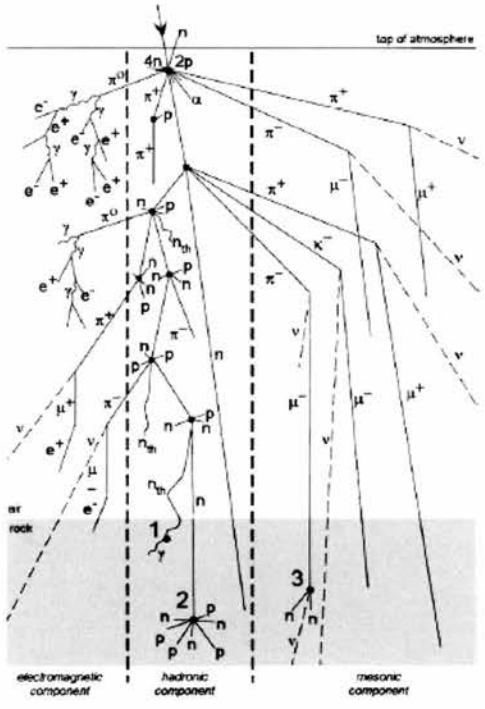

Figure 2.2.2 Secondary cosmic ray cascade (Gosse & Phillips, 2001). (see text for glossary of symbols).

As cosmic rays reach the atmosphere, they undergo further attenuation depending on atmospheric pressure, which varies with latitude and altitude and hence production rates must be scaled to account for this effect (see section 2.3). Different particles, e.g. neutrons and muons, are attenuated to differing degrees in the atmosphere hence they should be scaled separately (Stone, 2000). Once secondary cosmic rays have passed through the atmosphere, the depth to which they are able to penetrate into rock is determined by the absorption coefficient, a variable with units of g cm^{-2}

which is proportional to the rock's density and inversely proportional to the attenuation length of the cosmic rays (Lal, 1991). Cosmic rays with higher energy, or which interact less with other particles, have a higher attenuation length and hence will penetrate more deeply into the rock surface. Reactions of secondary cosmic rays with earth surface materials take the form of spallation and muogenic reactions as described below.

2.2.3 Spallation production

Spallation reactions account for over 97% of the total ^{10}Be and ^{26}Al production at sea level (Stone, 2000). Fast neutrons produced as part of the secondary hadronic cascade are sufficiently energetic to be able to shatter nuclei in rock surfaces and thus generate cosmogenic nuclides including ^{10}Be and ^{26}Al. ^{10}Be is normally produced from the spallation of ^{16}O in quartz (SiO_2) in the following reaction:

$$n + {}^{16}O \longrightarrow {}^{10}Be + 4p + 3n \qquad (2.2.1)$$

Where n is a neutron, p is a proton.

^{26}Al is normally produced from the spallation of ^{28}Si in quartz (SiO_2) in the following reaction:

$$n + {}^{28}Si \longrightarrow {}^{26}Al + 2p + n \qquad (2.2.2)$$

Where n is a neutron, p is a proton.

Due to its global ubiquity and favourable chemical properties, quartz is an ideal target mineral for cosmogenic nuclide analysis of ^{10}Be and ^{26}Al (Bierman *et al.*, 2002). As spallation reactions occur, energy is lost from fast neutrons until they reach energies of ~ 0.1-0.5 MeV, and later they become thermal neutrons (energy ~ 0.025 eV) and are unable to cause further spallation, although they can still produce cosmogenic ^{36}Cl and ^{41}Ca by neutron capture. Spallation reactions have an attenuation length of ~ 160 g cm^{-2} in most types of bedrock and decrease

exponentially with depth until spallation becomes relatively insignificant compared with muogenic production below ~ 6 m depth.

2.2.4 Muogenic production

Muogenic production accounts for around 3% of surface cosmogenic nuclide production. When deriving denudation rates, muons must be considered since a column of rock undergoing denudation will, depending on the rate of denudation, effectively have been brought up from a depth where muogenic production exceeds spallation. Muogenic production can be by negative muons (μ^-) which are short-lived ($t_{1/2} = \sim 2x10^{-6}$ seconds) products of the decay of negative pions. Negative muons may be captured by a charged nucleus which then emits nucleons and neutrinos as it becomes excited (Heisinger *et al.*, 2002a, 2002b). The muogenic production of ^{10}Be in quartz targets occurs thus (Nishiizumi *et al.*, 1989):

$$\mu^- + {}^{16}O \longrightarrow {}^{10}Be + 3p + 3n \qquad (2.2.3)$$

Muogenic production of ^{26}Al is by the following nuclear reaction.

$$\mu^- + {}^{28}Si \longrightarrow {}^{26}Al + 2n \qquad (2.2.4)$$

Muogenic production also results from deceleration of fast muons (μ_f) causing further secondary particles which generate cosmogenic nuclides (Gosse & Phillips, 2001). Muons are less strongly attenuated than neutrons (attenuation length ~ 1500 g cm^{-2}) and therefore can penetrate more deeply into bedrock surfaces. Fast and slow muons attenuate to different degrees and require separate scaling (Gosse & Phillips, 2001). The relative role of production by muons compared to spallation in very slowly eroding landscapes is discussed in Section 3.4 in the context of also considering radioactive decay of the cosmogenic nuclide over those long timescales.

2.2.5 Non-cosmogenic production

There are other, non-cosmogenic, production pathways of ^{10}Be and ^{26}Al, including from ^{7}Li, where alpha particles and protons from the decay of U and Th may react with ^{7}Li to produce ^{10}Be. The amounts of ^{10}Be produced in this way are usually

negligible (Gosse & Phillips, 2001). The decay of U and Th can produce considerable amounts of ^{26}Al by an alpha particle and neutron reaction with ^{23}Na, again with the alpha particle coming from the decay of U or Th, although this effect is negligible in quartz where U is not normally found.

2.2.6 Estimating *in-situ* denudation rates

In situ cosmogenic production rates in bedrock outcrops are determined by the location of the bedrock, its altitude and its depth (Bierman & Nichols, 2005). Modelling production rates requires scaling for all of these factors and also requires a number of shielding factors, including shielding by soil, vegetation, local and distant topography and slope, to be taken into account. These are considered in detail in section 2.3. The fundamentals of calculating *in-situ* denudation rates is examined below as a means of introducing the 'catchment-averaged' technique for determining denudation rates over a large area, which is discussed in the next section.

Lal and Arnold (1985) and later Lal (1991) introduced the concept of using *in-situ* produced cosmogenic nuclides to estimate denudation rates. Lal (1991) developed production rate scaling factors (discussed in detail in a later section) and calculated the *in-situ* cosmogenic nuclide concentration as a function of production rate, decay, time, and the shielding depth of the sample within the bedrock. This is summarised in Equation (2.2.5):

$$N(x,t) = N(x,0)\, e^{-\lambda t} + \frac{P(x,t)}{\lambda + \mu E}\, e^{-\mu x}\left(1 - e^{-(\lambda + \mu E)t}\right) \qquad (2.2.5)$$

(Lal, 1991)

Where:

N is the concentration of cosmogenic nuclides (atoms g^{-1});

P is the production rate (atoms g^{-1} a^{-1})

λ is the radioactive decay constant (a^{-1})

E is denudation rate (cm a^{-1})

μ is the absorption coefficient (cm^{-1})[1]

x is the shielding depth of the sample within the bedrock (cm)

t is the time in years, starting with an initial cosmogenic nuclide concentration at $t=0$

If it can be assumed that the production rate P has not varied significantly over time (this assumption is tested in the section on geomagnetic variability in the Section 3.4), then certain simplifications can be made to the above formula. If the system under consideration has been undergoing a constant rate of denudation and has reached secular equilibrium between accumulation of cosmogenic nuclides by production from incoming radiation and loss of cosmogenic nuclides through radioactive decay and denudation, then time essentially ceases to be a factor in Equation 2.2.5. If we can also assume that the material at the surface has not been exposed to cosmic radiation prior to being exposed by denudation of the overlying material, then t becomes zero and N(x,t) disappears. However, at any time the shielding depth of the sample within the eroding bedrock will still play a role in terms of nuclide production. With these assumptions in mind, production at the surface (P_0), nuclide concentration at the surface (N_0), radioactive decay (λ) and the penetration coefficient (z^*) are the only factors that need to be considered. By simplifying Equation 2.2.5 (Lal, 1991) as described above and solving for denudation rate, the following equation is given:

$$E = \left(\frac{P_0}{N_0} - \lambda \right) z^* \qquad (2.2.6)$$

(Lal, 1991)

Note that the above assumptions are discussed in the context of the sampled locations in section 3.1. The next section discusses a modification of the *in-situ* approach to estimate denudation rates for entire catchments.

[1] The absorption coefficient represents the attenuation that occurs as the cosmogenic nuclide passes through a material. It is a function of the material's density ρ (g/cm^{-3}, taken here to be 2.6) divided by its attenuation length Λ (g/cm^{-2}, taken to be 155 here), i.e. $\mu = \rho/\Lambda$. It also can be expressed as the coefficient of penetration, z^*, the depth in cm that cosmic radiation will reach before the intensity drops to a factor of 1/e (Gosse & Phillips, 2001). The penetration coefficient is the inverse of the absorption coefficient, i.e. $z^* = \Lambda/\rho$

2.3 The catchment-averaged approach to cosmogenic nuclide inventories: a review

2.3.1 Introduction

In this section, an introduction to quantifying denudation rates over large areas using the catchment-averaged approach is given. This is complemented by a discussion of how denudation rates are computed from the catchment-averaged approach in section 2.4. The catchment-averaged approach has the potential to quantify denudation rates on the scale of an individual hillslope to a sub-continental scale drainage system (Bierman & Nichols, 2004).

In the past decade, a number of authors have attempted to measure the cosmogenic nuclide concentration in alluvial sediment, as opposed to a bedrock surface, and in doing so to estimate a basin-wide, or catchment-averaged, denudation rate over large areas, from 10^2 to 10^6 km^2 (e.g. Bierman & Steig, 1996, Granger *et al.*, 1996, Schaller *et al.*, 2001). The basis of the technique is that individual clasts in a sediment sample represent a diversity of exposure histories from when the clasts were part of an intact bedrock surface. Thus, if the production rate of the source areas are known, and a number of other assumptions are met, a sediment sample can reveal the average denudation rate of its source areas. The technique has been largely applied to fluvial systems, where well-mixed sediments meet the assumptions of the model, but it has also been applied in a number of other systems to give an average denudation rate for a larger area, e.g. desert pavements and hillslopes (Bierman & Caffee, 2001).

2.3.2 Theoretical basis of the catchment-averaged approach

Mathematically, calculating a catchment-averaged denudation rate is similar to calculating *in-situ* denudation rates for bedrock surfaces and, as such, the assumptions of Lal's model of secular equilibrium between production, decay and denudation (summarised in Equation 2.2.6), must be met.

a. Assumption 1: Constant production rate

The model assumes that production of cosmogenic nuclides is temporally constant and can be averaged spatially. The temporal consistency of production is subject to the same large- and small- scale considerations as bedrock surfaces. Large-scale considerations include that the earth's geomagnetic field strength and non-dipole field have not varied sufficiently to affect production over the exposure history of the area being studied (Valet *et al.*, 2005). This is discussed further in relation to Southern African locations in section 2.4. Smaller scale considerations include that shielding, by topography, rock, or soil, of the area being studied has not changed significantly over the history of the site. Where production has varied over time, it is assumed that this variation can be modelled, e.g. by referring to published records of geomagnetic variability (Ohno & Hamano, 1992), or estimating shielding extent and duration by the use of paired radionuclides (^{10}Be and ^{26}Al).

With the *in-situ* approach to cosmogenic nuclides, spatial variation in production rates is not a problem, however for the catchment-averaged approach, areas of different production rates need to be considered. As production rates are governed by geomagnetic location and altitude, for small basins, this normally means just calculating the average elevation of the basin by GIS analysis of a digital elevation model (see section 3.4). For larger basins which cover several degrees of geomagnetic longitude and latitude (e.g. the Orange River), the total catchment area can be divided up into tributary catchments and the production rate calculated for each basin sub-unit based on the average elevation and latitude of that sub-unit calculated by GIS techniques (Section 3.2).

It is assumed that the inclination of a basin is, to a first order approximation, constant across the whole basin and so local slopes, which may be important when calculating *in-situ* bedrock sample production rates, do not significantly affect the overall production within the basin. It can be assumed that the inclination angle of the catchment under consideration is constant on the largest scale (Figure 2.3.1) hence the landsurface is at a constant angle with respect to the incoming 'cone' of cosmic

rays regardless of the exact location within the basin. Therefore topographic shielding corrections do not need to be carried out for catchment-averaged samples.

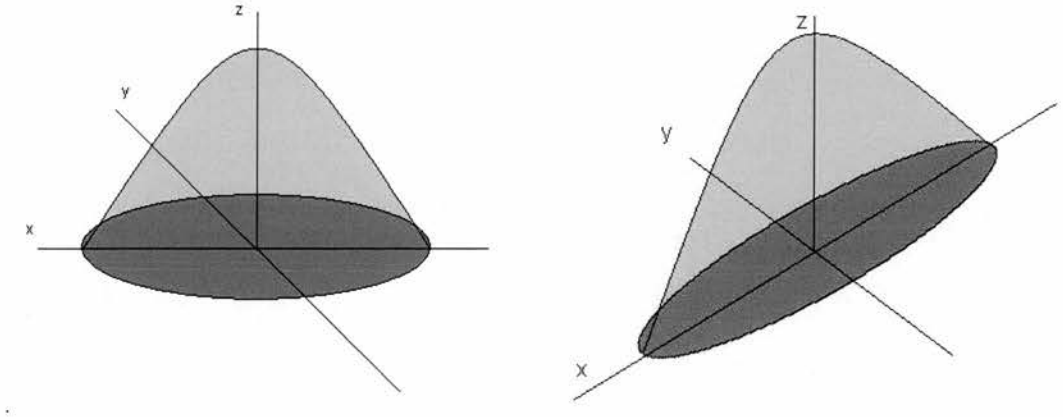

Figure 2.3.1 Cone of incoming cosmic radiation on (A) flat basin, (B) basin tilted at ~ 30 degrees – total incoming cosmic radiation for each basin is the same (*after* Codilean, 2006).

b. Assumption 2: Secular Equilibrium

Another assumption in common with the *in-situ* cosmogenic nuclide approach is that the system is in secular equilibrium with respect to production, decay and denudation (Lal, 1991, Bierman & Steig, 1996). If production, as discussed above, is constant this requires denudation to have been temporally consistent across the basin, although not necessarily spatially consistent as different basin sub-units may erode more quickly than others depending on site-specific considerations such as lithology and aspect. Note that the achievement of secular equilibrium is predicated by the rate of denudation: i.e. the time to reach secular equilibrium will be longer for systems which have a slow rate of denudation and quicker for those with rapid denudation (Figures 2.3.2, 2.3.3).

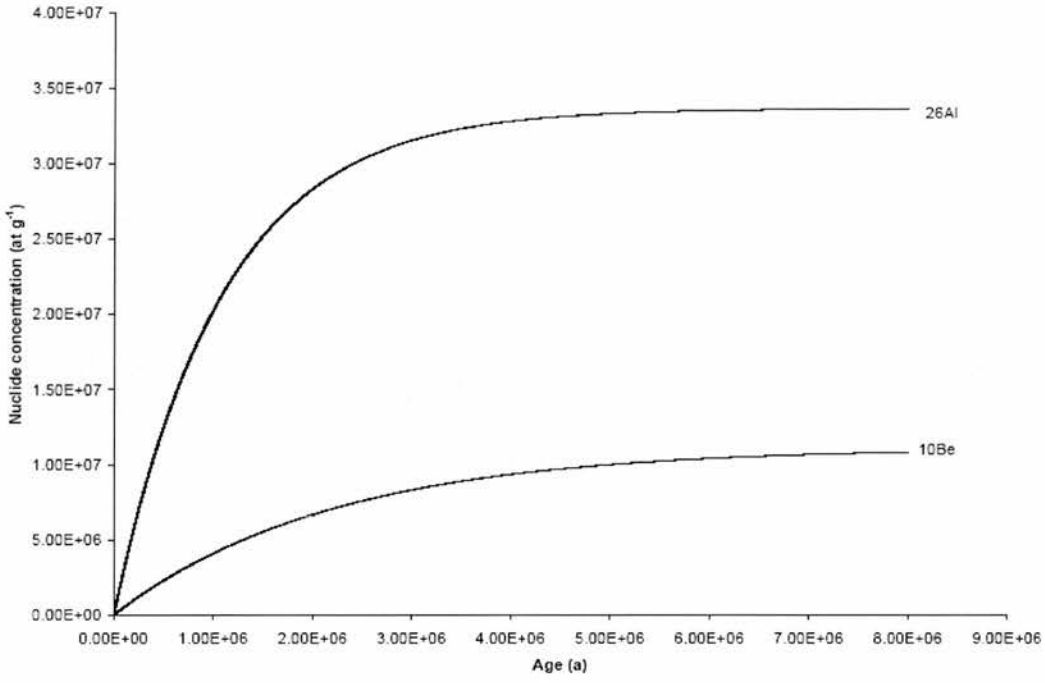

Figure 2.3.2 Graph showing build-up of cosmogenic nuclides with time, eventually reaching secular equilibrium (where plots level off). This graph assumes zero denudation, just decay and is based on Equation 2.2.5 (Lal, 1991). The faster the denudation rate, the quicker secular equilibrium between production, decay and denudation will be reached (see Figure 2.3.3).

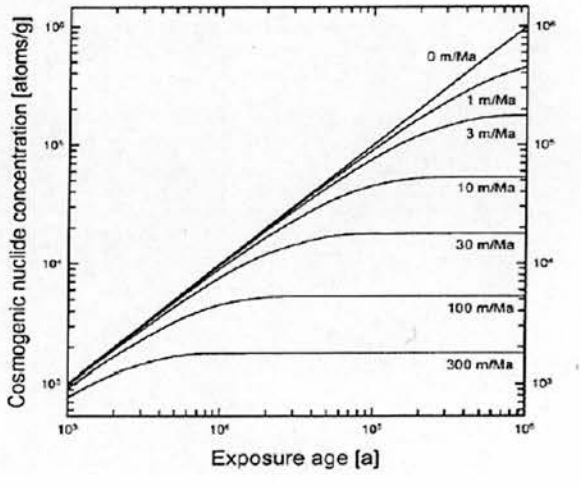

Figure 2.3.3 Effect of denudation on cosmogenic nuclide concentration, ignoring decay (Stuart, personal communication, 2006).Higher denudation rates allow secular equilibrium between production and denudation to be reached sooner.

c. Assumption 3: Well-mixed sediment

The principal assumption underpinning the catchment-averaged approach is that sediment must be both well-mixed and representative of its source area (Granger *et al.*, 1996, Schaller *et al.*, 2001). A well –mixed sediment will include clasts from all of the sub-catchments above it and so will be representative of denudation rates over the area from which it is derived. Areas of the catchment that erode more rapidly than others may be over-represented even in a well-mixed sediment and it is important that the sediment source areas are weighted according to their total area so as not to over-represent any one area of the catchment. A further, related assumption, is that the target mineral (in this case quartz) is distributed uniformally throughout the catchment (Bierman & Nichols, 2004). The Orange River contains a major tributary, the Vaal, which drains an area largely consisting of non-quartz lithology. The extent to which the Orange catchment meets this assumption, is discussed in Section 3.1.

Similarly, certain grain-size fractions may contain a greater concentration of cosmogenic nuclides than others, hence in a poorly-mixed sediment, there may be an over-representation of a particular size fraction which would lead to an inaccurate overall denudation rate being calculated. Authors such as Clapp *et al.* (2000, 2001) have shown that there is no relationship between nuclide concentration and grain size in some arid regions, however different size fractions of the same sediment are tested for variation in cosmogenic nuclide concentration.

d. Assumption 4: Incremental 'steady state' denudation

In contrast to the assumption of secular equilibrium (often mis-termed steady state) is the assumption that denudation is occurring by incremental denudation – i.e. by denudation occurring by low magnitude, high frequency means such as exfoliation of bedrock surfaces and not high magnitude, low frequency events such as landslides and mining of stored sediment. This assumption can be tested by careful field evaluation of the geomorphology of the basin under analysis.

2.3.3 Limitations

Note that the assumption of incremental denudation across the catchment does not necessarily mean that all parts of the catchment will be undergoing denudation at the same rate. Indeed, it is the lack of consistency in denudation rates across sub-catchments which presents one of the main limitations to the catchment-averaged technique. Bierman & Steig (1996) have demonstrated that for a catchment composed of multiple sub-catchments, the total denudation rate for the whole catchment will not equal the sum of the denudation rates of the individual sub-catchments. This is because of the influence of the decay constant, λ. The decay constant is calculated from the inverse of the radioactive half-life multiplied by ln2, i.e. λ = ln2/half life of nuclide. The half lives of ^{10}Be and ^{26}Al are 1.52 Ma and 0.71 Ma, respectively (Gosse & Phillips, 2001). After a cosmogenic radionuclide forms, it will undergo decay at an exponential rate determined by the decay constant. How much decay occurs is determined by how much time has passed since the formation of a cosmogenic nuclide. The formation of a cosmogenic nuclide is in part determined by the depth of the target mineral and therefore the denudation rate (how quickly it is being exposed), and by the penetration depth of radiation. Once the cosmogenic nuclide has been formed, assuming the penetration depth is constant, in a slowly denuding system the nuclide will undergo decay before it reaches the surface of the earth. In a rapidly denuding system, the nuclide will undergo less decay before reaching the surface. If sub-catchments are undergoing denudation at different rates, then so too will the effect of exponential decay be different for each sub-catchment and therefore impossible to quantify by a simple mixing model of denudation rates. However, as shown below, a simple mixing model of concentrations and the back-calculation of the denudation rates can be used to quantify catchment-averaged denudation.

Given that the nuclides under analysis (^{10}Be and ^{26}Al) have relatively long half-lives, and therefore low decay constants, provided that denudation is sufficiently rapid, in the order of several meters per million years and sediment storage is negligible, then loss by decay can be ignored (Bierman & Steig, 1996). In reality, and as discussed in Chapter 3, ignoring decay does not make a large difference to the final calculated

denudation, but may introduce a significant source of uncertainty. Therefore, by not considering decay, the total nuclide concentration in a well-mixed sediment sample which is representative of its source area is the sum of the concentration in each of the sub-units of a catchment for which production and denudation rates are known, expressed as Equation 2.3.1:

$$\bar{N} = \frac{\bar{P}}{\mu \bar{E}} = \frac{P_1}{\mu E_1} + \frac{P_2}{\mu E_2} \qquad (2.3.1)$$

(Bierman & Steig, 1996)

Where:

$\bar{N}$ is the catchment-averaged cosmogenic nuclide concentration (atoms g^{-1})

$\bar{P}$ is the catchment-averaged production rate (atoms g^{-1} a^{-1})

P_1 is the production rate in sub-catchment 1 (atoms g^{-1} a^{-1})

P_2 is the production rate in sub-catchment 2 (atoms g^{-1} a^{-1})

$\bar{E}$ is the catchment-averaged denudation rate (cm a^{-1})

E_1 is the denudation rate in sub-catchment 1 (cm a^{-1})

E_2 is the denudation rate in sub-catchment 2 (cm a^{-1})

μ is the absorption coefficient (cm^{-1})

The relative effects of rapidity of denudation, the decay constant and the effect of muogenic production are explored in section 2.5 in the context of the relatively low denudation rates calculated for Southern Africa.

2.4 Calculating ^{10}Be and ^{26}Al cosmogenic denudation rates

2.4.1 Production rates and scaling factors

A spreadsheet was constructed in order to compute ^{10}Be/^{26}Al denudation rates. Full details are given in Appendix 1. The following details specific corrections made to the production rate scaling factors which are well documented by Dunai (2000) and

Stone (2000) which this study uses. A number of authors have developed scaling factors to account for differences in production rates at different altitudes, latitudes, and dipole and non-dipole changes with time. The classic work on scaling was presented by Lal (1991), who bases his scaling factors on different altitudes and latitudes. An updated version of Lal's (1991) scaling factors based on pressure at different altitudes and latitudes, with updated scaling values for spallogenic and muogenic production is presented by Stone (2000).

Dunai (2000) presents a new set of scaling factors based on neutron cutoff rigidities and atmospheric palaeo-pressure rather than altitude which shows that for low latitudes (20-40°) scaling factors are significantly different to those of Lal (1991) and Stone (2000). This is because of the effects of the non-dipole field, believed to account for 20% of the earth's magnetic field and not accounted for in either Lal or Stone's factors, and the uncertainty associated with neutron absorption mean free path length (Λ) which is believed to vary with altitude and is also not considered in either Lal or Stone's factors.

Both Stone's and Dunai's schemes are used to calculate production rates of ^{10}Be. In this study, the denudation rates in the results chapters are given using Stone's (2000) scaling factors using spallation and muogenic production. Denudation rate data are presented using both Stone's (2000) and Dunai's (2000) scaling factors, with and without muons, for all samples in Appendixes 4 and 5.

2.4.2 Production rate correction factors

Before calculating production rates, production needs to be corrected for topographic shielding and sample thickness (Gosse & Phillips, 2001). Production rate also decreases with depth in rock (Kim & Englert, 2004). The thickness shielding coefficient T(Z) is calculated by Equation 2.4.1:

$$T(Z) = \frac{\Lambda}{\rho Z}\left(1 - e^{\frac{-\rho Z}{\Lambda}}\right) \qquad (2.4.1)$$

(Kim & Englert, 2004)

Where: Z is sample thickness (cm); ρ is rock density (g cm^{-3}); and Λ is the absorption mean free path length for spallation (g cm^{-2}) – a value that varies with latitude but, for the purposes of the spreadsheet, is taken to be 155 g cm^{-2} at latitudes <20°, 160 g cm^{-2} at latitudes 20-50°, and 150 g cm^{-2} at latitudes greater than 50° (Balco, 2000).

Topographic shielding is generally measured in the field as a blocked section of the horizon when the horizon is broken up into a number of straight line sectors. For a rectangular obstruction that blocks incident cosmic rays from the ground up at a constant inclination angle θ_i and extends through an azimuth angle $\Delta\phi_i$ the missing flux (δF) is given by (2.4.2) (Dunne *et al.*, 1999).

$$\delta F = \frac{I_0 \Delta \phi}{m+1} \sin^{m+1}(\theta_0) \qquad (2.4.2)$$

(Dunne *et al.*, 1999)

Where m = 2.3. For n obstructions, each with its own inclination and azimuth angles, a production shielding factor can be (S) can be calculated as the ratio of the remaining flux to the maximum flux (2.4.3):

$$S = 1 - \frac{1}{360^\circ} \sum_{i=1}^{n} \Delta \phi_i \sin^{m+1}\theta_i \qquad (2.4.3)$$

(Dunne *et al.*, 1999)

2.4.3 Slope angle shielding correction

If the surface being sampled is sloped, the effect of geometric shielding and attenuation length on production rates is more complicated than for a flat surface. The model below (Dunne *et al.*, 1999) assumes that the slope is uniform, with a dip angle of α. Equation (2.4.4) describes the slope angle shielding factor as a function of dip angle (α) and depth (z), where Λ is the absorption mean free path length for spallogenic production in rock (g cm^{-2}), taken to be 155 g cm^{-2} for all latitudes in this spreadsheet.

$$S(z,\alpha) = (1 - 3.6 \times 10^{-6}\alpha^{2.64})e^{-\left(\frac{z}{\Lambda}\right)\left(1+\frac{\alpha^2}{5000}\right)} \quad (2.4.4)$$

(Dunne *et al.*, 1999)

2.4.4 Overall production rate

With the above correction factors computed, overall production rate at the earth's surface can be calculated by combining them with the scaled production rates (2.4.5)

$$P = P_0 \; F \; T \; S \; S(z\,\alpha) \quad (2.4.5)$$

(Stone, 2000)

Where P_0 is production rate (taken as 5.1±0.3 atoms g^{-1} a^{-1} for ^{10}Be and 31.1±1.9 atoms g^{-1} a^{-1} (Stone, 2000)), F is combined scaling functions for muogenic and spallogenic production, T is the thickness correction factor.

2.4.5 Geomagnetic variations

Geomagnetic variations occur in two ways. Firstly, the position of the earth's magnetic pole changes on a scale of thousands of years, and thus affects the production rate of a sample throughout its exposure history. The geomagnetic pole location is believed to average out to the geographical pole over tens of thousands of years and so is changes in pole location are only significant for Holocene-age samples (Ohano & Hamano, 1992). Secondly, the overall intensity of the magnetic field changes over time (and indeed switches periodically – e.g. the geomagnetic reversal at ~ 750 ka BP at the boundary between the Bruhns and Matayama chrons (Guyodo & Valet, 1999). This causes changes in the intensity of cosmic rays near the earth and affects the production rates of cosmogenic nuclides. Changes in the position of the earth's magnetic pole over the last ~ 10 ka have been documented by Ohno & Hamano (1996) based on virtual geomagnetic pole positions from palaeomagnetic data (Table 2.4.1, Figure 2.4.1).

Age (a)	Øp (Lat, degrees)	Øp (Long, degrees)
500	86.6	216.3
100	80.2	65.1
1500	88.4	9.6
2000	85.5	358.0
2500	83.9	26.0
3000	82.9	68.7
3500	82.6	48.5
4000	86.3	180.0
4500	87.3	98.1
5000	86.1	181.2
5500	88.8	80.3
6000	86.7	145.5
6500	85.2	127.1
7000	86.7	136.4
7500	88.2	202.3
8000	83.6	5.5
8500	87.0	54.5
9000	86.1	122.0
9500	86.1	206.8
10000	82.5	94.6

Table 2.4.1 Location of north geomagnetic pole (Øp) in 500 a intervals for the past 10 ka (Ohno & Hamano, 1996).

To account for variations in the intensity of earth's geomagnetic field, a chronology has been constructed by Guyodo & Valet (1999) from sedimentary records for the last 200 ka. A more recent record of 2 Ma can also been used (Valet, personal communication, 2005). Together with a Holocene record by McIlhenny and Senanayake (1982), one has sufficient information to iteratively correct ages and denudation rates for geomagnetic variations once an initial age has been calculated.

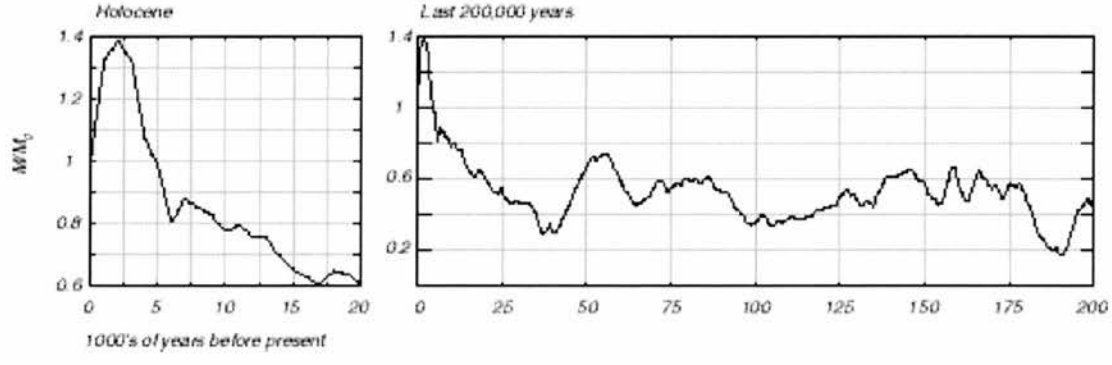

Figure 2.4.1 Variations in geomagnetic intensity (M/M_0) on 20- and 200-ka timescales. (Balco *et al.*, 2005).

Using Figure 2.4.1 for (M/M_0) and the values of $\emptyset p$ from Table 2.4.1, a new 'effective latitude' ($\emptyset m$) (2.4.6) can be calculated (Nishizumi *et al.*, 1994; cited in Dunne *et al.*, 1999) which together with the scaling factors described above can be used to calculate a geomagnetic-corrected exposure age. This is done over successive iterations until a new, consistent, geomagnetic latitude is worked out.

$$\phi_M = \arccos\left[\left(\frac{M}{M_0}\right)^{1/4} \cos(\phi_p)\right] \quad (2.4.6)$$

(Dunne *et al.*, 1999)

2.4.6 Erosion rate determination

Once the production rate (P) is calculated, and the number of atoms of ^{10}Be or ^{26}Al (N) has been measured by AMS, denudation rate (E) can be calculated by (2.4.7)

$$E = \left(\frac{P_o}{N_o} - \lambda\right) z^* \quad (2.4.7)$$

(Lal, 1991)

Where z* is the attenuation coefficient, i.e. the ratio of absorption mean free path length for spallogenic production in rock (Λ, 155 g cm^{-2}) to bulk rock density (ρ, 2.6 g cm^{-3}). The uncertainties associated with these calculations and specific considerations for the catchment-averaged approach are documented in Appendix 1.

2.5 Modelling cosmogenic production scenarios

A number of factors which affect cosmogenic production rates must be considered. These include the influence of fast and slow muons, radioactive decay and the role of past geomagnetic variability. These are considered in turn below.

2.5.1 Muogenic production

In order to assess the relative importance of spallation, and fast and slow muogenic production, the production rate of these three components was modelled for a range of denudation rate scenarios. In environments undergoing low rates of denudation, cosmogenic nuclide production is dominated by spallation (Stone, 2000). Muogenic production accounts for a low proportion of the total ^{10}Be and ^{26}Al concentration at the surface because muons are attenuated less and therefore penetrate more deeply than neutrons involved in spallation (Heisinger *et al.* 2002s, 2002b). Hence under conditions of low denudation rates, most of the muogenic produced ^{10}Be and ^{26}Al will have decayed before reaching the earth's surface. As denudation rates increase, there is less time for the cosmogenic nuclides to decay before reaching the earth's surface and so muogenic production increases relative to spallation (Schaller *et al.*, 2001). This is illustrated with reference to the calculations of Granger *et al.* (2001) (Eq.2.5.1)

$$N_{(0)} = \left(\frac{P_{(0)}}{\lambda + \frac{\rho\varepsilon}{\Lambda}}\right) + \left(\frac{YA_1}{\lambda + \frac{\rho\varepsilon}{L_1}}\right) + \left(\frac{YA_2}{\lambda + \frac{\rho\varepsilon}{L_2}}\right) + \left(\frac{B}{\lambda + \frac{\rho\varepsilon}{L_3}}\right) \quad (2.5.1)$$

(Granger *et al.*, 2001)

Where:

Symbol	Meaning (unit)	Value
P	Production rate (at g^{-1} a^{-1})	5.1
λ	Decay coefficient (a^{-1})	4.59E-07
ρ	Bedrock Density (g cm^{-3})	2.6
Λ	Nuclide Attenuation (g cm^{-2})	155
A1	Slow muon capture constant 1 (at g^{-1} a^{-1})	170.6
A2	Slow muon capture constant 2 (at g^{-1} a^{-1})	36.75
Y	Constant (unitless)	5.60E-04
B	Fast muon production (at g^{-1} a^{-1})	0.026
L1	Constant (g cm^{-2})	738.6
L2	Constant (g cm^{-2})	2688
L3	Constant (g cm^{-2})	4360
ε	Denudation rate (cm a^{-1})	Unknown

Table 2.5.1 Explanation of units used in Equation 2.5.1 for ^{10}Be (*after* Granger *et al.*, 2001). N.B. The factors above are for sea level high latitude (SLHL) production.

By plotting a range of denudation rates against the three different production pathways (spallation, fast muons, slow muons), it can be seen that muons are less important in terms of production as they are more slowly attenuated in the atmosphere than spallation-producing nucleons (Granger *et al.* 2001). In theory, muons should be important at SLHL for moderate denudation rates as shown in Figure 2.5.1. However, at the latitudes and altitudes being dealt with in this study, calculations in Chapter 5 show that muons affect denudation rates by less than 5% (this is well within the uncertainties on the denudation rates). In relatively slowly eroding environments, radioactive decay reduces the fraction of nuclides produced by muons at depth. Indeed, as the influence of muons relative to spallation becomes less with elevation and lower latitudes the effects, even over the 'problematic' range of denudation rates (1-10 mm ka^{-1}), are unlikely to prevent valid application of the model (Binnie, personal communication, 2005). However, given that it is conventional to include muogenic production in cosmogenic-derived erosion rates, even if the relative contribution of production by muons is small, the erosion rates presented in this study, scaled by both Stone's (2000) and Dunai's (2000) factors, include muons.

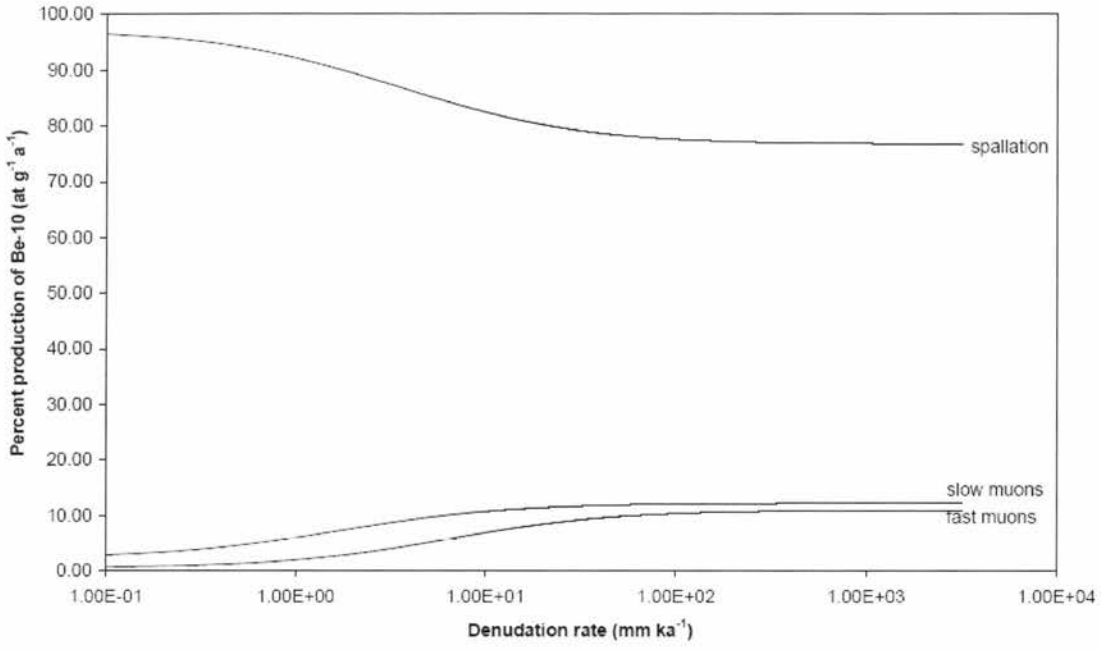

Figure 2.5.1 Relative contribution of spallation and muogenic production at sea level, high latitude (based on Stone 2000 scaling factors).

2.5.2 The influence of radioactive decay

The effect of radioactive decay is to reduce the concentration of ^{10}Be and ^{26}Al in a sample as a function of time. Under condition of rapid denudation (greater than several tens of millimetres per thousand years), the effect of decay on the cosmogenic nuclide concentration may be negligible (Bierman & Steig, 1996). For lower denudation rates, decay may have a significant effect on the concentration of cosmogenic nuclides. For the denudation rates considered here (in the order of 10^1-10^2 mm ka^{-1}) decay is considered to have a significant effect on cosmogenic nuclide concentration and hence is considered in the calculations here. Consideration of radioactive decay takes on a special significance in the context of basin-wide denudation rates. Uniform denudation rates across a basin are unlikely, due to local variations in lithology, slope and aspect and therefore the influence of decay across a basin will be variable. The influence of decay on a variable-denudation basin can be modelled for different scenarios of denudation variability with a basin. As each sediment grain in a basin effectively has a unique exposure history, the decay correction applied to basin-wide calculations of denudation assumes ^{10}Be behaves as a stable nuclide – i.e. decay is not considered. However, as demonstrated in Chapter

5, not considering decay makes very little difference to the calculations of denudation rates, while at the same time introducing significant uncertainty to basin-wide calculations.

2.5.3 The influence of geomagnetic variability

The earth's magnetic field exerts a strong influence over the attenuation of incoming cosmic rays (Figure 2.5.2). The earth's magnetic field is variable both spatially (it is strongest at the poles and high latitude regions), and temporally (it has periodically experienced both major and minor reversals, notably a major reversal at 780,000 years ago (the Brunhes-Matuyama boundary) and a partial reversal of smaller magnitude around 40,000 years ago (known as the Laschamp excursion). Constable & Korte (2006) have published data that suggests that although the earth's dipole field has been diminishing in strength, a reversal is not imminent although the time scale is unpredictable. Using a variety of sedimentological records from the terrestrial and marine environments, Valet *et al.* (2005) have constructed a record of geomagnetic variability extending back 2 Ma. This record of variability can be used to model the effective change in geomagnetic latitude associated with magnetic excursions and hence the effective changes in production rates over the averaging time of the sample (Guyodo & Valet, 1999). The averaging time is the time taken for a sample to pass through one attenuation length (z) of bedrock, where most of its cosmogenic nuclide content is accumulated. This, for a southern African bedrock sample, is around 60 cm and is calculated by dividing the absorption mean free path length for spallation (Λ, 155 g cm^{-2}) by the bedrock density (ρ, 2.65 g cm^{-3}). The averaging time of a slowly eroding sample is close to, but not identical to, its exposure age assuming zero erosion (the small amount of erosion accounting for the difference).

Over the past 800,000 years, the Earth's dipole strength has remained between 0.3 and 1.4 times the current field strength, as presented by Guyodo & Valet (1999). In addition, a more detailed, high resolution record has been presented for the last 10,000 years by Ohno & Hamano (1992). With this information, denudation rate

estimates can be corrected for geomagnetic variability (as described in section 2.4). Secular variation in geomagnetic field strength may be a more important concern and there is currently a need for improved understanding of the impact of geomagnetic field strength on the production rates of cosmogenic nuclides (Constable & Korte, 2006).

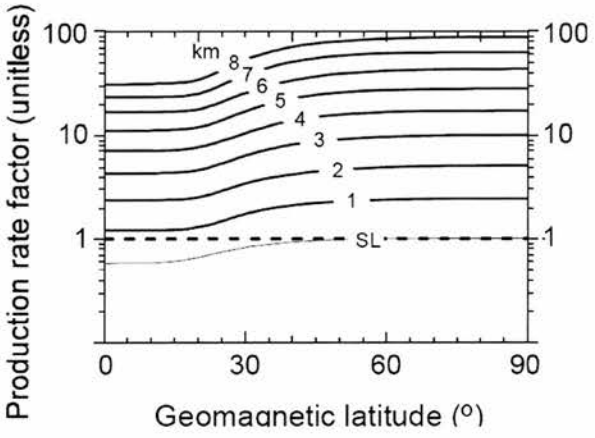

Figure 2.5.2 Variation in cosmogenic nuclide production with geomagnetic latitude and elevation (SL= sea level) (Lal, 1991).

The locations in this study are subject to geomagnetic variability. Low latitudes (of around 30 degrees or less, such as those in this study) are generally subject to variations in the geomagnetic field on timescales of thousands to hundreds of thousands of years (Gosse & Phillips, 2001). The averaging times of the samples presented here are between thousands and hundreds of thousands of years and hence production rates are likely to have varied considerably in response to geomagnetic changes over this time. As such, geomagnetic variation in production rates is considered in the erosion rate calculations for all bedrock samples. The catchment-averaged samples presented here, which by nature come from a range of latitudes, are not subject to geomagnetic variability corrections as to correct them would introduce greater uncertainty to the calculated erosion rates than leaving them out (see section 3.6.5).

2.5.4 Scaling factors

As discussed in Section 2.4, there are several different scaling factor schemes which can be used to calculate cosmogenic nuclide production rates (e.g. Lal, 1991, Dunai,

Stone, 2000). In this study, calculations are expressed using both the Dunai (2001) and Stone (2000) scaling factors. Spreadsheets have been constructed to calculate denudation rates for this study using both schemes. Lifton *et al.* (2005) have recently presented scaling factor schemes that take into account solar modulation of the secondary cosmic ray flux responsible for cosmogenic nuclide production. The dynamic solar wind effects on the Earth's magnetosphere influences the measured cosmic ray intensities. Solar activity varies in a cyclic manner over a variety of timescales; including the 11-year sunspot (Schwabe) cycles, the 22 year magnetic (Hale) cycle, the 88 year Gleissberg cycle, the 208 year Suess cycle and the 2300 year Halstatt cycle (Lifton *et al.*, 2005). These variations can lead to potentially significant scaling model uncertainties that have not previously been addressed in detail. As the effect is greater at higher latitudes than lower ones, Lifton's new scaling factors are not used in this study.

2.5.5 Catchment-averaged considerations: variation in production rate with elevation

Production of cosmogenic nuclides is strongly dependent on elevation. Production is highest at higher elevations, where there is less atmospheric shielding. The relationship between production rate and elevation is not linear (Figure 2.5.3) and increases very rapidly at higher elevations. As an example of the likely range of variation in production rates across the whole Orange basin, the nuclide concentrations for two extreme but possible sample locations are compared, other factors being equal but one sample is from a very low elevation (200 m) and one from a very high elevation (2000 m) (Table 2.5.2). This demonstrates that in the basin-wide fluvial samples, clasts could come from either of these locations and therefore have a large range of possible denudation rates (27.2% difference in this case). Therefore, rather than a mean elevation for the whole basin being used, the production rate is weighted according to the percentage of each basin at each elevation as described in Section 4.2. The underlying assumption of the catchment-averaged technique is that samples are well-mixed and representative of their source area (Granger *et al.*, 1996).

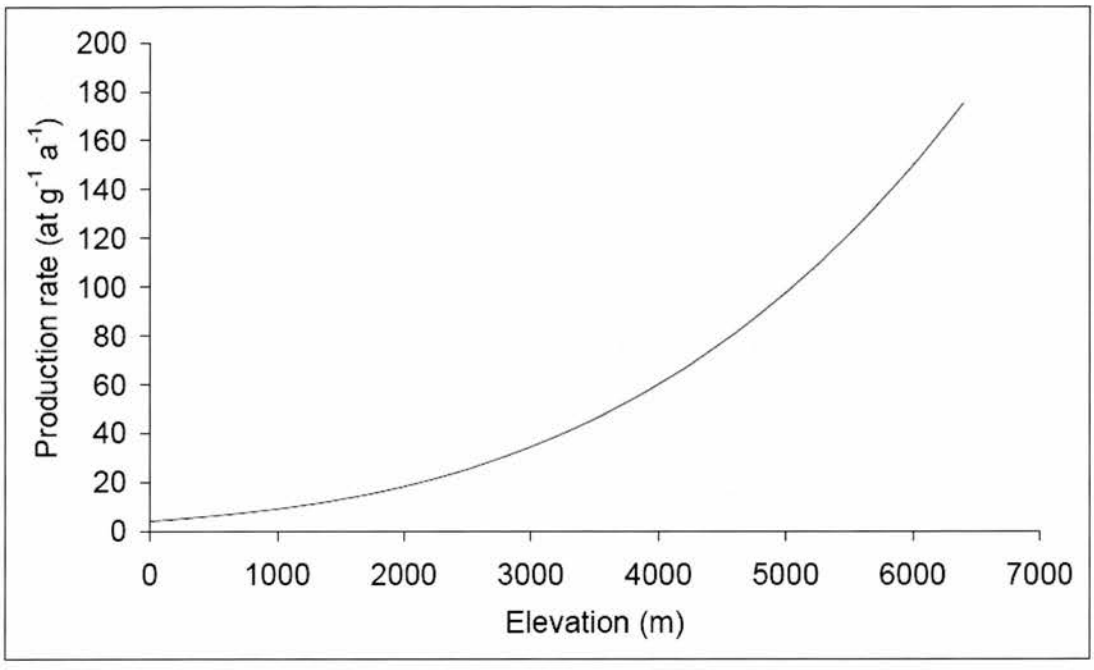

Figure 2.5.3 Non-linearity of production rate with elevation. This is for a 30 degree sample using Stone's (2000) scaling factors.

Sample	Latitude (degrees)	Elevation (m)	Stone's scaling factor	Production rate (at g^{-1} a^{-1})	Nuclide concentration (at g^{-1})
Low elevation	28	200	0.94	4.79	1.44E+06
High elevation	28	2000	3.47	17.67	5.30E+06

Table 2.5.2 Differences in nuclide concentration with elevation (other things being equal, assuming continuous exposure of 300 ka).

2.5.6 Catchment-averaged considerations: variation in production rate with latitude

Cosmogenic nuclide production is also dependent on latitude (though it is not as strongly dependent on latitude as elevation – Figure 2.5.2). The range of latitudes in the Orange basin covers from 27.5 to 32 degrees latitude (from 24.5 degrees to 32 degrees if the Fish River tributary is included) Variation in latitude can also result in a significant variation in cosmogenic nuclide concentration (90% difference in the example considered in Table 2.5.2). In reality both latitude and altitude will vary in the basin and therefore large differences in nuclide concentration will result between

high latitude, high elevation and low latitude, low elevation samples (Tables 2.5.3, 2.5.4). This is corrected by taking an average latitude for the basin in the way described in Section 4.2.

Sample	Latitude (degrees)	Elevation (m)	Stone's scaling factor	Production rate (at g^{-1} a^{-1})	Nuclide concentration (at g^{-1})
Low latitude	27	500	1.16	5.92	1.77E+06
High latitude	32	500	1.28	6.53	1.96E+06

Table 2.5.3 Differences in nuclide concentration with latitude (other things being equal, assuming continuous exposure of 300 ka). Nuclide concentrations are calculated using Stone's scaling factors as described above.

Sample	Latitude (degrees)	Elevation (m)	Stone's scaling factor	Production rate (at g^{-1} a^{-1})	Nuclide concentration (at g^{-1})
Low latitude, low elevation	27	200	0.92	4.69	1.41E+06
Low latitude, high elevation	27	2000	3.40	17.34	5.20E+06
High latitude, low elevation	32	200	1.01	5.14	1.54E+06
High latitude high elevation	32	2000	3.79	19.34	5.80E+06

Table 2.5.4 Differences in nuclide concentration with both varying elevation and latitude. The values of elevation and latitude are extreme examples for the Orange Basin. Note maximum difference in nuclide concentration is 25%, between high latitude high elevation sample and low latitude, low elevation sample. Nuclide concentrations are calculated using Stone's scaling factors as described above.

2.5.7 The sediment mixing 'problem'

It has been noted that for catchment-averaged samples, sediment clasts are assumed to be well-mixed and representative of their source area. If a small area of the basin (e.g. 10% of the area) is producing a large amount of sediment (e.g. 90% of the

sediment), then clearly the catchment-averaged denudation rate will not reflect the true rate of denudation in that 10% of the basin. However, in this extreme example, the other 90% of the basin can be assumed to be producing only 10% of the sediment, therefore the basin-wide denudation rate derived from a well-mixed sediment will indeed reflect the average rate of denudation for the whole basin, although there will obviously be local variations in the basin. Thus the axiom 'let nature do the averaging' (von Blanckenburg, 2006) is key to the basin-wide approach – as long as the sediment is well mixed, it will represent the average rate of denudation of the upstream area. Finer resolution sampling of sub-catchments will reveal local variations in denudation rates.

2.5.8 Topographic shielding

As described above, topographic shielding is not a significant problem for catchment-averaged samples given the multiplicity of exposure geometries of different clasts in a sediment sample and the fact that an entire basin ultimately receives a finite amount of comic radiation. It is however a significant source of uncertainty for bedrock samples, and strategies to quantify topographic shielding are described in Chapter 3. What is even more uncertain, however, is how topographic shielding has varied over time: there is no absolute method of quantifying how a slope has developed, for example, and how the changing slope angle will have resulted in varying *in situ* cosmogenic nuclide production. Nor is there any reliable method of quantifying how a bedrock channel has been differentially shielded over its lifetime – this is especially a source of uncertainty where incision results in shielding from the sidewalls of a bedrock channel – depending on the rate of incision, the bedrock channel sample will have been shielded to a greater or lesser extent over time. Thus, palaeo-shielding of bedrock samples is a classic tautology: the denudation rate estimation is critically dependent on adequate quantification of the amount of shielding in the past, and the amount of shielding in the past is dependent on how quickly the landform has eroded. Given the extreme uncertainties, particularly in bedrock channels, palaeo-shielding is not quantified in this study: greater uncertainty would be introduced by including it than by leaving it out.

2.5.9 Specific catchment-averaged considerations for the Orange basin

As discussed in Chapter 4, The Vaal catchment mainly consists of Ecca and Dwyka shales and tillites. As a major tributary, it contributes a large amount of sediment to the Orange River, however little of this is quartz. Indeed, field studies of the Vaal, discussed in the next Chapter, revealed it to contain little quartz of a sufficiently coarse grain size to survive chemical treatment. Therefore, the sediment collected from downstream of the Vaal confluence with the Orange will not contain a significant denudation signal from the Vaal basin. The sediment derived from the Vaal that ends up in the Orange will only serve to decrease the concentration of quartz in the Orange River's sediment. Since only pure quartz is used to measure the cosmogenic nuclide component, this dilution effect will not have any effect on the measured concentrations of ^{10}Be and ^{26}Al. Therefore, although the Vaal is a major tributary of the Orange, this study does not consider the denudation history of the Vaal by virtue of the fact that it does not capture any quartz (therefore no ^{10}Be or ^{26}Al signal) from the Vaal. Perhaps future studies that target a different lithology may be able to elucidate the denudation history of this major tributary (Figure 2.5.4).

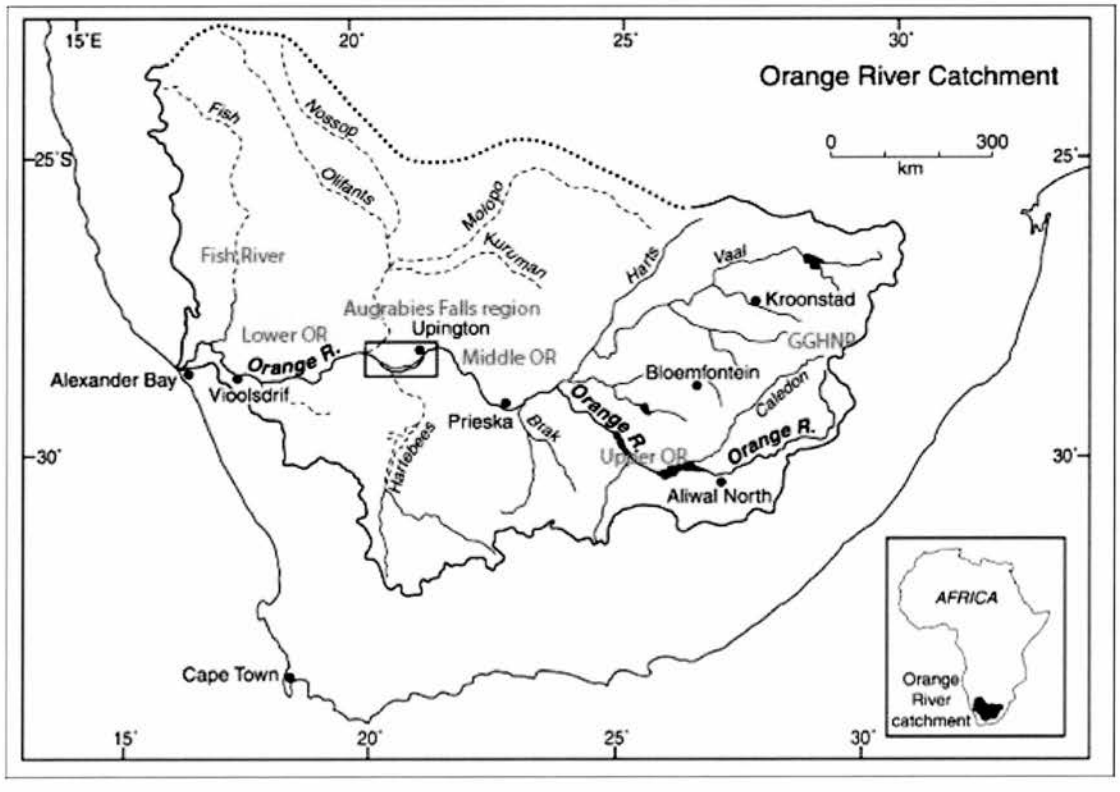

Figure 2.5.4 Principal regions in the Orange basin (OR- Orange River; GGHNP – Golden Gate Highlands National Park). Image adapted from Tooth & McCarthy (2004).

The Molopo, a large northern catchment covering parts of Botswana and entering the Orange close to Upington is not considered here on hydrological grounds: the majority of the Molopo catchment (the northern component) is hydrologically isolated from the southern component and therefore the Orange. From the Late Cretaceous onwards, the Molopo was hydrologically linked to its upper part and was a major north bank tributary of the Orange (Goudie, 2005). Subsequent tectonism in the Miocene and the development of the Kalahari basin resulted in its demise as a major tributary and the effective isolation of its northern and southern components. Thus the contribution of ancient quartz grains from the palaeo-Molopo to the present Orange River is not a problem since the Molopo was a major tributary at a time well outwith the timescales covered by cosmogenic ^{10}Be and ^{26}Al. However, some now-obsolete drainage systems in the Kalahari that link the Molopo may have been active during the Late Quaternary and Holocene (Stokes *et al.*, 1997). Luminescence dating of sand dunes in the Kalahari reveal there to have been numerous arid-humid cycles in the Quaternary. During the humid periods, the Molopo channels could have been re-activated and sediment delivered by them to the Orange River. The possibility that some quartz grains from the Molopo may be present in an Orange River sediment sample therefore cannot be excluded. However, the preponderance of bedrock channels and the relative lack of alluvium and colluvium in the lower Orange River suggests that sediment moves rapidly downstream and it is unlikely that clasts from the Molopo would be sampled as part of an Orange River sample. The record of high magnitude floods events in the lower Orange (as described in Chapter 1) also suggests that sediment is rapidly flushed from the system, thus justifying the exclusion of the Molopo from this study. The Molopo catchment also contains abundant areas of aeolian-deposited sand which is unrepresentative of the catchment-averaged denudation rate and may lead to uncertainties in calculations.

In contrast, the middle and upper parts of the Orange basin do contain local accumulations of sediment stored as alluvium and colluvium, and the low topographic gradients there could mean that this sediment is stored for periods of time that could significantly affect the concentration of cosmogenic nuclides in a sample. However, for such a large basin, the Orange does not have a significant

floodplain and the stretches of river where the Orange flows in its own alluvium are limited. There are extensive mixed bedrock-alluvial stretches in the lower part of the Orange River (Springer et al., 2006). Although there are alluvial floodplains in the middle course of the Orange which date from the Late Cenozoic, only a tiny proportion of their volume is currently being mined by the river (Granger, personal communication, 2006).

The presence of large dams in the middle course of the Orange could reduce the concentration of sediment travelling downstream. If sediment is buried and stored, or stored at or near the surface, its cosmogenic nuclide concentration could be significantly affected. However, many of the dams have only been constructed in the last 50-100 years, and any sediment storage that has resulted from their construction is insignificant on cosmogenic timescales. Sediment storage would have to be for several tens or hundreds of thousands of years to significantly affect the ^{10}Be or ^{26}Al concentrations in the clasts. This effect is explored in a discussion of relative ^{10}Be and ^{26}Al concentrations from fluvial sediment in Chapters 4 and 5.

Muzikar & Granger (2006) have described that surface processes not only move sediment, they also control concentrations of ^{10}Be in certain geomorphic units. The ^{10}Be concentration in fluvial sand bars is a balance between nuclide production in the target secondary material, and the addition from bedrock substrate during surface lowering, and the rate of denudation of any transported boulders, as well as nuclide removal from decay and transport. Thus a catchment-averaged sediment sample may reflect a strong local denudation rate signal, especially if the nuclide component from bedrock and boulders in transport is high (this point is discussed further in Chapter 9 with respect to sediment samples that were taken in the vicinity of bedrock bar samples). A further observation that Muzikar & Granger (2006) make is that the ^{10}Be concentration in swale sediment is balanced between production (in the target material and the supply from the bars) and removal (decay and transport of sediment off the fan). Thus there may be a difference in the nuclide concentration between bar samples and swale samples which increases to a maximum until the relief between bars and swales is minimized, resulting in a common surface lowering rate and

common ^{10}Be concentration across the fan. For the reasons of this potential difference in nuclide concentration between bar and swale samples, fluvial samples were taken where possible from *in-situ* sand bars, although this was not always practically possible. Nonetheless, any difference in the nuclide concentration in these different sampling locations is believed to be less important than some of the other uncertainties associated with the catchment-averaged technique. Another factor potentially biasing the catchment-averaged results may be the influence of sediment which runs off from unsealed roads. Motha *et al.* (2004) have estimated that unsealed roads are the main source of suspended sediment in an agricultural catchment in south eastern Australia. Although there are many such roads in southern Africa, the climate over much of the area is semiarid to arid therefore there is less runoff to move sediment clasts from unsealed roads into rivers, in contrast with the temperate Australian environment described by Motha *et al.*, (2004).

Chapter 3 - Methods

3.1 Sampling in the field

3.1.1. General

Sampling rocks and sediments for cosmogenic nuclide analysis is a relatively straightforward procedure. In this section, sampling is divided into that which is done using the catchment-averaged approach, and that which utilises site-specific *in-situ* sampling of bedrock. Successful sampling is predicated on the field worker having a good knowledge of the geomorphic setting of the sampled material, and being able to quantify variables such as geomagnetic location, topographic and other shielding and probable site history, all of which influence production rates of cosmogenic nuclides. The following guide to field sampling is based on various sources, including Gosse & Phillips (2001), Schaller *et al.* (2002), and others.

3.1.2. Catchment-averaged sampling

a. Fluvial material

When using the catchment-averaged approach to cosmogenic nuclide analysis (Kirchner *et al.*, 2001) it is desirable to collect well-mixed fluvial sediment that is representative of the cosmic-ray exposure history of a variety of locations (Kirchner *et al.*, 2001). This means sampling on a well-mixed part of the river, the thalweg, where the most sediment is entrained (Plate 3.1.1). Clearly, sampling the thalweg of a river is not always practical and so the worker in the field must select a location which is both accessible and contains well-mixed material. Often this is on the bluff of a river or on lateral sand bars where flood-deposited fluvial sand is present in abundance. It is unlikely in a currently active river that fluvial sand will have been stored on a sand bar for a geomorphically significant amount of time hence there is no need to employ correction factors for storage when calculating cosmogenic production rates. Most likely the material will have been deposited in a flood event in the recent past (~ last 10-100 years). Of course, the subjectivity of this statement emphasises the critical importance of a sound understanding of the geomorphic history of a sampling location. In the Orange River basin, the recurrence interval of major floods (several thousands of cubic meters per second discharge) is around a

decade, so the material currently found on bluffs and sand bars can be assumed to have undergone little storage that will affect its inventory of long-lived cosmogenic nuclides such as ^{10}Be and ^{26}Al. This is discussed in the light of ^{26}Al and ^{10}Be evidence in Chapter 6.

Another factor in selecting a suitable site is ensuring the sediment is well mixed and representative of the source area. One way of doing this is to take sand from beneath the water level in the present river channel. Cursory analysis of this material with a hand-lens and comparison with material found on bluffs and sand bars reveal any significant textural and compositional differences. Samples are taken from both the active channel and the banks for comparison. The general procedure for sampling fluvial sediment both from active channels and dry river channels is as follows:

1. Measure the longitude, latitude and local elevation of the site;
2. Note surroundings in 360° by means of field sketches/photographs;
3. Excavate ~ 1cm of top surface material to exclude aeolian sediments;
4. Collect a spade-full of sediment and separate the 250-710μm[1] fraction by sieving.
5. Continue collection and sieving until ~ 500g of sediment is collected.

b. Other catchment-averaged sampling

Hillslope colluvium and desert pavement regolith, like fluvial sediment, can be assumed to be well mixed and representative of its source area. As such, it is amenable to the catchment-averaged approach to quantify its cosmogenic nuclide inventory. A sound knowledge of the geomorphic setting of the colluvial material is

[1] N.B. This is the ideal size fraction for working with in the laboratory, however it is not always the most representative size fraction, particularly for low-energy fluvial environments. The size fraction to be collected may therefore be determined by site-specific considerations such as the size of material likely to be transported most often by the river – this is sometimes of the 125-250 μm fraction. This size fraction will experience considerable losses during the etching stage due to its fine-grained nature and it is therefore important that a large amount of material is collected. Similarly, in high fluvial energy environments there may be material much larger than 710 μm being regularly transported. In this case, material of a larger size than will be used in the lab may be collected and crushed prior to etching. The issue of grain size and its influence on cosmogenic nuclide concentration is explored in Chapter 6.

essential, especially since colluvium may be reworked and therefore have a multiplicity of exposure histories. Failure to appreciate that long-term storage of colluvium may have taken place may result in a significant under-estimation of erosion history of the sediment. This constitutes one of the principal challenges to applying the catchment-averaged approach to colluvial material and is explored further in subsequent sections.

The most meaningful results may be gleaned from colluvial material in a relatively simple geomorphic setting, for instance where colluvial material is deposited at the base of a hillslope. This allows the average erosion rate of that hillslope to be quantified. The generalised protocol for sampling is:

1. Measure the longitude, latitude and local elevation of the site;
2. Note surroundings in 360° by means of field sketches/photographs;
3. Excavate ~ 1cm of top surface material to exclude aeolian sediments;
4. Collect ~ 1 kg of sediment. Note that sieving at 250-710μm is likely to be difficult due to the indurated and lithified nature of the sediments. It is best to leave this until the sediments can be wet-sieved in a laboratory.
5. Individual clasts of country rock/colluvial conglomerate may be collected close to colluvial deposits.

3.1.3 Site-specific sampling

Bedrock outcrops are especially well-suited to site specific sampling. Their very nature as residuals in a denuded landscape makes their erosion history of particular interest. In this study, bedrock channels, interfluves, and inselbergs are all of great interest. Inselbergs and interfluves are particularly suited to sampling owing to the usual lack of shielding from overlying material. Vertical sections of bedrock may also be sampled, but care must be taken to adequately quantify the amount of shielding in each case, and it is usually best to calculate the likely amount of material needed to generate useful results prior to sampling. Bedrock bars in river channels, such as those in the Augrabies Falls region, are suited to site-specific sampling provided that due consideration is given to the shielding effect of the channel sides in

deeply incised locations (Plate 3.1.2). Exposed bedrock locations may be sampled in the following way for $^{10}Be/^{26}Al$ analysis:

1. Identify a suitable area of rock to sample. Ideally this will be horizontal or near-horizontal, contain a plane of weakness which may be exploited with a hammer and chisel to loosen the rock, and will spall off relatively easily to leave a surface that is virtually indistinguishable from naturally weathered rock. Eye protection must be worn;
2. Note geomorphic setting, longitude, latitude and altitude of location;
3. Note shielding from surficial cover and topography in 360°. Measure the horizontal angle of the surface using an Abney level and take repeat readings to generate an average.

3.1.4 Non-sampled locations

Many more locations were sampled than are dealt with in this study. This is partly due to time constraints- not all samples collected were processed, but also due to practical difficulties particularly with reference to quartz-poor lithologies and fine grained sediments which resulted in large losses of quartz during processing. Some of these problems were overcome by adapting the lab methods to include novel techniques (see next section) but inevitably, some samples did not produce cosmogenic data.

As noted above, the Vaal River tributary is not dealt with in this study due to problems of lack of quartz (<1%). The same problem was experienced with the Molopo catchment and extensive reconnaissance in both the Vaal and Molopo catchments failed to produce any useful samples. The same problem also applied to smaller tributaries of the Orange River, particularly those in the central Karoo, where lack of quartz and the problem of extensive re-working of colluvial material made the locations unsuitable for cosmogenic nuclide analysis. This was disappointing given that extensive work on contemporary erosion rates is currently being carried out in this area (e.g. Keay-Bright & Boardman, 2006) and cosmogenic-derived long term erosion rates would have complemented these studies.

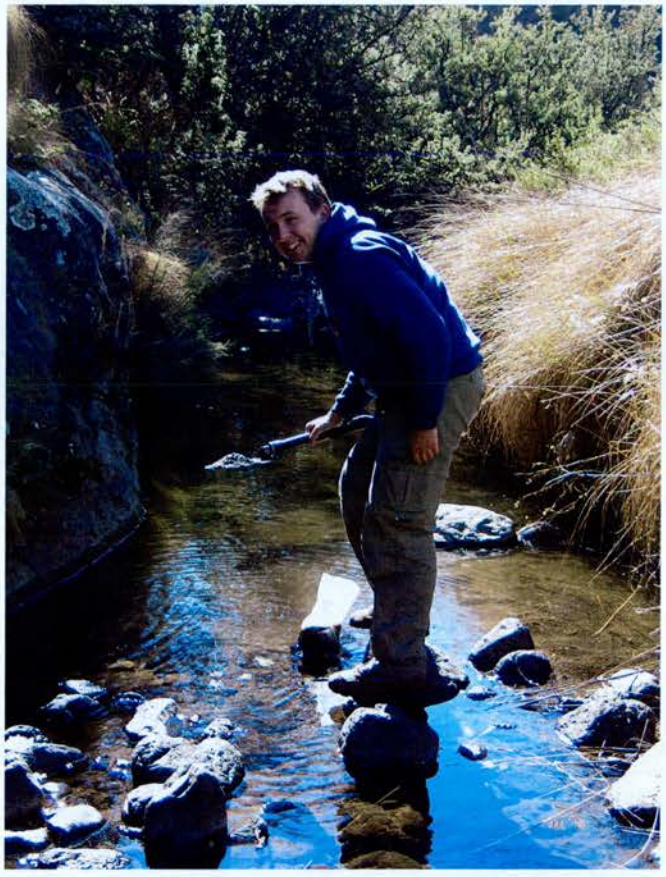

Plate 3.1.1 Sampling a stream in the Golden Gate Highlands National Park.

Plate 3.1.2 Sampling a bedrock bar in the Augrabies Falls region.

Other problems encountered were the low quartz concentrations in sediment in some rivers, particularly tributaries draining the Elliot, Clarens and Burgersdorp formations. It was necessary to hand-pick quartz grains from a large volume of sediment in order to get an erosion rate for some of these locations, and for others to integrate quartz from different tributaries (e.g. sample SA05-14-1 from the Golden Gate Highlands National Park).

Time and budgetary constraints prevented a number of *in-situ* cosmogenic ^{3}He samples from being analysed. These samples were collected from a range of locations, mostly as exposed dolerite cappings on the tops of koppies, which are extensive and ubiquitous in southern Africa. These samples may at some future point be processed and add to the overall picture of erosion rates in southern Africa attempted to be portrayed here.

3.2 Protocol for cosmogenic ^{10}Be and ^{26}Al sample preparation

3.2.1 Preparation of quartz separates

When preparing samples for cosmogenic ^{10}Be and ^{26}Al analysis, the aim is to isolate the quartz fraction, from which in-situ produced ^{10}Be and ^{26}Al can be separated. The following describes the standard protocol for ^{10}Be and ^{26}Al separation from quartz, based on Bierman *et al.* (2002) and others. It is a multi-step process involving the progressive refinement of quartz in the 250-710 μm size fraction. Bedrock samples need to be sawed, split, crushed and ground to 250-710μm prior to sieving. For fluvial and colluvial material, refinement may begin with sieving although some milling of coarser colluvial material may be required. Full details of laboratory protocols used in this study can be found in Appendix 2.

Once the desired size fraction has been obtained, mafic material can be removed by running a hand magnet over the sample and/or putting the sample through an Franz isodynamic mineral separator. Once this stage has been carried out, the material can be treated in dilute hydrochloric acid (HCl) in order to remove iron (Fe) and aluminium (Al) coatings from the mineral grains. The next stage is a 'junk' etch

using several hundred grams of sample in 1l of ~ 1% hydrofluoric acid (HF) left over several days on a shaker table or ultrasonic bath. This is intended to remove the atmospheric ^{10}Be-contaminated outer layer of quartz and begin to break up composite quartz grains and remove feldspars. Around 25 g of sample is then given at least 3 etches in ~ 1% HF and 2% nitric acid (HNO_3) left overnight in an ultrasonic bath. The dilute HF removes non-quartz minerals and etches the surface of the quartz grains. HNO_3 is used for safety reasons. Note that at this stage, large amounts of quartz are likely to be lost, especially if grains are small to begin with. Smaller grains will have a larger surface area to volume ratio and so be more susceptible to acid attack. To produce the desired ~ 30 g of pure quartz at the end of etching often required at least ten times that amount of fluvial sediment from the Orange River. For granite-gneiss samples from the Augrabies Falls region, with a quartz content of ~ 30% and generally larger grain sizes, proportionately smaller sample volumes were required. For samples with a low initial quartz content, a new approach to quartz refinement involving hexaflorosilicic acid (H_2SiF_6) was used (see below). After etching, the concentration of impurities remaining in the quartz sample can be checked by analysis of a dry sample under the microscope.

When all feldspar material is removed, any remaining heavy minerals can be separated using lithium metatungstate (LST) solution. LST is a heavy liquid with a density of 2.80 g cc^{-1} which is mixable with water. It is important that the LST solution has the correct density so that the quartz will float and the heavy minerals will sink. A new approach was implemented which involved the placement of ~ 15g of sample in a centrifuge tube to which ~ 30 ml of LST was added. The sample was in contact with LST solution for around half an hour to allow heavy minerals (e.g. ilmenite) to separate from the quartz. The sample was then centrifuged for ~ 30 minutes, after which the quartz was floated off and dried, while the heavy minerals stayed in the tube. The LST solution was then recycled for further use (see Appendix 2). After rinsing, the quartz is given a final etch in order to remove any residual LST. Before the Be and Al isolation stage is begun, Inductively Coupled Argon Plasma Spectrometry, Optical Emission (ICP-OES) is carried out on a ~ 1g assay of the quartz sample. This reveals the concentration of Be, B, Al, Ti and Fe. The native Be

concentration will reveal whether the native Be can be neglected compared to the Be carrier. The concentration of Al shows whether or not it is necessary to add a ^{27}Al carrier prior to dissolution. It also reveals remaining feldspars in the sample if Al concentrations are greater than ~ 200 ppm. In such a case further etching needs to be carried out to increase the $^{26}Al/^{27}Al$ ratio to make sure that the uncertainty obtained from the AMS measurement is not too high. The quartz assay also gives a guide as to the likely problems that might be encountered with e.g. high Ti, B and Fe content in the samples and how this might be dealt with.

3.2.2 Isolation of ^{26}Al and ^{10}Be

By this stage, ~ 30g of pure quartz should be available for each sample. A process blank is introduced at this stage to measure loading of the sample with contaminants (Bierman *et al.*, 2002). Since ^{9}Be occurs rarely in samples, a known quantity must be added so that the accelerator mass spectrometer can measure the ratio of $^{10}Be/^{9}Be$. ^{9}Be carrier is added to all the samples, including the blank. The amount of carrier used in each sample is a trade-off between handling of the Be target and uncertainties in AMS measurement (Binnie, personal communication, 2005). Whilst a larger amount of carrier makes physical handling of the target easier and allow a longer AMS beam time, more carrier will lower the $^{10}Be/^{9}Be$ ratio of the target and making it difficult to measure the ^{10}Be target signal above the ^{9}Be carrier signal and therefore increase the uncertainties. For a sample-specific discussion of type and amount of carrier used, see below. For Al targets, a ^{27}Al carrier is only generally used if the Al assay reveals samples to have <3000 μg Al (Bierman *et al.*, 2002). As most samples contain considerable natural concentrations of ^{27}Al (as revealed by the Al assay), an Al carrier is not essential. The cleaned quartz plus carriers are dissolved in concentrated HF over several days on a hotplate.

Samples are then fumed using perchloric acid ($HClO_4$). This step is intended to remove fluorides and boron by evaporation of a high boiling point compound. It is particularly important to include this step where the quartz assay reveals there to be a high proportion of Fe in the sample. Care must be taken at this stage not to allow the hotplate temperature to become to high, otherwise Al complexes may evaporate,

affecting the $^{26}Al/^{27}Al$ ratio (see Section 3.3). After this the anion column stage is designed to remove anions (e.g. $FeCl_4^-$) from the sample using resin-filled columns and varying strengths of HCl. Titanium can be removed as oxide-hydrate from the eluted sample at pH 4. This stage is essential for most samples, and particularly so for South African bedrock samples which have been revealed by ICP-OES to contain a high proportion of Ti, which can reduce Be beam currents (Binnie, personal communication, 2005). The cation column stage is then carried out and is where Be and Al are split into separate aliquots. Acids of different molarity are used to selectively adsorb and desorb cations onto resin beads, and separate the Be and Al. The procedure is similar to the anion column stage (see Appendix 2).

An aliquot of sample is taken to assess whether the column stages have been effective in separating Al and Be. A small aliquot is taken from the Be fraction for Al and diluted then sent for ICP-OES analysis. Those samples with high (>400ppm Al) are likely to run badly in the AMS due to Al swamping the Be and lowering the beam current. It may therefore be prudent to repeat the cation column stage so that a better Be-Al separation is obtained (Binnie, personal communication, 2005). A final perchloric fume of the Be sample is carried out prior to precipitation of $Be(OH)_2$ in order to remove B, which contains ^{10}B at 20% abundance (atom ratio), which is an isobar of ^{10}Be and thus can interfere with AMS measurement of ^{10}Be (Bierman *et al.*, 2002). Hydroxides of Al and Be are then precipitated from solution by adjusting pH to between pH 9 and 10 (for Be) and between pH 8 and 9 for Al. In the next stage, hydroxides of Be or Al are baked to their oxides, then packaged for shipping to the AMS laboratory. The very last step in the long process of obtaining Be and Al from bedrock or sediment samples involves mixing the sample with Niobium (Nb) powder (for Be) and Ag for Al, inert metals that are pressed into the targets to provide thermal and electrical conductivity and thereby prevent sparking of the sample in the AMS.

3.3 Sample specific considerations

A number of problems presented themselves in the course of field sampling that had implications for laboratory analysis. These necessitated special treatment of certain samples, and the employment of novel laboratory techniques that add to the standard preparation technique following Bierman *et al.* (2002) described in Section 3.2. The problems, and their solution where appropriate, are given below.

3.3.1 Low quartz content

This was a problem both for samples derived both from low quartz lithologies and samples which contained small size fractions of quartz (Table 3.3.1). In general the volume of the 125-250 μm size fraction was severely reduced during sample processing due to dissolution by HF at the etching stage. For bedrock samples, this was not a problem since the 250-710 μm size fraction was selected after crushing and sieving. For most catchment-averaged samples, particularly those derived from the coarser Molteno sandstones, those from the Augrabies Falls region and that from the Fish River predominantly contained single quartz grains in the 250-710 μm size fraction (Section 4.1). The problem was first encountered with the first batch of samples to be processed (SA03 series). After etching, a small amount of quartz resulted, which was partly from having fine grained sediment to begin with, and also the result of having to repeat etchings several times more than usual (6 times in total) in order to eliminate composite grains (dealt with separately below). These low quartz masses at dissolution nonetheless gave reliable results (Table 3.3.2), which is testament to both the sensitivity of AMS analysis and the dedication of the SUERC AMS team.

Unit	Quartz	Feldspar	Rock fragments	Other	Interstitial material	Samples
Molteno	64.3	9.7	0.1	1.0	24.7	SA04-35-1, 36-1, 42-1
Elliot	58.0	11.7	0.5	1.9	28.3	SA04-37-1
Clarens*	53.5	14.7	0.1	1.5	30.2	SA04-14-1

Table 3.3.1 Typical quartz content of Karoo Supergroup sandstones. All values are average percentages (Eriksson *et al.*, 1994). The Clarens value (*) is an average of the wet desert Clarens sandstone and the aeolian Clarens sandstone).

Sample	Mass at dissolution (g)	Blank corrected $^{10}Be/^{9}Be$ ratio	Standard Uncertainty
SA03-5-1	1.831	2.03 E-13	2.74 E-14
SA03-6-1	0.713	4.56 E-14	5.23 E-15
SA03-7-1	0.817	4.22 E-14	4.86 E-15

Table 3.3.2 Initial batch of samples, showing low initial quartz mass and extremely low measured $^{10}Be/^{9}Be$ ratios. Blank ratio was $2.15x10^{-14} \pm 6.21x10^{-15}$.

The next batch of fluvial samples to be analysed (including those samples that were derived from fine grained Clarens, sandstone, fine grained Molteno sandstone and fine grained grussified granite) were treated with a great deal of care at the etching stage and ~ 350 μg of a special low ratio carrier with a $^{10}Be/^{9}Be$ ratio of $3x10^{-15}$ was added (kindly donated to the NERC CIAF by F. v. Blanckenburg, University of Hannover). For the other samples, ~ 250 μg of Spectrosol ^{9}Be carrier ($^{10}Be/^{9}Be$ ratio of $2x10^{-14}$) was used. This was combined with the technique of using hexaflorosilicic acid (H_2SiF_6) to carry out the initial etching stages. The H_2SiF_6 attacks most minerals in a sample apart from quartz, thus the quartz concentration in a sample can actually be increased with successive treatments and is followed by three etches in HF to remove atmospheric ^{10}Be contamination from the grain (Binnie, personal communication, 2005). This technique seemed to be reasonably effective at preventing quartz loss to the extent of making a sample impossible to run. These samples would have been impossible to run without these techniques, and they represent some of the lowest $^{10}Be/^{9}Be$ ratios yet measured at SUERC (Table 3.3.3)

Sample	Quartz mass (g)	Blank Corrected ratio	Standard Uncertainty
SA04-19-1-A	0.43	8.77 E-15	1.89 E-15
SA-04-30-1-A	5.36	4.59 E-13	1.77 E-14
SA04-41-1	3.41	8.41 E-14	3.90 E-15
SA04-42-1	4.46	2.06 E-13	6.91 E-15
SA05-14-1	5.53	7.13 E-14	4.33 E-15

Table 3.3.3 Samples with low initial quartz mass. Blank ratio was $4.40x10^{-15} \pm 9.18x10^{-16}$ (low ratio carrier, one of the lowest measured at SUERC).

3.3.2 Quartz inclusions and composite grains

One of the problems encountered which affected some bedrock samples was high titanium (Ti) content. This was not initially realised hence some samples (samples SA04-22 to 24) suffered from high Ti content during AMS, which reduced the Be beam currents and consequently the number of ^{10}Be atoms counted, thus increasing the statistical uncertainty. This was subsequently rectified for other samples by re-introducing a vigorous Ti precipitation step, as well as carrying out an assay of samples prior to dissolution to test the concentration of common trace metals such as Fe and Ti. This allowed the anion column and Ti steps to be carried out more vigorously in samples which suffered from high concentrations of these metals. There was a subsequent improvement in the ^{10}Be/^{9}Be ratios after this step was introduced. These problems were encountered during the author's first experience with preparing cosmogenic ^{10}Be targets and the technique was later refined and developed.

3.3.3 Cosmogenic Helium-3 samples

A number of dolerite samples were collected from bedrock interfluves on residual koppie landforms across the Republic of South Africa. The intention was to carry out cosmogenic ^{3}He analysis on the samples in order to quantify benchmark rates of erosion on these most resistant landscape features and compare the rates with rates derived from cosmogenic ^{10}Be and ^{26}Al from fluvial and bedrock samples. Of the samples collected, several were taken from shielded sites in order to assess the non-cosmogenic component of ^{3}He in the samples, including one from ~ 70 m below the surface. Whilst these samples proved relatively easy to extract suitable clinopyroxenes, the nucleogenic component was calculated to be sufficiently high that relatively large volumes of material would be required (Stuart, personal communication, 2004). Numerous problems were encountered during sample processing of exposed samples, notably the lack of suitable cosmogenic ^{3}He-retaining clinopyroxene and olivine minerals. The exposed bedrock samples were extremely well-weathered and clinopyroxenes had apparently begun to break down and form plagioclase. Olivine was not widespread in the Karoo dolerites sampled. As plagioclase does not retain cosmogenic ^{3}He, the samples were not suitable for ^{3}He

analysis. Whilst unlimited time and the freedom from budgetary constraints could undoubtedly have yielded sufficient clinopyroxenes for ^{3}He analysis, this was not possible in the course of this project.

3.4 Accelerator mass spectrometry analysis

Accelerator mass spectrometry is crucial for analysis of cosmogenic ^{10}Be and ^{26}Al. Indeed, before the advent of high resolution accelerator mass spectrometers (AMS) in the mid- 1980s, routine measurement of terrestrial ^{10}Be concentrations was extremely difficult. The basic principle of an AMS is that atoms are extracted from a sample by ionisation, acceleration and then separation on the basis of their momentum, charge and energy (Tuniz *et al.*, 1998). The ions are deflected by powerful magnets and their relative concentrations are measured. Accelerator mass spectrometers have five basic components (as shown in Figure 3.4.1): an ion source; an injection system; an accelerator (either of the tandem, Van de Graff, cyclotron or linear type); high energy selectors (electromagnets) and a detection system incorporating an electrostatic analyser.

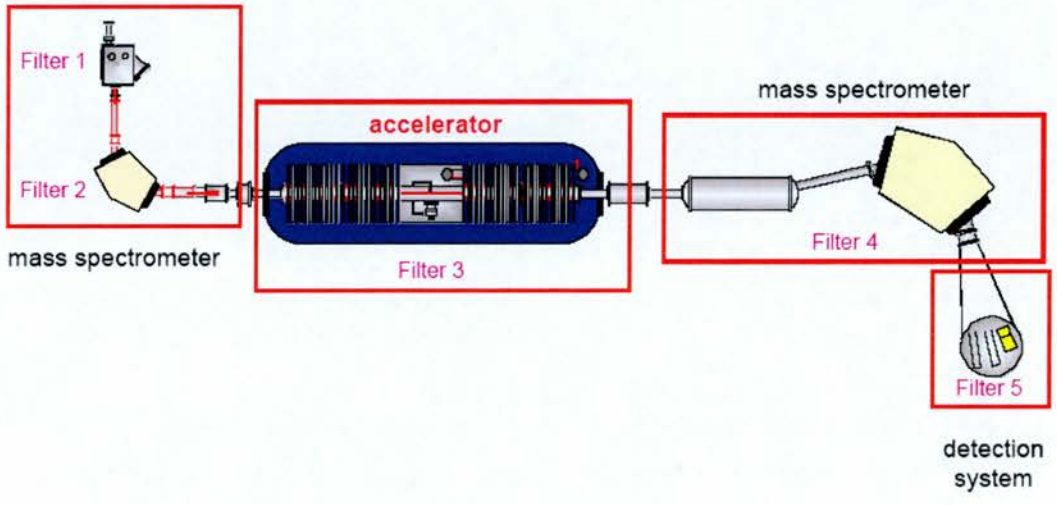

Figure 3.4.1 Schematic diagram of an accelerator mass spectrometer (Kubik, personal communication, 2006).

In the AMS at SUERC, sample targets are placed before a negative ion sputter source. Sputter ion sources use a Cs reservoir which is heated and the resulting Cs^{+} beam is focused on the samples and accelerated to form negative secondary ions

from BeO or Al_2O_3 sample targets. The resulting ions ($^{10}Be^{16}O^-$ and $^{9}Be^{17}O^-$ ions in the case of Be, Al^{3-} in the case of Al) are then focused through a lens and electromagnet before being injected into the van der Graff accelerator. There, the ion beam is accelerated towards the high voltage positively charged terminal. For Be, upon reaching the terminal the $^{10}Be^{16}O^-$ and $^{9}Be^{17}O^-$ are stripped of their ions by a gas or foil stripper or both to produce $^{10}Be^{3+}$ or $^{10}Be^{2+}$ charge states (Tuniz *et al.*, 1998). The positive ^{10}Be ions are then repelled away from the terminal.

In the detector, a gas filled chamber slows the ^{10}Be ions and produces electrons. These electrons drift toward anodes along the length of the chamber where the charge is recorded. Because the isobars ^{10}Be and ^{10}B lose energy at different rates they have unique identifiable signatures. These signatures are recorded by the anodes along the detector which allows discrimination between the isobars ^{10}Be and ^{10}B. Each sample is run, typically, for a period of several minutes and these runs are usually repeated two or three times if there is enough sample left. National Institute of Standards and Technology (NIST) standards are run with every ~ 10 samples to track any drift in the accelerator and to correct the $^{10}Be/^{9}Be$ ratios (Binnie, 2004, Tuniz, 1998).

AMS has been put to use in determining exposure ages of meteorites, in identifying glacial events, dating landforms, volcanic events and quantifying earth surface processes. There are also multiple uses of AMS in archaeological dating, biomedicine, industry and in atomic, nuclear and particle physics. Some of the range of applications and principal achievements of accelerator mass spectrometry are summarised in Table 3.4.1.

Application	Details
Extraterrestrial	Supernovae explosion dating
	Geomagnetic field variations
	Solar minima dating
	Meteoritic dating
Environmental sciences	Atmospheric circulation
	Oceanography
	Glaciology - flow parameters, ice dating
	Hydrology - groundwater flows, pollution
Geosciences	Impact cratering
	Volcanic event dating
	Fluvial system quantification
Material science	Radioisotope production
Medical science	Radioisotope production

Table 3.4.1 Applications and principal achievements of accelerator mass spectrometry from Tuniz *et al.*, 1998 and Jull and Burr, 2006.

^{10}Be and ^{26}Al are now routinely measured by AMS around the world (Table 3.4.2). The AMS used in this study is a 5 MV terminal-class machine from the National Electrostatics Corporation based at the Scottish Universities Environmental Research Centre (SUERC) at East Kilbride. The spectrometer features two high-intensity sputter ion sources, one with a 134 sample capacity and the other with a solid and gas sample capability. All rare ion detection is with a single versatile gas ionisation detector using thin SiN windows for heavy-ion analysis ^{10}Be is measured at SUERC at 1-3% precision with characteristic ^{10}Be/^{9}Be ratios in the order of 1×10^{-15} (Maden, personal communication, 2005).

Facility	Maximum terminal voltage (MV)
Scottish Universities Environmental Research Centre (SUERC), UK	5
Australian National University, Canberra, Australia	15.5
Gif-sur-Yvette, France	3
Lawrence Livermore National Laboratory, University of California, USA	10
Australian Nuclear Science and Technology Organisation (ANSTO), Lucas Heights, Australia	10
Purdue Rare Isotope Measurement Laboratory (PRIME), USA	8
Swiss Federal Institute of Technology (ETH), Zurich, Switzerland	6

Table 3.4.2 AMS Facilities around the world engaged in routine measurement of both ^{10}Be and ^{26}Al (*after* Cockburn & Summerfield, 2004).

3.5 GIS Analysis

A combination of approaches was used in calculating data about the sample sites, particularly the basin-wide samples, including GIS analysis of SRTM-derived 90 m resolution digital elevation models (DEMs), DEMs derived from 10 m resolution aerial photographs as well as analysis of 1:50,000 topographic sheets, 1:250,000 geological and topographic maps, and 1:10,000 aerial photographs (Plate 3.5.1). The technique used depended on the spatial scale of the required data, as described below.

3.5.1 Basin-wide elevation

When a sample of sediment is collected for basin-wide cosmogenic analysis, its location at the point of collection clearly does not represent the elevation of the clasts that make up the sample when they were in-situ. Therefore an average elevation for the basin, representative of the source of the clasts, must be calculated. For both the main channel of the Orange River and the tributary channels, this was done using

Plate 3.5.1 Satellite image of the Augrabies Falls region labelled with location of main Augrabies Falls, Twin Falls (a knickpoint on a tributary anabranch), the inselberg Moon Rock and the Swartrante Hills. Note that flow of the Orange River is from the bottom right to the top left of the image (*from* Google Earth).

topographic maps where the appropriate contour intervals (either 50 m or 100 m) were taken and the percentage of the total basin area at that elevation was worked out. The production rates were then calculated for these elevations and weighted according to area. To get the total elevation-scaled production rate for the basin, the area weighted average production rate was used.

3.5.2 Basin area

The area of each basin was again calculated by a combination of DEM and topographic map analysis. The area of the main Orange River was worked out from the 90 m DEM whilst the area of smaller tributary catchments was calculated by detailed analysis of 1:250,000 and 1:50,000 scale topographic maps. In both cases, the area was calculated from drainage lines and interfluve contour lines. Once again, some of the tributaries were extremely small (<10 km^2) and therefore it was impossible to accurately quantify their area using the 90 m resolution DEM.

3.5.3 Basin-wide lithology

The relevant geological maps were used to work out the proportion of which principal lithologies made up each basin area (see Appendix 3). This was aided by B. King (unpublished data) who has constructed a detailed dataset of dominant lithological units in each of the 1:50,000 geological sheets for South Africa. This dataset was adapted to cover the Orange River basin (see Appendix 3), and information on lithology of each tributary basin sampled is given in the Results section.

3.5.4 Latitude

Basin-wide samples cover a range of latitudes as well as altitudes. For very small tributary basins (<100 km^2) the local latitude where the sample was taken was used in calculations of scaling factors. Where the main Orange River channel was sampled, the area upstream covered often a large latitude belt. Where this was the case, an area-weighted average latitude was used for scaling factor calculations, and

the average latitude was calculated in the same way as described for calculating basin-wide elevations.

3.5.5 Gradient and relief

The gradient of the main Orange River channel was calculated using river long profile plots based on 1:50,000 topographic maps (Summerfield *et al.*, unpublished data) covering the mouth of the river at Alexander Bay to approximately 350 km inland. This included the stretch of the river in the Augrabies Falls region. The gradient was measured over ~ 20 km stretches of the river and the change in elevation noted to give the gradient in m km^{-1}. The basin relief was calculated as the maximum to minimum basin elevation derived from the maximum elevation of the basin (3282 m at Mont aux Sources (Wellington, 1955)) and the elevation of the local sampling point. The relief ratio was calculated as the basin relief divided by the maximum length of the river (2090 km, Wellington, 1955). The calculations described above follow the methods of Summerfield & Hulton (1994).

3.6 General comments on the data

3.6.1 Scaling factors

The results presented here use the scaling factors of both Dunai (2000) and Stone (2000) (based on Lal, 1991) as described in previous sections to calculate erosion rates in millimetres per thousand years (mm ka^{-1}). Averaging times are also calculated in thousands of years. The higher the erosion rate, the faster the memory of previous denudation rates is erased - i.e. the averaging time is smaller (Schaller & Ehlers, in press). It will be noted from the full set of results presented in Appendix 4 that there is considerable difference in the erosion rates calculated from the two methods – there is around 12% difference in erosion rates calculated using the Dunai (2000) and Stone (2000) scaling factors (Table 3.6.1, Plate 3.6.1). Stone's (2000) scaling factors transform Lal's (1991) polynomials from being based on altitude to being based on air pressure. Stone (2000) includes data for Antarctica so that production rates can be calculated for regions of abnormal air pressure.

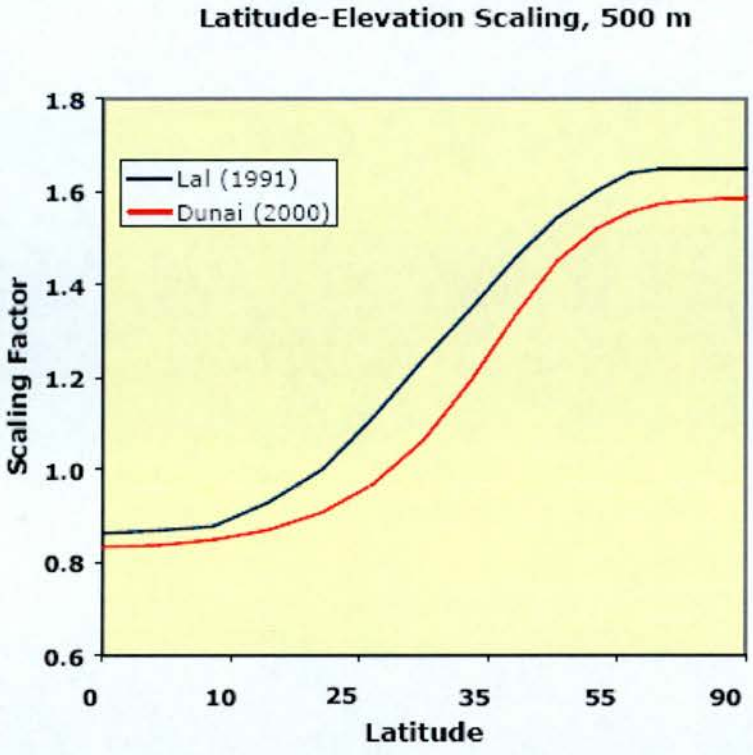

Plate 3.6.1 Latitude elevation scaling for 500 m elevations using the Lal (1991) and Dunai (2000) scaling factors (Dunai, personal communication, 2006). Stone (2000) uses Lal (1991) as its basis.

Dunai's (2000) scaling factors, also based on air pressure, incorporate non-dipole contributions to the geomagnetic field and use data with "known" geomagnetic parameters. As can be seen from Table 3.6.1, the difference in the erosion rates compared by the two different methods are roughly twice the percent uncertainty on the calculated erosion rates.

Sample	Geographic Latitude (degrees south)	Elevation (m)	Stone production rate spallation only (at $g^{-1} a^{-1}$)	Dunai production rate spallation only (at $g^{-1} a^{-1}$)	10Be (at g^{-1})	Std uncertainty (at g^{-1})	ε (mm ka^{-1}) Spallation only (Stone)	± std uncertainty	ε (mm ka^{-1}) Spallation only (Dunai)	± std uncertainty	% Difference (Stone/ Dunai)
SA04-28-1	28.0	683.7	6.9	6.03	6.73E+05	7.77E+02	6.15	0.36	5.07	0.42	17.6
SA04-29-1	25.9	1216.1	10.7	8.69	1.53E+06	1.77E+03	3.83	0.23	3.12	0.26	18.5
SA04-35-1	31.0	1762.0	16.0	14.62	1.73E+06	1.99E+03	5.52	0.32	4.76	0.40	13.8
SA04-37-1	31.0	1966.0	18.4	16.91	4.63E+05	5.43E+02	23.69	1.39	21.48	1.79	9.3
SA04-42-1	29.0	1296.0	11.1	9.86	9.43E+05	3.16E+04	6.72	0.72	5.96	0.40	11.3
SA05-14-1	28.0	2314.0	21.7	19.74	2.62E+05	1.59E+04	49.08	5.82	44.60	3.77	9.1

Table 3.6.1 Differences between Dunai and Stone calculated erosion rates for selected samples chosen for their contrasting latitude and elevations. Full sample details are given in Appendix 4.

Given that there is still considerable uncertainty in scaling factors (as evidenced by the multiplicity of scaling schemes including Desilets & Zreda (2006), Lifton (2005), and shielding correction factors (e.g. Dunne *et al.*, 1999)), the data presented here contain full sample details (Appendix 4) as well as the methods used to calculate the erosion rates (Section 3.2) so that the data may be corrected if a single set of scaling factors are agreed upon at some future dates (it is the aim of the sister projects CRONUS-EU and CRONUS-Earth to do this). The arguments in the forthcoming sections will not be substantially altered by any minor revisions to the absolute rates of erosion. This thesis is primarily concerned with elucidating the first order of magnitude rates of erosion for large parts of the Orange River and Augrabies Falls region and many of the arguments here on the evolution of the southern African landscape hinge on the relative, rather than absolute, differences in rates of denudation between various areas.

3.6.2 Half-life of ^{10}Be

There is ongoing debate as to the true half life of ^{10}Be, it has been reported as, variously, as being between 1.51 Ma (Hofmann *et al.*, 1987) and 1.34 Ma (Inn *et al.*, 1987). Middleton (1993) determined ^{10}Be's half life to be 1.5 Ma. All calculations have been carried out using the conventionally accepted ^{10}Be half-life of 1.51 Ma and an ^{26}Al half-life of 0.70 Ma. These are the values used in determination of the ratios of NIST standards in use at SUERC, where analyses were carried out. Unless otherwise stated, the data presented here are normalised using a primary standard material where ^{10}Be/^{9}Be = 3.00 x10^{-11}. This corresponds to a ^{10}Be production rate of 5.1 ± 0.3 at g^{-1} a^{-1} and a ^{10}Be half-life of 1.51 Ma. The CIAF samples presented here (see Chapters 7 and 8) use NIST SRM 4325 as primary standard for normalisation, where the ^{10}Be/^{9}Be ratio is 3.06 x10^{-11}. The CIAF sample concentrations must therefore be multiplied by 1.02 to make them comparable with the rest of the samples presented in this study.

3.6.3 Muogenic production

As discussed in Section 2.5, muogenic production is not considered to be a major factor in cosmogenic production rate calculations in southern Africa. Erosion rates were calculated for spallation only and with both spallation and muons to assess the difference that inclusion of muogenic production makes to the erosion rate estimates. All were calculated using Stone's (2000) scaling factors (Table 3.6.2).

It can be seen from Table 3.6.2 that there is no significant difference (< 4%) between the erosion rates calculated using Stone's spallation only and combined spallation and muogenic production. Indeed, the difference in erosion rates calculated by the two methods is less than the uncertainty on the erosion rate estimates (~ 6%). Table 3.6.3 shows the difference in erosion rates calculated using Dunai's scaling factors assuming spallation and no muogenic production and assuming spallation and 2% muogenic production. It can be seen that once again there is no significant variation in erosion rate calculated using the two methods (~ 1%). Indeed, once again the variation is less than the uncertainty on the erosion rates for a range of different altitudes and latitudes. As muons are a part of cosmogenic nuclide production (albeit a small part, ~ 3% of total contribution at the surface) their inclusion is justified (Dunai, personal communication, 2006). All erosion rates unless otherwise stated include production from both muons and spallation.

Sample	Geographic Latitude (degrees south)	Elevation (m)	Stone production rate spallation only (at g^{-1} a^{-1})	Stone production rate spallation and muons (at g^{-1} a^{-1})	^{10}Be (at g^{-1})	Std uncertainty (at g^{-1})	ε (mm ka^{-1}) Spallation only (Stone)	± std Uncert.	ε (mm ka^{-1}) Spallation and muons (Stone)	± std uncertainty	% Difference (Spallation/ spallation & muons)
SA04-28-1	28.0	683.7	6.94	6.91	6.7E+05	7.8E+02	6.15	0.51	5.85	0.49	4.8
SA04-29-1	25.9	1216.1	9.82	9.74	1.5E+06	1.8E+03	3.83	0.32	3.53	0.29	7.8
SA04-35-1	31.0	1762.0	16.03	15.86	1.7E+06	2.0E+03	5.52	0.46	5.19	0.43	6.0
SA04-37-1	31.0	1966.0	18.42	18.21	4.6E+05	5.4E+02	23.69	1.97	23.15	1.93	1.1
SA04-42-1	29.0	1296.0	11.07	10.98	9.4E+05	3.2E+04	6.72	0.06	6.67	0.07	0.7
SA05-14-1	28.0	2314.0	21.71	21.45	2.6E+05	1.6E+04	49.08	0.06	48.47	0.08	1.2

Table 3.6.2 Comparison of erosion rates calculated with spallation only, and spallation and muogenic production for selected samples, using Stone's (2000) scaling factors and a production rate of 5.1 at $g^{-1}a^{-1}$ in both cases. Percent difference is between erosion rates calculated from spallation scaling only and spallation and muogenic production. Full sample details can be found in Appendix 4. These samples are taken from the main channel of the Orange River and are representative of a range of altitudes and latitudes.

Sample	Geographic Latitude (degrees south)	Elevation (m)	Dunai production rate spallation only (at g^{-1} a^{-1})	Dunai production rate spallation and 2% muons (at g^{-1} a^{-1})	^{10}Be (at g^{-1})	Std uncertainty (at g^{-1})	ε (mm ka^{-1}) Spallation only (Dunai)	± std uncertainty	ε (mm ka^{-1}) Spallation and 2% muons (Dunai)	± std uncertainty	% Difference (Spallation/ Spallation & muons)
SA04-28-1	28.0	683.7	6.03	6.01	6.73E+05	7.77E+02	5.07	0.30	5.05	0.30	0.35
SA04-29-1	25.9	1216.1	8.69	8.64	1.53E+06	1.77E+03	3.12	0.18	3.10	0.18	0.63
SA04-35-1	31.0	1762.0	14.62	14.49	1.73E+06	1.99E+03	4.76	0.28	4.72	0.28	0.94
SA04-37-1	31.0	1966.0	16.91	16.75	4.63E+05	5.43E+02	21.48	1.26	21.27	1.25	0.96
SA04-42-1	29.0	1296.0	9.86	9.79	9.43E+05	3.16E+04	5.96	0.07	5.92	0.07	0.74
SA05-14-1	28.0	2314.0	19.74	19.54	2.62E+05	1.59E+04	44.60	0.08	44.14	0.08	1.02

Table 3.6.3 Comparison of erosion rates calculated with spallation only, and spallation and muogenic production for selected samples, using Dunai's (2000) scaling factors. Percent difference is between erosion rates calculated from scaling only and spallation and 2% muons production. Full sample details can be found in the Appendix. These samples are taken from the main channel of the Orange River and are representative of a range of altitudes and latitudes.

3.6.4 Decay constant

Not only does the value of the decay constant (λ) vary with the half life of ^{10}Be, the inclusion of the decay constant in catchment-averaged calculations may also affect the resulting erosion rate. The decay constant is the inverse average life-time of ^{10}Be. The average life-time of ^{10}Be is its half-life (1.51×10^6 times ln(2)). As discussed in Section 2.5, the effect of the decay constant will be different for each individual clast of sediment, therefore the inclusion of an incorrect value of the decay constant in calculations will result in inaccurate erosion rates. On the other hand, its exclusion (i.e. neglection from the calculations) may introduce a greater source of error into the calculations than if it were left in. To investigate this problem, the erosion rate of a number of samples from contrasting elevation and latitudes are calculated both including the decay constant and leaving it out. The results are given in Table 3.6.4. As can be seen, there is little difference in the erosion rate with and without decay (< 4%). As radioactive decay is a reality, the decay constant is justifiably included in this study (Dunai, personal communication, 2006).

Sample	Geographic Latitude (degrees south)	Elevation (m)	Stone production rate spallation only (at $g^{-1} a^{-1}$)	^{10}Be (at g^{-1})	Std uncertainty (at g^{-1})	ε (mm ka^{-1}) (including decay)	± std uncertainty	Av. time (ka)	ε (mm ka^{-1}) (no decay)	± std uncertainty	Averaging time (ka)	% Difference (decay/no decay
SA04-28-1	28.0	683.7	6.9	6.73E+05	7.77E+02	5.88	0.35	101.37	6.15	0.36	96.87	4.4
SA04-29-1	25.9	1216.1	10.7	1.53E+06	1.77E+03	3.56	0.21	167.41	3.83	0.23	155.46	7.0
SA04-35-1	31.0	1762.0	16.0	1.73E+06	1.99E+03	5.25	0.31	113.63	5.52	0.32	108.00	4.9
SA04-37-1	31.0	1966.0	18.4	4.63E+05	5.43E+02	23.42	1.38	25.46	23.69	1.39	25.16	1.1
SA04-42-1	29.0	1296.0	11.1	9.43E+05	3.16E+04	6.72	0.06	88.66	7.00	0.06	85.19	4.0
SA05-14-1	28.0	2314.0	21.7	2.62E+05	1.59E+04	49.08	0.06	12.15	49.35	0.06	12.08	0.5

Table 3.6.4 Variation in erosion rate for selected samples from contrasting elevation and latitudes where the decay constant of 4.59×10^{-7} is used (based on ^{10}Be half-life of 1.51×10^{6}). Percent difference relates to the difference between erosion rate calculated with and without decay.

3.6.5 Geomagnetic variability

As discussed in Chapter 2, geomagnetic variability over time has been quantified and cosmogenic production rates can be corrected for variation in the earth's geomagnetic field. As described in Chapter 3, a new effective latitude can be calculated for a sample on the basis of the SINT-800 (or SINT-2000) record (Guyodo & Valet, 1999, Valet, 2005). This uses the averaging time of a sample to calculate the variation in the strength of the earth's magnetic field and a scaling factor which can be then used to calculate a new 'effective latitude', from which production rates and a geomagnetic corrected erosion rate can be calculated. Geomagnetic corrected erosion rates are presented in Table 3.6.5 for samples with a range of averaging times. As can be seen from Table 3.6.5, the inclusion of the geomagnetic correction factor can lead to significant differences in the calculated erosion rates (average difference ~16%). As such, it is too important a factor to leave out of erosion rate calculations and all bedrock samples (Chapters 7-9) are calculated with a geomagnetic correction. Catchment averaged samples (Chapters 4-6) are not subject to these corrections. Each quartz grain in a catchment averaged sample may represent a different part of the basin and therefore a different original latitude (and hence a different new effective latitude when subject to geomagnetic correction). The question of palaeo-geomagnetic latitude in large basins is likely to be complicated by the wide range of latitudes spanned by basins such as the Orange River, and the uncertainties in the former extent of such basins.

Sample	Lat.	Height (m)	Stone production rate spallation muons (at g^{-1} a^{-1})	[10Be]	±	ε (mm ka^{-1}) (no geomag)	±	Av. time (ka)	New eff. lat.	New eff. P rate (at g^{-1} a^{-1})	ε (mm ka^{-1}) (with geomag)	±	# of iterations	% diff.
SA04-17-1	28	655	6.91	2.42E+04	1.67E+03	143.23	13.08	4.16	41.16	7.37	181.22	16.41	2	20.97
SA04-15-1	28	670	9.74	4.55E+05	7.66E+03	8.60	0.54	69.32	36.43	7.93	10.11	0.62	3	14.91
SA04-9-2	28	660	15.86	7.81E+04	4.50E+03	49.64	4.13	12.01	35.71	7.54	57.24	4.71	2	13.29
SA04-6-1	28	664	18.21	1.21E+06	2.35E+04	3.06	0.19	194.88	37.40	8.03	3.69	0.23	3	17.14
SA04-3-2	28	451	10.98	4.20E+05	8.43E+03	7.50	0.47	79.46	37.97	6.47	8.91	0.55	2	15.82

Table 3.6.5 Showing variation in erosion rates with and without geomagnetic shielding correction for selected samples with different averaging times. Percent difference reflects the difference between the uncorrected erosion rate and geomagnetic corrected erosion rate.

3.6.6 Blank corrections

Calculations of ^{10}Be concentration were carried out with respect to a number of process blanks (containing only ^{9}Be carrier). Each batch of samples contained at least one process blank. Where large relative standard uncertainties (>25%) were associated with a process blank, a weighted average of several process blanks including the imprecisely determined process blank was used (See Appendix 4 for which blanks were used for which samples). Some samples were anticipated to have extremely low numbers of ^{10}Be atoms as a result of very low quartz masses at dissolution. Where this was the case, a special low ^{10}Be concentration carrier (SA05-Y-1) was used in the process blank as described in Section 4.2. The details of the blanks used in this study are given in Table 3.6.6.

Blank	^{9}Be Mass (g)	[^{10}Be/^{9}Be]	St uncertainty [^{10}Be/^{9}Be]
Average of Good blanks	3.15×10^{-4}	1.58×10^{-14}	3.43×10^{-15}
AFB	3.11×10^{-4}	1.52×10^{-14}	2.93×10^{-15}
SA04-X-4	3.03×10^{-4}	1.23×10^{-14}	1.88×10^{-15}
SA05-X-2	3.58×10^{-4}	1.41×10^{-14}	2.72×10^{-15}
SA05-Y-1	3.54×10^{-4}	4.40×10^{-15}	9.184×10^{-16}

Table 3.6.6 Blanks used in this study. The carrier used in all the blanks apart from SA05-Y-1 has an inherent ^{10}Be/^{9}Be ratio of above 1×10^{-14} and consequently these blanks are not contaminated with ^{10}Be from sample processing. The blank SA05-Y-1 contains carrier kindly donated by Friedhelm von Blanckenburg and has a ^{10}Be/^{9}Be ratio of above 3×10^{-15} which agrees to within uncertainties with the 4.4×10^{-15} measured here. Note that for the CIAF samples, a separate process blank was used. Details of this are given in Appendix 5.

3.6.7 Aluminium data

It will be noticed that in general there are few Al samples. This is due to difficulties with the perchloric fuming stage after separating the Al fraction. During the fuming stage, the samples reached too high a temperature and some sample was lost as $AlCl_3$ vapour. This resulted in a lack of measured ^{26}Al in some samples, and in others, a spuriously low ratio, which gave on analysis with ^{10}Be data too high a ^{26}Al/^{10}Be (i.e.

ratio >6.1 ± 0.5, in the forbidden zone of the graph of ^{10}Be vs. ^{26}Al (see next Chapters).

3.6.8 Uncertainties

Unless otherwise stated, the uncertainties reported here are total uncertainties: i.e. they incorporate the analytical uncertainty on the analytical data and the uncertainty associated with production rates and in the chemistry (e.g. uncertainty of the sample mass). The method of calculating the uncertainties is described in Chapter 2. The uncertainties are reported as standard uncertainties (i.e. one sigma). They are calculated by adding the squares of the relative uncertainties for the AMS measurement, the production rates and chemistry uncertainties under the square root. As each uncertainty is one sigma, the resulting uncertainty is also one sigma. Much of the argument in subsequent chapters hinges on small relative differences in erosion rates between different samples. Since all samples are subject to roughly the same production rate uncertainties, it may be more revealing to just consider analytical uncertainties (i.e. the uncertainty on the measured $^{10}Be/^{9}Be$ ratio, presented together with the erosion rate data). This makes for less crossover of different samples' uncertainties and may strengthen the argument presented in subsequent Chpaters.

3.6.9 CIAF samples

In addition to the 50 samples presented as part of this PhD thesis, an additional 16 samples processed at the NERC Cosmogenic Isotope Analysis Facility (CIAF) as part of a project awarded to M.A. Summerfield are presented in Appendix 5. These samples were collected from a range of locations in the Augrabies region at the same time as sampling for the PhD was carried out. The denudation rates derived for the CIAF samples from various locations are presented at the end of the discussion of the PhD samples from similar locations. The denudation rates derived from the CIAF samples provide a useful check on the rates presented in this thesis, which were processed in a different lab but using similar procedures[2].

[2] Note that these samples were normalised using a primary standard with a $^{10}Be/^{9}Be$ ratio of $3.06x10^{-11}$. The PhD samples were normalised using a standard with a $^{10}Be/^{9}Be$ of $3.00x10^{-11}$. The CIAF ^{10}Be concentrations are therefore ~2% lower than the PhD samples.

Chapter 4 Catchment-averaged denudation rates from the main Orange River channel – results and analysis

4.1 Field sampling results and descriptions

A full description of the Orange River catchment is given in Chapter 1. The following section deals with the field sampling strategy together with some site-specific considerations for the samples collected. The sampling locations are split into those on the trunk channel of the Orange River (dealt with in this Chapter) and a variety of tributaries (dealt with in Chapter 5) (Table 4.1.1). The denudation rates derived from these samples help to answer questions of how large parts of the southern African landscape have evolved over Quaternary timescales (tens of thousands to hundreds of thousands of years). How these rates compare with geological timescale (millions to hundreds of millions of years) denudation rates derived from thermochronologic and offshore sedimentary methods and what this means for theories of long-term landscape evolution is discussed in Chapter 6.

Environment	Aim	Sampling/analysis strategy
Main Orange River channel	Quantify catchment denudation rates	Catchment-averaged $^{10}Be/^{26}Al$
Orange River tributary channel	Quantify catchment denudation rates	Catchment-averaged $^{10}Be/^{26}Al$
Main Orange River channel above Falls	Quantify bedrock channel incision rates	In situ $^{10}Be/^{26}Al$
Main Orange River channel below Falls	Quantify bedrock channel incision rates	In situ $^{10}Be/^{26}Al$
Orange River anabranch and tributary channels	Quantify bedrock channel incision rates	In situ $^{10}Be/^{26}Al$
Bedrock interfluves	Quantify 'background' denudation rates	In situ $^{10}Be/^{26}Al$
Bornhardt	Quantify denudation history	In situ $^{10}Be/^{26}Al$

Table 4.1.1 Showing environment, aim and sampling/analysis strategy.

The catchment-averaged approach has been used fairly widely (e.g. Clapp *et al.*, 2001; Schaller *et al.*, 2001), but at present there is a lack of data on the technique applied to large basins. In this study, a number of small, high relief, relatively undisturbed tributary catchments in the uppermost part of the Orange basin have been studied (Chapter 5) (Figure 4.1.1). These are compared with a number of locations in the middle and lower part of the Orange which were sampled with the intention of gaining the first quantitative estimate of denudation rates on Quaternary

timescales. A detailed study has been made of the rates of bedrock denudation in the Augrabies Falls region, the principal knickpoint on the Orange River and the main controlling landform of the middle and upper parts of the basin (dealt with in Chapters 7-9).

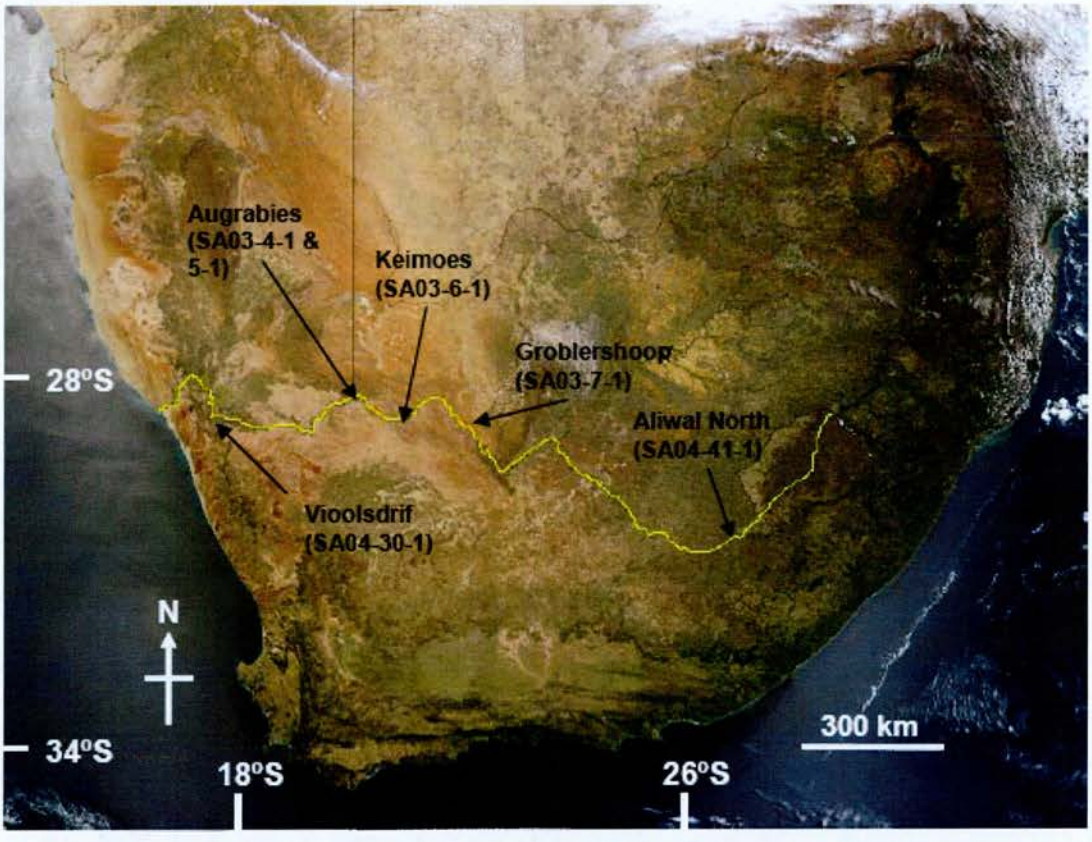

Figure 4.1.1 Map of southern Africa showing principal sampling locations on the trunk channel of the Orange River. The trunk channel of the Orange River is traced in yellow. Based on a composite satellite image of southern Africa taken by the Aqua (left half) and Terra (right half) satellites. (http://Earthobservatory.nasa.gov/Newsroom/NewImages/images.php3?imd=10823)

4.1.1 Sampling the main channel of the Orange River (catchment-averaged approach)

There is currently a lack of data on the evolution of the Orange basin on timescales of tens to hundreds of thousands of years. This study aims to redress this by quantifying catchment-averaged rates of denudation over Quaternary timescales. The sampled parts of the main channel are summarised in Table 4.1.2 and described below. Note that some catchment-averaged sample descriptions contain details of grain size fractions. Note also that many samples contain significant volumes of

larger size fractions (>710 μm). This fraction is unlikely to be transported in suspension in the river except in exceptionally high flood flows. Therefore, the 125-710 μm size fraction (that which will be transported in the river in normal flows – discharges of the order of tens to hundreds of $m^3 s^{-1}$) is the main focus for cosmogenic nuclide analysis. There may be a disproportionate loss of finer size fractions during sample processing, leading to an under-representation of these fractions in the final analysis. This is tested by measuring nuclide concentrations of different size fractions of the same sample. Several studies show no dependence of cosmogenic nuclide concentration on grain size in arid regions (Clapp *et al.*, 2000, 2001, Bierman & Caffee, 2001), and this is now tested for the Orange basin.

Sample	Geographic Latitude (Degrees south)	Geographic Longitude	Elevation (m)	Basin Lithology	Basin area (km^2)	Mean Basin altitude (m)	Climate	Grain size (µm)	Local Gradient ($m\ km^{-1}$)	Basin relief (m)	Basin Relief ratio
SA03-4-1	28° 32' 49"	20° 17' 15"	440	Shale, sandstone and basic	410500	1383	Arid (<250 $mm\ a^{-1}$)	125-710	3.1	2608	0.0017
SA03-5-1	28° 32' 37"	20° 20' 27"	614	Shale, sandstone and basic	410500	1383	Arid (<250 $mm\ a^{-1}$)	125-710	2.0	2434	0.0016
SA03-6-1	28° 43' 40"	20° 59' 07"	727	Shale, sandstone and basic	408000	1456	Arid (<250 $mm\ a^{-1}$)	125-710	2.0	2321	0.0016
SA03-7-1	28° 52' 37"	21° 59' 15"	837	Shale, sandstone and basic	408000	1456	Semiarid (<500 $mm\ a^{-1}$)	125-710	0.63	2211	0.0017
SA04-30-1-A	28°46'37''	17°38'27''	161	Shale, sandstone and basic	656000	1230	Hyperarid (<100 $mm\ a^{-1}$)	125-250	0.50	2887	0.0015
SA04-30-1-B	28°46'37''	17°38'27''	161	Shale, sandstone and basic	656000	1230	Hyperarid (<100 $mm\ a^{-1}$)	250-500	0.50	2887	0.0029
SA04-30-1-C	28°46'37''	17°38'27''	161	Shale, sandstone and basic	656000	1230	Hyperarid (<100 $mm\ a^{-1}$)	500-710	0.50	2887	0.0029
SA04-41-1	31°41'18''	26°42'36''	1294	Molteno sandstone and Drakensberg basalt	85000	1984	Seasonal rainfall (500-750 $mm\ a^{-1}$)	125-710	1.70	1754	0.0066

Table 4.1.2 (previous page) Summary of characteristics of main channel samples. Lithology is taken from Kent *et al.*, (1980). Local gradient is taken over 20 km stretches from river long profile plots by Summerfield *et al.*, (unpublished data), corroborated by Wellington (1955). Basin relief is calculated from maximum basin height (3048 m) minus local height at sampling location. Relief ratio is basin relief divided by maximum channel length from the location of maximum basin height to the sampling location. The total channel length is 2173 km (Zawada, 2000).

4.1.2 Aliwal North (SA04-41-1)

A number of locations were selected for analysis of catchment-averaged denudation rates from the trunk channel of the Orange River. The most upstream of these (SA04-41-1) was at Aliwal North, a few hundred kilometres from the river's source in the Lesotho Highlands (Plate 4.1.1). Aliwal North marks the downstream edge of the upper part of the Orange River, with the middle part defined as being between Aliwal North and the Augrabies Falls, and the lower part between the Augrabies Falls and the coast (Wellington, 1955). This sample should incorporate the denudation signal of the tributaries draining from Lesotho and also tributaries of the Kraai River draining the south of the region inland of the Great Escarpment, and including the sampling locations near Stormberg and Indwe (SA04-35, -36, -37, described in section 4.1.2). The sample was taken by the General Hertzhog bridge (30°41'18''S 26°42'36''E, 1294 m) and was fairly fine-grained but contained a large amount of quartz. A large amount of wet sample (~ 10 kg) was gathered ~ 2 m from the south bank of the river. Drying and sieving of the 125-250 μm size fraction was carried out later. The predominant size fraction in this sample was 125-250 μm (Figure 4.1.2). The fine grained nature of this sample necessitated special lab treatment in order to separate the quartz from other material (see Chapter 3).

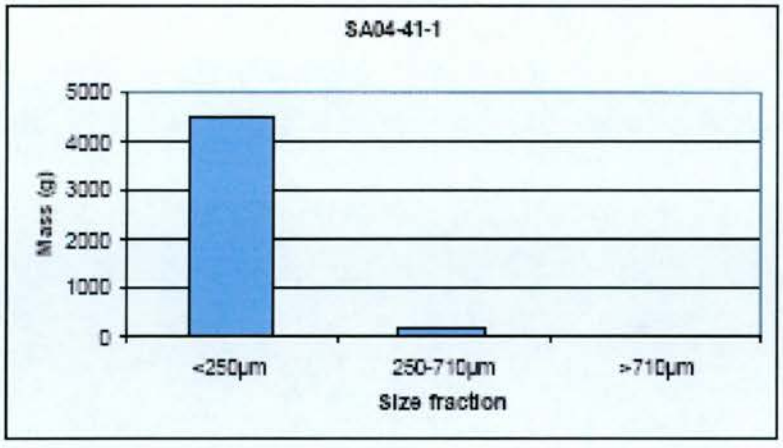

Figure 4.1.2 Grain size fractions of sample SA04-41-1.

4.1.3 Groblershoop (SA03-7-1)

This location is in the low gradient alluvial middle course of the Orange River (1.29 m km^{-1} Wellington, 1955), which predominantly flows over the lower Karoo sedimentary sequence (Plate 4.1.2). The rationale for sampling this location was to gain a catchment-averaged denudation rate for the middle course of the Orange River which incorporates the denudation rate signal coming from the Karoo region, as well as upstream regions and, if any, the denudation signal from the Vaal tributary, (although given the dearth of suitable quartz lithology in that basin, it is unlikely that any denudation signal from there will be captured.

4.1.4 Keimoes (SA03-6-1)

In common with SA03-7-1, this sample is taken from the middle course of the Orange River close to the town of Keimoes (Plate 4.1.3). This is in the mixed bedrock-alluvial stretch of the Orange River that extends ~ 250 km upstream of the Augrabies Falls (Tooth *et al.*, 2005). This sample complements two of the above-Falls bedrock channel samples described below (SA05-3-1, -2). This sample was fairly fine grained and, as with other catchment-averaged samples, the 125-250 µm size fraction was analysed after drying and sieving. The problems associated with loss of quartz during analysis are described in Section 4.2.

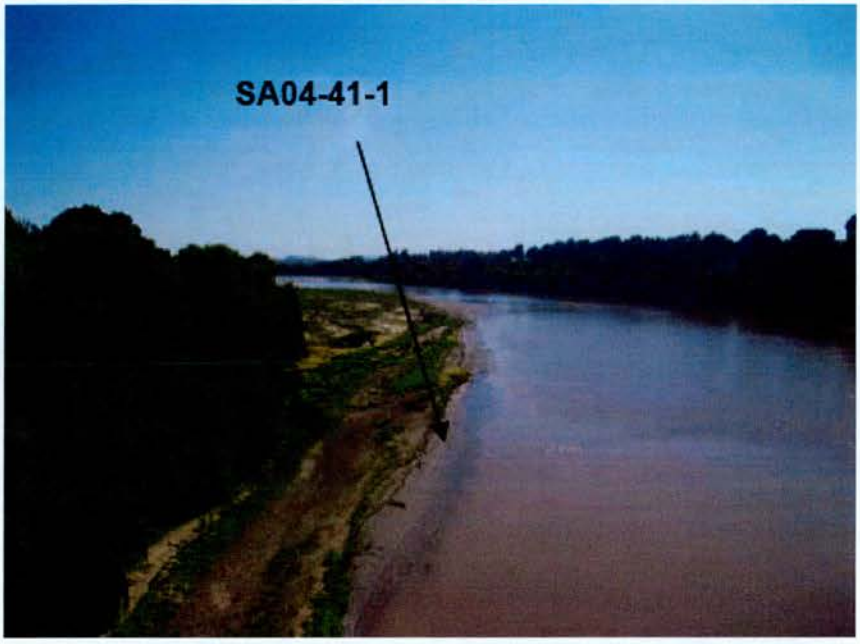

Plate 4.1.1 Location of sampling at Aliwal North. Sample was taken on left bank of the river. Flow of the Orange River is away from the picture.

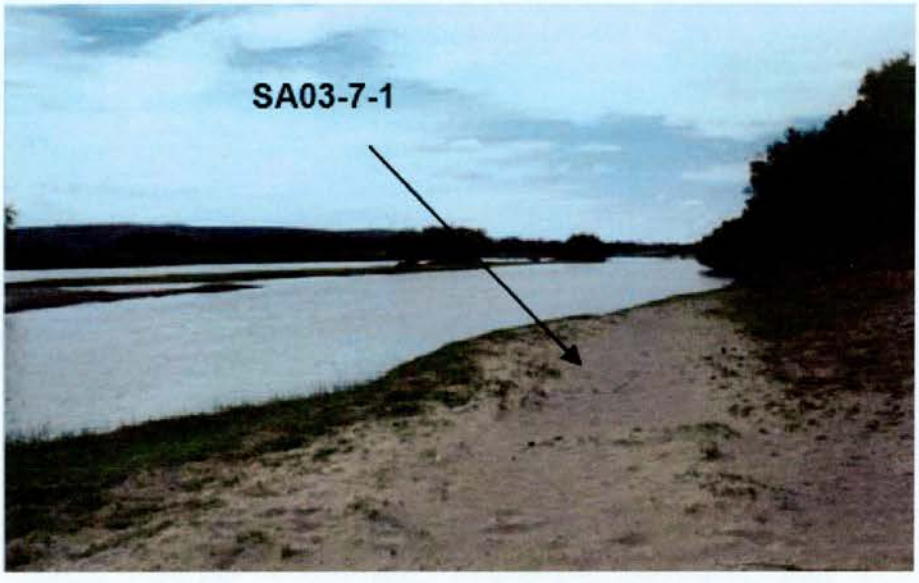

Plate 4.1.2 Sampling near Groblershoop. Sample was taken on the sand bar seen on the right of the picture.

4.1.5 Upstream of the Augrabies Falls knickpoint (SA03-5-1)

The Augrabies Falls marks the upstream edge of the third major zone of the Orange basin, the lower Orange River (Wellington, 1955). The rationale of sampling this location and the main channel immediately downstream of the knickpoint (sample SA03-4-1) by the catchment-averaged approach is to assess the denudation rate on either side of a high energy, steep gradient environment and compare it with bedrock incision rates from the channels above and below the knickpoint (see Chapter 7). The upstream sample is taken from an area of sediment ~ 1 km upstream of the main Falls in an area of bedrock interfluve on which fluvial sand has been deposited. This deposit is likely to date from the last major flood event (1988) when floodwater inundated this region, including the Visitor Centre. There is also evidence of the 1988 flood in the form of boulders and organic material suspended far above the present level of the river (Plate 4.1.4). This sample complements bedrock channel samples (SA05-4-1, -2, 5-1) taken from nearby locations and described in Chapter 7. The sample is fairly coarse-grained (Figure 4.1.3) and is extremely quartz-rich, perhaps reflecting the local derivation of many of the grains from the quartz-rich granite gneiss that is ubiquitous in the Augrabies region.

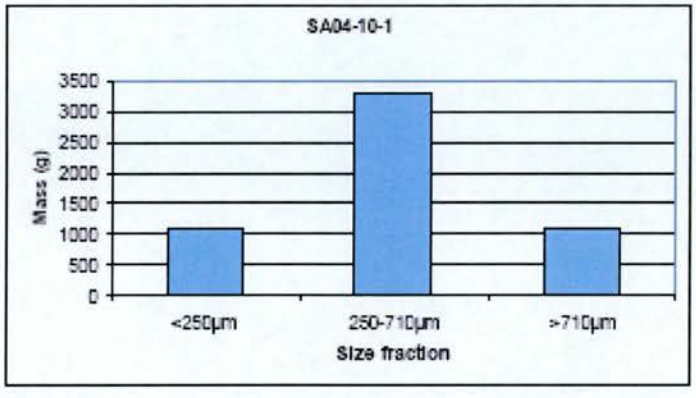

Figure 4.1.3 Grain size fractions for sediment taken from above the Augrabies knickpoint (Note that the sample illustrated here is SA04-10-1 and was taken from the same location as SA03-5-1).

4.1.6 Augrabies Falls, downstream of knickpoint (SA03-4-1)

Complementing sample SA03-5-1, this is taken from some 10 km downstream of the Augrabies Falls, a location closer to the knickpoint could not be accessed (Pl. 4.1.5).

Plate 4.1.3 Sampling at Keimoes. Fluvial sample was taken from the sand bar on the left of the picture.

Plate 4.1.4 (left) Sampling location SA03-5-1 above the Augrabies Falls. Boulders are most likely from the high magnitude 1988 flood, as is the fluvial sand collected here; (right) Organic Material transported and deposited high above the present river channel by the 1988 flood.

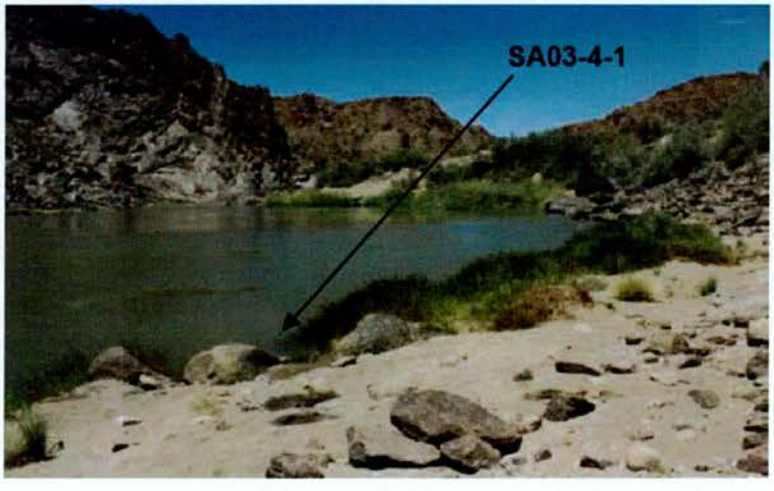

Plate 4.1.5 Location of sample SA03-4-1, downstream of Augrabies Falls.

This sample is complemented by a number of bedrock channel samples from the same area (SA04-3-1, 23-2, 24-1), which help to address questions of the evolution of the Augrabies Falls region. This sample is just upstream of a small tributary channel which was independently sampled (sample SA03-2-1, SA04-19-1-A to C, described below); however, mixing of the main channel sediment with sediment from this tributary may mean that there is an denudation rate signal coming from the tributary channel reflected in this sample. This is discussed further in Section 7.2.

4.1.7 Vioolsdrif (SA04-30-1)

This sample is the most downstream sample taken from the trunk channel of the Orange River just south of the border with the Republic of Namibia at Noordoewer and east of Vioolsdrif in the Republic of South Africa (28°46'37''S, 17°38'27''E, 161 m). This is a catchment-averaged sample from just south of the main channel. The area sampled is clearly inundated regularly by floodwaters (evidence for this is in the lack of older vegetation - Plate 4.1.6). The sample was composed of quartz grains and some finer material, generally all >125 μm (Figure 4.1.4). Since this was the most downstream sample, it ought to capture the denudation rate signal of the entire Orange River upstream and be representative of the average denudation rate of all the upstream sampled locations, including tributaries. In order to test whether there is any variation in nuclide concentration with grain size, and therefore whether any one size fraction is over-represented in terms of denudation rate signal, a number of different size fractions were analysed (125-250 μm, 250-500 μm, 500-750 μm) and the results are presented in Chapter 5.

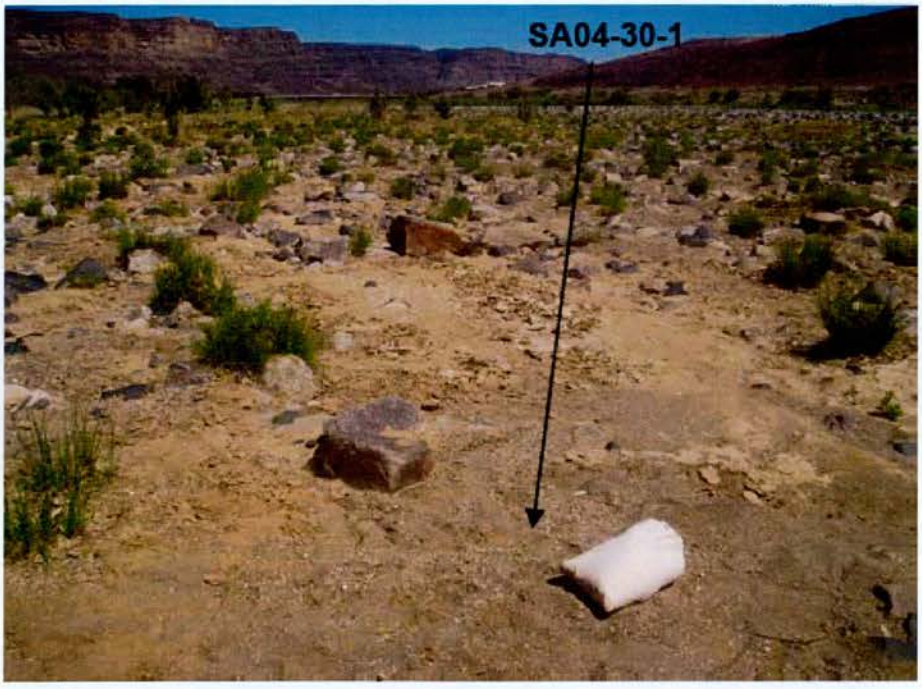

Plate 4.1.6 Location of sample SA04-30-1. This is the most downstream sample taken from the Orange River hence it represents the denudation rate of the entire area upstream.

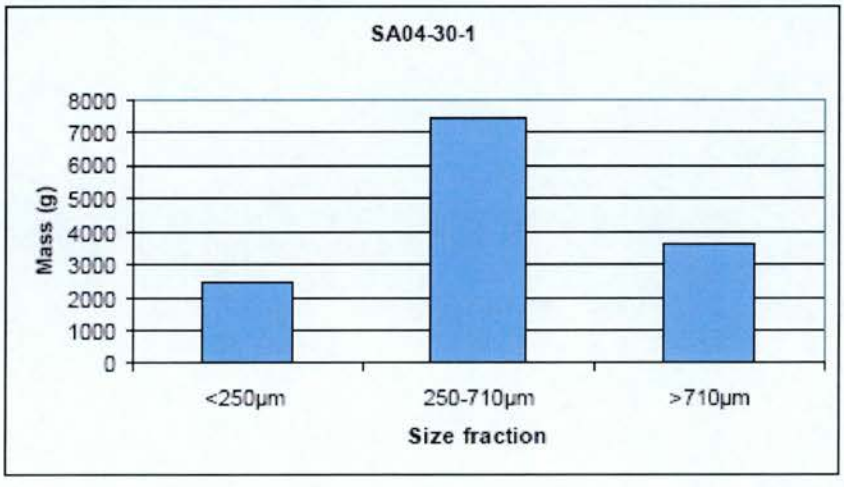

Figure 4.1.4 Grain size fractions of sample SA04-30.

4.2 Catchment-averaged denudation rates from the main channel of the Orange River

The catchment-averaged samples taken from the main channel of the Orange River are summarised in Table 4.1.1 and the summary of results is given in Table 4.2.1. Full sample details can be found in Appendix 4.

4.2.1 Variation in nuclide concentration with grain size

The sample of sediment (SA04-30-1) from the main Orange River near Vioolsdrif was split into three size fractions and processed as three separate ^{10}Be targets and the resulting nuclide concentrations were then measured. The results are presented in Figure 4.2.1. As with sample SA04-19-1, a tributary sample which was tested for variation in nuclide concentration, the smallest grain size fractions (125-250 μm) has the highest nuclide concentration and the lowest denudation rate, whilst the largest size fractions (500-710 μm) have the lowest nuclide concentration. Overall, however, the variation in nuclide concentration with grain size results in denudation rates that are insignificant to within standard uncertainties (Table 4.2.1). The smaller clasts may form by attrition of larger clasts, therefore they may inherit some of the concentration from the large clasts as well as accumulating their own cosmogenic nuclide concentration, hence have a slightly higher cosmogenic nuclide concentration than larger clasts. The lack of dependence of nuclide concentration on grain size is in common with findings from other arid regions: from Israel (Clapp *et al.*, 2000); the United States (Clapp *et al.*, 2001, 2002); and Namibia (Bierman & Caffee, 2001).

Sample	Average latitude (degrees south)	Average elevation (m)	Stone prn. rate (at g^{-1} a^{-1})	^{10}Be (10^5 atom g^{-1})	Denudation rate (mm ka^{-1})	^{10}Be averaging time (ka)
SA03-4-1	29.6	1383.3	12.27	14.16 ± 0.43	4.89 ± 0.32	121.86
SA03-5-1	29.6	1383.3	12.27	21.15 ± 2.85	3.18 ± 0.47	187.20
SA03-6-1	29.6	1456.7	12.42	12.27 ± 1.41	5.76 ± 0.74	103.50
SA03-7-1	29.6	1456.7	12.48	9.90 ± 1.14	7.24 ± 0.94	82.34
SA04-30-1-A	29.0	1230.0	10.42	15.76 ± 0.61	3.61 ± 0.33	165.121
SA04-30-1-B	29.0	1230.0	10.42	14.13 ± 0.28	4.13 ± 0.35	128.09
SA04-30-1-C	29.0	1230.0	10.42	10.98 ± 2.15	5.39 ± 0.43	98.26
SA04-41-1	29.1	1984.6	18.29	4.55 ± 0.21	23.71 ± 2.26	25.34

Table 4.2.1 Cosmogenic nuclide data and basin-wide denudation rates for the main channel of the Orange River. The altitude-latitude scaling factor is calculated according to Stone (2000). Be data are normalised using the SUERC NIST standard with a nominal $^{10}Be/^{9}Be$ ratio of 3.00×10^{-11}. Denudation rates are calculated using sea level, high latitude ^{10}Be production rate (Stone, 2000). See Appendix 4 for full details of data. ± uncertainties are standard uncertainties.

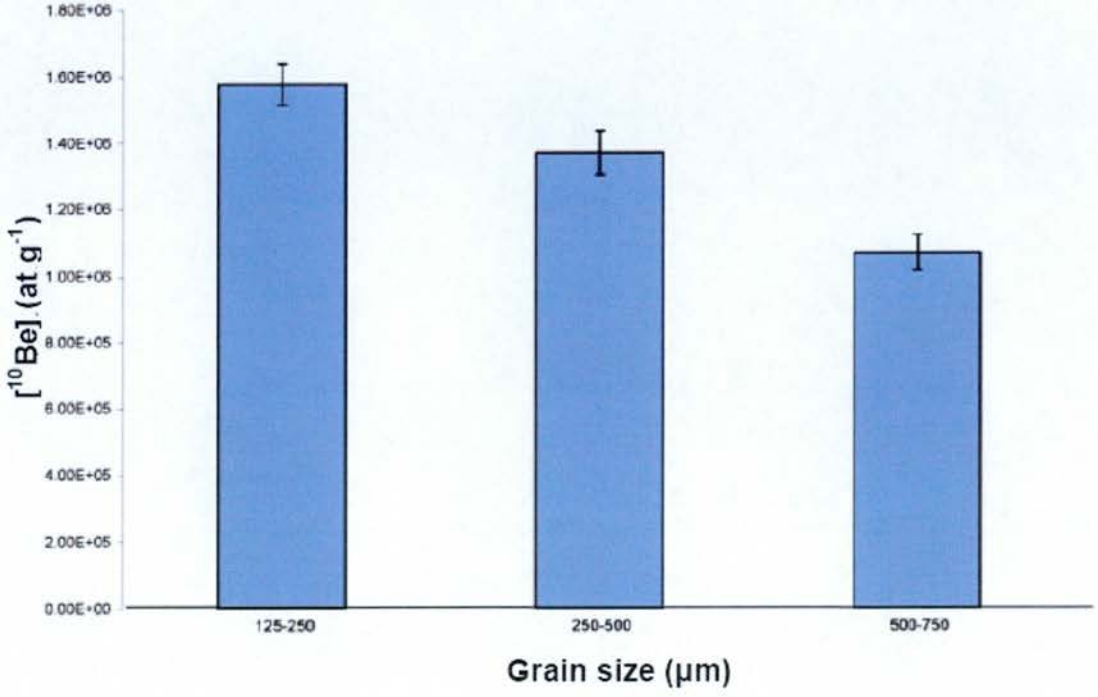

Figure 4.2.1 (previous page) Comparison of nuclide concentration and grain size for sample SA04-30-1, the most downstream sampling point on the main Orange River. Samples are, left to right SA04-30-1-A, SA04-30-1-B, SA04-30-1-C, respectively.

4.2.2 The upper Orange River

The most upstream sample taken on the trunk channel of the Orange River was from Aliwal North, a few hundred kilometres from the river's source in the Lesotho Highlands, draining an area of some 85,000 km^2 (Figure 4.2.2). The denudation rate of this sample is ~ 24 mm ka^{-1}, the highest rate recorded in the trunk channel of the Orange River. This high denudation rate reflects the high denudation rates in the upstream region, where high seasonal rainfall, high relief ratio (0.007); the highest gradient of the main channel samples (1.70 m km^{-1}); and erodible lithologies (including the Clarens sandstone) may combine to give high denudation rates. This is discussed further below. In addition, high production rates are directly proportional to high denudation rates. Since local production rate is strongly dependent on local altitude, higher altitudes may give apparently higher denudation rates. However, given that production rates are weighted by how much area covers a particular elevation (Section 3.4), this is not believed to be a significant problem.

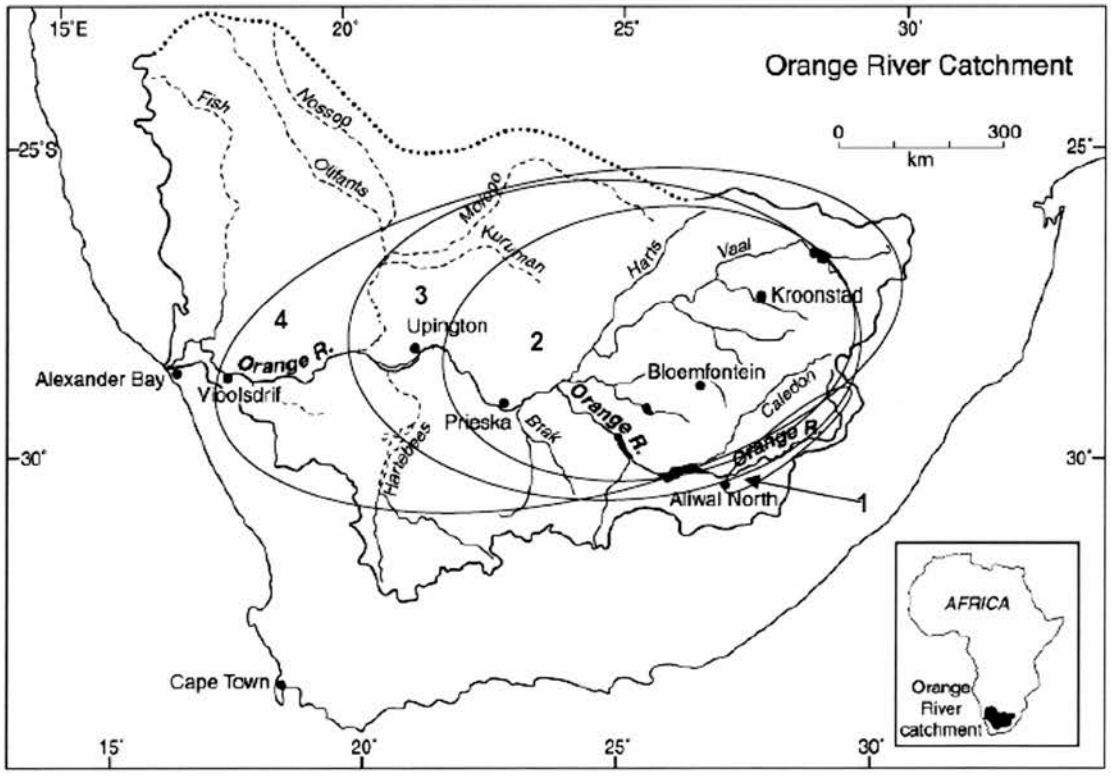

Figure 4.2.2 (previous page) Summary diagram of catchment-averaged denudation rates in (1) Upper Orange River averaged upstream of Aliwal North (23.71 ± 2.26 mm ka^{-1}); (2) middle Orange River taken as average denudation rate upstream of Groblershoop and Keimoes (6.50 ± 0.84 mm ka^{-1}); (3) Average denudation rate upstream of the Augrabies region (from samples above and below main Falls (4.04 ± 0.40 mm ka^{-1}); (4) Average denudation rate upstream of Vioolsdrif (4.37 ± 0.37 mm ka^{-1}). Based on an original diagram by Tooth & McCarthy, 2004.

4.2.3 The middle Orange River

In the middle course of the Orange River, around Keimoes and Groblershoop the average upstream denudation rate, draining an area of some 408,000 km^2, is less than 10 mm ka^{-1} (5.76 ± 0.74 and 7.24 ± 0.94 mm ka^{-1} for Keimoes and Groblershoop, respectively). These low rates compared with the trunk channel upstream at Aliwal North could be due to the sediment yield decreasing with increasing basin area as more sites in the basin become available for sediment storage (Schumm, 1977; Walling, 1983). This is a function of relief, rather than basin area, as the downstream region below Aliwal North is low relief and appears to produce far less sediment than the high relief upstream region. The denudation rates measured in the middle course of the Orange River, between Aliwal North and the Augrabies Falls, are around 4 times lower than those measured at Aliwal North. The much lower gradient in the middle course of the river (2.00 m km^{-1} and 0.63 m km^{-1} respectively for samples SA03-6-1 and -7-1, and average relief ratio of 0.16) may be responsible for less overall sediment production than the upstream region.

4.2.4 The lower Orange River

This region, defined as being between the Augrabies Falls and the mouth of the Orange River, experiences some of the lowest rates of denudation of the entire Orange River. Just upstream of the Augrabies Falls, sample SA03-5-1 has a denudation rate of 3.18 ± 0.47 mm ka^{-1}. A few kilometres downstream of the knickpoint, sample SA03-4-1 has a rate of 4.89 ± 0.32 mm ka^{-1}. The difference in denudation rates above and below the Falls is extremely small and indicates that there is little storage of sediment, which would affect the total ^{10}Be concentration, occurring either just above or just below the knickpoint. These very low rates of denudation from the lower Orange River may reflect the fact that the high denudation

signal from upstream is being effectively diluted by a great deal of low denudation signal sediment from the considerably larger downstream catchment area. One of the principal reasons for the low rates of denudation in the Augrabies region may be the low topographic relief (average relief ratio 0.0016) in much of the upstream middle course of the Orange, and the arid to semiarid climate in the Orange basin.

4.2.5 Discussion

The lowermost sediment samples taken from the Orange River at Vioolsdrif have an average denudation rate of 4.37 ± 0.37 mm ka^{-1}, one of the lowest rates recorded in this study. This represents the denudation rate of the entire upstream region (over 600,000 km^2) in one of the largest basins that the catchment-averaged technique has been used on. This compares well, within standard uncertainty, to the estimated average denudation rate for the Orange River of 6.8 mm ka^{-1} (Dingle & Hendey, 1984).

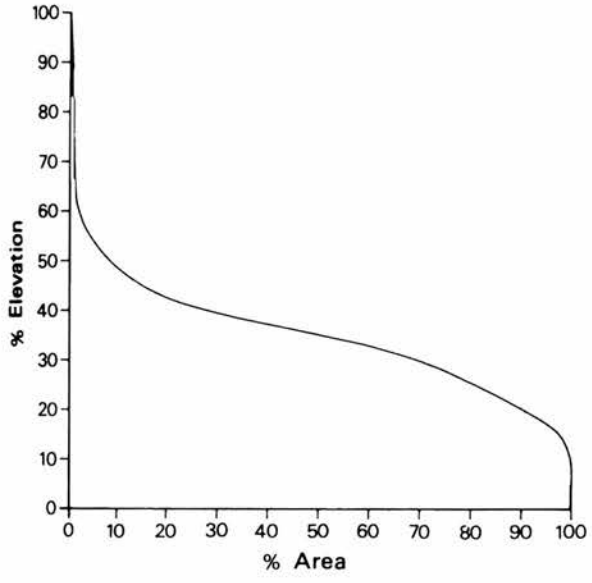

Figure 4.2.3 Hypsometry of the Orange River basin (from Summerfield, 1991b).

Given the variability in climate and hypsometry (Figure 4.2.3) and therefore sediment supply at different times in very large basins, sediment may be stored in floodplains for thousands of years or more (Summerfield & Hulton, 1994). Summerfield & Hulton state that for such river systems, sampling at the basin mouth may provide an unrepresentative snapshot of the long-term mean sediment flux – the

key issue is the timescale involved. Indeed, the sample taken at Vioolsdrif may not be representative of the long term flux, and may only capture the present cycle of sediment deposition, rather than the longer term mean of the denudation-deposition cycles. On the other hand, the samples presented here integrate denudation rates over fairly long averaging times (the time taken for a sample to move up a bedrock column through one attenuation length of bedrock, around 60 cm, and equivalent to tens to hundreds of thousands of years). Therefore they ought to capture a number of denudation-deposition cycles over the last glacial-interglacial cycle and give the mean denudation rate for this time. While some samples may be over-represented in terms of deposited sediment, since the catchment-averaged technique aims to capture the long-term average denudation rate of a large number of individual clasts, which all have a unique denudation history of the time when they were on a hillslope, the technique will indeed capture that long-term denudation history capturing successive climatically-driven cycles of accelerated and decelerated denudation in the basin as a whole.

Denudation involves both *in situ* chemical and physical weathering of material (as discussed by Raymo *et al.*, 1988) followed by the removal of weathered material. Summerfield & Hulton (1994) observe that chemical weathering is low with respect to physical weathering in the Orange basin, especially compared with other major drainage basins of the world (Figure 4.2.4). Raymo *et al.* (1988) contend that temperature plays no part in controlling rates of chemical denudation. They propose that efficient removal of weathered regolith occurs by continuous advection of rock into the weathering zone, i.e. by denudation. This is held to be the critical determinant of the rate of chemical weathering. However, it must be recognised that climate is the key determinant of chemical weathering and, more specifically, humidity affects the rate and style of chemical weathering. The quartz –rich sandstone lithologies of the Karoo Supergroup are strongly affected by humidity and weather very easily in humid conditions (Cox *et al.*, 1990). Physical weathering is also important in terms of enabling the detachment of previously chemically-weathered bedrock which eventually reaches the Orange River as eroded sediment clasts. In this study, the dataset is not sufficiently large to categorically identify the

topographic, climatic and lithological factors that control denudation in the Orange basin, although some attempt is made to do this in Appendix 6. However, varying climate, relief and lithology clearly all have strong controls on the rate and style of denudation (this is well established in the literature, e.g. by Ahnert (1970) who presented a seminal paper on the dependence of denudation on relief), although their relative roles are difficult to address given the limited number of samples and relatively few sampling environments in this study. The role of climate in controlling denudation may be difficult to evaluate given that it has changed over time.

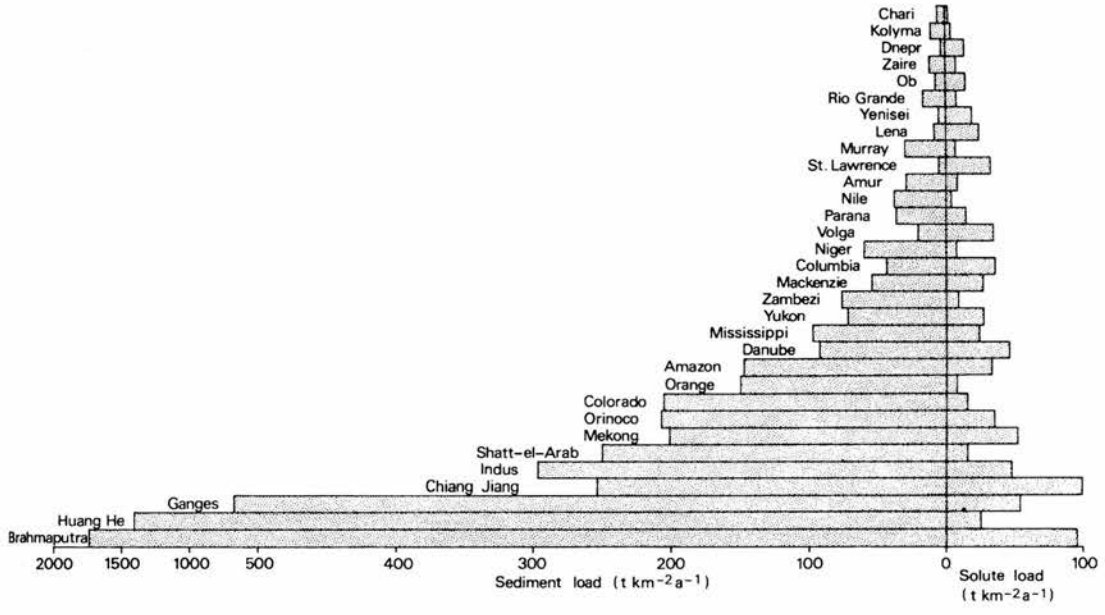

Figure 4.2.4 Sediment and solute loads for the world's largest drainage basins. Note that the Orange River has a low proportion of solute load (representing chemical weathering) with respect to sediment load (representing physical weathering) (Summerfield, 1991b).

The trend described in the results above for catchment-averaged denudation rates to decrease as one travels further downstream could be explained by the fact that sediment yield decreases with increasing basin area as more sites in the basin become available for sediment storage (Schumm, 1977; Walling, 1983). Walling (1983) states that it is well known that only a fraction, and perhaps rather a small fraction, of the sediment eroded within a drainage basin will find its way to the basin outlet and be represented in the long term sediment yield (Walling, 1983). This explanation is backed up by observations by Annandale (1987) that regions of lower relief deliver

less sediment than those of high relief. Annandale (1987) describes sediment yields of 600-1000 t km^{-2} a^{-1} in high relief regions of South Africa and 50-150 t km^{-2} a^{-1} for regions of lower relief (Thomas, 1994). The decrease in denudation rates as one travels downstream is exactly to be expected given the spatial variability of denudation rates. Small, high relief, high runoff tributary catchments (described in Chapter 5) denude faster than large, low relief, low runoff catchments. Owing to their greater size, the larger catchments overall contribute more sediment (though their sediment contribution per unit area is smaller). This has the effect of effectively diluting the high denudation upstream signal.

Changes in sediment supply over time may be attributed to climatic fluctuations (Leopold *et al.*, 1966). Cycles of incision and deposition may have gone on in the past, particularly in the middle course of the Orange River. During colder or drier periods (such as during the LGM) colluvium may have accumulated on hillslopes (Holmes *et al.*, 2004). During periods of high precipitation intensity (such as during glacial-interglacial transitions) the stored sediment is stripped from hillslopes and transported to fluvial systems by vegetation disturbance and bedrock weathering (as with Anders *et al.*, 2005). In such a situation, the Orange River would change from being a weathering-limited to a transport-limited regime (i.e. in the latter, there is unlimited colluvium to be transported). Such cycles of incision and deposition occur as sediment supply changes in response to external climatic forcing. It is likely that the response of the Orange River to climate changes is controlled by the weathering limited nature of the upstream hillslope sediment supply and the transport limited nature of the middle course of the Orange River. The interplay between these two environments results in cycles of sediment storage and remobilisation that are ultimately regulated by the pace and style of climatic change. The intermediate- and long-term trends of denudation in the Orange basin are discussed in Chapter 6 with the aid of data from small tributary catchments, presented in Chapter 5.

Chapter 5 – catchment-averaged analysis of tributaries of the Orange River

5.1 Tributaries of the Orange River

Tributaries of the Orange River were sampled for catchment-averaged denudation rates in a range of environments, from high relief tributary catchments, to lower relief environments in the middle and lower courses of the Orange River (Figures 5.1.1, 5.1.2). A number of upstream tributaries such as the Caledon River which marks the northern Lesotho border were sampled. Several northward draining catchments south of Lesotho were also sampled (Table 5.1.1). These tributaries drain the quartz-rich Molteno Formation of the Upper Karoo Supergroup and show little evidence of disturbance by human activity. In contrast with the Caledon River, the channel gradients in this region are lower and although there is potential for sediment storage, there is little evidence that old river terraces are being actively mined (Granger, personal communication, 2006) and in any case river terraces represent a small proportion of the total area of the Orange basin. Downstream tributaries (particularly in the Augrabies region) were also sampled, both to answer questions of how small tributaries in the lower Orange River are related to the development of the main Orange River, and also how the Augrabies region has evolved. The Fish River, a major tributary that drains southern Namibia, was also sampled in order to get a regional picture of Quaternary timescale denudation rates from an area that has had its longer term denudation history reconstructed from thermochronological methods. The Fish River is the westernmost major tributary of the Orange and the confluence is just west of Vioolsdrif.

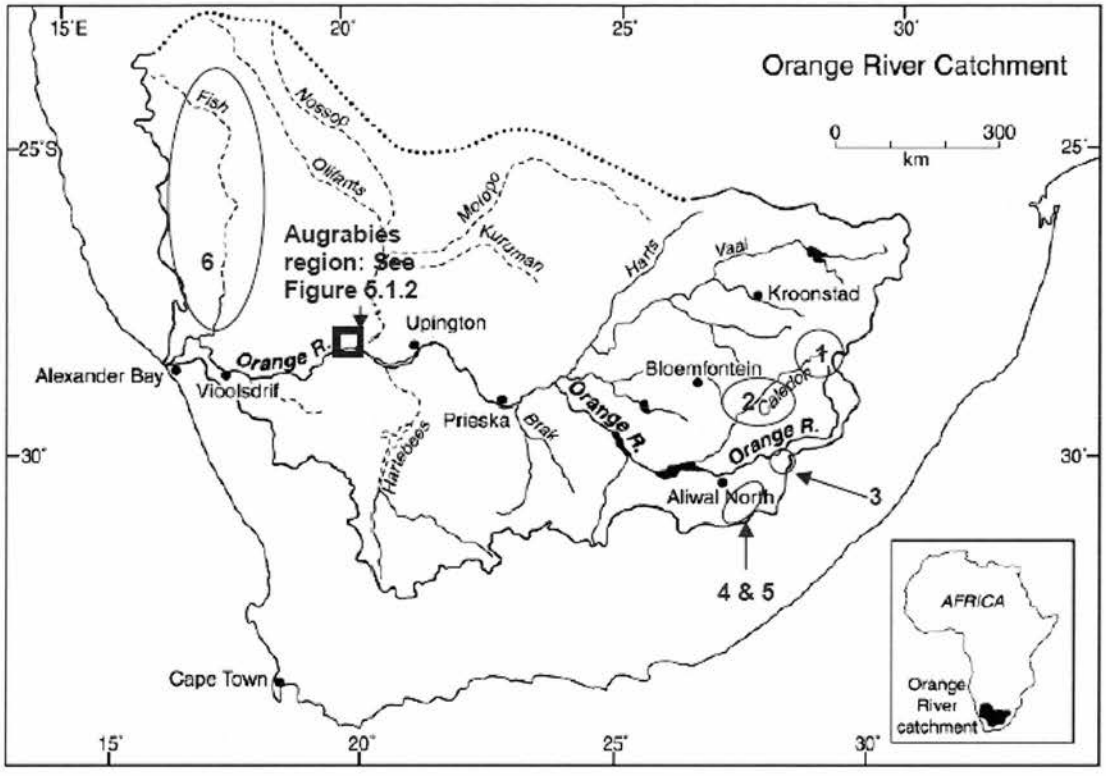

Figure 5.1.1 Map of principal tributary catchments sampled in the Orange basin: (1) Little Caledon River in the Clarensformation (SA05-14-1); (2) Caledon River (SA04-42-1); (3) Elliot Formation on a small unnamed tributary draining into the Orange River (SA04-37-1); (4 & 5) Molteno Formation on the Sterkspruit River (SA04-35-1, SA04-36-1; (6) Fish River (SA04-29-1). Map based on Tooth & McCarthy, 2004).

5.1.1 The Little Caledon River (SA05-14-1)

The Little Caledon River is a tributary of the Caledon River, which itself is a major tributary of the Orange River. It flows along the eastern margin of the Orange catchment close to Lesotho and drains an area of some 200 km^2 in the Golden Gate Highlands National Park before reaching the town of Clarens, and eventually reaches the Caledon River south of Fouriesburg. Geologically, it incises through the uppermost part of the Karoo Supergroup, comprising the Clarens Formation a fine-grained aeolian sandstone-mudstone unit deposited ~ 200 Ma BP. The Clarens sandstone (formerly known as the Cave Sandstone, Dardis & Moon, 1988) forms striking cliffs of bright red sandstone and lighter mudstone rocks which have been eroded by wind and water to form caves high up on the cliffs above the Golden Gate Highlands National Park. The sandstone is capped by the Drakensberg volcanic group (Ar/Ar dated to ~ 185 Ma) and there is abundant basalt on the tops of the hills

around the Golden Gate Highlands Park and numerous outcrops of basalt at lower levels in the Park.

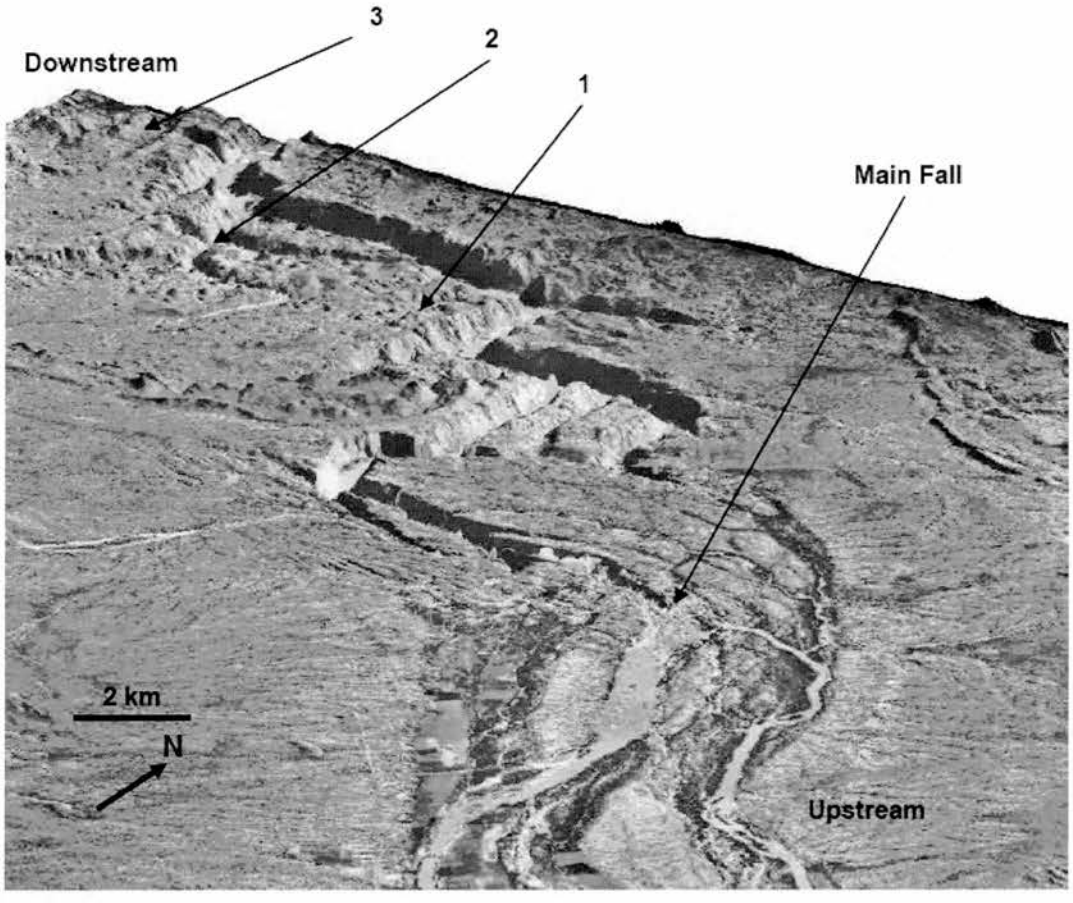

Figure 5.1.2 Digital elevation model of principal tributary catchments sampled in the Augrabies Falls region: (1) Echo Corner tributary (SA03-2-1, SA04-19-1-A, SA04-19-1-B, SA04-19-1-C); (2) Unnamed tributary (SA04-28 1); (3) Unnamed western tributaries (SA05-8-1, SA05-9-1). DEM derived from 10 m aerial photographs, by Walcott *et al.* (unpublished).

Sample	Latitude	Longitude	Elevation (m)	Basin Lithology	Basin area (km^2)	Mean Basin altitude (m)	Climate (rainfall)	Grain size (µm)	Channel gradient ($m\ km^{-1}$)	Basin Relief (m)	Relief ratio
SA03-2-1	28°33'20"S	20°17'01"E	566	Cape Granite	14.1	637.8	Arid (100-250 mm a^{-1})	125-710	38.9	210	0.04
SA04-19-1-A	28°33'58"S	20°16'56"E	566	Cape Granite	14.1	637.8	Arid (100-250 mm a^{-1})	125-250	34.6	187	0.03
SA04-19-1-B	28°33'58"S	20°16'56"E	566	Cape Granite	14.1	637.8	Arid (100-250 mm a^{-1})	250-500	34.6	187	0.03
SA04-19-1-C	28°33'58"S	20°16'56"E	566	Cape Granite	14.1	637.8	Arid (100-250 mm a^{-1})	500-710	34.6	187	0.03
SA04-28-1	28°32'59''S	20°15'41''E	447	Cape Granite	34.0	683.7	Arid (100-250 mm a^{-1})	125-710	85.4	726	0.09
SA04-29-1	27°54'29''S	17°30'03''E	203	Richtersveld Granite	73750.0	1216.1	Hyperarid (<100 mm a^{-1})	125-710	2.86	797	0.0023
SA04-35-1	31°27'56''S	26°21'09''E	1600	Molteno sandstone	12.0	1762.0	Seasonal rainfall (500-750 mm a^{-1})	125-710	62.3	467	0.06
SA04-36-1	31°25'02''S	26°22'06''E	1625	Molteno sandstone	71.8	1766.0	Seasonal rainfall (500-750 mm a^{-1})	125-710	58.9	442	0.06
SA04-37-1	31°26'55''S	27°22'52''E	1335	Elliot and Burgersdorp Formations	125.0	1966.0	Seasonal rainfall (500-750 mm a^{-1})	125-710	41.6	583	0.04
SA04-42-1	29°09'07''S	27°35'10''E	1296	Molteno sandstone	770.1	1296.0	Seasonal rainfall (750-1000 mm a^{-1})	125-710	103.0	412	0.10
SA05-8-1	28°33'02.6"S	20°07'31.9"E	602	Cape Granite	28.5	709.1	Arid (100-250 mm a^{-1})	125-710	16.7	251	0.02
SA05-9-1	28°33'36.6"S	20°09'39.0"E	596	Cape Granite	116.0	804.9	Arid (100-250 mm a^{-1})	125-710	17.1	257	0.01
SA05-14-1	28°30'44.2"S	28°35'00.7"E	1876	Clarens sandstone	63.0	2314.0	Seasonal rainfall (750-1000 mm a^{-1})	125-710	127.1	953	0.13

Table 5.1.1 (previous page) Summary of sampled tributary catchments. Basin lithology is taken from Kent (1980). Local gradient is taken the upstream length of the river from topographic maps, as described in Chapter 3. Basin relief is calculated from maximum basin height minus local height at sampling location. Relief ratio is basin relief divided by maximum channel length from the location of maximum basin height to the sampling location.

The Little Caledon River is one of the most upstream tributaries of the Orange River, with steep relief and a range of small tributaries at different altitudes; it drains a quartz-rich lithology; it is relatively undisturbed by human activity as a large part of its course lies within a National Park. The main channel and two small tributaries of the Little Caledon River were sampled for analysis of ^{10}Be using the catchment-averaged approach. The aim of this is to quantify denudation of a small tributary catchment with steep relief (Plate 5.1.1). In addition, an amalgamated sample of 10 small (<200 g) bedrock samples across a ~ 20 m transect of Clarens Sandstone bedrock outcrop was sampled in order to quantify bedrock denudation and to compare this with the denudation rate derived from the catchment-averaged approach. Owing to the extremely fine-grained nature of the material and high losses during processing, it proved impossible to generate sufficient quartz from these samples separately, therefore the samples were amalgamated after the etching stage to form one single catchment-averaged sample.

5.1.2 The Caledon River (SA04-42-1)

This catchment-averaged sample was taken from a tributary of the Caledon River close to Ladybrand. There was not a great deal of fluvial sand here as the channel was to a large degree bedrock-dominated. The small amount of sediment that was present was fairly quartz-rich, albeit fine-grained (Plate 5.1.2). Problems with the fine-grained nature of this sample necessitated special lab treatment (see Section 3.3). The lithology in this area is Molteno sandstone, which is quartz rich, but here in the northern area, fine grained (as described by Catuneanu *et al.*, 2005). The rationale for sampling in this location is to get the catchment-averaged denudation rate of one of the major north-eastern tributaries of the Orange River, and one that should incorporate the denudation rate signal of the Little Caledon River, further upstream. This, together with other tributary channel samples should help to address questions

of local scale (tens to hundreds of km^2) denudation trends over tens to hundreds of thousands of years. These rates can be compared with regional-scale (thousands to hundreds of thousands of km^2) rates for the wider Orange basin over similar timescales. These Quaternary-timescale local and regional denudation rates can then be compared with millions to hundreds of millions of year timescale regional denudation rates from thermochronologic studies, and different theories of local and regional landscape evolution discussed.

5.1.3 Molteno Formation (SA04-35, -36)

Two samples were taken in the Molteno Formation type locality, close to the town of Stormberg (Plate 5.1.3, Figure 5.1.3.-4). This location is underlain almost exclusively by Molteno Formation sedimentary rocks, in contrast with the Little Caledon River, underlain by Clarens sandstones, and the next sample described, which is in the Elliot Formation. This location also has low gradient relief, which contrasts with the relief in the Caledon River region, also underlain by Molteno Formation rocks. In common with the previous two, this is in a relatively high rainfall zone (500-750 mm a^{-1}). This contrasts with some of the tributary channel samples in the Augrabies region, which also have low channel gradients and quartz-rich lithology, but are in an arid climate (100-250 mm a^{-1} rainfall) (Tyson, 1986).

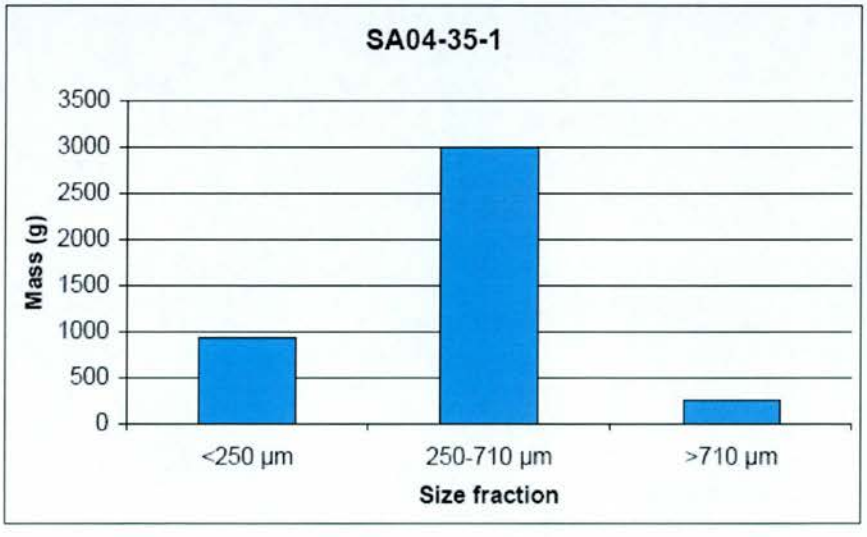

Figure 5.1.3 Grain size fractions of sample SA04-35-1.

Plate 5.1.1 Steep-sided tributary catchment of the Little Caledon River, GGHNP.

Plate 5.1.2 Caledon River site: sample SA04-42-1 was taken here. Note the Molteno sandstone proximate to the main channel.

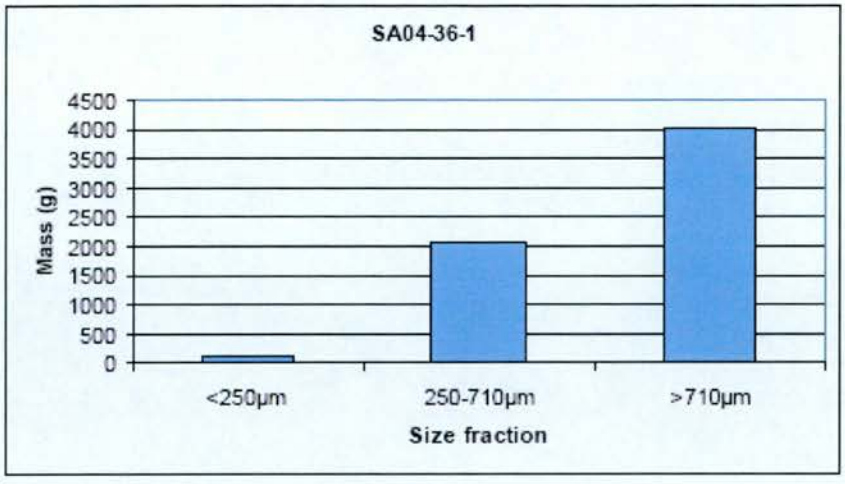

Figure 5.1.4 Grain size fractions of sample SA04-36-1.

5.1.4 Elliot Formation (SA04-37-1)

This is a catchment-averaged sample taken from a stream draining the Elliot Formation and Drakensberg lavas around 6 km east of Indwe (Plate 5.1.4, Figure 5.1.5). The catchment above the sampling location is largely undisturbed by dams and other anthropogenic modifications and incises deeply into the Elliot Formation. It was inevitable that a great deal of fine-grained and organic material had to be collected with this sediment, hence around 16 kg of sediment was collected, most of which was lost during processing.

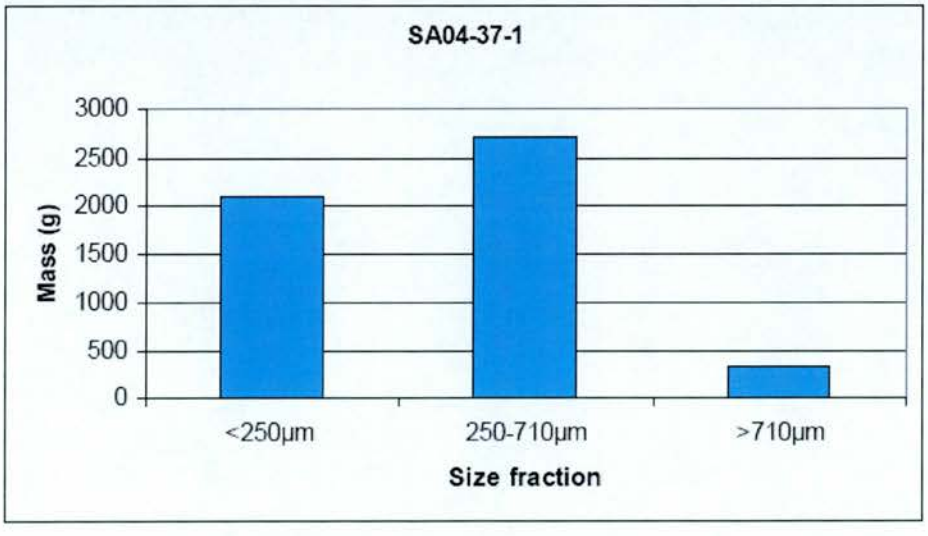

Figure 5.1.5 Grain size fraction of sample SA04-37-1.

Plate 5.1.3 Sample locations on the Molteno Formation near Stormberg, on the Sterkspruit tributary. On the left is the upstream sample (SA04 35-1), on the right is the downstream sample (SA04-36-1).

Plate 5.1.4 Sample locations on the Elliot Formation near Indwe.

5.1.5 Catchment-averaged tributary channels in the Augrabies Falls Region (SA03-2-1, SA04-19-1-A to C, SA04-28-1, SA05-8-1, -9-1)

A number of different tributaries were sampled for catchment-averaged denudation rates in the Augrabies Falls region (Figure 5.1.6). A number of samples were taken from areas which are complemented with bedrock channel samples taken from the tributary channels. One such channel drains into the main Orange River close to Echo Corner. This location also contains a number of bedrock samples taken from the channel and the interfluves. The sample location is a discrete, isolated valley (area of basin ~ 14 km^2) which has had no significant flows for several years at least (evident from the large trees close to the channel (Plate 5.1.5). In order to test whether there is systematic variation in nuclide concentration with grain size, four different samples were selected from this location, each covering different grain size fractions (see Table 5.1.1). The results of this are discussed in Section 5.2.

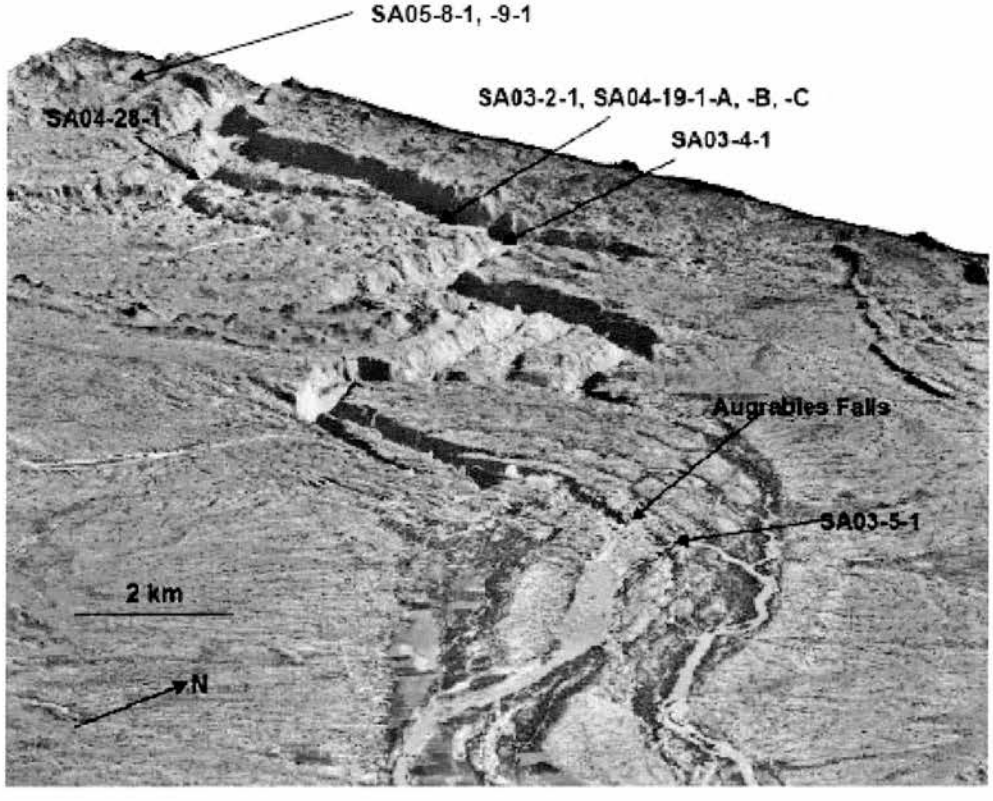

Figure 5.1.6 DEM derived from 10 m aerial photographs showing sample locations for catchment-averaged denudation rates in the Augrabies Falls region. (Walcott *et al.*, unpublished data).

Plate 5.1.5 Sample location of SA03-2-1, SA04-19-1-A to –C.

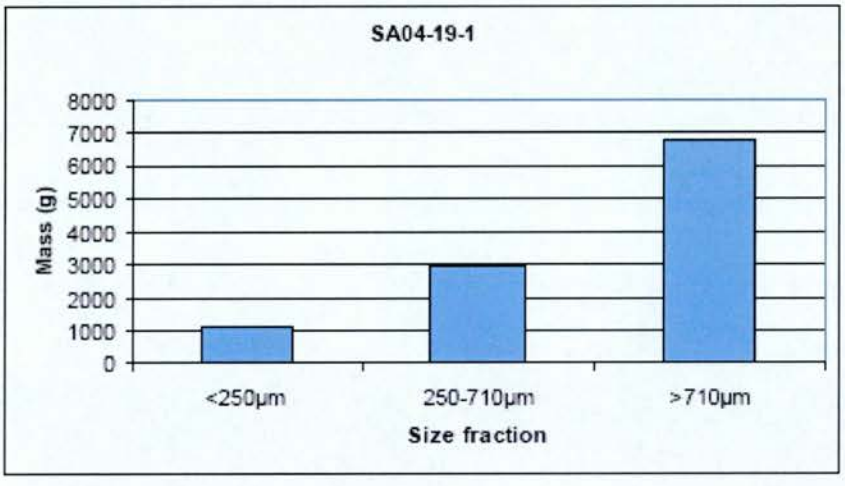

Figure 5.1.7 Grain size fractions of sample SA04-30-1 prior to splitting into the respective size fractions.

A catchment-averaged sample (SA04-28-1) is also taken from the most downstream portion of a bedrock-alluvial tributary channel west of the sample described previously (Plate 5.1.6; Figure 5.1.8). This sample is complemented by three bedrock samples taken from the tributary walls next to it (SA04-27-1, -2, -3, described below). This sample ought to capture the catchment-averaged denudation rate signal of the tributary basin above it (~ 34 km^2) and enable comparison with the rate of denudation in the adjacent main channel (from catchment-averaged sample SA03-4-1 and bedrock bar samples SA04-23-1 and -24-1).

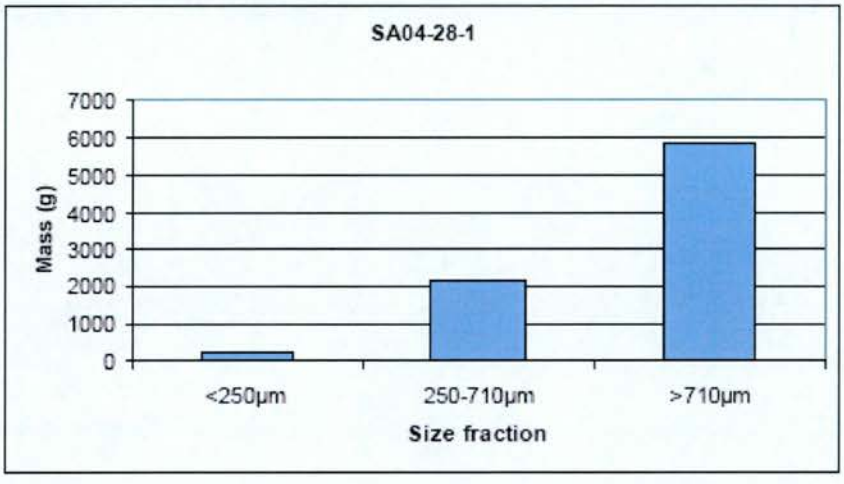

Figure 5.1.8 Grain size fractions of sample SA04-28-1.

In the far western edge of the Augrabies region (28°33' S, 20°08' E), two catchment-averaged samples were taken from a large complex tributary system on the south bank of the main Orange River (Plates 5.1.7, 5.1.8). These samples SA05-8-1 and SA05-9-1, covering a drainage area of 28.5 km^2 and 116 km^2, respectively, are like all sediment samples taken in the Augrabies Falls region extremely quartz rich. They are from very low gradient channels (16.7 and 17.1 m km^{-1}, respectively), in common with some of the tributary samples from much further upstream, but have the contrast of lying in a arid climatic environment. Storage in the basin is not believed to be a problem due to periodic (decadal-scale) high magnitude flows in the region as described by Zawada (1996).

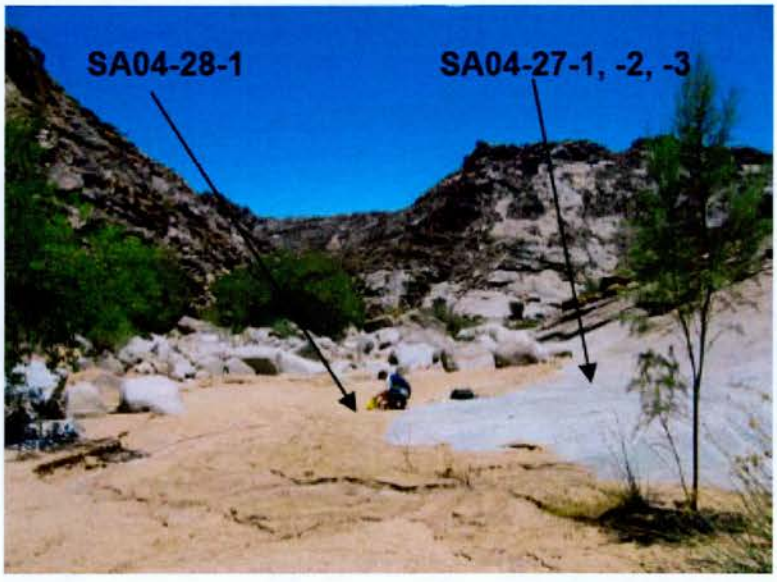

Plate 5.1.6 Location of sample SA04-28-1. Note the nature of the mixed bedrock-alluvial channel here. The bedrock is sampled as SA04-27-1, -2, and -3.

Plate 5.1.7 Location of sample SA05-8-1 taken from a low gradient, granite gneiss dominated region in the far west of the Augrabies Falls National Park. The picture on the right shows megacrystic clasts of quartz dominate the sediment. Braided channels on the surface of the river channel suggest periodic (and recent) fluvial activity in this tributary.

5.1.6 The Fish River tributary (SA04-29-1)

This is the most downstream major tributary of the Orange River, lying ~ 100 km from the Orange River's mouth. It drains a large part of Namibia and has a nominal drainage area of 73,750 km^2 (Figure 5.1.9, Table 5.1.1) although it is uncertain when in the Quaternary the upper parts of the basin were hydrologically active. Nonetheless, in calculating latitude and altitude scaled production rates (Section 3.4) the value of 73,750 km^2 is used. The sample location is just upstream of Ai-Ais (27°54' S, 17°30' E). The sample was extremely quartz rich and generally fairly coarse grained (>250μm).

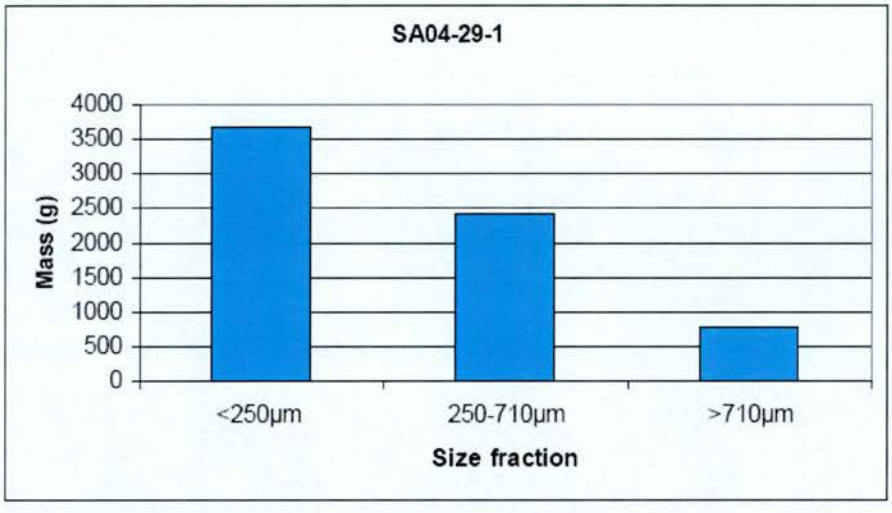

Figure 5.1.9 Grain size fractions of Fish River sample.

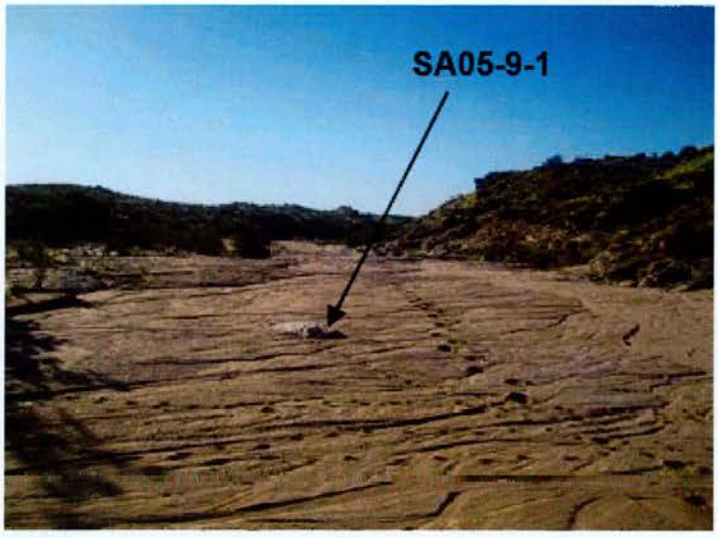

Plate 5.1.8 Location of sample SA05-9-1: taken from a different branch of the tributary described above. Giraffe footprints for scale.

Plate 5.1.9 Fish River sample location, and (right) the Fish River Canyon upstream of the sample location.

5.2 Catchment-averaged denudation rates from tributary channels of the Orange River

As described in the previous section, a number of tributary channels were selected for sampling on the basis of size, lithology and relief (Table 5.1.1). These samples span the Stormberg group of sandstones- i.e. the Molteno, Elliot, and Clarens units – which form the upper part of the Karoo Supergroup. The cosmogenic-derived denudation rate data are presented in Table 5.2.1. This follows the catchment-averaged technique described in Chapter 3 and by Granger *et al.* (1996), Schaller *et al.* (2001), Bierman & Nichols (2004), von Blanckenburg (2006), and others.

5.2.1 Variation in nuclide concentration with grain size

The first four samples in Table 5.2.1 are taken from the same location, a small (~ 14 km^2), dry tributary channel in the Augrabies Falls region, downstream of the main knickpoint. These samples were tested for variation in cosmogenic nuclide concentration with grain size by sieving into four different size fractions prior to chemical treatment. These were: 250-710 μm (medium to large size fraction); 125-250 μm (small size fraction); 250-500 μm (medium size fraction); 500-710 μm large size fraction. As can be seen from Figure 5.2.1, there is no significant variation (R^2 = 0.05) in nuclide concentration with grain size, and variation occurs mostly within the errors on the data. This is in common with the findings of other studies in arid regions (Bierman *et al.*, 2001; Clapp *et al.*, 2000; 2001; 2002).

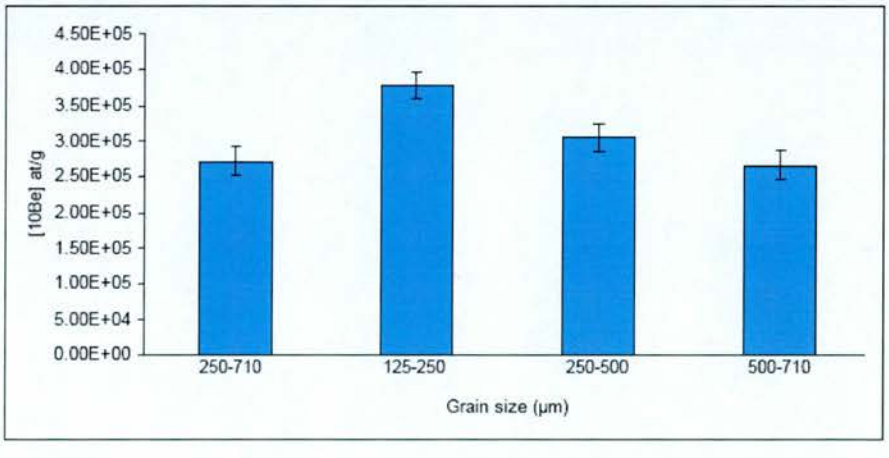

Figure 5.2.1 Variation in cosmogenic nuclide concentration with grain size for tributary samples SA03-2-1, SA04-19-1-A, SA04-19-1-B, SA04-19-1-C, respectively.

Sample	Average latitude (degrees south)	Average elevation (m)	Stone scaling factor	^{10}Be (10^5 at g^{-1})	^{26}Al (10^5 at g^{-1})	^{10}Be denudation rate (mm ka^{-1})	^{10}Be averaging time (ka)	^{26}Al denudation rate (mm ka^{-1})	^{26}Al averaging time (ka)	^{26}Al/^{10}Be
SA03-2-1	28.0	637.8	1.31	2.72 ± 0.20		14.36 ± 1.34	41.52			
SA04-19-1-A	28.0	637.8	1.31	3.78 ± 0.81		10.26 ± 2.29	58.09			
SA04-19-1-B	28.0	637.8	1.31	3.05 ± 0.09		12.76 ± 0.75	46.70			
SA04-19-1-C	28.0	637.8	1.31	2.66 ± 0.14		14.67 ± 1.14	40.65			
SA04-28-1	28.0	683.7	1.45	6.73 ± 0.01		5.85 ± 0.49	101.88			
SA04-29-1	25.9	1216.1	1.92	15.3 ± 0.02	74.27 ± 2.24	3.53 ± 0.29	168.80	4.18 ± 0.29	142.55	4.85 ± 0.32
SA04-35-1	31.0	1762.0	3.14	17.31 ± 0.02	91.69 ± 1.83	5.19 ± 0.43	114.89	5.70 ± 0.37	104.54	5.30 ± 0.33
SA04-36-1	31.0	1766.0	3.13	12.22 ± 0.25		7.43 ± 0.44	80.26			
SA04-37-1	31.0	1966.0	3.61	4.63 ± 0.01	25.37 ± 0.78	23.15 ± 1.93	25.75	25.51 ± 1.74	23.37	5.47 ± 0.36
SA04-42-1	29.0	1296.0	2.17	9.43 ± 0.32		6.67 ± 0.45	89.41			
SA05-8-1	28.0	709.1	1.43	18.18 ± 0.46		2.03 ± 0.13	293.01			
SA05-9-1	28.0	804.9	1.43	18.00 ± 0.39		2.23 ± 0.14	267.48			
SA05-14-1	28.0	2314.0	3.36	2.62 ± 0.16		48.47 ± 4.10	12.30			

Table 5.2.1 (previous page) Cosmogenic nuclide data and basin-wide denudation rates for tributary channels of the Orange River. The altitude latitude scaling factor is calculated according to Stone (2000) using combined spallation and muogenic production. Total Al concentration in quartz is determined by ICP-AES at 2% uncertainty. Be data are normalised using the SUERC NIST standard with a nominal $^{10}Be/^{9}Be$ ratio of 3.00×10^{-11}. Al data are normalised using Z92-0222 standard with a nominal $^{26}Al/^{27}Al$ ratio of 4.11×10^{-11}. Denudation rates are calculated using sea level, high latitude ^{10}Be and ^{26}Al production rates (Stone 2000). See Appendix 4 for full details of data. ± represents standard uncertainty.

5.2.2 Tributary catchments in the upper Orange River

A number of contrasting lithological and relief environments were selected in the upper Orange basin. Samples SA04-35-1, SA04-36-1 and SA04-42-1 are from the Molteno sandstone Formation. They have a comparably low rate of denudation (5-7 mm ka^{-1}) in contrast with sample SA04-37 from the Elliot Formation (23 mm ka^{-1}). Sample SA05-14-1, from the Clarens sandstone Formation, has a denudation rate of almost 50 mm ka^{-1}. The Clarens and Elliot Formations appear to be slightly more erodible than the Molteno Formation, and the Clarens Formation appears more erodible than the Elliot Formation. The higher quartz content of the Molteno Formation makes it fairly resistant to denudation, whereas the Elliot formation has a lower quartz concentration and higher feldspar content, making it less resistant to denudation. The Clarens Formation has lower quartz content, and a higher feldspar content (Eriksson *et al.*, 1994). Differential denudation of the sandstone and mudstone units of the Clarens formation has resulted in the formation of spectacular high relief sandstone cliffs in the Golden Gate sampling region (Plate 5.2.1). Runoff and relief play a role in the higher denudation rates in Golden Gate region – the region is wetter than the Elliot and Molteno regions (750-1000 mm a^{-1} as compared with 500-750 mm a^{-1}) leading to greater runoff and potential for erosion in the former. The Golden Gate region has much steeper topography partly due to it being on the edge of the high relief Lesotho Highlands – the Clarens Formation sampling location has a relief ratio of 0.13; whereas the Elliot Formation and Molteno sampling regions have relief ratios of 0.04 and 0.06, respectively. Thus a combination of high relief, high potential for runoff from high rainfall and relatively erodible lithology, as expected, explain the high denudation rates (Ahnert, 1970).

Plate 5.2.1 (top) High relief Clarens vs. (bottom) low relief Molteno sandstone Formations.

5.2.3 Tributary catchments in the lower Orange River

Four samples (SA03-2-1, SA04-19-1-A, -B, -C) were taken from a small (~ 14 km^2) a dry tributary channel in the Augrabies Falls region, downstream of the main knickpoint. The denudation rates of between ~ 10 and 15 mm ka^{-1} (average 13.01 ± 1.38 mm ka^{-1}) are comparable and consistent. A tributary basin (~ 34 km^2) just west of the basin described above was sampled (SA04-28-1). The average denudation rate of ~ 6 mm ka^{-1} is consistent with other samples in the Augrabies region. Two samples taken from two different branches of a larger (~ 16-17 km^2) tributary on the south bank of the Orange River in the far west of the Augrabies National Park (SA05-8-1, -9-1) have denudation rates of 2.03 and 2.23 mm ka^{-1}, respectively which is similar to the other tributary samples in the region (Table 5.2.2). These tributaries have relatively low relief ratios of 0.02-0.03.

Sample	^{10}Be erosion rate (mm ka^{-1})			^{10}Be averaging time (ka)
SA03-2-1	14.36	±	1.34	41.52
SA04-19-1-A	10.26	±	2.29	58.09
SA04-19-1-B	12.76	±	0.75	46.70
SA04-19-1-C	14.67	±	1.14	40.65
SA04-28-1	5.85	±	0.34	101.88
SA05-8-1	2.03	±	0.13	293.01
SA05-9-1	2.23	±	0.14	267.48
Average	8.88	±	1.00	121.33

Table 5.2.2 Showing variation in denudation rates of tributary channels in the Augrabies Falls region.

It can be seen from Table 5.2.2 that catchment-averaged denudation rates of tributary channels in the Augrabies region are generally low (average <10 mm ka^{-1}). The rapidly eroding tributaries in the upper part of the basin can be explained with reference to the high relief and high rainfall, and the slowly eroding tributaries in the Augrabies region can be explained with reference to the relatively low topographic gradients in the channel (average relief ratio of 0.03) and the arid climate (100-250 mm a^{-1}). The Fish River tributary has an extremely low catchment-averaged denudation rate (5.85 ± 0.34 mm ka^{-1}) consistent with the extremely low rates of denudation in Namibia reported by Cockburn & Summerfield (1999) and Bierman &

Caffee (2001). This river is in a hyperarid (< 100 mm a^{-1} rainfall) setting and has a very low relief ratio (0.002) and a relatively resistant granite lithology in much of the basin. This results in one of the lowest measured catchment-averaged denudation rates for the wider Orange basin.

5.2.4 Aluminium data

As can be seen from Table 5.2.1 and Figure 5.2.2., the $^{26}Al/^{10}Be$ ratio for the samples from the main channel of the Orange River is 4.85 ± 0.32; 5.30 ± 0.33 and 5.47 ± 0.36 mm ka^{-1}, for samples SA04-29-1, -35-1 and SA04-37-1, respectively. The ideal ratio assuming no burial or shielding is 6.1 ± 0.5. A ratio of less than 6.1 may suggest that some burial and shielding of the sample has occurred. Given that the uncertainties on the values of 5.30 and 5.47 are within 1 standard deviation uncertainty of the idealised ratio of 6.1, any shielding of samples SA04-35-1 and -37-1 is therefore insignificant. There is no apparent complexity in the exposure history of samples SA04-35-1 and SA0-37-1, given that both plot on the steady state denudation island to within 1 standard deviation uncertainty (Small, 1997).

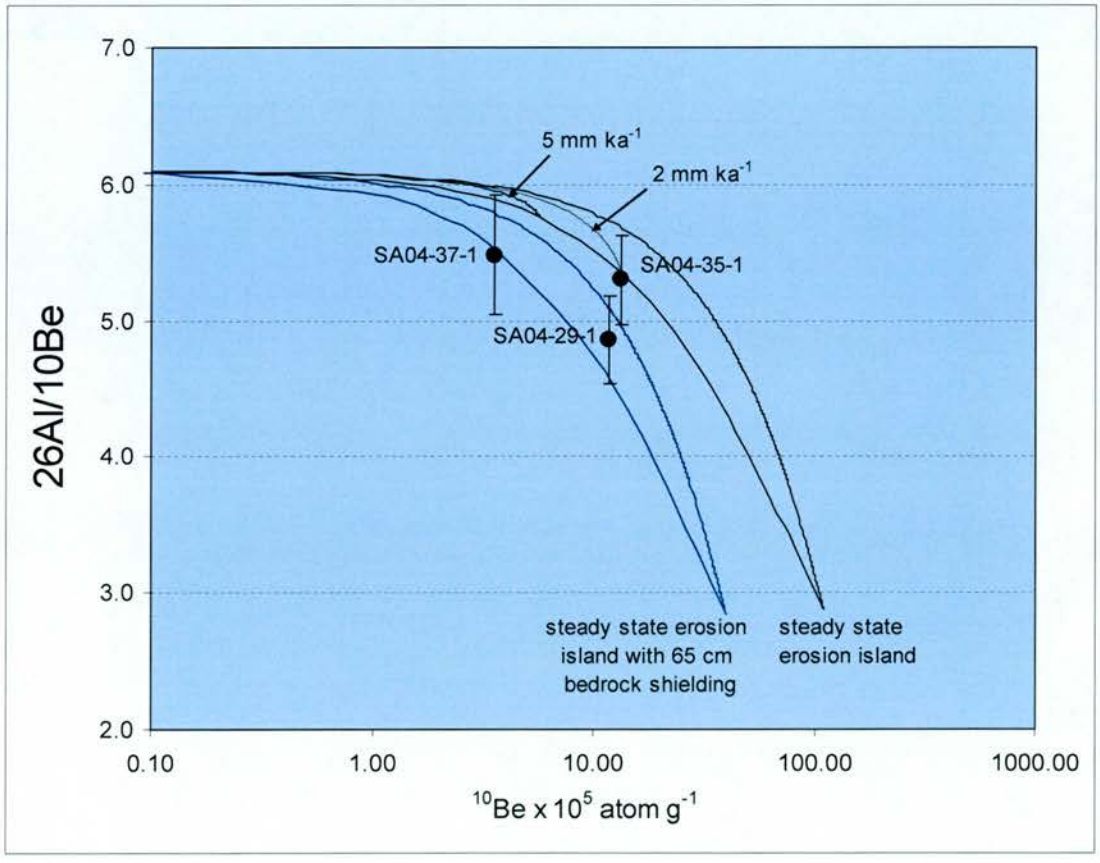

Figure 5.2.2 (previous page) Plot showing ^{10}Be concentration against ^{26}Al/^{10}Be ratios for tributary samples. Upper line in the 'banana' shaped plots show scenario for a sample experiencing constant exposure. Lower line shows scenario for a sample experiencing steady state erosion. The scythe shaped windows show the region where samples have either been continuously exposed or steadily eroding. The upper scythe-shaped plot shows a normal, non complex exposure history. The lower plot shows a complex exposure history where the samples would have been covered by ~ 90 cm of sediment. Error bars show total uncertainties (i.e. production rate and analytical uncertainties).

Sample SA04-35-1, which is taken from a small tributary basin in the Molteno Formation, has an ^{26}Al-derived denudation rate which is consistent with that of the ^{10}Be derived rate (5.19 ± 0.31 mm ka^{-1} compared with 5.70 ± 0.37 mm ka^{-1}). This sample plots on the steady state erosion island (Figure 5.2.2). Sample SA04-37-1, from a small tributary basin in the Elliot Formation, has an ^{26}Al derived denudation rate of 23.15 ± 1.36 mm ka^{-1} compared with a ^{10}Be derived rate of 25.54 ± 1.56 mm ka^{-1}. These rates are virtually indistinguishable to within 1 standard deviation uncertainty and emphasise a consistently fairly high denudation rate for these tributary samples. The uncertainties on the Al/Be ratio of this sample overlap with the ideal ratio of 6.1 ± 0.3. Figure 5.2.2 shows that the ^{26}Al/^{10}Be ratio of sample SA04-29-1 is 4.85 ± 0.32, suggesting that the sample has undergone some burial and shielding in the past. Indeed, it could be that the sample was shielded by bedrock, sediment or water. Calculations show that shielding by at least 65 cm of bedrock, or ~ 90 cm of sediment, or ~ 150 cm of water, would be required to shield the sample for over 432 ± 46 ka (the burial time, calculated according to Granger & Muzikar (2001)). Sustained shielding by water is unlikely in this semi-arid basin, leaving rock and sediment shielding as possible factors. Quartz clasts could have been shielded *in-situ* on a hillslope by bedrock before becoming detached, or clasts could have been shielded by boulders whilst entrained in the river's sediment. Given that this sample represents a large part of the Fish River basin, it is unlikely that the clasts in the sample would all have been equally affected by bedrock shielding to the extent that it shows in the Al/Be ratio. A more likely scenario is that many of the clasts in the sample were shielded by sediment for a significant period (tens to hundreds of thousands of years) while entrained in the river. Given that the Fish River tributary is currently hydrologically discontinuous and large parts of the upstream region are

effectively separated from the downstream region, it is not surprising that some degree of storage has apparently gone on in the basin. The sample was apparently buried for around 432 ka. It can be seen from Figure 5.2.2 that prior to burial, the sample would have had a denudation rate of between 2 and 5 mm ka^{-1}, not dissimilar to the denudation rate averaged over the last 169 ka, of 3.53 ± 0.21 mm ka^{-1}.

5.3 Comparison of tributary and main channel catchment-averaged samples

5.3.1 Upper Orange River

As a general trend, the highest denudation rates are from the main channel and tributaries upstream of Aliwal North (Table 5.3.1). In particular, samples SA04-41-1 and SA05-14-1 have the highest denudation rates, with rates of 23.71 ± 2.26 and 48.47 ± 0.08 mm ka^{-1}, respectively – the highest rates measured. Sample SA05-14-1 is from a high relief area (relief ratio 0.13) and SA04-41-1 from a low relief area (relief ratio 0.007, though locally relief will be much higher than this). Both are taken from seasonally wet areas with a wide variety of lithologies in the case of SA04-41-1 and fairly uniform, and high relief in the case of SA05-14-1. Tributaries upstream of Aliwal North include those taken in the Elliot and Molteno Formations (SA04-37-1 and SA04-35-1, -36-1, -42-1, respectively). These sampling locations, by virtue of their moderate relief (relief ratio 0.04-0.10) and lower denudation rates are in fact more characteristic of the middle course of the Orange River than the upper Orange. Even taking into account the lower denudation rate samples, the upper Orange River region still has an average denudation rate higher than the other two areas, of 19.10 ± 1.6 mm ka^{-1}.

5.3.2 The middle Orange River

The average denudation rate of the middle course of the Orange River is 6.50 ± 0.84 mm ka^{-1} (Table 5.3.2). As mentioned above, certain samples from the Upper Orange tributaries have more in common in terms of geomorphic environment with the low-relief middle course of the Orange River, and indeed the denudation rate in these areas is comparable to that of the middle course of the river (<10 mm ka^{-1}). This

emphasises that despite the Orange basin being arbitrarily divided into upper, middle and lower regions, a very small proportion of the total Orange basin is true upland, high relief catchment, and for the most part it is low relief and low channel gradient (average 1.70 m km^{-1}, Summerfield & Hulton, 1994).

5.3.3 The lower Orange River

The samples taken from the lower part of the Orange River in the Augrabies Falls region are also discussed with respect to bedrock incision rates at Augrabies in Chapters 7-9. The tributaries in the lower Orange River are generally eroding faster than the trunk channel (See chapter 7, Table 5.3.3). This may be a response of the tributary channels incising to keep track of changes in local base level, but overall the difference in rates is too small to draw significant conclusions from. The rates experienced here are all fairly consistent and in the range of 3-15 mm ka^{-1}. They are also some of the lowest denudation rates measured anywhere in the Orange basin. Note that these rates represent catchment-averaged rates, and bedrock incision rates are presented in Chapters 7-9.

Sample	Average latitude (degrees south)	Average elevation (m)	Stone shielded scaling factor	^{10}Be (10^5 atom g^{-1})	^{26}Al (10^5 atom g^{-1})	^{10}Be Denudation rate (mm ka^{-1})	^{10}Be averaging time (ka)
						23.71 ± 2.26	25.34
SA04-41-1	29.1	1984.6	3.53	4.55 ± 0.21			
						5.19 ± 0.43	114.89
SA04-35-1	31.0	1762.0	3.14	17.31 ± 0.02	91.69 ± 1.83		
						7.43 ± 0.44	80.26
SA04-36-1	31.0	1766.0	3.10	12.22 ± 0.25			
						23.15 ± 1.93	25.75
SA04-37-1	31.0	1966.0	3.61	4.63 ± 0.01	25.37 ± 0.78		
SA04-42-1	29.0	1296.0	2.17	9.43 ± 0.32		6.67 ± 0.45	89.41
						48.47 ± 4.10	12.30
SA05-14-1	28.0	2314.0	3.36	2.62 ± 0.16			
average						19.10 ± 1.60	57.99

Table 5.3.1 Results from the upper Orange River. Denudation rates are calculated using Stone's (2000) SLHL scaling factors for spallation and muogenic production. Be data are normalised using the SUERC NIST standard with a nominal ^{10}Be/^{9}Be ratio of 3.00 x10^{-11}. Denudation rates are calculated using sea level, high latitude ^{10}Be production rate (Stone 2000). See Appendix 4 for full details of data.

Sample	Average latitude (degrees south)	Average elevation (m)	Stone shielded scaling factor	^{10}Be (10^5 atom g^{-1})	Denudation rate (mm ka^{-1})			^{10}Be averaging time (ka)
SA03-6-1	29.6	1456.7	2.46	12.27 ± 1.41	5.76	±	0.74	103.50
SA03-7-1	29.6	1456.7	2.43	9.90 ± 1.14	7.24	±	0.94	82.34
average					6.50	±	0.84	92.92

Table 5.3.2 Results from the middle course of the Orange River. Wellington's (1955) value for the gradient for this part of the river (from Aliwal North to the Augrabies Falls) is 1.70 m km^{-1} (corroborated by Summerfield & Hulton, 1994). Denudation rates are calculated using Stone's (2000) SLHL scaling factors for spallation and muogenic production.

Sample	Average latitude (degrees south)	Average elevation (m)	Stone shielded scaling factor	^{10}Be (10^5 atom g^{-1})	Denudation rate (mm ka^{-1})			^{10}Be averaging time (ka)
SA03-4-1	29.6	1383.3	2.43	14.16 ± 0.43	4.89	±	0.32	121.86
SA03-5-1	29.6	1383.3	2.43	21.15 ± 2.85	3.18	±	0.47	187.20
SA04-30-1-A	29.0	1230.0	2.31	15.76 ± 0.61	3.61	±	0.33	165.121
SA04-30-1-B	29.0	1230.0	2.31	14.13 ± 0.28	4.65	±	0.40	128.09
SA04-30-1-C	29.0	1230.0	2.31	10.98 ± 2.15	6.07	±	0.46	98.26
SA03-2-1	28.0	637.8	2.5	2.72 ± 0.20	14.36	±	1.34	41.52
SA04-19-1-A	28.0	637.8	2.5	3.78 ± 0.81	10.26	±	2.29	58.09
SA04-19-1-B	28.0	637.8	2.5	3.05 ± 0.09	12.76	±	0.75	46.70
SA04-19-1-C	28.0	637.8	2.5	2.66 ± 0.14	14.67	±	1.14	40.65
SA04-28-1	28.0	683.7	6.9	6.73 ± 0.01	5.85	±	0.49	101.88
SA04-29-1	25.9	1216.1	10.7	15.3 ± 0.02	3.53	±	0.29	168.80
SA05-8-1	28.0	709.1	7.1	18.18 ± 0.46	2.03	±	0.13	293.01
SA05-9-1	28.0	804.9	7.6	18.00 ± 0.39	2.23	±	0.14	267.48
average					6.78	±	0.66	132.20

Table 5.3.3 Results from the lower Orange River. Denudation rates are calculated as in Table 5.3.1.

Chapter 6 – Discussion of catchment-averaged samples

6.1 Comparison of intermediate- and short-term denudation rates

This chapter discusses the catchment-averaged rates of denudation presented in Chapters 4 and 5 with respect to short-term denudation rates (10^1-10^3 a); existing intermediate-term cosmogenic derived denudation rates (10^4-10^6 a) from southern Africa and elsewhere; and long term denudation rates (>10^6 a) from thermochronological methods and the offshore sedimentary record. Different models of landscape evolution and theories of denudation history are then assessed in the light of the new, regional scale, intermediate-term denudation rates from cosmogenic nuclides and existing, regional, long term denudation rate data.

6.1.1 Comparison with decadal-scale denudation rates

The catchment-averaged technique allows quantification of denudation rates over large parts of the Orange basin. These rates can be compared with published values of modern (10^1 a) denudation rates in order to assess the 'benchmark' pre-anthropogenic denudation rates against modern rates and consider the relative influence of climate and human activity on these rates (Plate 6.1.1). This assumes that deposition rates can be taken as a proxy for erosion rates. The data presented below are from published sources on the Quaternary rates of sediment deposition in small farm dams in the Sneeuberg Uplands ~ 70 km north of Graaf Reinet, South Africa in the Klein Seekoei River valley, which drains north towards the Orange River in central South Africa (Figure 6.1.1). Sedimentation rates were studied in two small catchments (<10 km^2) in the headwaters of the Klein Seekoei River by Foster *et al.* (2005) using ^{137}Cs inventories (Table 6.1.1). Sediment yields are averages for the last ~ 70 years based on extrapolated depths to the original ground surface based on 7 cores from Dam 7 and Dam 10 and give total sediment yields of 271 t km^{-2} yr^{-1} and 512 t km^{-2} yr^{-1}, respectively (Foster, personal communication, 2006). The dams are evident on a 1945 aerial photographic survey and thus pre-date the onset of southern hemisphere ^{137}Cs post-bomb testing in the 1950s (Foster *et al.*, 2005). The sediments in the dam are labelled with the atmospheric fallout radionuclide ^{137}Cs and have a high inventory compared with the reference site. This suggests that the dam sediments have derived largely from topsoil sources that are also enriched in ^{137}Cs.

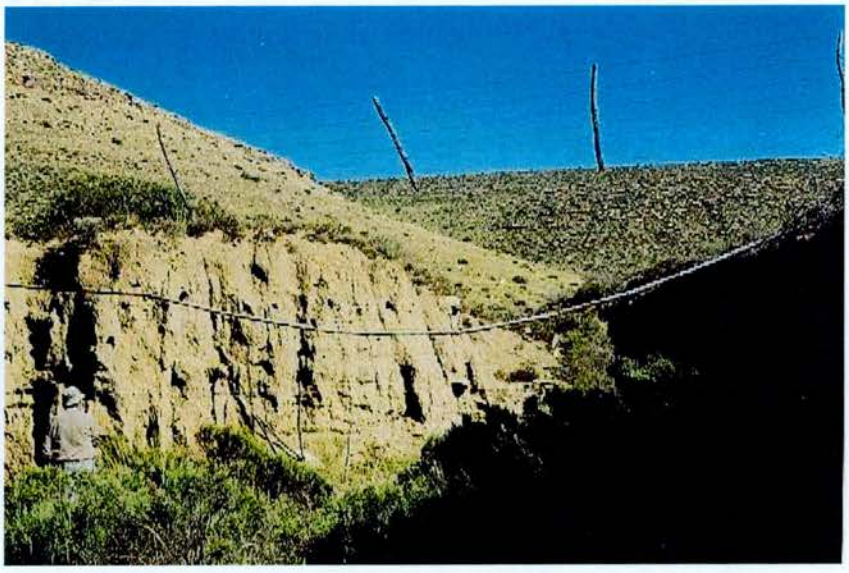

Plate 6.1.1 Evidence of soil erosion in the central Karoo. The fence was constructed in 1937, at a time when the eroded gully system would have been less extensive (as suggested by the presence of fence posts across the gully). Photograph courtesy of John Boardman.

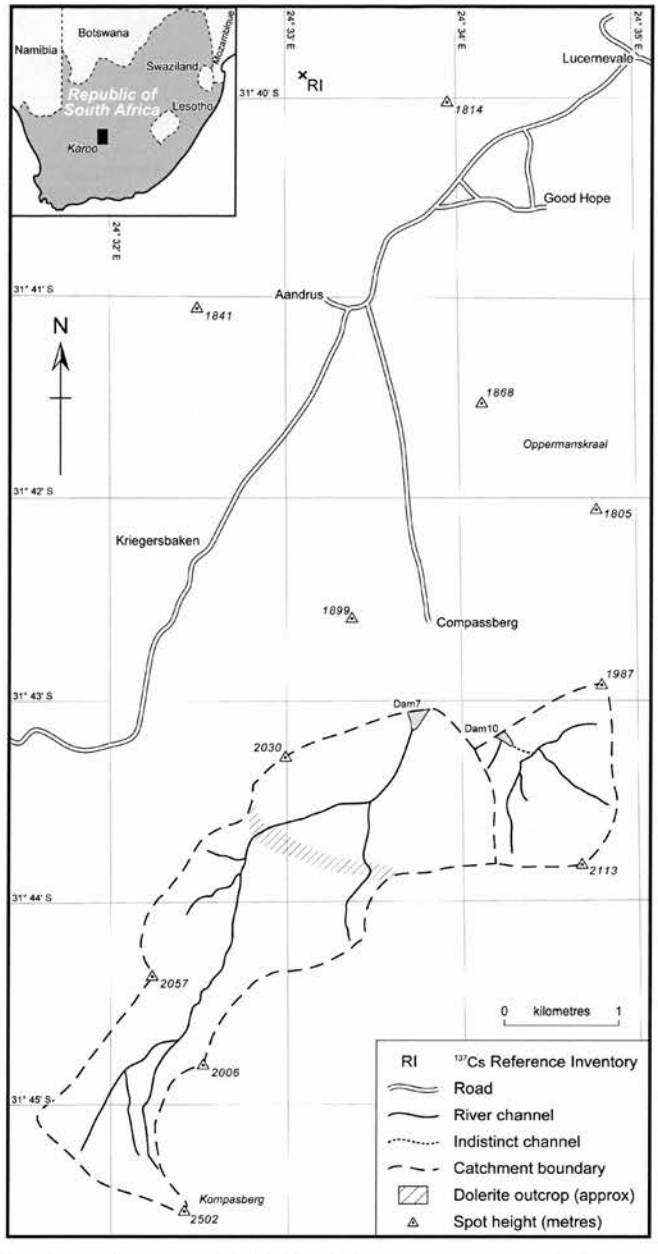

Figure 6.1.1 Location and details of the research catchments and sampling sites used in Foster *et al.* (2005). The gully wall sediments in this study contain no detectable ^{137}Cs (Foster, personal communication, 2006).

Characteristic	Dam 7	Dam 10
Catchment area (excluding reservoir) (km^2)	6.30	1.48
Reservoir area (km^2)	0.03	0.02
Maximum altitude (m)	2502	2113
Minimum altitude (m) (approx.)	1840	1860
Relative relief (m)	662	253
Sediment yield (t km^{-2} a^{-1})	271	512
Denudation rate (mm ka^{-1})*	104.23	196.92
Denudation rate (mm ka^{-1})**	180.67	341.33

Table 6.1.1 Characteristics of Dam 7 and Dam 10, their catchments and average denudation rates (based on Foster *et al.* (2005). * Calculated assuming bedrock density of 2.6 kg m^{-3}. ** Calculated assuming soil density of 1.5 kg m^{-3}.

The average yields in Table 6.1.1 were adjusted for catchment area and the denudation rates derived from these yields (assuming a sediment density of 2.6 t m^{-3}) are 104.23 mm ka^{-1} for Dam 7 and 196.92 mm ka^{-1} for Dam 10, both averaged over the entire catchments. This assumes a steady state thickness for the weathering mantle – as much rock is converted at depth to lower density weathered material/soil as is being removed from the surface. If it is assumed that just soil is being removed (which, given the ^{137}Cs content of the sediment, is probably more accurate) then a soil density of 1.5 kg m^{-3} can be assumed in the calculations and the denudation rates for Dam 7 and Dam 10 are 180.67 and 341.33 mm ka^{-1}, respectively. These denudation rates greater than, but not massively greater than, the cosmogenic-derived denudation rates from the central Orange basin. Problems with processing sufficient volumes of quartz from the fine-grained lithology of the Sneeuberg Uplands region precluded obtaining denudation rates from nearer Foster *et al.*'s (2005) sampling sites. The catchment-averaged denudation rate of the sample taken at Groblershoop (the closest sampling site) is 7.24 ± 0.94 mm ka^{-1} averaged over ~ 80 ka. This represents an increase in denudation of around 25 times and 50 times for Dam 7 and Dam 10 respectively (or around two orders of magnitude for both) between the early to mid-Pleistocene and the last ~ 80 years.

6.1.2 Denudation and degradation in the Karoo

Natural (pre-anthropogenic) denudation rates in the Sneeuberg Uplands would be expected to be higher than those averaged for the whole area upstream of Groblershoop. The catchments studied by Foster *et al.* (2005) are of much higher relief than the average relief upstream of Groblershoop (the average topographic gradients of the catchment upstream of Dams 7 and 10 are ~ 132 m km^{-1} and 169 m km^{-1}, respectively, compared with 0.625 m km^{-1} upstream of Groblershoop). However, the short-term denudation rates in the Sneeuberg Uplands are around 3 to 7 times higher than the intermediate term rates from a similarly high relief region, the Golden Gate Highlands region, where the Little Caledon River catchment has a topographic gradient of 127.1 m km^{-1} and a denudation rate of ~ 48 mm ka^{-1}. Therefore part of the higher recent denudation rates in the Sneeuberg Uplands can be explained by the region having higher relief than the larger catchment with which it is being compared. However, this only explains part of the higher denudation rates in the short-term compared with the intermediate-term. By its nature, a longer record will capture a wider range of events of differing frequency and magnitude – in this case the cosmogenic record seems to be capturing high frequency, low magnitude denudation events whereas the sedimentary record may have captured low frequency high magnitude events. These events could have been driven by climate, humans or a combination of both.

The debate over recent land degradation in the Karoo has centred on the relative influence of climate and anthropogenic disturbance as major contributing factors (Plate 6.1.1; Boardman *et al.*, 2003, Keay-Bright & Boardman, 2006). There is some debate whether pre-colonial herders caused irreversible damage to the landscape by overgrazing (Lovegrove, 1993); though Fox (2000) and Keay-Bright & Boardman (2006) suggest that European colonists are responsible for the dramatic increase in degradation over the last 200 years. Denudation is particularly apparent in the post-1945 period in the form of extensive colluvial 'badland' gully systems (mapped by contemporary aerial photography), although it is clear that the vast majority of this degradation occurred before the first aerial photographs were taken in 1945 and there appears to have been some recovery of degraded land since then (Keay-Bright &

Boardman, 2006). The sedimentary record from farm dams covering the last ~ 80 years also indicates accelerated denudation in the middle part of that period (Foster *et al.*, in review). Keay-Bright & Boardman (2006) conclude that cultivation of land has led to locally extensive denudation and, whilst climatic change has occurred in the form of increased rainfall intensity, this does not appear to have led to an increase in denudation. The cosmogenic derived denudation rates, which are integrated over several climatic cycles and should therefore 'smooth out' temporal variations in climate, are around two orders of magnitude lower than the rates for the last few decades, a time when anthropogenic activity has demonstrably increased denudation rates whilst climate appears to have had less of an impact. This suggests that humans, rather than climate, have been mainly responsible for accelerated denudation.

Gellis *et al.* (2004) raise the question about the sediment sources for cycles of aggradation and filling in a similar semi-arid setting in New Mexico. They question whether channel filling is a result of redistribution of sediment stored in the alluvial valleys or from upland denudation of recently generated regolith (Gellis *et al.*, 2004). Since Foster *et al.*'s sediment contained high ^{137}Cs, activities the sediment was predominantly topsoil rather than reworked alluvial or colluvial material. Sediment yields are averages for the last ~ 80 years based on extrapolated depths to the original ground surface based on 7 cores from each dam. No account is taken of dam trap efficiency or changing trap efficiency through time, a possible limitation of the short-term data (Foster, personal communication, 2006). These sedimentation estimates assume that there is no sediment loss over the dam during high flow events, clearly an unrealistic assumption (Keay-Bright & Boardman, 2006) therefore the sediment yields represent minimum yields. A possible limitation of the comparison with intermediate-term data is that the Sneeuberg Uplands and the wider Orange basin are topographically, lithologically and climatically different. This means that part of the difference in denudation rates may be explained by these factors. Nonetheless, the samples described in Chapters 4 and 5 are also taken from topographically, lithologically and climatically different parts of the Orange basin yet this accounts for a maximum of only around one order of magnitude difference in the rates. Since the short- and intermediate- term rates are around two orders of magnitude different,

human activity clearly has a significant part to play in influencing the short term rates. The comparison of short and intermediate-term rates suggests that it is anthropogenic activity, rather than climatic change, that is the driver of short-term increased denudation rates. Cosmogenic nuclide analysis can thus be a useful tool for benchmarking intermediate-term, pre-anthropogenic denudation rates in sensitive, degraded landscapes.

6.1.3 Benchmarking natural denudation rates

There are a number of well-known studies in the cosmogenic literature that compare cosmogenic-derived long term denudation rates with measured short term rates, such as Hewawasam *et al.* (2003) who find that in the tropical highlands of Sri Lanka, the 'benchmark' cosmogenic derived denudation rates are exceeded by several orders of magnitude by modern human-induced denudation (measured from stream sediment), and agricultural soil being lost 10 to 100 times faster than it is produced. The natural, background, pre-anthropogenic denudation rates derived from cosmogenic nuclide analysis are ~ 10 to 48 mm ka^{-1}. The stream sediment data suggest that there has been a 10 to 100-fold recent (last ~ 250 a) increase in spatially averaged soil erosion. The long term cosmogenic derived erosion rates are comparable to natural rates of soil production (Heimsath et al., 1997), suggesting that the recent, human driven rate of soil loss in Sri Lanka is resulting in the loss of a non-renewable resource. This is similar to the pattern in the Karoo, where denudation rates in the past ~ 80 years are around 2 orders of magnitude higher than the intermediate term (~ 80 ka) rates.

In contrast, Kirchner *et al.* (2001) find that denudation rates were around seventeen times higher on timescales of tens of thousands of years than over decadal timescales (derived from modern stream sediment fluxes) in high relief Idaho catchments (hillslope gradients 23% to 57%). The long term rates are consistent with denudation rates on 10 Ma timescales measured by apatite fission tracks. From small experimental catchments (0.2 km^2) to large river basins (35 000 km^2), long-term sediment yields are consistently much greater than conventional measurements over years or decades would suggest (Kirchner *et al.*, 2001). The fact that the cosmogenic derived rates agree with thermochronologic derived rates suggests the cosmogenic

rates are not anomalously high. Discounting climatic change as being responsible for the observed differences in sediment yield, Kirchner *et al.* suggest extremely episodic sediment delivery, dominated by events that are large but rare, as being responsible for the higher long term sediment yield. These events are so rare that they are unlikely to be reflected in measurements over years or decades. They conclude that incremental erosion prevails most of the time, but accounts for a small fraction of the total sediment yield; by contrast, catastrophic erosion events are rare and brief, but dominate the long-term sediment yield. This seems to agree with the long-term cosmogenic derived sediment-generation rates in central Europe, which are 1.5–10 times higher than short-term sediment yields (Schaller *et al.*, 2001). One possible explanation is that cosmogenic nuclides inherit an elevated late Pleistocene erosion signal from periglacial processes (Schaller *et al.*, 2001, 2002). Other comparison studies also illustrate that short-term sediment delivery is not in steady state with long-term sediment generation (Brown *et al.*, 1995; Clapp *et al.*, 2000; Hewawasam *et al.*, 2001).

6.2 Comparison with existing intermediate-term denudation rates in southern Africa from cosmogenic nuclide analysis

Relatively few studies have characterised intermediate-term (10^3-10^6 a) denudation rates in southern Africa using cosmogenic nuclides (Fleming *et al.*, 1999; Cockburn & Summerfield; Cockburn *et al.*, 2000; Bierman & Caffee, 2001; van der Wateren & Dunai, 2001). All of these studies have emphasised the essential stability of the southern African landscape over at least hundreds of thousands of years. The denudation rates presented in these studies are low (generally ~10 mm ka^{-1}) and are of a similar order of magnitude as the results presented here. Many of these studies derive denudation rates of rock outcrops, whose denudation rates are generally lower than the surrounding terrain. Rates from these outcrops are difficult to translate into landscape erosion rates, since the rocks crop out precisely because their erosion history differs from that of the surrounding terrain (Cockburn & Summerfield, 2000). This study has tried to quantify rates of denudation for large areas of the southern Africa landscape and, accordingly, several areas have denudation rates higher than those recorded in bedrock outcrops by previous studies. However, the average rate of

denudation for all samples from the Orange basin is 10.79 ± 1.03 mm ka^{-1}, with a range of rates between 2.03 ± 0.13 to 48.47 ± 4.10 mm ka^{-1}, which is a similar value to the previously published average rates. The range of rates cover the natural, pre-anthropogenic rate of 28 mm ka^{-1} derived for the Orange by Summerfield and Hulton (1994) based on mean annual solid load data from Rooseboom & Harmse (1979) and mean annual solute data from Meybeck *et al.* (1976). They are also similar to the preliminary rates of between 7 and 114 mm ka^{-1} by Rust and Summerfield (1990) from offshore sedimentary evidence.

6.2.1 The western margin of southern Africa

Bierman & Caffee (2001) analysed a large number of samples for ^{10}Be and ^{26}Al from the Namib Desert and Namibian Escarpment and showed that bedrock samples both inland and seaward of the Escarpment were indistinguishable (3.2 ± 1.5 mm ka^{-1} and 3.6 ± 1.9 mm ka^{-1}, respectively). These rates are very similar to the catchment-averaged denudation rate for the Fish River catchment, the nearest location sampled, of 3.53 ± 0.21 mm ka^{-1}. Bierman and Caffee also derived catchment-averaged denudation rates for the western margin of Namibia from four large river basins (ranging from $1.6x10^4$ to $1.2x10^5$ km^2) which gave an average denudation rate of 7.91 mm ka^{-1} (Table 6.2.1) once again of a similar order of magnitude to the rates derived in this study. From a comparison of bedrock and catchment-averaged derived denudation rates, they found that the bedrock samples generally have lower denudation rates than the catchment-averaged samples – hence explaining why bedrock outcrops are positive relief features. This trend is also observed in the data presented in this study – tributaries in the lower Orange region have an average denudation rate of 6.78 ± 0.66 mm ka^{-1}, compared with 5.29 ± 0.40 mm ka^{-1} for bedrock outcrops (see Chapter 7). Note that whilst these differences are small, it is precisely the small relative rate differences that have generated the landscape we currently see. Bierman & Caffee find that small tributaries generally have higher denudation rates than larger catchments, in common with the findings presented in Chapters 4 and 5, where small tributaries (up to 10^3 km^2) are eroding on average at 12.79 ± 0.68 mm ka^{-1} compared with the large catchment (10^4-10^6 km^2) rate of 7.00 ± 0.59 mm ka^{-1}. This is largely due to the higher relief in tributary catchments (high

relief is positively correlated with denudation (Ahnert, 1970; Summerfield & Hulton, 1994)) and the lower relief and large area available for sediment storage in the Orange basin (which may effectively dilute a high-denudation signal).

Sample	Area (km^2)	Mean ^{10}Be denudation rate ($mm\ ka^{-1}$)
NAM-08	53.00	5.30
NAM-09	13.00	16.10
NAM-16	16000.00	9.00
NAM-43	0.50	8.30
NAM-46	4100.00	7.30
NAM-52	120000.00	2.60
NAM-57	28000.00	6.80
average	**24023.79**	**7.91**

Table 6.2.1 Catchment-averaged denudation rates from Namibian sediment samples. Note that denudation rates are of the same order of magnitude as the Orange basin samples described in Chapters 4 and 5. The average denudation rate of all samples is similar to that for the Orange basin, 10.31 ± 0.64 mm ka^{-1} (Bierman & Caffee, 2001).

The samples presented by Bierman & Caffee do not support a model of significant and ongoing retreat of the Namibian Escarpment. This conclusion was also reached previously by Cockburn & Summerfield (2000) and Cockburn *et al.* (2000). Cockburn *et al.* (2000) derived denudation rates from ^{10}Be and ^{26}Al analysis of free face and granite ridge bedrock samples on an 800 m escarpment in the Gamsberg region of Namibia ~ 150 km inland of the coast (Table 6.2.2). They found that the average denudation rate of the free face averaged 7.08 mm ka^{-1}, and the denudation rate on the coastal plain bornhardts averaged 0.45 mm ka^{-1}. Once again, these bedrock denudation rates are of the same order of magnitude as catchment-averaged denudation rates in the western part of the Orange basin. The previously published bedrock denudation rates are lower than the catchment-averaged rates as would be expected for bedrock samples that stick out from the surrounding landscape and have clearly undergone a different rate of denudation to the rest of the landscape. Using in-situ ^{21}Ne dating of pediment surfaces, river terraces and river cut bedrock benches, Van der Wateren & Dunai (2001) present denudation rates for the central Namib desert which are even lower than the ones presented above (of the order of 0.5 to 1 mm ka^{-1}). These rates are integrated over the last 5 Ma and, like the data presented above, are in good agreement with the data presented from thermochronologic

methods (discussed below). The rates presented by Van der Wateren & Dunai (2001) are an order of magnitude lower than the rates presented in the previous chapters. This emphasises the extreme stability of the central Namib in contrast to the more geomorphically active Orange River basin.

Sample	Location	Mean ^{10}Be erosion rate (mm ka^{-1})	± Standard uncertainty
8/95	Free Face	6.2	1.3
9/95	Free Face	5.9	1.2
11/95	Free Face	11.7	2.5
15/94	Free Face	4.5	1
average		**7.08**	**1.5**
10/95	Summit	0.40	0.1
10R/95	Summit	0.40	0.1
12/95	Summit	0.5	0.1
14/95	Summit	0.5	0.1
average		**0.45**	**0.1**

Table 6.2.2 Rates of denudation of summit and free face samples in the Gamsberg region, Namibia from Cockburn *et al.* (2000).

6.2.2 The south-east margin of southern Africa

In the far south east of the Orange basin, a study using cosmogenic ^{36}Cl concentrations in basalt samples gives denudation and scarp retreat rates of the Drakensberg Escarpment (Fleming *et al.*, 1999). The average summit denudation rate of 6 mm ka^{-1} is lower than the catchment-averaged denudation rate from the eastern part of the Orange basin (average denudation rate in the upper Orange River 19.10 ± 1.60 mm ka^{-1}, Chapters 4 and 5). Fleming *et al.* (1999) derive free-face bedrock denudation rates that suggest that the Escarpment has been retreating at between 50 and 95 m Ma^{-1}, 2-3 times higher than denudation rates on the summit (Table 6.2.3). These retreat rates are comparable to some of the denudation rates in the similarly high-relief Golden Gate region, on the north-eastern edge of the Drakensberg Escarpment, where a catchment-averaged rate of 48.47 ± 4.10 mm ka^{-1} was presented in Chapter 5. Fleming *et al.* (1999) contend that the rates of summit denudation, although low, are sufficient to prevent the intact preservation of erosion surfaces over geological time. Given that the catchment-averaged rates of denudation presented in previous Chapters an order of magnitude higher than those presented by Fleming *et al.*, it is very unlikely that erosion surfaces would be preserved in the Orange basin, a point that is discussed further in section 6.4.

Sample	Location	Mean ^{36}Cl erosion rate (mm ka^{-1})	± Standard uncertainty
	Free Face	47.8	6.3
	Free Face	62.3	6.8
average		**55.05**	**6.55**
	Summit	6.70	0.5
	Summit	10.00	0.5
	Summit	1.4	0.1
	Summit	26.9	1.7
average		**11.25**	**0.7**

Table 6.2.3 Rates of denudation of summit and free face samples on the Drakensberg Escarpment from Fleming *et al.* (1999)

6.3 Long-term rates of denudation from offshore sedimentary data and thermochronologic methods

6.3.1 Comparison with the offshore sedimentary record

Quantifying the denudation and landscape evolution of passive continental margins is fundamental to understanding the interactions between tectonics and topography. Regional, intermediate term denudation rates from ^{10}Be and ^{26}Al cosmogenic nuclides were presented in Chapters 4 and 5. These regional scale patterns of denudation are now compared with existing long-term regional patterns derived from thermochronologic methods and the offshore sedimentary record. Note that it is most appropriate to quote denudation rates in m Ma^{-1} when discussing long-term rates of denudation. In doing this the values remain the same since, dimensionally, mm ka^{-1} is the same as m Ma^{-1}. Rust and Summerfield (1990) present isopach and borehole data along the western margin of southern Africa which suggests that the palaeo-Orange River became established in the Late Cretaceous in the vicinity of the present Orange River mouth. Rust & Summerfield use borehole and isopach data, combined with a drainage model, to infer the spatial and temporal patterns over southern Africa from ~ 150 Ma to the present. They estimate an average depth of post-rifting denudation for the present day catchment of being around 1.8 km and an associated denudation rate over this period as 12 m Ma^{-1} (with a potential range of values between 7 and 114 mm ka^{-1} depending on which drainage model is used). The

intermediate-scale average Quaternary denudation rate from all Orange basin samples in this study is 10.79 ± 1.03 m Ma^{-1}; – virtually indistinguishable from the long term rate over the last 150 Ma. Four distinct denudational periods (Table 6.3.1) are identified in the isopach data; the first period between ~ 152 and 113 (contemporaneous with rifting of the western margin of southern Africa ~ 130 Ma ago) when rates averaged between 41 and 82 m Ma^{-1}; the second period ~ 113 Ma to around 60 Ma ago when denudation ranged between 41-114 m Ma^{-1}; the third period between ~ 60 Ma to ~ 37 Ma when denudation ranged between 16 and 32 m Ma^{-1}; and ~ 37 Ma to the present when denudation ranged between 7-9 m Ma^{-1}. This final period of deposition closely corresponds with the average denudation rate of all cosmogenic samples in the Orange basin of 10.79 ± 1.03 m Ma^{-1} (and the average denudation rate of the most downstream sample, taken at Vioolsdrif, of 4.37 ± 0.37 mm ka^{-1}). The correspondence between long term sediment data and intermediate term cosmogenic data emphasises the essential stability of the southern African landscape over very long timescales (since at least the mid Tertiary). Regional denudation rates are very low both on timescales of tens of thousands of years and tens of millions of years, suggesting that the processes operating over long and intermediate terms have been essentially the same. Rust and Summerfield (1990) state that there is a great deal of spatial and temporal variability within these rates, just as there is a large degree of spatial and temporal variability in the cosmogenic-derived rates. The high rates of denudation co-incident with rifting and the immediate post-rifting period are analogous with the rates in the present day upper Orange basin, suggesting that locally the rate and style of fluvial denudation on Quaternary timescales is similar to that over tens to hundreds of millions of years timescales.

Time period (Ma)	Sedimentary sequence	Average depth of denudation for each sequence (km)	Average denudation rate (m Ma^{-1})
0 - 37	4	0.26 - 0.32	7.1 - 8.7
37 - 60	3	0.47 - 0.95	16 – 24
60 - 113	2	1.3 - 5.3	29 – 114
113-152	1	1.6 - 3.2	41 – 82

Table 6.3.1 Estimates of total average rates of denudation from offshore sedimentary sequences in southern Africa (Rust & Summerfield, 1990).

6.3.2 Comparison with the thermochronological record

Although Rust & Summerfield's data was a huge step in quantifying long term regional denudation rates, the major limitation with using offshore sedimentary data is the uncertainty in quantifying former basin extents. The onshore denudation pattern is likely to be very variable and dependent on post-breakup tectonics, the pattern of drainage development, and the style of landscape evolution and long term climatic and lithological variations (Gallagher *et al.*, 1999). Low temperature thermochronology (specifically, apatite fission track thermochronology (AFTT)), which began to be applied to questions of southern African landscape development in the late 1980s and early 1990s, provides a direct measure of rates of denudation based on the cooling history of a near-surface sample (the technique is described fully in Chapter 1). Brown *et al.* (1990) presented denudation rates for the south-western margin of southern Africa using a combination of AFTT data and the offshore sedimentary record. They infer a period of accelerated denudation in the early Cretaceous, broadly synchronous with the break up of Gondwana and resulting in ~ 3 km of regional denudation assuming a palaeo-geothermal gradient of 30°C km^{-1} (equivalent to ~ 23 m Ma^{-1} denudation since continental breakup ~ 130 Ma ago (Brown *et al.*, 1990)).

For the western margin of southern Africa, quantitative thermal histories have been modelled from AFTT data and mean denudation rates estimated from modelled palaeo-temperatures (Gallagher *et al.*, 1995, 1999; Gallagher & Brown, 1999a, 1999b). Estimated total post-breakup denudation is 800-1000 m, equivalent to a rate of 6-7 m Ma^{-1} (Figure 6.3.1) and very similar to the cosmogenic-derived denudation rates for the western region of southern Africa (average of 6.78 ± 0.66 m Ma^{-1} for samples in the lower Orange basin).

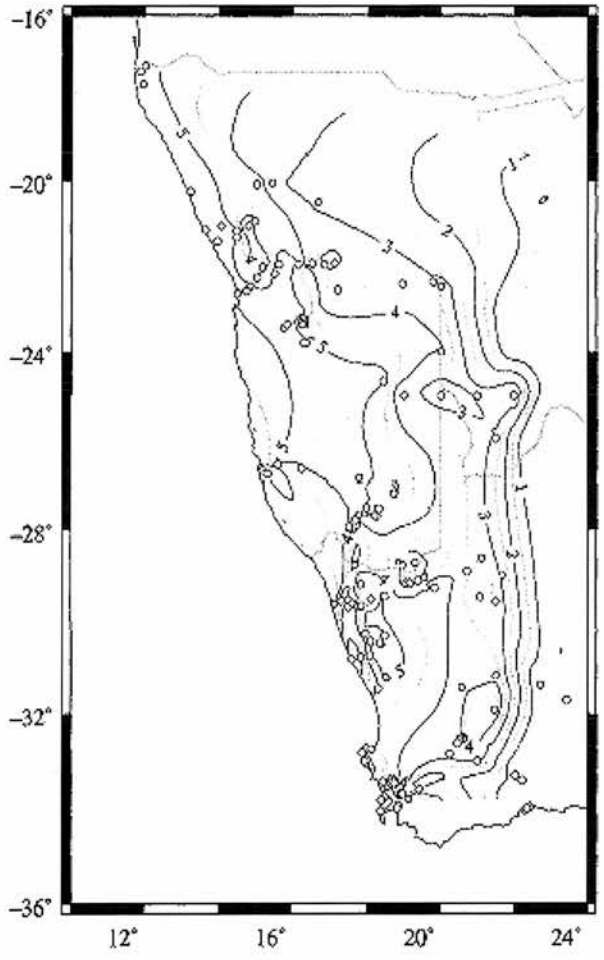

Figure 6.3.1 Total amount of denudation in western southern Africa since ~ 140 Ma. Contours are in kilometres. Note that the central part of the Orange basin has undergone between 1 and 3 km of denudation (average rate of 7 – 21 m Ma^{-1}) (Gallagher & Brown, 1999a).

Denudation is not uniform temporally – there are periods of enhanced denudation at ~ 100 Ma, ~ 75 Ma and ~ 40 Ma ago (Gallagher *et al.*, 1999). Gallagher & Brown (1998) and Gallagher *et al.* (1998) give estimates of syn- and post-rifting denudation on the Atlantic margin of southern Africa and show that the largest amount of post-rift denudation went on in the coastal region, with less further inland. There are some notable spatial and temporal anomalies e.g. 4 km of denudation 400 km inland, occurring between 100 and 60 Ma; equivalent to a local denudation rate of 100 m Ma^{-1}. The post-breakup denudation chronology shows that relatively little post-breakup denudation occurred on the southern African margin immediately following rifting, then rates increased dramatically in the Late Cretaceous-Early Tertiary, more than 50 Ma after initial rifting (Gallagher & Brown, 1999a). The estimated rates of

denudation vary between ~ 25 m Ma^{-1} at the coast and ~ 6 m Ma^{-1} inland for western southern Africa for the syn-rifting period 158-118 Ma (Figure 6.3.2). The post-rifting period (118-0 Ma) shows that there has been an average denudation rate of between ~ 8 and 25 m Ma^{-1} – broadly the same rates as experienced over Quaternary timescales in various parts of the Orange basin, although there are likely to be some local anomalies. For the central Orange basin, total denudation since 140 Ma was estimated by Gallagher and Brown (1999a, 1999b) as being between 1 and 3 km, equivalent to a denudation rate of between 7 and 21 m Ma^{-1} – very similar to the intermediate-term rates of denudation presented in this study (average of 10.79 ± 1.03 for all Orange basin samples).

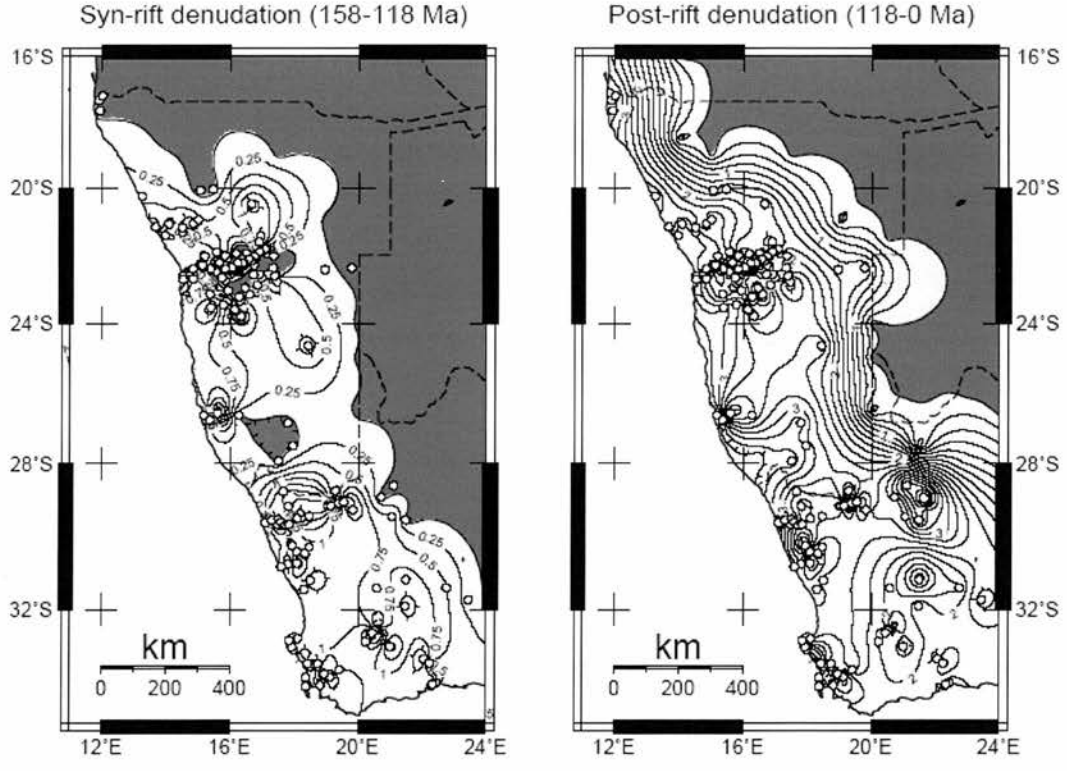

Figure 6.3.2 Estimated syn- and post-rift denudation in kilometres for western southern Africa (Gallagher *et al.*, 1998).

In the eastern part of the Orange basin, AFTT studies suggest that less than 1 km of denudation has gone on in the Lesotho Highlands region since the basalt was emplaced in the Jurassic ~ 185 Ma ago (Brown *et al.*, 1990). Assuming around 1 km of denudation has occurred in the past 130 Ma, an average regional denudation rate of around 7 m Ma^{-1} would have been maintained. This is lower than the cosmogenic-derived average denudation integrated over ~ 60 ka in the upper Orange basin of

19.10 ± 1.60 m Ma^{-1} (Figure 6.3.3). Summerfield (1991a) suggests that the relatively high local relief of the Lesotho Highlands could mean that current rates of denudation are >100 m Ma^{-1}. The intermediate-term cosmogenic data suggest that rates have been somewhere between the long and short term average rates. The highest measured cosmogenic rates, of 48.47 ± 4.10 mm ka^{-1} are in the high runoff, high relief Golden Gate region. This emphasises the spatially variable nature of denudation, particularly in areas such as the Lesotho Highlands which have undergone considerable climatic changes in the Quaternary (Holmgren, *et al.*, 2003). A possible explanation for the slow long term rates of denudation could be that the phase of accelerated denudation began 130 Ma after the tectonic event that formed the south east African margin (Brown *et al.*, 1990). More recent high rates of denudation only became established once the headwaters of the Orange River cut through the Drakensberg basalt into the more readily erodible sediments of the underlying Karoo sequence, such as the Clarens Formation which cosmogenic nuclide analysis now reveals to be eroding rapidly in the Golden Gate region.

Brown *et al.* (2002) estimate from a borehole near Ladybrand, north of Lesotho and close to the Caldeon River cosmogenic sampling location (SA04-42-1), that 1.7 km of denudation has occurred since ~ 78 Ma. This gives an average denudation rate of 21 m Ma^{-1}, although Brown *et al.* describe an accelerated phase of denudation in the Late Cretaceous between 78 and 64 Ma of around 82 ± 43 m Ma^{-1} and an average rate of ~ 10 m Ma^{-1} from the end of the Cretaceous and for much of the Tertiary. This compares well with the catchment-averaged denudation rate for the Caledon River over the last ~ 90 ka of 6.67 ± 0.45 m Ma^{-1} (sample SA04-42-1). As described above, other samples in the upper Orange basin have a higher average denudation rate of 19.10 ± 1.60 m Ma^{-1}– still similar in magnitude to the average long term rate of Brown *et al.* (2002), but reflecting the fact that denudation can be spatially and temporally variable. The AFTT data and cosmogenic data presented above suggests that long term low denudation rates (since at least the mid Tertiary) have carried over into the Quaternary period, suggesting that the denudational processes have been essentially the same on these different timescales. This is explored further in the next section in the context of theories and models of landscape evolution.

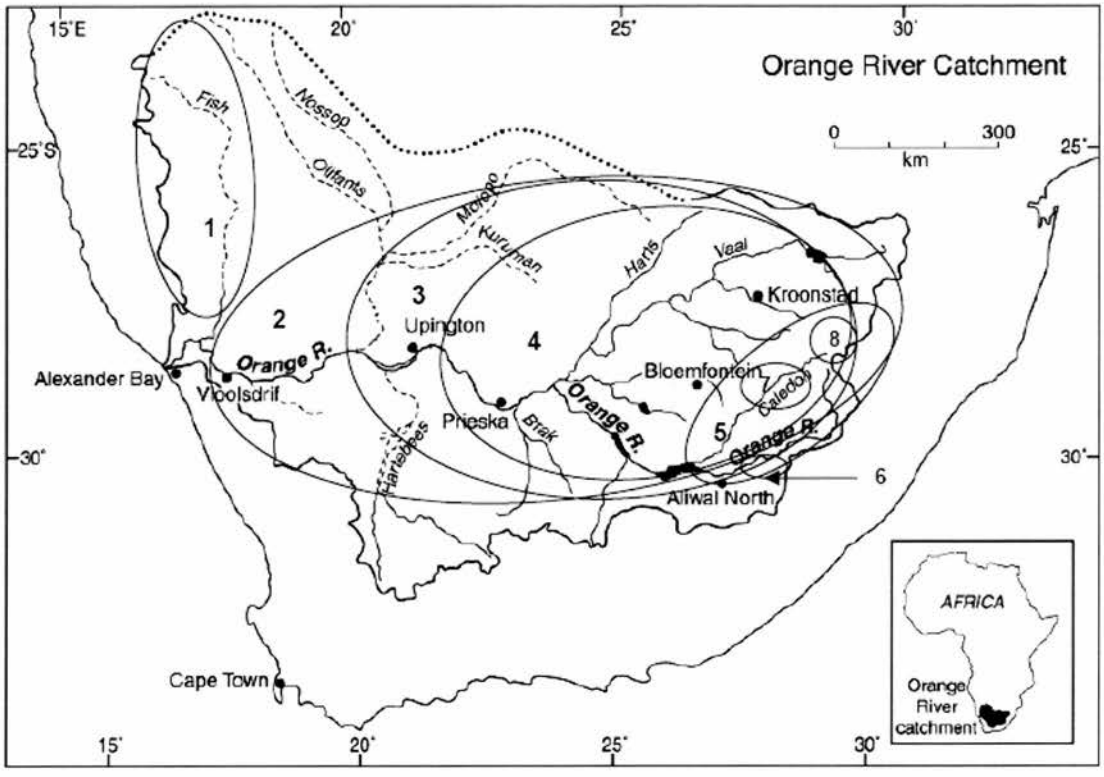

Figure 6.3.3 Catchment-averaged denudation rates in the Orange River catchment: (1) Fish River average denudation rate 3.53 ± 0.29 m Ma^{-1}; (2) average denudation rate upstream of Vioolsdrif 4.37 ± 0.37 m Ma^{-1}; (3) average denudation rate upstream of Augrabies Falls region 4.04 ± 0.40 m Ma^{-1}(calculated from two samples in the main channel of the Orange River, downstream and upstream of the Augrabies Falls); (4) Average denudation rate upstream of Keimoes and Groblershoop 6.50 ± 0.84 m Ma^{-1} (average of two samples); (5) Average denudation rate upstream of Aliwal North 23.53 ± 2.76 m Ma^{-1}; (6) Average of three tributary samples east of Aliwal North in the Karoo Supergroup (11.92 ± 0.93 m Ma^{-1}); (7) average denudation rate of the Caledon River tributary 6.67 ± 0.45m Ma^{-1}; (8) Little Caledon basin average denudation rate of 48.47 ± 4.10 m Ma^{-1}. (Image adapted from Tooth & McCarthy, 2004).

6.4 Implications for models of landscape evolution

6.4.1 General implications

The southern African landscape has been essentially stable with regional scale denudation rates of the order of less than 10 m Ma^{-1} for most of the Cenozoic. These low regional-scale rates of denudation have continued into the Quaternary. Both fission track (AFTT) and cosmogenic techniques indicate spatially-limited accelerated denudation with rates up to tens of metres per million years in some parts of the Orange basin. Such rates have been experienced in high relief, high rainfall

tributary catchments in the upper Orange basin on timescales of tens of thousands of years, and are also evident in the AFTT record as periods of regional accelerated denudation in the Late Cretaceous. This emphasises the essential stability of the southern African landscape, suggesting denudation rates occur at a constant low rate on a regional scale and change little over time, as reported for Namibia by Bierman & Caffee (2001). The rates of denudation over much of the Orange basin are not sufficiently different to generate high relief topography at the local scale (although clearly the topography changes on the largest scale with respect to sea level). The rates of denudation from the middle Orange basin indicate that the landscape would have changed very little visually over long periods of time. Nonetheless, the long term rates of denudation revealed in this study, backed up by AFTT data, suggest that the landscape is eroding sufficiently quickly that characteristic erosion surfaces (or pediments), a canonical landform in King's (1953, 1967) theories of landscape evolution, will not be preserved unmodified in the landscape on timescales of hundreds of millions of years. The cosmogenic ^{10}Be and ^{26}Al data presented here confirm that denudation has been occurring actively over 10^4-10^5 a in the Orange basin at rates of the order of meters to tens of meters per million years. If these data are representative of bedrock outcrops, then, like the study of denudation rates on Drakensberg basalts by Fleming *et al.* (1999), these data have important implications for denudation chronologies that assume that erosion surfaces are preserved unmodified over geological timescales.

6.4.2 Implications for traditional denudation chronologies

Partridge & Maud's (1987) modification of King's (1967) scheme argues for the initiation of the Great Escarpment at continental breakup (evidence to the contrary is discussed below). They propose a subsequent 'African' cycle of denudation from the Late Jurassic to the Early Miocene occurring above and below the Great Escarpment. A subsequent 'Post African I' cycle persisting until the late Pliocene, followed by a 'Post African II' cycle of denudation since the Pliocene. This study, backed up by independent fission track data, shows rather than there having been discrete episodes of denudation characterised by remnant erosion surfaces, low to moderate rates of denudation have prevailed in the Orange basin for 10^4 to 10^5 years, and fission track

data indicate that denudation rates of the same order of magnitude have prevailed throughout the Tertiary. Furthermore, denudation rates have been too high for characteristic erosion surfaces such as the 'African' surface to have been preserved unmodified over hundreds of thousands (and by implication millions to tens of millions) of years. Thus this study provides further evidence against traditional 'denudation chronology' narratives of southern African landscape evolution based on correlation of widely scattered erosion surfaces.

Traditional models of long-term landscape evolution in southern Africa have assumed that development is dominated by the retreat of a major escarpment initiated along the coast at the time of continental breakup (King, 1951; Partridge & Maud, 1987). More recently, numerical surface process models backed up by long term denudation data from AFTT and the offshore sedimentary record have questioned this and suggested a range of possible landscape evolution models (Gilchrist *et al.*, 1994). Three principal styles of escarpment formation are proposed by Gallagher & Brown (2002); the downwarp model, scarp retreat and the pinned drainage divide model. Downwarping models neglect the isostatic response to denudational unloading and thus fail even on a theoretical level (Gallagher & Brown, 2002). The spatial and temporal patterns of denudation revealed by AFTT, both on the western margin of southern Africa and on the eastern Drakensberg Escarpment, are incompatible with a model of landscape development involving constant retreat of an escarpment originally formed at the coast at the time of breakup (Brown *et al.*, 2002). For the western margin of southern Africa, a combination of AFTT data and cosmogenic nuclide data show that denudation rates oceanward of the Namibian Escarpment have been low (<20 m Ma^{-1}) with an estimated rate of escarpment retreat of ~ 10 m Ma^{-1} (Cockburn *et al.*, 2000). This rate is consistent with a model of landscape evolution where the escarpment is pinned at an inland drainage divide and retreat occurs only slowly (~ 100 m Ma^{-1}, less than that required for the escarpment to have originated at the coast). Brown *et al.*'s (2002) fission track data from the Drakensberg Escarpment are consistent with a model of development where an escarpment initiated at the coast is rapidly destroyed by rivers draining from an interior divide. The present escarpment formed, became pinned at this divide and

subsequently retreated inland relatively slowly. Cosmogenic and AFTT data from the Drakensberg Escarpment also support the model of a pinned drainage divide. Fleming *et al.* (1999) show that the rate of retreat for the past ~ 10^4 a is an order of magnitude lower than would be required for the escarpment to have originated at the coast, and thus a combination of pinned drainage divide and slow escarpment retreat must be invoked to explain the development of the escarpment, rather than solely escarpment retreat, as suggested by the traditional models of King (1967) and Partridge & Maud (1987). Although this study does not quantify actual rates of denudation on the southern African escarpment, the average denudation rate of the Orange basin is sufficiently low (<10 m Ma^{-1}) as to be consistent with a slowly retreating escarpment model, thus providing further evidence in favour of a combined pinned drainage/slowly retreating escarpment model of landscape development.

6.4.3 The future of landscape evolution models

With the growth in cosmogenic and fission track techniques for quantifying landscape development comes enormous potential for combining complimentary data sources to develop quantitative models for the evolution and long-term development of passive margins. This is being explored for the south east African margin by numerical surface process models backed by cosmogenic and fission track data. Numerical modelling results by van der Beek *et al.* (2002) support a scenario of rapid post-breakup river incision seaward of a pre-existing drainage divide, located close to its present position, and subsequent escarpment retreat at rates of ~ 100 m Ma^{-1}. Pre-breakup topography of the margin has exerted a fundamental control on subsequent margin evolution. This 'inheritance' and the importance of initial conditions on subsequent rates of landscape evolution can also be seen in the denudation rates presented in this study. On a regional scale, the Quaternary denudation rates are virtually indistinguishable from long term rates, emphasising the primary control that the long term post-breakup evolution has on intermediate term rates and style of denudation. Van der Beek *et al.*'s model suggests an inland base level fall, possibly related to back-cutting of the Orange River drainage system, around 40–50 Ma after breakup. The denudation rates of tens of metres per million

years (Brown *et al.*, 2002) during this period are revealed in this study to have occurred over tens of thousands of years in some of the high relief tributary catchments in the upper Orange basin, suggesting that both the rate and the style of denudation in the Orange River basin has been essentially the same, though the temporal and spatial extents differ. On a regional scale, southern Africa has been relatively stable in terms of denudation from tens of millions of years through to tens of thousands of year timescales. This scenario, predicted by van der Beek *et al.*'s model, is backed up by the cosmogenic data in this study.

The data presented here argue strongly against the traditional denudation chronology approach to landscape reconstruction based on long term survival of erosion surfaces and the idea that tectonic and base level change is reflected in erosion surfaces in the modern landscape. This study adds to a growing body of evidence that refutes the idea that erosion surfaces are preserved in the landscape over long periods. The body of evidence incorporates cosmogenic and fission track studies from, as well as southern Africa, a range of passive margin environments on the former Gondwana supercontinent: south eastern Brazil (Harman *et al.*, 1998; Brown *et al.*, 2000); and south eastern Australia (Gleadow *et al.*, 2002; Kohn *et al.*, 2002). These studies emphasise that establishing variations in denudation rates across landscapes reveals more about landscape evolution than attempting to diagnose the amount and timing of denudation from apparently correlated erosion surface remnants (Brown *et al.*, 2002).

Chapter 7 –
Bedrock channels in the Augrabies Falls region

In order to characterise the evolution of the Augrabies region, a number of bedrock samples were taken from the trunk channel of the Orange River in the area upstream and downstream of the Augrabies main Falls (Chapter 4). In addition, a number of samples were taken from anabranches that bypass the main Falls as well as from bedrock interfluves. The bedrock interfluves should give an order of magnitude estimation of the background bedrock lowering rates which can be compared with both rates of bedrock incision in the trunk channel, anabranches and tributary channels which were also sampled (Chapter 9). Chapter 8 deals with denudation rates from interfluves and also the evolution of a unique granite-gneiss bornhardt landform in the Augrabies region, Moon Rock, and uses cosmogenic derived denudation rates to work out how quickly this feature is eroding relative to the surrounding landscape. Chapter 9 synthesises all of the data presented in the preceding sections, together with catchment-averaged denudation rate data to give an overall picture of the denudation history of the Augrabies Falls region.

7.1 Bedrock channel samples from the Augrabies Falls region

The Augrabies Falls region separates the middle and upstream components of the Orange basin from base level changes affecting the lower part of the basin. As such, the Augrabies Falls region ultimately controls the evolution of around 80% of the total drainage area of the Orange basin (excluding the Fish River tributary, which enters the Orange below the Falls region). The Augrabies main Falls is the principal knickpoint on the Orange River and is over 90 m high, with a free fall of 60 m (van der Walt, 2000). There are several other, smaller subsidiary knickpoints in the Augrabies Falls region, including Twin Falls and Bride's Veil Falls, here collectively termed the 'Augrabies Falls system'. The region of study lies primarily within the Augrabies Falls National Park, Northern Cape, Republic of South Africa. The region above the main Falls consists of a complex series of anabranching channels. The region below the main Falls is characterised by deeply incised (~ 100 m deep) steep, narrow bedrock channels the orientation of which is structurally controlled and results in the river flowing through a spectacular series of 90° bends (Plate 7.1.1, Table 7.1.1). A full description of the region is given in Chapter 1.

Plate 7.1.1 Map of Augrabies Falls region with numbers to denote sample locations (see Table 7.1.5 for key to sample locations) (*based on* SANParks map of Augrabies Falls National Park, 2005, Robin Frandsen). Blue colour denotes river channels, red denotes access roads.

Below the Augrabies main Falls the Orange River flows in a narrow, deeply incised bedrock gorge for ~ 18 km. Upstream of the main Falls the channel gradient is 1.55 m km^{-1} (Plates 7.1.2, 7.1.3) and downstream the gradient increases to over 2.0 m km^{-1} (averaged over 20 km stretches). Immediately upstream of the main Falls for a few hundred meters there is a steep knickpoint drawdown zone. Upstream of the main Falls, there is a complex array of anabranches, some of which completely bypass the main Falls. These anabranches re-join the main channel downstream of the main Falls. In addition, a number of tributary channels flow into the main channel downstream of the Falls system (Plate 7.1.1).

Number	Environment	Sample type	Sample name
1	Trunk channel above main Falls	Bedrock	SA04-9-2
2	Trunk channel above main Falls	Bedrock	SA05-4-1
3	Trunk channel above main Falls	Bedrock	SA05-4-2
4	Trunk channel above main Falls	Bedrock	SA05-5-1
5	Trunk channel above main Falls	Fluvial sand (catchment-averaged)	SA03-5-1
6	Trunk channel above main Falls	Bedrock	SA04-3-1
7	Trunk channel above main Falls	Bedrock	SA04-23-1
8	Trunk channel above main Falls	Bedrock	SA04-24-1
9	Trunk channel above main Falls	Fluvial sand (catchment-averaged)	SA03-4-1
10	Anabranch channel	Bedrock	SA04-17-1
11	Tributary channel	Bedrock	SA04-27-1
12	Tributary channel	Bedrock	SA04-27-2
13	Tributary channel	Bedrock	SA04-27-3
14	Tributary channel	Fluvial sand (catchment-averaged)	SA04-28-1
15	Tributary channel	Fluvial sand (catchment-averaged)	SA03-2-1
16	Tributary channel	Fluvial sand (catchment-averaged)	SA04-19-1-A
17	Tributary channel	Fluvial sand (catchment-averaged)	SA04-19-1-B
18	Tributary channel	Fluvial sand (catchment-averaged)	SA04-19-1-C
19	Interfluve	Bedrock	SA04-15-1
20	Interfluve	Bedrock	SA04-18-1
21	Interfluve	Bedrock	SA04-18-2
22	Interfluve	Bedrock	SA04-20-1
23	Interfluve	Bedrock	SA04-21-1
24	Interfluve	Bedrock	SA04-21-2
25	Interfluve	Bedrock	SA04-22-1
26	Interfluve	Desert pavement	SA05-6-1
27	Inselberg	Bedrock	SA04-6-1
28	Inselberg	Bedrock	SA05-1-1
29	Inselberg	Bedrock	SA05-1-2
30	Inselberg	Bedrock	SA05-1-3
31	Inselberg	Bedrock	SA05-2-1
32	Inselberg	Bedrock	SA05-2-2
33	Inselberg	Bedrock	SA05-2-3

Table 7.1.1 Key to sample locations indicated in Plate 7.1.1.

Flows in the Augrabies region at the time of sampling were ~ 50 $m^3 s^{-1}$ (~ 40 $m^3 s^{-1}$ in December 2003, 2004 and ~ 60 $m^3 s^{-1}$ in July 2005) and confined to the topographically lowest channels in the region. These represent base flows, as can be seen from Figure 7.1.1 where the average discharge for the period 1935-1997 is 214.3 $m^3 s^{-1}$. The monthly discharge data at Upington (Figure 7.1.2) further support the case that the flows at the time of sampling are base flows as the average December flows for the period 1974-1986 are roughly four times higher than the average for December 2003-4. Looking at the twentieth century instrumental record (Figure 7.1.2), it can be seen that discharges were somewhat higher in the period prior to the 1970s, after which the construction of large upstream dams may have lowered the flow at Upington. In the period since the 1970s, there have been several years of low average flows (<100 $m^3 s^{-1}$) suggesting that the base flows witnessed at the time of sampling are not unusual. High flows (>400 $m^3 s^{-1}$) are evident in the record and occur with a roughly decadal frequency. These high flows are over an order of magnitude higher than the base flows. The instrumental record indicates that during the major floods of 1974 and 1988, discharge reached over 9,000 $m^3 s^{-1}$ and 7,000 $m^3 s^{-1}$, respectively (Zawada, 1996). During these high magnitude events, topographically higher bedrock channel anabranches in the Augrabies region (Tooth *et al.*, 2004) became re-activated and 'short circuited' the narrow main channel and flowed along wider, high-level channels. The trunk channel, bedrock anabranches and bedrock from tributary channels were sampled for this study and are described below.

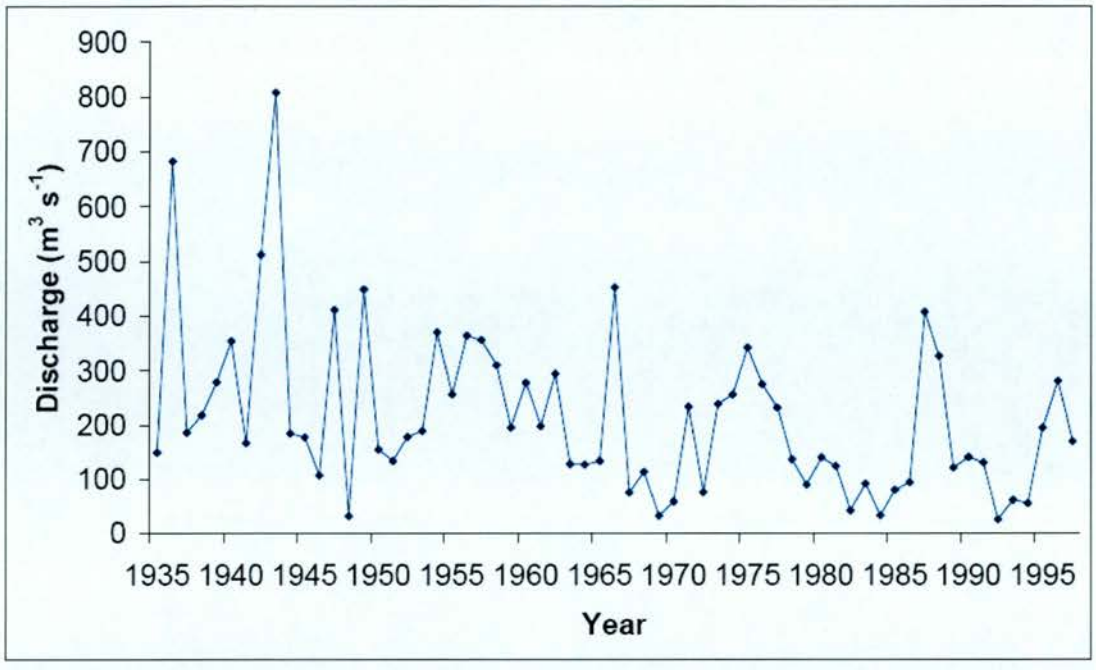

Figure 7.1.1 Annual flow of the Orange River at Upington (~ 100 km upstream of the Augrabies Falls region) 1935 – 1997 [1]. Note the high base flows prior to large dam construction in the 1970s, and the lower base flows, punctuated by roughly decadal-scale peak flows, since the 1970s.

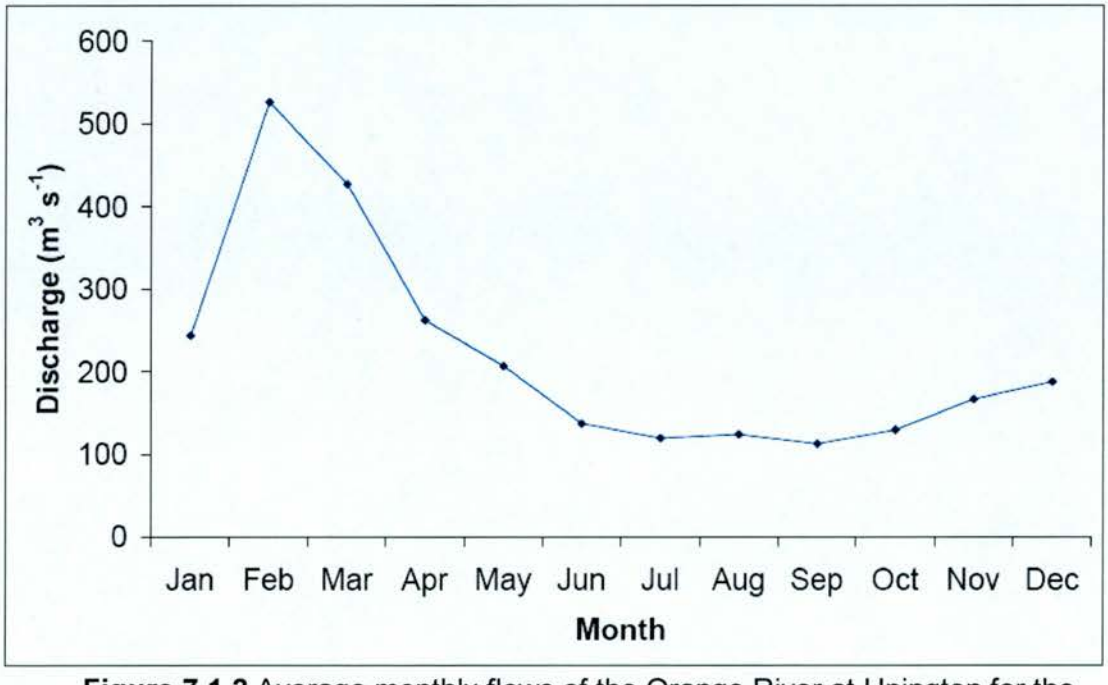

Figure 7.1.2 Average monthly flows of the Orange River at Upington for the period 1974-1986[2].

[1] Department of Water Affairs and Forestry (http://www-dwaf.pwv.gov.za/watres)
[2] UNESCO Global Monthly River Discharge Data (http://www-eosdis.ornl.gov/rivdis/STATIONS.HTM)

7.1.1 Main bedrock channel above the main Falls

The locations sampled here include channel anabranches that flow over the main Falls. Anabranches that flow over the other falls in the system are dealt with in section 7.1.3. The principal aim of sampling in the Augrabies Falls region was to determine the denudation rates of bedrock channels above and below the knickpoint (Plate 7.1.2). On the largest spatial scale, quantifying the rates of denudation of the Augrabies Falls region helps to understand better the long term evolution of the landform that exerts the primary control over development of the Orange basin as a whole. On a smaller scale, quantifying rates of denudation helps better constrain the duration and timing of bedrock incision processes, in particular joint exploitation and potholing, which appear to be the principal means of bedrock channel development over bedrock-dominated stretches of the Orange River (Springer *et al.*, 2006). It is not possible to measure directly the rate of retreat of the main Falls owing to the difficulty in accessing the appropriate locations (Plate 7.1.3). A great deal of topographic shielding is experienced by the channel walls and this means that a large amount if bedrock material would have to be collected to yield sufficient ^{10}Be to derive a denudation rate estimate. This was not possible due to restrictions on the amount of material that could be collected in the Augrabies National Park.

The evolution of the Orange River basin is already well constrained on tens of millions of year timescales from thermochronological studies (Brown *et al.*, 1990). Knowledge of denudation rates on millions of year timescales does not reveal much about rates of landscape evolution on tens to hundreds of thousands of year timescales. Cosmogenic nuclide analysis now allows denudation rates to be determined over these timescales and is a useful tool to quantify rates of geomorphological processes that still continue today. If rates of processes over thousands of years and millions of years are similar, then it can be assumed that the processes operating over those timescales have been similar. Rates of evolution of the Augrabies region over thousands of years can therefore be used as a proxy for the rate and style of evolution of the region over millions of years. Since the Augrabies Falls is the principal controlling landform in the Orange basin, we also have a basis for studying the wider evolution of the Orange River basin.

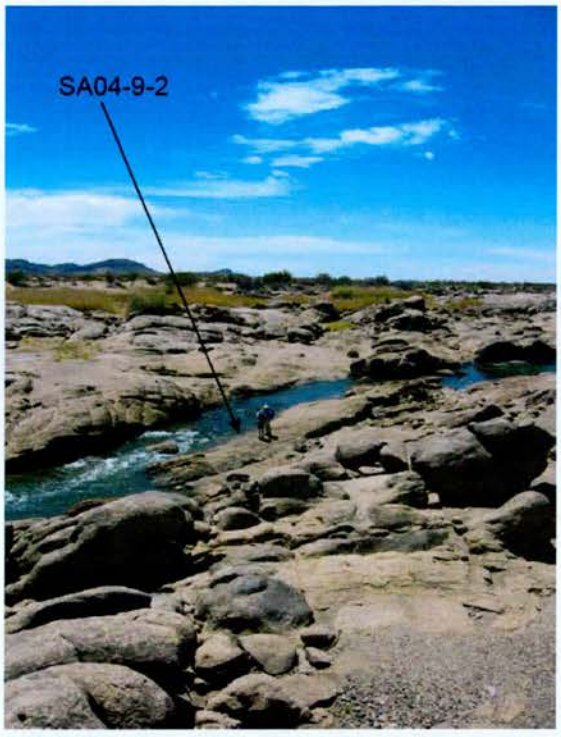

Plate 7.1.2 Typical bedrock channel above the Augrabies main Falls.

Plate 7.1.3 The main channel just below the Augrabies main Falls, note the difficulty in accessing the vertical sides of the Falls.

This study also has the benefit of providing an opportunity for estimating the vertical retreat rates of the side channels in the Augrabies region. This was done by determining the vertical incision rates of bedrock channels both above and below the Falls system. Six bedrock channel samples both above and below the Falls system were therefore analysed for cosmogenic ^{10}Be and ^{26}Al derived denudation rates (see section 7.2). To gain a representative sample of the incision rate of areas both above and below the Falls system, bedrock bars were sampled in the main channel above the main Falls as far east as Keimoes (~ 100 km from the main Falls) and several kilometres downstream of the main Falls, as well as anabranches and tributary channels that bypass the main Falls (described in the next sections).

Sample	Latitude	Longitude	Elevation (m)	
SA04-9-2	28°36'09"S	20°20'45"E	660	Granite-gneiss
SA05-3-1	28°42'42"S	20°59'06"E	724	Granite-gneiss
SA05-3-2	28°43'41"S	20°59'06"E	720	Granite-gneiss
SA05-4-1	28°35'39"S	20°20'41"E	613	Granite-gneiss
SA05-4-2	28°35'39"S	20°20'41"E	613	Granite-gneiss
SA05-5-1	28°35'10"S	20°20'02"E	613	Granite-gneiss

Table 7.1.2 Summary data for the samples above the main Falls (includes samples SA05-3-1 and -3-2 taken at Keimoes).

Above the main Falls (Table 7.1.2), two samples (SA05-3-1, -3-2) were taken from Keimoes, the same sample location as the catchment-averaged sample discussed in previous Chapters (SA03-6-1) (Plate 7.1.4). Here, the granite-gneiss bedrock channel was sampled in order to determine bedrock incision rates. The location of the samples on the west side of the river by a road bridge means that the river may periodically cover the sampled sites with either water or sediment, a factor which may be revealed by the Al/Be ratio in the samples, although around 20 m of water would be required to significantly affect the Al/Be ratio. Within the Augrabies Falls region, three samples were taken from a few tens of metres upstream of the main

Falls in the drawdown zone upstream of the knickpoint, on an area of bedrock in the principal trunk channel of the Orange River (SA05-4-1, 4-2, 5-1; Plate 7.1.5). Given the complex nature of the anabranching river channel upstream of the main Falls (Tooth *et al.*, 2005) it proved necessary to sample other bedrock channels above the Falls (SA04-9-2, Plate 7.1.2). The lithology of all the bedrock bars is granite-gneiss with abundant quartz veins. All four samples upstream of the main Falls are from a region that shows much evidence of fluting and potholing (Plate 7.1.6), as observed by Springer *et al.*, (2006), a phenomenon that is discussed further in the light of incision rate data from ^{10}Be in Section 7.2.

7.1.2 Main bedrock channel below the main Falls

Three bedrock samples were taken from the trunk channel below the main Falls (Table 7.1.3) from bedrock bars in the channel above the level of the river at the time of sampling. The bedrock bars are the highest points in the bedrock channel, and the denudation rates derived from these samples could be seen as minimum channel lowering rates. On the other hand, the whole channel could be incising at the same rate, but the bars are manifested as higher points in the channel due to minor lithological differences with other parts of the channel. This stretch of the Orange River is deeply incised into a gorge (a minimum of 100 m from the top of the interfluves to the level of the river – Plate 7.1.7). Sample SA04-3-1 was from a bedrock bar that extends ~ 21 m into river the channel. This bar will be submerged during peak flows. There is evidence of incremental denudation in the form of exfoliation features and an undulating surface around tens of centimetres high. There is also evidence of high energy flows where pebbles have been wedged into joint cracks.

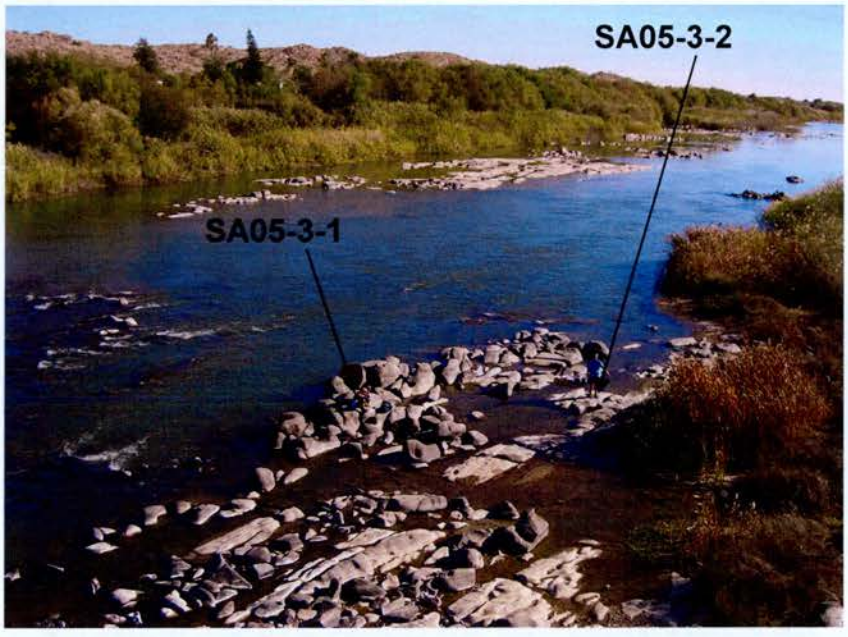

Plate 7.1.4 Sample location SA05-3-1, -3-2 near Keimoes, some 100 km upstream of the main Falls. Samples were taken from bedrock bar on right hand side of picture.

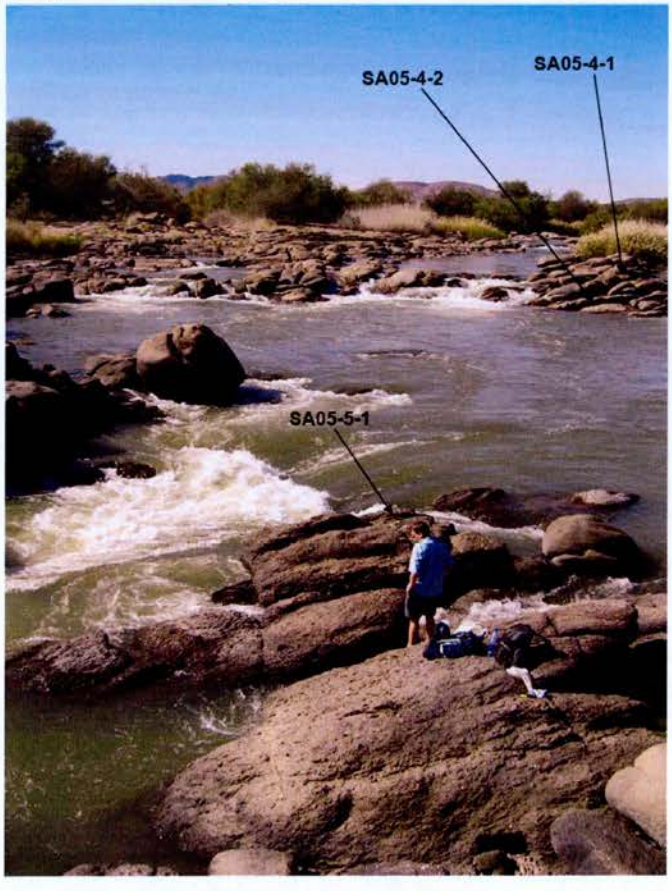

Plate 7.1.5 Sample locations SA05-4-1, -4-2, -5-1 in the northern bedrock anabranch a few hundred metres upstream of the main Falls. This location is

just upstream of the confluence between the western, northern, and eastern anabranches.

Plate 7.1.6 Potholes and fluted bedforms just upstream of the Falls close to the sample location shown in Plate 7.1.5.

Plate 7.1.7 Samples taken from the bedrock channel some 4 km below the main Falls.

Sample no.	Latitude	Longitude	Elevation (m)	Lithology
SA04-3-2	28°32'45''S	20°17'07''E	451	Granite-gneiss
SA04-23-1	28°32'47''S	20°16'22''E	431	Granite-gneiss
SA04-24-1	28°32'45''S	20°16'20''E	430	Granite-gneiss

Table 7.1.3 Summary sample characteristics for locations below the main Falls.

Samples SA04-23 and -24 (Plate 7.1.8) were reached by travelling downstream of Echo Corner by canoe. SA04-23 was from a bedrock bar in the Orange River, ~ 20 m from either bank and ~ 5 m long. Bluffs of fluvial material (most of it too fine grained to sample for cosmogenic catchment-averaging) were seen on both sides of the river. SA04-24-1 was from the midstream section of the river, ~ 10 m from the north bank and 15 m downstream of 23-1. Given that the discharge of the river was around 50 $m^3 s^{-1}$ at the time of sampling and this discharge represents base flow of the river the bars would almost certainly have been covered by water in the recent past (average discharges for the periods 1974-1986 and 1935-1997 are 214.3 $m^3 s^{-1}$ and 220 $m^3 s^{-1}$, respectively (Figures 7.1.1, 7.1.2)). There is also strong observational evidence to suggest that peak flows would have completely submerged the bedrock bars – for instance, there is an absence of vegetation on the bars themselves and little mature vegetation on adjacent bluffs at the same level as the bars, suggests that the bars will be covered by high flows on at least annual timescales.

7.1.3 Bedrock anabranch channels

This section describes all the sampled anabranches that bypass the main Falls and re-enter the main gorge of the river below the Falls after flowing over knickpoints such as Twin Falls. A notable feature of the entire Augrabies region is that there are master joints orientated at 110° and 10° respectively (Moen, 1984, cited in van der Walt, 2000) or, more generally, roughly perpendicular east-west and north-south

(Plate 7.1.9). A number of inferior joints cut across the granite in all directions, but these are less exploited than the master joints (Moen, 1984, cited in van der Walt, 2000). The master joints account for much of the large-scale topography seen at Augrabies, particularly the 90° switches in orientation of the main channel below the Falls and the formation of angular, cube-like blocks which fall from the sidewalls of the anabranch channels. Many of the major anabranch channels begin as small (<1 m wide) fissures orientated parallel to the main channel and within a short distance (<100 m) rapidly become both wider and deeper. A detailed description is given below of one such anabranch channel which was sampled (the results are discussed in Chapter 5). Summary characteristics of the anabranch samples are given in Table 7.1.4.

Sample	Latitude	Longitude	Elevation (m)	Lithology
SA04-17-1	28°35'34"S	20°19'37"E	655	Granite gneiss

Table 7.1.4 Summary sample characteristics for anabranch channel location.

The bedrock bases of anabranch channels, like the main channel of the Orange River, were sampled for *in-situ* cosmogenic nuclide content in order to reveal both the incision rate of the channels and, indirectly, to estimate the vertical retreat rate of the channels' sidewalls. Since the channels appear to maintain their basic morphology whatever their stage of development, downwearing of the base of the channel appears to occur at roughly the same rate as backwearing of the vertical sidewalls. Sample SA04-17-1 (Plate 7.1.10) was taken from the base of a southern anabranch that enters the main channel below the main Falls via Twin Falls (Plate 7.1.11). In this region, there is a remarkable series of interlocking potholes and cavities, suggesting that the nearby Twin Falls knickpoint is retreating by pothole coalescence (Springer et al., 2006; Tooth & McCarthy, 2004). The channel was sampled at low flow though it is clear from the depth of incision that this anabranch channel acts as a 'short circuit' for the main channel during high flows. Given that even at low flow (50 $m^3 s^{-1}$) there was some flow in this channel, it can be expected that considerably higher flows will be experienced periodically near Twin Falls.

Plate 7.1.8 SA04-23-1 (top), -24-1 (bottom) taken from the bedrock channel below the main Falls.

Plate 7.1.9 90-degree joint orientation in granite-gneiss bedrock.

Plate 7.1.10 'Fissure Canyon'. Note that the basic geometry of the channel is maintained as the channel becomes both wider and deeper. Note also vertical retreat of the sidewalls by block falls. CIAF sample SA04-14-4 was taken from where the people are standing. Sample SA04-14-1 was taken from the far end of the channel.

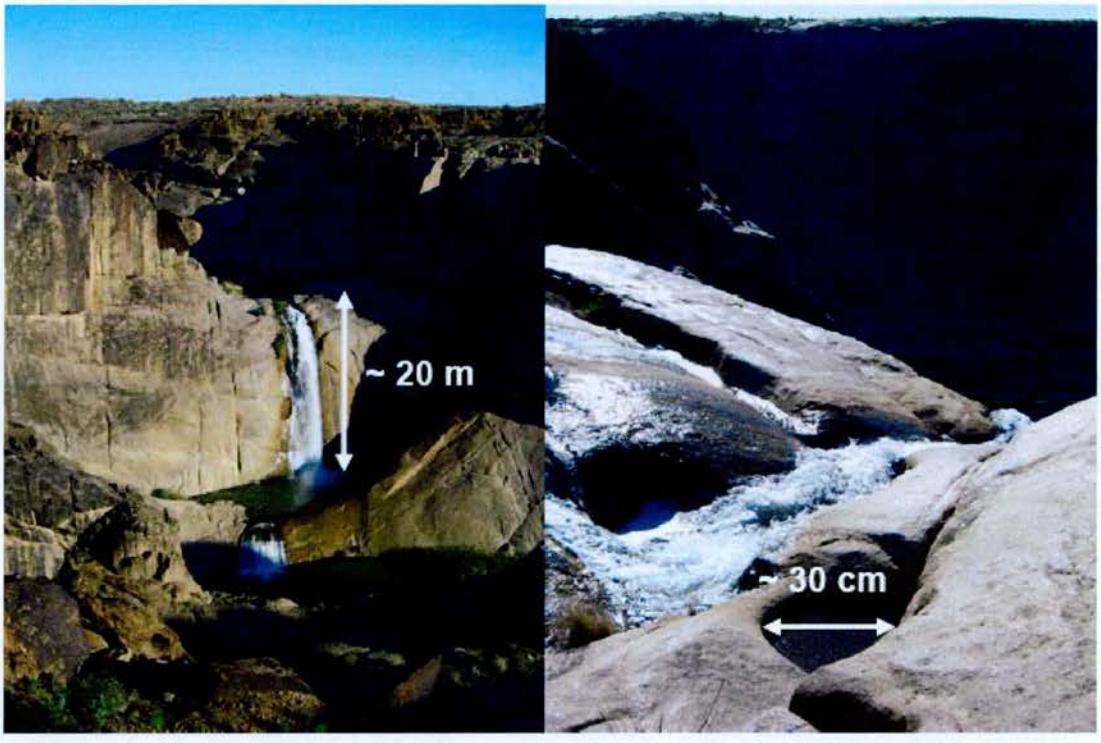

Plate 7.1.11 Twin Falls sampling location. Left hand picture shows potholes and joints immediately above the Falls.

Another anabranch ('Fissure Canyon') which bypasses the main Falls to the south of the main channel anabranches was sampled as part of the CIAF project (discussed in sections 7.1.4 and 7.2.5). This channel is orientated parallel (east-west) to the main channel and begins at the level of the surrounding landsurface (~ 630 m) and within a few hundred metres becomes markedly wider and deeper, reaching a depth of some 10 m and 10 m wide at the point where it can be observed to end, with a break in slope, in a sharp drop into a larger channel. The flow in this anabranch varies, e.g. from completely dry in November 2004 to having flowing water in its base in July 2005.

This channel, like several others around Augrabies, seems to maintain its basic geometry throughout its course. The explanation for this is that the channel develops principally by vertical incision of the channel floor driven by water flow. This is complemented by block retreat from the sidewalls, which occurs where the blocks contain horizontal structural discontinuities. It is telling that on the right side of the channel, where an incipient channel is developing, the geometry is disproportionately deeper than it is wide. This is due to the fact that there are very few horizontal discontinuities in the sidewalls of the bedrock. It may be that pressure release associated with denudation causes master joints to open up and blocks to form, this is discussed with respect to the bedrock incision results in Chapter 6.

Incision in the main part of 'Fissure Canyon' was being carried out by flowing water as observed on 12/7/05. This is in marked contrast to the situation in November 2004, when the channel was observed to be dry and it seemed that the channel only re-activated during high magnitude, low frequency events such as the 1988 flood. Given that the discharge of the Orange River as recorded at Upington was only one third higher in July 2005 than November 2004 (~ 60 $m^3 s^{-1}$ compared with ~ 40 $m^3 s^{-1}$) it is likely that low magnitude high frequency events are responsible for vertical and lateral incision, at least in the anabranch channels.

7.1.4 Tributary channels

This section deals with small tributary channels (as distinct from anabranches) that meet the Orange River downstream of the main Falls (Table 7.1.5). In the west of the Augrabies Falls region, three bedrock samples were taken from the base of a tributary channel draining into the south bank of the Orange River, close to where the catchment-averaged sample SA04-28-1 was taken (Plate 7.1.12). Three samples were taken from the gully on the south side of the Orange River. On the eastern flank of this gully, a sheet of granite-gneiss ~ 20 cm thick, dipping at about 15° appears to be eroding as a sheet from the underlying granite-gneiss which appears identical in lithology. It appears that the granite has been eroding by block release. Sampling this location will reveal how rapidly the tributaries are cutting down to local base level (i.e. the level of the main Orange River channel).

The stream power incision model (Whipple and Tucker, 1999) explains river incision as a function of basin area and channel gradient. Other things being equal, tributaries usually have steeper channel gradients and a smaller area than the main channel they feed into. This is true of this tributary which has an average gradient of 40 m km^{-1} as compared with a local channel gradient of the main channel of the river of 3.1 m km^{-1} (measured over a 20 km stretch of river) and a drainage area of ~ 34 km^2 compared with 410,000 km^2. Due to its steeper gradient, this tributary would be expected to be undergoing more rapid incision than the main channel. The sample location is also likely to experience higher stream power per unit area as discharge is funnelled down a steep, narrow channel with a smaller cross sectional area than the main channel.

At some point in the past, the knickpoint system has probably migrated upstream and passed the mouth of this tributary, resulting in a change of base level. However, given that the tributary is several kilometres downstream of the knickpoint, this event would have occurred millions to tens of millions of years ago, far outwith the averaging time of this sample. Therefore, any erosion signal from this location will not represent a re-grading in response to the knickpoint having passed by.

Sample	Latitude	Longitude	Elevation (m)	Lithology
SA04-27-1	28°32'59''S	20°15'41''E	448	Granite gneiss
SA04-27-2	28°32'59''S	20°15'41''E	448	Granite gneiss
SA04-27-3	28°32'59''S	20°15'41''E	448	Granite gneiss

Table 7.1.5 Summary sample characteristics for tributary channel locations.

7.1.5 CIAF samples

The samples described above were complemented by a number of samples which were collected together with the SA04- suite of samples but analysed as part of a separate but related project at the NERC Cosmogenic Isotope Analysis Facility (CIAF). These samples were taken from locations similar to the samples presented above and provide further data from which interpretations of the long term denudation rates in the Augrabies Falls region can be made (Table 7.1.6; Figure 7.1.3). Further CIAF samples, from interfluve locations, are discussed in Chapter 8.

The samples from above the main Falls (Table 7.1.6) were taken from numerous bedrock bars along several kilometres of the eastern anabranch. This was the same anabranch as that which sample SA04-9-2 came from (described above, Plate 7.1.2). Sample SA04-9-1 was taken from the same bedrock bar as SA04-9-2. Samples SA04-11-1 and SA04-12-1 were taken from similar granite gneiss bedrock bars containing fluted forms and numerous potholes, indicative of high flows which will periodically cover the bars. These locations were upstream of the samples described in section 7.1.1 and, as such, were not in the steep knickpoint drawdown zone. Samples SA04-13-1 and -13-2 were taken from an area of exposed bedrock proximate to the channel above the Falls (Plate 7.1.13). This area is clearly inundated by flood flows, as indicated by the presence of debris from fluvial sand to boulders and the absence of mature vegetation, suggesting that this area may re-activate as an anabranch channel during peak flows (which appear to occur on inter-annual timescales – Figure 7.1.2).

Plate 7.1.12 Location of samples SA04-27-1 to -3. Note the pegmatite vein running across the centre of the picture.

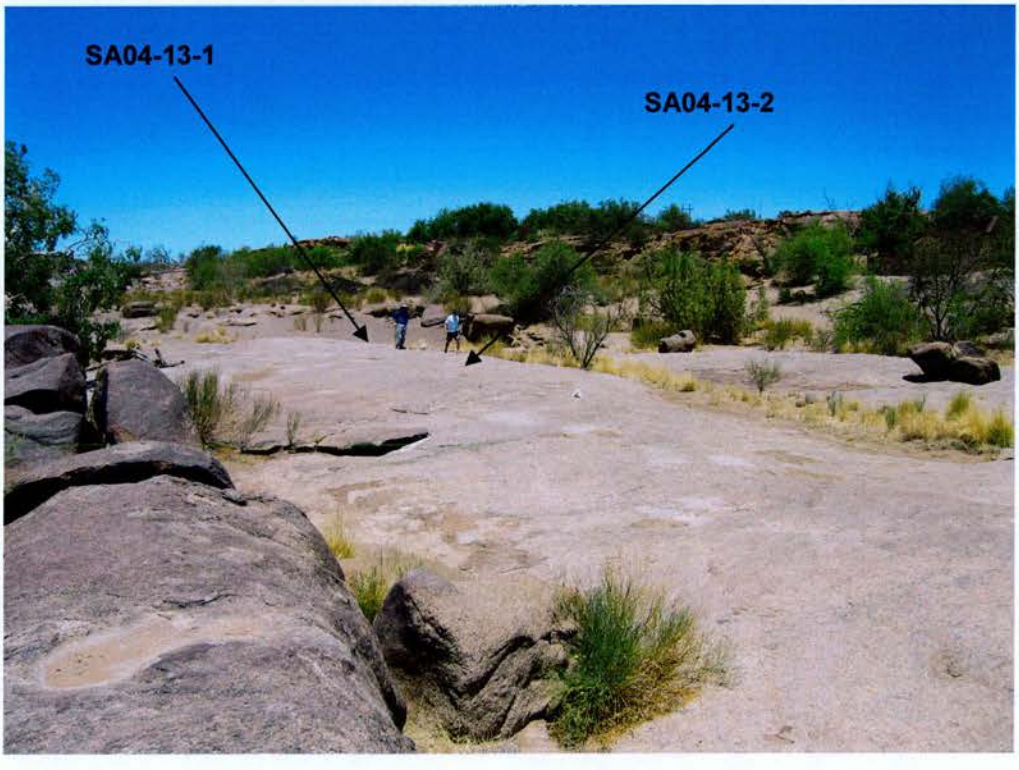

Plate 7.1.13 Anabranch channel close to the main channel above the main Falls, location of samples SA04-13-1, -13-2.

The samples from below the Falls were taken from bedrock bars in the main channel. Sample SA04-3-1 was taken from the same location as SA04-3-2 (Plate 7.1.7), described above. Samples SA04-4-1 and -4-2 were taken from a bedrock bar in the main channel near the mouth of Echo Corner tributary.

Sample	Location	Latitude	Longitude	Altitude (m)
SA04-09-1	Bedrock channel above main Falls	28°36'S	20°20'E	660
SA04-11-2	Bedrock channel above main Falls	28°36'S	20°20'E	620
SA04-12-1	Bedrock channel above main Falls	28°36'S	20°20'E	622
SA04-13-1	Bedrock channel above main Falls	28°36'S	20°20'E	679
SA04-13-2	Bedrock channel above main Falls	28°36'S	20°20'E	679
SA04-03-1	Bedrock channel below main Falls	28°33'S	20°17'E	448
SA04-04-1	Bedrock channel below main Falls	28°33'S	20°17'E	400
SA04-04-2	Bedrock channel below main Falls	28°33'S	20°17'E	439
SA04-14-1	Anabranch channel ('Fissure Canyon')	28°35'S	20°19'E	615
SA04-14-4	Anabranch channel ('Fissure Canyon')	28°35'S	20°19'E	657
SA04-05-1	Tributary channel (Echo Corner tributary)	28°33'S	20°17'E	446
SA04-05-2	Tributary channel (Echo Corner tributary)	28°33'S	20°17'E	458

Table 7.1.6 Summary of samples collected as part of the CIAF project. Full sample details are given in Appendix 5.

'Fissure Canyon', the anabranch channel described above, had samples SA04-14-1 and SA04-14-4 collected from the base of it. This anabranch bypasses the main Falls and over ~ 500m rapidly becomes steeper and wider, though maintaining a width of ~ 50m for much of its downstream length. Fissure Canyon ends with a ~ 10 m knickpoint as it drops into a deeper canyon, both of which were dry at the time of sampling (Plates 7.1.10, 7.1.13, 7.1.14). The canyon into which this anabranch drops starts off as a narrow fissure adjacent to this anabranch, but rapidly deepens to that

eventually it becomes deep enough for 'Fissure Canyon' to lie as a 'hanging valley' above it (Plate 7.1.14).

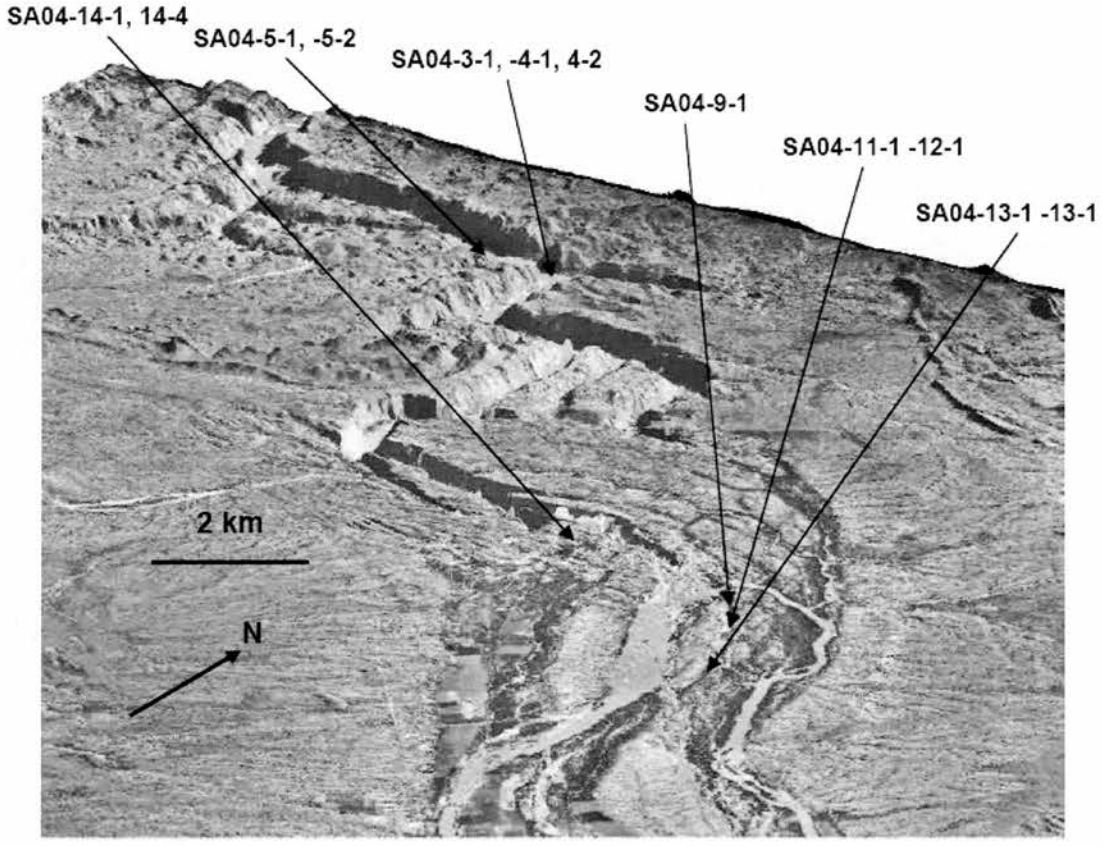

Figure 7.1.3 DEM showing locations of CIAF samples referred to in Table 7.1.5 (from Walcott *et al.*, unpublished).

The tributary that drains into the main channel below the Falls at Echo Corner was also sampled (samples SA04-5-1, -5-2). Further upstream, this tributary was sampled for the catchment-averaged denudation rate (see Chapter 5), and the interfluves surrounding this basin are discussed in Chapter 8. Sample SA04-5-1 was a near vertical bedrock sample taken from a mini-knickpoint close to the tributary's confluence with the main channel (Plate 7.1.15). Sample SA04-5-2 was taken from a horizontal part of the same bedrock exposure (Plate 7.1.16). These two samples should allow quantification of the rate of downwearing and beackwearing of the knickpoint that marks the end of the tributary and its steep descent to join the main Orange River. The retreat rate of this knickpoint could be a useful proxy for the retreat of other tributaries, and indeed main channel anabranches in the Augrabies Falls system.

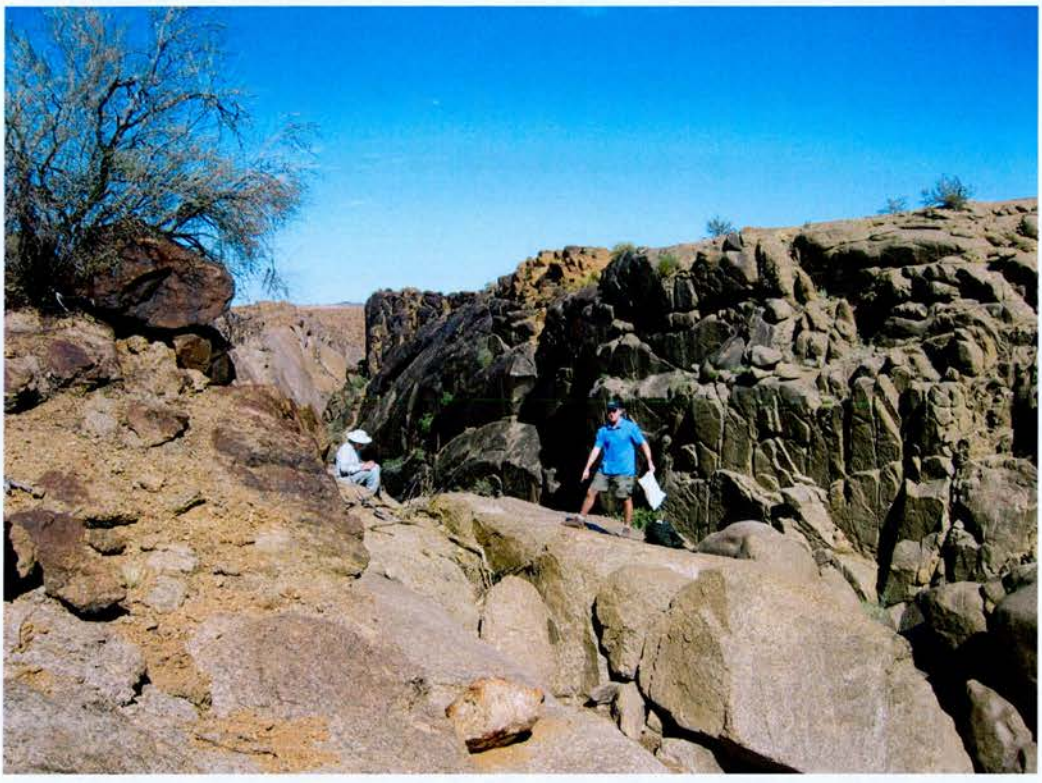

Plate 7.1.14 Western (downstream) end of Fissure Canyon anabranch, at the point where the anabranch becomes a hanging valley and drops ~ 10 m down to a deeper anabranch channel, which starts off as a narrow fissure adjacent to this anabranch (Plate 7.1.15).

Plate 7.1.15 Western (downstream) end of Fissure Canyon anabranch, where the anabranch drops ~ 10 m down to a deeper anabranch channel. In the middle distance the point at which the anabranch re-joins the main channel below the Falls can be seen. Note the boulders in the deeper anabranch channel.

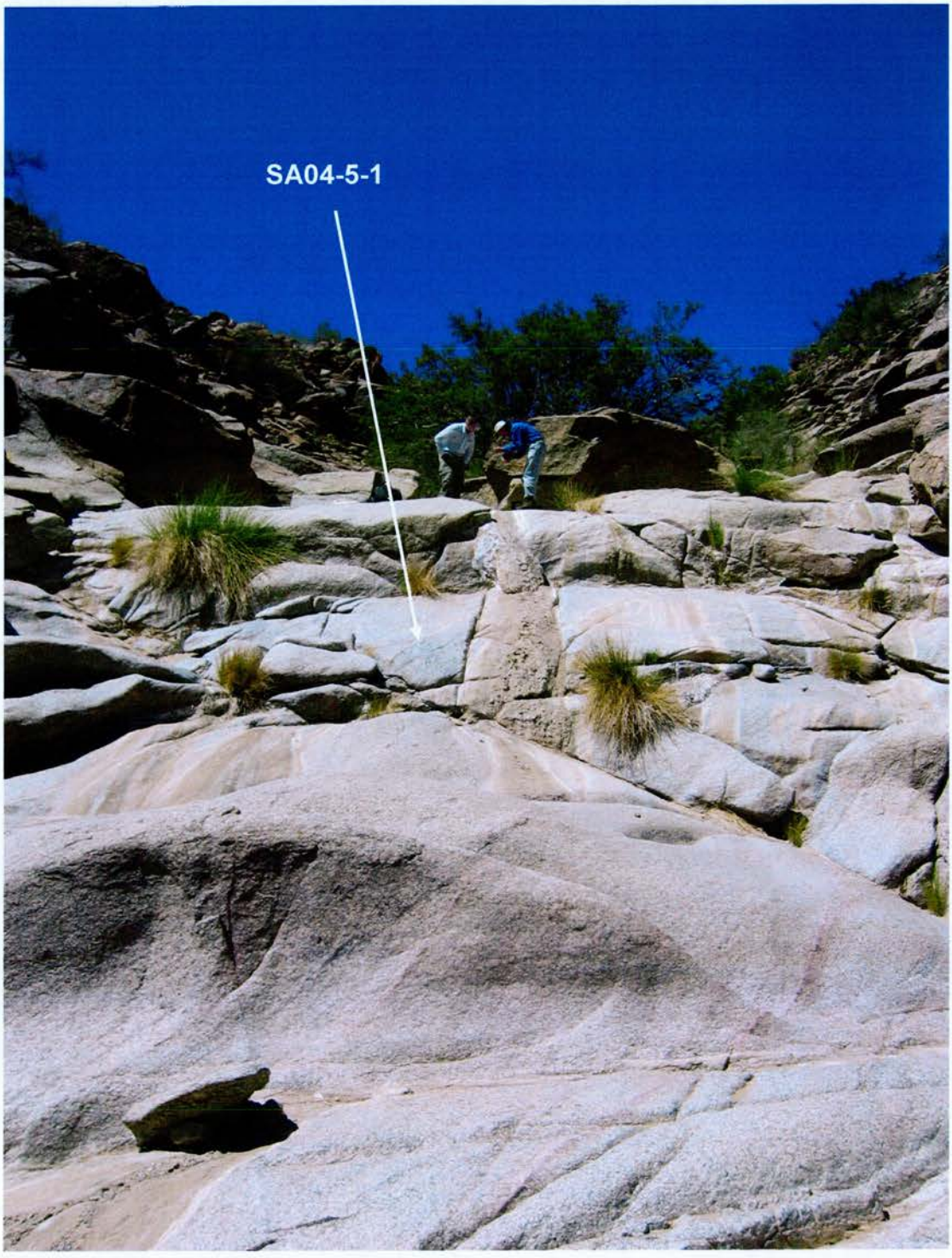

Plate 7.1.16 Echo Corner looking upstream (south) showing location of SA04-5-1 sample on the mini-knickpoint. Sample SA04-5-2 was a horizontal sample taken from where the people are standing.

7.2 Cosmogenic derived bedrock channel denudation rate estimates in the Augrabies Falls region

7.2.1. The trunk channel above the main Falls

The region above the main Falls consists of an anabranching, bedrock-dominated channel which extends for over 150 km upstream of the Falls where the discharge is distributed among several anabranches (Springer et al., 2006; Tooth *et al.*, 2004; Tooth & McCarthy, 2004) (Plate 7.2.1). The bedrock channels are dominated by potholed, fluted bedforms (Plate 7.2.2). Several bedrock bars in the channel, some several tens of kilometres upstream of the main Falls, were sampled in order to gain an understanding of the incision rate above the main Falls. Summary cosmogenic nuclide data is given in Table 7.2.1. Full details of cosmogenic nuclide data are given in Appendix 4.

As can be seen from Table 7.2.1, the bedrock channel in the anabranching region immediately above the Augrabies main Falls has a mean rate of incision of ~ 68.20 ± 6.40 mm ka^{-1} (this mean rate does not include sample SA05-4-2, for reasons discussed below). Samples SA05-3-1 and -3-2 are taken from the trunk channel at Keimoes, as described in Chapter 4, several tens of kilometres upstream of the Falls system on a granite-gneiss bedrock bar. The denudation rates of 4.50 ± 0.30 and 12.12 ± 0.79 mm ka^{-1}, respectively, are fairly consistent with each other. This region has an average incision rate of 8.31 ± 0.55 mm ka^{-1}, considerably lower than the rates immediately upstream of the main Falls in the knickpoint drawdown zone (the northern anabranch, discussed below, has an average rate of 73.68 ± 7.25 mm ka^{-1}). Sample SA05-3-1 has an $^{26}Al/^{10}Be$ ratio greater that 6.1, and is not plotted on the $^{26}Al/^{10}Be$ concentration plot (Figure 7.2.1). It is likely that this spurious $^{26}Al/^{10}Be$ ratio is due to loss of ^{26}Al during processing as described in Chapter 3.

Sample	Latitude	Long.	Elev. (m)	Lithology	Shielding correction	Stone scaling factor	^{10}Be (10^5 atom g^{-1})	^{26}Al (10^5 atom g^{-1})	^{10}Be denudation rate (mm ka^{-1})	^{10}Be Av. time (ka)	^{26}Al denudation rate (mm ka^{-1})	^{26}Al Av. time (ka)	^{26}Al /^{10}Be
SA04-9-2	28°36'09 "S	20°20'4 5"E	660	Granite-gneiss	0.96	1.54	0.78 ± 0.05	4.66 ± 0.34	57.24 ± 4.71	13.3	58.21 ± 5.47	13.4	5.97 ± 0.56
SA05-3-1	28°42'42 "S	20°59'0 6"E	724	Granite-gneiss	0.94	1.69	10.11 ± 0.30	87.76 ± 2.84	4.50 ± 0.30	132.4	2.75 ± 0.18	216.8	8.68 ± 0.64
SA05-3-2	28°43'41 "S	20°59'0 6"E	720	Granite-gneiss	0.96	1.64	3.86 ± 0.10		12.12 ± 0.79	49.2			
SA05-4-1	28°35'39 "S	20°20'4 1"E	613	Granite-gneiss	0.99	1.48	0.58 ± 0.04		76.99 ± 6.52	7.7			
SA05-4-2	28°35'39 "S	20°20'4 1"E	613	Granite-gneiss	0.99	1.47	38.59 ± 0.91	117.34 ± 2.3	0.87 ± 0.06	683.1	1.79 ± 0.11	332.8	3.04 ± 0.20
SA05-5-1	28°35'10 "S	20°20'0 2"E	613	Granite-gneiss	0.93	1.48	0.59 ± 0.05		70.37 ± 7.98	8.5			

Table 7.2.1 Cosmogenic nuclide data and denudation rates for bedrock channels above the main Falls. Thickness and shielding corrections are calculated using a rock density of 2.65 g cm^{-3} and a cosmic ray attenuation length of 155 g cm^{-2}. The altitude-latitude scaling factor is calculated according to Stone (2000). Total Al concentration in quartz is determined by ICP-AES at 2% uncertainty. Be data are normalised using the SUERC NIST standard with a nominal ^{10}Be/^{9}Be ratio of 3.00 x10^{-11}. Al data are normalised using Z92-0222 as the primary standard, with a nominal ^{26}Al/^{27}Al ratio of 4.11x10^{-11}. Denudation rates are calculated using sea level, high latitude ^{10}Be and ^{26}Al production rates (Stone 2000). Denudation rates are corrected for geomagnetic variation. See Appendix 4 for full details of data.

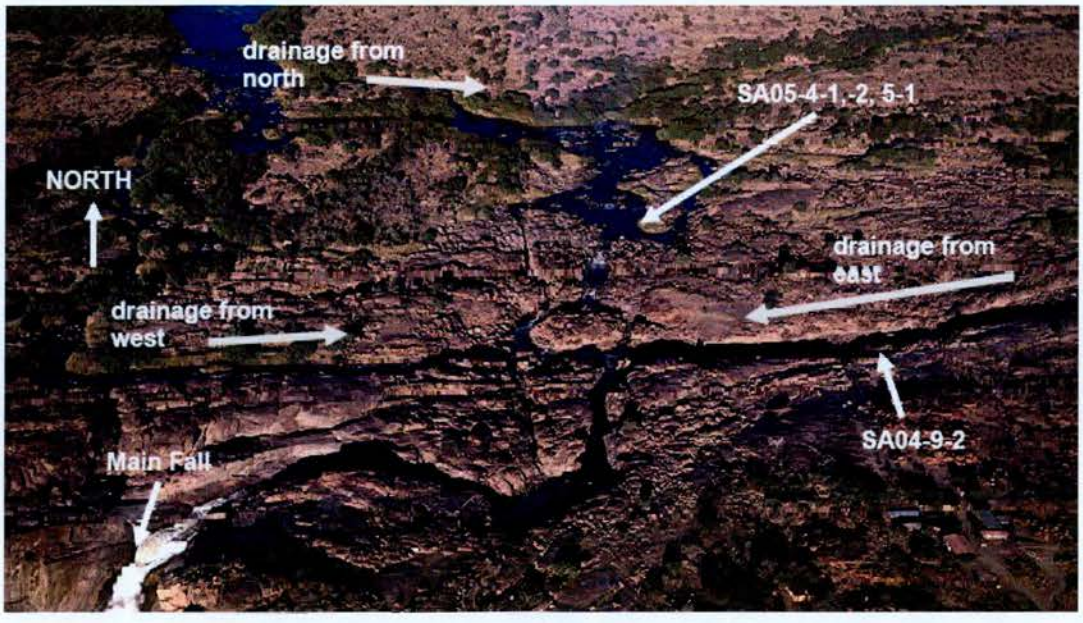

Plate 7.2.1 Western, northern and eastern anabranches just above the main Falls. The eastern anabranch ultimately captures flow from the northern and western anabranches. Photograph courtesy of S. Tooth.

Plate 7.2.2 Bedrock anabranching channel above the Augrabies main Falls (left) with evidence of potholing compared with deeply incised bedrock channel below the main Falls (right), at a 90-degree bend at Ararat.

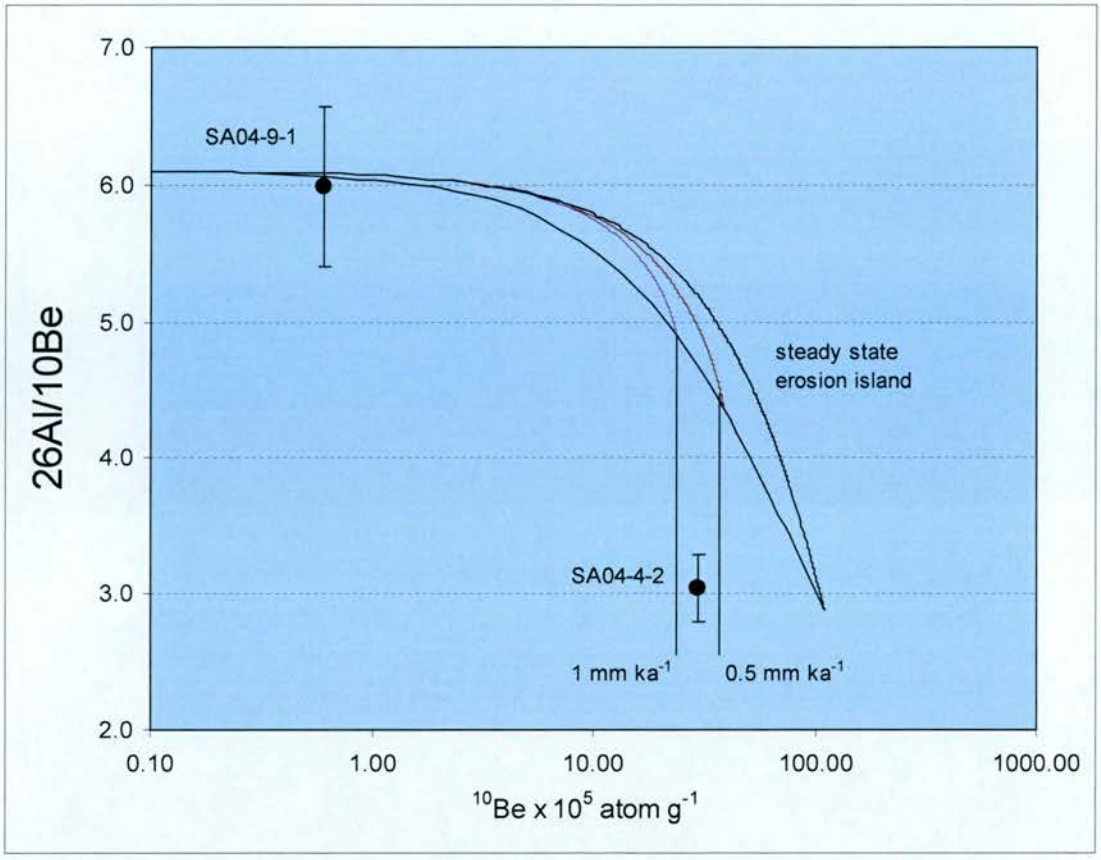

Figure 7.2.1 Steady state denudation island plot for bedrock channel samples above the main Falls. Note that sample SA05-3-1, with an $^{26}Al/^{10}Be$ ratio of >6.1 does not plot on this graph. This spurious ratio was caused by loss of Al during fuming, as described in Chapter 3. SA04-9-1 has undergone continuous exposure and incremental erosion, whilst SA04-4-2 may have had a more complex history or, more likely, was subject to analytical error, as described below.

Samples SA05-4-1, -4-2, and -5-1 are taken from a northern anabranch which joins with an eastern and western anabranch of the Orange River a few tens of meters above the main Falls (Plate 7.2.2). The samples from the northern anabranch give a cosmogenic-derived denudation rate of 76.99 ± 6.52, 0.87 ± 0.06, and 70.37 ± 7.98 mm ka^{-1}, respectively. Samples SA05-4-1 and SA05-5-1 are consistent and give a nominal average incision rate of ~ 74 mm ka^{-1}. Clearly sample SA05-4-2 is not consistent with the other two samples, as analysis of its $^{26}Al/^{10}Be$ ratio shows (3.04 ± 0.20, Figure 7.2.1). One possible scenario to account for the measured concentration is that the sample was buried by rock, sediment or water. To account for the measured concentration, sample SA05-4-2 would have had to have been covered by ~ 70 cm of rock; or 120 cm of sediment; or 180 cm of water for around 58 ka (from

Granger & Muzikar, 2001, equation 6). Since samples SA05-4-1 and SA05-4-2 were taken from the same bedrock bar and the difference in their elevation is only a few centimetres, SA05-4-2 could not have experienced shielding by any material without SA05-4-1 also being shielded. Sample SA05-4-1 has experienced no such shielding, making the argument for a complex exposure history of SA05-4-2 somewhat spurious. The Be concentration data in Table 5.2.1 and Appendix 4 are more revealing: they show sample SA05-4-2 to have an anomalously high ^{10}Be concentration; around sixty times higher than concentrations for the nearby samples SA05-4-1 and SA05-5-1 (which have concentrations of $0.58 \pm 0.04 \times 10^5$ and $0.59 \pm 0.05 \times 10^5$ at g^{-1}, respectively, as compared with $38.59 \pm 0.91 \times 10^5$ at g^{-1}). It is this high ^{10}Be concentration relative to the ^{26}Al concentration that gives sample SA05-4-2 its unusual position on Figure 7.2.1. Accidental addition of double (or even treble) the normal amount of ^{10}Be carrier to SA05-4-2 still would not account for the measured ^{10}Be concentration. It can only be concluded that this sample suffered some other form of ^{10}Be contamination which the other samples in the batch did not. Therefore, whilst would be conventional to construct an argument invoking complex exposure for a sample that lies in SA05-4-2's position on Figure 5.2.1 (one that includes complete burial for a prolonged period, preceded by slow erosion of between 0.5 and 1 mm ka^{-1} (Figure 5.2.1), such an argument makes no geomorphological sense as any burial would also have affected the neighbouring samples.

Another of the anabranches of the river immediately above the main Falls was sampled for both cosmogenic Be and Al (sample SA04-9-2). The location is on fluvially eroded bedrock on a protruding bedrock bar in the middle of the channel of the eastern anabranch that ultimately captures the northern and western anabranches and diverts their flow over the main Falls (Plate 7.2.2). Although there is a thin, localised cover of pebbles and cobbles along parts of the channel bank, flood deposits are not accumulating at the sampled sites. As shown by its ^{26}Al/^{10}Be ratio of 5.97 ± 0.56 and its presence on the steady state denudation island on Figure 5.2.1, this sample has not had a complex exposure history. The denudation rate of 57.24 ± 4.71 mm ka^{-1} suggests that incision is going on at much the same order of magnitude

in this anabranch as in the main channel described above, albeit at a slightly higher rate – something that is significant in terms of stream capture and is discussed fully in Chapter 9. Again the high rate of incision may be explained with reference to the proximity of the knickpoint drawdown zone, where the local channel gradient is steepest and river flow is most concentrated. The steep gradient leads to an increase in local velocity and therefore in the specific stream power per unit area. The high rates of incision experienced immediately above the knickpoint contrast with the relatively low rates some tens of kilometres upstream at Keimoes.

All locations immediately above the main Falls, whether in the main channel or in the anabranch, display potholes and fluting the bedrock (Plate 7.2.3). Potholes have been recognised as important components of channel incision by Gilbert (1906), Alexander (1932) and Wohl (1993) and may be the principal means by which channel margins are worn away in massive strata (cited in Hancock *et al.*, 1999). Springer *et al.* (2006) have described potholing as the dominant mechanism of channel incision in the anabranching region above the Augrabies main Falls. They propose that the main knickpoint is retreating by coalescence of potholes that form even where joints are absent. Joints may also be exploited and deepen by flowing water where potholes are absent, as described above. The bedrock above the main Falls is massive and is able to support large potholes that are likely to coalesce. This contrasts with the nature of the bedrock below the Falls, where joints exert strong controls on the direction of the trunk channel and the tributary networks south of the Orange River. It may be that bedrock incision by potholing strips the first few meters of bedrock from the channel, causing incipient joints to open up as denudational unloading features, thus explaining why joints are more apparent downstream of the knickpoint, although it is uncertain how much bedrock needs to be stripped before these incipient joints open up (Tooth, personal communication, 2006). Cylindrical potholes tend to grow in a systematic manner so that pothole walls are eroded faster than floors (Figure 7.2.2). This may be due to a combination of 'grinders', large boulders which systematically grind out the potholes, and cavitation – where pressure changes exerted by water rushing into and out of the pothole help weaken the rock and expand the pothole. The relative volume of denudation from wall versus

floor reflects the relative roles of descending erosive fluids versus basal erosive fluids and grinders in a pothole (Tooth, personal communication, 2006).

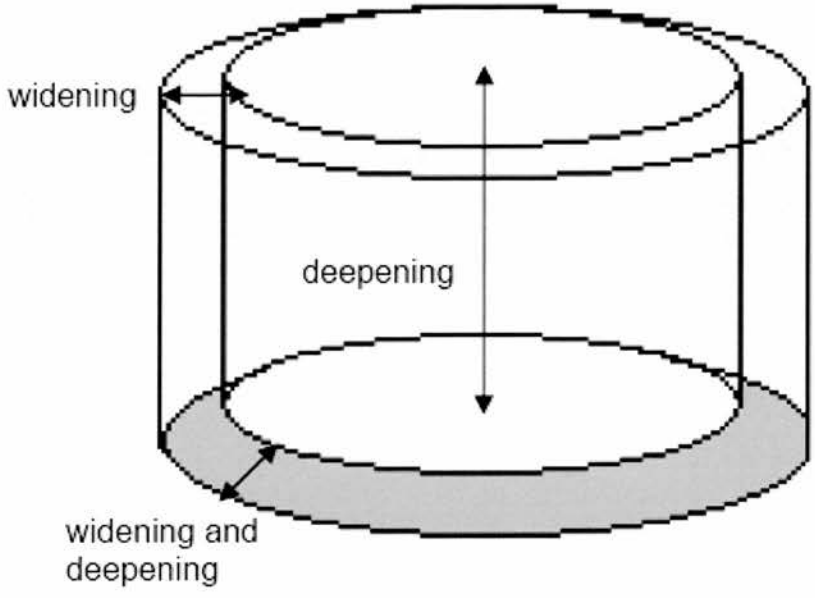

Figure 7.2.2 Schematic diagram of pothole development. Note that potholes are rarely symmetrical. Depth and radii increase simultaneously with vertical translation of the pothole base caused by bedrock denudation (*after* Springer *et al.* (2006); Springer and Wohl, (2002)).

Springer et al. (2006) observe that the largest potholes are found at the downstream terminus of the river where they have coalesced, and smaller potholes dominate the upstream terminus where bedrock banks slope down to sub-metre scale potholes that have coalesced to form the rudiments of an inner channel. Small, young potholes are found on the inclined banks and nearby surfaces (Plate 7.2.4). They propose that the passage of a knickpoint creates an inner channel which is enlarged further by undercutting of the walls and sheet collapse downstream of the potholes. Joints play less of a role in pothole development just upstream of the Augrabies main Falls than at other locations they studied in the bedrock dominated reaches of the Orange River. They observe that only 51% of joints intersect potholes, which are sparse at this knickpoint.

Plate 7.2.3 (left) Potholes and fluting in microcrystalline mafic bedrock; (right) mega-pothole (~ 5 m deep) adjacent to the main Falls. Note person for scale in right hand photograph.

Plate 7.2.4 Different sizes of potholes upstream (left); and downstream (right) of Augrabies main Falls. Note that the downstream area shows both massive jointing and potholes.

7.2.2 The channel below the main Falls

Table 7.2.2 shows the results of cosmogenic isotope analysis for a number of samples taken from the trunk channel downstream of the Augrabies main Falls. It can be seen from the ^{10}Be data that there is a consistent denudation rate of less than 10 mm ka^{-1} (mean 7.83 ± 0.64 mm ka^{-1}, range of 5.41 to 9.16 mm ka^{-1}). This rate is much lower than the average rate observed immediately upstream of the knickpoint (average 68.20 ± 6.40 mm ka^{-1}).

Sample SA04-3-2 is taken from the bed of the Orange River around 100 m upstream of a 90-degree bend in the river. The bedrock bar sticks out 15 m into the trunk channel, and although it is exposed at low (~ 50 m^3 s^{-1}) flows, it may be covered during floods. What this means in terms of cosmogenic shielding is uncertain since the Al sample was lost during processing. However, since shielding is not significant for sample SA04-9-1, in a topographically similar position, it is not believed to be significant at this location. Burial by water, sediment or rock would have to take place over tens of thousands of years to significantly affect the nuclide concentrations. This location, given the lack of anabranches, has been the main channel for possibly millions of years. It is unlikely that in this environment, rock or sediment would remain in the channel for long enough to exert a significant shielding effect. In contrast to the samples above the main Falls, the bedrock outcrops in the channel show minimal fluting and potholing, however wedged pebbles in joint cracks give evidence of high energy flows.

Sample no.	Latitude	Longitude	Elevation (m)	Lithology	Thickness and shielding correction	Stone scaling factor	^{10}Be (10^5 atom g^{-1})	^{10}Be denudation rate (mm ka^{-1})
SA04-3-2	28°32'45''S	20°17'07''E	451	Granite-gneiss	0.94	1.64	4.20 ± 0.08	8.91 ± 0.55
SA04-23-1	28°32'47''S	20°16'22''E	431	Granite-gneiss	0.74	1.36	5.39 ± 0.50	5.41 ± 0.60
SA04-24-1	28°32'45''S	20°16'20''E	430	Granite-gneiss	0.74	1.34	3.20 ± 0.19	9.16 ± 0.76

Table 7.2.2 Cosmogenic nuclide data and denudation rates for bedrock channels below the main Falls. Thickness and shielding corrections are calculated using a rock density of 2.65 g cm^{-3} and a cosmic ray attenuation length of 155 g cm^{-2}. The altitude-latitude scaling factor is calculated according to Stone (2000). Be data are normalised using the SUERC NIST standard with a nominal ^{10}Be/^{9}Be ratio of 3.00 x10^{-11}. Denudation rates are calculated using sea level, high latitude ^{10}Be production rates (Stone 2000) with spallation and muons. Denudation rates are corrected for geomagnetic variation. See Appendix 4 for full details of data.

Samples SA04-23-1 and -24-1 are the most downstream samples of bedrock taken from the Orange River. SA04-23-1 is a bedrock bar in the Orange River, ~ 20 m from either bank and ~ 5 m long. SA04-24-1 is a bedrock bar in the midstream section of the river, ~ 10 m from the north bank and 15 m down river from 23-1. There is possible periodic coverage of these bedrock bars by sediment and/or water during floods, however the extent and duration of such coverage is difficult to discern. The low denudation rates in the Orange River downstream of the Falls suggest that the style of denudation in the downstream zone is qualitatively different from that upstream, a feature that is discussed in more detail in the next section.

7.2.3 Anabranch channels

Sample SA04-17-1 was taken from a bedrock channel anabranch close to one of the smaller knickpoints (Twin Falls) in the Augrabies region (Plates 7.2.5, 7.2.6). This site is on a southern anabranch that completely bypasses the main Falls and re-enters the main Orange River downstream of the main Falls (Figure 7.2.1). The sample is taken from the base of the bedrock channel, proximate to but not covered by water at the time of sampling, although the bedrock is likely to be covered by high flows just upstream of Twin Falls. The bedrock is fluted and pot-holed with a remarkable network of interlocking potholes and cavities suggesting the knickpoint is retreating by the same mechanism as illustrated in Section 7.2. Table 7.2.3 shows the cosmogenic nuclide details for this and other anabranch channel samples, which are supplemented by full details in the Appendix. Sample SA04-17-1 is eroding quickly (181.22 ± 16.41 mm ka^{-1} from ^{10}Be and 193.54 ± 20.84 mm ka^{-1} from ^{26}Al data – the fastest rates measured in the Augrabies region). These rates are consistent within standard uncertainties. The ^{26}Al/^{10}Be ratio of 5.19 ± 0.59, agrees with the 'ideal' ratio of 6.1 ± 0.5 to within standard uncertainty, suggesting that there has been minimal shielding of the sample during its history (Figure 7.2.3). The rapid rates measured for Twin Falls anabranch suggests that incision is still actively going on.

Plate 7.2.5 Location of sample SA04-17-1. Note the presence of potholes upstream.

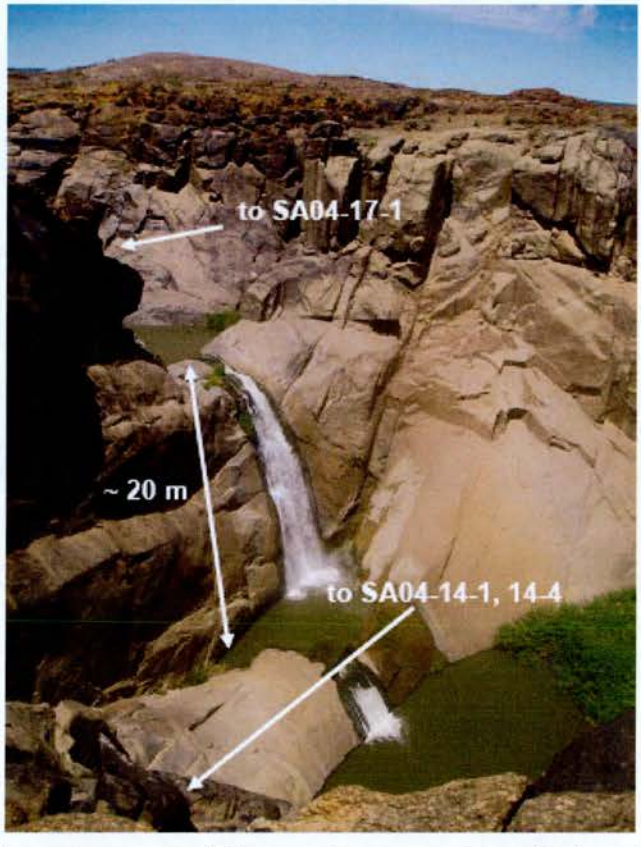

Plate 7.2.6 western end of Fissure Canyon, where that anabranch joins with the Twin Falls anabranch. Twin Falls is incising around three times faster than Fissure Canyon.

If sample SA04-17-1 is compared with the trunk channel bedrock samples both downstream and upstream of the Falls system discussed in the last section, it can be seen that the Twin Falls anabranch at this particular point is incising at a rate two orders of magnitude more quickly than the main channel below the Falls system, and an order of magnitude more quickly than the main channel above the Falls system. One explanation could be that Twin Falls bedrock channel is incising rapidly to keep track of changes in local base level – in this case the local base level is the main channel of the Orange River which lies at an elevation some 20 m below the sampling location at Twin Falls. However, the sampled location has no 'knowledge' that base level lies 20 m below it and so another explanation must be invoked to explain its high rate of incision.

The flow of the Orange above the Augrabies Falls system is distributed among several anabranches. Twin Falls anabranch becomes re-activated as a 'short circuit' for the main river channel when the Orange is in flood, completely bypassing the main Falls (Springer *et al.*, 2006). This leads to concentrated high flows which can rapidly deepen the anabranch by abrasion and potholing of the bedrock. Invoking the stream power incision model (Whipple & Tucker, 1999), the specific stream power of the Twin Falls anabranch is clearly high during floods due to the discharge being confined to a small cross-section of channel, thus funnelling the discharge and increasing the velocity (and incision power) per unit area. This has a positive feedback effect, by increasing the gradient of the channel, and leading to a further increase in velocity and local stream incision power. Figures 7.1.1 and 7.1.2 reveal that the River has experienced high discharge (~ 500 $m^3 s^{-1}$) for only a small proportion of the last few decades. If this trend is extrapolated back, it may not be sufficient to account for the high incision rate at Twin Falls. If, however, large floods in the past led to deposition of debris which diverted most of the Orange's flow over one of the other knickpoints in the Augrabies system (such as Twin Falls) then the sustained high flow in a confined cross section could explain the high denudation rate seen at Twin Falls. If the flow was subsequently diverted again to another of the anabranches (perhaps as a result of sediment or bedrock deposited after peak flows), the previous main channel would be left as a dry 'ghost' channel, cut off from the

Augrabies system as flow was diverted away. This mechanism would account for the observed state of Twin Falls as a 'hanging valley', left high and dry after the majority of discharge switched from Twin Falls to its present location at the main Falls (Plate 7.1.11). Given the short averaging time of this sample (~ 3 ka) it is likely that there was high discharge at Twin Falls at some point in the recent past, and that future flood events could lead to a diversion of flow and re-activation of the Twin Falls anabranch as the major conduit for flow in the Augrabies system for a prolonged period of time. Thus peak flows can affect the routing of the channel network by depositing debris (mainly boulders) which diverts subsequent flow. These antecedent conditions are responsible for the channel switching that has clearly gone on in the Falls system.

7.2.4 Tributary channels

The other tributary samples are taken from a sheet of granite gneiss bedrock downstream of a ~ 34 km^2 mixed alluvial-bedrock tributary on the south bank of the Orange River, close to its confluence with the trunk channel (Figure 7.2.4). The three samples (SA04-27-1, -2, -3) give an average ^{10}Be derived denudation rates of 14.63 ± 3.28 mm ka^{-1}. These results are fairly consistent with each other and are of the same order of magnitude. Samples SA04-27-1 and -27-3 have very similar rates, whilst SA04-27-2 has a higher rate, albeit with a larger uncertainty (Table 7.2.3). There is no significant shielding of the samples – SA04-27-1 gives a $^{26}Al/^{10}Be$ ratio of 6.1 to within one standard deviation of error (Figure 7.2.3). This sample also has similar ^{26}Al and ^{10}Be derived denudation rates. The lack of shielding (particularly by bedrock) suggests that denudation is going on incrementally rather than by removal of large blocks.

Sample	Lat.	Long.	Elev. (m)	Lith.	Shielding correction	Stone scaling factor	^{10}Be (10^5 at g^{-1})	^{26}Al (10^5 at g^{-1})	^{10}Be denudation rate (mm ka^{-1})	Av. time (ka)	^{26}Al denudation rate (mm ka^{-1})	Av. time (ka)	^{26}Al/^{10}Be
SA04-17-1	28°35'34"S	20°19'37"E	655	Granite gneiss	0.86	1.53	0.24 ± 0.02	1.26 ± 0.11	181.22 ± 16.41	3.29	193.54 ± 20.84	3.08	5.19 ± 0.59
SA04-27-1	28°32'59"S	20°15'41"E	448	Granite gneiss	0.91	1.32	3.13 ± 0.12	17.78 ± 0.67	10.67 ± 0.74	55.87	12.20 ± 0.85	48.88	5.37 ± 0.42
SA04-27-2	28°32'59"S	20°15'41"E	448	Granite gneiss	0.91	1.29	1.69 ± 0.63	17.78 ± 0.67	22.03 ± 8.37	27.06			
SA04-27-3	28°32'59"S	20°15'41"E	448	Granite gneiss	0.91	1.30	3.13 ± 0.10	17.78 ± 0.67	11.19 ± 0.74	53.26			

Table 7.2.3 Cosmogenic nuclide data and denudation rates for anabranch channel (SA04-17-1) and tributary channel samples (SA04-27-1, -2, -3) in the Augrabies Falls region. Thickness and shielding corrections are calculated using a rock density of 2.65 g cm^{-3} and a cosmic ray attenuation length of 155 g cm^{-2}. The altitude-latitude scaling factor is calculated according to Stone (2000). Total Al concentration in quartz is determined by ICP-AES at 2% uncertainty. Be data are normalised using the SUERC NIST standard with a nominal ^{10}Be/^{9}Be ratio of 3.00 x10^{-11}. Al data are normalised using standard Z92-0222 with a nominal ^{26}Al/^{27}Al ratio of 4.11x10^{-11}. Denudation rates are calculated using sea level, high latitude ^{10}Be and ^{26}Al production rates (Stone 2000). Denudation rates are corrected for geomagnetic variation. See Appendix 4 for full details of data.

The denudation rates in this bedrock channel are roughly two times higher than those in the main channel of the Orange River. The sample location is only ~ 5 m above the level of the main channel of the Orange River, suggesting that the tributary has incised almost down to base level and that more rapid denudation went on some time in the past and has since slowed as the local base level has almost been reached. The main period of incision went on perhaps millions to tens of millions of years ago when the knickpoint retreated up the main channel resulting in lowering of local base level and associated rapid denudation in the tributary. The tributary and the main channel can be seen to be incising at similar rates (~ 14 mm ka^{-1} in the tributary as compared with ~ 4 mm ka^{-1} in the main channel below the Falls). The slightly higher rate in the tributary channel might be explained by its steeper channel gradient with respect to the main channel and therefore its higher specific stream power. Flood discharges will be much higher overall in the main channel, however per unit area the stream incision power is likely to be greater in the tributary channel, thus accounting for a slightly higher incision rate. Since this location is a true tributary and not an anabranch of the main Orange River, its discharge is much lower, therefore the incision power is less than in the Twin Falls anabranch.

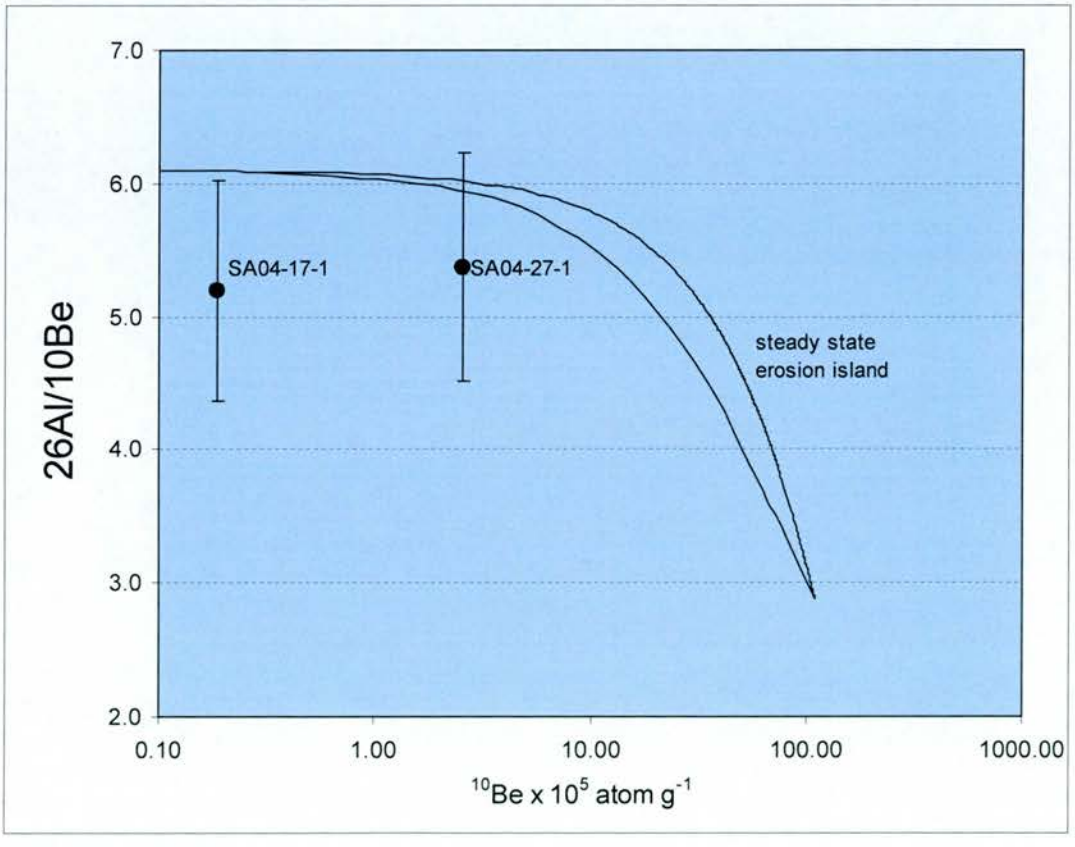

Figure 7.2.3 (previous page) Steady state denudation island plot for anabranch and tributary channel samples.

The catchment-averaged denudation rate for a fluvial sample from the same tributary is 5.85 ± 0.49mm ka^{-1}, of a similar order of magnitude but slightly lower than the rate of bedrock incision. This reflects that this mixed alluvial-bedrock tributary catchment is undergoing denudation on average more slowly than the bedrock stretch at the base of the tributary. There is no evidence of potholing in the bedrock in this tributary channel, suggesting that the tributary experiences neither the high magnitude flows nor the boulder-dominated bedload of the main trunk channel and its anabranches and that incision of the bedrock here is incremental.

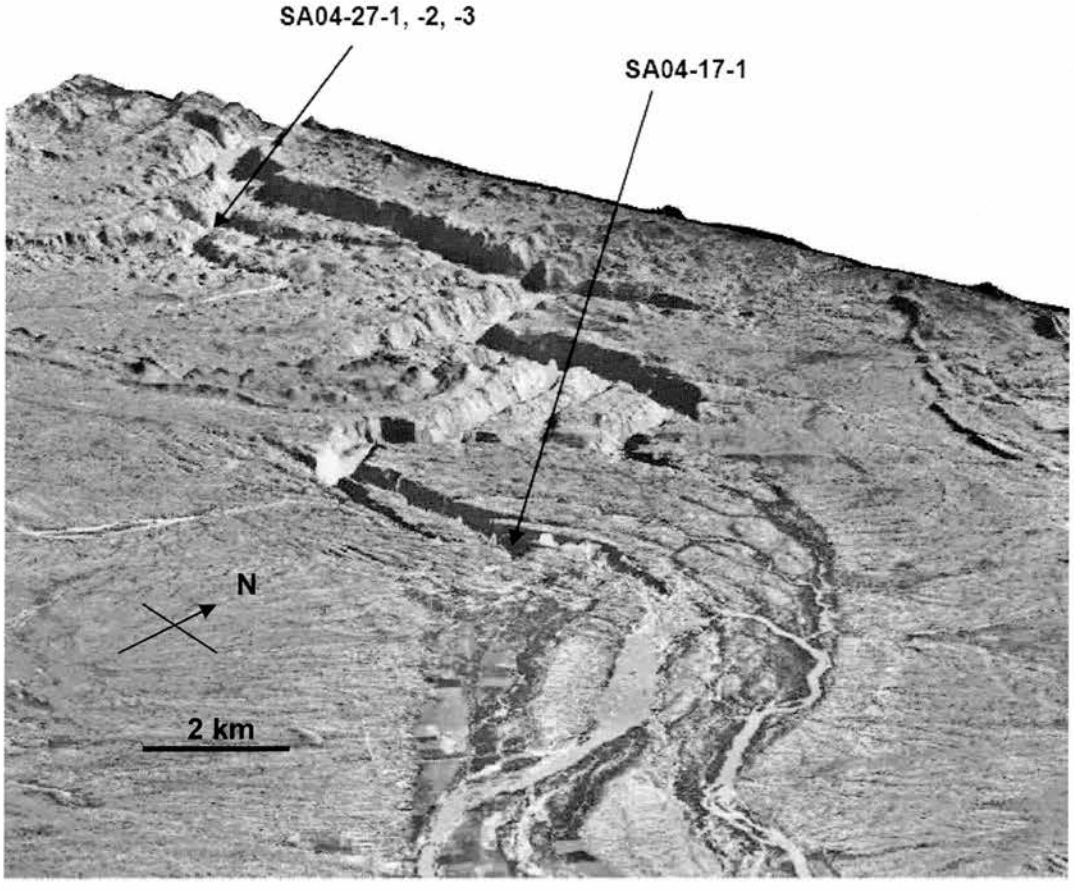

Figure 7.2.4 Location of SA04-27- series and SA04-17-1 tributary samples (DEM from Walcott *et al.*, unpublished data).

7.2.5 CIAF samples

In general, the samples analysed by the Cosmogenic Isotope Analysis Facility (CIAF) back up the data already presented above. The denudation rates calculated from this data are very similar and reinforce the trends described above. Specific samples and locations are discussed below. The results from the main channel above the Augrabies Falls are given in Table 7.2.4. In common with the samples from above the main Falls discussed above, the channel incision rate is of the order of tens of millimetres per thousand years. The average channel incision rate for the CIAF samples from above the main Falls is ~ 43 mm ka^{-1}. This compares well with the average rate of ~ 44 mm ka^{-1} from all the samples above the main Falls presented in Table 7.2.1. Samples SA04-9-1 and -9-2 are from the same bedrock bar and have similar denudation rates (74.94 ± 5.44 and mm ka^{-1} and 57.24 ± 4.71 mm ka^{-1}, respectively), despite the samples having been processed in different laboratories. A clear trend is seen in the CIAF samples that denudation rates decline further upstream. Samples SA04-9-1 to SA04-12-1 were taken progressively further upstream on a ~ 2 km stretch of the eastern anabranch above the Augrabies main Falls. The decline in denudation rates upstream is likely to be due to the gradient becoming steeper downstream as it approaches the knickpoint drawdown zone which results in higher flow velocities and higher specific stream power. Narrowing of the channel downstream will also result in a higher specific stream power, reflected in a high denudation rate. Samples SA04-13-1 and -13-2 were taken from a region of bedrock that is not part of the channel but is likely to be a conduit for peak flows. Evidence for this comes from its topographic position at a local low point, and the presence of boulders, sand and absence of vegetation. As might be expected for an area of bedrock that only acts as a channel during peak flows, the average incision rate of this location is ~ 12.75 mm ka^{-1}, which is around 3 times lower than the average for the samples from the main anabranch channel. Taking just the CIAF samples there is an average rate of incision for the eastern anabranch of 62.56 ± 6.05 mm ka^{-1}. This compares well to within standard uncertainties with the rate of 57.24 ± 4.71 mm ka^{-1} for sample SA04-9-2 from the same anabranch.

Sample	Latitude	Altitude (m)	Shielding scaling factor	Stone's SEL scaling (spallation and muons)	Production rate spallation and muons (at $g^{-1} a^{-1}$) (Stone)	$^{10}Be/^{9}Be$	σ ($^{10}Be/^{9}Be$)	ε (mm ka^{-1}) spallation & muons (Stone)	± Standard Uncertainty	Averaging time (ka)
SA04-09-01	28°36'S	660	0.96	1.53	7.49	5.94E+04	2.52E+03	74.94	5.44	7.96
SA04-11-02	28°36'S	620	0.98	1.48	7.40	6.63E+04	8.25E+03	66.23	9.11	9.00
SA04-12-01	28°36'S	622	0.97	1.50	7.42	9.46E+04	4.78E+03	46.50	3.61	12.82
SA04-13-01	28°36'S	679	0.98	1.58	7.90	4.44E+05	1.22E+04	10.33	0.67	57.72
SA04-13-02	28°36'S	679	0.98	1.69	8.45	3.26E+05	9.06E+03	15.16	0.99	39.31

Table 7.2.4 Cosmogenic nuclide data and denudation rates for bedrock channel samples above the Augrabies main Falls. Samples were processed at the NERC Cosmogenic Isotope Analysis Facility (CIAF), SUERC. Thickness and shielding corrections are calculated using a rock density of 2.65 g cm^{-3} and a cosmic ray attenuation length of 155 g cm^{-2}. The altitude-latitude scaling factor is calculated according to Stone (2000) and includes spallogenic and muogenic production. Be data are normalised using NIST SRM 4325 as primary standard with a nominal $^{10}Be/^{9}Be$ ratio of $3.06x10^{-11}$. Note that this means the ^{10}Be concentrations are some 2% lower than those measured using the SUERC NIST standard with a nominal $^{10}Be/^{9}Be$ ratio of $3.00x10^{-11}$. Denudation rates are corrected for geomagnetic variation. See Appendix 5 for full details of data. ± uncertainties are standard uncertainties.

The results of the CIAF samples taken from below the Falls are given in Table 7.2.5. In general, the mean rate of incision below the Falls (~ 13 mm ka^{-1}) is similar to that presented above for similar locations (~ 7.8 mm ka^{-1}). Given the low overall rates, and the fact that the samples are from very similar locations, this is not believed to be significant. Indeed samples SA04-3-1 and -3-2 have rates that are very similar to each other within standard uncertainty (9.64 ± 0.63 and 8.91 ± 0.55 mm ka^{-1}, respectively). Overall, the trend that the main gorge below the Augrabies Falls system is incising much more slowly than the channels above the main Falls is backed up by the CIAF data; the range of denudation rates above the Falls is ~ 46 – 75 mm ka^{-1} for the CIAF samples and ~ 57 – 76 mm ka^{-1} for the PhD samples. Below the Falls, a range of rates between ~ 10 – 19 mm ka^{-1} and ~ 5 – 9 mm ka^{-1} were derived for the CIAF and PhD samples, respectively. Mean rates of all samples (CIAF and PhD) are: above the main Falls 65.4 mm ka^{-1}; below the main Falls 8.8 mm ka^{-1}. Although the absolute rate differences are not always very big, it is the relative rate differences that are responsible for generating the spectacular topography of the Augrabies Falls region.

The CIAF samples from an anabranch that bypasses the main Falls and a tributary channel are summarised in Table 7.2.6. Samples SA04-14-1 and SA04-14-4 were taken from an anabranch channel that bypasses the main Falls but is part of a complex series of deeply incised anabranches that end in knickpoints. This anabranch is incising fairly rapidly (between 50.82 ± 4.09 at its western downstream end; and 48.02 ± 3.22 mm ka^{-1} at the upstream, eastern end). However, it is incising more slowly than the Twin Falls anabranch which is incising at a rate of 181.22 ± 16.41 mm ka^{-1}, around three times faster. This could be partly explained by Twin Falls being a wider channel and thus not subject to the same funnelling effect of peak discharges (Plates 7.2.5, 7.2.6), which leads to high stream power and higher denudation rates. If rates such as these are maintained over tens to hundreds of thousands of years, Twin Falls would be expected to out-compete Fissure Canyon and capture drainage from it. At present, Twin Falls appears to be out-competed by a small channel running adjacent to it, which rapidly becomes wider and deeper and which Fissure Canyon eventually descends into via a knickpoint.

Sample	Latitude	Altitude (m)	Shielding scaling factor	Stone's scaling factor	Production rate (at g^{-1} a^{-1})	$^{10}Be/^{9}Be$	σ ($^{10}Be/^{9}Be$)	ε (mm ka^{-1}) spallation & muons (Stone)	± Standard Uncertainty	Averaging time (ka)
SA04-04-01	28°33'S	400	0.89	1.25	5.67	2.98E+05	7.72E+03	11.05	0.71	53.93
SA04-04-02	28°33'S	439	0.87	1.34	5.95	1.82E+05	4.96E+03	19.21	1.25	31.04
SA04-03-01	28°33'S	448	0.94	1.35	6.47	3.89E+05	10720.00	9.64	0.63	61.83

Table 7.2.5 Cosmogenic nuclide data and denudation rates for bedrock channel samples below the Augrabies main Falls. Samples were processed at the NERC Cosmogenic Isotope Analysis Facility (CIAF), SUERC. Thickness and shielding corrections are calculated using a rock density of 2.65 g cm^{-3} and a cosmic ray attenuation length of 155 g cm^{-2}. The altitude-latitude scaling factor is calculated according to Stone (2000) and includes spallogenic and muogenic production. Be data are normalised using NIST SRM 4325 as primary standard with a nominal $^{10}Be/^{9}Be$ ratio of $3.06x10^{-11}$. Note that this means the ^{10}Be concentrations are some 2% lower than those measured using the SUERC NIST standard with a nominal $^{10}Be/^{9}Be$ ratio of $3.00x10^{-11}$. Denudation rates are corrected for geomagnetic variation. See Appendix 5 for full details of data. ± uncertainties are standard uncertainties.

Sample	Latitude	Altitude (m)	Shielding factor	Stone scaling factor	Production rate spallation and muons (at $g^{-1} a^{-1}$) (Stone)	$^{10}Be/^{9}Be$	σ ($^{10}Be/^{9}Be$)	ε (mm ka^{-1}) spallation & muons (Stone)	± Standard Uncertainty	Averaging time (ka)
SA04-14-01	28°35'S	615	0.97	1.49	7.37	8.60E+04	4.72E+03	50.82	4.09	11.73
SA04-14-04	28°35'S	657	0.94	1.54	7.38	9.11E+04	2.93E+03	48.02	3.22	12.41
SA04-05-01	28°33'S	446	0.59	1.40	7.25	1.53E+05	5.32E+03	16.32	1.12	36.53
SA04-05-02	28°33'S	458	0.84	1.35	5.78	1.28E+05	5.69E+03	26.56	1.96	22.44

Table 7.2.6 Cosmogenic nuclide data and denudation rates for anabranch channel samples (that bypass the main Falls, 'Fissure Canyon', first two samples in the table) and tributary channel samples (from Echo Corner tributary, third and fourth samples in the table). Samples were processed at the NERC Cosmogenic Isotope Analysis Facility (CIAF), SUERC. Thickness and shielding corrections are calculated using a rock density of 2.65 g cm^{-3} and a cosmic ray attenuation length of 155 g cm^{-2}. The altitude-latitude scaling factor is calculated according to Stone (2000) and includes spallogenic and muogenic production. Be data are normalised using NIST SRM 4325 as primary standard with a nominal $^{10}Be/^{9}Be$ ratio of $3.06x10^{-11}$. Note that this means the ^{10}Be concentrations are some 2% lower than those measured using the SUERC NIST standard with a nominal $^{10}Be/^{9}Be$ ratio of $3.00x10^{-11}$. Denudation rates are corrected for geomagnetic variation. See Appendix 5 for full details of data. ± uncertainties are standard uncertainties.

The samples from the Echo Corner tributary were taken on a small knickpoint – a ~ 5m exposure of bedrock which was sampled for both downwearing and backwearing rates. Sample SA04-5-1 was the near-vertical sample which gave a backwearing rate of 16.32 ± 1.12 mm ka^{-1}, which is a fairly rapid rate of retreat. This may be driven by high magnitude low frequency rainfall events which, given the boulders in the tributary, are responsible for high flows, and high specific stream power. The relatively high backwearing rate could be interpreted as a response to base level lowering in the main channel, which has initiated a wave of incision which is now travelling upstream in the tributary basin. The tributary channel downwearing rate from sample SA04-5-2 is 26.56 ± 1.96 mm ka^{-1}, a relatively rapid rate of incision that is comparable with the catchment-averaged rate of denudation for this tributary of 13.0 mm ka^{-1}, discussed in Chapter 5.

Chapter 8 – Interfluves in the Augrabies region

8.1 Field descriptions of interfluves and inselbergs

8.1.1 Interfluves: background denudation rates

In order to gain an estimate of relief development rates in the Augrabies region, 'background' interfluve denudation rates were compared with channel denudation rates. Interfluve locations were chosen carefully in order to be representative of both the interfluves proximate to river anabranches that flow over the main Falls and anabranches that bypass the main Falls as well as interfluves close to tributaries. The lithology of the interfluves, in common with the rest of the region, is mainly a mixture of Augrabies granite and Riemsvasmaak gneiss. Owing to the quartz-rich nature of these rocks, with quartz veins visible in the field, they are eminently well-suited to *in-situ* ^{10}Be and ^{26}Al analysis. The interfluves are some of the most resistant landforms of the Augrabies region and represent some of the highest altitude points in the region (~ 660 m, compared with a surrounding landsurface altitude of 620 m and altitude of ~ 610 m and 430 m, respectively, in sampled bedrock channels above and below the main Falls). The following section gives an introduction to the interfluves sampled near the main channel; those near anabranch channels that bypass the main Falls; and those near tributary channels.

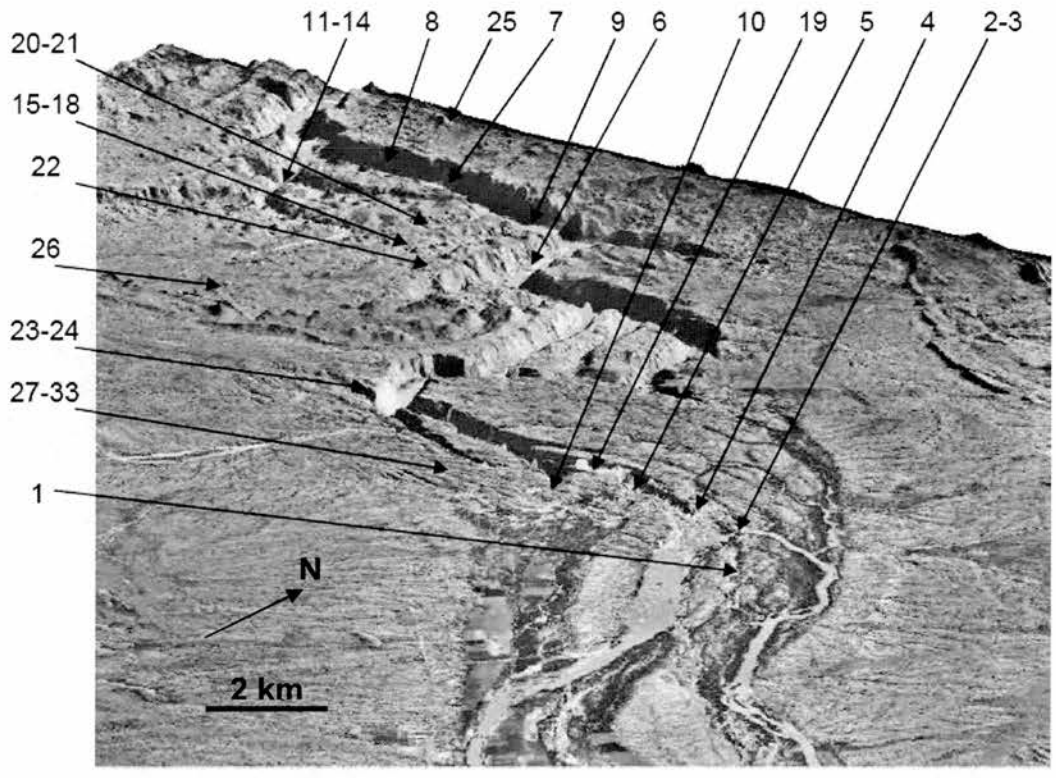

Figure 8.1.1 Sampling locations in the Augrabies Falls region (refer to Table 8.1.1 for locations) DEM from Walcott *et al.* (unpublished data).

Two samples were taken from the interfluves adjacent to the main Orange River channel on the south bank at Ararat, a viewpoint where two deeply incised anabranch channels can be seen (Plate 8.1.1). Samples were taken from a very well weathered, grussified granite (SA04-21-1) that was superposed over a less grussified, but still well weathered granite undergoing spallation weathering (SA04-21-2) – similar to that on the Moon Rock bornhardt (described below). The main research question in this location was to determine the rate of incision of the interfluve given that it lies proximate to two deeply incised bedrock channels that may in the past have been locations of knickpoints within the Augrabies Falls System. Indeed, just upstream of Ararat is Twin Falls and a complex series of deeply incised bedrock anabranches that have clearly carried significant flows in the past. Incision rates established from this location can be compared with a nearby sample from the main channel (SA04-3-2). The interfluve on the northern side of the Orange River was also sampled (SA04-22-1). This is one of the highest points in the Augrabies region (Plate 8.1.2).

Number	Environment	Sample type	Sample name
1	Trunk channel above main Falls	Bedrock	SA04-9-2
2	Trunk channel above main Falls	Bedrock	SA05-4-1
3	Trunk channel above main Falls	Bedrock	SA05-4-2
4	Trunk channel above main Falls	Bedrock	SA05-5-1
5	Trunk channel above main Falls	Fluvial sand (catchment-averaged)	SA03-5-1
6	Trunk channel below main Falls	Bedrock	SA04-3-1
7	Trunk channel below main Falls	Bedrock	SA04-23-1
8	Trunk channel below main Falls	Bedrock	SA04-24-1
9	Trunk channel below main Falls	Fluvial sand (catchment-averaged)	SA03-4-1
10	Anabranch channel	Bedrock	SA04-17-1
11	Tributary channel	Bedrock	SA04-27-1
12	Tributary channel	Bedrock	SA04-27-2
13	Tributary channel	Bedrock	SA04-27-3
14	Tributary channel	Fluvial sand (catchment-averaged)	SA04-28-1
15	Tributary channel	Fluvial sand (catchment-averaged)	SA03-2-1
16	Tributary channel	Fluvial sand (catchment-averaged)	SA04-19-1-A
17	Tributary channel	Fluvial sand (catchment-averaged)	SA04-19-1-B
18	Tributary channel	Fluvial sand (catchment-averaged)	SA04-19-1-C
19	Interfluve	Bedrock	SA04-15-1
20	Interfluve	Bedrock	SA04-18-1
21	Interfluve	Bedrock	SA04-18-2
22	Interfluve	Bedrock	SA04-20-1
23	Interfluve	Bedrock	SA04-21-1
24	Interfluve	Bedrock	SA04-21-2
25	Interfluve	Bedrock	SA04-22-1
26	Interfluve	Desert pavement	SA05-6-1
27	Bornhardt	Bedrock	SA04-6-1
28	Bornhardt	Bedrock	SA05-1-1
29	Bornhardt	Bedrock	SA05-1-2
30	Bornhardt	Bedrock	SA05-1-3
31	Bornhardt	Bedrock	SA05-2-1
32	Bornhardt	Bedrock	SA05-2-2
33	Bornhardt	Bedrock	SA05-2-3

Table 8.1.1 Sampling locations in the Augrabies Falls region. Fluvial samples are included in this table for comparison.

Plate 8.1.1 Samples taken adjacent to the main Orange River at Ararat (SA04-21-1, -2) are off to the left hand side of the image. Note the 90-degree switchbacks in the river looking downstream and the deeply incised bedrock channel.

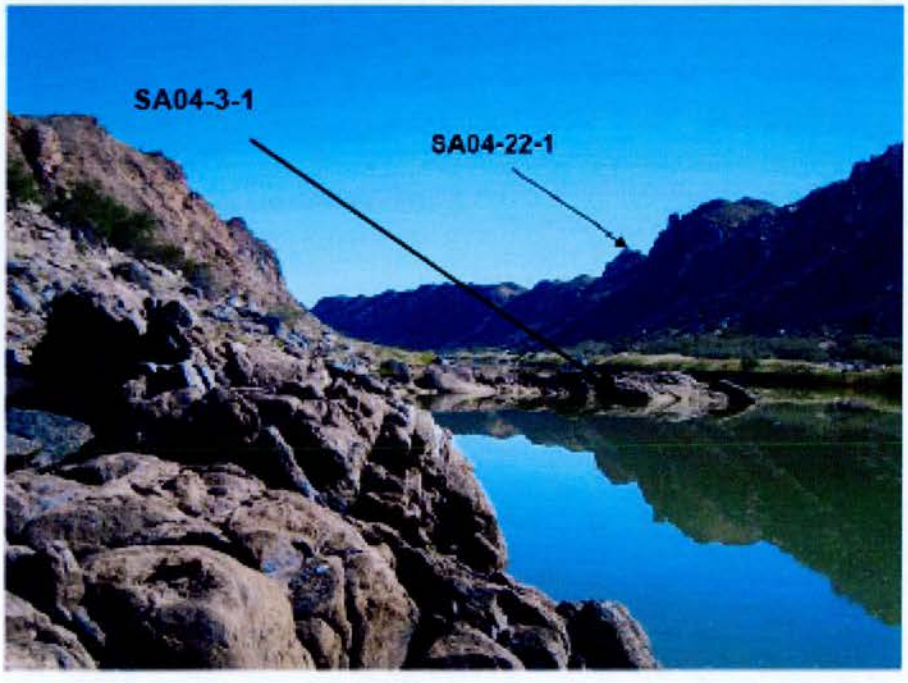

Plate 8.1.2 Sample SA04-22-1 taken from the northern interfluve of the Orange River. Picture also shows location of one of the sampled bedrock bars in the main channel below the main Falls.

Like the samples described above, this should allow quantification of the 'background' downwearing rate of the interfluve and comparison with the samples from the main bedrock channel below the Falls in order to understand how relief has developed in the Augrabies region by comparing denudation rates in the bedrock channels and denudation rates on interfluves. A sample was taken from the interfluve between the southern anabranch that bypasses the main Falls ('Fissure Canyon') and the Orange River channel below the main Falls. This sample consists of grussified granite material that is well-weathered and contains abundant weathered feldspars. Obtaining an incision rate for this interfluve allows benchmark interfluve incision rates to be established. The bedrock interfluve surfaces are too high above the channels to have been flooded at any time – the lowering rates therefore represent minimum denudation rates. Also, this means no shielding by boulders or sediment will have been experienced by the sample (Plate 8.1.3). Comparing interfluve incision rates with channel incision rates has the added advantage of potentially allowing the retreat rates of the sidewalls of the channels to be calculated, without the need for collecting large numbers of shielded samples from the sidewalls. This assumes that incision (i.e. lowering) of the channels rather than backwearing of the sidewalls is the dominant mechanism of landscape development.

Three samples (SA04-18-1, 18-2, 20-1) were taken from interfluves adjacent to the Echo gully tributary channel described previously (Plate 8.1.4). This was in order to determine the relative rate of denudation of these apparently resistant parts of the landscape compared with the catchment-averaged denudation rate for this gully, captured by samples SA03-2-1 and SA04-19. The aim of sampling in this location was also to determine the relative rates of incision on each side of the tributary. Two samples (SA04-18-1, -2) were located on a granite-gneiss interfluve adjacent to upper part of Echo Corner gully where the granite-gneiss is well-weathered and grussified. This was a quartz-rich sample and other, less resistant minerals appear to have weathered out. The interfluve on the east side of the tributary consists of in-situ weathered bedrock that has broken down to form large angular boulders. The largest, topmost, boulder was sampled. Possible burial and movement of the boulder cannot be excluded. The topmost block was sampled, which appears to be undergoing incremental exfoliation weathering.

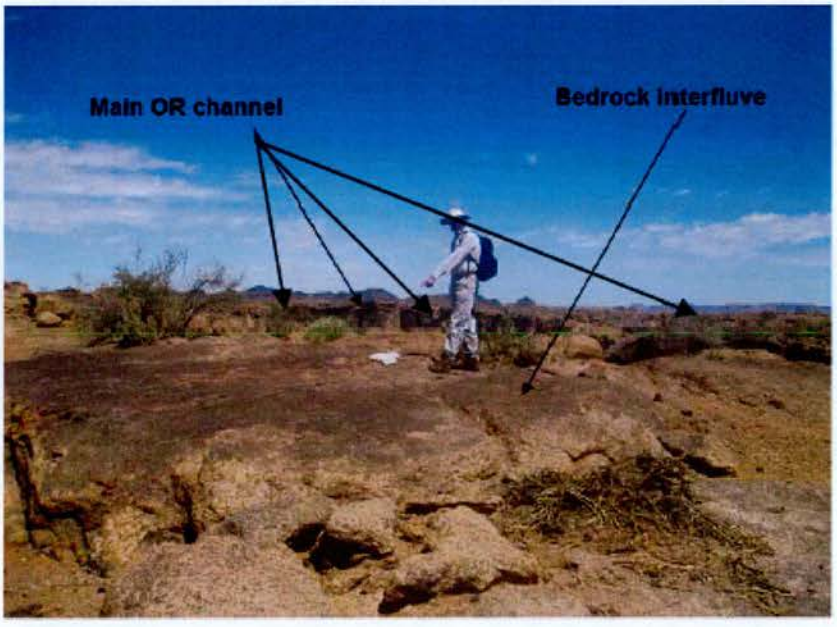

Plate 8.1.3 Location of sample SA04-15-1. Note Orange River channel in background. Picture was taken looking north and anabranch channel sampled as SA05-17-1 is behind photographer.

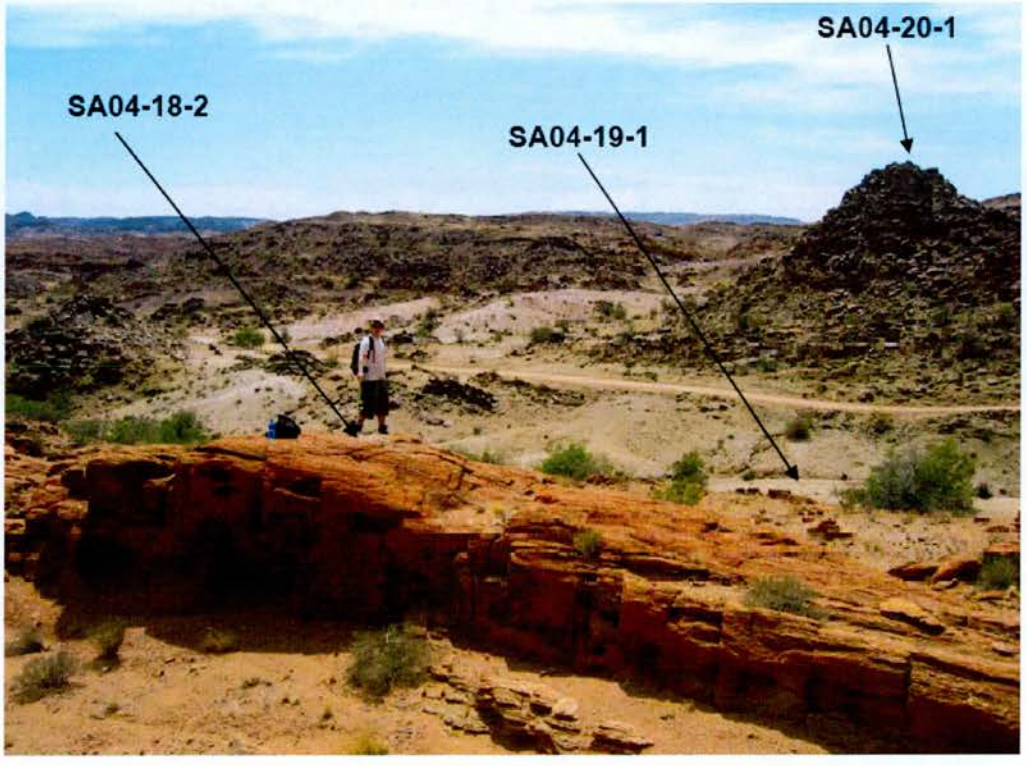

Plate 8.1.4 Interfluves and koppies bordering Echo gully (SA04-18-1, -2, 20-1).

A sample of alluvial/colluvial quartz clasts from a desert pavement in the Augrabies region (close to the Swartrante hills, Plate 8.1.5) was taken (SA05-6-1). The sampling procedure was to measure out a 20x20 m square and to collect 40 quartz clasts from the surface of that area, all in the order of 2-5 cm in diameter. These were then crushed and treated as a catchment-averaged sample of sediment. This technique follows similar ones used by Bierman & Caffee (2001) and Dunai *et al.* (2005). This ought to give the denudation history of a part of the desert pavement surface which, given that it lies on a shallow gradient is ultimately derived from the Swartrante hills.

8.1.2 Moon Rock

A number of massive, rounded inselbergs are found in granite lithologies of southern Africa. These rounded forms have characteristic 'whaleback' morphologies and are more accurately termed bornhardts (Twidale, 1982; Cockburn & Summerfield, 2000). Moon Rock is one such bornhardt (Plate 8.1.6), reaching over 25 m above the surrounding landsurface at its highest point. It is composed of granite-gneiss bedrock that is clearly undergoing incremental weathering by exfoliation of sheets of granite generally <1 cm thick on its summit. Moon Rock raises a number of interesting geomorphological questions as a particular type of topography found on the interfluves of the Augrabies Falls region. Moon Rock is similar to other bornhardts in semi-arid regions that have been studied (e.g. Bierman & Turner, 1994; Cockburn & Summerfield, 2000; Bierman & Caffee, 2001; Bierman & Caffee, 2002). One of the principal questions is how quickly Moon Rock is eroding and where the fastest denudation is occurring, i.e. what is the rate and style of its development over thousands of years. The rate of denudation of Moon Rock was thought likely to be as low as some of lowest rates reported for other parts of hyperarid southern Africa by e.g. Cockburn *et al.* (1999), Bierman & Caffee (2001) – of the order of meters per million years. Another major question is how does Moon Rock's denudation rate compare with other bedrock interfluve locations and also how does it compare with channel bedrock incision rates. Analysis from individual and amalgamated samples from the summit of Moon Rock helps to quantify rates of denudation this local high point in the landscape.

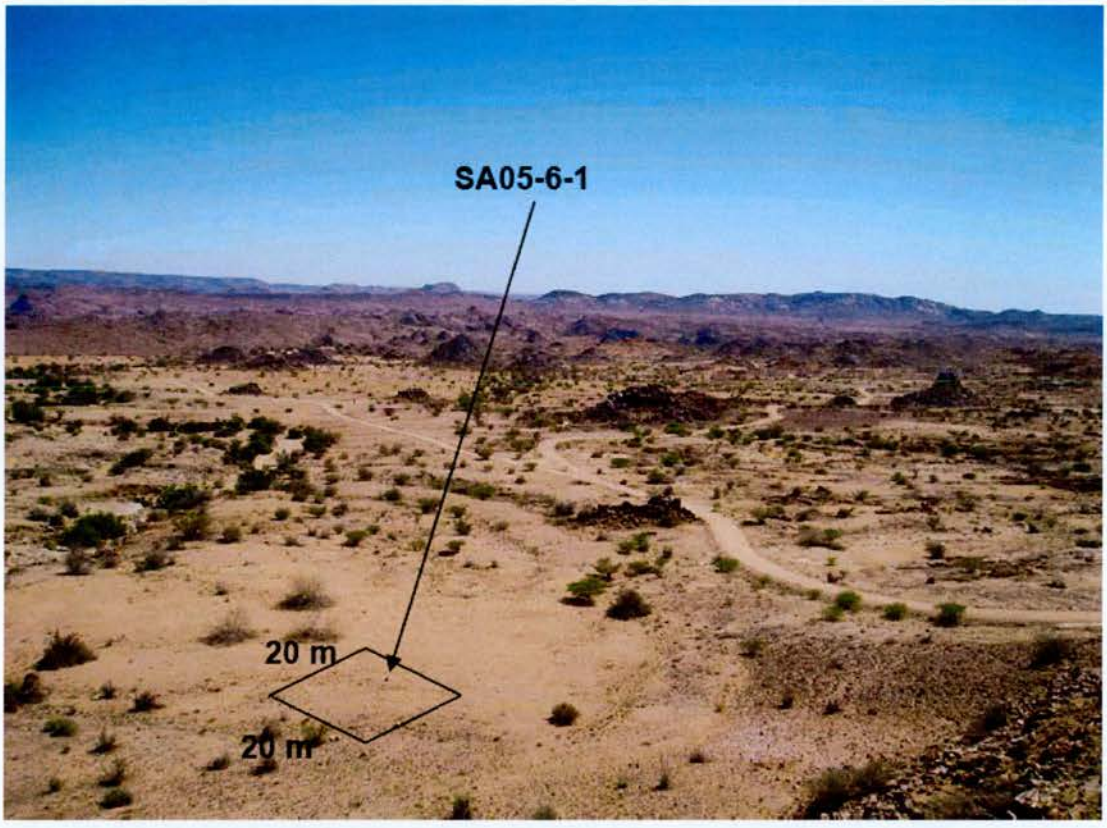

Plate 8.1.5 Location of SA05-6-1 on the desert pavement.

Plate 8.1.6 Moon Rock: a classic granite 'whaleback' bornhardt feature.

Another pertinent question regarding the evolution of Moon Rock is how quickly the slopes are eroding both vertically and laterally and whether the landform is maintaining its overall morphology. These questions are addressed by means of a number of samples taken from different elevations on the sides of Moon Rock (Plate 8.1.7).

Moon Rock is composed of fairly uniform massively jointed granite gneiss. Its primary means of denudation is by incremental exfoliation of massive (>1 m^2), thin (<10 cm) sheets of granite gneiss. In some areas, exfoliation is manifested as spectacular 'popup' features which may be related to pressure release arising from denudational unloading (Plate 8.1.8). Moon Rock is approximately 1.5 km long, 500 m wide, and is 25 m above the surrounding landsurface at its highest point (Figure 8.1.2). It emerges abruptly from the surrounding landsurface and there is almost no regolith surrounding its base. The lack of regolith may be explained by both human and natural mechanisms. Large blocks that fall from the bornhardt may be removed by humans for ornamental stone (although removal from the bornhardt itself is prohibited). Sheetwash from occasional high magnitude flood events may remove smaller clasts that fall from the bornhardt. Moon Rock is orientated roughly east-west along its long axis. Its north-facing side is steepest and the south-facing side shallower (Figure 8.1.3). Three ~ 3 kg samples were taken at the top, middle and bottom of the north and south sides of Moon Rock (Samples SA05-1-1, -2, -3, and SA04-2-1, -2, and -3, respectively). An amalgamated sample containing 30 individual rock chips from all over the summit of Moon Rock was taken (SA05-6-1).

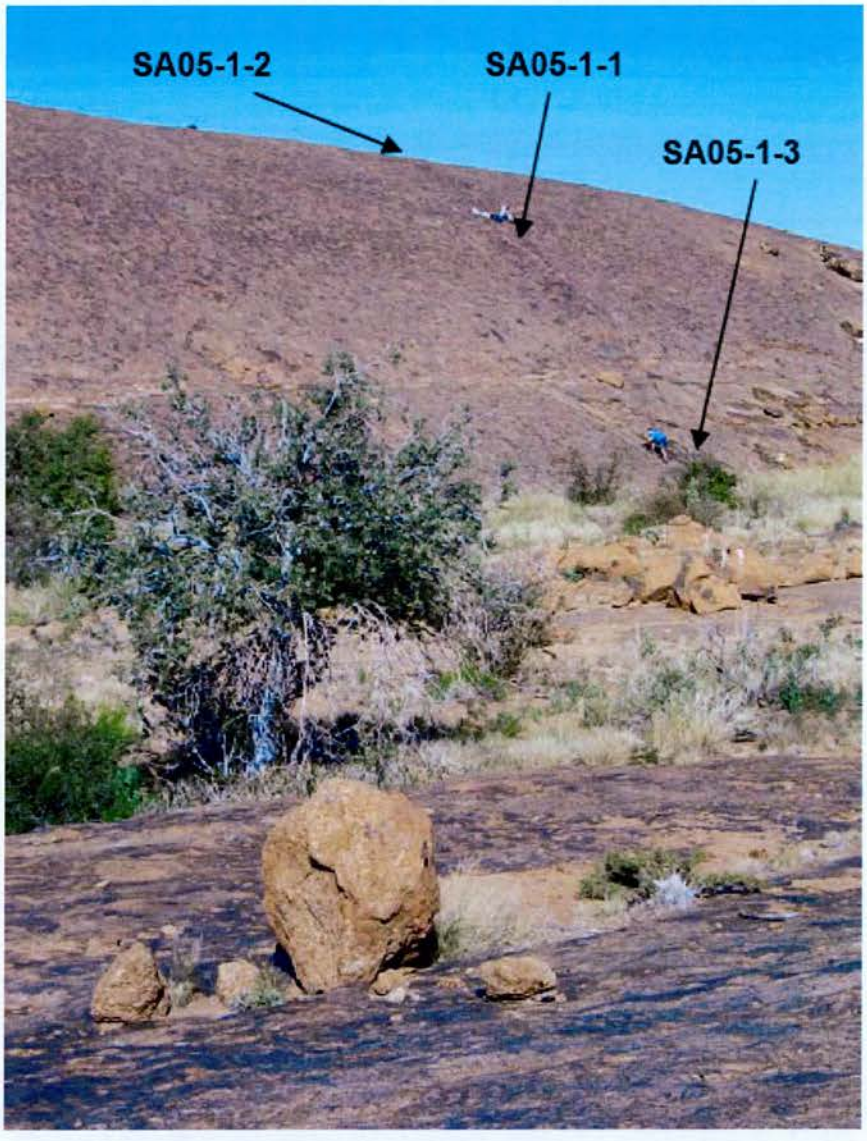

Plate 8.1.7 Sampling on the north side of Moon Rock.

Plate 8.1.8 Popup on Moon Rock. Thickness of the rock here is approximately 10 cm.

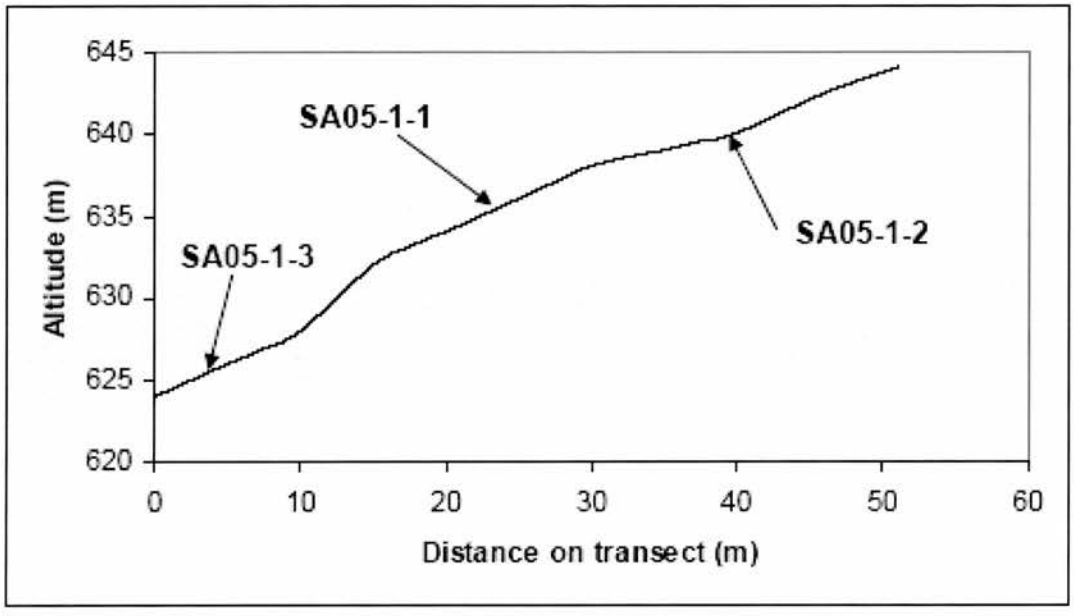

Figure 8.1.2 North profile of Moon Rock showing sample locations.

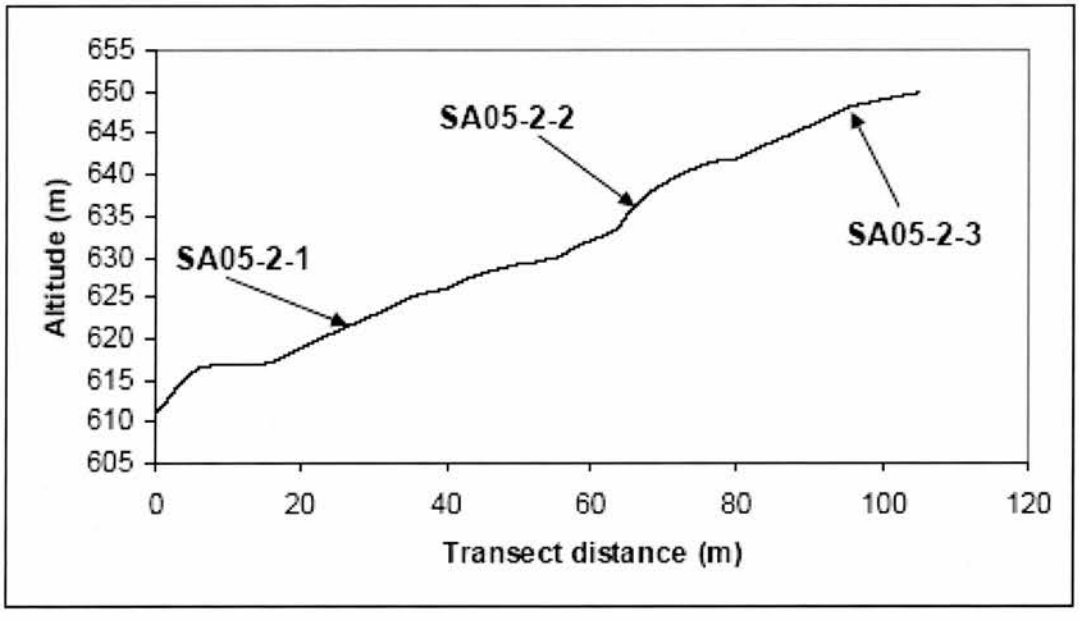

Figure 8.1.3 South profile of Moon Rock showing sample locations.

8.1.3 CIAF samples

Several samples were taken from interfluve areas (Figure 8.1.4) and prepared at the SUERC cosmogenic isotope analysis facility (CIAF) (Table 8.1.2). Sample

SA04-7-1 was taken from a bedrock interfluve adjacent to Moon Rock and gives a denudation rate that can be compared with the summit denudation rate on Moon Rock in order to quantify the rate of development of Moon Rock as a positive bedrock feature. Sample SA04-16-1 is from the interfluve area that lies between two anabranches, Fissure Canyon and Twin Falls, described in the last Chapter. This sample provides a useful 'background' rate of denudation which can be compared with the incision rates in the two anabranch channels. Samples SA04-6-2 and -6-3 come from the summit of Moon Rock and expand the dataset on the rate of summit lowering.

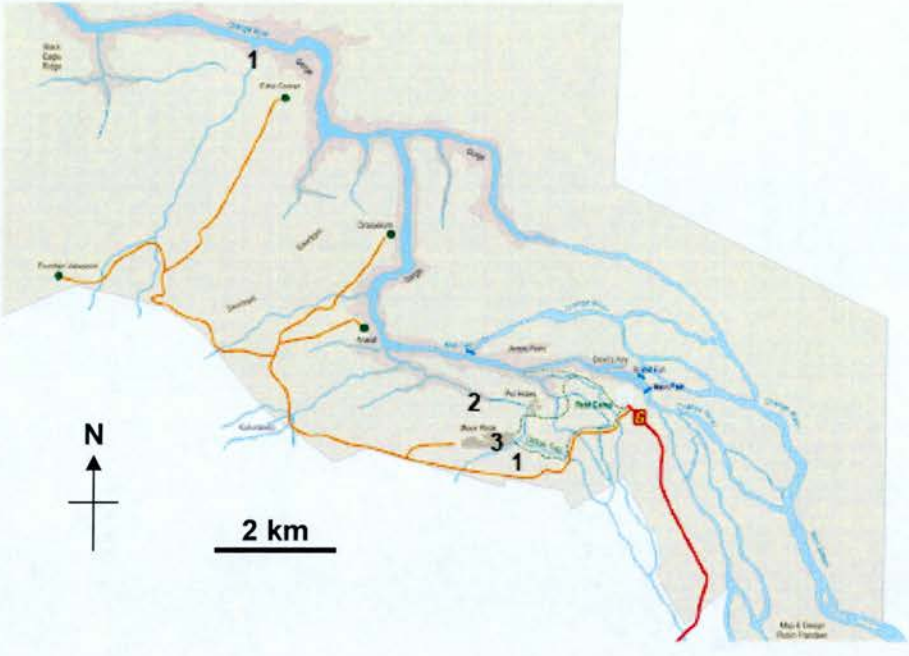

Figure 8.1.4 Sample locations for CIAF samples: (1) Interfluve area adjacent to Moon Rock; (2) Interfluve between 'Fissure Canyon' and Twin Falls anabranches; (3) summit of Moon Rock.

Sample	Environment	Latitude	Longitude	Altitude (m)
SA04-07-01	Interfluve	28°36'S	20°18'E	645
SA04-16-01	Interfluve	28°36'S	20°19'E	679
SA04-06-02	Moon Rock summit	28°36'S	20°19'E	721
SA04-06-03	Moon Rock summit	28°36'S	20°19'E	721

Table 8.1.2 Summary of CIAF samples taken from interfluve locations. Full sample details can be found in Appendix 5.

8.2 Cosmogenic denudation rate data from interfluves: 'background' rates

8.2.1 Bedrock interfluves

In order to quantify 'background' rates of bedrock lowering in the Augrabies Falls region and compare them with rates of incision of bedrock channels in the trunk channel, anabranches, and tributary channels, several bedrock samples were taken from interfluves proximate these channels. It was anticipated that the interfluve samples would have among the lowest rates of denudation of any samples measured in the Augrabies region. Indeed, from Table 8.2.1, it can be seen that there is a low average rate of denudation of 6.40 ± 0.42 mm ka^{-1} and that all samples have denudation rates of around 10 mm ka^{-1} or less (not including sample SA05-6-1, which is discussed separately, below). This puts these bedrock sample denudation rates alongside those extremely low rates measured by Cockburn *et al.* (1999) and Bierman & Caffee (2001) for morphologically- and lithologically-similar bedrock exposures in Namibia.

Sample	Lat.	Long.	Elevation (m)	Lithology	Thickness and shielding correction	Stone factor	^{10}Be (10^5 atom g^{-1})	^{26}Al (10^5 at g^{-1})	^{10}Be denudation rate (mm ka^{-1})	Av. time (ka)	^{26}Al denudation rate (mm ka^{-1})	Av. time (ka)	^{26}Al/^{10}Be
SA04-15-1	28°35'21"S	20°19'44"E	670	Granite gneiss	0.99	1.57	4.55 ± 0.08	26.80 ± 0.63	10.11 ± 0.62	58.99	10.17 ± 0.64	58.65	5.89 ± 0.39
SA-18-1	28°33'48"S	20°16'22"E	624	Granite gneiss	0.97	1.30	5.07 ± 0.10		8.81 ± 0.55	67.71			
SA-18-1	28°33'48"S	20°16'22"E	620	Granite gneiss	0.94	1.29	5.39 ± 0.11		7.89 ± 0.49	75.58			
SA04-20-1	28°34'00"S	20°16'58"E	610	Granite gneiss	0.99	1.29	6.52 ± 0.19		6.79 ± 0.45	87.79			
SA04-21-1	28°35'17"S	20°18'03"E	635	Granite gneiss	0.98	1.12	14.23 ± 0.72		3.16 ± 0.24	188.51			
SA04-21-2	28°35'17"S	20°18'05"E	635	Granite gneiss	0.96	1.31	10.45 ± 0.21		3.61 ± 0.23	165.02			
SA04-22-1	28°32'37''S	20°16'13''E	590	Granite gneiss	0.98	1.17	9.61 ± 0.50		4.44 ± 0.35	134.24			
SA05-6-1	28°34'22''S	20°17'21''E	623	Quartz	1.00	1.29	0.47 ± 0.04	4.49 ± 0.33	84.14 ± 8.90	7.09	52.85 ± 5.05	11.28	9.63 ± 1.10

Table 8.2.1 Cosmogenic nuclide data and denudation rates for interfluves in the Augrabies Falls region. Thickness and shielding corrections are calculated using a rock density of 2.65 g cm^{-3} and a cosmic ray attenuation length of 155 g cm^{-2}. The altitude-latitude scaling factor is calculated according to Stone (2000). Total Al concentration in quartz is determined by ICP-AES at 2% uncertainty. Be data are normalised using the SUERC NIST standard with a nominal ^{10}Be/^{9}Be ratio of 3.00 x10^{-11}. Al data are normalised using Z92-0222 as the primary standard, with a nominal ^{26}Al/^{27}Al ratio of 4.11x10^{-11}. Denudation rates are calculated using sea level, high latitude ^{10}Be and ^{26}Al production rates (Stone 2000). Denudation rates are corrected for geomagnetic variation. See Appendix 4 for full details of data.

Samples SA04-21-1 and -2 were taken from a bedrock high above the main channel on the south side of the Orange River at Ararat (Plate 8.2.1). This location is significant as it is a topographically high interfluve adjacent to two deeply incised channel anabranches. These samples give very similar, low rates of denudation (3.16 ± 0.24 and 3.61 ± 0.23 mm ka^{-1}, respectively). These two samples gave the lowest denudation rates of any interfluve samples. They also lie at one of the highest elevations in the region (635 m) and almost 200 m higher than the level of the present river channel. Therefore, at this location, inundation by the river over the averaging time of ~ 165- 188 ka is extremely unlikely.

Sample SA04-22-1 was taken from one of the highest points on the bedrock interfluve on the north side of the Orange River (Figure 8.1.2). This sample also has an extremely low denudation rate (4.44 ± 0.35 mm ka^{-1}) consistent with its high point on the landscape, suggesting that this is an extremely resistant feature. If this and the previous two interfluve samples are compared with the incision rates in the main channel of the Orange River, one can determine the rate of relief development in this part of the Augrabies region. The average rate of denudation of 7.83 ± 0.64 mm ka^{-1} for the channel is similar to that of the interfluves proximate to the channel (3.74 ± 0.27 mm ka^{-1}), but the important thing is the relative rate difference. The main channel is incising roughly twice as fast as the interfluves. Constant relative rates of incision over tens of thousands of years can be said to have existed in the region below the main Falls, resulting in net positive relief developing between the interfluves and the channel, albeit at an extremely slow rate.

Sample SA04-15-1 lies on an interfluve between an anabranch channel and the main channel of the Orange River (Figure 8.1.3). Obtaining a lowering rate for this interfluve and comparing it with bedrock incision rates in the adjacent channels may allow the retreat rates of the sidewalls of the channels to be estimated indirectly. This assumes that incision of the channels floors has predominated over backwearing of the sidewalls. This possibility is discussed in the following section. This bedrock interfluve surface is too high above the channels to have been inundated with water or sediment. The denudation rate of 10.11 ± 0.62 mm ka^{-1} is of the same order of magnitude as the other interfluves measured in the area.

Plate 8.2.1 View from Ararat bedrock interfluve, location of SA04-21-1 and -2 samples. Note the deeply incised trunk channel (left) and equally deeply incised tributary anabranch (right). It is highly likely that the right hand channel was the main channel at some point in the past.

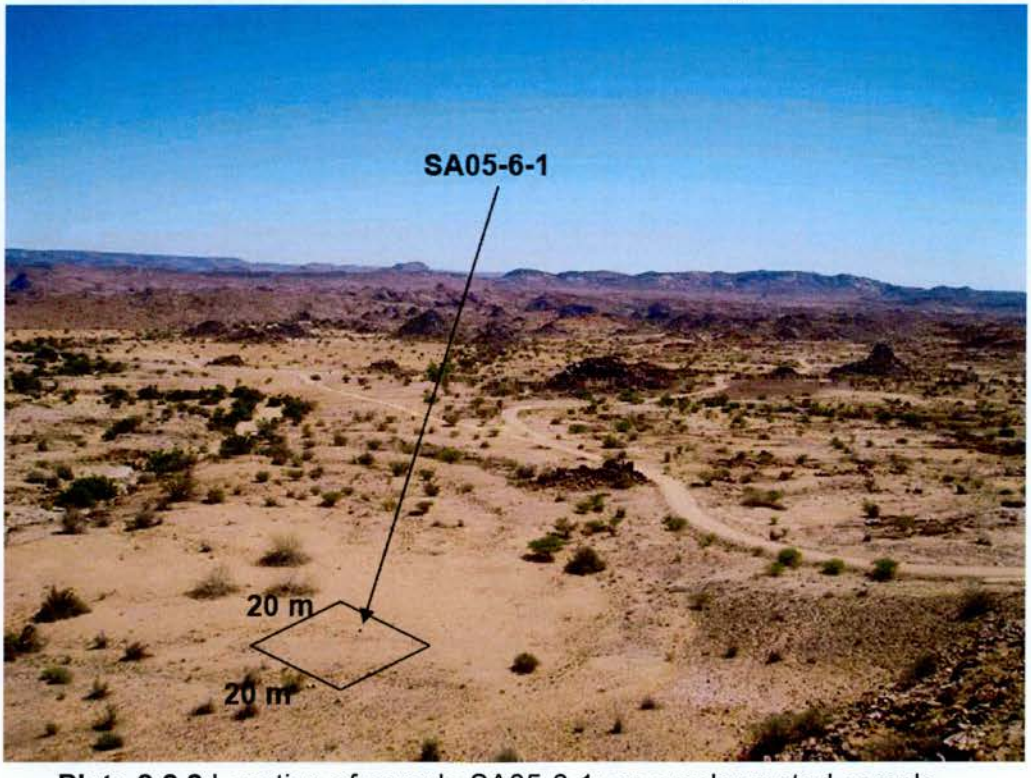

Plate 8.2.2 Location of sample SA05-6-1: an amalgamated sample consisting of quartz clasts from an interfluve.

This is the highest attitude (670 m) interfluve sample measured. Indeed, the $^{26}Al/^{10}Be$ ratio (5.89 ± 0.39) shows, to within standard uncertainty, there has been no significant burial or shielding of the sample (Figure 8.2.1).

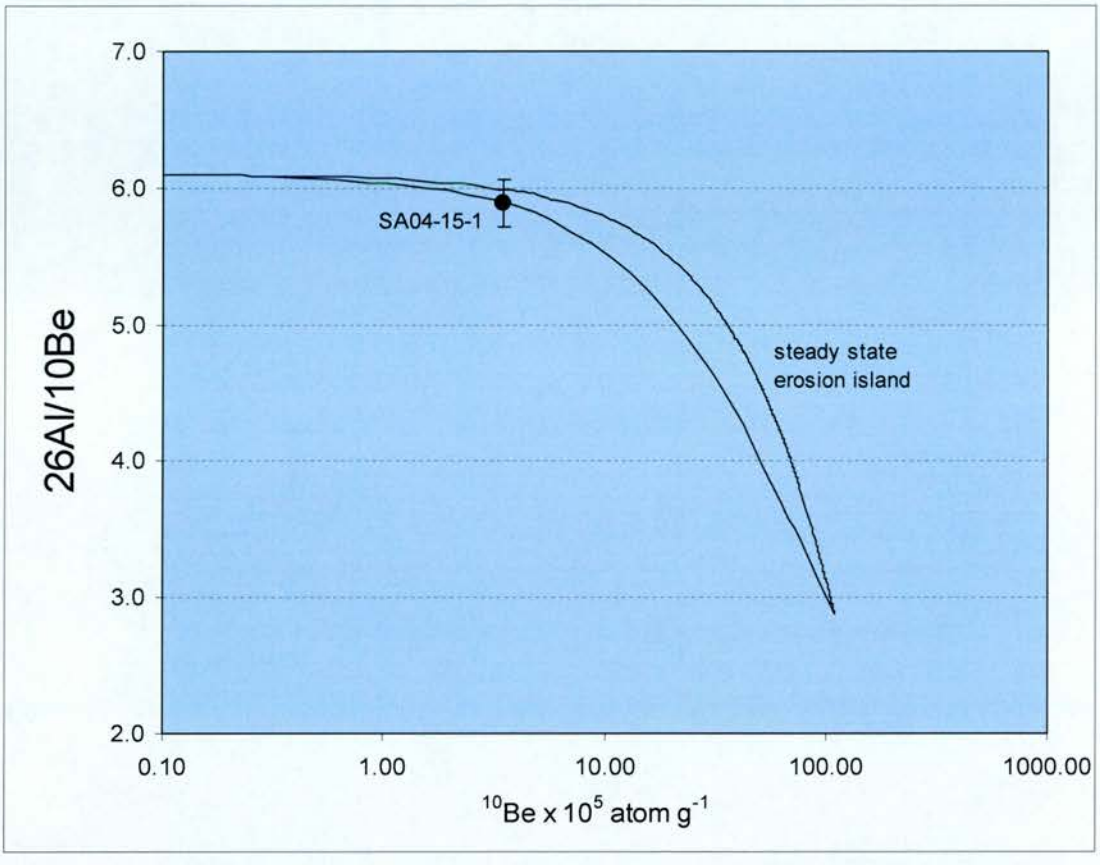

Figure 8.2.1 Steady state denudation island plot for interfluve samples. Note that sample SA04-15-1 plots in the scythe-shaped steady state erosion island and therefore has undergone no significant shielding. Sample SA05-6-1 has a spuriously high ratio of >6.1 to within standard uncertainty and therefore plots in the 'forbidden zone' above the steady state erosion island (not shown on this diagram).

Samples SA04-18-1, -18-2 and 20-1 are from the west and east interfluves, respectively, of the Echo Corner tributary channel. This tributary has a catchment-averaged denudation rate of 13.01 ± 1.38 mm a^{-1}. The average interfluve denudation rate is 7.83 ± 0.31 mm ka^{-1}. Once again, the interfluve lowering rate is approximately half that of the average channel lowering rate. This leads to the conclusion that for the Echo Corner tributary channel, a dynamic equilibrium between rates of incision in the channel and the interfluves has been maintained. Over the averaging time of the samples (~ 77 ka), denudation of both the interfluves and the tributary channel

has been slow and an effective dynamic equilibrium has been maintained between lowering of the interfluves and slightly more rapid lowering of the channel, overall resulting in positive relief being generated over hundreds of thousands to millions of year timescales. Note that for this location, no bedrock exposures were found in the channel, so catchment-averaged denudation rates are used for comparison with the bedrock interfluve samples. The catchment-averaged samples give denudation rates averaged over a large area and therefore can be seen as minima. Denudation of the tributary channel (particularly in the steeper downstream section) may have been more rapid than this average rate. The same basic relative rate difference has been maintained between incision of interfluves and incision of both anabranch and tributary channels.

Sample SA05-6-1 was an amalgamated sample of 20 quartz desert pavement clasts collected from the interfluve area just north of the Swartrante hills (Plate 8.2.2). As can be seen from Table 8.2.1 the sample gives a suspiciously high denudation rate of 84.14 ± 8.90 mm ka^{-1}, which is considerably higher than some of the rates calculated from actively incising bedrock channels in the Augrabies region. Since this sample incorporates clasts from over a potentially wide area, it could be that a disproportionate number of clasts capture extremely high denudation rate signals which are reflected in the high overall denudation rate. Alternatively, burial of the clasts could have occurred over their history, resulting in an over-estimated apparent denudation rate. This sample is from a fairly high elevation, 623 m, and too high to be affected by flow from the Orange River. There is, however, a small ephemeral stream close to where this sample was taken, although the clasts were taken from upstream of the channel. Possibly the clasts in this sample have been buried by alluvial/colluvial material over their history, resulting in a low average ^{10}Be concentration (0.47 ± 0.04 at g^{-1}). The lack of any geomorphic evidence for high denudation rates, and this sample's inconsistency with other interfluve denudation rates, means that this sample is excluded from the discussion in Chapter 9.

8.3 Moon Rock

8.3.1 Moon Rock – a classic bornhardt

Inselbergs are isolated rocky outcrops that are well documented in granite landforms around the world (Twidale, 1982). Inselbergs are often fracture-controlled, steep sided granite domes that rise out of a flat surrounding landscape. Many types of inselbergs have been identified, including bornhardts (Boornhardt, 1900; Willis, 1934; 'whalebacks in Wellington's (1955) terminology) which are bald, unvegetated, steep sided domes; and koppies which are angular, blocky, landforms common in the flat lying lithology of the Karoo (King, 1967). An introduction to Moon Rock, a classic bornhardt, is given in Section 8.1. The cosmogenic results from Moon Rock are presented in Table 8.3.1

Sample	Lat.	Long.	Elev. (m)	Lith.	Sh. correct.	Stone scaling factor	^{10}Be (10^5 at g^{-1})	^{26}Al (10^5 at g^{-1})	^{10}Be denudation rate (mm ka^{-1})	^{10}Be av. time (ka)	^{26}Al denudation rate (mm ka^{-1})	^{26}Al av. time (ka)	^{26}Al/^{10}Be
SA05-1-1	28°3 5'50" S	20°18' 59"E	631	Granite-gneiss	0.95	1.30	4.31 ± 0.12	27.02 ± 0.93	10.04 ± 0.88	59.35	9.65 ± 0.66	61.78	6.27 ± 0.46
SA05-1-2	28°3 5'50" S	20°18' 59"E	635	Granite-gneiss	0.96	1.31	8.63 ± 0.30	48.75 ± 2.10	5.14 ± 0.46	116.03	5.29 ± 0.39	112.66	5.65 ± 0.46
SA05-1-3	28°3 5'49" S	20°18' 59"E	625	Granite-gneiss	0.93	1.30	3.39 ± 0.16	24.81 ± 1.59	12.48 ± 1.18	47.78	9.98 ± 0.87	59.75	7.31 ± 0.57
SA05-2-1	28°3 5'55" S	20°19' 06"E	624	Granite-gneiss	0.96	1.30	5.06 ± 0.18	32.07 ± 1.33	8.67 ± 0.75	68.77	8.02 ± 0.58	74.37	6.34 ± 0.48
SA05-2-2	28°3 5'54" S	20°19' 06"E	636	Granite-gneiss	0.95	1.31	11.46 ± 0.49	67.43 ± 1.27	3.63 ± 0.34	164.05	3.46 ± 0.21	172.20	5.89 ± 0.44
SA05-2-3	28°3 5'53" S	20°19' 06"E	646	Granite-gneiss	0.93	1.32	12.07 ± 0.32		3.43 ± 0.30	173.98			
SA04-6-1	28°3 5'53" S	20°19' 06"E	664	Granite gneiss	0.99	1.33	12.07 ± 0.24	60.81 ± 1.15	3.69 ± 0.23	161.49	4.15 ± 0.26	143.56	5.04 ± 0.33

Table 8.3.1 Cosmogenic nuclide data and denudation rates for the Moon Rock bornhardt. Thickness and shielding corrections are calculated using a rock density of 2.65 g cm^{-3} and a cosmic ray attenuation length of 155 g cm^{-2}. The altitude-latitude scaling factor is calculated according to Stone (2000). Total Al concentration in quartz is determined by ICP-AES at 2% uncertainty. Be data are normalised using the SUERC NIST standard with a nominal ^{10}Be/^{9}Be ratio of 3.00 x10^{-11}. Al data are normalised using Z92-0222 as the primary standard, with a nominal ^{26}Al/^{27}Al ratio of 4.11x10^{-11}. Denudation rates are calculated using sea level, high latitude ^{10}Be and ^{26}Al production rates (Stone 2000). Denudation rates are corrected for geomagnetic variation. See Appendix 4 for full details of data.

8.3.2 Transect and summit data

On both transects, there is a trend of decreasing denudation rates as one moves up the transect (Figure 8.3.1). The denudation rates are quoted as rates corrected for the slope of the sampled surface (i.e. to give the resultant of vertical and lateral denudation), although there is little difference in this and vertical denudation. Some of the lowest rates of time-integrated denudation are at the summit of Moon Rock (Figure 8.3.1). There is consistency in the estimates of denudation from the summit of Moon Rock, particularly when the amalgamated sample is compared with the point sample, suggesting that the summit is undergoing fairly uniform rates of denudation. This is also evident in the field by the relatively flat summit surface and evidence for incremental denudation in the form of small pits and sheets of granite spalling consistently off across the surface. This surface has been slowly but constantly eroding. The sides of Moon Rock appear to be eroding roughly twice as fast as the summit, meaning that the bornhardt will become narrower over time.

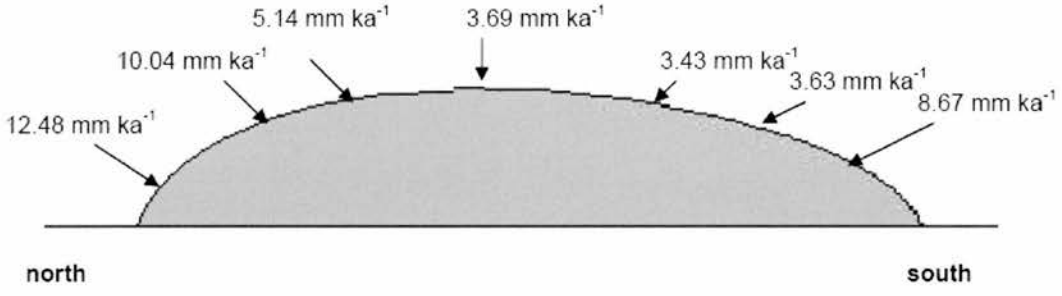

Figure 8.3.1 Schematic diagram showing denudation rates of Moon Rock. These denudation rates have been corrected for the slope of the sampled surface. These rates suggest that the bornhardt will become narrower over time and maintain its relative height as the summit is denuding at roughly the same rate as the surrounding land surface (see section 8.3.4).

The highest rates of vertical denudation are apparent at the bases of the two transects (samples SA05-1-3 and SA05-2-1, with denudation rates of 12.48 ± 1.18 and 8.67 ± 0.75 mm ka^{-1} from ^{10}Be data and 9.98 ± 0.87 and 8.02 ± 0.58 mm ka^{-1} from ^{26}Al data, respectively). The ^{10}Be and ^{26}Al data are in good agreement, to within standard uncertainties. The high denudation rates at the base of the slopes suggests that the greatest amount of denudation is going on at the foot of the scarp, leading to steepening and recession of the surrounding bornhardt slope (Tricart, 1957). The

higher denudation on steeper slopes could be due to greater runoff and precipitation leading to dissolution and loss of material as solutes given sufficient time. Like in a karst landscape, precipitation and runoff from the summit collects in hollows at the base of slopes where solutional weathering may go on. Although granite is only slightly soluble in water, given sufficient time, solutional weathering can occur, as described for the Kimberleys in north western Australia (Young, 1988). Karstic forms can eventually develop in quartzite rocks, e.g. the sandstone karst of the Bungle Bungle range in western Australia (Young, 1986; 1987) and the dendritic forms observed by Cockburn *et al.* (1999) on Namibian bornhardts. Denudation is highest at the foot of the steep northern side of Moon Rock where, perhaps due to greater runoff from the steep slope, more solutional weathering is occurring. This is contributing to the overall steepened profile and the recession of the north side of Moon Rock. The foot of the shallower south side, in comparison, has a denudation rate of 8.67 ± 0.75 mm ka^{-1}. This slower rate of denudation explains the relatively shallow slope on this side. Overall, the bases of the slopes are eroding the most rapidly of all the sections which were sampled – this could be due to a positive feedback between steep slopes, and increased runoff and solutional weathering. As expected, the samples taken at the mid-point of the transects have denudation rates in-between those of the summit surface and the base of the bornhardt. After correction for slope angle (to give lateral rates of retreat), the sides are retreating faster than the summit, indicating that the bornhardt will become narrower over time. Since the mean summit lowering rate is similar to that of the surrounding landsurface (see section 8.3.4) the relative height of the bornhardt will be maintained, causing the landform to undergo 'parallel retreat' on its sides.

The sidewall samples from Moon Rock, with $^{26}Al/^{10}Be$ ratios of 6.1 ± 0.5 to within standard uncertainty (Figure 8.3.2), show no evidence of burial or shielding apart from SA05-1-3, with a spuriously high $^{26}Al/^{10}Be$ ratio, which is not considered here. The northern and southern sides of Moon Rock appear to be too steep to sustain sheets of eroded bedrock and so have not experienced significant shielding by bedrock (Plate 8.3.1). This justifies the assumption made in the field that if large blocks were to detach from the sides of Moon Rock, the sides are steep enough to

ensure rapid falling of the blocks down the slope and insignificant shielding of the sampled locations during that time. The only sample that shows a $^{26}Al/^{10}Be$ ratio of less than 6.1 is SA04-6-1, the amalgamated sample from the summit of Moon Rock. Clearly some shielding has gone on here. Given the high elevation at this point, shielding by sediment or water can be discounted and shielding must have been effected by at least 60 cm of bedrock for around 38 ka (as shown by the lower erosion island on Figure 8.3.2). Before this, the sample would have eroded at between 1 and 5 mm ka^{-1}, which is in keeping with the denudation rate of the other Moon Rock samples. Since SA04-6-1 an amalgamated sample containing rock chips from all over the summit, shielding of individual rock chips could have been greater or less than that described above. Clearly some significant shielding of a large proportion of the rock sampled has gone on to show up in the $^{26}Al/^{10}Be$ plots. In the absence of other mechanisms for rock removal on this flat part of the bornhardt with clear evidence of incremental erosion, it can only be assumed that rock has been removed by humans for ornamental stone at some point in the past (a point confirmed by the Augrabies Park Manager, Steven Smith (pers. comm., 2005)).

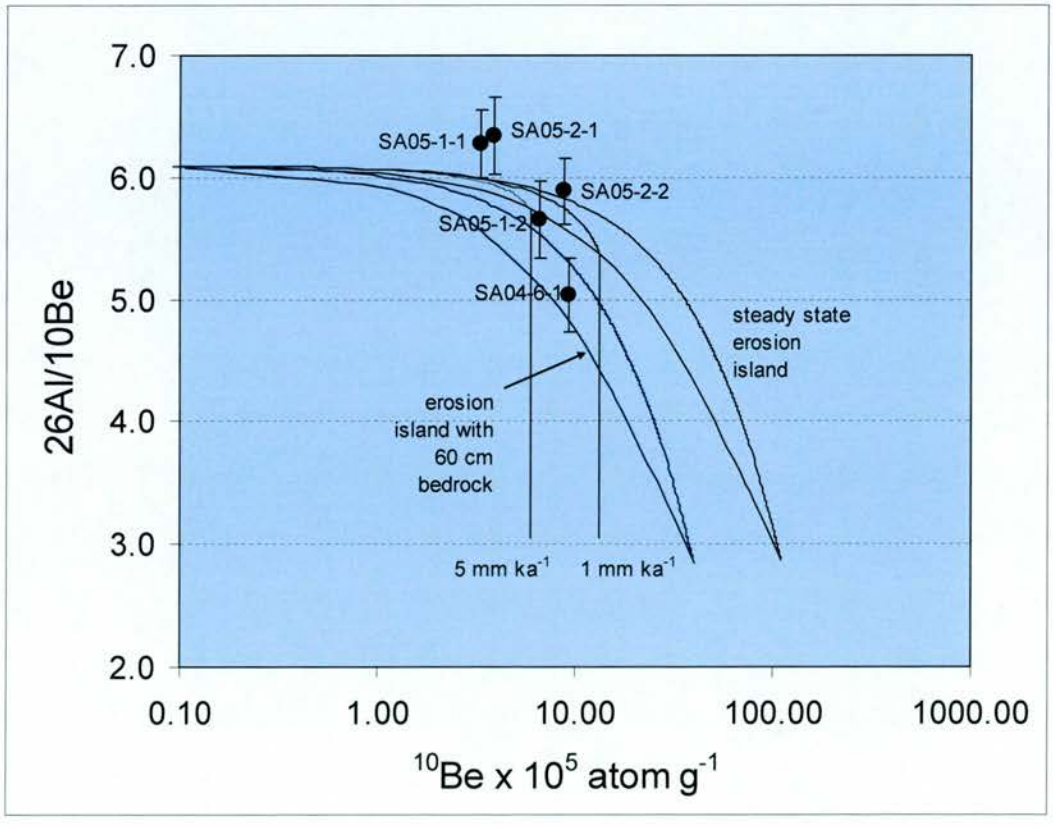

Figure 8.3.2 (previous page) Steady state denudation island plot for Moon Rock samples. Note samples SA05-1-1, -1-2, 2-1 and 2-2 plot on the steady state erosion island to within standard uncertainty. Sample SA05-1-3 does not, due to a spuriously high $^{26}Al/^{10}Be$ ratio of 7.31 ± 0.57. Even this sample, however, would plot on the steady state erosion island at 2 sigma standard uncertainty. Sample SA04-6-1 does not plot on the steady state erosion island, suggesting it has had a complex history. The graph above shows that it could have been shielded by ~ 60 cm of bedrock and previously may have eroded at between 1 and 5 mm ka^{-1}.

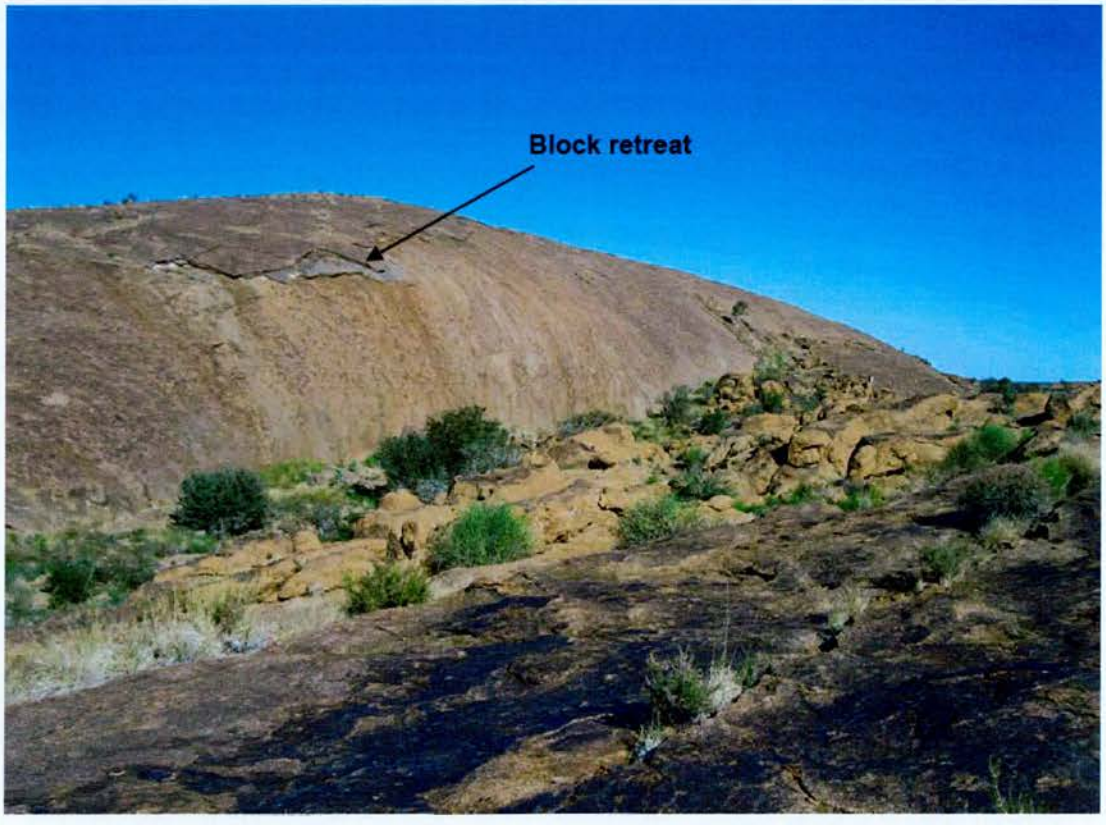

Plate 8.3.1 Exfoliation and block retreat on the north side of Moon Rock. Note that the slope is sufficiently steep that detached blocks will immediately move down slope, and not cause shielding to the underlying rock.

8.3.3 Discussion of the evolution of Moon Rock

There has been much debate on the origin of bornhardts (e.g. King, 1949; Twidale, 1982), ranging from their formation as marine features (Boornhardt, 1900), glacial rouche moutonées (Agassiz, 1965, cited in Twidale, 1982), sculpted aeolian features, the result of differential fluvial denudation and the end-form of a series of wetting and drying events. It appears that, like quartzite bornhardts in Namibia and Australia, Moon Rock is evolving by solutional weathering, which is primarily concentrated on its slopes and is responsible for the landform undergoing parallel retreat. King (1949) argues that bornhardts are strongly structurally controlled by joints and are features in a long-term cycle of landscape development. Whilst Moon Rock does indeed appear to be undergoing parallel retreat (one of King's 1953 canons of landscape evolution) it is not experiencing it in the sense that King meant it (in the context of the formation of characteristic erosion surfaces). Moon Rock appears not to be structurally controlled (apart from being orientated north-south, in common with the master joint orientation) and is not large enough or denuding rapidly enough to be emerging from the subsurface (a mechanism suggested by Tricart, 1957). Nor does Moon Rock appear to be denuding rapidly enough for pressure release joints to be opening up as they are elsewhere in the Augrabies region. Rather, the denudation rate data suggests that parallel retreat of slopes is occurring driven by solution weathering coming from runoff from the summit and high magnitude seasonal rainfall in the region (~ 220 mm a^{-1}) which might remain at the base of the bornhardt for some time. The highest denudation rates are at the bases of the slopes, where most runoff accumulates.

Cockburn *et al.* (1999) attribute the moderate rates of denudation of Namibian coastal plain bornhardts to salt weathering resulting from fog precipitation. Since fog precipitation generally penetrates only ~ 60 km inland, it is extremely rare in the Augrabies region (van der Walt, 2000) and cannot be invoked to explain the moderate rates of denudation on Moon Rock. Salt weathering could still be an important mechanism driving denudation where high rates of evaporation leave salt crystals at the surface, although no salt precipitates were seen at the time of sampling (Plate 8.3.2), in common with Cockburn *et al.* (1999). Effective salt weathering is

driven by hydration at the surface. High magnitude seasonal rainfall events are perhaps sufficient to cause hydration and dehydration of the salts which may promote accelerated salt weathering (Goudie & Viles, 1997). The rainfall experienced at Moon Rock normally occurs as high intensity, short rainfall event in the summer months (van der Walt, 2000). This rainfall is likely to immediately run off the surface of the bornhardt due to the lack of soil or regolith and into the hollows at the base of the bornhardt. After it eventually evaporates, it may leave salts at the surface which cause salt weathering and further denudation on the sides of the landform.

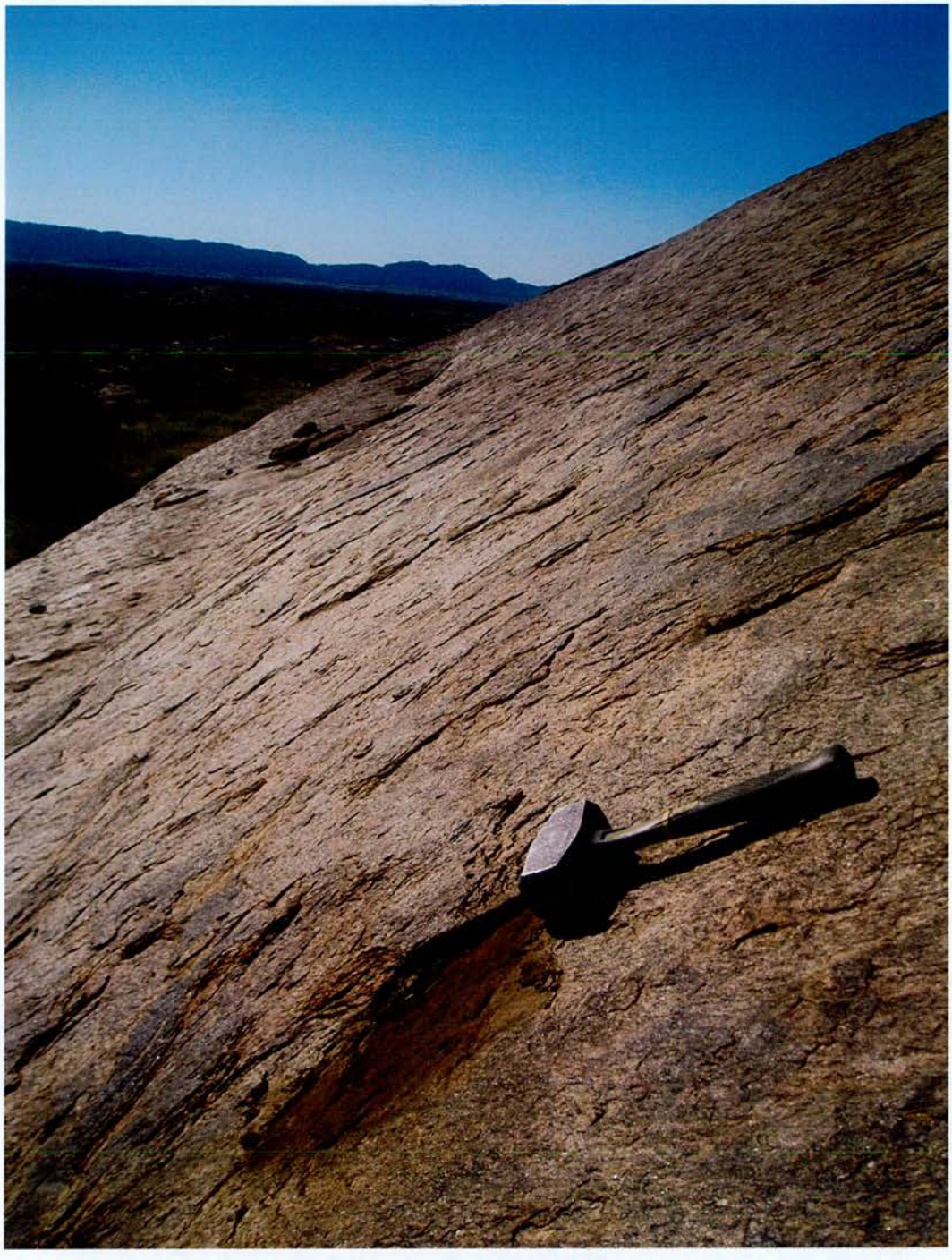

Plate 8.3.2 North side of Moon Rock displaying exfoliation weathering as well as micro-solutional features manifested as a pitted surface.

Assuming denudation rates have been constant, and taking the average interfluve denudation rate of 7.97 mm ka^{-1} as the denudation rate of the surrounding landsurface and the average rate of denudation of the summit of Moon Rock as 3.69 ± 0.23 mm ka^{-1}, and the height of Moon Rock as 25 m above the surrounding landsurface at its highest point, it would have taken around 6 Ma for Moon Rock to reach its present height above the landsurface. Lateral retreat (which is much faster than denudation on the summit) is likely to have considerably altered the morphology of Moon Rock over this time, in particular by maintaining steep sides on the bornhardt.

Several studies have used cosmogenic nuclide analysis to understand the evolution of bornhardts in arid regions. Cockburn *et al.* (1999) studied the bornhardts on the coastal plain of Namibia. ^{10}Be analysis showed these to be eroding at a mean rate of 5.1 ± 1.1 mm ka^{-1}, almost identical to the average rate of erosion of Moon Rock (5.66 ± 1.21 mm ka^{-1}). Bierman & Caffee (2001) also describe bedrock inselbergs in Namibia as having average rates of erosion of 3.5 ± 1.8 mm ka^{-1}, with a range of rates between 1.1 and 7.5 mm ka^{-1} – once again very similar to the rates measured for Moon Rock. Bierman & Caffee describe a lack of complex exposure histories in their bornhardts, something that is generally observed for Moon Rock. Cockburn *et al.* observe the $^{26}Al/^{10}Be$ ratio of their samples to be below the steady state erosion island, implying complex exposure histories which they ascribe to burial by the Namib Sand Sea at some point in the past.

Studies of bornhardt evolution in other arid regions of the world, such as the Eyre Peninsula of south Australia (Bierman & Turner, 1994; Bierman & Caffee, 2002) reveal the denudation rates to be an order of magnitude lower than those recorded in southern Africa. Bierman & Caffee (2002) present ^{10}Be-derived rates between 0.3 ± 0.1 and 5.7 ± 1.0 mm ka^{-1} on the summits and flanks of bornhardts and Bierman & Turner (1995) present average rates of ~ 0.7 mm ka^{-1} for the summits of bornhardts in the Eyre Peninsula. These authors describe the bornhardts as developing in dynamic equilibrium where the same overall morphology of the bornhardt is maintained but subtle differences in rates on the flanks and summit of the boornhardt

result in the landform becoming narrower. These low, but still finite, denudation rates cause positive relief features to develop over very long timescales. Bierman & Caffee (2001) note the agreement between bornhardt denudation rates and long term fission track derived denudation estimates and emphasise that although the bornhardts may date from at least the Tertiary, sufficient denudation has gone on since then for the bornhardts not to have been preserved unmodified in the landscape (as King's denudation chronology approach would have them). Since Moon Rock is eroding at around an order of magnitude faster than the Australian bornhardts it is even more unlikely that Moon Rock has been preserved in the landscape unmodified over long timescales. Indeed, some of the denudation rates on the flanks on the bornhardt apparently exceed some of the incision rates in the main channel of the Orange River. How real these apparent differences are is a matter of debate, however. For if these rates were to endure over millions of years, they would clearly result in a landscape that is the 'inverse' landscape of the one we see today. The reason for the apparently high rates of denudation on the flanks of Moon Rock may be that blocks are being shed from the steep sides, and the sampled rock consequently has a relatively low cosmogenic nuclide concentration (and artificially high denudation rate). It is important to consider that the timescales over which the relatively rapid rates endure on Moon Rock will be shorter than the timescale over which denudation in the main channel occurs – otherwise Moon Rock would be deeply incised and the main channel would be an interfluve area. While the denudation rates measured on Moon Rock may be in some cases higher than those in the main channel they are likely only to have lasted for thousands, rather than tens or hundreds of thousands of years. This invokes Schumm & Lichty's (1965) idea of episodic erosion, where high magnitude denudation only endures for a relatively short time. Denudation in the main channel may be lower in magnitude, but, since it endures for longer, is ultimately responsible for more geomorphic work. The cosmogenic nuclide technique integrates denudation over time and will 'smooth out' the record of episodic erosion over a long period to give an apparently low erosion rate. It could be said that Moon Rock has undergone episodic erosion relatively recently, reflected in the high denudation signal in the samples. The main channel on the other hand, may have only undergone low magnitude, high frequency erosion

events, thus the time-integrated denudation rate is low. Even high magnitude episodes of erosion (such as those driven by large floods) may become smoothed out over the long history of the river channel to give an apparently low denudation rate.

8.3.4. CIAF samples

The CIAF interfluve samples are presented in Table 8.3.2. They show a striking similarity to the rates presented above. The interfluve sample adjacent to Moon Rock (SA04-7-1) has a denudation rate of 3.25 ± 0.21 mm ka^{-1} compared with the denudation rates of 2.85 ± 0.18 and 3.19 ± 0.21 mm ka^{-1} for the summit of Moon Rock. Although these rates are very similar, the small relative rate differences will generate positive topography over long timescales. When the mean summit lowering rate from all samples (CIAF and PhD samples) from the summit of Moon Rock (3.24 mm ka^{-1}) is compared with the 'background' mean interfluve lowering rate for all samples (4.50 mm ka^{-1}), it can be seen that although the relative rate differences are small (net denudation rate 1.26 mm ka^{-1}), over long timescales (~ 16 Ma) a landform of this size (~20 m high) can be generated. As shown above, denudation is more rapid on the sides of Moon Rock, causing it to undergo 'parallel retreat' as its sides become narrower while its summit lowers much more slowly. The summit of Moon Rock is eroding at a rate similar to the incision rate of the main channel below the Falls. Both have relatively low time-integrated erosion rates suggesting that they are not undergoing episodic erosion, unlike the sides of Moon Rock, which are apparently undergoing an episode of erosion on a much shorter timescale.

Sample	Latitude	Altitude (m)	Shielding scaling factor	Stone's SEL scaling (spallation and muons)	Production rate spallation and muons (at $g^{-1} a^{-1}$) (Stone)	$^{10}Be/^{9}Be$	σ ($^{10}Be/^{9}Be$)	ε (mm ka^{-1}) spallation & muons (Stone)	± Standard Uncertainty	Averaging time (ka)
SA04-07-01	28°36'S	645	0.99	1.61	8.13	1.33E+06	3.52E+04	3.25	0.21	183.40
SA04-16-01	28°36'S	679	0.98	1.58	7.90	1.84E+06	4.94E+04	2.29	0.15	260.00
SA04-06-02	28°36'S	721	0.96	1.66	8.21	1.57E+06	4.19E+04	2.85	0.18	209.48
SA04-06-03	28°36'S	721	0.99	1.76	8.89	1.49E+06	3.95E+04	3.19	0.21	186.61

Table 8.3.2 Cosmogenic nuclide data and denudation rates for interfluve locations in the Augrabies region. Samples were processed at the NERC Cosmogenic Isotope Analysis Facility (CIAF), SUERC. Thickness and shielding corrections are calculated using a rock density of 2.65 g cm^{-3} and a cosmic ray attenuation length of 155 g cm^{-2}. The altitude-latitude scaling factor is calculated according to Stone (2000) and includes spallogenic and muogenic production. Be data are normalised using NIST SRM 4325 as primary standard with a nominal $^{10}Be/^{9}Be$ ratio of $3.06x10^{-11}$. Note that this means the ^{10}Be concentrations are some 2% lower than those measured using the SUERC NIST standard with a nominal $^{10}Be/^{9}Be$ ratio of $3.00x10^{-11}$. Al data are normalised using Z92-0222 as the primary standard, with a nominal $^{26}Al/^{27}Al$ ratio of $4.11x10^{-11}$. Denudation rates are corrected for geomagnetic variation. See Appendix 5 for full details of data. ± uncertainties are standard uncertainties.

The interfluve that lies between two anabranch channels, Fissure Canyon and Twin Falls (SA04-16-1) has a denudation rate of 2.29 ± 0.15 mm ka^{-1}, around 5 times lower but still similar to the rate on an adjacent interfluve, that separating Fissure Canyon and the main channel of the river (SA04-15-1), of 10.11 ± 0.62 mm ka^{-1}. Due to their position high above the main channel and anabranch channels, these locations are unlikely to have undergone fluvial driven incision. Lowering rates of the interfluves are, as expected, the lowest of any location sampled in the Augrabies region. Further discussion of interfluve lowering in the context of anabranch channel development is given in Chapter 9. The CIAF samples from Moon Rock compare well with the sample from the summit of Moon Rock presented above. Sample SA04-6-1 (presented above), which was an amalgamated sample of 20 rock chips from across the summit of Moon Rock, had a denudation rate of 3.69 ± 0.23 mm ka^{-1}. Samples SA04-6-2 and -6-3 were site-specific samples from the summit. They have rates of 2.85 ± 0.18 and 3.19 ± 0.21 mm ka^{-1}, respectively – similar rates that give an overall mean summit lowering rate of 3.24 mm ka^{-1}. The fact that these rates are similar but not identical – all overlap to within two sigma standard uncertainty – indicates that with site-specific samples there is natural variability in denudation rates which is a function of their particular history and position in the landscape. That the rates are low, and also quite similar, in the Augrabies landscape emphasises how small differences in denudation rates can, over long timescales, be responsible for spectacular features such as the 100 m deep gorges and hanging anabranch channels. This study shows that it is not the absolute rates (since the interfluves, Moon Rock summit and main channel below the Falls all have rates of <10 mm ka^{-1}), so much as the relative rate differences that are responsible for generating the Augrabies landscape over long timescales. The role of contingency in the extremely complex landscape of the Augrabies region is thus emphasised.

Chapter 9 – Discussion of the evolution of the Augrabies region

9.1 Discussion – evolution of the river long profile

9.1.1 Above and below the Falls

This section deals with the small- and medium- scale processes that can now be quantified using the denudation rate data presented in the preceding Chapters. The next section deals with the large-scale landscape evolution that can be inferred from cosmogenic-derived denudation rates and the implications in the context of existing long-term denudation rates and models of large scale landscape evolution. Detailed hypsometric plots of the Orange River in the Augrabies Falls region (Figures 9.1.1) aid the interpretation of denudation rates above and below the main Falls and channel anabranch Falls (Summerfield *et al.*, unpublished data). These plots allow the mapping of detailed channel gradients for upstream and downstream of the main Falls (Table 9.1.1).

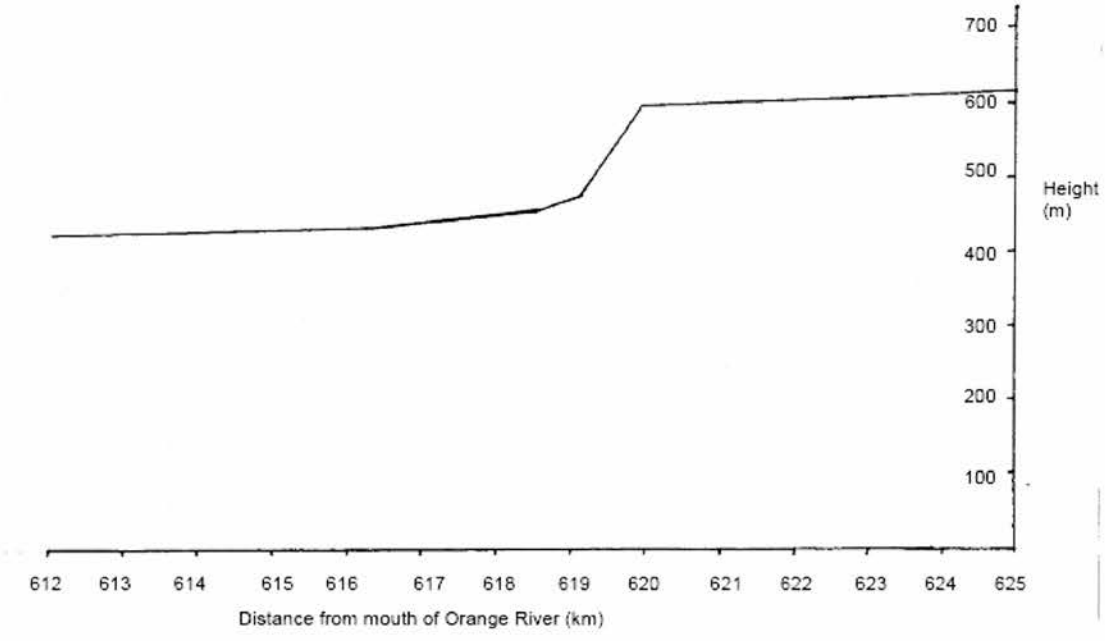

Figure 9.1.1 High resolution long profile plot of the Augrabies Falls region (*after* Summerfield *et al.*, unpublished data) Left of graph is west, right is east.

The main channel above the main Falls has a higher denudation rate than the area below the main Falls. Although the gradient measured over 20 km stretches of river is steeper downstream of the main Falls than upstream of the main Falls (3.10 vs. 2.07 m km^{-1}) immediately above the main Falls in the knickpoint drawdown zone,

where several anabranches merge, the gradient is relatively steep and step-like as the river flows over a number of actively incising potholes. The high rates of incision immediately above the main Falls (average ~ 68 mm ka^{-1}) can be explained by the increase in potential energy of the river as it flows into the knickpoint drawdown zone and has a higher specific stream power. Further upstream, near Keimoes where the gradient is shallower, incision rates are much slower (average of ~ 8 mm ka^{-1}). These rates compare well with rates of incision downstream of the main Falls in the gorge section, which have average rates of ~ 8 mm ka^{-1}. This shows that it is in the steep gradient knickpoint drawdown zone where the most rapid incision occurs. The style of this incision is discussed below.

Sample no.	Location	Channel gradient (m km^{-1})
SA04-3-2	Below Falls	3.10
SA04-23-1	Below Falls	3.10
SA04-24-1	Below Falls	3.10
Average		3.10
SA04-9-2	Above Falls	2.00
SA05-3-1	Above Falls	2.20
SA05-3-2	Above Falls	2.20
SA05-4-1	Above Falls	2.00
SA05-4-2	Above Falls	2.00
SA05-5-1	Above Falls	2.00
Average		2.07

Table 9.1.1 Summary of channel gradient, basin relief and relief ratio calculated from Summerfield *et al.*'s hypsometric plots (unpublished data). Gradients are local and measured over 20 km stretches of river from Figure 9.1.1.

9.1.2 Anabranches

Immediately above the main Falls there is a complicated system of anabranches flowing from three separate directions, the north, east and west (Plate 9.1.1). The north and east anabranch channels were sampled and appear to have similar rates of incision. The highest rate of incision is in the northern anabranch (average 73.68 ± 7.25 mm ka^{-1}), with a slightly lower rate (57.24 ± 4.71 mm ka^{-1}) in the anabranch that joins the eastern anabranch from the east. The western anabranch was not sampled, although it is clear that the northern anabranch, which is incising more quickly, is capturing the drainage from the west (S. Tooth, personal communication,

2006). The reason for the eastern anabranch capturing the other channels appears to be that the eastern anabranch is incising along a north-orientated master joint which is deepening fairly rapidly. This line of structural weakness appears to be a favourable location for potholes to develop. The drainage capture above the main Falls also partly explains how the Orange River goes from anabranching upstream of the main Falls to being confined within a single channel below the main Falls by being captured by the most quickly incising channel. With reference to the stream power incision model (Whipple & Tucker, 1999), whilst the eastern anabranch does not appear to carry the majority of discharge (this is done by the northern anabranch), the flow velocity in the channel appears to be faster than that that of the other anabranches, possibly owing to its confined nature (it has a width of around 3 m for most of its length immediately upstream of the main Falls, compared with a width between 5 and 10 m of the northern anabranch). The increased velocity results in higher stream power per unit area despite the lower discharge in this anabranch, resulting in it capturing the other two anabranches. Although the denudation rate data for the sampled point in the eastern anabranch (SA04-9-2) is slightly lower than for the northern anabranch, this merely reflects natural variability at the different sampling locations and is consistent with this model. However, the lack of quantitative data on the roughness and gradient of the different anabranches precludes a fuller discussion of the stream power incision model and requires further investigation.

9.1.3 Incision mechanisms

In the Augrabies region, there is a distinction between massive, pothole dominated bedrock upstream of the Falls system (including the main Falls) where knickpoint retreat is going on by pothole coalescence usually along joints and the area downstream of the Falls system which is massively jointed and incision appears to occur by joint exploitation only (Figure 9.1.2 Plates 9.1.2 – 4). The fact that joints are much more apparent in the downstream region could be because the downstream region has undergone significant bedrock denudation by potholing (of the order of tens of meters of denudation) which has resulted in the formation of deep bedrock channels (Plate 9.1.5). As these channels have formed, incipient pressure release joints may have opened up in the underlying and adjacent bedrock, resulting in large bedrock blocks beginning to fall from the sides of the channel. The river below the Falls system appears to be exploiting joints at the base of the channel, accounting for the observed pattern of kilometre-scale 90-degree turns and switchbacks in the river downstream of the Falls system (following the predominant 90-degree master joint orientations). This pattern is not seen above the Falls system, where the river anabranches and is clearly not structurally controlled (Plate 9.1.6).

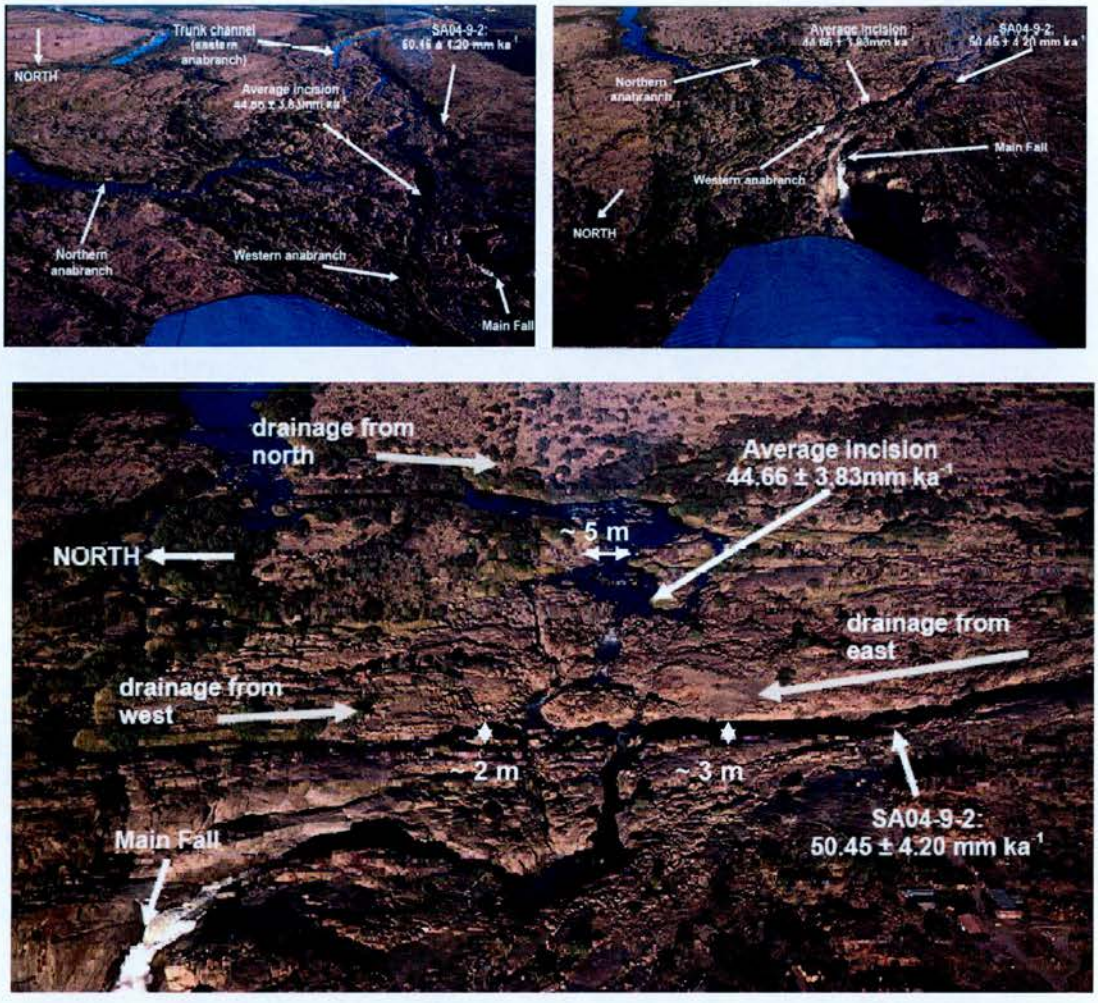

Plate 9.1.1 Aerial views of the drawdown zone immediately above the Augrabies main Falls. Note that drainage from the west is captured by that coming from the east and flows towards the main Falls. Photographs courtesy of S.Tooth.

Plate 9.1.2 (left) Massively jointed bedrock (right) bedrock joint is being exploited by flowing water.

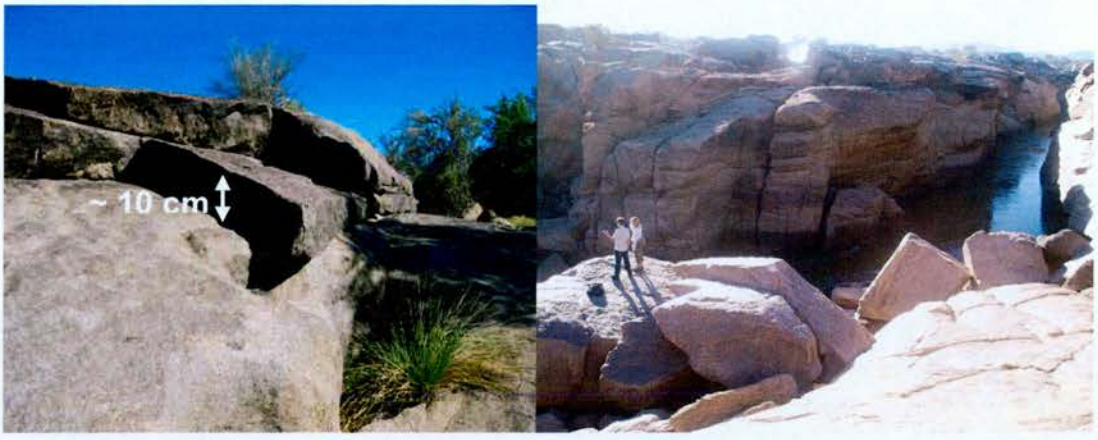

Plate 9.1.3 Joint exploitation: once a joint has been exploited, bedrock may become detached, as is about to happen in the left hand picture, and has happened on a large scale in the right hand picture, which is taken from the eastern anabranch just before it captures the northern and western anabranches above the main Falls.

Plate 9.1.4 Massive block retreat (left) in Fissure Canyon anabranch channel (right) and next to the main Falls (the waterfall can be seen in the far bottom right of the picture).

Plate 9.1.5 (left) Massively jointed bedrock on interfluves downstream of the main Falls (right) a massive bedrock block on an interfluve downstream of the main Falls, possibly formed after pressure release joints developed (note people for scale in both plates).

Plate 9.1.6 Large potential blockfalls (left) above the main channel, (right) in an anabranch channel that bypasses the main Falls (note person for scale).

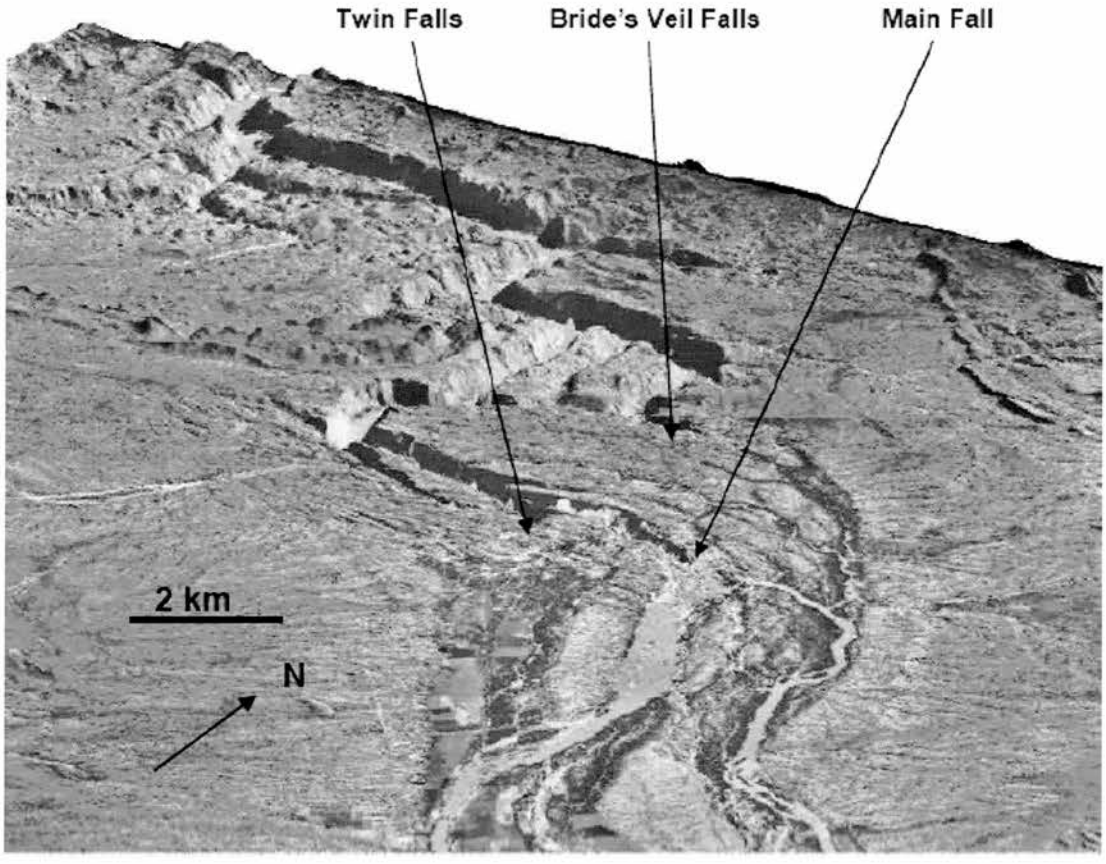

Figure 9.1.2 DEM of Augrabies region showing the main Falls and Falls systems that bypass the main Falls. Note the structurally-controlled nature of the river below the three Falls, and the anabranching nature of the river above the Falls system. DEM is by Walcott *et al.* (unpublished).

Tooth & McCarthy (2004), McCarthy & Tooth (2004) and Springer et al. (2006) suggest that bedrock channels above the main Falls develop by water running along incipient joints or into potholes. To this mechanism can now be added actual incision rate data derived from cosmogenic nuclides. A linear low point develops where a joint is exploited and a deepening and widening pothole may develop by the grinding action of boulders. Both features attract surface flow during floods and give rise to a very rapid increase in discharge and stream power. The channel may become deepened at one end, forming a mini-knickpoint. If the main river flow is diverted into the joint or pothole, this will create a constant high flow which will concentrate incision at the initiation lower part of the gorge. As potholes deepen, the erosive power declines, hence potholes tend to remain wide and shallow, and rapidly coalesce (Plate 9.1.7).

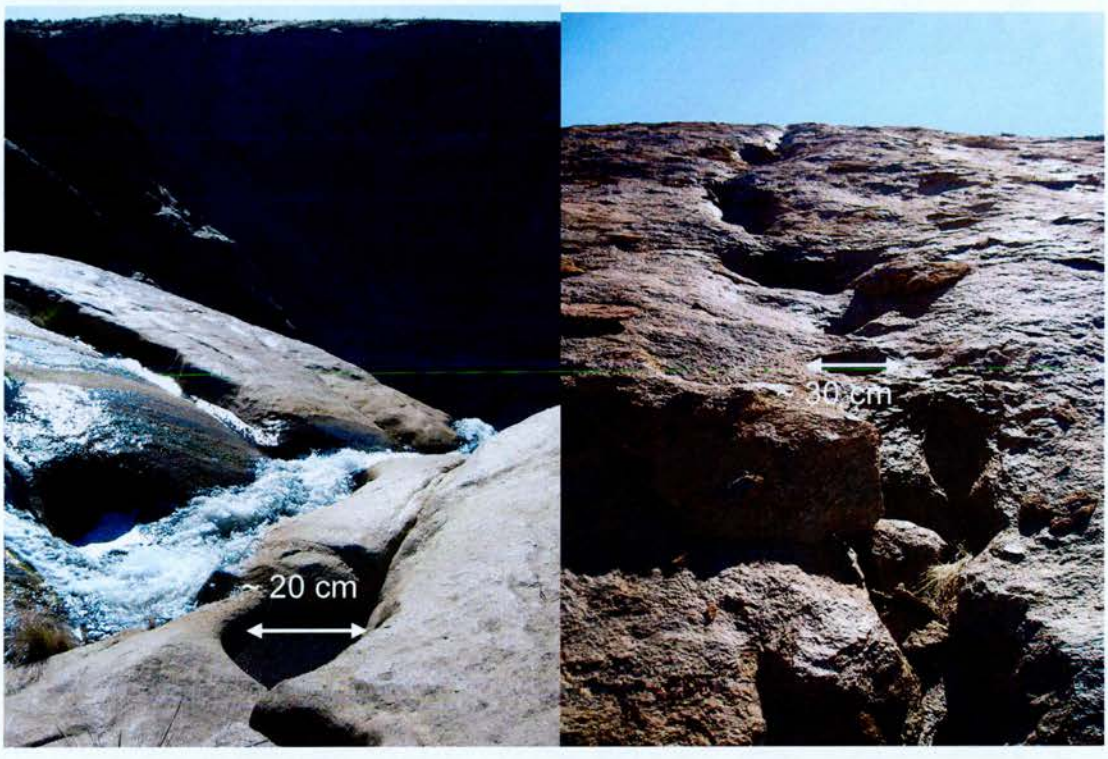

Plate 9.1.7 (left) Pothole incision immediately above Twin Falls; (right) incipient potholing down a bedrock slope near Ararat.

As they do so, bedrock surrounding the potholes may become detached as large blocks, resulting in surface lowering. This process could create a gorge from where the width declines only slightly to the gorge head, as seen in the main gorge and main Falls at the present day. The knickpoint would then retreat but at a rate which is slow in relation to the initial downcutting phase. This is the model proposed here for retreat of the Augrabies main Falls (Figures 9.1.3 & 9.3.4) and is backed up strongly by cosmogenic nuclide evidence that the channels upstream of the main Falls erode much more rapidly (an order of magnitude higher) than the channel downstream. Although actual rates of downcutting in potholes are still unknown, minimum rates of incision on bedrock bars are relatively rapid – of the order of several tens of millimetres per thousand years. Rates of incision in the potholes are likely to be around an order of magnitude higher than this, at least over short timescales, and may be responsible for up to meters of denudation after they widen and coalesce. Pressure release following this denudation may cause joints to widen and for blocks to become detached, forming a stepped knickpoint as seen at the Augrabies main Falls (Figure 9.1.3, 9.1.4).

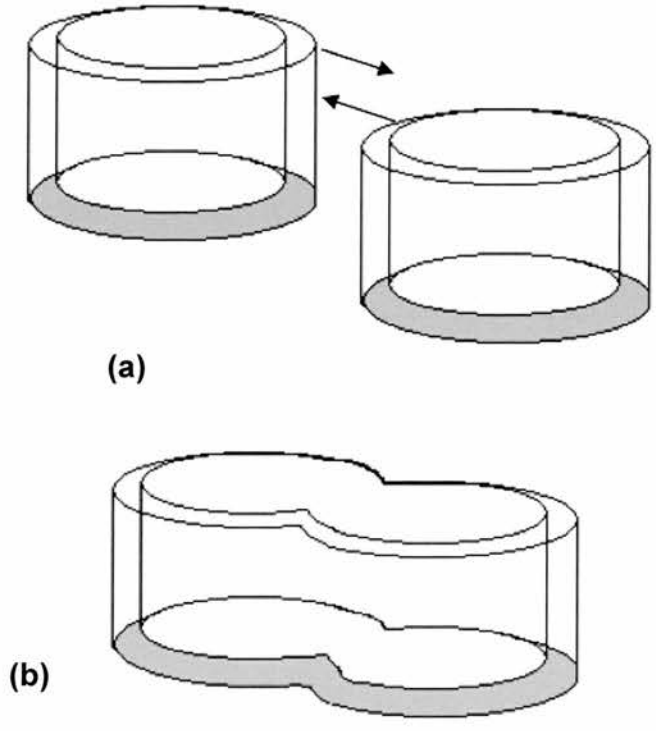

Figure 9.1.3 Pothole coalescence: (a) two potholes widen and deepen and become closer to each other (b) eventually they merge, creating a local bedrock low wider than it is deep. Where many potholes merge, and

bedrock retreat occurs, a knickpoint is created which may subsequently retreat.

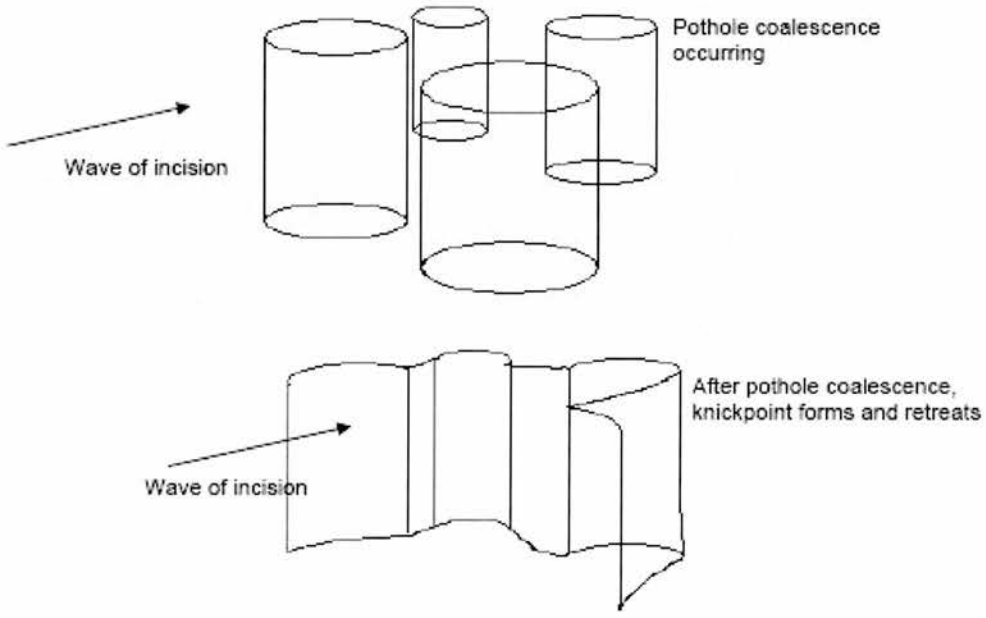

Figure 9.1.4 Model of development of the main Falls by pothole coalescence and knickpoint retreat (*based on* Springer *et al.* (2006) and others).

9.1.4 Knickpoint retreat

King (1963) suggested that the Augrabies Falls system represents the most inland portion of the Great Escarpment, which was initiated at the coast at the time of continental breakup around 130 Ma ago, and has since retreated to its present position. There is an order of magnitude difference in the channel incision rates upstream and downstream of the main Falls, suggesting that the Falls are rotating, rather than undergoing parallel retreat as proposed by King (although since the rates are very low, the Falls would appear to undergo parallel retreat on timescales of hundreds of thousands of years). Since the Falls lie some 620 km inland of the coast, King's model would have required an average rate of retreat of some 4.7 km per million years; or, 4700 mm ka^{-1} to have been maintained since continental breakup – clearly faster than the Falls have been retreating. The proposed style of knickpoint development, described above, is by potholing. In this mechanism, the rate of widening (backwearing) of the pothole seems to be roughly the same order of

magnitude as its rate of deepening (downwearing). This means that the knickpoint should be retreating at a rate of the order of tens, rather than thousands, of meters per million years. Clearly, these rates are inconsistent with a model of the knickpoint having originated at the coast and subsequently retreated. The idea that the Great Escarpment (and possibly the Falls system) originated as a marginal upwarp some hundreds of kilometres inland of the coast at the time of rifting must therefore be taken into account (van der Beek, 2002). With this model, the Falls would have retreated tens, rather than hundreds of kilometres, since breakup. Alternatively, the Falls system may have originated as a local drainage divide that underwent backwearing from the Late Cretaceous onwards, first by the Molopo River and later by the proto-Orange River after the Kalahari and Karoo rivers joined up (Goudie, 2005). The joining of these two rivers may have increased the overall discharge and stream power and driven higher rates of channel downwearing and associated knickpoint backwearing. Another possibility is that the Falls could be a local feature resulting from differential incision into bedrock of varying resistance, although this is unlikely given the similar bedrock incision rates above the Falls. Whatever the ultimate origin of the Falls system, this study gives the first actual bedrock channel incision rates that reveal the evolution of the region over tens to hundreds of thousands of years.

The rates of incision downstream of the main Falls are low (<10 mm ka^{-1}) and are integrated over ~ 90 ka. Clearly given the distance of several kilometres between the sampling locations and the knickpoint, the knickpoint retreated upstream of the sampling locations at a time far outwith the averaging times of the samples. There is also no clear trend of cosmogenic nuclide concentration with distance downstream of the main Falls. Although this study did not sample sufficiently close to the knickpoint to derive exposure ages of bedrock proximate to the knickpoint due to problems with access, this would not necessarily have given a reliable estimate of the knickpoint retreat rate. As discussed in the next section, it is highly unlikely that the present main Falls would have been the main knickpoint in the past. The complex anabranching nature of the area above the Falls system means that there has been re-

routing of flow over time and de-activation and re-activation of various anabranch channels at different times resulting in switching of the location of the main Falls.

9.2 Discussion of the evolution of anabranches, tributary channels and interfluves

9.2.1 Geometry and orientation

The perpendicular master joints in the Augrabies region account for the right-angle switches in orientation of the main channel below the Falls system, as noted previously (Plate 9.2.1). Broadly speaking, the main channel and principal tributaries of the Orange River are oriented in an east-west direction, whilst there are several north-south oriented structural discontinuities cutting between the Orange River and the major parallel tributaries. One of the southern anabranches, 'Fissure Canyon', is a case in point which illustrates the above observation. This channel is orientated parallel (east-west) to the main channel and begins at the level of the surrounding landsurface (~ 630 m). Within a few hundred meters it becomes markedly wider and deeper, reaching a depth of some 10 m and 10 m wide at the point where it can be observed to end, with a break in slope, in a sharp drop into a larger channel (Plate 9.2.2). This anabranch is revealed by the CIAF samples to have a mean denudation rate of ~ 49 mm ka^{-1}. This channel, like several others around Augrabies, seems to maintain its basic geometry throughout its course – i.e. the channel seems to be as wide as it is deep throughout its course. An explanation for this is that the channel develops principally by vertical incision of the channel floor driven by water flow. This is complemented by block retreat from the sidewalls, which occurs where the blocks contain horizontal structural discontinuities. In more energetic fluvial environments, such as the anabranches of the main Orange River, bedrock incision is carried out by the process of potholing in massive joined bedrock, followed by block retreat or pothole coalescence. It is telling that on the right side of the Fissure Canyon, where an incipient channel is developing, the geometry is disproportionately deeper than it is wide (Plate 9.2.2). This may be due to the fact that there are very few horizontal discontinuities in the sidewalls of the bedrock – further evidence, perhaps, that incipient joints open up primarily in response to denudational unloading. Anabranch channels that bypass the main Falls appear to begin as minor

flows along sub-vertical joints. These become topographic lows which then collect overflow discharge from elsewhere (Plate 9.2.3). Where large boulders and high flows exist, deepening can be carried by the process of potholing. As further deepening occurs more flow is concentrated, joints widen and undermine adjacent blocks which then collapse into the channel causing it to widen (Plate 9.2.4). Where incipient joints lie sub-parallel to the slope, their opening up by flowing water and/or potholing, can cause slabs of bedrock to break off and move down the slope as appears to be happening in Figure 9.2.1.

9.2.2 Mechanism of anabranch development

Evidence of this method of development of some of the anabranch channels comes from flowing water in Fissure Canyon which was present in July 2005 when the flow of the Orange River was ~ 60 $m^3 s^{-1}$. This was in marked contrast to the situation in November 2004, when the channel was observed to be dry and it was postulated then that the channel only carried flow during high magnitude, low frequency events such as the 1988 flood (Bremner *et al.*. 1990). Given that the discharge of the Orange River as recorded at Upington is only a third higher in July 2005 than November 2004 (~ 60 $m^3 s^{-1}$ compared with ~ 40 $m^3 s^{-1}$) these base flows are unlikely to be responsible for significant incision into bedrock anabranch channels. More likely is that during high magnitude flood events, flow becomes diverted from the main channel to these anabranches. The flow velocities are increased as the high discharges are funnelled into narrow anabranches, and the specific stream power therefore increases, and results in incision by potholing and cavitation. It may be that as high magnitude flood events wane, they leave debris which block the previous main channel so that anabranches become the 'main channel' until the next major flood occurs. This could account for the high incision rate (> 180 mm ka^{-1}) measured in one of the anabranches currently experiencing low flow (discussed in Chapter 7).

Plate 9.2.1 Showing block retreat in a southern anabranch channel of the River that bypasses the main Falls.

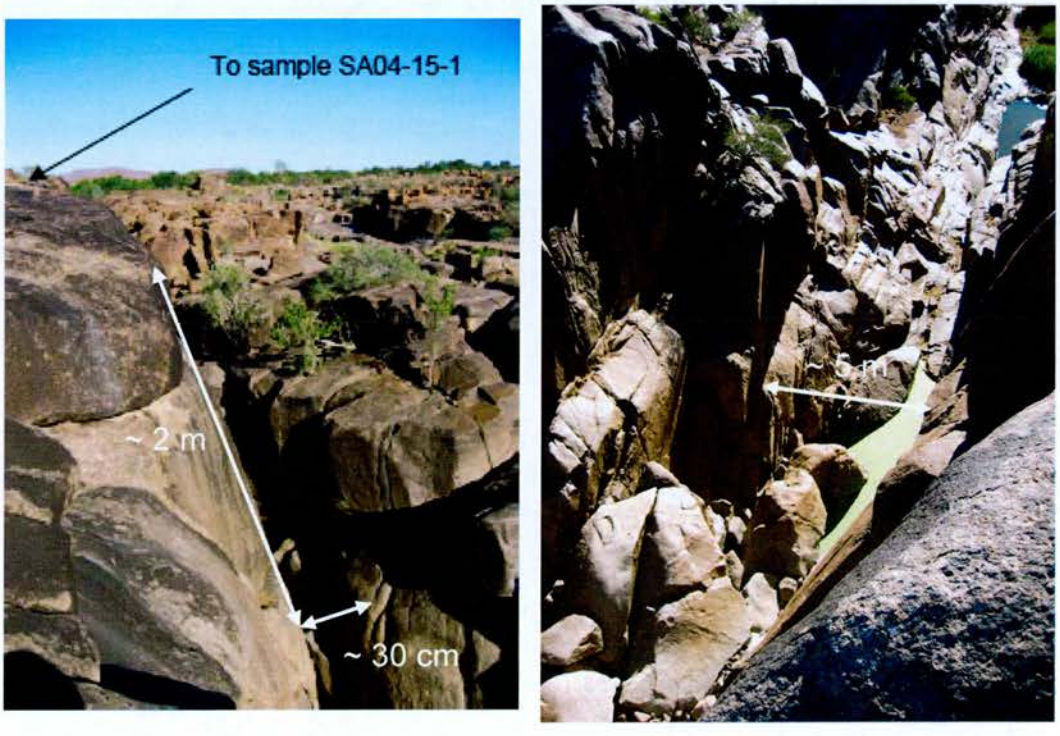

Plate 9.2.2 Initiation of deeply incised anabranch channel adjacent to sample SA04-15-1 and sample SA04-14-1, -14-4 (Fissure Canyon).

Plate 9.2.3 Evidence of block retreat on bedrock interfluves proximate to (left) anabranch channel and (right) main channel below Falls.

Plate 9.2.4 Perpendicular orientated joints on a small scale (left), and manifested on a large scale (right).

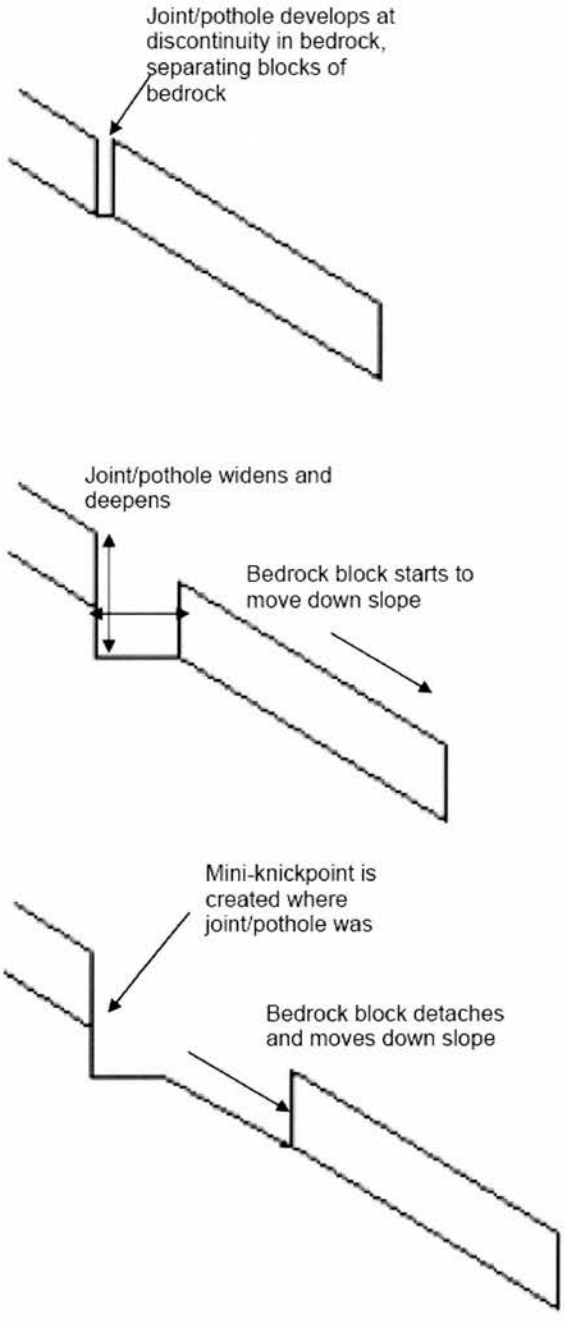

Figure 9.2.1 Model of development of anabranch bedrock channels by block retreat sub-parallel to the slope initiated by joint or pothole exploitation.

9.2.3 Positive relief development

When the channel bed lowering rate is known, and interfluve lowering rate is known, then the rate of vertical incision of channels relative to interfluves (i.e. the rate of change of relief) can be calculated. On average, from the cosmogenic nuclide data presented above, channel beds are deepening twice as quickly as the surrounding

interfluves are lowering. If these rates are assumed constant and extrapolated back over a time interval needed to form the observed channel depth then the time taken to form the feature is known, and the rate of channel widening is also known. For the main channel, the rate of lowering of the interfluves at Ararat are known from samples SA04-21-1 and -2 and the rate of lowering of the main channel in the same vicinity is known from sample SA04-3-2. With an elevation difference of 184 m and average denudation rates of 3.39 ± 0.24 mm ka^{-1} on the interfluve and 8.91 ± 0.55 mm ka^{-1} in the channel, there is a denudation ratio of ~ 2.6. Assuming these denudation rates are constant, there is an effective channel incision rate of 5.53 mm ka^{-1} and it would take ~ 33 Ma to form the main channel. Doing the same further downstream in the main channel, (sample SA04-22-1 on the interfluve, SA04-23-1 and -24-1 in the channel) gives a formation time of ~ 56 Ma (Table 9.2.1). The upstream site has a higher gradient than the downstream site, and therefore should have a greater local velocity and higher specific stream power. It will also experience higher local stream power due to its relative proximity to the knickpoint, where a large discharge travels at high velocity. In contrast, the downstream location has a lower gradient and, although it may have a slightly higher discharge due to it being downstream of where the anabranches re-join the main channel, its gradient and distance from the knickpoint means that it has a lower specific stream power and therefore a lower net denudation rate. Using the same method, the Echo Corner tributary has a formation time of 4.25 Ma. Formation times are also calculated for two anabranch channels using the CIAF samples presented in the last two chapters. The Fissure Canyon anabranch has a formation time of < 1 Ma whilst Twin Falls anabranch has a formation time of around 130 ka, due to its rapid incision rate and small topographical differences (Table 9.2.1). Clearly, these two anabranches have much greater rate differences between the base of the channels and the interfluves than the samples discussed above. The incision rate in the channel is out of equilibrium with the rate on the interfluves, thus generating positive topography more rapidly. The anabranches appear to be incising rapidly by high magnitude, low frequency flows (see discussion below). Assuming that the basic internal geometry of the channels is maintained, the incision rate is also a proxy for backwearing of the channel sides. Therefore, the backwearing rate of the main channel sides can be said

to be of the order of less than ten millimetres (~ 2-3 mm ka^{-1}) per thousand years, or less than ten meters per million years on the appropriate, longer timescale. This compares well with the rate of knickpoint retreat of ~ 10 mm ka^{-1} for the Echo Corner tributary and discussed in the previous chapter. The formation of this tributary channel could be linked to the onset of more humid conditions in the area in the Quaternary, which resulted in greater potential for runoff (Tyson, 1986).

Location	Sample(s)	Average erosion rate (mm ka^{-1})	Erosion rate ratio	Net erosion rate (mm ka^{-1})	Average altitude (m)	Altitude Difference (m)	Formation time (a)
Interfluve (near Echo Corner)	SA04-22-1	4.44	1.64	2.85	590	159.5	$55.96x10^6$
Channel (main)	SA04-23-1, -24-1	7.29			430.5		
Interfluve (Ararat)	SA04-21-1, -2	3.39	2.63	5.52	635	184	$33.27x10^6$
Channel (main)	SA04-3-2	8.91			451		
Interfluve	SA04-18-1, -2, 20-1	7.83	1.66	5.18	618.0	22.0	$4.25x10^6$
Channel (tributary)	SA03-2-1, SA04-19-1-A, -B, -C	13.01			596.0		
Interfluve	SA04-15-1, SA04-16-1*	6.20	7.97	43.22	674.5	38.5	$0.89x10^6$
Anabranch (Fissure Canyon)	SA04-14-1* SA04-14-4*	49.42			636.0		
Interfluve	SA04-16-1*	2.29	79.1	178.93	679	24	$0.13x10^6$
Anabranch (Twin Falls)	SA04-17-1	181.22			655		

Table 9.2.1 Showing formation time of bedrock channels. The first two sets of columns are samples from the main channel and the third from a tributary channel upstream of Echo Corner. * denotes CIAF sample.

Clearly the critical assumption here is that denudation has been going on at a constant rate, and also that the basic morphology of the channels is constant over time. It was observed in some of the tributary channels that deepening occurs much

more rapidly than widening as the channel starts off as a joint or fissure that becomes exploited by flowing water. Therefore the channel backwearing rates inferred from the downwearing rates must be thought of as maxima since downwearing tends to exceed backwearing at least in the initial stage of channel development.

9.2.4 Overall development of the Augrabies region

For the first time, the model of channel development in the Augrabies region, discussed by Springer et al. (2006), Tooth & McCarthy (2005) can be backed up with cosmogenic derived incision rate data. This is reinforced by catchment-averaged data from tributaries and the main channel of the Orange River, which show similar orders of magnitude denudation rates as the bedrock channels, although given that the catchment-averaged technique integrates denudation signals from over a wide area, the latter are generally lower. There are large parts of the basin where little denudation is going on, and relatively small 'hotspots' of denudation, particularly in parts of the bedrock channel immediately upstream of the knickpoint. A catchment-averaged sediment sample may reflect a strong local denudation rate signal, especially if the nuclide component from bedrock and boulders in transport is high (Kirchner *et al.*, 2006). Certain samples collected in the vicinity of denudation 'hotspots', e.g. sediment sample SA04-28-1, collected next to the relatively rapidly eroding sample site SA04-27 (average 14.63 ± 3.28 mm ka^{-1}). However, the low denudation rate of SA04-28-1 (5.85 ± 0.49 mm ka^{-1}) suggests that the well-mixed sediment assumption holds and there is no disproportionate influence of one area of bedrock. For the main channel, sample SA03-5-1 has an extremely low rate of denudation (3.18 ± 0.47 mm ka^{-1}) and reflects the upstream denudation rate signal, rather than the locally high bedrock incision rate (e.g. sample SA05-4-1: 76.99 ± 6.52 mm ka^{-1}). Given the very low rates of denudation in general in the Augrabies region and the lack of major differences in denudation rates between sites, Kirchner *et al.*'s (2006) anticipated bias does not hold true.

It appears that potholing and joint widening along east-west or north-south trending incipient joint systems (Plate 9.2.4) rapidly results in a very deep and wide channel developing. There appears to be a positive feedback at work whereby an existing

joint is exploited by flowing water and this causes widening and deepening eventually forming a large channel and a surrounding upstanding area (bedrock interfluve). Such upstanding areas (their orientation locally controlled by both master joints and inferior joints (Moen, 1984, cited in van der Walt, 2000)) are manifested as features such as Arrow Point and, on a smaller scale, the upstanding area between Fissure Canyon and the channel running parallel to it (sampled as SA04-15). Indeed, it could be argued that the entire Augrabies landscape below the Falls system exhibits a 'self replicating' landscape on a variety of scales: joints are exploited to form channels running with a generally east-west orientation; these channels coalesce (especially where the inferior joints meet, like the spokes on a wheel) to form ever larger channels with corresponding upstanding areas; the channels thus formed coalesce with other channels forming yet more upstanding areas ('Arrow Points') which are correspondingly larger.

Clearly, high magnitude, low frequency events are ultimately responsible for shaping the Augrabies landscape, both in the sense that they are responsible for rapid incision by potholing and in that they control which anabranches become activated and which become cut off from the main channel system by depositing debris during peak flows that can re-route subsequent flows. Critical to this idea is the concept of stream power (Whipple & Tucker, 1999). Although discharge is clearly important in incision; the gradient, cross sectional area and roughness may control incision in anabranches. Occasional high magnitude flood events may lead to high specific stream power in an anabranch and cause it to rapidly widen and deepen (Plate 9.2.2). Eventually it may become deep enough to capture base flows from the main channel, and effectively 'short circuit' the main channel. This is believed to have gone on as the Augrabies region has developed, and the location of the main Falls has accordingly switched as different anabranches have captured flow. This mechanism is responsible for the complexity of the Augrabies Falls system. Anabranches that have failed to deepen sufficiently quickly, and therefore capture flow from the main channel, have been left high and dry as 'hanging valleys' such as Twin Falls or Fissure Canyon. Given sufficient time, the rapid incision rate in the Twin Falls anabranch may mean it captures more flow from the main channel and itself becomes

the main channel, as it may have been in the past. As Twin Falls is incising roughly three times faster than Fissure Canyon, it may eventually form a new local base level and capture the flow from Fissure Canyon.

In the bedrock channels of the Augrabies region, incision rates in anabranches and tributaries are ultimately controlled by the local base level of the main channel of the Orange River (Tooth *et al.*, 2004). This contrasts with studies of mixed bedrock alluvial rivers, e.g. the Klip River, eastern Free State (Howard, 1998; Tooth *et al.*, 2002; 2004). Dolerites form local base levels impeding incision and promoting lateral denudation in upstream reaches underlain by more erodible sandstone and shale. As descried by Nanson & Croke (1992) river floodplains are constructed by a complex interaction of fluvial processes but their character is essentially the product of stream power and sediment character. The uniform, massively jointed granite gneiss bedrock at Augrabies controls the style of fluvial incision and the resulting spectacular landforms. The rate of fluvial incision and knickpoint retreat is controlled by stream power. In the past, due to the lack of upstream flow control, discharges were higher, and the stream power would have accordingly been higher. This resulted in the moderately high time-integrated denudation rate of tens of millimetres per thousand years above the knickpoint and well over 100 mm ka^{-1} in anabranch channels. Rates of knickpoint retreat in these environments are likely to mirror the incision rates. The incision rate in the main channel below the main Falls is less than 10 mm ka^{-1}, reflecting the low denudation and the morphological 'steady state' that has existed between the rates of interfluve and channel incision over hundreds of thousands of years. Base flows measured at Upington over the last 70 years or so have averaged ~ 200 $m^3 s^{-1}$, with peak flows of several thousand $m^3 s^{-1}$ (Zawada, 1996; UNEP, 2006). Prior to the regulation of the Orange by dams, base flows and peak flows would have been correspondingly higher. Indeed, there is evidence from undated slackwater deposits that floods in the past had peak flows as high as 30,000 $m^3 s^{-1}$ (Zawada, 1996). The stream power in the Augrabies region would have been correspondingly higher. It may be postulated that the rates of incision and retreat in the Augrabies region will not be maintained as long as the flow of the Orange River is regulated by large dams and water abstraction upstream. This may have

implications for the long term rate of unroofing of kimberlite pipes, hydrocarbons and other resources along the Orange River.

9.3 Regional scale, long term landscape development

9.3.1 Importance of Quaternary-scale denudation rate data

The low rates of incision measured from cosmogenic nuclide analysis of bedrock interfluves are of the order of millimetres per thousand years, or meters per million years to state the rates in units more relevant to the development of the southern African landscape. These rates are comparable and, indeed, somewhat higher than those measured for other low relief regions (e.g. Bierman & Turner, 1994; Bierman & Caffee, 2002). Parts of the Augrabies region are undergoing moderate rates of denudation – bedrock channels upstream of the main Falls are incising at rates of the order of tens of meters per million years, while some of the rates above one of the anabranch Falls in the Falls system are of the order of hundreds of meters per million years. The data presented here allows processes of bedrock incision to be better understood by presenting the first actual bedrock incision rates for the Orange River. Although small-scale processes such as potholing and joint exploitation appear to be the main mechanisms of incision, the rate of incision in individual potholes remains to be quantified. On a regional scale, the Augrabies Falls region ultimately controls the evolution of some 80% of the Orange basin, and provides a local base level down to which the rest of the Orange River is incising. The Augrabies region controls the propagation upstream of denudation that has gone on in the lower Orange River. Quantifying the rates of evolution of the Augrabies region consequently helps our understanding of the Orange basin's evolution over Quaternary timescales, which complement published studies of the evolution of the Orange over much longer timescales based on offshore sediment and thermochronological studies.

Fission track thermochronology provides a readily accessible framework for quantifying the otherwise undetectable, i.e. the timing and magnitude of long term denudation over tens to hundreds of millions of years (Kohn *et al.*, 2002). Rates and patterns of denudation provide a fundamental insight into the response of landscapes

to various tectonic processes and allow a quantitative calibration of the evolution of the Earth's surface (Gleadow & Brown, 2000). What has been lacking until now are data on Quaternary timescales to answer questions of whether rates of processes have been constant over geological (millions of years), geomorphological (thousands of years) and anthropogenic (hundreds of years) timescales. This also helps answer questions of what the main formative events in landscapes are (Brunsden & Thornes, 1979) and to test long-standing models of landscape evolution, in particular the idea that erosion surfaces are preserved in the landscape over long periods.

9.3.2 Regional-scale denudation trends

Gallagher & Brown (1999a, 1999b) have produced denudation plots derived from palaeotemperature maps for the western margin of southern Africa. The Augrabies region has a total inferred amount of denudation of around 3 km since 140 Ma, which is equivalent to 21 m Ma^{-1} of denudation. Generally low rates of denudation would have prevailed across southern Africa after a phase of locally high rates immediately post break-up. This value is not dissimilar to the average rates of denudation of around 15 m Ma^{-1} from catchment-averaged tributary samples in the Augrabies region. Gallagher *et al.* (1999) show that the largest amount of post-rift denudation was close to the coast, with less further inland, although there are some notable anomalies e.g. 4 km of denudation 400 km inland, occurring between 100 and 60 Ma: equivalent to a denudation rate of 100 m Ma^{-1}. Gallagher *et al.* (1999) have identified two time periods when denudation was most active (Table 9.3.1). As can be seen from Table 9.3.1, denudation was greatest in the Augrabies region in the Lower Cretaceous, immediately following continental breakup ~ 130 Ma. There then followed a long period of low denudation until the early Cenozoic when rates of denudation of the order of tens of meters per million years prevailed (not dissimilar to the rates experienced over Quaternary timescales, as revealed by cosmogenic nuclides).

Time interval (Ma ago)	Denudation (km)	Equivalent Denudation rate (m Ma^{-1})
0-40	1	25
40-70	0	0
70-100	0	0
100-140	2	50

Table 9.3.1 Equivalent denudation rates for the Augrabies region taken from denudation plots derived from palaeotemperature maps derived from palaeotemperature maps using present-day heat-flow data (Gallagher & Brown (1999a, 1999b).

On a larger scale, the post-breakup denudation chronology for southern Africa presented by Gallagher & Brown (1999b) shows that on the western margin of southern Africa there was relatively little post-breakup denudation and then a dramatic increase in denudation rates in the Late Cretaceous-Early Tertiary, more than 50 Ma after initial rifting. Average rates of post-breakup denudation of were estimated at 800-1000 m, equivalent to 6-7 m Ma^{-1} of denudation. Periods of enhanced denudation occurred well after breakup, at around ~ 100 Ma, 75 Ma and 40 Ma ago. Gallagher *et al.* (1998) have presented estimates of syn-rift (158-118 Ma) and post-rift (118-0 Ma) denudation on the western margin of southern Africa (Figure 9.3.1). In the Augrabies region, which lies on the 0.5 km denudation contour for the syn-depositional period, an average denudation rate of 12.5 m Ma^{-1} appears to have prevailed. For the period since rifting (118-0 Ma) around 3 km of denudation has occurred near the Augrabies region, giving an equivalent denudation rate of ~ 25 m Ma^{-1}. Once again, the rates during these enhanced periods of denudation are comparable with the denudation rates derived from cosmogenic nuclide analysis over tens to hundreds of thousands of years.

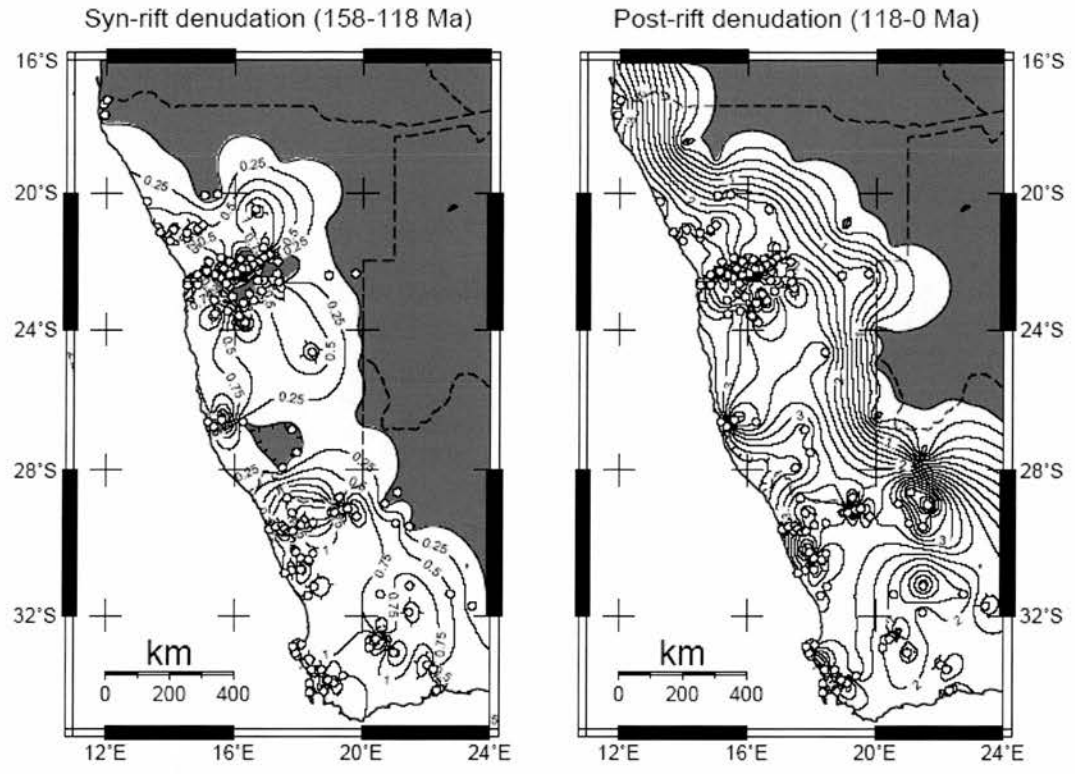

Figure 9.3.1 Estimated syn- and post- rift denudation in kilometres for western southern Africa (Gallagher *et al.*, 1998).

From temperature histories combined with heat flow data, the equivalent depth of denudation can be estimated and used to calculate average denudation rates for the Atlantic margin of southern Africa. Integrated over the whole western margin, the rates are of the order of a few tens of meters per million years, though with temporal and spatial variations which imply complex patterns of denudation (Gallagher *et al.*, 1999). The assumption is that there was a phase of high denudation rates soon after continental break-up. The similarity of rates of denudation over tens of millions of years (from thermochronologic data) and those over tens of thousands of years (from cosmogenic methods) are striking. They are of the same order of magnitude (meters to tens of meters per million years) and suggest that the processes operating on the southern African landscape over tens of millions or tens of thousands of years have been essentially the same. This suggests that the small scale processes operating during the Quaternary on tens of thousands of year timescales (e.g. potholing and block retreat in bedrock channels) have been going on over millions of year timescales. This detail is not resolvable by thermochronologic methods. The rates also suggest that the legacy of continental breakup inherited from the early- to mid-

Cretaceous has effectively been maintained in the rates of landscape denudation almost to the present day.

On a regional scale, Gallagher *et al.* (1999) use the thermochronological data in support of a scarp retreat or pinned drainage divide model of development of the southern African passive margin escarpment. They argue against downwarping of the marginal escarpment after breakup (as proposed by Ollier & Pain (1997)) as downwarping models neglect the isostatic response to denudational unloading. Neither the thermochronologic data nor the results of modelling support the idea of marginal downwarping. Gallagher *et al.* (1999) suggest that scarp retreat or the pinned drainage divide model both operate to some extent and are manifested on different length scales. Assuming that the rates and processes over Quaternary timescales are representative of those operating on millions of year timescales (and given that the rates over different timescales are similar, this is a reasonable assumption), the cosmogenic data, at least in the Augrabies region, would appear to suggest that a downwearing model is applicable owing to the differential denudation rates above and below the Falls system. If these rates measured over tens thousands of years are maintained for millions of years, the Falls system will be eventually worn down. Over tens of thousands of year timescales, this downwearing would be manifested as parallel retreat, reflecting the small relative differences in denudation rates above and below the main Falls, although this is ultimately part of a longer process of downwearing. Perhaps the downwearing model, rather than the parallel retreat model, can be applied to the western escarpment as a whole, although more work to confirm the cosmogenic derived erosion rates above and below the western escarpment is required to confirm this.

The thermochronological data from southern Africa generally suggests an Early Cretaceous phase of erosion linked to rifting, and a later more variable phase of denudation with denudation 'hotspots' experiencing denudation rates of tens of metres per million years. The pattern of many areas undergoing low rates of denudation and relatively few areas denuding rapidly is seen in the cosmogenic derived denudation data from the Augrabies region where large areas of interfluves are eroding at rates of the order of metres per million years and a small area of active

Chapter 10 – Summary and Conclusions

10.1 Summary of findings

10.1.1 Catchment-averaged denudation rates

The main achievement of this study is that for the first time, Quaternary timescale denudation rates derived from cosmogenic ^{10}Be and ^{26}Al have been quantified for the Orange basin, the primary drainage basin in southern Africa. The rates have been revealed to vary between ~2 and ~50 mm ka^{-1}, comparable with existing cosmogenic-derived rate estimates (e.g. Cockburn *et al.*, 1999; Fleming, 1999; Bierman & Caffee, 2001) and also with the total denudation rate of 28 mm ka^{-1} for the Orange derived from sediment yield data (Summerfield & Hulton, 1994 based on Rooseboom & Harmse, 1979). The rates are also compatible with regional-scale denudation rates derived from the offshore sedimentary record and low-temperature thermochronological data over longer timescales. These data indicate generally low rates of denudation across southern Africa over millions of years following locally high rates in the period following the break-up of the Gondwana supercontinent and the formation of new base levels (Rust & Summerfield, 1990; Brown *et al.*, 1990; Gallagher & Brown, 1999a, 1999b). Denudation rates for much of the Tertiary have been estimated from low-temperature thermochronology at ~ 10 m Ma^{-1} (Brown *et al.*, 2002). These rates are very similar to the average rate of 9.6 mm ka^{-1} presented here for the whole Orange basin. Despite the low rates presented here, it is evident that low-relief erosion surfaces in the Orange basin could not have survived unmodified over geological timescales, as suggested by traditional denudation chronology approaches to landscape reconstruction.

Most of the middle and lower parts of the Orange basin are eroding relatively slowly ~ 2 to ~ 15 mm ka^{-1} and the catchment-averaged rates derived from different parts of the middle and lower basin are essentially in agreement to within standard uncertainties. The sampled upper parts of the basin are eroding at rates of between ~ 5 and ~ 50 mm ka^{-1}. Tributary catchments are generally eroding more quickly, ~ 12 mm ka^{-1} than the main Orange catchment, ~ 7 mm ka^{-1}. The catchment-averaged denudation rates, ~ 10 mm ka^{-1}, are generally higher than bedrock interfluve denudation rates, ~ 6 mm ka^{-1}, indicating that local relief will increase slowly over time. With the limited number of samples presented here, no attempt is made to

elucidate the relative controls on denudation from climate, lithology and relief over different spatial scales. This study provides the first 'background' rates of Quaternary-scale denudation for the Orange basin and further study may reveal the precise nature of the controls on these rates.

The cosmogenic-derived denudation rates presented here provide mean rates over timescales of 10^4 to 10^5 years and therefore provide a benchmark against which other rate estimates on shorter timescales can be compared. When the cosmogenic-derived denudation rates presented here were compared with short-term (~ 80 year) denudation rates derived from dated sedimentary sequences in small farm dams (Foster *et al.*, 2005), the short-term rates were found to be around two orders of magnitude higher than the average rates for the upper and middle Orange derived from cosmogenic data over the last ~ 80 ka. Whilst some of this difference may be accounted for by local variations in lithology and relief, it is clear that in the central Karoo, there has been a considerable increase in denudation rates in the last few decades compared with the benchmark intermediate-term rates. This may be partly an artefact of the data – a longer record will incorporate a larger number of events of different frequency and magnitude than the short-term record, which may only capture events that are unrepresentative of the longer record. However, given that the longer-term record captures part of a glacial-interglacial cycle (Partridge, 1997b), it ought to 'smooth out' the effects of a changing climate. It is very difficult to unravel the effects of climate change on denudation in semiarid landscapes – with an increase in precipitation, vegetation could increase leading to a decline in denudation (Schumm & Lichty, 1965). With a decrease in precipitation, the runoff and transport capacity could be reduced, also leading to a decrease in denudation. The increase in denudation rates in the recent period is unlikely to be driven by climate change alone and is more likely to be a result of anthropogenic modification of the landscape, in particular the over-stocking of sheep in the area in the 1940s-1970s period (Keay-Bright & Boardman, 2006; Meadows & Hoffman, 2006). Undoubtedly, climatic change may have played a role alongside grazing pressures, however human-induced land use changes are most likely to be responsible for the recent accelerated denudation rates compared with the 'benchmark' cosmogenic-derived rates. This

further demonstrates the utility of cosmogenic-derived catchment-averaged denudation rates as tools for informing environmental management.

10.1.2 Bedrock denudation rates in the Augrabies region

The major knickpoint on the Orange River, the Augrabies Falls, exerts a fundamental control on landscape evolution across two thirds of the basin upstream. Rates of incision above and below the Falls are constrained here for the first time. This has allowed actual rates to be applied to existing models of bedrock incision by potholing and joint exploitation (Tooth *et al.*, 2004; Springer *et al.*, 2006). Average rates of channel incision in anabranches above the Augrabies main Falls knickpoint are ~ 70 mm ka^{-1} compared with average incision rates below the Falls of < 10 mm ka^{-1}. Stream incision power (Whipple & Tucker, 1999) explains the rapid denudation rates (mean ~ 96 mm ka^{-1}) in relatively narrow anabranches – in one narrow anabranch, the flow is accelerated leading to increased specific stream power and a higher denudation rate (~ 180 mm ka^{-1}), causing it to capture other, more slowly incising anabranches. The precise nature of the relationship between stream power and denudation needs to be investigated further, with reference to changes in gradient, roughness and discharge in the different anabranches.

Average interfluve lowering rates of ~ 6 mm ka^{-1} have been derived, and account for low background rates of erosion in the Augrabies region. The difference between incision rates in the main channel below the Falls and on interfluves is low but local relief will increase over long timescales. A detailed study was made of a characteristic type of interfluve, a bornhardt, which is denuding at a rate comparable with bornhardts on the coastal plain of Namibia (Cockburn *et al.*, 1999). By comparing the rates of incision on the summit (downwearing) and the sides (backwearing), it appears that backwearing is going on at a rate roughly twice as fast as downwearing, suggesting that the bornhardt will become narrower over time. Its height relative to the surrounding landsurface will be maintained, however, since the summit is denuding at a rate similar to that of the surrounding interfluve (~ 3 mm ka^{-1}). Clearly if these rates were maintained for a long period of time, they would result in the inverse of the landscape we see today. The critical factor is the

timescale over which these rates endure: rapid rates operate over shorter timescales than the slower rates. This argument invokes ideas of timescale first put forward by Schumm & Lichty (1965) and involves episodic erosion. The mechanism of denudation is believed to be solutional weathering from runoff which occurs on the bornhardt following high magnitude, low frequency storm events. Runoff and precipitation, and therefore denudation, are most concentrated on the sides of Moon Rock, leading to apparent 'parallel retreat' of the sides of the bornhardt.

Anabranch channels which bypass the main Falls and re-join the channel below the Falls appear to be incising rapidly (~ 50 to ~ 180 mm ka^{-1}), on a local scale at least. The anabranches that bypass the main Falls appear to be highly significant in the overall evolution of the Augrabies Falls system. Their high denudation rates can be explained by periodically high discharge associated with high magnitude, low frequency flood events. During floods, discharge may be diverted from the anabranches above the main Falls to narrow bedrock anabranches such as the Twin Falls anabranch that bypasses the main Falls. High specific stream power will result from the high flows in the confined channel, giving high time-integrated incision rates. At different times, certain channels will have been activated or de-activated after debris from peak flows diverted the flow. As flood flows recede, sediment or boulders may block the original flow route, resulting in certain anabranches becoming active even during base flows. The antecedent flow routing will affect the routing of the next flood – emphasising the importance of contingency in this landscape (Brunsden & Thornes, 1979). If flow is sustained in an anabranch for thousands of years, considerable denudation by potholing and joint exploitation may occur. If the flow is again re-routed, the anabranch may become de-activated and left as a 'hanging valley' if it has failed to incise down to the local base level of the main channel. This is believed to have gone on in the past and is responsible for the complex Augrabies Falls system of knickpoints.

10.2 Conclusions

10.2.1 Erosion history of the Orange basin

The denudation rates presented here from catchment-averaged and in-situ ^{10}Be and ^{26}Al data significantly improve our knowledge of Quaternary scale denudation rates across the Orange basin in general, and the key Augrabies Falls knickpoint in particular. They support the characterisation of the Orange as a low gradient, slowly eroding river basin (Summerfield & Hulton, 1994). Since the intermediate-term cosmogenic-derived denudation rates (mean ~10 mm ka^{-1}) are broadly comparable with long-term thermochronological rates over the Tertiary, it could be argued that the southern African landscape has been relatively stable since at least the mid-Tertiary, with moderate regional-scale rates of denudation. The low rates mean that locally on thousands of year timescales, the overall appearance of the southern African landscape would not have changed much. On a smaller scale, there may have been some regions of relatively rapid erosion, such as in the headwaters of the Orange River, where cosmogenic-derived denudation rates are as high as 48 mm ka^{-1}. Other parts of the Orange basin, particularly the middle and lower parts, may have maintained low rates of denudation (<10 mm ka^{-1}) over hundreds of thousands, if not millions, of years.

Bedrock channels below the Augrabies main Falls appear to have maintained constant differences in rates with the channels incising roughly twice as fast as the interfluves. As a result, they would have taken up to tens of millions of years to form. Although the result of faster denudation rates in the channels is overall positive relief developing over time, the absolute rates are so low that the same basic morphology would appear to be maintained over tens to hundreds of thousands of years, at least on a local scale, although positive relief would be seen to develop on longer timescales. A similar situation was observed by Bierman & Caffee for the Namibian landscape, where rates are sufficiently low that topography takes many millions of years to develop and, over cosmogenic timescales at least, little change would be seen in the large-scale geomorphology. The importance of local rate differences is emphasised by Moon Rock, whose sides are denuding more rapidly than its summit,

leading to progressive narrowing or 'parallel retreat' following solutional weathering.

10.2.2 Models of landscape evolution

Although the rates of denudation have been fairly low over tens to hundreds of thousands of years (and, indeed, over millions to tens of millions of years from fission track evidence), they have been sufficiently high that Mesozoic erosion surfaces would not have been preserved unmodified in the landscape. Thus a key canon of traditional denudation chronology models of southern African landscape development is undermined. If millimetres to tens of millimetres per thousand years rates of denudation have been maintained over hundreds of thousands of years (which cosmogenic data reveals they have), then the characteristic erosion surfaces of King (1953) and Partridge & Maud (1987) would have been significantly modified over geological time. This provides further evidence to refute the idea that erosion surfaces can be used as a basis for reconstructing landscape history. Even before ideas of denudation chronology became firmly entrenched, Wellington (1955) argued against multiple, discrete erosion events that resulted in the formation of characteristic erosion surfaces. This critique continued with qualitative, theoretical arguments against erosion surfaces for several decades (e.g. de Swardt & Bennett, 1974) until the emergence of the first quantitative data on denudation history from offshore sedimentary records and thermochronology (Rust & Summerfield, 1990; Brown *et al.*, 1990) which categorically showed that denudation has been too rapid to preserve erosion surfaces unmodified over geological timescales. Further thermochronological evidence (e.g. Gleadow and Brown, 2000) and new small-scale cosmogenic data (e.g. Cockburn, 1999; Fleming *et al.*, 1999) discredited traditional denudation chronology theories. Notwithstanding the proposed mechanism of parallel retreat of Moon Rock, the cosmogenic evidence presented here puts the final nail in the coffin of denudation chronology by providing a regional-scale picture of denudation rates for the whole Orange basin over tens of thousands of years which suggests there has been a single, sustained and ongoing 'cycle' of erosion which affects all parts of the landscape.

Low-temperature thermochronological techniques are now complemented by cosmogenic techniques that allow long- and intermediate- term denudation rates to be compared. This study represents one of the few attempts to reconcile long-term low temperature thermochronology-derived denudation rates and intermediate-term cosmogenic-derived regional denudation rates for southern Africa. This comparison has highlighted the essential similarity between long-term and intermediate term rates at the sub-continental scale, and linked the cosmogenic data to more recent decadal scale denudation rates derived from sediment deposits. On a variety of scales, from small catchments to large regional basins, both thermochronological- and cosmogenic-derived denudation rates are very similar. This study represents a significant step in the development of consistent data with which to back up models of southern African landscape evolution (e.g. van der Beek *et al.*, 2002).

The linking of different temporal and spatial scales has been one of the more elusive goals of geomorphology for several decades. The inability to link small temporal and spatial scale processes with large-scale, long-term landform development was arguably one of the reasons for the emergence of the 'two geomorphologies' from the 1950s onwards (Summerfield, 2005b), a schism that still haunts the discipline. Now that cosmogenic techniques provide a means to link small-scale processes with local and regional denudation rates over thousands to hundreds of thousands of years (and, indeed, longer), perhaps geomorphologists have at their disposal a tool that can bring about the 're-enchantment' of geomorphology (Baker & Twidale, 1991; Tooth, 2006). A re-engagement with large scale geomorphology and the reconciliation of small, process-oriented geomorphology and large scale, contingent, landform-oriented geomorphology perhaps awaits. Geomorphologists already have the visual tools for re-engaging with large scale geomorphology (in the form of increasingly sophisticated DEMs and 'virtual globes' such as Google Earth (Tooth, 2006)); they have myriad theoretical models of landscape evolution (which draw to a greater or lesser extent on tectonics and climate as the controlling variables). To echo Molnar (2003), what is now needed is robust data to prove or disprove different theories and models of landscape evolution, to reconcile processes operating on different spatial and temporal scales, to settle the debate on the role of climate and tectonics in

landscape evolution, to quantify the role of denudation in CO_2 drawdown and global climate regulation, and provide 'benchmark' estimates of pre-anthopogenic denudation rates which may be useful in environmental management and the emerging research area of 'earth system science'. Cosmogenic nuclide data, together with fission track and short-term sediment data, provides the means to do this.

10.2.3 Wider significance

The denudation rates reported here provide further evidence to refute 'classical' models of landscape evolution and provide important constraints for numerical surface process models. Combining cosmogenic nuclide analysis with fission track thermochronology provides a powerful means of constraining such models. The data presented here back up data in similar integrated studies from across southern Africa (Fleming *et al.*, 1999; Cockburn *et al.*, 2000; Bierman & Caffee, 2001; van der Wateren & Dunai, 2001). These studies all emphasise the variation in denudation rates on high elevation passive margins on a range of temporal and spatial scales. Thermochronological techniques reveal rates to have been higher in the past, but low to moderate on a regional scale since at least the Tertiary (Gallagher *et al.*, 1999) and indeed into the Quaternary as revealed by cosmogenic techniques. Within this general pattern, rates may vary locally on different timescales.

10.3 Further study

As demonstrated above, establishing the rate and timing of denudation seems to be a much more rewarding area for study rather than correlating erosion surface remnants in order to understand landscape evolution. Cosmogenic nuclide analysis of catchment-averaged sediment offers great potential for understanding regional landscape evolution, particularly where fission track data is also available. Fission track data exist for the major passive margins of southern Africa, Australia and south-eastern Brazil, yet there remains a relative lack of denudation rate data on Quaternary timescales, which could be addressed by cosmogenic techniques. The data presented here represent only a small sample of selected sites in the Orange basin and whilst the data serve to provide the first Quaternary-scale denudation rates

for the Orange, a more systematic approach with many more samples is required to properly understand the evolution of this basin. In particular, the role of lithology and relief in controlling denudation requires study in much greater detail, incorporating sample locations representative of those areas, to properly understand the denudation history of the Orange. Given that climate has varied over much of the period covered by cosmogenic averaging times, unravelling its influence on denudation rates may be much more difficult. Climate is the one variable which trying to understand by means of denudation rates may be something of a tautology and represents a significant challenge to understand properly. A more extensive study is also required to establish whether cosmogenic-derived denudation rates are properly comparable with short-term denudation rates from sediment data, or whether natural differences in lithology and relief can explain the apparent differences between the rates of denudation on short and intermediate timescales. More bedrock samples, in particular from outcrop samples on interfluves across the Orange basin, are required for the fission track data to be directly comparable with the cosmogenic data.

The role of sediment storage has not been fully quantified in this study, so although the catchment-averaged technique is applied to a large basin, the full implications of sediment storage in a potentially sediment-rich basin have not been fully explored. Precisely how much sediment is in the Orange needs to be addressed, as do questions of average travel times of quartz clasts through the basin. Aspects of large river basins which require further study are how large landslides and other high magnitude, low frequency events affect the cosmogenic nuclide concentration of river sediments. In particular, how much, if at all, does mining of river terraces bias cosmogenic nuclide concentrations by adding inherited ^{10}Be concentrations to river sediment. Also, how biased are the rates by landslides which may serve to remove cosmogenic nuclides from a surface and give it, in effect, a 'zero' erosion rate signal, and introduce low nuclide concentration material to a river system. Similarly, the role of large tributaries that either do not contribute quartz or are not hydrologically continuous (in particular the Vaal and the Molopo Rivers) has not been addressed here but remains a potentially significant source of uncertainty in catchment-averaged studies.

The cosmogenic data from the Augrabies region presented here provide important constraints on the timing and extent of denudation of the key controlling landform in the Orange basin. However, time and budgetary constraints prevented a full appraisal of the role of local gradients in different sections of the channels and how this affects stream power, which is manifested in the stream incision rate. The Augrabies region is complex, and large variations in channel widths and depths, stream gradients and discharge essentially control the incision rates. A future study could build on the denudation rates presented here and compare how gradient, discharge, channel roughness and other variables affect incision rates in different anabranches. This would allow the nature of stream capture above the Augrabies main Falls to be elucidated and a more robust discussion of how anabranches 'short circuit' the main Falls in the overall evolution of the Falls system. The background interfluve lowering and channel incision rate data presented here are consistent with the topography of the region, although further work is required to find out the precise nature of the relationships.

The utility of the catchment-averaged technique for large basins has been demonstrated here and adds to a growing body of research being carried out in large basins of the world, e.g. the Yangtze (Chappell, personal communication, 2005) and the Amazon (von Blackenburg, personal communication, 2006). These studies are collectively pushing the boundaries of the cosmogenic technique yet many uncertainties remain, some of which may remain even after better quantification of nuclide production systematics by the CRONUS-EU and CRONUS-Earth projects. Greater attention by geomorphologists to problems of sediment mixing, differential production of sediment, storage and the role of long-term climate change should help to address this.

Reconstructing the Quaternary denudation history of the Orange River basin, southern Africa using cosmogenic ^{10}Be and ^{26}Al analysis

Jonathan J Butler

Volume 2: References and Appendices

PhD

The University of Edinburgh

2007

References

Ahnert, F. (1970). "Functional relationships between denudation, relief, and uplift in large mid-latitude drainage basins." *American Journal of Science* **268**: 243-263.

Allen, P. (2005). "Striking a chord. Landscapes: when perturbed by climatic and tectonic changes, landscapes resonate with a range of frequencies." *Nature* **434**: 961.

Anders, M. D., Pederson, J.L., Rittenour, T.M., Sharp, W.D., Gosse, J.C., Karlstrom, K.E., Crossey, L.J., Goble, R.J., Stockli, L., Yang, G. (2005). "Pleistocene geomorphology and geochronology of eastern Grand Canyon:linkages of landscape components during climate changes." *Quaternary Science Reviews* **24**: 2428-2448.

Annandale, G. W. (1987). *Reservoir sedimentation.* Amsterdam, Elsevier.

Baker, V. R., Twidale, C.R. (1991). "The reenchantment of geomorphology." *Geomorphology* **4**: 73-100.

Balco, G., Stone, J.O.H., Mason, J.A.. (2005). "Numerical ages for Plio-Pleistocene glacial sediment sequences by 26Al/10Be dating of quartz in buried palaeosols." *Earth and Planetary Science Letters* **232**: 179-191.

Bamford, M. K., Grab, S.W. (2005). "Highlights of Quaternary research in Southern Africa, and proceeding forwards." *Quaternary International* **129**(1): 1-3.

Barrows, T. T., Stone, J.O., Fifield, L.K., Cresswell, R.G. (2001). "Late Pleistocene Glaciation of the Kosciuszko Massif, Snowy Mountains, Australia." *55*(179-189).

Beaumont, C. K., H. & Willet, S. (2000). Coupled tectonic-surface process models with applications to rifted margins and collisional orogens. *Geomorphology and Global Tectonics.* M. A. Summerfield. London, Wiley.

Berner, R. A., Lasaga, A. C. and Garrels, R. M. (1983). "The Carbonate-Silicate Geochemical Cycle and Its Effect on Atmospheric Carbon Dioxide over the Past 100 Million Years." *American Journal of Science* **283**: 641-683.

Bezuidenhout, H. (1996). "The maajor vegetation communities of the Augrabies Falls National Park, Northern Cape." *Koedoe* **39**: 7-24.

Bierman, P., Caffee, M.W. (2001). "Slow rates of rock surface erosion and sediment production across the Namib Desert and Escarpment, Southern Africa." *American Journal of Science* **301**: 326-358.

Bierman, P., Caffee, M.W. (2002). "Cosmogenic exposure and erosion history of Australian bedrock landforms." *Geological Society of America Bulletin* **114**(7): 787-803.

Bierman, P., Steig, E.J. (1996). "Estimating rates of denudation using cosmogenic isotope abundances in sediment." *Earth Surface Processes and Landforms* **21**(2): 125-139.

Bierman, P., Turner, (1994). "Using in situ produced cosmogenic isotopes to estimate rates of landscape evolution: A review from the geomorphic perspective." *Journal of Geophysical Research* **99**(B7): 13,885-13,896.

Bierman, P. R., Caffee, M.W., Thomson Davis, P., Marsella, K., Pavich, M., Coglan, P., Mickelson, D., Larsen, J. (2002). "Rates and Timing of Earth Surface Processes from *In Situ*-Produced Cosmogenic Be-10." *Reviews in Mineralogy and Geochemistry* **50**: 147-205.

Bierman, P. R., Nichols, K.K. (2004). "Rock to Sediment - Slope to Sea with 10Be - Rates of Landscape Change." *Annual Review of Earth and Planetary Sciences* **32**: 215-155.

Bierman, P. R., Turner, J. (1995). "10Be and 26Al evidence of exceptionally low rates of bedrock ersoion and the likely existence of pre-Pleistocene landscapes." *Quaternary Research* **44**: 378-382.

Bierman, P. R., Turner, J. (1997). "Reply to Comment by C. Rowland Twidale." *Quaternary Research* **48**: 386-389.

Binnie, S. (2004). 'Deriving basin-wide denudation rates from cosmogenic radionuclides, San Bernardino Mountains, California'. PhD thesis, School of Geosciences, University of Edinburgh.

Boardman, J., Parsons, A.J., Holland, R., Holmes, P.J., Washington, R. (2003). "Development of badlands and gullies in the Sneeuberg, Great Karoo, South Africa." *Catena* **50**: 165-184.

Boaretto, E., Berkovits, D., Hass, M., Hui, S.K., Kaufman, A., Paul, M., Weiner, S. (2000). "Dating of prehistoric caves sediments and flints using 10Be and 26Al in quartz from Tabun Cave (Israel): Progress report." *Nuclear Instruments and Methods in Physics Research B* **172**: 767-771.

Bordy, E. M., Hancox, P.J., Rubidge (2004). "Basin development during the deposition of the Elliot Formation (late Triassic - Earlt Jurassic), Karoo Supergroup, South Africa." *South African Journal of Geology* **107**: 397-412.

Bordy, E. M., Hancox, P.J., Rubidge (2004). "Fluvial syle variations in the Late Triassic-Early Jurassic Elliot formation, main Karro Basin, South Africa." *Journal of African Earth Sciences* **38**: 383-400.

Bornhardt, W. (1900). *Zur Oberflächengestaltung und Geologie Deutsch Ostafrikas.* Berlin, Reimer.

Braucher, R., Bourlès, D.L., Brown, E.T., Colin, F., Muller, J.-P., Braun, J.-J., Delaune, M., Minko, A.E., Lescouet, C., Raisbeck, G.M., Yiou, F. (2000). "Application of in situ-produced cosmogenic 10Be and 26Al to the study of lateritic soil development in tropical forest: theory and examples from Cameroon and Gabon." *Chemical Geology* **170**: 95-111.

Braucher, R., Bourlès, D.L., Colin, F., Brown, E.T., Boulangé, B. (1998). "Brazilian laterite dynamics using in situ-produced 10Be." *Earth and Planetary Science Letters* **163**: 197-205.

Bremner, J. M., Rogers, J., Willis, J.P. (1990). "Sedimentological aspects of the 1988 Orange River floods." *Transactions, Geological Society of South Africa* **47**(3): 247-294.

Brocard, G. Y., van der Beek, P.A., Bourlès, D.L., Siame, L.L., Mugnier, J.-L. (2003). "Long term fluvial incision rates and postglacial river relaxation time in the French Western Alps from 10Be dating of alluvial terraces with assessment of inheritance, soil development and wind ablation effects." *Earth and Planetary Science Letters* **209**: 197-214.

Brown, E. T., Bendick, R., Bourlès, D.L., Gaur, V., Molnar, P., Raisbeck., G.M., Yiou, F. (2002). "Slip rates of the Karakoram fault, Ladakh, India, determined using cosmic ray exposure dating of debris flows and moraines." *Journal of Geophysical Research* **207**(B9).

Brown, E. T., Bourlès, D.L., Colin, F., Raisbeck, G.M., Yiou, F., Desgareaux, S. (1995). "Evidence for muon-induced production of 10Be in near-surface rocks from the Congo." *Geophysical Research Letters* **22**(6): 703-706.

Brown, E. T., Colin, F., Bourlès, D.L. (2003). "Quantitative evaluation of soil processes using in situ-produced cosmogenic nuclides." *Competes Rendus Geoscience* **335**: 1161-1171.

Brown, E. T., Molnar, P., Bourlès, D.L. (2005). "Comment on 'slip rate measurements on the Karakorum Fault may imply secular variations in fault movements'." *Science* **309**: 1326.

Brown, E. T., Stallard, R.F., Larsen, M.C., Bourlès, D.L., Raisbeck., G.M., Yiou, F. (1998). "Determination of predevelopment denudation rates of an agricultural watershed (Cayaguás River, Puerto Rico) using in-situ-produced 10Be in river-borne quartz." *Earth and Planetary Science Letters* **160**: 723-28.

Brown, R. W., Gallagher, K., Gleadow, A.J.W. and Summerfield, M.A. (2000). Morphotectonic evolution of the South Atlantic margins of Africa and South America. *Geomorphology and Global Tectonics*. M. A. Summerfield. Chicheter, John Wiley and Sons Ltd**:** 257-283.

Brown, R. W., Rust, D.J., Summerfield, M.A., Gleadow, A.J.W., de Wit, M.C.J. (1990). "An Early Cretaceous phase of accelerated erosion on the south-western margin of Africa: evidence from apatite fission track analysis and the offshore sedimentary record." *International Journal of Radioation Applications and Instrumentation. Part D. Nuclear Tracks and Radiation Measurements* **17**(3): 339-350.

Brown, R. W., Summerfield, M.A., Gleadow, A.J.W. (2002). "Denudational history along a transect across the Drakensberg Escarpment of southern Africa derived from apatite fission track thermochronology." *Journal of Geophysical Research* **107**(B12): 11-1-11-13.

Brunsden, D., Thornes, J.B. (1979). "Landscape sensitivity and change." *Transactions, Institute of British Geographers* **4**(4): 449-462.

Burbank, D. W., Blythe, A.E., Pratt-Sitaula, B., Gabet, E., Oskin, M., Barros, A., Ojha, T.P. (2003). "Decoupling of erosion and precipitation in the Himalayas." *Nature* **426**: 652-655.

Burke, K. (1996). *South African Journal of Geology* **99**(341).

Büdel, J. (1982). *Climatic Geomorphology*. Princeton, New Jersey, Princeton University Press.

Butzer, K. W., Helgren, D.M., Fock, G.J., Stuckenrath, R. (1973). "Alluvial terraces of the Lower Vaal River, South Africa: a reappraisal and reinvestigation." *Journal of Geology* **81**: 341-162.

Carr, A. S., Thomas, D.S.G., Bateman, M.D. (2006). "Climatic and sea level controls on Late Quaternary eolian activity on the Agulhas Plain, South Africa." *Quaternary Research* **65**: 252-263.

Catuneanu, O., Hancox, P.J., Rubidge, B.S. (1998). "Reciprocal flexural behaviour and contrasting stratigraphies: a new basin development model for the Karoo retroarc foreland system, South Africa." *Basin Research* **10**: 417-39.

Catuneanu, O. (2004). "Basement control on fluxural profiles and the distribution of foreland facies: The Dwyka Group of the Karoo Basin, South Africa." *Geology* **32**(6): 517-520.

Catuneanu, O., Wopfner, H., Eriksson, P.G., Cairncross, B., Rubidge, B.S., Smithm R.M.H., Hancox, P.J. (2005). "The Karoo Basins of south-central Africa." *Journal of African Earth Sciences* **43**: 211-253.

Chevalier, M.-L., Ryerson, F.J., Tapponier, P., Finkel, R.C., Van Der Woerd, J., Haibing, L., Qing, L. (2005). "Slip-rate measurements on the Karakoram Fault may imply secular variations in fault motion." *Science* **307**: 411-414.

Chorley, R. J. (1963). "Diastrophic Background to Twentieth-Century Geomorphological Thought." *Geological Society of America Bulletin* **74**: 953-970.

Chorley, R. J. (1965). A re-evaluation of the Geomorphic System of W.M.Davis. *Frontiers in Geographical Teaching*. R. J. Chorley, Haggett. London, Methuen.

Church, M. (1996). Space, time and the mountain - how do we order what we see? *The Scientific Nature of Geomorphology*. B. Rhoads, Thorn, C.E. London, John Wiley & Sons Ltd.

Church, M. (2005). "Continental drift." *Earth Surface Processes and Landforms* **30**: 129-130.

Clapp, E. M., Bierman, P.R., Caffee, M. (2002). "Using 10Be and 26Al to determine sediment generation rates and identify sediment source areas in an arid region drainage basin." *Geomorphology* **45**: 89-104.

Clapp, E. M., Bierman, P.R., Nichols, K.K., Pavich, M. Caffee, M. (2001). "Rates of sediment supply to arroyos from upland erosion determined using in situ cosmogenic 10Be and 26Al." *Quaternary Research* **55**: 235-245.

Clapp, E. M., Bierman, P.R., Schick, A.P., Lekach, J., Enzel, Y., Caffee, M. (2000). "Sediment yield exceeds sediment production in arid region drainage basins." *Geology* **28**(11): 995-998.

Cockburn, H. A. P., Brown, R.W., Summerfield, M.A., Seidl, M.A. (2000). "Quantifying passive margin denudation and landscape development using a combined fission-track thermochronology and cosmogenic isotope analysis approach." *Earth and Planetary Science Letters* **179**: 429-435.

Cockburn, H. A. P., Seidl, M.A., Summerfield, M.A. (1999). "Quantifying denudation rates on inselbergs in the central Namib Desert using in-situ produced cosmogenic 10Be and 26Al." *Geology* **27**(5): 399-402.

Cockburn, H. A. P., Summerfield, M.A. (2000). "A progress report on the use of *in-situ*-produced cosmogenic isotopes to evaluate rates of landscape development in central Namibia." *Communications, Geological Survey of Namibia* **12**: 403-408.

Cockburn, H. A. P., Summerfield, M.A. (2004). "Geomorphological applications of cosmogenic isotope analysis." *Progress in Physical Geography* **27**(4): 612-653.

Codilean, A. T. (2006). "Calculation of the cosmogenic nuclide production topographic shielding scaling factor for large areas using DEMs." *Earth Surface Processes and Landforms* **31**: 785-794.

Constable, C., Korte, M. (2006). "Is Earth's magnetic field reversing?" *Earth and Planetary Science Letters* **246**: 1-16.

Cox, K. G. (1988). The Karoo Province. *Continental Flood Basalts*. J. D. Macdougall, Kluwer: 239-271.

Dadson, S. J., Hovius, N., Chen, H., Dade, W.B., Hsleh, M.L., Willett, S.D., Hu, J.C., Horng, M.J., Chen, M.J., Stark, C.P., Lague, D., Lin, J.C. (2003). "Links between erosion, runoff variability and seismicity in the Taiwan orogen." *Nature* **426**: 648-651.

Dardis, G. F., Moon, B.P. (eds) (1988). *Geomorphological Studies in Southern Africa*. Rotterdam, A.A.Balkema.

Davis, W. M. (1899). "The geographical cycle."

De Wit, M. C. J. (1999). "Post-Gondwana drainage and the development of diamond placers in western South Africa." *Economic Geology* **94**: 721-40.

de Wit, M. C. J., Marshall, T.R., Partridge (2000). Fluvial deposits and drainange evolution. *The Cenozoic of southern Africa*. T. C. Partridge, Maud, R.R. Oxford, Oxford University Press.

De Wit, M. J., Ransome, I.G.D. (1992). *Inversion tectonics of the Cape Fold Belt, Karoo and Cretaceous of southern Africa*. Rotterdam, A.A. Balkema.

De Swart, A. M. I. B., G. (1974). "Structure and physiographic development of Natal since late Jurassic times." *Transactions, Geological Society of South Africa* **77**(309-32).

Desilets, D., Zreda, M. (2006). "Extended scaling factors for in situ cosmogenic nuclides: New measurements at low latitude." *Earth and Planetary Science Letters* **246**: 265-276.

Dingle, R. V., Hendey, Q.B. (1984). "Late Mesozoic and Tertiary sediment supply to the Eastern Cape Basin (SE Atlantic) and palaeo-drainage systems in Southwestern Africa." *Marine Geology* **56**: 13-26.

Dingle, R. V., Siesser, W.G., Newton, A.R. (1983). *Mesozoic and Tertiary Geology of Southern Africa*. Rotterdam, A.A.Balkema.

Dunai, T. J. (2000). "Scaling Factors for production rates of in situ produced cosmogenic nuclides: a critical reevaluation." *Earth and Planetary Science Letters* **176**: 157-169.

Dunai, T. J., González López, G.A., Juez-Larré, J. (2005). "Oligocene-Miocene age of aridity in the Atacama Desert revealed by exposure dating of erosion-sensitive landforms." *Geology* **33**(4): 321-324.

Dunne, J., Elmore, D., Muzikar, P. (1999). "Scaling factors for the rates of production of cosmogenic nuclides for geometric shielding and attenuation at depth on sloped surafces." *Geomorphology* **27**: 3-11.

Dupont, L., Behling, H. (2006). "Land-sea linkages during deglaciation: High-resolution records from the eatern Atlantic off the coast of Namibia and Angola." *Quaternary International* **148**: 19-28.

Dury, G. H. (1976). *The Face of the Earth.* Harmondsworth, Penguin.

Einsele, G., Hinderer, M. (1997). "Terrestrial sediment yield and the lifetimes of reservoirs, lakes and larger basins." *Geol Rundsch* **86**: 288-310.

Eriksson, P. G., McCourt, S., Snyman, C.P. (1994). "A note on the petrology of upper Karoo sandstones in the Natal Drakensberg: implications for the Clarens Formation palaeoenvironment." *South African Journal of Geology* **97**(1): 101-103.

Fabel, D., Fink, D., Fedin, O., Harbor, J., Stroeven, A.P. (2006). "Exposure ages from relict lateral moraines overriden by the Fennoscandian ice sheet." *Quaternary Research* **65**: 136-146.

Ferrier, K. L., Kirchner, J.W., Finkel, R.C. (2005). "Erosion rates over millennial and decadal timescales at Caspar Creek and Redwood Creek, Northern California Coast Ranges." *Earth Surface Processes and Landforms* **30**: 1025-1038.

Fjellanger, J., Sorbel, L., Linge, H., Brook, E.J., Raisbeck, G.M., Yiou, F. (in press). "Glacial survival of blockfields on the Varanger Peninsula, northern Norway." *Geomorphology.*

Fleming, A., Summerfield, M.A., Stone, J.O., Fifield, L.K., Cresswell, R.G. (1999). "Denudation rates for the southern Drakensberg escarpment, SE Africa, derived from *in-situ*-produced cosmogenic 36Cl: initial results." *Journal of the Geological Society of London* **156**: 209-212.

Foster, I. D. L., Boardman, J, Keay-Bright, J. & Meadows, M.E. (2005). Land degradation and sediment dynamics in the South African Karoo. *Sediment Budgets 2 (IAHS Symposium, Foz do Iguacu, Brazil, April 2005).* A. J. W. Horowitz, D.E., IAHS Publication. **292:** 207-213.

Foster, I. D. L., Boardman, J. & Keay-Bright (in press). "The contribution of sediment tracing to an investigation of the environmental history of two small catchments in the uplands of the Karoo, South Africa." *Geomorphology.*

Fox, R. (2000). Agriculture and rural development. *The Geography of South Africa in a Changing World.* R. Fox, Rowntree, K. Cape Town., Oxford University Press.

Frye, J. C. (1958). "Climate and Lester King's 'Uniformitarian nature of hillslopes'." 111-113.

Gallagher, K. a. Brown., R.W (1999a). The Mesozoic denudation history of the Atlantic margins of southern Africa and southeast Brazil and the relationship to offshore sedimentation. *The Oil and Gas Habitats of the South Atlantic*. R. B. N. Cameron, V. Clure. London, The Geological Society. **153:** 41-53.

Gallagher, K. a. Brown., R.W (1999b). "Denudation and uplift at passive margins: the record on the Atlantic Margin of southern Africa." *Philosophical Transactions of the Royal Society, London* **357**: 835-859.

Gallagher, K., Brown, R.W. and Johnson, C. (1998). "Fission track analysis and its applications to geological problems." *Annual Review of Earth and Planetary Sciences* ***26***: 519-572.

Gellis, A. C., Pavich, M.J., Bierman, P.R., Clapp, E.M., Ellevein, A., Aby, S. (2004). "Moden sediment yield compared to geological rates of sediment production in a semi-arid basin, New Mexico: assessing the human impact." *Earth Surface Processes and Landforms* **29**: 1359-1372.

Gilchrist, A. R., & Summerfield, M.A. (1990). "Differential denudation and flexural isostacy in formation of rifted-margin upwarps." *Nature* **346**: 739-742.

Gilchrist, A. R., & Summerfield, M.A. (1991). "Denudation, isostacy and landscape evolution." *Earth Surface Processes and Landforms* **16**: 555-562.

Gilchrist, A. R., Kooi, H., Beaumont, C. (1994). "Post-Gondwana geomorphic evolution of southwestern Africa: Implications for the controls on landscape development from observations and numerical experiments." *Journal of Geophysical Research* **99 B6**: 12,211-12,228.

Gleadow, A. J. W., Kohn, B.P., Brown, R.W., O'Sullivan, P.B. and Raza, A. (2002). "Fission track thermotectonic imaging of the Australian continent." *Tectonophysics* **349**: 5-21.

Gleadow, A. J. W., Brown, R.W. (2000). Fission track thermochronology and the long-term denudational response to tectonics. *Geomorphology and Global Tectonics*. M. A. Summerfield. Chichester, John Wiley and Sons Ltd**:** 57-75.

Gosse, J. C., Evenson, E.B., Klein, J., Lawn, B., Middleton, R. (1995). "Precise cosmogenic 10Be measurements in western North America: support for a global Younger Dryas cooling event." *23* **10**(877-880).

Gosse, J. C., Phillips, F.M. (2001). "Terrestrial in situ cosmogenic nuclides: theory and application." *Quaternary Science Reviews* **20**: 1475-1560.

Goudie, A. S. (1997). The geomorphology of the seasonal tropics. *The physical geography of Africa*. W. M. Adams, Goudie, A.S., Orme, A.R. Oxford, Oxford University Press**:** 148-172.

Goudie, A. S. (2005). "The drainage of Africa since the Cretaceous." *Geomorphology* **67**: 437-456.

Granger, D. E., Fabel, D., Palmer, A.N. (2001). "Pliocene-Pleistocene incision of the Green River, Kentucky, determined from radioactive decay of cosmogenic 26Al and 10 Be in Mammoth Cave sediments." *GSA Bulletin* **113**(July 2001): 825-836.

Granger, D. E., Kirchner, J.W., Finkel, R. (1996). "Spatially averaged long-term erosion rates measured from in situ produced cosmogenic nuclides in alluvail sediment." *The Journal of Geology* **104**: 249-257.

Granger, D. E., Kirchner, J.W., Finkel, R. (1997). "Quaternary downcutting rate of the New River, Virginia, measured from differential decay of cosmogenic 26Al and 10 Be in cave-deposited alluvium." *Geology* **25**(2): 107-110.

Granger, D. E., Muzikar, P.F. (2001). "Dating sediment burial with in-situ produced cosmogenic nuclides: theory, techniques and limitations." *Earth and Planetary Science Letters* **188**: 269-281.

Green, E. G., Dietrich, W.E., Banfield, J.F. (2006). "Quantification of chemical weathering rates across an actively eroding hillslope." *Earth and Planetary Science Letters* **242**: 155-169.

Guyodo, Y., Valet, J. (1996). "Relative variations in geomagnetic intensity from sedimentary records: the past 200,000 years." *Earth and Planetary Science Letters* **143**: 23-36.

Guyodo, Y., Valet, J. (1999). "Global changes in intensity of the earth's magnetic field during the past 800kyr." *Nature* **399**: 249-252.

Hack, J. (1960). "Interpretation of erosional topography in humid temperate regions:." *American Journal of Science* **257A**: 80-97.

Hancock, G. S., Anderson, R.S., Chadwick, O.A., Finkel, R.C. (1999). "Dating fluvial terraces with 10Be and 26Al: application to the Wind River, Wyoming." *Geomorphology* **27**: 41-60.

Harman, R., Gallagher, K., Brown, R., Raza, A. and Bizzi, L. (1998). "Accelerated denudation and tectonic/geomorphic reactivation of the cratons of northeastern Brazil during the Late Cretaceous." *Journal of Geophysical Research* **103**: 27,091-27,105.

Heimsath, A. M., Chappell, J., Dietrich, W.E., Nishiisumi, K., Finkel, R.C. (2000). "Soil production on a retreating escarpment in southeastern Australia." *Geology* **28**(9): 787-790.

Heimsath, A. M., Dietrich, W.E., Nishiizumi, K., Finkel, R.C. (2001). "Stochastic Processes of Soil Production and Transport: Erosion Rates, Topographic Variation

and Cosmogenic Nuclides in the Oregon Coast Range." *Earth Surface Processes and Landforms* **26**: 531-552.

Heimsath, A. M., Dietrich., W.M., Nishiizumi, K., Finkel, R.C. (1997). "The soil production function and landscape equilibrium." *Nature* **388**(358-361).

Heisinger, B., Lal, D., Jull, A.J.T., Kubik, P., Ivy-Ochs, Knie, K., Nolte, E. (2002b). "Production of selected cosmogenic radionuclides by muons: 2. Capture of negative muons." *Earth and Planetary Science Letters* **200**: 357-369.

Heisinger, B., Lal, D., Jull, A.J.T., Kubik, P., Ivy-Ochs, S., Neumaier, S., Knie, K., Lazarev, V., Nolte, E. (2002a). "Production of selected cosmogenic radionuclides by muons 1. fast muons." *Earth and Planetary Science Letters* **200**: 345-355.

Helgren, D. M. (1979). *River of Diamonds: an alluvial history of the Lower Vaal River*. Chicago, University of Chicago Press.

Helgren, D. M., Butzer, K.W. (1974). "Alluvial terraces of the Lower Vaal River, South Africa: a reappraisal and reinvestigation: A reply." *Journal of Geology* **82**: 665-667.

Hewawasam, T., von Blanckenburg, F., Schaller, M., Kubik, P. (2003). "Increase of human over natural erosion rates in tropical highlands constrained by cosmogenic nuclides." *Geology* **31**(7): 597-600.

Holmes, P. J., Boardman, J., Parsons, A.J., Marker, M.E. (2004). "Geomorphological palaeoenvironments of the
Sneeuberg Range, Great Karoo, South Africa." *Journal Of Quaternary Science* **18**(8): 801-813.

Holmgren, K., Lee-Thorp, J.A., Cooper, G.R.J., Lundblada, K., Partridge, T.C., Scott, L., Sithaldeen, R., Talmaf, A.S., Tyson, P.D. (2003). "Persistent millennial-scale climatic variability over the past 25,000 years in Southern Africa." *Quaternary Science Reviews* **22**: 2311-2326.

Ivy-Ochs, S., Schülter, C., Kubik, P.W., Denton, G.H. (1999). "Moraine exposure dates imply synchronous Younger Dryas glacier advances in the European Alps and in the Southern Alps of New Zealand." *Geografiska Annaler* **81**(2): 313-323.

Jackson, J., Ritz, J., Siame, L., Raisbeck, G., Yiou, F., Norris, R., Youngson, J., Bennett, E. (2002). "Fault growth and landscape development rates in Otago, New Zealand, using in situ cosmogenic 10Be." *Earth and Planetary Science Letters* **195**: 185-193.

Jull, A. J. T., Burr, G.S. (2006). "Accelerator mass spectrometry: is the future bigger or smaller?" *Earth and Planetary Science Letters* **243**: 305-325.

Kaplan, M. R., Douglass, D.C., Singer, B.S., Ackert, R.P., Caffee, M.W. (2005). "Cosmogenic nuclide chronology of pre-last glacial maximum moraines at Lago Buenos Aires, 46°S, Argentina." *Quaternary Research* **63**: 301-315.

Keay-Bright, J., Boardman, J. (2006). "Changes in the distribution of degraded land over time in the central Karoo, South Africa." *Catena* **67**: 1-14.

Kent, L. E. (1980). Stratigraphy of South Africa: Lithostratigraphy of the the Republic of South Africa, South West Africa/Namibia and the Republics of Bophuthatswana, Transkei and Venda. Pretoria, Republic of South Africa Department of Mineral and Energy Affairs.

Kim, K. J., Englert, P.A.J. (2004). "Profiles of in situ 10Be and 26Al at great depths in the Macraes Flat, East Otago, New Zealand." *Earth and Planetary Science Letters* **223**: 113-126.

Kim, K. J., Imamura, M. (2004). "Exposure dating of underwater rocks: potential application to studies of land bridges during the Ice Ages." *Nuclear Instruments and Methods in Physics Research B* **223-224**: 608-612.

King, L. C. (1944). "Geomorphology of the Natal Drakensberg." *Transactions, Geological Society of South Africa* **47**(255-282).

King, L. C. (1949). "A theory of bornhardts." *Geographical Journal* **112**: 83-87.

King, L. C. (1951). *South African Scenery: A textbook of geomorphology.* Edinburgh, Oliver & Boyd.

King, L. C. (1953). "Canons of landscape evolution." *Bulletin of the Geological Society of America* **64**: 721-752.

King, L. C. (1962). *Morphology of the Earth. First Edition.* Edinburgh, Oliver & Boyd.

King, L. C. (1967). *Morphology of the Earth. Second Edition.* Edinburgh, Oliver & Boyd.

King, L. C. (1976). "Comment upon two papers concerning the geomorphology of Natal." *Transactions, Geological Society of South Africa* **79**(1): 149-151.

Kirby, E., Burbank, D.W., Reheis, M., Phillips, F. (in press). "Temporal variations in slip rate of the White Mountain Fault Zone, Eastern California." *Earth and Planetary Science Letters.*

Kirchner, J. W., Finkel, R.C., Riebe, C.S., Granger, D.E., Clayton, J.L., King, J.G., Megahan, W.F. (2001). "Mountain erosion over 10yr, 10k.y., and 10m.y. time scales." *Geology* **29**(7): 591-594.

Kirchner, J. W., Riebe, C.S., Ferrier, K.L., Finkel, R.C. (2006). "Cosmogenic nuclide methods for measuring long-term rates of physical erosion and chemical weathering." *Journal of Geochemical Exploration* **88**: 296-299.

Kohn, B. P., Gleadow, A.J.W., Brown, R.W., Gallagher, K., O'Sullivan, P.B., Foster, D.A. (2002). "Shaping the Australian crust over the last 300 million years: Insights from fission track thermotectonic and denudation studies of key terranes, Australian." *Australian Journal of Earth Sciences* **153**: 41-53.

Kooi, H., Beaumont, C. (1996). "Large-scale geomorphology: Classical concepts reconciled and integrated with contemporary ideas via a surface process model." *Journal of Geophysical Research* **101 B2**: 3361-3386.

Kutzbach, J., Bonan, G., Foley, J., Harrison, S.P. (1996). "Vegetation and soil feedbacks on the response of the African monsoon to orbital forcing in the early to middle Holocene." *Nature* **384**: 623-626.

Kutzbach, J., Liu, Z. (1997). "Response of the African Monsoon to Orbital Forcing and Ocean Feedbacks in the Middle Holocene." *Science* **278**: 440-443.

Lal, D. (1988). "In situ-produced cosmogenic isotopes in terrestriral rocks." *Annual Review of Earth and Planetary Sciences* **16**: 355-88.

Lal, D. (1991). "Cosmic ray labelling of erosion surfaces: in situ nuclide production rates and erosion models." *Earth and Planetary Science Letters* **104**: 424-439.

Lal, D., Arnold, J.R. (1985). "Tracing quartz through the environment." *Proceedings, Indian Academy of Sciences (Earth Science)* **94**(1).

Lal, D., Gallup, C.D., Somayajulu, B.K., Vacher, L., Caffee, M.W., Jull, A.J.T., Finkel, R. Speed, R.C., Winters, A. (2005). "Records of cosmogenic radionuclides 10Be, 26Al and 36Cl in corals: First studies on coral erosion rates and potential of dating very old corals." *Geochimica et Cosmochemica Acta* **69**(24): 5717-5728.

Lal, D., Harris, N.B.W., Sharma, K., Gu, Z., Ding, L., Liu, T., Dong, W., Caffee, M.W., Jull, A.J.T. (2003). "Erosion history of the Tibetan Plateau since the last interglacial: constraints from the first studies of cosmogenic 10Be from Tibetan bedrock." *Earth and Planetary Science Letters* **217**: 33-42.

Leopold, L. B., Emmett, W.W., Myrick, R.M. (1966). "Channel and hillslope processes in a semi-arid area, New Mexico." *United States Geological Survey Profesional Paper* **352G**: 153-253.

Lewis, C. A. (2005). "Late Glacial and Holocene palaeoclimatology of the Drakensberg of the Eastern Cape, South Africa." *Quaternary International* **129**(1): 22-48.

Lifton, N. A., Jull, A.J.T., Quade, J. (2001). "A new extraction technique and production rate estimate for in situ cosmogenic 14C in quartz." *Geochimica et Cosmochimica Acta* ***65***(12): 1953-1969.

Lifton, N. A., Bieber, J.W., Clem, J.M., Duldig, M.L., Evenson, P., Humble, J.E., Pyle, R. (2005). "Addressing solar modulation and long-term uncertainties in scaling secondary cosmic rays for in situ cosmogenic nuclide applications." *Earth and Planetary Science Letters* **239**(140-161).

Lorenc, M. w., Barco, P.M., Saavedra, J. (1994). "The evolution of potholes in granite bedrock, W Spain." *Catena* **22**: 265-274.

Lovegrove, B. (1993). *The Living Deserts of Southern Africa*. Vlaeberg, South Africa, Fernwood
Press.

Lowe, J. J., Walker, M.J.C. (1997). Reconstructing Quaternary Environments. London, Prentice Hall.

Margerison, H. R., Phillips, W.M., Stuart, F.M., Sugden, D.E. (2005). "Cosmogenic 3He concentrations in ancient flood deposits from the Coombs Hills, northern Dry Valleys, East Antarctica: interpreting exposure ages and erosion rates." *Earth and Planetary Science Letters* **230**: 163-175.

Masarik, J., Reedy, R.C. (1995). "Terrestrial cosmogenic-nuclide production systematics calculated from numerical simulations." *Earth and Planetary Science Letters* **136**: 381-395.

Matmon, A., Bierman, P.R., Larsen, J., Southworth, S., Pavich, M., Caffee, M. (2003). "Temporally and spatially uniform rates of erosion in the southern Appalachian Great Smoky Mountains." *Geology* **32**(2): 155-158.

Mc Carthy, T. S., Tooth, S. (2004). "Incised meanders along the mixed bedrock-alluvial Orange River, Northern Cape Province, South Africa." *Zietschrift fur Geomorphologie N.F.* **48**(3): 273-292.

Mc Clymont, E. L., Rosell-Melè, Giraudeau, J., Pierre, C., Lloyd, J.M. (2005). "Alkenone and coccolith records of the mid-Pleistocene in the south-east Atlantic: Implications for the U^K^37 index and South African climate." *Quaternary Science Reviews* **24**: 1559-1572.

Mc Ilhenny, Senanayake, (1982). "Variations in the Geomagnetic Dipole I: The Past 50000 years." *J. Geomag. Geoelectr* **34**: 39.

Meadows, M. E., Hoffman, M.T. (2002). "The nature, extent and causes of land degradation in South Africa: legacy of the pas, lessons for the future?" *Area* **34**(4): 428-437.

Meybeck, M. (1976). "Total mineral dissolved transport by world major rivers." *Hydrological Sciences Bulletin* **21**(265-284).

Meybeck, M. (1987). "Global chemical weathering of surficial rocks estimated from river dissolved loads." *American Journal of Science* **287**: 401-428.

Middleton, R., Brown, L., Dezfouly-Arjomandy, B., Klein, J. (1993). "On 10Be standards and the Half-life of 10Be." *Nuclear Instruments and Methods in Physics Research B* **82**(399).

Milliman, J. D., Meade, R.H. (1983). "World-wide delivery of river sediments to the oceans." *Jounal of Geology* **91**(1): 1-21.

Millot, R., Gaillardet, J., Dupré, B., Allègre, C.J. (2002). "The global control of silicate weathering rates and the coupling with physical erosion: new insights from the rivers of the Canadian Shield." *Earth and Planetary Science Letters* **196**: 83-98.

Mills, S. C., Grab, S.W. (2005). "Debris ridges along the southern Drakensberg escarpment as evidence for Quaternary glaciation in southern Africa." *Quaternary International* **129**(1): 61-73.

Moen, H. F. G. (1984). Die geologie can die Riemsvasmaakgebied en die Augrabies Nasionale Park, Council for Geoscience.

Molnar, P., England, P. (1990). "Late Cenozoic uplift of mountain ranges and global climate change: chicken or egg?" *Nature* **346**(6279): 29-34.

Molnar, P. (2003). "Nature, Nurture and landscape." *Nature* **426**: 612-614.

Morel, P., von Blanckenburg, F., Schaller, M., Kubik, P.W., Hinderer, M. (2003). "Lithology, landscape dissection and glaciation controls on catchment erosion as determined by cosmogenic nuclides in river sediment (the Wutach Gorge, Black Forest)." *Terra Nova* **15**(6): 398-404.

Motha, J. A., Wallbrink, P.J., Hairsine, P.B., Grayson, R.B. (2004). "Unsealed roads as suspended sediment sources in an agricultural catchment in south-eastern Australia." *Journal of Hydrology* **286**: 1-18.

Mountjoy, A. B., Mountjoy, C. (1965). *Africa, A Geographical Study*. London, Hutchinson.

Munyikwa, K. (2005). "Synchrony of Southern Hemisphere Late Pleistocene arid episodes: A review of luminescence chronologies from arid aeolian landscapes south of the Equator." *Quaternary Science Reviews* **24**: 2555-2583.

Muzikar, P., Granger, D. (2006). "Combining cosmogenic, stratigraphic, and paleomagnetic information using a Bayesian approach: General results and an application to Sterkfontein." *Earth and Planetary Science Letters* **243**: 400-408.

Nanson, G. C., Croke, J.C. (1992). "A genetic classification of floodplains." *Geomorphology* **4**: 459-486.

Nichols, K. K., Bierman, P.R., Caffee, M., Finkel, R., Larsen, J. (2005). "Cosmogenically enabled sediment budgeting." *Geology* **33**(2): 133-136.

Nichols, K. K., Bierman, P.R., Hooke, R.LeB., Clapp, E.M., Caffee, M. (2002). "Quantifying sediment transport on desert piedmonts using 10Be and 26Al." *Geomorphology* **45**: 105-125.

Nishiizumi., K., C.P., K., Arnold, J.R., Klein, J., Fink, D., Middleton, R. (1991). "Cosmic ray produced 10Be and 26Al in Antarctic rocks: exposure and erosion history." *Earth and Planetary Science Letters* **104**: 440-454.

Nishiizumi, K., Finkel, R.C., Ca!ee, M.W., Southon, J.R., Kohl, C.P., Arnold, J.R., Olinger, C.T., Poths, J. and Klein, J., (1994). "Cosmogenic production of ^{10}Be and ^{26}Al on the surface of the earth and underground, Eighth International Conference on Geochronology, Cosmochronology and Isotope Geochemistry (U.S. Geol. Surv. Circular 1107), Berkeley, California, 234 pp.

Nishiizumi., K., Winterer, E.L., Kohl, C.P., Klein, J. (1989). "Cosmic Ray Production Rates of 10Be and 26Al in Quartz From Glacially Polished Rocks." *Journal of Geophysical Research* **94**(B12): 17,907-17,915.

Ohno, M., Hamano, Y. (1992). "Geomagnetic poles over the past 10,000 years." *Geophysical Research Letters* **19**(16): 1715-1718.

Ollier, C. (1995). "Classics in physical geography revisited: King, L.C., Canons of landscape evolution." *Progress in Physical Geography* **19**(3): 371-377.

Ollier, C. D., Pain, C.F. (1997). "Equating the basal unconformity with the palaeoplain: a model for passive margins." *Geomorphology* **19**: 1-15.

Osmaston, H. A., Harrison, S.P. (2005). "The Late Quaternary glaciation of Africa: A regional synthesis." *Quaternary International* **138-139**: 32-54.

Owen, L. A., Finkel, R.C., Barnard, P.L., Haizhou, M., Asahi, K., Caffee, M.W., Derbyshire, E. (2005). "Climatic and topographic controls on the style and timing of Late Quaternary glaciation throughout Tibet and the Himalaya defined by 10Be cosmogenic surafce exposure dating." *Quaternary Science Reviews* **24**: 1391-1411.

Partridge, T. C. (1997). "Cainozoic environmental change in southern Africa, with special emphasis on the last 200,000 years." *Progress in Physical Geography* **21**(1): 3-22.

Partridge, T. C. (1997). Evolution of Landscapes. *Vegetation of Southern Africa*. R. M. Cowling, Richard, D.M., Pierce, S.M. Cambridge, Cambridge University Press: 5-20.

Partridge, T. C., Brink, A.B.A. (1974). "Alluvial terraces of the Lower Vaal River, South Africa: a reappraisal and reinvestigation: A discussion." *Journal of Geology* **82**: 663-665.

Partridge, T. C., Maud, R.R. (1987). "Geomorphic evolution of southern Africa since the Mesozoic." *South African Journal of Geology* **90**(2): 179-208.

Partridge, T. C., Maud, R.R. (2000). *The Cenozoic of Southern Africa*. Oxford, Oxford University Press.

Penck, W. (1953). *Morphological Analysis of Landforms (translated by H. Czech & K.C. Boswell.* London, Macmillan.

Phillips, W. M. (2000). "Estimating cumulative soil accumulation rates with in situ-produced cosmogenic nuclide depth profiles." *Nuclear Instruments and Methods in Physics Research B* **172**: 817-821.

Pinet, P., Souriau, M. (1988). "Continental erosion and large-scale relief." *Tectonics* **7**: 563-582.

Raymo, M. E., Lisiecki, L.E., Nisancioglu, K.H. (2006). "Plio-Pleistocene Ice Volume, Antarctic Climate, and the Global 18O Record." *Science* **313**(5786): 492 - 495.

Raymo, M. E., W.F. Ruddiman, and P.N. Froelich (1988). "Influence of late Cenozoic mountain building on ocean geochemical cycles." *Geology* **16**: 649-653.

Riebe, C. S., Kirchner, J.W., Finkel, R.C. (2003). "Long-term rates of chemical and physical erosion from cosmogenic nuclides and geochemical mass balance." *Geochimica et Cosmochimica Acta* **67**(22): 4411-4427.

Riebe, C. S., Kirchner, J.W., Finkel, R.C. (2004). "Sharp decrease in long-term chemical weathering rates along an altitudinal transect." *Earth and Planetary Science Letters* **218**: 421-434.

Riebe, C. S., Kirchner, J.W., Granger, D.E., Finkel, R.C. (2000). "Erosional equilibrium and disequilibrium in the Sierra Nevada, inferred from cosmogenic 26Al and 10Be in alluvial sediment." *Geology* **28**(9): 803-806.

Riebe, C. S., Kirchner, J.W., Granger, D.E., Finkel, R.C. (2001a). "Strong tectonic and weak climatic control of long-term chemical weathering rates." *Geology* **29**(6): 511-514.

Riebe, C. S., Kirchner, J.W., Granger, D.E., Finkel, R.C. (2001b). "Minimal climatic control on erosion rates in the Sierra Nevada, California." *Geology* **29**(5): 447-450.

Rooseboom, A., Harmse, H.J. (1979). "Changes in the sediment load of the Orange River during the period 1929-1969." *International Association of Hydrological Sciences Publication* **128**: 459-70.

Ruddiman, W. F. (2001). *Earth's climate: past and future*, W.H.Freeman & Co Ltd.

Rust, D. J., Summerfield, M.A. (1990). "Isopach and borehole data as indicators of rifted margin evolution in southwestern Africa." *Marine and Petroleum Geology* **7**: 277-288.

Schäfer, J. M., Baur, H., Denton, G.H.S., Ivy-Ochs, S., Marchant, D.R., Schlüchter, C., Wieler, R. (2000). "The oldest ice on Earth in Beacon Valley, Antarctica: new evidence from surface exposure dating." *Earth and Planetary Science Letters* **179**: 91-99.

Schäfer, J. M., Tschudi, S., Zhao, Z., Wu, X., Ivy-Ochs, S., Wieler, R., Leya, I., Baur, H., Denton, G.H., Kubik, P.W., Schlüchter, C. (2002). "The limited influence of glaciations in Tibet on global climate over the past 170,000yr." *Earth and Planetary Science Letters* **194**: 287-297.

Schaller, M., Ehlers, T.A. (in press). "Limits to quantifying climate driven changes in denudation rates with cosmogenic radionuclides." *Earth and Planetary Science Letters*.

Schaller, M., von Blanckenburg, F., Hovius, N., Kubik, P.W. (2001). "Large-scale erosion rates from in-situ produced cosmogenic nuclides in European river sediments." *Earth and Planetary Science Letters* **188**: 441-458.

Schaller, M., von Blanckenburg, F., Hovius, N.,Veldkamp, A., van den Berg, M.W., Kubik, P.W. (2004). "Palaeoerosion rates from cosmogenic 10Be in a 1.3Ma terrace sequence: response of the river Meuse to changes in climate and rock uplift." *The Journal of Geology* **112**: 127-144.

Schaller, M., von Blanckenburg, F., Veldkamp, A., Tebbens, L.A., Hovius, N., Kubik, P.W. (2002). "A 30 000 yr record of erosion rates from cosmogenic 10Be in Middle European river terraces." *Earth and Planetary Science Letters* **204**: 307-20.

Schulmeister, J., Fink, D., Augustinus, P.C. (2005). "A cosmogenic nuclide chronology of the last glacial transition in North-West Nelson, New Zealand-new insights in Southern Hemisphere climate forcing during the last deglaciation." *Earth and Planetary Science Letters* **233**: 455-466.

Schumm, S. A. (1977). *The Fluvial System*. Chichester, Wiley.

Schumm, S. A., Lichty, R.W. (1965). "Time, Space and Causality in Geomorphology." *American Journal of Science* **263**(February 1965): 110-119.

Seidl, M. A., Dietrich, W.E., Kirchner, J.W. (1994). "Longitudinal profile development into bedrock: an analysis of Hawaiian channels." *The Journal of Geology* **102**: 457-474.

Seidl, M. A., Finkel, R.C., Caffee, M.W., Hudson, G.B., Dietrich, W.E. (1997). "Cosmogenic isotope analyses applied to river longitudinal profile evolution: problems and interpretations." *Earth Surface Processes and Landforms* **22**: 195-209.

Shone, R. W., Booth, P.W.K. (2005). "The Cape Basin, South Africa: A review." *Journal of African Earth Sciences* **43**: 196-210.

Small, E. E., Anderson, R.S., Hancock, G.S. (1999). "Estimates of the rate of regolith production using 10Be and 26Al from an alpine hillslope." *Geomorphology* **27**: 131-150.

Smith, R. M. H. (1990). "A review of stratigraphy and sedimentary environments of the Karoo Basin of South Africa." *Journal of African Earth Sciences* **10**(1/2): 117-137.

Springer, G. S., Tooth, S., Wohl, E.E. (2004). *A geometry-based theoretical estimation of the role of abrasion by suspended sediment in a pothole-dominated knickpoint, Orange River, Republic of South Africa*. American Geophysical Union Fall Meeting 2005, San Francisco.

Springer, G. S., Tooth, S., Wohl, E.E. (2006). "Theoretical modeling of stream potholes based upon empirical observations from the Orange River, Republic of South Africa." *Geomorphology* **82**(1-2): 160-176.

Stock, G. M., Anderson, T.S., Finkel, R.C. (2005a). "Rates of erosion and topographic evolution of the Sierra Nevada, California, inferred from cosmogenic 26Al and 10Be concentrations." *Earth Surface Processes and Landforms* **30**: 985-1006.

Stock, G. M., Granger, D.E., Sasowsky, I.D., Anderson, R.S., Finkel, R.C. (2005b). "Comparison of U–Th, paleomagnetism, and cosmogenic burial methods for dating caves: Implications for landscape evolution studies." *Earth and Planetary Science Letters* **236**: 388-403.

Stone, J., Evans, J.M., Fifield, L.K., Allan, G.L., Cresswell, G. (1998). "Cosmogenic chlorine-36 production in calcite by muons." *Geochimica et Cosmochemica Acta* **62**(3): 433-454.

Stone, J. O. (2000). "Air pressure and cosmogenic isotope production." *Journal of Geophysical Research* **105**(B10): 23,753-23,759.

Stone, J. O., Balco, G.A., Sugden, D.E., Caffee, M.W., Sass, L.C., Cowdery, S.G., Siddoway, C. (2003). "Holocene deglaciation of Marie Byrd Land, West Antarctica." *Science* **299**: 99-102.

Sugden, D. E., Summerfield, M.A., Denton, G.H., Wilch, T.I., McIntosh, W.C., Marchant, D.R., Rutford, R.H. (1999). "Landscape development in the Royal Society Range, southern Victoria Land, Antarctica: stability since the mid-Miocene." *Geomorphology* **28**: 181-200.

Summerfield, M. A. (1981). "Nature and occurrence of silcrete, southern Cape Province, South Africa." *School of Geography, University of Oxford Research Papers* **28**.

Summerfield, M. A. (1985). Plate tectonics and the evolution of the African landscape. *Tectonic Geomorphology.* M. M. a. J. T. Hack. Boston, Allan and Unwin**:** 27-51.

Summerfield, M. A. (1988). "Global tectonics and landform development." *Progress in Physical Geography* **12**: 389-404.

Summerfield, M. A. (1989). "Tectonic geomorphology: convergent plate boundaries, passive continental margins and supercontinent cycles." *Progress in Physical Geography* **13**: 431-491.

Summerfield, M. A. (1990). "Geomorphology and mantle plumes." *Nature* **344**(44): 387-388.

Summerfield, M. A. (1991a). "Sub Aerial Denudation of Passive Margins." *Earth Surface Processes and Landforms* **102**: 460-69.

Summerfield, M. A. (1991b). *Global Geomorphology: An introduction to the study of landforms*. London, Longman.

Summerfield, M. A. (1991c). "Tectonic Geomorphology." *Progress in Physical Geography* **15**(2): 193-205.

Summerfield, M. A. (1996). Tectonics, Geology and Long-Term Landscape Development. *The Physical Geography of Africa.* W. M. Adams, Goudie, A.S., Orme, A.R. Oxford, Oxford University Press**:** 1-17.

Summerfield, M. A. (2000). *Geomorphology and Global Tectonics*. Chichester, John Wiley and Sons.

Summerfield, M. A. (2005a). "The changing landscape of geomorphology." *Earth Surface Processes and Landforms* **30**: 779-781.

Summerfield, M. A. (2005b). "A tale of two scales, or the two geomorphologies." *Transactions, Institute of British Geographers* **30**: 402-415.

Summerfield, M. A., Brown, R.W. (1998). Geomorphic factors in the interpretation of fission-track data. *Advances in Fission-Track Geochronology*. P. Van den Haute, De Corte, F. Amsterdam, Kluwer: 269-289.

Summerfield, M. A., Hulton, N.J. (1994). "Natural controls of fluvial denudation rates in world drainage basins." *Journal of Geophysical Research* **99**(B7): 13,871-13,883.

Thomas, D. S. G., Shaw, P.A. (1990). "The deposition and development of the Kalahari Group sediments, Central Southern Africa." *Journal of African Earth Sciences* **10**(1/2): 187-197.

Thomas, M. F. (1994). *Geomorphology in the tropics: a study oin weathering and denudation rates in low latitudes*. Chichester, Wiley.

Tooth, S. (2006). "Virtual globes: a catalyst for the re-enchantment of geomorphology." *Earth Surface Processes and Landforms* **31**: 1192-1194.

Tooth, S., Brandt, D., Hancox, P.J., McCarthy, T.S. (2004). "Geological controls on alluvial river behaviour: a comparative study of three rivers on the South African Highveld." *Journal of African Earth Sciences* **38**: 79-97.

Tooth, S., McCarthy, T.S. (2004). "Anabranching in mixed bedrock-alluvial rivers: the example of the Orange River above Augrabies Falls, Northern Cape Province, South Africa." *Geomorphology* **57**: 235-262.

Tricart, J. (1957). "Mise en point: l'évolution des versants." *L'Inf. Géogr.* **21**: 108-115.

Tuniz, C., Bird, J.R., Fink, D., and Herzog, G.F., (1998). *Accelerator Mass Spectrometry: Ulatrasensitive Analysis for Global Science*. Boca Raton, CRC Press.

Twidale, C. R. (1982). *Granite Landforms*. Amsterdam, Elsevier.

Twidale, C. R. (1990). "The origin and implications of some erosional landforms." *Journal of Geology* **98**(343-64).

Tyson, P. D. (1986). *Climate change and variability in Southern Africa*. Oxford, Oxford University Press.

Tyson, P. D., Partridge, T.C. (2000). Evolution of Cenozoic climates. *The Cenozoic of southern Africa*. T. C. Partridge, Maud, R.R. Oxford, Oxford University Press.

Valet, J. P., Meynadier, L., Guyodo, Y (2005). "Geomagnetic dipole strength and reversal rate over the past two million years." *Nature* **435**: 802-805.

van der Beek, P., Summerfield, M.A., Braun, J., Brown, R.W., Fleming, A. (2002). "Modeling postbreakup landscape development and denudational history across the southeast African (Drakensberg Escarpment) margin." *Journal of Geophysical Research* **107**(B12).

van der Walt, P. T. (2000). *Augrabies Splendour: a guide to the natural history of the Augrabies Falls National Park and the Riemvasmaak wildlife area*. Pretoria, Info Naturae.

Van der Wateren, F. M., Dunai, T.J. (2001). "Late Neogene passive margin denudation history - cosmogenic isotope measurements from the central Namib desert." *Global and Planetary Change* **30**: 271-307.

von Blanckenburg, F. (2006). "The control mechanisms of erosion and weathering at basin scale from cosmogenic nuclides in river sediment." *Earth and Planetary Science Letters* **242**: 224-239.

von Blanckenburg, F., Hewawasam, T., Kubik, P.W. (2004). "Cosmogenic nuclide evidence for low weathering and denudation in the wet, tropical highlands of Sri Lanka." *Journal of Geophysical Research* **109**: 1-22.

Wakasa, S., Matsuzaki, H., Horiuchi, K., Tanaka, Y., Matsukura, Y. (in press). "Estimation of episodic exfolifation rates of rock sheets on a granite dome in Korea from cosmogenic nuclide analysis." *Earth Surface Processes and Landforms*.

Walling, D. R. (1983). "The Sediment Delivery Problem." *Journal of Hydrology* **65**: 209-237.

Watchman, A. L., Twidale, C.R. (2002). "Relative and 'absolute' dating of land surfaces." *Earth-Science Reviews* **58**(1-49).

Wellington, J. H. (1955). *Southern Africa: A Geographical Study*. Cambridge, Cambridge University Press.

Whipple, K. X., Tucker, G. (1999). "Dynamics of the stream-power river incision model: Implications for height limits of mountain ranges, landscape response timescales and research needs." *Journal of Geophysical Research* **104**(B8): 17,661-17,674.

Williams, A. J., Stuart, F.M., Day, S.J., Phillips, W.M. (2005). "Using pyroxene microphenocrysts to determine cosmogenic 3He concentrations in old volcanic rocks: an example of landscape development in central Gran Canaria." *Quaternary Science Reviews* **24**: 211-222.

Willis, B. (1934). "Inselbergs." *Annals of the Association of American Geographers* **24**: 123-129.

Wobus, C. W., Hodges, K.V., Whipple, K.X. (2003). "Has focused denudation sustained active thrusting at the Himalayan topographic front?" *Nature* **31**(10): 861-864.

Wooldridge, S. W., Linton, D.L. (1955). *Surface, Structure and Drainage in South-East England (2nd Edn)*. London, George Philip.

Wooldridge, S. W. (1957). The progress of geomorphology. *Geography in the twentieth century*. G. Taylor. London, Methuen.

Yokoyama, Y., Caffee, M.W., Southon, J.R., Nishiizumi, K. (2004). "Measurements of in situ produced 14C terrestrial rocks." *Nuclear Instruments and Methods in Physics Research B* **223-224**: 253-258.

Young, R. (1986). "Tower Karst in Sandstone: Bungle Bungle massif, northwestern Australia." *Zietschrift fur Geomorphologie N.F.* **30**(2): 189-202.

Young, R. (1987). "Sandstone landforms of the tropical East Kimberley Region, Northwestern Australia." *Jounal of Geology* **95**: 205-218.

Young, R. (1988). "Quartz etching and sandstone Karst: Examples from the East Kimberleys, Northwestern Australia." *Zeitschrift Fur Geomorphologie* **32**(4): 409-423.

Zawada, P. K. (2000). Slackwater sediments and Paleofloods. *The Cenozoic of southern Africa*. T. C. Partridge, Maud, R.R. Oxford, Oxford University Press.

Zawada, P. K., Hattingh, J., van Bladeren (1996). Palaeoflood Hydrological Analysis of Selected South African River. Report to the Water Research Commission by the Council for Geoscience.

Appendix 1 – Calculating cosmogenic ^{10}Be and ^{26}Al erosion rates

A.1.1 Production rates and scaling factors

A spreadsheet was constructed in order to compute $^{10}Be/^{26}Al$ exposure ages and erosion rates. The aim was to create a spreadsheet that would allow calculation of ages and rates given specific inputs of sample mass, carrier mass, $^{10}Be/^{9}Be$ ratio etc. (Table A.1.1). The following sections describe how this spreadsheet was constructed.

Parameter	Typical Input
Sample mass of SiO2 (g)	20
9Be carrier mass (mg)	2.50E-04
10Be/9Be carrier ratio	5E-14
Sample thickness (Z) (cm)	10
Rock bulk density (ρ) (g cm^{-3})	2.7
Distant Shielding (Σ)	0.29
Latitude	55
Altitude (A) (m)	500

Table A.1.1 Principal spreadsheet parameters and typical inputs. Note these are not measured values but arbitrary values used to 'tune' the spreadsheet.

A number of authors have developed scaling factors to account for differences in production rates at different altitudes, latitudes, and dipole and non-dipole changes with time. The classic work on scaling was presented by Lal (1991), who bases his scaling factors on different altitudes and latitudes. An updated version of Lal's (1991) scaling factors based on pressure at different altitudes and latitudes, with updated scaling values for spallogenic and muogenic production is presented by Stone (2000).

Dunai (2000) presents a new set of scaling factors based on neutron cutoff rigidities and atmospheric palaeo-pressure rather than altitude which shows that for low latitudes (20-40°) scaling factors are significantly different to those of Lal (1991) and Stone (2000). This is because of the effects of the non-dipole field, believed to account for 20% of the earth's magnetic field and not accounted for in either Lal or Stone's factors, and the uncertainty associated with neutron absorption mean free path length (Λ) which is believed to vary with altitude and is also not considered in either Lal or Stone's factors.

Both Stone's and Dunai's schemes are used to calculate production rates of ^{10}Be. Stone's scaling factors are described below, whilst Dunai's production rates are calculated with reference to the 2000 paper and a spreadsheet (Dunai, personal communication). Pressure is first calculated using the standard atmosphere approximation (A.1.1) (Stone, 2000)

$$P(z) = P_S \exp\left\{-\frac{gM}{R\xi}\left[\ln T_S - \ln(T_S - \xi z)\right]\right\} \quad \text{(A.1.1)}$$

(Stone, 2000)

Where: P_s is standard atmospheric pressure (1013.25hPa); T_s is sea level temperature (288.15K); ξ is adiabatic lapse rate (0.0065 Km^{-1}); and gM/R is a constant 0.03417 Km^{-1}). The standard atmosphere approximation holds true for most of the earth's surface apart from Antarctica, for which there is a separate approximation, not considered here.

Stone (2000) presents scaling coefficients as a function of pressure at seven index latitudes (Table A.1.2). The overall spallogenic scaling equation is (A.1.2):

$$S_\lambda(P) = a + b\exp[-P/150] + cP + dP^2 + eP^3 \quad \text{(A.1.2)}$$

(Stone, 2000)

latitude	a	b	c	d	e	M
0	31.8518	250.3193	-0.083393	7.4260E-05	-2.2397E-08	0.587
10	34.3699	258.4759	-0.089807	7.9457E-05	-2.3697E-08	0.600
20	40.3153	308.9894	-0.106248	9.4508E-05	-2.8234E-08	0.678
30	42.0983	512.6857	-0.120551	1.1752E-04	-3.8809E-08	0.833
40	56.7733	649.1343	-0.160859	1.5463E-04	-5.0330E-08	0.933
50	69.0720	832.4566	-0.199252	1.9391E-04	-6.3653E-08	1.000
>60	71.8733	863.1927	-0.207069	2.0127E-04	-6.6043E-08	1.000

Table A.1.2 Scaling coefficients (Stone, 2000)

In the spreadsheet, these index scaling coefficients are entered and the spallogenic scaling factor is calculated by linear interpolation of latitudes lying between the

reference values. The error introduced by this simple method is believed to be less than 1% (Balco, 2001).

The muogenic scaling factor is calculated with reference to (A.1.3) and the 'M' values in Table 2 for different latitudes. Linear interpolation is once again used to calculate scaling factors for intermediate latitudes.

$$M_{\lambda}(P) = M_{\lambda,1013.25} \exp[(1013.25 - P)/242] \quad \text{(A.1.3)}$$

(Stone, 2000)

The spallogenic and muogenic scaling factors are combined to calculate the overall scaling factor (A.1.4):

$$F(P) = f_{SP} S(P) + (1 - f_{SP}) M(P) \quad \text{(A.1.4)}$$

(Stone, 2000)

Where f_{sp} is the fraction of production due to spallation (0.974 for ^{10}Be and 0.978 for ^{26}Al).

A.1.2 Production rate correction factors

Before calculating production rates based on the scaling factors above, production needs to be corrected for topographic shielding and sample thickness (Gosse & Phillips, 2001). Production rate also decreases with depth in rock (Kim & Englert, 2004). The thickness shielding coefficient T(Z) is calculated using (A.1.5):

$$T(Z) = \frac{\Lambda}{\rho Z}\left(1 - e^{\frac{-\rho Z}{\Lambda}}\right) \quad \text{(A.1.5)}$$

(Gosse & Phillips, 2001)

Where: Z is sample thickness (cm); ρ is rock density (g cm^{-3}); and Λ is the absorption mean free path length for spallation (g cm^{-2}) – a value that varies with

latitude (170 g cm^{-2} at latitudes <20°, 160 g cm^{-2} at latitudes 20-50°, and 150 g cm^{-2} at latitudes greater than 50° (Balco, 2000)).

Topographic shielding is generally measured in the field as a blocked section of the horizon when the horizon is broken up into a number of straight line sectors. For a rectangular obstruction that blocks incident cosmic rays from the ground up at a constant inclination angle θ_i and extends through an azimuth angle $\Delta\phi_i$ the missing flux (δF) is given by (A.1.6) (Dunne *et al.*, 1999).

$$\delta F = \frac{I_0 \Delta \phi}{m+1} \sin^{m+1}(\theta_0) \qquad \text{(A.1.6)}$$

(Dunne *et al.*, 1999)

Where m = 2.3. For n obstructions, each with its own inclination and azimuth angles, a production shielding factor (S) can be calculated as the ratio of the remaining flux to the maximum flux (A.1.7):

$$S = 1 - \frac{1}{360^\circ} \sum_{i=1}^{n} \Delta\phi_i \sin^{m+1}\theta_i \qquad \text{(A.1.7)}$$

(Dunne *et al.*, 1999)

A.1.3 Slope angle shielding correction

If the surface being sampled is sloped, the effect of geometric shielding and attenuation length on production rates is more complicated than for a flat surface. The model below (Dunne *et al..*, 1999) assumes that the slope is uniform, with a dip angle of α. Equation (A.1.8) describes the slope angle shielding factor as a function of dip angle (α) and depth (z), where Λ is the absorption mean free path length for spallogenic production in rock (g cm^{-2}), is 155 g cm^{-2} latitudes in this study (27-35°S)

$$S(z,\alpha) = (1 - 3.6 \times 10^{-6}\alpha^{2.64}) e^{-\left(\frac{z}{\Lambda}\right)\left(1+\frac{\alpha^2}{5000}\right)}$$

(A.1.8) (Dunne *et al.*, 1999)

A.1.4 Overall production rate

With the above correction factors computed, overall production rate at the earth's surface can be calculated by combining them with the scaled production rates (A.1.9)

$$P = P_0 \, F \, T \, G \, S(z, \alpha) \qquad \text{(A.1.9)}$$

(Stone, 2000)

Where P_0 is production rate (taken as 5.1±0.3 atoms g^{-1} a^{-1} (Stone, 2000)), F is combined scaling functions for muonic and spallogenic production, T is the thickness correction factor, and G is the geometric shielding correction factor and S is the topographic shielding correction.

A.1.5 Geomagnetic variations

Geomagnetic variations occur in two ways. Firstly, the position of the earth's magnetic pole changes on a scale of thousands of years, and thus affects the production rate of a sample throughout its exposure history. The geomagnetic pole location is believed to average out to the geographical pole over tens and thousands of years and so changes in pole location are only significant for Holocene-age samples (Ohano & Hamano, 1992). Secondly, the overall intensity of the magnetic field changes over time (and indeed switches periodically – e.g. the geomagnetic reversal at ~780 ka BP at the boundary between the Brunhes and Matuyama chrons (Guyodo & Valet, 1999). This causes changes in the intensity of cosmic rays near the earth and effects the production rates of cosmogenic nuclides.

Changes in the position of the earth's magnetic pole over the last ~10ka have been documented by Ohno & Hamano (1996) based on virtual geomagnetic pole positions from palaeomagnetic data (Table A.1.3). To account for variations in the intensity of earth's geomagnetic field, a chronology has been constructed by Guyodo & Valet (1999) from sedimentary records for the last 200 ka. A more recent record of 2Ma

can also been used (Valet, personal communication). Together with a Holocene record by McIlhenny and Senanayake (1982), one has sufficient information to iteratively correct ages and erosion rates for geomagnetic variations once an initial age has been calculated (Figure A.1.1).

Age (a)	Øp
500	86.6
100	80.2
1500	88.4
2000	85.5
2500	83.9
3000	82.9
3500	82.6
4000	86.3
4500	87.3
5000	86.1
5500	88.8
6000	86.7
6500	85.2
7000	86.7
7500	88.2
8000	83.6
8500	87.0
9000	86.1
9500	86.1
10000	82.5

Table A.1.3 Location of north geomagnetic pole (Øp) in 500a intervals for the past 10ka (Ohno & Hamano, 1996).

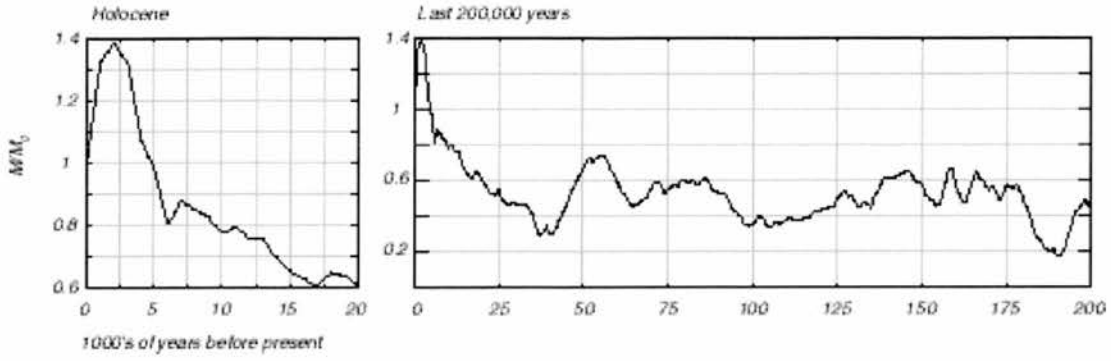

Figure A.1.1 Variations in geomagnetic intensity (M/M_0) on 20- and 200-ka timescales. (Balco, 2001)

Using Figure A.1.1 for (M/M_0) and the values of $\emptyset_P$ from Table A.1.3, a new 'effective latitude' ($\emptyset_m$) (A.1.10) can be calculated, which together with the scaling factors described above can be used to calculate a geomagnetic-corrected exposure age.

$$\phi_M = \arccos\left[\left(\frac{M}{M_0}\right)^{1/4}\cos(\phi_P)\right] \qquad \text{(A.1.10)}$$

(Dunne *et al.*, 1999)

A.1.6 Calculation of number of atoms of ^{10}Be

While tuning this spreadsheet, and before ^{10}Be AMS data became available, it was necessary to estimate the nuclide concentration in a typical sample from first principles. In order to compute an erosion rate/exposure age, the number of ^{10}Be atoms in the sample must be calculated. Some authors (e.g. Balco, 2001) have used a number of additional estimates of ^{10}Be from various other sources, such as from the ^{9}Be carrier (N_{10C}), from sample processing (N_{10P}) and the from AMS itself (N_{10A}). Whilst this may be desirable in circumstances where ^{10}Be contamination during sample processing may be a particular problem, or where cross-talk between high- and low-level samples during AMS analysis is especially marked, the error introduced from these other sources is generally very low (Balco, 2001) and is not considered in the spreadsheet being described here.

Normally, the measured $^{10}Be/^{9}Be$ ratio (R_M) is given from the AMS output. However, for the purposes of the spreadsheet, this must be calculated from first principles. An input of AMS current beam (in the order of hundreds of nA) and likely beam time (characteristically in the order of several minutes for each sample – an arbitrary 30 minute beam time is used for the spreadsheet calculations) is required to do this. The number of atoms in the AMS detector can then be calculated assuming there are 3 electrons released per atom of Be (A.1.11):

$$N_{10M} = \frac{(B_s / 3) B_t}{e} R_A \qquad \text{(A.1.11)}$$

(based on Lal, 1991)

Where: B_s is beam strength (nA); B_t is beam time (seconds); and e is the charge on an electron (1.6×10^{-19} C). Using the value for N_{9C}, the measured $^{10}Be/^{9}Be$ ratio (R_M) can be calculated and using (A.1.15) the number of ^{10}Be atoms in the sample N_{10S} can be worked out. R_A is the carrier ratio. The number of ^{10}Be atoms per gram of quartz sample can be calculated using (A.1.12):

$$N_{10S} = N_{10M} \cdot M_Q \qquad \text{(A.1.12)}$$

(Gosse & Phillips, 2001)

Where M_Q is the mass of the quartz sample (g). Once N_{10} is calculated, and P is known from section A.1.1, one is in a position to determine age and erosion rates of samples.

The above describes how a nuclide concentration would be calculated from first principles. In reality, one has a ratio of $^{10}Be/^{9}Be$ atoms as an output from the AMS. In this case, the number of ^{10}Be atoms (N) can be calculated by the following formula (A.1.13):

$$N = \frac{((^{10}Be/^{9}Be)*c*(a/A))-((^{10}Be_{blank}/^{9}Be_{blank})*c*(a/A))}{m} \quad \text{(A.1.13)}$$

(based on Lal, 1991)

Where:

a = Avagadro's number (6.022×10^{23})

A_N = atomic number of the element being measured (9.012182 for Be)

$^{10}Be/^{9}Be$, $^{10}Be_{blank}/^{9}Be_{blank}$ = ratios measured by AMS for the sample and blank, respectively

c = mass of carrier added (g)

m = mass of pure quartz separates which was dissolved (g)

A.1.7 Age and erosion rate determination

There are three principal scenarios which are computed by the spreadsheet (all assuming zero inherited nuclide component). These are:

i) Exposure age assuming zero erosion

ii) Exposure age with an erosion rate correction;

iii) Erosion rate assuming steady state has been reached (i.e. production of nuclides in balanced by their radioactive decay.

Considering exposure age under the zero erosion scenario (i), age is calculated using (A.1.14) (Lal, 1991):

$$t = -\frac{1}{\lambda} \ln \left(1 - \frac{N\lambda}{P}\right) \quad \text{(A.1.14)}$$

(Lal, 1991)

For scenario (ii), exposure age with an erosion rate correction, (A.1.15) is used Lal (1991):

$$t = -\frac{1}{A} \ln \left(1 - \frac{NA}{P}\right)$$

(A.1.15)

(Lal, 1991)

Where: A is given in (A.1.16); N is the number of ^{10}Be atoms per gram of quartz (N_{10}) given in (A.1.13); and P is overall production rate given in (A.1.9).

$$A = \lambda + \frac{\rho E}{\Lambda}$$

(A.1.16)

(based on Lal, 1991)

Where: λ is the decay constant (4.62×10^{-7} for ^{10}Be); ρ is rock bulk density (g cm^{-3}) (2.6 for granite-gneiss); and E is erosion rate (cm a^{-1}). Λ is the absorption mean free path length for spallogenic production in rock (g cm^{-2}) (155 g cm^{-2}). For scenario (iii), assuming steady state, maximum erosion rate (E) can be determined using the following method

$$E = \left(\frac{P_o - \lambda}{N_o}\right) z^*$$

(A.1.17)

(Lal, 1991)

Where z* is the attenuation coefficient, i.e. ratio of Λ is the absorption mean free path length for spallogenic production in rock (g cm^{-2}) (155 g cm^{-2}) to ρ is rock bulk density (g cm^{-3}) (2.6 for granite-gneiss)).

A.1.8 Uncertainties

Uncertainties in exposure ages and erosion rates were calculated based on uncertainties in the input values. Typical uncertainties for the main input parameters are given in Table A.1.4:

Input parameter	Typical ± uncertainty
Sample mass of SiO2 (g)	0.001
9Be carrier mass (mg) (Mc)	1.00E-05
10Be/9Be carrier ratio (Ra)	5E-15
Sample thickness (Z) (cm)	0.1
Rock bulk density (ρ) (g cm^{-3})	0.1
Distant Shielding (Σ)	0.14
Latitude (°)	0.08
Altitude (A) (m)	0.5

Table A.1.4 Typical input values and their ± uncertainties.

These uncertainties must be propagated through all the stages of calculation that lead to an output of exposure age/erosion rate. This is done by a combination of calculating absolute uncertainties (A.1.18) where the arithmetic function in the calculation is addition/subtraction, and calculating percent relative uncertainties (A.1.19) where division/multiplication is involved and a combination of the two for mixed functions.

$$e_4 = \sqrt{e_1^2 + e_2^2 + e_3^2} \qquad \text{(A.1.18)}$$

(Schnabel, personal communication, 2005)

Where e is the uncertainty associated with various values (n).

$$e_4 = \left(\sqrt{(e_1/n_1)^2 + (e_2/n_2)^2 + (e_3/n_3)^2} \right) n_4 \qquad \text{(A.1.19)}$$

(Schnabel, personal communication, 2005)

A.1.9 Uncertainties in production rate calculation

From Table A.1.4, the uncertainty in altitude and latitude measurements are given to be ±0.08° (0.5 minutes) and ±0.5 m respectively. Whilst these errors are associated with the scaling factors given by Stone (2000), in general they are <1% and are not considered in the spreadsheet. Errors associated with the thickness, depth and geometric shielding correction factors are computed by a combination of (A.1.18) and (A.1.19) and propagated through to the combined production rate calculation (A.1.9).

Uncertainties associated with the concentration of ^{10}Be atoms from various sources are propagated in a similar way to the above, so that the error in the final exposure age (Δt) for scenarios (i) and (ii) can be calculated thus (A.1.20):

$$\Delta t = \sqrt{\left(\frac{1}{P - NA}\right)^2 \Delta N^2 + \left(\frac{-N}{P^2 - NAP}\right)^2 \Delta P^2} \qquad \text{(A.1.20)}$$

(Balco, unpublished)

Where: ΔN is the error on N_{10} (the number of ^{10}Be atoms per gram of silica); ΔP is the error on the combined production rate P and A is the constant given in (A.1.21).

The error in the calculated erosion rate (ΔE) can be calculated as follows:

$$\Delta E = \sqrt{\Delta P^2 \left[\frac{\Lambda}{\rho N}\right]^2 + \Delta N^2 \left[\frac{-\Lambda P}{\rho N^2}\right]^2} \qquad \text{(A.1.21)}$$

(Balco, unpublished)

Where: ρ is rock bulk density (g cm^{-3}); and E is erosion rate (m a^{-1}). Λ is the absorption mean free path length for spallogenic production in rock (g cm^{-2}) (taken to be: 170 g cm^{-2} at latitudes 0-20°; 160 g cm^{-2} at latitudes 20-50°; and 150 g cm^{-2} at latitudes >50°).

A.1.10 Catchment-averaged erosion rates

Several authors have demonstrated the potential of quantifying the cosmogenic nuclide component of a well-mixed representative sample of sediment from a drainage basin in order to estimate time-averaged erosion for that basin (Brown *et al.*, 1995; Bierman & Steig, 1996; Granger *et al.*, 1996; Schaller *et al.*, 2001). An attempt is made to quantify erosion in this way using the spreadsheet. Calculation of an average erosion rate depends on knowing the effective cosmogenic production (P_{eff}) rate for the entire basin under consideration, and also the average nuclide concentration of the sediment (N_{sed}), assuming that it is well-mixed and representative of its source area (A.1.22).

$$\overline{\varepsilon} = \frac{\Lambda\,(P_{0eff} - \overline{N}_{sed}\lambda)}{\overline{N}_{sed}} \qquad \text{(A.1.22)}$$

(Based on Granger *et al.*, 1996 and others)

Where: $\overline{\varepsilon}$ is catchment-averaged erosion rate; P_{0eff} is effective production rate across the whole basin; $\overline{N}_{sed}$ is average nuclide concentration in sediment across the whole basin; and λ is the decay coefficient.

Production rates are calculated for a number of sub-catchments using the latitude/altitude scaling factors and topographic shielding factors described in (A.1.1 – A.1.7). Taking into account all subcatchments, P_{0eff} is calculated using (A.1.23):

$$P_{0eff} = \frac{1}{a_T} \sum a\,P \qquad \text{(A.1.23)}$$

(Balco, unpublished)

Where: a_T is the total area of the catchment; a is the area of each subcatchment, and P is the combined production rate for each catchment calculated from (A.1.9).

With the effective production rate calculated above, and the average concentration of nuclides calculated from AMS (or Equation A.1.12), average erosion rate for the catchment can be calculated from (A.1.22). N.B. A sample that contains sediment from both a rapidly eroding- and a slowly eroding- sub-catchment within a single main catchment will still give an average rate of erosion that is equal to if all sub-catchments were eroding at the same rate. This is because the mixed nuclide concentrations reflect the size of each subcatchment and its rate of erosion, and it is assumed that all parts of the catchment undergo erosion, however slowly (S.Binnie, 2004, Pers. Comm.).

Appendix 2 - Protocol for cosmogenic ^{10}Be and ^{26}Al sample preparation

A2.1 General

When preparing samples for cosmogenic ^{10}Be and ^{26}Al analysis, the aim is to isolate the quartz fraction, from which the ^{10}Be and ^{26}Al is produced. The following describes the standard protocol for ^{10}Be and ^{26}Al separation from quartz, based on Bierman *et al.* (2002) and others. It is a multi-step processes involving the progressive refinement of quartz in the 250-710 μm size fraction. The following protocol describes that which can be used for a variety of rock types but is most suitable for granite-gneisses.

Samples which are collected as whole rock samples need to be sawed, split, crushed and ground (Stages 1-4) prior to sieving at 250-710 μm. For fluvial and colluvial material, refinement may begin with sieving (Stage 5) although some milling of coarser colluvial material may be required.

A2.1. Sawing

Larger samples of rock (>10 cm diameter) may have to be sawed. This is done on a tungsten-carbide diamond-tipped rock saw at the Department of Geology. The protocol for use of the saw is as follows:

1. Ensure that personal protective equipment is worn at all times. This includes ear protection, goggles, a fine particulate dust mask, lab coat and optional waterproof gear;
2. Turn on the water-cooling system;
3. Position rock sample on a flat surface;
4. Turn on the saw;
5. Keeping a firm grip on the rock sample, away from the saw, gently lower the saw onto the edge of the sample which is being cut, keeping hold of the handle of the saw so that it can be lifted up;
6. Move the rock along as the saw blade cuts through it;
7. If the saw becomes stuck, lift the handle to release it;

8. Between samples, clean the area where the rock has been cut by using the water hose.

A2.2. Splitting

Sawed rock samples can be further reduced in size by using the hydraulic splitter. This machine works by producing tension on the surface of the rock by means of two hydraulic springs, which can be tightened and loosened as required. The procedure for use is as follows:

1. Place the shatter-box around the splitter to prevent loss of sample;
2. Place the rock under the 'teeth' of the splitter;
3. Gently turn the top handle until the teeth are lowered onto the surface of the rock;
4. Tighten the springs by turning both spring handles simultaneously until the rock splits;
5. Remove the rock and ensure springs are untightened.

A2.3. Crushing

This is done in a large jaw-crusher to produce fine chips of rock that can be further reduced in size in the Fritsch jaw-crusher or the Gy-RoMill. Both jaw crushers work by two metal plates grinding together as a sample of rock passes between the two plates. Note that this procedure, as well as grinding, must be done wearing personal protective equipment comprising dust mask, eye protection, ear protection and lab coat. To use the large jaw-crusher:

1. Clean down with paper towels and air hose. Turn on the extractor fan;
2. Close the doors of the jaw crusher and firmly clamp the doors in place;
3. Turn on the jaw crusher. Ensure the sample collection drawer is in place;
4. Carefully place a small sample of rock in the top of the jaw crusher;
5. Wait for the crushed sample to fall into the sample collection drawer below;

6. Repeat the process as necessary, until fine rock chips (1-2 cm diameter) are produced;
7. Note that Jaw crusher needs to be cleaned between samples. This is done by wiping and air-hosing the machine itself, and washing the plates in H_2O, ensuring that they are fully dry before being replaced.

The Fritsch jaw-crusher is used to crush small rock chips (from the above stage) to the desired size fraction. It is operated as follows:

1. Remove tungsten carbide plate and clean down with paper towels and air hose;
2. Re-fit the tungsten carbide plate;
3. Turn on the jaw crusher. Ensure the sample collection drawer is in place;
4. Carefully place a few small rock chips in the top of the jaw crusher;
5. Wait for the crushed sample to fall into the sample collection drawer below;
6. Repeat the process as necessary, until desired size fraction (250-710 μm) is achieved;
7. Note that Jaw crusher needs to be cleaned between samples. This is done by wiping and air-hosing the plates.

A2.4. Grinding

If the Fristch jaw crusher has been used to produce the desired size fraction, this step can normally be skipped. Grinding is done in a Gy-RoMill, a device that uses a rotating tungsten carbide barrel to grind the rock. At this stage, it is easy to grind the rock to too fine a powder, which makes refinement of quartz difficult. It is therefore advisable to use the Gy-RoMill for only short bursts of time (~ 5 seconds) and to repeatedly sieve the resulting powder at the desired size fraction until sufficient sample is collected. Note that use of the Gy-RoMill can often result in too fine-fraction samples than is desirable for cosmogenic ^{10}Be isolation, so great care must be taken in its operation:

1. Ensure the tungsten carbide barrels are clean and dry;

2. Fit the barrels together (centre, ring, main barrel, rubber seal and lid);
3. Place a small amount of rock chips in the barrel;
4. Ensure rubber seal is in place and attach lid;
5. Place in the Gy-RoMill, clamping the lid firmly down;
6. Turn on Gy-RoMill for 5 seconds;
7. Sieve the resulting powder at 250-710 μm;
8. Grind the sample further as necessary.
9. Note that barrels must be cleaned and dried thoroughly between samples.

A2.5. Further refinement of 250-710 μm fraction

1. Wet sieving can be carried out to discard fine material (<250 μm).
2. In a fume hood, wearing gloves, labcoat and safety glasses, 1:1 ratio 15MΩ distilled and ~ 37% HCl (cation waste) is added to the sample in a polypropelene bottle and is agitated on a shaker table for ~ 8 hours. This is to separate composite grains to leave single grains of quartz and other materials
3. Acid is discarded. Samples are rinsed thoroughly with 15MΩ distilled H_2O (10 rinses).
4. Using Stokes' settling law fine suspended material is rinsed off after leaving the samples to settle for ~ 30 seconds, leaving only the coarser, more easily settled material. Samples are dried down overnight in a 40°C oven.
5. Analysis under a microscope at this stage should reveal single grains of quartz and heavy minerals that can be separated out in the heavy liquid stage. Quartz is the transparent to translucent white grains (Bishop *et al.*, 2001).

A2.6. Junk etch

This stage is carried out using ~ 1% HF and should remove the outer layer of quartz and begin to break up composite quartz grains and remove feldspars. Wearing full HF personal protective equipment (nitrile and black gloves, face mask, labcoat, neoprene apron), it is carried out in a HF fume hood as follows:

1. Place sample (~ 100 g) in a clean 1l polypropylene bottle;
2. Add 900 ml 15MΩ H_2O;
3. Add 20 ml 40% HF to the bottle,
4. Ensure lid is screwed firmly on bottle, place bottles on a shaker table for 48 hours.
5. Rinse sample with copious amounts of 15MΩ H_2O and dry down sample.

A2.7. Magnetic Separation

This step is not always necessary but can be carried out to remove mafic material from the sample prior to etching. It is done on an isodynamic magnetic separator ('Franz'), a device that uses mineral magnetic susceptibility and gravity to separate different grains. Before commencing use of this device, the highly-magnetic magnetite grains, which would stick to and clog the separator, must be removed. This is done by covering a bar magnet with paper, and running the magnet along a thinly spread (~ 1-2 grains thick) layer of the sample. The magnetite grains will adhere to the paper and can be removed for collection.

After removing the magnetite, the isodynamic magnetic separator can be used. The device consists of a large electromagnet with a two-channelled separator running between it. The vertical angle of the magnet and separator can be adjusted so that when a sample is introduced to the separator, it will flow downhill naturally under gravity. The lateral angle of the separator and electromagnet can also be adjusted so that when the electromagnet is switched off, the sample will only flow down one channel (the one at the lower lateral angle). When the electromagnet is turned on, magnetic minerals are dragged up into the channel at the higher lateral angle. The separator works on the principle that magnetic minerals, such as ilmenite and clinopyroxene will separate out from the non-magnetic quartz. A degree of fine-tuning is required until the device effectively separates the minerals:

1. Ensure that the separator is clean. Use iso-propanol to clean the machine if required;

2. Adjust the vertical angle to ~ 15° so that a sample will flow easily, but not too rapidly, down the separator;
3. Adjust the lateral angle so that the sample will not flow down the upper channel unless the electromagnet is turned on;
4. Turn the magnetic field on to a low setting (~ 0.1 Amps). Turn on the vibrator and introduce the sample into the separator via the hopper. Note that the speed at which the sample goes into the separator can be adjusted by screwing/unscrewing the hopper;
5. As the sample travels down the separator, it should be apparent from the colour difference in the grains that the ilmenite (black) is travelling down the upper channel (i.e. has magnetically separated) whilst the quartz is travelling down the lower channel. Cups should be placed on the end of each channel to collect the separates;
6. Once the ilmenite has been removed, tilt the entire machine downhill and turn on the vibrator to clean the channels.
7. Collect the quartz, ilmenite and magnetite. Store in separate labelled glass vials.

A2.8. Etching stage

The aim of this and the following stages is to produce ~ 30 g of pure quartz by the start of stage 11. At least three 24-hour etches in ~ 1% HF are required to remove feldspars and other materials from the sample. Wearing full HF personal protective equipment as in stage 6, the protocol below should be followed:

1. Transfer samples to large (4litre) bottles. Weigh out ~ 50 g of sample and add to each bottle;
2. Fill bottle with 4litres of 15MΩ H_2O;
3. Add 35 ml of 70% HNO_3;
4. Add 60 ml of 40% HF;
5. Secure lids on bottles, and place in heated ultrasonic baths (on 30 minute ultrasonic bursts) for 24 hours;

6. Discard acid and rinse with copious amounts of 15MΩ H_2O until sample runs clean;
7. Repeat steps 2-6 two more times. If necessary repeat further until sample runs clean;
8. Dry down sample.

A2.9. Heavy liquid separation

This stage focuses on the separation of any remaining heavy minerals from the quartz. It uses lithium heterotungstate (LST) a heavy liquid with a density of 2.65 g cc^{-1} which is soluble in water. It is important that the LST is at the correct density so that the quartz will float and the heavy minerals will sink. 18MΩ water is used throughout this procedure. A new protocol has been developed in the Edinburgh labs which involves using a centrifuge to separate the quartz from heavy minerals. This protocol is much more effective at separating grains and less clumsy than the old method involving stoppered funnels.

1. Check the density of the LST by taking a 10 ml bottle, weigh the bottle, fill the bottle with LST, weigh the combined bottle and LST. The mass of the LST must be 2.65 g cc^{-1}. If the liquid is not up to density, place the LST on a hotplate to evaporate off excess water. Correct density will be indicated when a piece of quartz will float on the top of the liquid.
2. Label a clean 50 ml centrifuge tube, and put ~ 20 g of sample in the bottom.
3. Fill the tube to about 3/4 full with LST;
4. Put the tube in the vortex mixer for a few seconds to allow mixing;
5. Leave the tube standing up in a tube rack for ~ 1 hr to allow mafic minerals which may have become caught up in the quartz floating on the top of the float to sink;
6. Place the tube in the centrifuge for ~ 30 minutes on 3000 rpm;
7. By now, heavy minerals should be seen at the bottom of the tube and quartz should be floating on top of the LST. Pour the quartz-LST mixture into filter

paper above a labelled beaker and allow the LST to drain off. Ensure the mafic minerals remain in the tube. The LST in the beaker can then be re-used;

8. Rinse the mafic minerals with 18 MΩ water several times and collect the rinse water to recover LST. Retain the tube containing mafics for possible later analysis;
9. Rinse the quartz with copious amounts of 18MΩ water and collect the rinse water. Dry down the quartz sample;
10. Rinse all equipment with 18MΩ water, collect all rinse water and place (LST and 18MΩ water mixture) on a hotplate at 80°C until the water has evaporated off. This may take several days.

A2.10. Final Etch

After the quartz has been separated by heavy liquid separation, a final HF etch must be carried out to remove any remaining contaminants (particularly LST). This is done using the highest-purity (ANLAR) reagents. Using full HF personal protective equipment:

1. To each sample, in a clean Nalgene bottle, add 900 ml of 18MΩ H_2O
2. Add 20 ml HF (48%)
3. Add 10 ml HNO_3
4. Place overnight in ultrasonic baths
5. Rinse thoroughly and dry down the samples

A2.11. Quartz Assay

This stage is carried out prior to dissolution to check the sample's purity. A small (~ 1g) aliquot of sample is taken, dissolved and analysed by inductively-coupled plasma mass spectrometry (ICP-MS) which reveals the concentration of Be, Ti, Al, B, and Fe. The concentration of Be will give an indication of likely beam currents during AMS analysis and the concentration of Al will show whether or not it is necessary to add a ^{27}Al carrier prior to dissolution. The quartz assay also gives a guide as to the likely problems that might be encountered with e.g. high Ti, B and Fe content in the

samples and how this might be dealt with. The procedure for preparing the quartz assay is as follows:

1. Label then weigh (with caps) a clean 60 ml Savillex jar and a clean 30 ml bottle for each sample.
2. Place jar on balance, tare, remove from balance and carefully add around 1g of sample. Weigh and record weight.
3. Wearing full personal protective equipment, dissolve in ~20 ml HF (48%, analytical grade) on setting 1 (S&J hotplate) overnight.
4. Before finishing clean workbench around balance to make sure there are no quartz grains.
5. The next day, add 1.5 ml HNO_3 (70% Primar) to dried, dissolved sample in jars, using digital pipette, in order to take up sample.
6. One sample at a time, tare a capped, labelled, 30 ml bottle then transfer the acid from the jar to the bottle using disposable pipettes. Keep disposable pipette in bottle.
7. Using dedicated measuring cylinder, add ~25ml of water (18 MΩ) to jar to rinse it then transfer the water to bottle using the disposable pipette from 5.
8. Weigh bottle and record weight.
9. Repeat 5-7 for all samples.
10. Dispose of Be waste and unused acid and dishwash empty bottles.
11. At the end of the procedure you should have a bottle for each sample and a written table with columns recording the weight of the empty jar, the empty 30 ml bottle, the weight of the quartz and the weight of the dissolved solution.

The samples are then sent off for ICP-MS analysis at the Department of Chemistry. The results are given as a concentration (μg/ml) of the different elements. For Ti, B, Fe, these can be interpreted qualitatively – if there is a particularly high concentration of any of these anions, extra care must be taken in the Ti precipitation, B diffusion, and anion column steps, respectively. The Be concentration (^{9}Be) will normally be <1.0 μg/ml and so a ^{9}Be carrier must always be added. The Al concentration (^{27}Al) may vary, and samples with low Al concentrations (<100 ppm)

must have a carrier added to them, otherwise, the naturally occurring ^{27}Al in the sample will act as a carrier. High Al concentrations will interfere with the Be target by swamping the Be at cation column stage and leaving Al in the Be target which will then lower AMS beam current) The ppm concentration of trace metals in the quartz can be calculated as follows:

$$\text{Ppm concentration of quartz} = \frac{\text{Liquid mass} \times (\text{ICP result}/1000)}{\text{Dissolved quartz mass}} \times 1\,000\,000 \quad \text{(A2.1)}$$

A2.12. Dissolution and carrier addition

By this stage, ~ 30 g of pure quartz should be available for each sample. Work is now done in the clean ^{10}Be-^{26}Al laboratory. Note that from now on, unless otherwise stated, clean-room personal protective equipment must be worn (nitrile gloves, clean room lab coat, clean room shoes, eye protection). Also, from this stage on, any material coming into contact with the sample (e.g. pipette tips, pastettes) represents a Be-hazard and must be placed in a sealed bag labelled 'Be waste' and disposed of in the Be-waste bin. The ~ 30 g sample is added to acid-cleaned Savillex beakers. At this stage a blank is made up (a clean Savillex beaker containing no sample is labelled and treated to the same steps as the samples). It is best to work with 7 samples and one blank from now on.

1. Weigh each beaker (with or without lid, make a note) prior to adding quartz
2. Weigh each beaker again once quartz is added
3. Before adding the ^{9}Be carrier, the pipette that will be used in this step needs to be calibrated. This is done by pipetting ~ 250 ml of H_2O from a bottle which is weighed before and after pipetting. This is done and noted ten times. This helps one to get used to operating the pipette and ensure consistency in adding carrier.
4. After adding a small amount of 18MΩ H_2O to each beaker hold the sample down, pipette ~ 250 mg ^{9}Be carrier into each Savillex container. Make a note of exactly how much carrier is used by weighing the carrier bottle before and

after adding the carrier into the quartz. Note the temperature in the lab when this is done.

5. If necessary, add ^{27}Al carrier to the sample in the same way as for ^{9}Be. The amount added will depend on the natural ^{27}Al concentration of the sample, as revealed by ICP-MS, but is likely to be in the order of 2.5 – 3.0 mg..
6. Add ANLAR reagent grade HF to each container. The amount added will depend on the volume of quartz in the container. As a rule, ~ 30 g of quartz will require ~ 80 ml of HF to dissolve.
7. Place the containers, without lids on a hotplate (set on '1'). The samples will need to stay on the hotplate until the quartz has visibly dissolved. This may take several days. Further acid may need to be added to the samples from time to time.
8. Once the quartz has dissolved, the acid can be evaporated off. This is done by leaving the container on the hotplate until all liquid has evaporated.

A2.13. Hydrochloric acid fume

This step is used to break down some of the iron complexes in the sample to make them easier to remove during the column stages. It is particularly important to include this step where the quartz assay reveals there to be a high proportion of Fe in the sample. It is done as follows:

1. In a fume cupboard, 1.0 ml of $HClO_4$ is added to each Savillex beaker using an acid-cleaned autopipette.
2. Samples are placed on small hot-plate (setting 7) until all acid is fumed off;
3. Beakers are taken off hot plate to cool down.

A2.14. Perchloric acid fume

Perchloric acid ($HClO_4$) is a very effective oxidising agent and will break down metal complexes which can then be removed in the anion and cation column stages. It is done in a number of steps:

1. Perchloric acid ($HClO_4$, 70%) is explosive on contact with organic material, and the fume hood in the ^{10}Be-^{26}Al laboratory must be washed down prior to work commencing;
2. In fume cupboard, 1.0 ml of $HClO_4$ is added to each Savillex beaker using autopipette.
3. Samples are placed on small hot-plate (setting 7) until all acid is fumed off;
4. Beakers are taken off hot plate to cool down. Steps 2 and 3 are then repeated three times;
5. Dry down samples completely. Cap the beakers and clean down fume hood after fuming is finished.

A2.15. Anion Columns

This stage is designed to remove anions (e.g. Fe^{3+}) from the sample using resin-filled columns and varying strengths of HCl. It is advisable to make up the various-strength acids and putting them into labelled bottles prior to commencing the column chemistry. The following protocol assumes that 8 cylinders are in use (7 samples plus blank), although this can be adjusted to suit the number of samples being prepared. The acids are made up as follows:

1. Prepare 0.5M HCl stock solution by adding 27ml of concentrated PRIMAR grade HCl (37%) to 623ml 18MΩ H_2O to make up 650 ml total volume. Transfer to 1l yellow-taped (colour coded with yellow tape for 0.5M) poly bottle;
2. Prepare 9M HCl stock solution by adding 632ml of concentrated PRIMAR grade HCl (37%) to 218ml 18MΩ H_2O to make up 850 ml total volume. Transfer to 1l red-taped (colour coded with red tape for 9M) poly bottle;
3. Using 100 ml graduated cylinder, fill 8 red-tipped 60 ml bottles (labelled 'A') with 9M HCl;
4. 16 or more pastettes and at least 8 autopipette tips should be acid cleaned in ~ 10% HNO_3 overnight;
5. Fill a red-tipped 60 ml poly bottle (labelled 'B') with 40 ml of 9M HCl;

6. Fill 8 red-tipped 60 ml poly bottles (labelled 'C') with 40 ml of 9M HCl;
7. Fill 8 yellow-tipped 125ml poly bottles (labelled 'D') with 80 ml of 9M HCl;
8. Fill 8 yellow-tipped 60 ml poly bottles (labelled 'E') with 60 ml of 18MΩ H_2O;
9. Set up 8 columns packed with anion resin in the recirculating fume cupboard. Each column should be labelled with a unique ID and this should be noted for each sample. The columns should be saturated with 18MΩ H_2O and contain no air bubbles (bubbles might need to be removed by forcing the air out using an acid-cleaned pastette filled with H_2O;
10. Position a 500 ml waste bottle beneath each column, each labelled with the sample ID and 'waste 1'. Open bottles and uncap columns;
11. Using the autopipette with an acid-cleaned tip, add 5ml of 9M HCl from red bottle B to each of the Savillex beakers containing the dissolved samples. The samples should completely dissolve leaving no residue;
12. Using a clean disposable pastette, add red bottle A to each of the columns. Catch the elutant in the anion waste bottles;
13. Using the pastette, add each sample from the Savillex beakers to the columns;
14. Using a clean new pastette, add a few ml of red bottle C to each of the Savillex beakers, wash the inside walls of the beaker, take up the solution and add to each column. Using a new pastette, add the rest of bottle C to the column. Immediately place the now-empty Savillex beaker beneath each column;
15. Once the column has finished dripping, place the Savillex beaker on a hotplate (setting 2) to dry down overnight in the fume hood. Place a 'waste 2' labelled bottle beneath each of the columns;
16. Add yellow bottle D to the columns, catching the waste;
17. Add white bottle E to the columns, catching the waste. When the H_2O level reaches the top of the resin, cap the columns an place in storage. Rinse the fume cupboard with 18MΩ H_2O. The waste bottles must be kept until the Be or Al has been successfully precipitated (otherwise, they can be dried down and the above protocol followed again). Upon successful Be/Al precipitation the acid contained in the waste bottles can be used in stage 5.

A2.16. Cation Columns

At this stage the Be and Al are split into separate aliquots. Acids of different molarity are used to selectively adsorb and desorb cations onto resin beads, and separate the Be and Al. The procedure is similar to the anion column stage, and is described below. Steps 1-12 deal with preparing the acids, the next five steps with priming the cation columns, and the remaining steps with collecting first the Be aliquot then the Al aliquot:

1. Prepare 9M HCl stock solution by adding 372ml of concentrated PRIMAR grade HCl (37%) to 118ml 18MΩ H_2O to make up 490 ml total volume. Transfer to 1l red-taped (colour coded with red tape for 9M) poly bottle;
2. Prepare 4.5M HCl stock solution by adding 429ml of concentrated PRIMAR grade HCl (37%) to 701ml 18MΩ H_2O to make up 1130 ml total volume. Transfer to 1l green-taped (colour coded with green tape for 4.5M) poly bottle;
3. Prepare 1M HCl stock solution by adding 169ml of concentrated PRIMAR grade HCl (37%) to 1831ml 18MΩ H_2O to make up 2-l total volume. Transfer to two separate l-l blue-taped (colour coded with blue tape for 4.5M) poly bottle. Add 79ml concentrated PRIMAR grade HCl (37%) to 851ml 18MΩ H_2O to make up 930 ml total volume. Transfer to a l-l blue-taped poly bottle. The total volume of 1M acid should be 2930 ml;
4. Put an additional 40 ml of 1M HCl into a 60 ml blue tape bottle labelled 'Bottle J <1M HCl'. Add 5ml of 18MΩ H_2O using an acid-cleaned autopipette;
5. Fill 8 60 ml red tape bottles labelled 'Bottle A' with 60 ml 9M HCl;
6. Fill 8 60 ml green tape bottles labelled 'Bottle B' with 60 ml 4.5M HCl;
7. Fill 8 60 ml blue tape bottles labelled 'Bottle C' with 60 ml 1M HCl;
8. Fill 8 60 ml blue tape bottles labelled 'Bottle D' with 60 ml 1M HCl;
9. Fill 8 250 ml blue tape bottles labelled 'Bottle E' with 160 ml 1M HCl;
10. Fill 8 125ml blue tape bottles labelled 'Bottle F' with 80 ml 1M HCl;
11. Fill 8 125ml green tape bottles labelled 'Bottle G' with 80 ml 4.5M HCl;
12. Fill 8 60 ml white tape bottles labelled 'Bottle H' with 60 ml 18MΩ H_2O,

13. Using the autopipette with an acid-cleaned tip, add 5ml from bottle J to each of the Savillex beakers. The dried down sample residue should dissolve completely.
14. Ensure the columns are filled with 18MΩ H_2O. Place labelled 500 ml cation waste bottles beneath the columns, uncap top and bottom of columns;
15. Add contents of bottle A to each column;
16. Add contents of bottle B to each column;
17. Add contents of bottle C to each column;
18. Add the contents of the Savillex beaker to each column using a clean pastette. Rinse the Savillex beaker with a few drops from bottle D and add to the column;
19. Slowly add the contents of bottle D to each column, using a pastette and taking care not to disturb the column resin. This acid should help to push the sample through the columns;
20. When fluid level in the columns reaches the top of the resin, immediately place used Savillex beaker beneath the column Add the contents of bottle E to the columns. The solution thus collected in the beakers will contain Be, whilst Al should remain adsorbed onto the resin beads in the column;
21. When the fluid level in the columns reaches the top of the resin, immediately place labelled cation waste bottles beneath each column and add the contents of bottle F;
22. The Savillex beakers containing Be should now be transferred to a hotplate in fume cupboard to dry down at ~ 80°C (hotplate setting 2) for 24 hours;
23. When fluid level in the columns reaches the top of the resin, immediately place new clean Savillex beaker labelled with sample number and 'Al aliquot' beneath each column. Add contents of bottle G. This will cause the Al to be desorbed from the resin and collect in the beaker;
24. When the fluid level reaches the top of the resin, immediately place cation waste bottle beneath column. Add contents of bottle H to clean the column;
25. Place the Al aliquot solution on hotplate in fume cupboard to dry down;
26. When fluid level in columns reaches just above the top of the resin, cap the columns and store. Cap and store cation waste bottle and store until

successful yield of Be and Al precipitates have been achieved. After this, the acids in the bottle can be used in stage 6 (HCl treatment).

A2.17. Aluminium aliquot

This stage is carried out to asses whether the column stages have been effective in separating Al and Be. A small aliquot is taken from the Be fraction for Al and diluted then sent for ICP-MS analysis:

1. Weigh the dried down sample jar with lid and record weight. (Note, before you take the jar from the hood you should make sure the outside is clean, if not wipe gently with a damp paper towel). Tare scale.
2. Add 5ml of ~70% Primar HNO_3 to the Savillex jar using a cleaned digital pipette, swirl to take the sample up into solution (note the Primar HNO_3 should come form a decanting bottle).
3. Add 50 ml of 18MΩ H_2O to the jar measured using the dedicated measuring cylinder and stir with a clean disposable pipette to make sure liquid is thoroughly mixed.
4. Cap and re-weigh jar, record weight as 'V1'.
5. Label a clean 30 ml bottle with the sample ID, date, initials and 'Al assay'. Weigh it and record weight. Tare scale.
6. Subtract 1ml of sample liquid from the jar and add to bottle (use a new digital pipette for each sample). Place jar on Juniper hotplate at setting 1 to dry overnight.
7. Weigh bottle and record weight as 'V2'.
8. Add 25 ml of the 4% HNO_3 solution to the 30 ml bottle using , weigh and record weight as 'V3'.
9. Record lab temperature.
10. Dispose of Be waste and unused acid and dishwash empty bottles.

At the end of the procedure there will be a bottle for each sample including the blank and a written table with columns recording the weight of the empty jar, V1, the empty 30 ml bottle, V2 and V3. Use lab temperature and solution density to convert the mass of the sample to a volume.

After ICP-MS analysis, the abundance of Al in the sample can be calculated as follows:

$$X(mg) = \left[\frac{C_1 V_3}{V_2}\right] V_1 \qquad \text{(A2.2)}$$

Where:

X (mg) = Abundance of Al in sample

C_1 (mg/l) = Concentration of Al in aliquot measured by ICP

V_1 (ml) = First dilution

V_2 (ml) = Second dilution

V_3 (ml) = Third dilution

The concentration of Al in the sample can be calculated thus:

$$C_0(ppm) = \frac{X.1000}{m} \qquad \text{(A2.3)}$$

Where:

C_0 (ppm) = Concentration of Al in sample

m (g) = Sample mass

Those samples with high (>400 ppm Al) are likely to run badly in the AMS due to Al swamping the Be and lowering the beam current. It may therefore be prudent to repeat stage 16 (cation columns) so that a better Be-Al separation is obtained.

A2.18. Titanium precipitation

This stage is essential for most samples, and particularly so for South African bedrock samples which have been revealed by ICP-MS to contain a high proportion of Ti. It is completed as follows:

1. Make up stock solutions for the following acids:

a. 170 ml 1.2M HCl;

b. 40 ml 3M HCl;

c. 20 ml 30% NH_4OH;

d. 30 ml 3% NH_4OH.

2. Add 20 ml of 1.2M HCl to each Savillex beaker using an acid-cleaned autopipette. Ensure sample has fully dissolved;

3. For each sample, label two 50 ml centrifuge tubes with 'sample# 1' and 'sample# 2'. Transfer each sample to tube labelled 'sample# 1';

4. Adjust the pH of each sample to between 3.8 and 4.1 using ~ 1.75 ml 30% NH_4OH and an autopipette. Add 3% NH_4OH dropwise until the desired pH is reached. Test acidity by dropping a small amount of sample onto pH paper Avoid adding too much NH_4OH which may cause the solution to become too alkaline and Be and Al to precipitate;

5. At about pH 3, a slight cloudiness indicates precipitation of Ti hydroxide. When the correct pH is reached, cap the centrifuge tube, and centrifuge at 3000 rpm for 10 minutes. The supernatant will then contain Be and Al and the Ti will be precipitated. Not all samples will yield Ti (the likely yield will be indicated by the quartz assay at stage 11);

6. Decant the supernatants into the tube labelled 'sample# 2'. These contain Al and Be which will be precipitated in the next stage;

7. Rinse the tube 'sample# 1' with 18MΩ water, the Ti precipitate should retained until after AMS analysis in case of any mistakes.

A2.19. Final perchloric fume

Compounds of Be or Al and remaining cations may cause the two metals to precipitate out of solution at a different pH to that which the metal on its own would. A final perchloric fume is therefore required to ensure that no such compounds remain:

1. In fume cupboard, 1.0 ml of $HClO_4$ is added to each Savillex beaker using autopipette.

2. Samples are placed on small hot-plate (setting 7) until all acid is fumed off;

3. Dry down samples completely. Cap the beakers and clean down fume hood after fuming is finished.

A2.20. Final hydroxide precipitation

Hydroxides of Al and Be are precipitated from solution by adjusting pH in this stage. The procedure is as follows:

1. Wash down the fume cupboard prior to perchloric acid fume;
2. Add 1ml $HClO_4$ to each beaker containing Be and Al fractions. Place on hot plate and fume with hotplate at around 200°C (Stuart scientific setting 9);
3. Make up 40 ml stock solution of 3M HCl. Add 10 ml 12.1M HCl to 60 ml poly bottle. Add 30 ml 18MΩ H_2O. Cap and mix;
4. After perchloric acid has been fumed off and beakers have cooled, dissolve samples by adding 2ml of 3M HCl to beakers using an acid-cleaned pastette;
5. Transfer the sample to a labelled 15ml centrifuge tube. Wash the sides and bottom of beaker with 2ml 18MΩ H_2O. Transfer the wash H_2O to the centrifuge tube;
6. Adjust the pH of the Be solution to between pH 9 and 10 by adding a few drops of ammonia to the tube. Check the pH by adding a small drop of solution to pH paper;
7. Once correct pH range has been reaches, a faint cloudiness may be noticed in the tube as hydroxides of Be. Vortex the sample for a few seconds then centrifuge at 3000 rpm for 15 minutes. After centrifuging a distinct precipitate MUST be visible at the tip of the tube, otherwise a mistake has been made in e.g. the cation column procedure. Be and Al hydroxide precipitates vary in colour from off-white to yellow-brown. There will almost always be a greater volume of Al than Be hydroxide in a sample;
8. Proceed with Al hydroxide precipitation using the same procedure as in steps 6 and 7 except bring the pH to between 8 and 9;
9. After centrifuging, decant the supernatants and discard carefully (beware of Be hazard). Re-precipitate the sample by dissolving in 5ml 18MΩ H_2O and add 3 drops of 3M HCl;

10. Adjust the pH of the sample to the correct range using a few drops of ammonia. Vortex the sample for a few seconds then centrifuge at 3000 rpm for 5 minutes. A precipitate should be now visible. This can be left overnight together with the supernatant in the tube to help transfer B (isobar of Be) into the supernatant;
11. Decant and discard supernatant. Add 5ml 18MΩ H_2O, vortex until sample is disrupted, then centrifuge at 3000 rpm for 5 minutes. A gel-like hydroxide must be present at the tip of the tube. Discard the supernatant and repeat the rinse. Remove the supernatant by decanting, the gel will stick to the end of the tube;
12. Cut the centrifuge tube so that they are about 2cm high; place the cut tubes into the clean Al block heater in a cleaned fume cupboard. Set the heater at 70°C and dry samples overnight.

A2.21. Oxidation procedure

In this stage, hydroxides of Be or Al are oxidised in a quartz vial in an open flame, then packaged for shipping to AMS laboratory. Procedure is as follows:

1. Clean 8 glass vials and plastic caps by rising in 18MΩ H_2O. Dry under filtered air flow;
2. Clean plastic funnels by immersing in 10% HNO_3 for a few minutes then rinsing in 18MΩ H_2O;
3. Clean quartz crucibles by placing in a beaker and covering with 1:1 HNO_3. Heat on a hotplate in fume cupboard for 1 hour at 100°C. Rinse vials in 18MΩ H_2O five times;
4. Rinse Al heater block with 18MΩ H_2O, write sample numbers on the block;
5. Clean metal tongs and tweezers in 18MΩ H_2O. Light gas torch and carefully position in the fume cupboard. Using tweezers, pick a quartz crucible out of the water and transfer to quartz tong. Pre-fire each quartz crucible by heating in outer part of flame for a few seconds. Place prefired quartz crucible in each labelled hole in Al block;

6. Carefully transfer the small bead of Al or Be hydroxide from the centrifuge tube to the quartz crucible using a clean microfunnel;
7. Carefully pick up the quartz crucible with quartz tong and place in the torch flame. Keep the vial in the hottest part of the flame for ~ 10 seconds. The bead of Al or Be should glow incandescently;
8. Let crucible cool and cap with plastic cap. Repeat for all samples. Package each crucible inside labelled glass vial.

A2.22. Mixing and pressing

This is the very last step in the long process of obtaining Be and Al from bedrock or sediment samples. It involves mixing the sample with Niobium (Nb) powder, an inert metal that is pressed into the target to prevent sparking of the sample in the AMS. This is done as follows:

1. In the labelled quartz crucible, crush the BeO sample using a quartz pestle;
2. Add 0.5mg Nb powder (record weight);
3. Assemble a copper cathode by carefully placing the bottom part on a steel pin;
4. Ensuring that the sample and powder are thoroughly mixed, pour out onto a small piece of Al foil then carefully transfer this to the cathode;
5. Ensuring that the steel pin stays in place at the bottom of the cathode to hold the sample in, place the cathode beneath the press and carefully bring down the press (with clean pin on the end) into the cathode to press the sample. Apply pressure up to 200 Pa so that the sample is properly pressed;
6. Place the cathode in a clean labelled cylinder ready for AMS analysis.

Appendix 3 – GIS analysis

In the following section the maps and GIS analytical tools used in this study can be found.

A3.1 Mapping

The following 1:250,000 Geological and Topographic maps published by the Chief Directorate of Surveys and Mapping, Republic of South Africa were used for detailed mapping of tributary catchments:

2816 Alexander Bay
2820 Upington
2826 Bloemfontein
2922 Prieska
3126 Queenstown

The following 1:50,000 Topographic maps published by the Chief Directorate of Surveys and Mapping, Republic of South Africa were used for detailed mapping of sampling locations:

2717DA Fish River Canyon
2717CD Ai-Ais
2820CB Augrabies
2820CA Bysteek
2828DA Golden Gate
2828CB Clarens

A3.2 Catchment averaged characterisation

A large geological map constructed from 1:50,000 Geological maps was used to calculate 'mean' lithology for the catchment averaged samples (Figure A3.1)

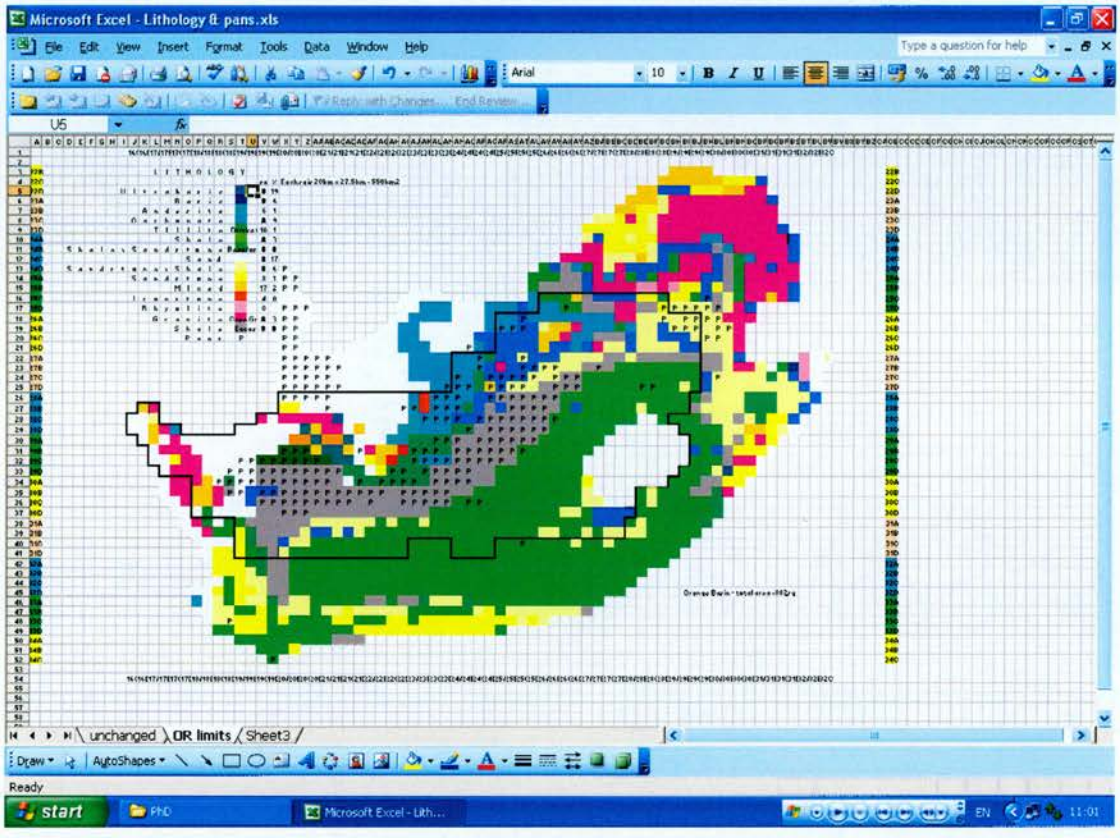

Figure A3.1 Graphic representation of South Africa showing average lithology for each 1:50,000 map sheet. (Each square represents a 1:50,000 Geological sheet (Courtesy of B. King, unpublished data)

Interpretation of the South African landscape was aided by a composite map derived from 1:50,000 topographic sheets (Figure A3.2).

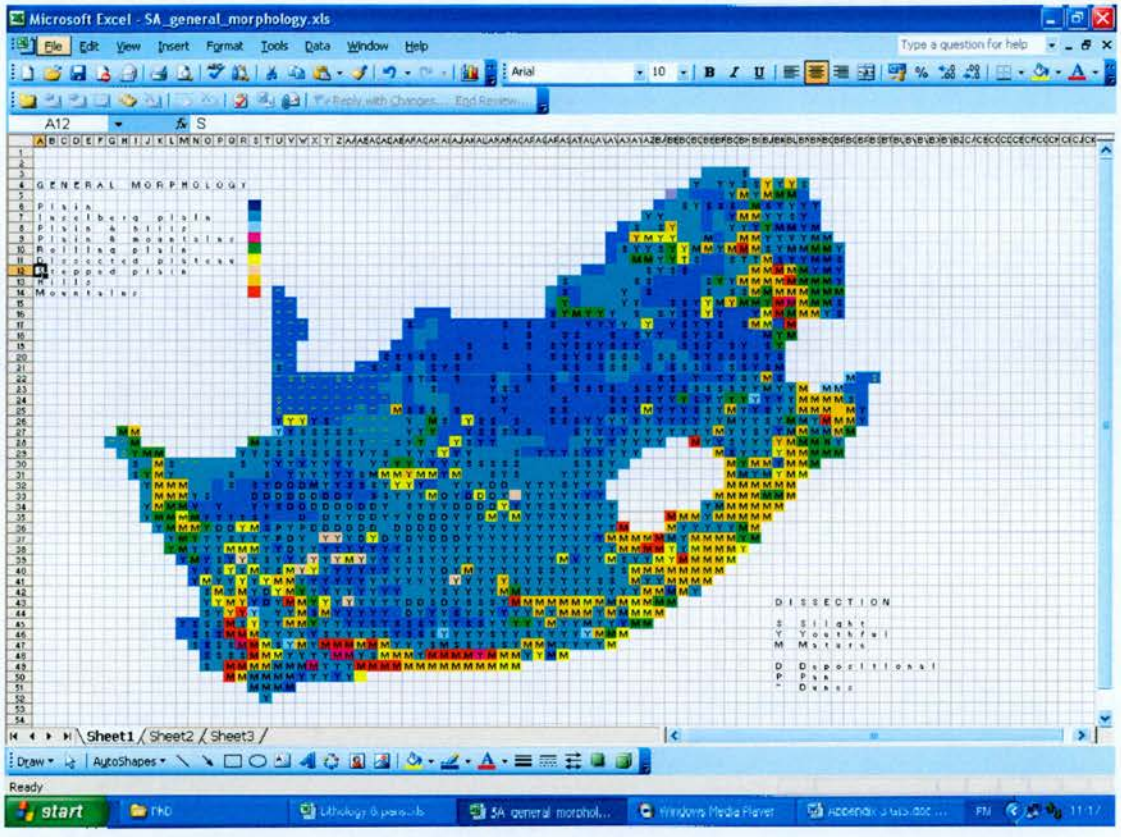

Figure A3.2 Composite map of South Africa derived from 1:50,000 topographic maps, with geomorphic interpretations (Courtesy of B. King, unpublished data)

A3.3 DEM of Augrabies Falls region

Field interpretation of the Augrabies Falls region was aided by the use of a Digital Elevation Model (DEM) derived from 1:10,000 scale aerial images and 1:50,000 topographic maps (Figure A3.3).

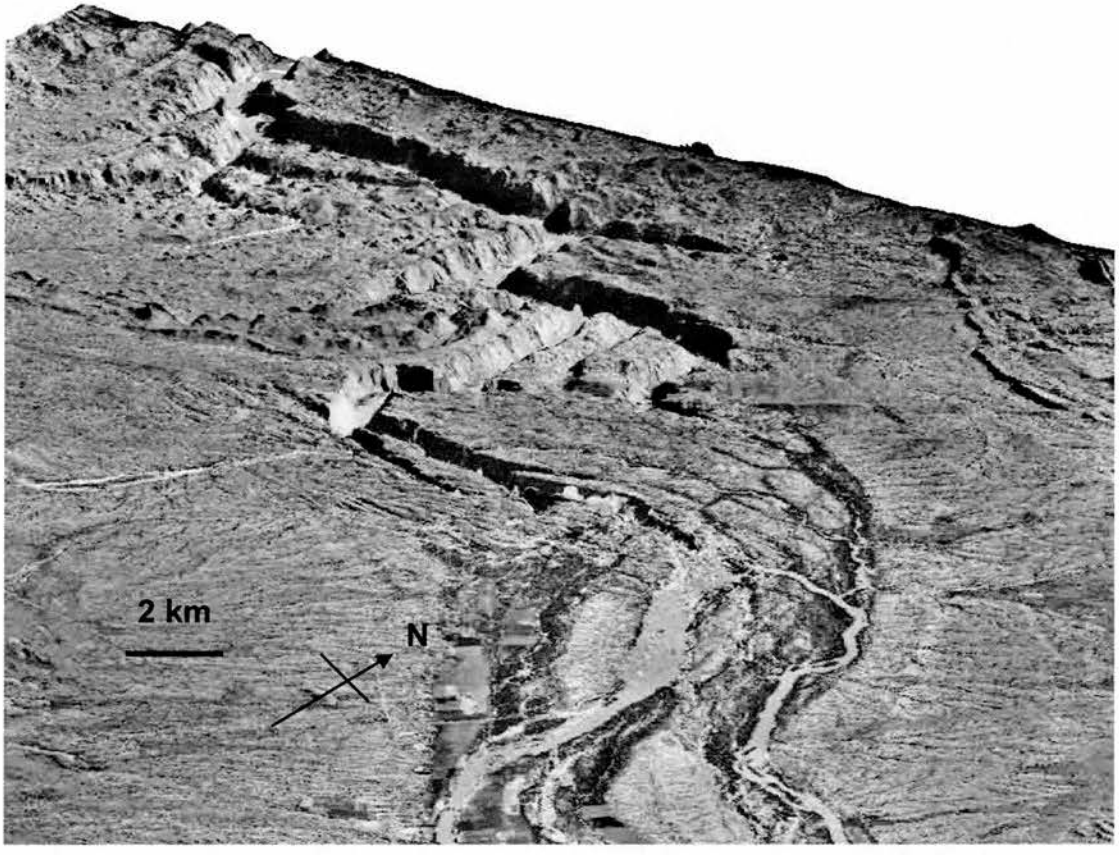

Figure A3.3 DEM of the Augrabies Falls region (Walcott *et al.*, unpublished data).

Appendix 4 – Analytical data (PhD samples)

Sample	Lat. (° S)	Altitude (m)	Basin Lithology (King)	Basin area (km^2)	Catchment averaged latitude (° south)	Mean Basin altitude (m)	Production rate spallation only (at g^{-1} a^{-1}) (Dunai)	±	Production rate spallation and muons (at g^{-1} a^{-1}) (Dunai)	±	Stone's SEL scaling	Production rate spallation only (at g^{-1} a^{-1}) (Stone)
SA03/2/1	28	543	Granite Gneiss	14.1	28.00	637.77	5.82	0.34	5.80	0.34	1.31	6.70
SA03/4/1	28	440	Shale, sandstone and basic	409050	29.57	1383.30	10.67	0.63	10.59	0.62	2.33	11.90
SA03/5/1	28	614	Shale, sandstone and basic	409050	29.57	1383.30	10.67	0.63	10.59	0.62	2.33	11.90
SA03/6/1	28	727	Shale, sandstone and basic	396550	29.57	1456.72	11.27	0.66	11.18	0.66	2.46	12.54
SA03/7/1	28	837	Shale, sandstone and basic	336600	29.57	1395.00	10.76	0.63	10.69	0.63	2.35	12.00

Table A.4.1 SA03 batch 1 analytical data. A weighted average of the SA03-X blank and other process blanks (see Chapter 3) was used to calculate ^{10}Be concentrations. These values were: blank mass = 3.15×10^{-4} g; $^{10}Be/^{9}Be = 1.58 \times 10^{-14} \pm 3.43 \times 10^{-15}$. Be data are normalised using the SUERC NIST standard with a nominal $^{10}Be/^{9}Be$ ratio of 3.00×10^{-11}. Denudation rates are calculated using sea level, high latitude ^{10}Be production rate (Stone, 2000). ± means plus or minus standard uncertainty.

Sample	±	Production rate spallation and muons (at $g^{-1} a^{-1}$) (Stone)	±	Sample mass (g)	±	Carrier mass (g)	± Standard Uncertainty	$^{10}Be/^{9}Be$	σ ($^{10}Be/^{9}Be$)	Blank corrected ratio	±	% uncert blank corr ratio
SA03/2/1	0.31	6.67	0.39	36.70	3.0E-04	2.53E-04	3.00E-07	6.07E-13	4.27E-14	5.92E-13	4.29E-14	7.25E+00
SA03/4/1	0.29	12.27	0.72	7.29	3.0E-04	2.79E-04	3.00E-07	5.70E-13	1.66E-14	5.54E-13	1.69E-14	3.05E+00
SA03/5/1	0.33	12.27	0.72	1.83	3.0E-04	2.86E-04	3.00E-07	2.19E-13	2.72E-14	2.03E-13	2.74E-14	1.35E+01
SA03/6/1	0.36	12.42	0.73	0.71	3.0E-04	2.87E-04	3.00E-07	6.14E-14	3.95E-15	4.56E-14	5.23E-15	1.15E+01
SA03/7/1	0.39	12.48	0.73	0.82	3.0E-04	2.87E-04	3.00E-07	5.80E-14	3.44E-15	4.22E-14	4.86E-15	1.15E+01

Table A.4.1 (continued from previous page)

Sample	N ^{10}Be (at g^{-1})	±	ε (mm ka^{-1}) Spallation only (Dunai)	±	Av. time (ka)	ε (mm ka^{-1}) Spallation and muons (Dunai)	±	Av. time (ka)	ε (mm ka^{-1}) Spallation only (Stone)	± Standard Uncertainty	Av. time (ka)	ε (mm ka^{-1}) spallation & muons (Stone)
SA03/2/1	2.72E+05	1.97E+04	12.48	1.38	47.75	12.44	1.16	47.92	14.42	1.51	41.33	14.36
SA03/4/1	1.42E+06	4.32E+04	4.22	0.37	141.32	4.18	0.28	142.45	4.74	0.33	125.86	4.89
SA03/5/1	2.12E+06	2.85E+05	2.73	0.43	218.08	2.71	0.40	219.89	3.08	0.46	193.49	3.18
SA03/6/1	1.23E+06	1.41E+05	5.20	0.74	114.64	5.16	0.67	115.61	5.81	0.77	102.52	5.76
SA03/7/1	9.90E+05	1.14E+05	6.21	0.88	96.05	6.16	0.80	96.71	6.95	0.93	85.72	7.24

Table A.4.1 (continued from previous page)

Sample	±	Averaging time (ka)
SA03/2/1	1.34	41.52
SA03/4/1	0.32	121.86
SA03/5/1	0.47	187.20
SA03/6/1	0.74	103.50
SA03/7/1	0.94	82.34

Table A.4.1 (continued from previous page)

Sample ID	Latitude (degrees south)	Longitude (degrees east)	Altitude (m)	Thickness correction	Topo shielding correction	Slope shielding correction	Total shielding scaling factor	Production rate spallation only (at g^{-1} a^{-1}) (Dunai)	±	Production rate spallation & muons (at g^{-1} a^{-1}) (Dunai)	±	Stone SEL scaling factor spallation only
SA04-21-1	28	20	635	0.98	1.00	1.00	0.98	5.71	0.75	5.68	0.33	1.13
SA04-22-1	28	20	590	0.98	1.00	1.00	0.98	5.51	0.48	5.48	0.32	1.18
SA04-23-1	28	20	431	0.97	0.77	1.00	0.74	3.66	0.33	3.65	0.21	1.12
SA04-24-1	28	20	430	0.97	0.77	1.00	0.74	3.66	0.33	3.65	0.21	1.12
SA04-27-2	28	17	448	0.98	0.93	1.00	0.91	4.56	0.57	4.53	0.27	1.14

Table A.4.2 SA04 batch 1 analytical data. A weighted average of the SA04-X blank and other process blanks (see Chapter 3) was used to calculate ^{10}Be concentrations. These values were: blank mass = 3.07×10^{-4} g; $^{10}Be/^{9}Be = 1.35 \times 10^{-14} \pm 3.04 \times 10^{-15}$. Be data are normalised using the SUERC NIST standard with a nominal $^{10}Be/^{9}Be$ ratio of 3.00×10^{-11}. Denudation rates are calculated using sea level, high latitude ^{10}Be production rate (Stone, 2000). ± means plus or minus standard uncertainty.

Sample ID	Prod. rate spalln. only (at g^{-1} a^{-1}) (Stone)	±	Stone SEL scaling factor with muons	Prod. rate spallation and muons (at g^{-1} a^{-1}) (Stone)	±	Sample mass (g)	±	Carrier mass (g)	± Standard Uncertainty	$^{10}Be/^{9}Be$	σ ($^{10}Be/^{9}Be$)	N ^{9}Be (at g^{-1})
SA04-21-1	5.66	0.75	1.12	5.64	0.33	25.01	1.00E-05	2.52E-04	1.00E-05	2.12E-12	6.56E-14	1.69E+19
SA04-22-1	5.90	0.48	1.17	5.88	0.35	25.90	1.00E-05	2.50E-04	1.00E-05	1.50E-12	4.99E-14	1.67E+19
SA04-23-1	4.26	0.33	1.12	4.24	0.25	24.54	1.00E-05	2.57E-04	1.00E-05	7.84E-13	6.54E-14	1.71E+19
SA04-24-1	4.25	0.33	1.12	4.24	0.25	48.04	1.00E-05	5.04E-04	1.00E-05	4.70E-13	2.47E-14	3.36E+19
SA04-27-2	5.29	0.57	1.14	5.28	0.31	24.25	1.00E-05	2.51E-04	1.00E-05	2.58E-13	9.11E-14	1.67E+19

Table A.4.2 (continued from previous page)

Sample ID	Blank Corrected Ratio	±	% uncert blank corr ratio	N ^{10}Be (at g^{-1})	±	Erosion rate spallation only (mm ka^{-1}) (Dunai)	±	Averaging time (ka)	Erosion rate spallation and muons (mm ka^{-1}) (Dunai)	± Standard Uncertainty	Averaging time (ka)
SA04-21-1	2.11E-12	6.56E-14	3.11E+00	1.42E+06	7.17E+04	2.12	0.30	281.12	2.11	0.16	282.77
SA04-22-1	1.49E-12	5.00E-14	3.36E+00	9.61E+05	5.01E+04	3.14	0.32	189.70	3.13	0.25	190.44
SA04-23-1	7.71E-13	6.55E-14	8.49E+00	5.39E+05	5.03E+04	3.78	0.49	157.84	3.77	0.42	158.18
SA04-24-1	4.57E-13	2.49E-14	5.46E+00	3.20E+05	1.86E+04	6.55	0.70	91.04	6.53	0.54	91.23
SA04-27-2	2.44E-13	9.12E-14	3.73E+01	1.69E+05	6.33E+04	15.83	6.27	37.66	15.80	6.00	37.73

Table A.4.2 (continued from previous page)

Sample ID	Erosion rate spallation only (mm ka^{-1}) (Stone)	±	Averaging time (ka)	Erosion rate spallation and muons (mm ka^{-1}) (Stone)	±	Averaging time (ka)	Geomag. corrected erosion rate (mm ka^{-1}) (Stone, spallation, muons)	±	Averaging time (ka)	Iterations	% diff with original
SA04-21-1	2.10	0.20	284.30	2.09	0.16	285.32	3.16	0.24	188.51	6.00	33.93
SA04-22-1	3.39	0.33	176.09	3.37	0.27	176.76	4.44	0.35	134.24	4.00	24.05
SA04-23-1	4.44	0.56	134.32	4.42	0.49	134.77	5.41	0.60	110.29	3.00	18.16
SA04-24-1	7.66	0.78	77.87	7.63	0.63	78.12	9.16	0.76	65.08	3.00	16.69
SA04-27-2	18.44	7.09	32.33	18.38	6.98	32.44	22.03	8.37	27.06	2.00	16.57

Table A.4.2 (continued from previous page)

Sample ID	Lat. (° S)	Long. (° E)	Altitude (m)	Basin Lithology	Basin area (km^2)	Mean Basin altitude (m)	Thickness scaling factor	Topo shielding factor	Slope shielding factor	Total Sheilding scaling factor	Production spallation only (at $g^{-1} a^{-1}$) (Dunai)	± Standard Uncertainty
SA-18-1	28	20	624	Granite Gneiss			0.97	1.00	1.00	0.97	5.57	0.33
SA-18-2	28	20	620	Granite Gneiss			0.97	0.97	1.00	0.94	5.41	0.32
SA-19-1C	28	20	566	Granite Gneiss	14.1	637.77	na	na	na	1.00	5.82	0.34
SA-27-1	28	20	448	Granite Gneiss			0.98	0.93	1.00	0.91	4.56	0.27
SA-27-3	28	20	448	Granite Gneiss			0.98	0.93	1.00	0.91	4.56	0.27
SA-30-1B	28	17	161	Shale, sandstone and basic	652800	1230.00	na	na	na	1.00	9.17	0.54
SA-30-1C	28	17	161	Shale, sandstone and basic	652800	1230.00	na	na	na	1.00	9.32	0.55

Table A.4.3 SA04 batch 2a analytical data. The process blank AFB (see Chapter 3) was used to calculate ^{10}Be concentrations. These values were: blank mass = 3.11×10^{-4} g; $^{10}Be/^{9}Be = 1.52 \times 10^{-14} \pm 2.93 \times 10^{-15}$. Be data are normalised using the SUERC NIST standard with a nominal $^{10}Be/^{9}Be$ ratio of 3.00×10^{-11}. Denudation rates are calculated using sea level, high latitude ^{10}Be production rate (Stone, 2000). ± means plus or minus standard uncertainty.

Sample ID	Prod. Rate spalln. and muons (at g^{-1} a^{-1}) (Dunai)	±	Stone's SEL production scaling spallation only	Stone SEL scaling factor spallation & muons	Production rate spallation only (at g^{-1} a^{-1}) (Stone)	±	Production rate spallation and muons (at g^{-1} a^{-1}) (Stone)	±	Sample mass (g)	±	Carrier mass (g)	±
SA-18-1	5.54	0.33	1.30	1.30	6.42	0.38	6.39	0.48	2.81E+01	3.00E-04	2.62E-04	3.00E-07
SA-18-2	5.39	0.32	1.30	1.29	6.23	0.37	6.21	0.61	3.50E+01	3.00E-04	2.57E-04	3.00E-07
SA-19-1C	5.80	0.34	1.31	1.31	6.70	0.39	6.67	0.39	3.46E+01	3.00E-04	2.59E-04	3.00E-07
SA-27-1	4.55	0.27	1.14	1.14	5.29	0.31	5.28	0.57	3.50E+01	3.00E-04	2.60E-04	3.00E-07
SA-27-3	4.55	0.27	1.14	1.14	5.29	0.31	5.28	0.57	3.45E+01	3.00E-04	2.58E-04	3.00E-07
SA-30-1B	9.11	0.54	2.04	2.04	10.35	0.63	10.42	0.61	1.98E+01	3.00E-04	2.58E-04	3.00E-07
SA-30-1C	9.11	0.54	2.04	2.04	10.35	0.63	10.42	0.52	3.15E+01	3.00E-04	2.59E-04	3.00E-07

Table A.4.3 (continued from previous page)

Sample ID	$^{10}Be/^{9}Be$	s ($^{10}Be/^{9}Be$)	N ^{9}Be (at g^{-1})	N ^{10}Be (at g^{-1})	±	Erosion rate (mm ka^{-1}) spallation only (Dunai)	±	Averaging time (ka)	Erosion rate (mm ka^{-1}) spallation and muons (Dunai)	±	Averaging time (ka)
SA-18-1	8.29E-13	1.54E-14	1.75E+19	5.07E+05	9.77E+03	6.28E+00	3.69E-01	8.85E+01	6.25	0.37	95.46
SA-18-2	1.11E-12	2.19E-14	1.72E+19	5.39E+05	1.09E+04	5.71E+00	3.36E-01	9.42E+01	5.69	0.33	104.75
SA-19-1C	5.47E-13	2.70E-14	1.73E+19	2.66E+05	1.36E+04	1.28E+01	7.50E-01	4.59E+01	12.71	0.75	46.91
SA-27-1	6.84E-13	2.39E-14	1.73E+19	3.31E+05	1.19E+04	7.89E+00	4.64E-01	6.64E+01	7.88	0.46	75.68
SA-27-3	6.41E-13	1.85E-14	1.73E+19	3.13E+05	9.39E+03	8.35E+00	4.91E-01	6.28E+01	8.34	0.49	71.50
SA-30-1B	1.63E-12	3.22E-14	1.73E+19	1.41E+06	2.82E+04	3.60E+00	2.12E-01	1.52E+02	3.57	0.21	166.95
SA-30-1C	2.01E-12	3.89E-14	1.73E+19	1.10E+06	2.15E+04	4.79E+00	2.82E-01	1.18E+02	4.67	0.27	127.57

Table A.4.3 (continued from previous page)

Sample ID	Erosion rate (mm ka^{-1}) spallation only (Stone)	±	Averaging time (ka)	Erosion rate (mm ka^{-1}) spallation and muons (Stone)	± Standard Uncertainty	Averaging time (ka)	Geomag. corrected erosion rate (mm ka^{-1}) (Stone, spallation, muons)	±	Averaging time (ka)	Iterations	% diff with original
SA-18-1	7.27	0.62	81.96	7.24	0.56	82.33	8.81	0.55	67.71	2.00	17.76
SA-18-2	6.62	0.57	90.05	6.59	0.66	90.46	7.89	0.49	75.58	2.00	16.45
SA-19-1C	14.73	1.44	40.47	14.67	1.14	40.65	na	na	na	na	na
SA-27-1	9.26	0.84	64.40	9.23	1.06	64.62	10.67	0.74	55.87	5.00	13.54
SA-27-3	9.79	0.87	60.86	9.76	1.10	61.07	11.19	0.74	53.26	3.00	12.79
SA-30-1B	4.10	0.36	145.57	4.13	0.35	144.51	na	na	na	na	na
SA-30-1C	5.35	0.47	111.47	5.39	0.43	110.67	na	na	na	na	na

Table A.4.3 (continued from previous page)

Sample ID	Lat. (° S)	Long. (° E)	Altitude (m)	Thickness shielding scaling factor	Topo shielding scaling factor	Slope shielding scaling factor	Total shielding scaling factor	Production rate spallation only (at $g^{-1} a^{-1}$) (Dunai)	±	Production rate spallation and muons (at $g^{-1} a^{-1}$) (Dunai)	±	Stone'sSEL scaling factor
SA04-17-1	28	20	655	0.96	0.90	1.00	0.86	5.13	0.48	5.07	0.30	1.33
SA04-15-1	28	20	670	0.99	1.00	1.00	0.99	5.97	0.35	5.95	0.35	1.35
SA04-9-2	28	20	660	0.97	1.00	1.00	0.96	5.80	0.60	5.59	0.33	1.34
SA04-6-1	28	20	664	0.99	1.00	1.00	0.99	5.94	0.35	5.92	0.35	1.34
SA04-3-2	28	20	451	0.99	0.95	1.00	0.94	4.63	0.61	4.62	0.27	1.14

Table A.4.4 SA04 batch 2b analytical data. The process blank AFB (see Chapter 3) was used to calculate ^{10}Be concentrations. These values were: blank mass = 3.11×10^{-4} g; $^{10}Be/^{9}Be = 1.52 \times 10^{-14} \pm 2.93 \times 10^{-15}$. Be data are normalised using the SUERC NIST standard with a nominal $^{10}Be/^{9}Be$ ratio of 3.00×10^{-11}. Denudation rates are calculated using sea level, high latitude ^{10}Be production rate (Stone, 2000). ± means plus or minus standard uncertainty.

Sample ID	Stone's scaling factor with muons	Production rate spallation only (at $g^{-1} a^{-1}$) Stone	±	Production rate spallation and muons (at $g^{-1} a^{-1}$) (Stone)	± Standard Uncertainty	Effective geomagnetic latitude (degrees south)	Geomagnetic shielded production rate (Stone, spallation only) (at $g^{-1} yr^{-1}$)	± Standard Uncertainty	Sample mass (g)	± Standard Uncertainty	Carrier mass (g)	± Standard Uncertainty
SA04-17-1	1.33	5.85	0.35	5.83	0.35	41.16	7.37	0.43	30.14	3.00E-04	3.14E-04	3.00E-07
SA04-15-1	1.34	6.81	0.41	6.78	0.41	36.43	7.93	0.47	29.38	3.00E-04	3.11E-04	3.00E-07
SA04-9-2	1.33	6.57	0.39	6.54	0.39	35.71	7.54	0.44	34.27	3.00E-04	3.11E-04	3.00E-07
SA04-6-1	1.33	6.78	0.41	6.75	0.40	37.40	8.03	0.47	28.02	3.00E-04	3.11E-04	3.00E-07
SA04-3-2	1.14	5.49	0.33	5.48	0.33	37.97	6.47	0.38	31.70	3.00E-04	3.12E-04	3.00E-07

Table A.4.4 (continued from previous page)

Sample ID	$^{10}Be/^{9}Be$	σ ($^{10}Be/^{9}Be$)	% Error	N ^{9}Be (at g^{-1})	Blank corrected ratio	±	% uncert. Blank corr ratio	N ^{10}Be (at g^{-1})	±	Erosion rate spallation only (mm ka^{-1}) (Dunai)	±	Averaging time (ka)
SA04-17-1	5.01E-14	2.40E-15	4.79E+00	2.09E+19	3.48E-14	2.40E-15	6.88E+00	2.42E+04	1.67E+03	126.02	14.56	4.73
SA04-15-1	6.59E-13	1.08E-14	1.64E+00	2.08E+19	6.44E-13	1.08E-14	1.68E+00	4.55E+05	7.66E+03	7.48	0.46	79.75
SA04-9-2	1.44E-13	7.42E-15	5.15E+00	2.08E+19	1.29E-13	7.42E-15	5.76E+00	7.81E+04	4.50E+03	43.27	5.22	13.78
SA04-6-1	1.64E-12	3.16E-14	1.92E+00	2.08E+19	1.63E-12	3.16E-14	1.94E+00	1.21E+06	2.35E+04	2.64	0.16	226.24
SA04-3-2	6.55E-13	1.28E-14	1.96E+00	2.08E+19	6.39E-13	1.28E-14	2.01E+00	4.20E+05	8.43E+03	6.44	0.84	92.58

Table A.4.4 (continued from previous page)

Sample ID	Erosion rate spallation and muons (mm ka^{-1}) (Dunai)	±	Averaging time (ka)	Erosion rate spallation only (mm ka^{-1}) (Stone)	±	Averaging time (ka)	Erosion rate spallation and muons (mm ka^{-1}) (Stone)	±	Averaging time (ka)	ε (mm ka^{-1}) (Stone) Geomag. corrected	±	Geomag. corrected erosion rate (mm ka^{-1}) (Stone, spallation, muons)
SA04-17-1	124.54	10.37	4.79	143.88	13.14	4.14	143.23	13.08	4.16	216.55	19.61	181.22
SA04-15-1	7.45	0.62	80.02	8.64	0.54	68.99	8.60	0.54	69.32	11.47	0.70	10.11
SA04-9-2	41.68	3.47	14.30	49.86	4.15	11.96	49.64	4.13	12.01	59.88	4.93	57.24
SA04-6-1	2.63	0.22	227.08	3.07	0.19	193.91	3.06	0.19	194.88	3.75	0.23	3.69
SA04-3-2	6.43	0.53	92.78	7.53	0.48	79.19	7.50	0.47	79.46	9.46	0.59	8.91

Table A.4.4 (continued from previous page)

Sample ID	±	Averaging time (ka)	Iterations	% diff with original
SA04-17-1	16.41	3.29	2	20.97
SA04-15-1	0.62	58.99	3	14.91
SA04-9-2	4.71	10.41	2	13.29
SA04-6-1	0.23	161.49	3	17.14
SA04-3-2	0.55	66.88	2	15.82

Table A.4.4 (continued from previous page)

Sample ID	Latitude (degrees south)	Longitude (degrees east)	Altitude (m)	Basin Lithology	Basin area (km^2)	Basin altitude (m)	Thickness shielding scaling factor	Topo shielding scaling factor	Slope shielding scaling factor	Total Shielding scaling factor	Production rate spallation only (at $g^{-1}a^{-1}$) Dunai	±
SA04-19-1-B	28	20	566	Granite-gneiss	14.10	637.77	0.99	1.00	1.00	0.99	5.82	0.34
SA04-20-1	28	20	610	Granite-gneiss	na	na	1.00	1.00	1.00	0.96	5.64	0.33
SA04-21-2	28	20	635	Granite-gneiss	na	na	0.98	0.98	1.00	0.96	5.58	0.33
SA04-36-1	31	27	1625	Molteno sandstone	71.78	1766.00	1.00	1.00	1.00	1.00	14.66	0.86

Table A.4.5 SA04 batch 3 analytical data. A weighted average of the SA04-X-3 blank and other process blanks (see Chapter 3) was used to calculate ^{10}Be concentrations. These values were: blank mass = 3.07×10^{-4} g; $^{10}Be/^{9}Be = 1.46 \times 10^{-14} \pm 3.05 \times 10^{-15}$. Be data are normalised using the SUERC NIST standard with a nominal $^{10}Be/^{9}Be$ ratio of 3.00×10^{-11}. Denudation rates are calculated using sea level, high latitude ^{10}Be production rate (Stone, 2000). ± means plus or minus standard uncertainty.

Sample ID	Production rate spallation and muons (at $g^{-1}a^{-1}$) Dunai	±	Stone's SEL scaling factor (spallation and muons)	Production rate spallation only (at $g^{-1}a^{-1}$) (Stone)	±	Production rate spallation and muons (at $g^{-1}a^{-1}$) Stone	± Standard Uncertainty	Sample mass (g)	±	Carrier mass (g)	±	$^{10}Be/^{9}Be$
SA04-19-1-B	5.80	0.34	1.31	6.70	0.39	6.67	0.39	35.35	3.00E-04	2.57E-04	3.00E-07	6.42E-13
SA04-20-1	5.62	0.33	1.28	6.51	0.38	6.48	0.38	32.24	3.00E-04	2.58E-04	3.00E-07	1.23E-12
SA04-21-2	5.56	0.33	1.31	6.43	0.59	6.40	0.59	26.40	3.00E-04	2.53E-04	3.00E-07	1.65E-12
SA04-36-1	14.53	0.85	3.10	15.95	0.94	15.78	0.93	22.21	3.00E-04	2.58E-04	3.00E-07	1.59E-12

Table A.4.5 (continued from previous page)

Sample ID	s ($^{10}Be/^{9}Be$)	N ^{9}Be (at g^{-1})	Blank corrected ratio	St Uncert blank corr ratio	N ^{10}Be (at g^{-1})	±	Erosion rate spallation only (Dunai) (mm ka^{-1})	±	Averaging time (ka)	Erosion rate spallation and muons (Dunai) (mm ka^{-1})	±
SA04-19-1-B	1.84E-14	1.72E+19	6.27E-13	1.84E-14	3.05E+05	8.96E+03	11.10	0.73	53.73	11.06	0.73
SA04-20-1	3.55E-14	1.73E+19	1.22E-12	3.55E-14	6.51E+05	1.90E+04	4.89	0.32	121.91	4.87	0.32
SA04-21-2	3.34E-14	1.69E+19	1.63E-12	3.34E-14	1.04E+06	2.14E+04	2.91	0.18	204.63	2.90	0.18
SA04-36-1	3.19E-14	1.73E+19	1.57E-12	3.19E-14	1.22E+06	2.49E+04	6.88	0.43	86.66	6.82	0.42

Table A.4.5 (continued from previous page)

Sample ID	Averaging time (ka)	Erosion rate spallation only (Stone) (mm ka^{-1})	±	Averaging time (ka)	Erosion rate spallation and muons (Stone) (mm ka^{-1})	±	Averaging time (ka)	Geomag corrected erosion rate	±	Av. Time (ka)	Iterations	% diff with non corrected
SA04-19-1-B	53.92	12.82	0.84	46.49	12.76	0.84	46.70	na	na	na	na	na
SA04-20-1	122.37	5.69	0.37	104.86	5.66	0.33	105.33	6.79	0.45	87.79	4.00	16.66
SA04-21-2	205.79	3.40	0.32	175.53	3.38	0.31	176.37	3.61	0.23	165.02	3.00	6.44
SA04-36-1	87.47	7.51	0.47	79.41	7.43	0.44	80.26	na	na	na	na	na

Table A.4.5 (continued from previous page)

Sample ID	Latitude (degrees south)	Long (degrees east)	Altitude (m)	Basin Lithology	Basin area (km^2)	Mean Basin altitude (m)	Basin latitude (degrees south)	Production rate spallation only (at g a^{-1}) (Dunai)	±	Production rate spallation and muons (at g a^{-1}) (Dunai)	±	Production rate spallation only (at $g^{-1}a^{-1}$) (Stone)
SA04-28-1	28	20	447	Cape Granite	34	683.73	28.00	6.03	0.35	6.01	0.36	6.94
SA04-29-1	27	17	203	Richtersveld Granite	73750	1216.10	25.87	8.69	0.51	8.64	0.51	9.82
SA04-35-1	31	26	1600	Molteno sandstone	12	1762.00	31.00	14.62	0.86	14.49	0.85	16.03
SA04-37-1	31	26	1335	Elliot and Burgersdorp Formations	125	1966.00	31.00	16.91	0.99	16.75	0.99	18.42

Table A.4.6 SA04 batch 4 analytical data. A weighted average of the SA04-X-4 blank and other process blanks (see Chapter 3) was used to calculate ^{10}Be concentrations. These values were: blank mass = 3.03×10^{-4} g; $^{10}Be/^{9}Be = 1.24 \times 10^{-14} \pm 1.88 \times 10^{-15}$. Be data are normalised using the SUERC NIST standard with a nominal $^{10}Be/^{9}Be$ ratio of 3.00×10^{-11}. Denudation rates are calculated using sea level, high latitude ^{10}Be production rate (Stone, 2000). ± means plus or minus standard uncertainty.

Sample ID	±	Production rate spallation and muons (at g^{-1} a^{-1}) (Stone)	±	Sample mass (g)	±	Carrier mass (g)	±	$^{10}Be/^{9}Be$	s ($^{10}Be/^{9}Be$)	N ^{9}Be (at g^{-1})	Blank corrected ratio
SA04-28-1	0.41	6.91	0.41	35.12	3.00E-04	2.60E-04	3.00E-07	1.3733E-12	3.608E-14	1.7353E+19	1.361E-12
SA04-29-1	0.58	9.74	0.57	29.03	3.00E-04	2.59E-04	3.00E-07	2.5744E-12	5.543E-14	1.7293E+19	2.562E-12
SA04-35-1	0.94	15.86	0.93	33.60	3.00E-04	2.61E-04	3.00E-07	3.3503E-12	1.032E-13	1.7427E+19	3.338E-12
SA04-37-1	1.08	18.21	1.07	25.94	3.00E-04	2.56E-04	3.00E-07	7.1483E-13	1.882E-14	1.7113E+19	7.025E-13

Table A.4.6 (continued from previous page)

Sample ID	St uncert. Blank corr. Ratio	% Uncert. Blank corr ratio	N ^{10}Be (at g^{-1})	±	Erosion rate spallation only (mm ka^{-1}) (Dunai)	±	Averaging time (ka)	Erosion rate spallation and muons (mm ka^{-1}) (Dunai)	±	Averaging time (ka)	Erosion rate spallation only (mm ka^{-1}) (Stone)
SA04-28-1	3.61291E-14	2.65E+00	6.73E+05	7.77E+02	5.07	0.42	117.55	5.05	0.42	117.96	5.88
SA04-29-1	5.5462E-14	2.16E+00	1.53E+06	1.77E+03	3.12	0.26	191.00	3.10	0.26	192.20	3.56
SA04-35-1	1.03217E-13	3.09E+00	1.73E+06	1.99E+03	4.76	0.40	125.22	4.72	0.39	126.40	5.25
SA04-37-1	1.8914E-14	2.69E+00	4.63E+05	5.43E+02	21.48	1.79	27.76	21.27	1.77	28.02	23.42

Table A.4.6 (continued from previous page)

Sample ID	± Standard Uncertainty	Averaging time (ka)	Erosion rate spallation and muons (mm ka^{-1}) (Stone)	±	Averaging time (ka)	Erosion rate spallation only. No decay (mm ka^{-1}) (Stone)	±	Averaging time (ka)
SA04-28-1	0.49	101.37	5.85	0.49	101.88	6.15	0.51	96.87
SA04-29-1	0.30	167.41	3.53	0.29	168.80	3.83	0.32	155.46
SA04-35-1	0.44	113.63	5.19	0.43	114.89	5.52	0.46	108.00
SA04-37-1	1.95	25.46	23.15	1.93	25.75	23.69	1.97	25.16

Table A.4.6 (continued from previous page)

Sample ID	Latitude (degrees south)	Longitude (degrees east)	Altitude (m)	Basin Lithology	Basin area (km^2)	Basin altitude (m)	Production rate spallation only (at g^{-1} a^{-1}) (Dunai)	±	Production rate spallation and muons (at g^{-1} a^{-1}) (Dunai)	±	Stone's SEL scaling factor	Production rate spallation only (at g^{-1} a^{-1}) (Stone)
SA04-19-1-A	28	20	566	Granite-gneiss	14.1	637.77	5.82	0.34	5.80	0.34	1.31	6.70
SA-04-30-1-A	28	17	161	Shale, sandstone and basic	652800	1230.00	9.17	0.54	9.32	0.55	2.11	11.78
SA04-41-1	31	26	1294	Molteno sandstone and Drakensberg basalt	85250	1984.60	17.13	1.01	16.07	0.95	2.87	18.36
SA04-42-1	31	26	1296	Molteno sandstone	770.0625	1296.00	9.86	0.58	9.79	0.58	2.17	11.07
SA05-14-1	28	28	1900	Clarens sandstone	63	2314.00	19.74	1.16	19.54	1.15	3.36	21.71

Table A.4.7 SA05 batch y analytical data. Process blank SA04-Y was used to calculate ^{10}Be concentrations. The values are: blank mass = 3.54×10^{-4} g; $^{10}Be/^{9}Be = 4.40 \times 10^{-14} \pm 9.18 \times 10^{-15}$. Be data are normalised using the SUERC NIST standard with a nominal $^{10}Be/^{9}Be$ ratio of 3.00×10^{-11}. Denudation rates are calculated using sea level, high latitude ^{10}Be production rate (Stone, 2000). ± means plus or minus standard uncertainty.

Sample ID	±	Production rate spallation and muons (at g^{-1} a^{-1}) (Stone)	±	Sample mass (g)	±	Carrier mass (g)	±	$^{10}Be/^{9}Be$	s ($^{10}Be/^{9}Be$)	% Error	N 9Be (at g^{-1})
SA04-19-1-A	0.39	6.67	0.39	0.43	3.00E-04	2.74E-04	3.00E-07	1.32E-14	1.65E-15	1.25E+01	1.83E+19
SA-04-30-1-A	0.69	11.68	0.69	5.36	3.00E-04	2.76E-04	3.00E-07	4.63E-13	1.77E-14	3.82E+00	1.84E+19
SA04-41-1	1.08	18.15	1.07	3.41	3.00E-04	2.76E-04	3.00E-07	8.85E-14	3.79E-15	4.28E+00	1.84E+19
SA04-42-1	0.65	10.98	0.65	4.46	3.00E-04	3.05E-04	3.00E-07	2.11E-13	6.66E-15	3.16E+00	2.04E+19
SA05-14-1	1.28	21.45	1.26	5.53	3.00E-04	3.04E-04	3.00E-07	7.58E-14	3.90E-15	5.15E+00	2.03E+19

Table A.4.7 (continued from previous page)

Sample ID	Blank (Y-1) corrected ratio	St uncert. Blank corr ratio	N 10Be (at g^{-1})	St uncert. N ^{10}Be	% Error	±	Erosion rate spallation only (mm ka^{-1}) (Dunai)	±	Averaging time (ka)	Erosion rate spallation and muons (mm ka^{-1}) (Dunai)	±
SA04-19-1-A	8.77E-15	1.89E-15	3.78E+05	8.12E+04	2.15E+01	8.12E+04	8.91	1.99	66.89	8.88	1.98
SA-04-30-1-A	4.59E-13	1.77E-14	1.58E+06	6.09E+04	3.86E+00	2.45E-04	3.19	0.19	179080.66	3.17	0.19
SA04-41-1	8.41E-14	3.90E-15	4.55E+05	2.11E+04	4.64E+00	1.02E-03	22.19	1.31	26695.85	21.98	1.29
SA04-42-1	2.06E-13	6.92E-15	9.43E+05	3.16E+04	3.36E+00	3.36E+00	5.96	0.07	99.99	5.92	0.07
SA05-14-1	7.14E-14	4.33E-15	2.62E+05	1.59E+04	6.07E+00	6.07E+00	44.60	0.08	13.37	44.14	0.08

Table A.4.7 (continued from previous page)

Sample ID	Averaging time (ka)	Erosion rate spallation only (mm ka^{-1}) (Stone)	±	Averaging time (ka)	Erosion rate spallation and muons (mm ka^{-1}) (Stone)	±	Averaging time (ka)
SA04-19-1-A	67.12	10.31	2.30	57.83	10.26	2.29	58.09
SA-04-30-1-A	0.19	3.64	0.26	163.75	3.61	0.25	165.12
SA04-41-1	1.31	23.98	1.80	24.86	23.71	1.78	25.14
SA04-42-1	100.74	6.72	0.06	88.66	6.67	0.07	89.41
SA05-14-1	13.51	49.08	0.06	12.15	48.47	0.08	12.30

Table A.4.7 (continued from previous page)

Sample ID	Latitude (degrees south)	Altitude (m)	Basin Lithology	Basin area (km^2)	Basin altitude (m)	Thickness shielding scaling factor	Topo shielding scaling factor	Slope shielding scaling factor	Shielded scaling factor	Production rate spallation only (at g^{-1} a^{-1}) (Dunai)	± Standard Uncertainty	Production rate spallation and muons (at g^{-1} a^{-1}) (Dunai)
SA05-3-1	28	724	Granite gneiss	na	na	0.94	1.00	1.00	0.94	5.88	0.37	5.85
SA05-3-2	28	720	Granite gneiss	na	na	0.96	1.00	1.00	0.96	5.96	0.37	5.93
SA05-4-1	28	613	Granite gneiss	na	na	0.99	1.00	1.00	0.99	5.66	0.34	5.63
SA05-4-2	28	613	Granite gneiss	na	na	0.99	1.00	1.00	0.99	5.66	0.34	5.63
SA05-6-1	28	623	Granite gneiss	na	na	1.00	1.00	1.00	1.00	5.75	0.34	5.73
SA05-8-1	28	602	Cape Granite	400	700	1.00	1.00	1.00	1.00	6.11	0.36	6.09
SA05-9-1	28	596	Cape Granite	400	700	1.00	1.00	1.00	1.00	6.11	0.36	6.09

Table A.4.8 SA05 batch 1 analytical data. Process blank SA05-X-1 was used to calculate ^{10}Be concentrations. The values are: blank mass = 5.13×10^{-4} g; $^{10}Be/^{9}Be = 1.41 \times 10^{-14} \pm 2.72 \times 10^{-15}$. Be data are normalised using the SUERC NIST standard with a nominal $^{10}Be/^{9}Be$ ratio of 3.00×10^{-11}. Denudation rates are calculated using sea level, high latitude ^{10}Be production rate (Stone, 2000). ± means plus or minus standard uncertainty.

Sample ID	±	Stone's SEL scaling	Production rate spallation only (at g^{-1} a^{-1}) (Stone)	±	Production rate spallation and muons (at g^{-1} a^{-1}) (Stone)	±	Sample mass (g)	±	Carrier mass (g)	±	$^{10}Be/^{9}Be$	Uncertainty ($^{10}Be/^{9}Be$)
SA05-3-1	0.50	1.40	6.75	0.50	6.71	0.39	22.68	3.00E-04	2.58E-04	3.00E-07	1.34E-12	3.92E-14
SA05-3-2	0.51	1.40	6.84	0.50	6.80	0.40	30.79	3.00E-04	2.59E-04	3.00E-07	7.00E-13	1.84E-14
SA05-4-1	0.33	1.29	6.53	0.50	6.50	0.38	26.75	3.00E-04	2.61E-04	3.00E-07	1.03E-13	4.66E-15
SA05-4-2	0.33	1.29	6.53	0.50	6.50	0.38	27.32	3.00E-04	2.54E-04	3.00E-07	6.21E-12	1.47E-13
SA05-6-1	0.34	1.30	6.63	0.50	6.60	0.39	30.39	3.00E-04	2.63E-04	3.00E-07	9.48E-14	6.54E-15
SA05-8-1	0.36	1.43	7.07	0.50	7.04	0.41	35.68	3.00E-04	2.58E-04	3.00E-07	3.77E-12	9.49E-14
SA05-9-1	0.36	1.43	7.60	0.50	7.56	0.44	34.99	3.00E-04	2.57E-04	3.00E-07	3.68E-12	7.99E-14

Table A.4.8 (continued from previous page)

Sample ID	N ^{9}Be (at g^{-1})	Blank corrected ratio	St Uncert. Blank corrected ratio	% st uncert. Blank corr. Ratio	N ^{10}Be (at g^{-1})	St Uncert. N 10Be	Erosion rate spallation only (mm ka^{-1}) (Dunai)	±	Averaging time (ka)	Erosion rate spallation and muons (mm ka^{-1}) (Dunai)	±	Averaging time (ka)
SA05-3-1	1.73E+19	1.33E-12	3.93E-14	2.96E+00	1.01E+06	2.99E+04	3.19	0.22	186.80	3.17	0.29	187.78
SA05-3-2	1.73E+19	6.86E-13	1.86E-14	2.71E+00	3.86E+05	1.05E+04	8.93	0.60	66.76	8.88	0.80	67.10
SA05-4-1	1.74E+19	8.84E-14	5.39E-15	6.10E+00	5.76E+04	3.52E+03	58.29	4.96	10.23	57.99	4.91	10.28
SA05-4-2	1.70E+19	6.20E-12	1.47E-13	2.36E+00	3.86E+06	9.13E+04	0.60	0.04	991.63	0.60	0.04	999.27
SA05-6-1	1.76E+19	8.06E-14	7.08E-15	8.79E+00	4.66E+04	4.10E+03	73.25	7.75	8.14	72.99	7.72	8.17
SA05-8-1	1.73E+19	3.76E-12	9.49E-14	2.53E+00	1.82E+06	4.60E+04	1.73	0.11	344.63	1.72	0.11	345.94
SA05-9-1	1.72E+19	3.67E-12	7.99E-14	2.18E+00	1.80E+06	3.93E+04	1.75	0.11	340.69	1.74	0.11	341.99

Table A.4.8 (continued from previous page)

Sample ID	Erosion rate spallation only (mm ka^{-1}) (Stone)	± Standard Uncertainty	Averaging time (ka)	Erosion rate spallation and muons (mm ka^{-1}) (Stone)	± Standard Uncertainty	Averaging time (ka)	Geomag corrected erosion rate (mm ka^{-1})	± Error	Averaging time (ka)	Iterations
SA05-3-1	3.70	0.29	160.98	3.68	0.24	161.84	4.50	0.30	132.44	3
SA05-3-2	10.29	0.80	57.92	10.24	0.66	58.21	12.12	0.79	49.20	3
SA05-4-1	67.23	6.57	8.79	67.50	5.72	8.83	76.99	6.52	7.74	2
SA05-4-2	0.73	0.06	802.23	0.74	0.05	806.96	0.87	0.06	683.08	5
SA05-6-1	84.50	9.78	7.05	84.14	8.90	7.09	n/a	n/a	n/a	n/a
SA05-8-1	2.05	0.15	291.39	2.03	0.13	293.01	n/a	n/a	n/a	n/a
SA05-9-1	2.24	0.16	265.85	2.23	0.14	267.48	n/a	n/a	n/a	n/a

Table A.4.8 (continued from previous page)

Sample ID	Latitude (degrees south)	Altitude (m)	Thickness shielding scaling factor	Topo shielding scaling factor	Slope shielding scaling factor	Shielded Scaling factor	Production rate spallation only (at $g^{-1} a^{-1}$) (Dunai)	±	Production rate spallation and muons (at $g^{-1} a^{-1}$) (Dunai)	±	Stone scaling factor with muons	Stone's altitude-latitude scaling factor
SA05-1-1	28	631	0.99	0.98	0.98	0.95	5.51	0.34	5.49	0.32	1.30	1.31
SA05-1-2	28	635	0.99	0.98	0.99	0.96	5.59	0.34	5.56	0.33	1.31	1.31
SA05-1-3	28	625	0.99	0.95	0.99	0.93	5.37	0.34	5.35	0.31	1.30	1.30
SA05-2-1	28	624	0.98	0.98	1.00	0.96	5.52	0.34	5.49	0.32	1.30	1.30
SA05-2-2	28	636	0.98	0.97	0.99	0.95	5.50	0.34	5.48	0.32	1.31	1.31
SA05-2-3	28	646	0.98	0.97	0.99	0.93	5.46	0.34	5.43	0.32	1.32	1.32
SA05-5-1	28	613	0.98	1.00	1.00	0.93	5.32	0.34	5.29	0.31	1.28	1.29

Table A.4.9 SA05 batch 2 analytical data. Process blank SA05-X-1 was used to calculate ^{10}Be concentrations. The values are: blank mass = 3.58×10^{-4} g; $^{10}Be/^{9}Be = 1.41 \times 10^{-14} \pm 2.72 \times 10^{-15}$. Be data are normalised using the SUERC NIST standard with a nominal $^{10}Be/^{9}Be$ ratio of 3.00×10^{-11}. Denudation rates are calculated using sea level, high latitude ^{10}Be production rate (Stone, 2000). ± means plus or minus standard uncertainty.

Sample ID	Production rate spallation only (at g^{-1} a^{-1}) (Stone)	±	Production rate spallation and muons (at g^{-1} a^{-1}) (Stone)	±	Sample mass (g)	±	Carrier mass (g)	±	$^{10}Be/^{9}Be$	s ($^{10}Be/^{9}Be$)	N ^{9}Be
SA05-1-1	6.67	0.39	6.32	0.31	24.78	3.00E-04	2.51E-04	3.00E-07	6.52E-13	1.75E-14	1.67E+19
SA05-1-2	6.69	0.39	6.41	0.34	16.47	3.00E-04	2.63E-04	3.00E-07	8.23E-13	2.77E-14	1.76E+19
SA05-1-3	6.64	0.39	6.16	0.28	9.45	3.00E-04	2.59E-04	3.00E-07	2.00E-13	8.02E-15	1.73E+19
SA05-2-1	6.64	0.39	6.33	0.32	20.06	3.00E-04	2.56E-04	3.00E-07	6.08E-13	1.35E-14	1.71E+19
SA05-2-2	6.70	0.39	6.31	0.25	20.00	3.00E-04	2.58E-04	3.00E-07	1.34E-12	5.65E-14	1.72E+19
SA05-2-3	6.75	0.40	6.25	0.26	16.67	3.00E-04	2.56E-04	3.00E-07	1.19E-12	3.13E-14	1.71E+19
SA05-5-1	6.58	0.39	6.10	0.27	35.05	3.00E-04	2.57E-04	3.00E-07	1.35E-13	8.91E-15	1.72E+19

Table A.4.9 (continued from previous page)

Sample ID	Blank corrected ratio	±	N ^{10}Be (at g^{-1})	±	Erosion rate spallation only (mm ka^{-1}) (Dunai)	±	Averaging time (ka)	Erosion rate spallation and muons (mm ka^{-1}) (Dunai)	±	Averaging time (ka)	Erosion rate spallation only (mm ka^{-1}) (Stone)
SA05-1-1	6.38E-13	1.77E-14	4.31E+05	1.20E+04	7.35	0.50	81.13	7.32	0.48	81.42	8.51
SA05-1-2	8.09E-13	2.78E-14	8.63E+05	2.97E+04	3.59	0.25	166.09	3.57	0.24	167.02	4.17
SA05-1-3	1.86E-13	8.47E-15	3.39E+05	1.55E+04	9.16	0.71	65.09	9.13	0.68	65.33	10.60
SA05-2-1	5.94E-13	1.38E-14	5.06E+05	1.17E+04	6.23	0.41	95.67	6.20	0.39	96.20	7.22
SA05-2-2	1.33E-12	5.66E-14	1.15E+06	4.88E+04	2.59	0.19	230.45	2.58	0.19	231.33	3.02
SA05-2-3	1.18E-12	3.14E-14	1.21E+06	3.22E+04	2.42	0.17	246.09	2.41	0.16	247.50	2.83
SA05-5-1	1.21E-13	9.32E-15	5.92E+04	4.56E+03	53.24	5.30	11.20	52.96	5.13	11.26	61.41

Table A.4.9 (continued from previous page)

Sample ID	±	Averaging time (ka)	Erosion rate spallation and muons (mm ka^{-1}) (Stone)	±	Averaging time (ka)	Geomag corrected erosion (mm ka^{-1})	± Error	Averaging time (ka)	Iterations	% difference with original
SA05-1-1	0.93	70.08	8.47	0.69	70.39	10.04	0.88	59.35	4.00	15.69
SA05-1-2	0.26	142.80	4.16	0.26	143.48	5.14	0.46	116.03	2.00	19.13
SA05-1-3	0.68	56.24	10.55	0.68	56.49	12.48	1.18	47.78	3.00	15.42
SA05-2-1	0.79	82.57	7.19	0.58	82.94	8.67	0.75	68.77	2.00	17.09
SA05-2-2	0.33	197.21	3.01	0.25	198.17	3.63	0.34	164.05	3.00	17.22
SA05-2-3	0.29	210.65	2.82	0.22	211.69	3.43	0.30	173.98	2.00	17.81
SA05-5-1	5.44	9.71	61.14	5.42	9.75	70.37	7.98	8.47	3.00	13.11

Table A.4.9 (continued from previous page)

Sample ID	Geomag corrected erosion rate (mm ka^{-1}) (Stone, spallation, muons)	± Error	Averaging time (ka)	Iterations	% diff corrected, uncorrected
SA05-1-1	9.65	0.66	61.78	3	17.94
SA05-1-2*	5.29	0.39	112.66	3	20.79
SA05-1-3*	9.98	0.87	59.75	7	15.34
SA05-2-1	8.02	0.58	74.37	2	17.77
SA05-2-2	3.46	0.21	172.20	5	18.71
SA05-3-1*	2.75	0.18	216.78	3	20.20
SA05-4-2	1.79	0.11	332.77	6	20.34
SA05-6-1	na	na	na	na	na
SA04-29-1	na	na	na	na	na
SA04-35-1	na	na	na	na	na

Table A.4.9 (continued from previous page)

Sample ID	Latitude (degrees south)	Altitude (m)	Geology	Basin averaged lat (degrees south)	Basin area (km^2)	Basin averaged altitude (m)	Thickness shielding scaling factor	Topo shielding scaling factor	Slope shielding scaling factor	Shielded Scaling factor	Production rate spallation only (at g^{-1} a^{-1}) (Dunai)
SA05-1-1	28	631	Granite gneiss	na	na	na	0.99	0.98	0.98	0.95	33.60
SA05-1-2*	28	635	Granite gneiss	na	na	na	0.99	0.98	0.99	0.96	34.06
SA05-1-3*	28	625	Granite gneiss	na	na	na	0.99	0.95	0.99	0.93	32.75
SA05-2-1	28	624	Granite gneiss	na	na	na	0.98	0.98	1.00	0.96	33.64
SA05-2-2	28	636	Granite gneiss	na	na	na	0.98	0.97	0.99	0.95	33.54
SA05-3-1*	28	724	Granite gneiss	na	na	na	0.94	1.00	1.00	0.94	35.83
SA05-4-2	28	613	Granite gneiss	na	na	na	0.99	1.00	1.00	0.99	34.51
SA05-6-1	28	623	Quartz	na	na	na	1.00	1.00	1.00	1.00	35.07
SA04-29-1	27	203	Richtersveld Granite	25.87	73750	1216.10	1.00	1.00	1.00	1.00	25.82
SA04-35-1	31	1600	Molteno sandstone	31	12	1762	1.00	1.00	1.00	1.00	84.67

Table A.4.10 SA05 Al analytical data 1. Al data are normalised using the Z92-0222 standard with a nominal $^{10}Be/^{9}Be$ ratio of 4.11 $x10^{-11}$. Denudation rates are calculated using sea level, high latitude ^{26}Al production rate (Stone, 2000). ± means plus or minus standard uncertainty.

Sample ID	±	Production rate spallation and muons (atoms g^{-1} a^{-1}) (Dunai)	±	Stone's altitude-latitude scaling factor	Production rate spallation only (at g^{-1} a^{-1}) (Stone)	±	Stone's scaling factor (spallation and muons)	Production rate spallation and muons (at g^{-1} a^{-1}) (Stone)	±	Sample mass (g)	±
SA05-1-1	2.11	33.46	2.04	1.3079	38.71	2.37	1.30	38.54	2.35	24.78	1.00E-05
SA05-1-2*	2.12	33.93	2.07	1.3119	39.25	2.40	1.31	39.07	2.39	16.47	1.00E-05
SA05-1-3*	2.10	32.63	1.99	1.3021	37.75	2.31	1.30	37.59	2.30	9.45	1.00E-05
SA05-2-1	2.10	33.52	2.05	1.3011	38.79	2.37	1.30	38.62	2.36	20.06	1.00E-05
SA05-2-2	2.12	33.40	2.04	1.3128	38.64	2.36	1.31	38.46	2.35	20.00	1.00E-05
SA05-3-1*	2.27	35.68	2.18	1.4019	41.14	2.51	1.39	40.93	2.50	22.68	1.00E-05
SA05-4-2	2.08	34.38	2.10	1.2904	39.80	2.43	1.28	39.63	2.42	27.32	1.00E-05
SA05-6-1	2.10	34.9	2.1	1.3001	40.43	2.47	1.29	40.26	2.46	30.39	1.00E-05
SA04-29-1	1.52	52.7	3.2	1.92	59.86	3.66	1.91	59.40	3.63	29.03	1.00E-05
SA04-35-1	4.98	88.34	5.40	3.14	97.75	5.97	3.11	96.73	5.91	33.60	1.00E-05

Table A.4.10 (continued from previous page)

Sample ID	Carrier mass (g)	± Standard Uncertainty	$^{26}Al/^{27}Al$	s ($^{26}Al/^{27}Al$)	^{27}Al content (g)	N ^{27}Al (at g^{-1})	N ^{26}Al (at g-1)	±	Erosion rate spallation only (mm ka^{-1}) (Dunai)	±	Averaging time (ka)
SA05-1-1	0.00E+00	1.00E-05	1.06E-12	3.62E-14	2.85E-03	6.35E+19	2.70E+06	9.28E+04	6.83	0.49	87.33
SA05-1-2*	0.00E+00	1.00E-05	2.18E-12	9.39E-14	1.65E-03	3.69E+19	4.88E+06	2.10E+05	3.58	0.27	166.56
SA05-1-3*	0.00E+00	1.00E-05	8.71E-13	5.58E-14	1.21E-03	2.69E+19	2.48E+06	1.59E+05	7.28	0.66	81.84
SA05-2-1	0.00E+00	1.00E-05	1.48E-12	6.11E-14	1.95E-03	4.36E+19	3.21E+06	1.33E+05	5.67	0.42	105.19
SA05-2-2	0.00E+00	1.00E-05	4.02E-12	7.55E-14	1.51E-03	3.36E+19	6.74E+06	1.27E+05	2.38	0.16	250.62
SA05-3-1*	0.00E+00	1.00E-05	4.96E-12	1.61E-13	1.80E-03	4.01E+19	8.78E+06	2.84E+05	1.85	0.13	322.55
SA05-4-2	0.00E+00	1.00E-05	6.80E-12	1.34E-13	2.11E-03	4.71E+19	1.17E+07	2.31E+05	1.17	0.10	510.80
SA05-6-1	0.00E+00	1.00E-05	2.14E-13	1.57E-14	2.86E-03	6.38E+19	4.49E+05	3.30E+04	45.96	5.18	12.97
SA04-29-1	0.00E+00	1.00E-05	9.50E-13	2.87E-14	1.02E-02	2.27E+20	7.43E+06	2.24E+05	1.49	0.13	401.05
SA04-35-1	0.00E+00	1.00E-05	2.86E-12	5.68E-14	4.84E-03	1.08E+20	9.17E+06	1.83E+05	4.92	0.43	121.20

Table A.4.10 (continued from previous page)

Sample ID	Erosion rate spallation and muons (mm ka^{-1}) (Dunai)	±	Averaging time (ka)	Erosion rate spallation only (mm ka^{-1}) (Stone)	±	Averaging time (ka)	Erosion rate spallation and muons (mm ka^{-1}) (Stone)	±	Averaging time (ka)
SA05-1-1	6.80	0.48	95.10	7.96	0.56	73.92	7.92	0.55	75.29
SA05-1-2*	3.56	0.27	167.33	4.21	0.32	139.01	4.19	0.31	142.22
SA05-1-3*	7.26	0.64	82.17	8.49	0.75	68.05	8.45	0.75	70.58
SA05-2-1	5.64	0.42	105.63	6.62	0.49	89.53	6.59	0.49	90.44
SA05-2-2	2.37	0.15	251.86	2.83	0.18	211.82	2.81	0.18	211.82
SA05-3-1*	1.84	0.13	324.35	2.21	0.15	265.69	2.19	0.15	271.64
SA05-4-2	1.16	0.07	513.68	1.44	0.09	400.67	1.43	0.09	417.75
SA05-6-1	45.79	4.38	13.02	53.08	5.07	11.22	52.85	5.05	11.28
SA04-29-1	3.64	0.25	163.74	4.22	0.29	140.14	4.18	0.29	142.55
SA04-35-1	5.16	0.33	115.59	5.77	0.37	102.71	5.70	0.37	104.54

Table A.4.10 (continued from previous page)

Sample ID	Latitude (degrees south)	Altitude (m)	Geology	Basin averaged lat (degrees south)	Basin area (km^2)	Basin averaged altitude (m)	Thickness shielding scaling factor	Topo shielding scaling factor	Slope shielding scaling factor	Shielded Scaling factor	Production rate spallation only (at g^{-1} a^{-1}) (Dunai)
SA04-37-1	31	1335	Elliot and Burgersdorp Formations	31	125	1966	1.00	1.00	1.00	1.00	102.11
SA04-27-1	28	448	Granite gneiss	na	na	na	0.98	0.93	1.00	0.91	27.71
SA04-17-1	28	655	Granite gneiss	na	na	na	0.96	0.90	1.00	0.86	30.88
SA04-15-1	28	670	Granite gneiss	na	na	na	0.99	1.00	1.00	0.99	35.95
SA04-9-2	28	660	Granite gneiss	na	na	na	0.97	1.00	1.00	0.96	34.68
SA04-6-2	28	664	Granite gneiss	na	na	na	0.99	1.00	1.00	0.99	35.78

Table A.4.11 SA05 Al analytical data 2. Al data are normalised using the Z92-0222 standard with a nominal $^{10}Be/^{9}Be$ ratio of 4.11 $x10^{-11}$. Denudation rates are calculated using sea level, high latitude ^{26}Al production rate (Stone, 2000). ± means plus or minus standard uncertainty.

Sample ID	±	Production rate spallation and muons (at g^{-1} a^{-1}) (Dunai)	±	Stone's altitude-latitude scaling factor	Production rate spallation only (at g^{-1} a^{-1}) (Stone)	±	Stone's scaling factor (spallation and muons)	Production rate spallation and muons (at g^{-1} a^{-1}) (Stone)	±	Sample mass (g)	±
SA04-37-1	6.24	97.47	5.73	3.61	112.31	6.86	3.57	111.05	6.78	25.94	1.00E-05
SA04-27-1	1.69	27.79	1.86	1.14	32.24	1.97	1.14	32.18	1.97	35.02	1.00E-05
SA04-17-1	1.89	31.00	2.20	1.33	35.67	2.18	1.33	35.53	2.17	30.14	1.00E-05
SA04-15-1	2.20	36.10	2.22	1.35	41.88	2.56	1.34	41.34	2.53	29.38	1.00E-05
SA04-9-2	2.12	34.82	2.21	1.34	40.74	2.49	1.33	39.90	2.44	34.27	1.00E-05
SA04-6-2	2.19	35.93	2.21	1.34	41.69	2.55	1.33	41.16	2.51	28.02	1.00E-05

Table A.4.11 (continued from previous page)

Sample ID	Standard Uncertainty	$^{26}Al/^{27}Al$	s ($^{26}Al/^{27}Al$)	^{27}Al content (g)	N ^{27}Al (at g^{-1})	N ^{26}Al (at g-1)	±	Erosion rate spallation only (mm ka^{-1}) (Dunai)	±	Averaging time (ka)	Erosion rate spallation and muons (mm ka^{-1}) (Dunai)
SA04-37-1	1.00E-05	7.64E-13	2.34E-14	3.86E-03	8.62E+19	2.54E+06	7.78E+04	22.32	2.01	26.71	23.41
SA04-27-1	1.00E-05	9.08E-13	3.43E-14	3.08E-03	6.86E+19	1.78E+06	6.71E+04	8.73	0.67	68.25	8.71
SA04-17-1	1.00E-05	6.70E-14	6.04E-15	2.54E-03	5.66E+19	1.26E+05	1.13E+04	146.48	16.80	4.07	145.91
SA04-15-1	1.00E-05	1.75E-12	4.14E-14	2.02E-03	4.50E+19	2.68E+06	6.33E+04	7.44	0.49	80.11	7.41
SA04-9-2	1.00E-05	2.89E-13	2.12E-14	2.48E-03	5.52E+19	4.66E+05	3.42E+04	43.92	4.26	13.57	43.75
SA04-6-2	1.00E-05	2.29E-12	4.31E-14	3.34E-03	7.44E+19	6.08E+06	1.15E+05	2.94	0.19	203.06	2.92

Table A.4.11 (continued from previous page)

Standard Uncertainty	Averaging time (ka)	Sample ID	Erosion rate spallation only (mm ka^{-1}) (Stone)	Standard Uncertainty	Averaging time (ka)	Erosion rate spallation and muons (mm ka^{-1}) (Stone)	Standard Uncertainty	Averaging time (ka)	Geomag corrected erosion rate (mm ka^{-1}) (spallation and muons, Stone)	±
SA04-37-1	1.60	25.47	25.80	1.76	23.10	25.51	1.74	23.37	na	na
SA04-27-1	0.63	68.47	10.24	0.74	58.21	10.21	0.73	58.41	12.20	0.85
SA04-17-1	15.90	4.09	168.74	18.38	3.53	167.97	18.30	3.55	193.54	20.84
SA04-15-1	0.49	80.46	8.65	0.57	68.91	8.61	0.56	69.26	10.17	0.64
SA04-9-2	4.18	13.63	50.65	4.84	11.77	50.42	4.81	11.82	58.21	5.47
SA04-6-2	0.19	204.07	3.47	0.22	171.95	3.45	0.22	172.88	4.15	0.26

Table A.4.11 (continued from previous page)

Sample	Averaging time (kyr)	Iterations	% diff corrected, uncorrected
SA04-37-1	na	na	na
SA04-27-1	48.88	2	16.33
SA04-17-1	3.08	2	13.21
SA04-15-1	58.65	4	15.32
SA04-9-2	10.24	2	13.38
SA04-6-2	143.56	4	16.96

Table A.4.11 (continued from previous page)

Appendix 5 – Analytical data (CIAF samples)

Sample	Environment	Latitude	Altitude (m)	Thickness (mm)	Angle of dip	Thickness shielding scaling factor	Topo shielding scaling factor	Slope shielding scaling factor	Shielding scaling factor	Production rate spallation only (at g^{-1} a^{-1}) (Dunai)	±
SA04-04-01	Main channel below Falls	28°33'S	400	20	0	0.98	0.91	1.00	0.89	4.30	0.25
SA04-06-02	Moon Rock	28°36'S	721	20	15	0.98	0.99	1.00	0.97	5.98	0.35
SA04-09-01	Main channel above Falls	28°36'S	660	40	0	0.97	1.00	1.00	0.96	5.71	0.34
SA04-03-01	Main channel below Falls	28°33'S	448	10	0	0.99	0.95	1.00	0.94	4.72	0.28
SA04-05-01	Tributary channel below Falls	28°33'S	446	10	20	0.99	0.61	0.99	0.60	2.93	0.17
SA04-05-02	Tributary channel below Falls	28°33'S	458	50	0	0.96	0.88	1.00	0.84	4.24	0.25
SA04-11-02	Main channel above Falls	28°36'S	620	20	0	0.98	1.00	1.00	0.98	5.63	0.33
SA04-12-01	Main channel above Falls	28°36'S	622	20	20	0.98	1.00	0.99	0.97	5.58	0.33

Table A.5.1 CIAF samples analytical data 1. A weighted average of the SA03-X blank and other process blanks (see Chapter 3) was used to calculate ^{10}Be concentrations. Full-chemistry blanks had $^{10}Be/^{9}Be$ of about $4*10^{-15}$. Be data are normalised using the NIST SRM 4325 standard with a nominal $^{10}Be/^{9}Be$ ratio of $3.06*10^{-11}$. ± means plus or minus standard uncertainty.

Sample	Production rate spallation and muons (at $g^{-1} a^{-1}$) (Dunai)	±	Stone's SEL scaling (spallation)	Stone's SEL scaling (spallation and muons)	Production rate spallation only (at $g^{-1} a^{-1}$) (Stone)	±	Production rate spallation and muons (at $g^{-1} a^{-1}$) (Stone)	±	N ^{10}Be	σ (N ^{10}Be)	ε (mm ka^{-1}) Spallation only (Dunai)
SA04-04-01	4.29	0.25	1.10	1.09	5.01	0.29	4.99	0.29	2.98E+05	7.72E+03	8.32
SA04-06-02	5.96	0.35	1.40	1.39	6.89	0.41	6.86	0.40	1.57E+06	4.19E+04	2.00
SA04-09-01	5.69	0.33	1.34	1.33	6.57	0.39	6.54	0.38	5.94E+04	2.52E+03	57.04
SA04-03-01	4.71	0.28	1.14	1.14	5.48	0.32	5.46	0.32	3.89E+05	1.07E+04	6.96
SA04-05-01	2.92	0.17	1.14	1.13	3.47	0.20	3.46	0.20	1.53E+05	5.32E+03	11.15
SA04-05-02	4.23	0.25	1.15	1.14	4.92	0.29	4.90	0.29	1.28E+05	5.69E+03	19.40
SA04-11-02	5.61	0.33	1.30	1.29	6.49	0.38	6.46	0.38	6.63E+04	8.25E+03	50.30
SA04-12-01	5.56	0.33	1.30	1.29	6.43	0.38	6.40	0.38	9.46E+04	4.78E+03	34.92

Table A.5.1 (continued from previous page)

Sample	± Standard Uncertainty	Averaging time (ka)	ε (mm ka^{-1}) Spallation and muons (Dunai)	±	Averaging time (ka)	ε (mm ka^{-1}) Spallation only (Stone)	±	Averaging time (ka)	ε (mm ka^{-1}) spallation & muons (Stone)	±	Averaging time (ka)
SA04-04-01	0.53	71.67	8.30	0.53	71.83	9.73	0.63	61.27	9.70	0.62	61.45
SA04-06-02	0.13	298.22	1.99	0.13	299.31	2.35	0.15	254.14	2.33	0.15	255.55
SA04-09-01	4.14	10.45	56.85	4.12	10.49	65.72	4.77	9.07	65.42	4.75	9.11
SA04-03-01	0.45	85.69	6.94	0.45	85.87	8.13	0.53	73.35	8.10	0.53	73.59
SA04-05-01	0.76	53.46	11.13	0.76	53.57	13.26	0.91	44.96	13.22	0.90	45.11
SA04-05-02	1.43	30.73	19.36	1.43	30.79	22.58	1.66	26.41	22.50	1.66	26.50
SA04-11-02	6.92	11.85	50.12	6.89	11.89	58.01	7.98	10.28	57.76	7.94	10.32
SA04-12-01	2.71	17.07	34.80	2.70	17.13	40.28	3.12	14.80	40.10	3.11	14.87

Table A.5.1 (continued from previous page)

Sample	Geomag. Corrected ε (mm ka-1) spallation & muons (Stone)	± Standard Uncertainty	Av. Time (ka)	No. of iterations	% diff with old geomag. Latitude
SA04-04-01	11.05	0.71	53.93	3	12.24
SA04-06-02	2.85	0.18	209.48	2	18.03
SA04-09-01	74.94	5.44	7.96	2	12.69
SA04-03-01	9.64	0.63	61.83	2	15.98
SA04-05-01	16.32	1.12	36.53	3	19.01
SA04-05-02	26.56	1.96	22.44	3	15.29
SA04-11-02	66.23	9.11	9.00	2	12.79
SA04-12-01	46.50	3.61	12.82	3	13.76

Table A.5.1 (continued from previous page)

Sample	Environment	Latitude	Altitude (m)	Thickness (mm)	Angle of dip	Thickness shielding scaling factor	Topo shielding scaling factor	Slope shielding scaling factor	Shielding scaling factor	Production rate spallation only (at g^{-1} a^{-1}) (Dunai)	±
SA04-14-01	Anabranch channel above Falls system	28°35'S	615	20	12	0.98	0.99	1.00	0.97	5.56	0.33
SA04-04-02	Main channel below Falls	28°33'S	439	40	0	0.97	0.90	1.00	0.87	4.35	0.26
SA04-06-03	Moon Rock	28°36'S	721	10	15	0.99	1.00	1.00	0.99	6.13	0.36
SA04-07-01	Interfluve	28°36'S	645	10	0	0.99	1.00	1.00	0.99	5.80	0.34
SA04-13-01	Anabranch channel above Falls system	28°36'S	679	20	0	0.98	1.00	1.00	0.98	5.91	0.35
SA04-13-02	Anabranch channel above Falls system	28°36'S	679	20	0	0.98	1.00	1.00	0.98	5.91	0.35
SA04-14-04	Anabranch channel above Falls system	28°35'S	657	40	0	0.97	0.97	1.00	0.94	5.55	0.33
SA04-16-01	Interfluve	28°36'S	679	20	0	0.98	1.00	1.00	0.98	5.91	0.35

Table A.5.2 CIAF samples analytical data 2. A weighted average of the SA03-X blank and other process blanks (see Chapter 3) was used to calculate ^{10}Be concentrations. Full-chemistry blanks had $^{10}Be/^{9}Be$ of about $4*10^{-15}$. Be data are normalised using the NIST SRM 4325 standard with a nominal $^{10}Be/^{9}Be$ ratio of $3.06*10^{-11}$. ± means plus or minus standard uncertainty.

Sample	Production rate spallation and muons (at $g^{-1} a^{-1}$) (Dunai)	±	Stone's SEL scaling (spallation)	Stone's SEL scaling (spallation and muons)	Production rate spallation only (at $g^{-1} a^{-1}$) (Stone)	±	Production rate spallation and muons (at $g^{-1} a^{-1}$) (Stone)	±	N ^{10}Be	σ (N ^{10}Be)	ε (mm ka^{-1}) Spallation only (Dunai)
SA04-14-01	5.53	0.33	1.29	1.29	6.41	0.38	6.38	0.38	8.60E+04	4.72E+03	38.29
SA04-04-02	4.33	0.25	1.13	1.13	5.04	0.30	5.03	0.30	1.82E+05	4.96E+03	13.95
SA04-06-03	6.11	0.36	1.40	1.39	7.07	0.42	7.04	0.41	1.49E+06	3.95E+04	2.18
SA04-07-01	5.78	0.34	1.32	1.32	6.68	0.39	6.65	0.39	1.33E+06	3.52E+04	2.32
SA04-13-01	5.89	0.35	1.36	1.35	6.80	0.40	6.77	0.40	4.44E+05	1.22E+04	7.66
SA04-13-02	5.89	0.35	1.36	1.35	6.80	0.40	6.77	0.40	3.26E+05	9.06E+03	10.52
SA04-14-04	5.52	0.32	1.33	1.33	6.39	0.38	6.36	0.37	9.11E+04	2.93E+03	36.05
SA04-16-01	5.89	0.35	1.36	1.35	6.80	0.40	6.77	0.40	1.84E+06	4.94E+04	1.65

Table A.5.2 (continued from previous page)

Sample	±	Averaging time (ka)	ε (mm ka^{-1}) Spallation and muons (Dunai)	±	Averaging time (ka)	ε (mm ka^{-1}) Spallation only (Stone)	±	Averaging time (ka)	ε (mm ka^{-1}) spallation & muons (Stone)	±	Averaging time (ka)
SA04-14-01	3.08	15.57	38.08	3.07	15.65	44.16	3.55	13.50	43.97	3.54	13.56
SA04-04-02	0.90	42.73	13.89	0.90	42.91	16.24	1.05	36.71	16.19	1.05	36.83
SA04-06-03	0.14	274.00	2.17	0.14	274.99	2.55	0.16	233.51	2.54	0.16	234.79
SA04-07-01	0.15	256.87	2.31	0.15	257.86	2.72	0.18	219.51	2.70	0.17	220.60
SA04-13-01	0.50	77.84	7.63	0.50	78.11	8.85	0.57	67.35	8.81	0.57	67.68
SA04-13-02	0.68	56.64	10.49	0.68	56.84	12.15	0.79	49.07	12.09	0.79	49.31
SA04-14-04	2.42	16.54	35.86	2.40	16.62	41.53	2.78	14.36	41.34	2.77	14.42
SA04-16-01	0.11	362.07	1.64	0.11	363.48	1.94	0.13	308.03	1.93	0.12	309.69

Table A.5.2 (continued from previous page)

Sample	Geomagnetic corrected erosion rate (mm ka^{-1}) (Stone, spallation, muons)	±	Averaging time (ka)	Iterations	% difference with original
SA04-14-01	50.82	4.09	11.73	2	13.48
SA04-04-02	19.21	1.25	31.04	3	15.71
SA04-06-03	3.19	0.21	186.61	7	20.52
SA04-07-01	3.25	0.21	183.40	7	16.86
SA04-13-01	10.33	0.67	57.72	2	14.71
SA04-13-02	15.16	0.99	39.31	5	20.27
SA04-14-04	48.02	3.22	12.41	5	13.92
SA04-16-01	2.29	0.15	260.00	5	16.05

Table A.5.2 (continued from previous page)

Appendix 6 – Correlation of denudation rates with other variables

A.6.1 Correlation of denudation rates with topographic gradient

Topographic maps, field observations and plots of the gradient of the Orange River (Summerfield *et al.*, unpublished data) were used to determine topographic gradients for the main channel and sampled tributary channels in the Orange basin. Normalised ^{10}Be concentration data were worked out from the ^{10}Be concentration multiplied by the average basin production rate divided by sea level high latitude production rate (5.1 at g^{-1} a^{-1}). Normalized data was used to eliminate bias from comparing different production rates. The resulting values are plotted in Figures A.6.1 - 3. In the following discussion, ^{10}Be concentration is used as a shorthand for denudation rate although it must be remembered that ^{10}Be concentration is inversely related to denudation rate, and that these are production-normalised concentrations.

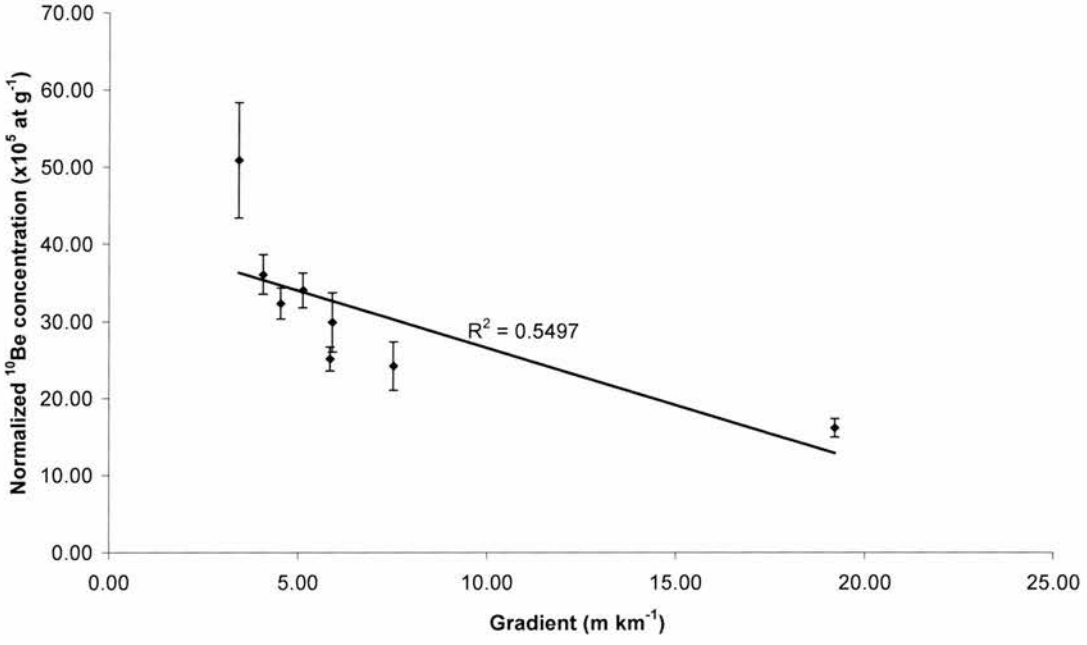

Figure A.6.1 Topographic gradient (m km^{-1}) plotted against normalised ^{10}Be concentration for main channel samples. Note that there is a weak negative correlation between ^{10}Be concentration and gradient.

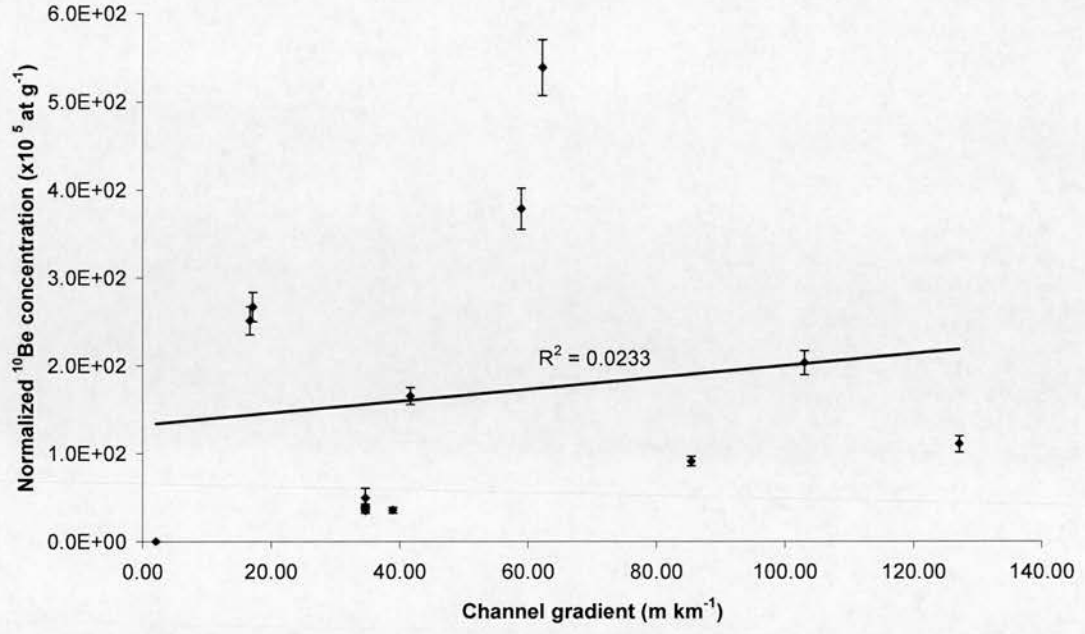

Figure A.6.2 Topographic gradient (m km^{-1}) plotted against normalised ^{10}Be concentration for tributary channel samples. Note that there is little apparent correlation between ^{10}Be concentration and gradient.

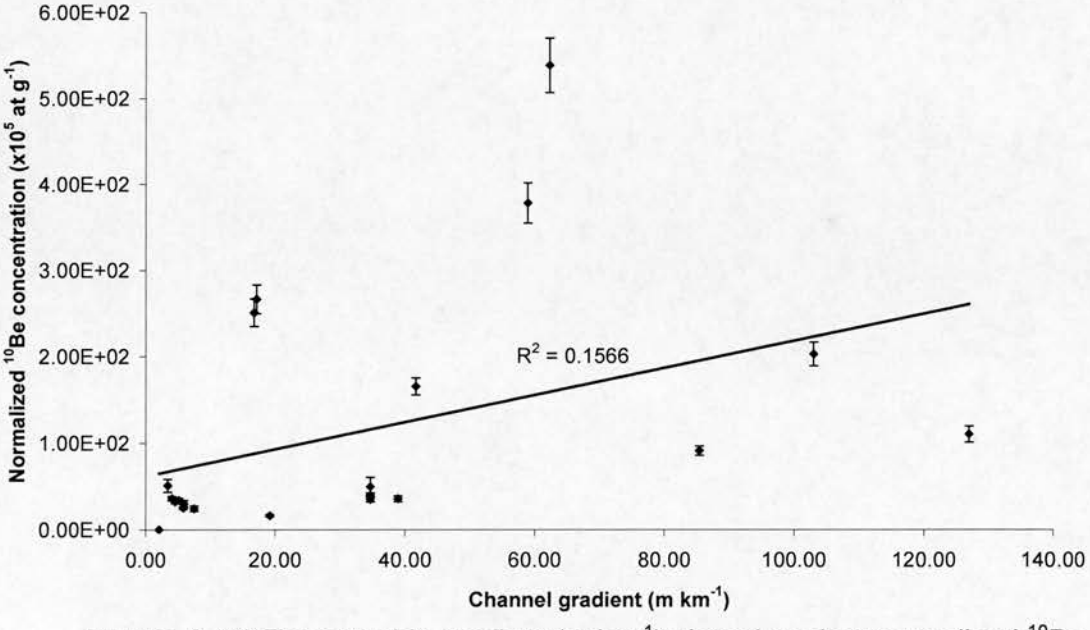

Figure A.6.3 Topographic gradient (m km^{-1}) plotted against normalised ^{10}Be concentration for all fluvial samples. Note that there is little apparent correlation between ^{10}Be concentration and gradient.

It can be seen from Figure A.6.1 that there is a weak negative correlation (R^2 = 55%) between topographic gradient and ^{10}Be concentration. Since concentration is inversely related to denudation rate, there is a weak positive correlation between gradient and denudation. Areas of high topographic gradient would be expected to have higher denudation rates, as there is more potential energy available in such areas, leading to greater erosion. The relationship between topography and denudation was made explicit by Ahnert (1970), in the context of the relationship between denudation and relief, which is discussed for the Orange River below. Figures A.6.2 and A.6.3 illustrate just how complex the relationship between gradient and denudation is – there is little apparent correlation between ^{10}Be concentration and gradient for either tributary channels or all fluvial samples.

A.6.2 Correlation of denudation rates with relief

^{10}Be concentration was plotted against basin relief (in metres, calculated from the highest and lowest points in the basin, as described in Appendix 3). As can be seen from Figures A.6.4 -6, there is little correlation between relief and concentration (and therefore denudation). Whilst this may seem surprising, given Ahnert's (1970) oft-cited relationship between denudation and relief, it must be remembered that the Orange basin is a highly complex environment where a number of factors (relief, climate and lithology included) can interact to generate different erosion rate scenarios. Although high relief is usually positively correlated with high denudation (and therefore low cosmogenic nuclide concentration), this does not appear to hold true for the sampled locations in the Orange basin. Although this is likely to be a function of the complexity of the Orange basin, it may also reflect the limited number of sampled locations in this study and a more systematic study may reveal stronger relief-denudation relationships.

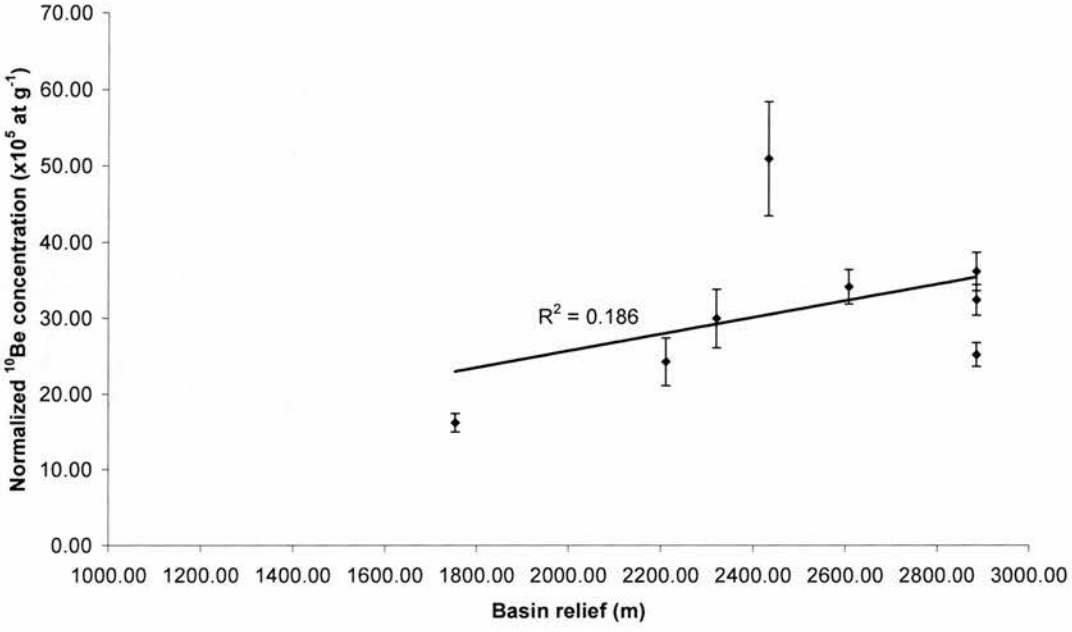

Figure A.6.4 Basin relief plotted against normalised ^{10}Be concentration for main channel samples.

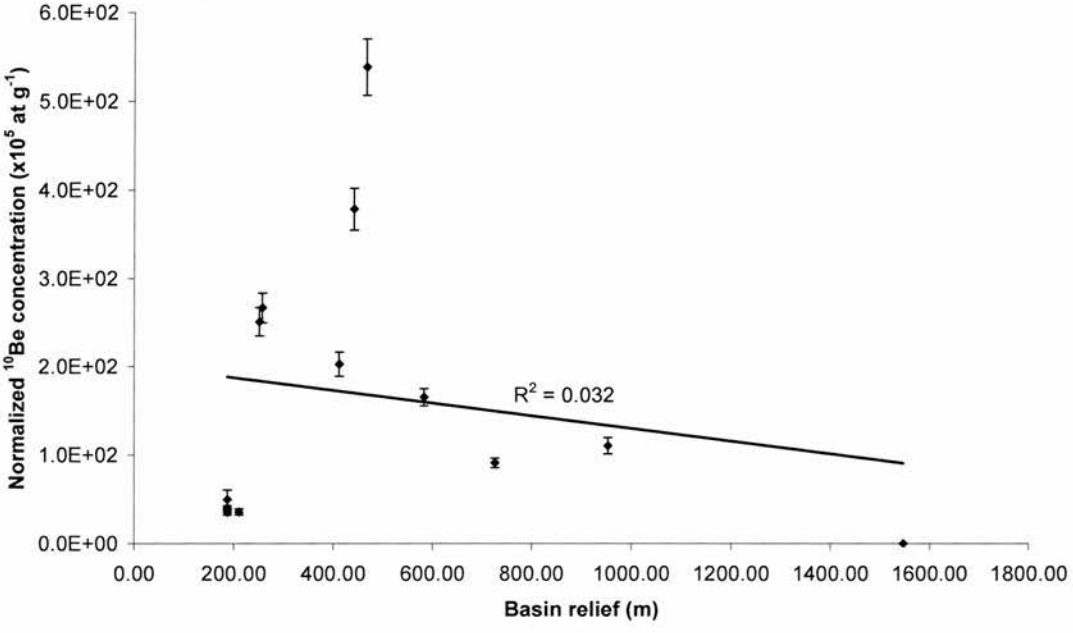

Figure A.6.5 Basin relief plotted against normalised ^{10}Be concentration for tributary channel samples.

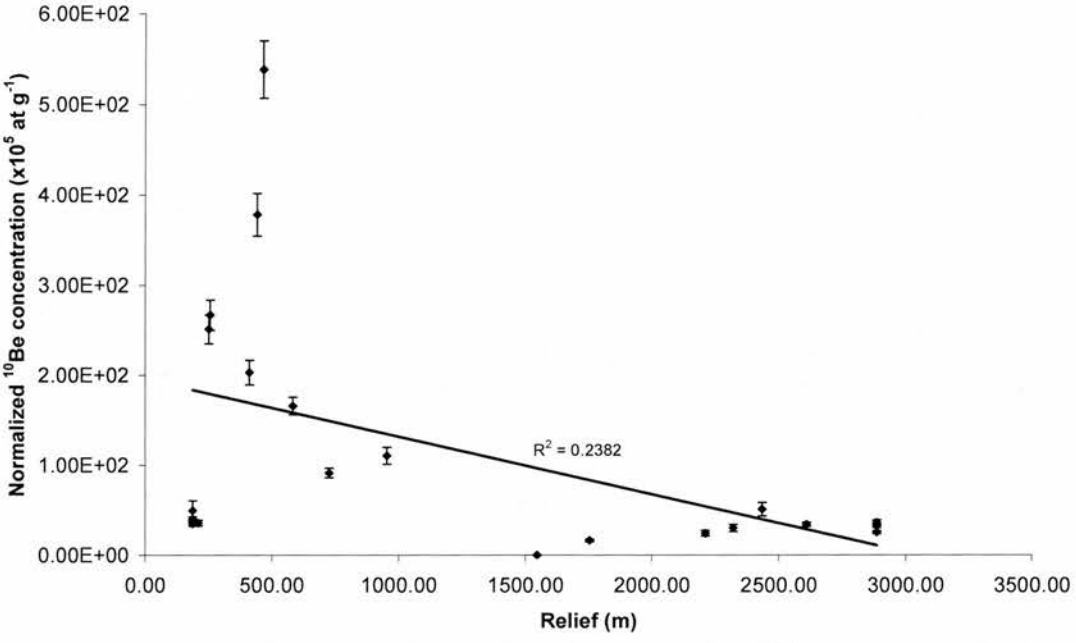

Figure A.6.6 Basin relief plotted against normalised ^{10}Be concentration for all fluvial samples.

A.6.3 Correlation of denudation rates with relief ratio

Relief ratio is the ratio of total basin relief to the maximum length of the basin and is measured according to Summerfield & Hulton's (1994) method as described in Appendix 4. Once again, there is no apparent relationship between relief ratio and nuclide concentration for either the main channel samples (Figure A.6.7), the tributary samples (Figure A.6.8) or all samples considered together (Figure A.6.9), showing that there is no correlation with denudation rate.

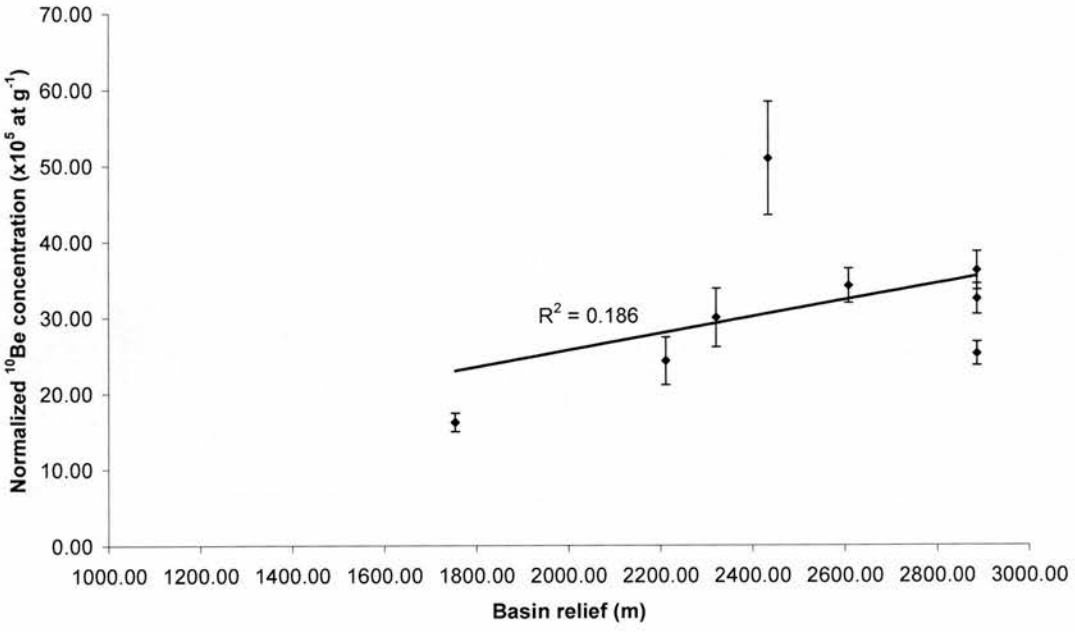

Figure A.6.7 Basin relief ratio plotted against normalised ^{10}Be concentration for main channel samples.

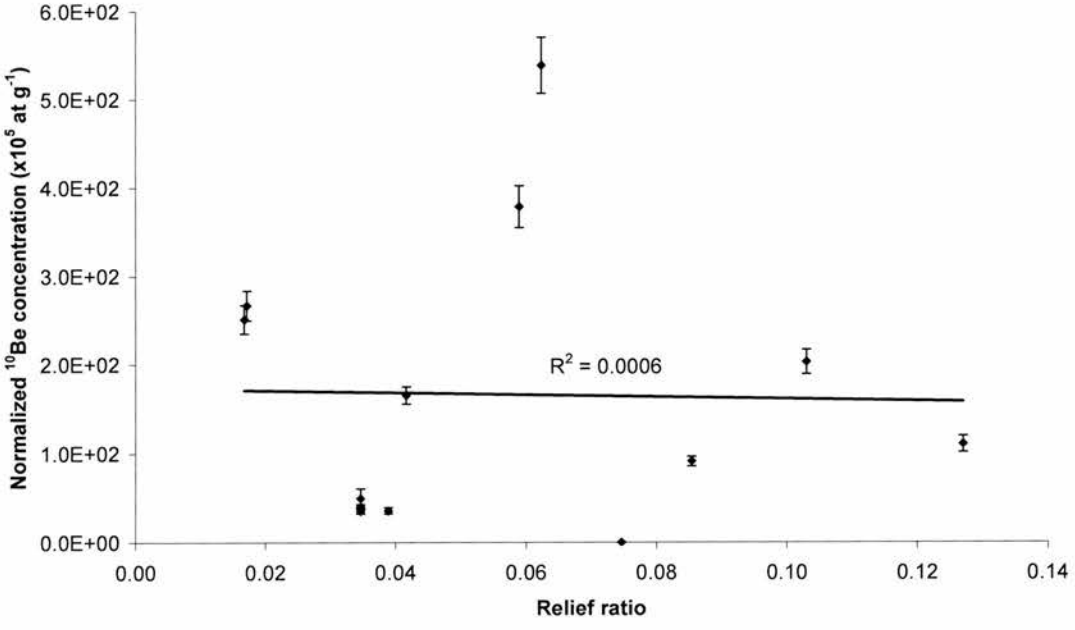

Figure A.6.8 Basin relief ratio plotted against normalised ^{10}Be concentration for tributary samples.

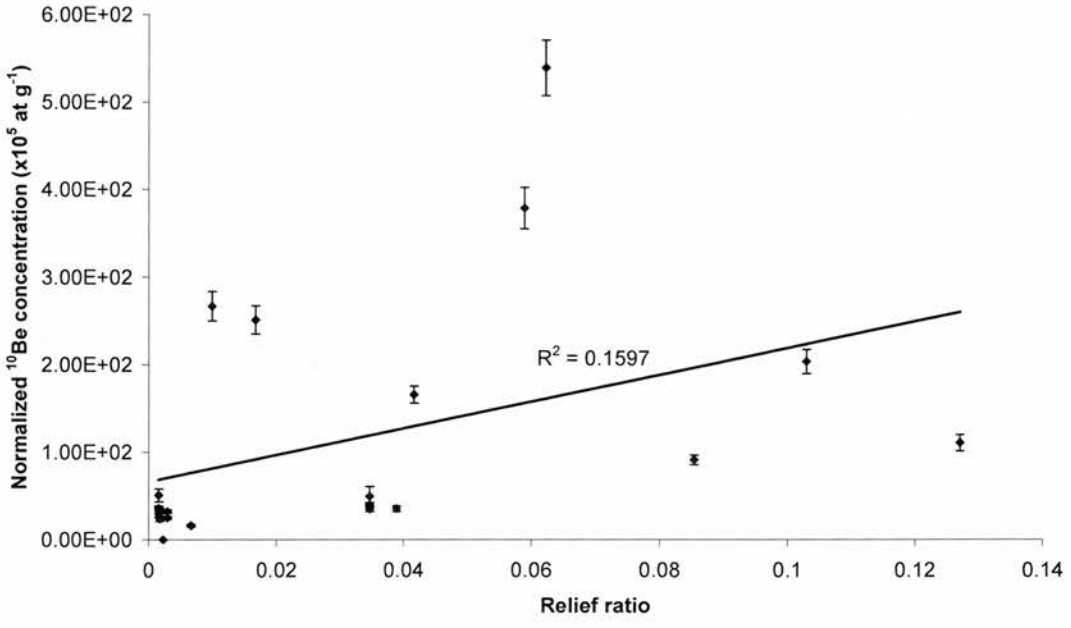

Figure A.6.9 Basin relief ratio plotted against normalised ^{10}Be concentration for all fluvial samples.

A.6.4 Correlation of denudation rates with basin area

Figures A.6.10-12 show that there is little correlation of denudation rates with basin area. It might be expected that denudation rates will decrease with greater basin area as more sites become available for sediment storage. The peculiar hypsometry of the Orange means that as basin area increases, more and more low relief, long-exposed sites (with a high cosmogenic nuclide content, hence low denudation rate signal) will be potentially incorporated into the river's sediment. This is discussed in Chapters 4-6 but, as illustrated here, does not appear to be a geomorphologically significant phenomenon.

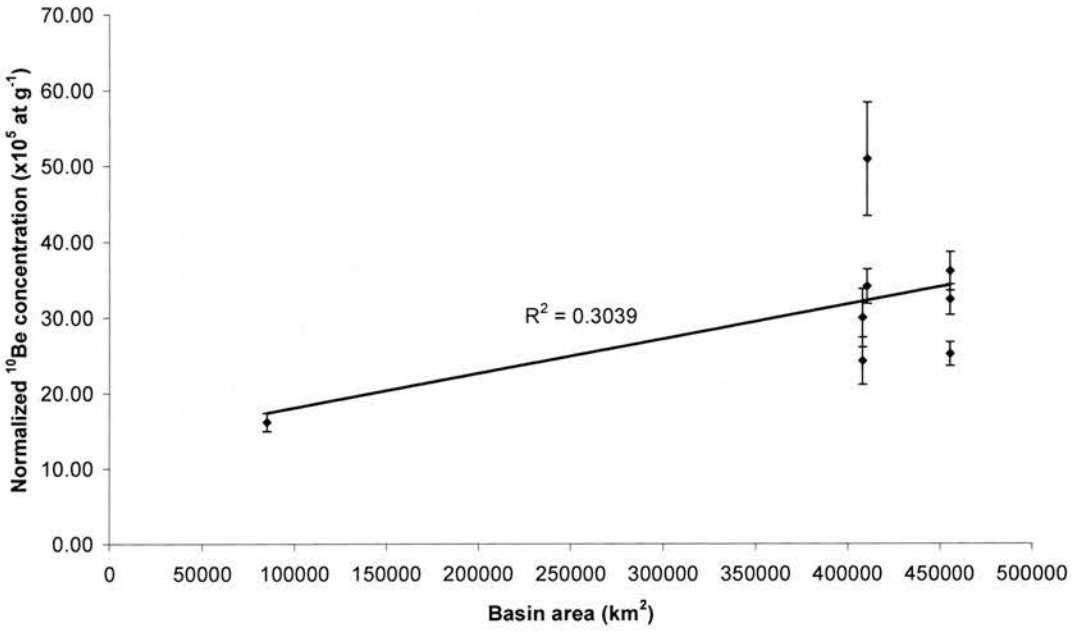

Figure A.6.10 Basin area plotted against normalised ^{10}Be concentration for main channel samples.

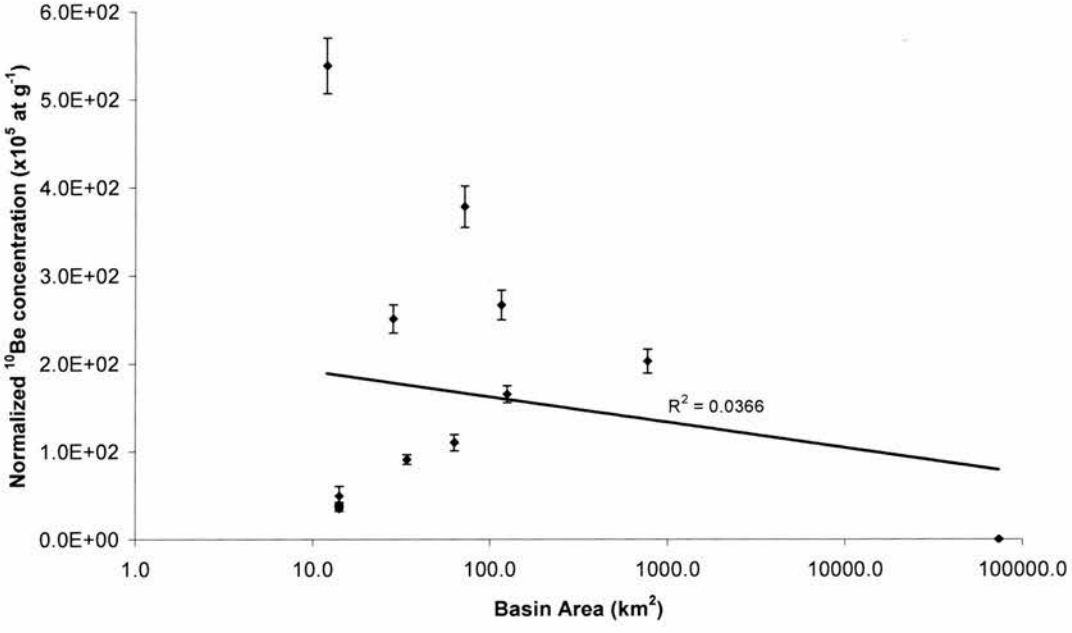

Figure A.6.11 Basin area plotted against normalised ^{10}Be concentration for tributary samples.

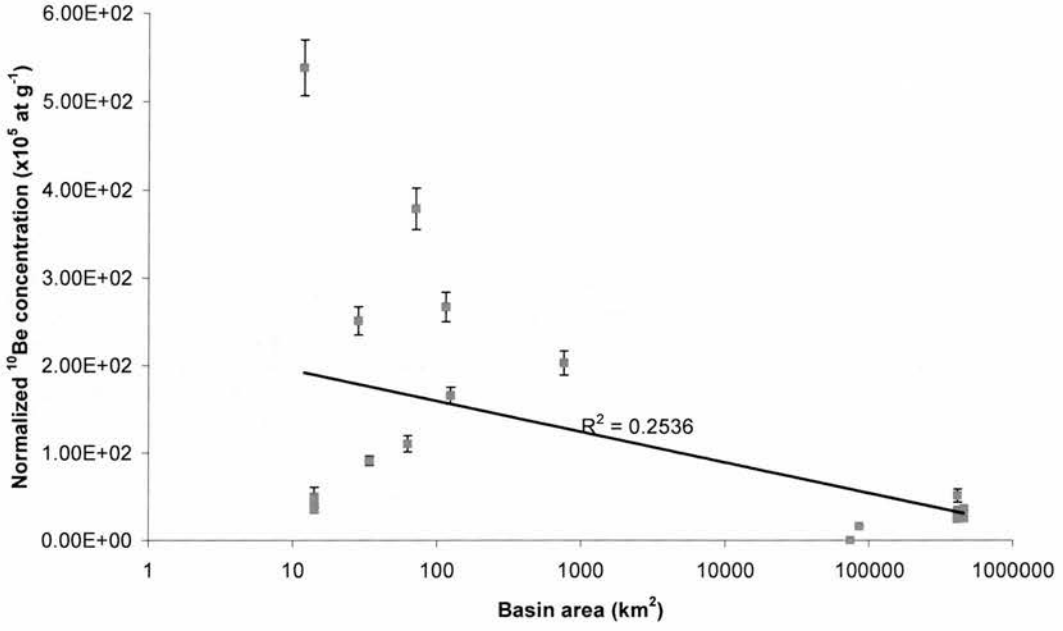

Figure A.6.12 Basin area plotted against normalised ^{10}Be concentration for all fluvial samples.

A.6.5 Correlation of denudation rates with basin altitude

Basin altitude was calculated as a weighted average according to the proportion of area which each latitude bin occupied out of the total basin area (described in Chapter 3 and Appendix 3). This average altitude was then used to calculate the basin average cosmogenic production rate. Figures A.1.13 to A.1.15 show the relationship between basin altitude and cosmogenic nuclide concentration. Once again, no significant relationship can be seen between altitude and nuclide concentration. Indeed, there is no reason why normalized nuclide concentration (and therefore denudation rate) should be correlated with denudation – since the data are normalized for production rate variation, there will be no dependence of denudation rate on altitude.

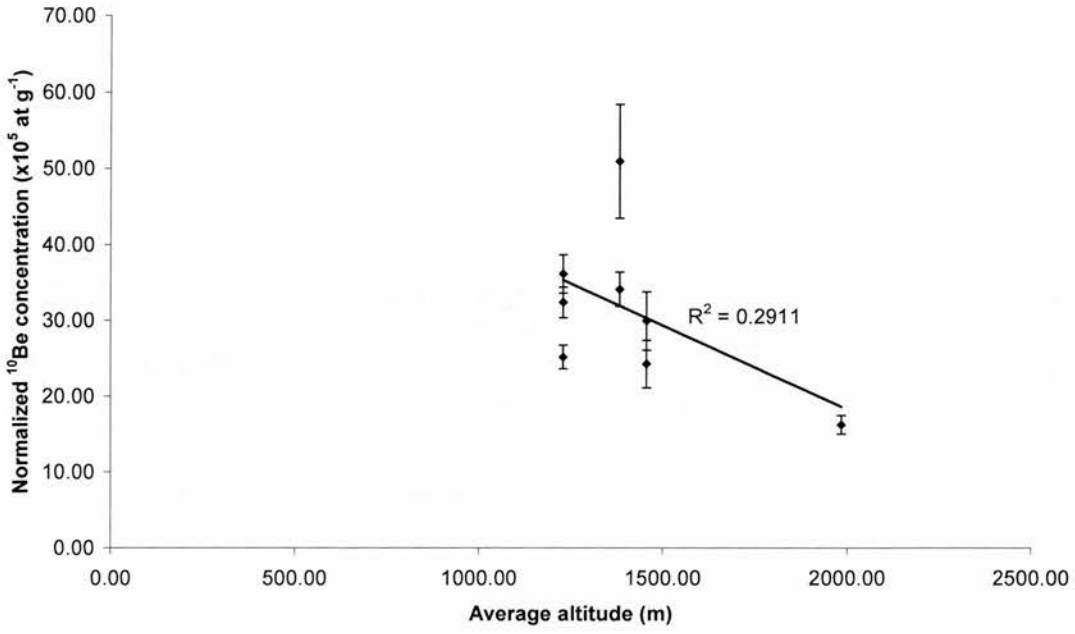

Figure A.6.13 Basin average altitude plotted against normalised ^{10}Be concentration for main channel samples.

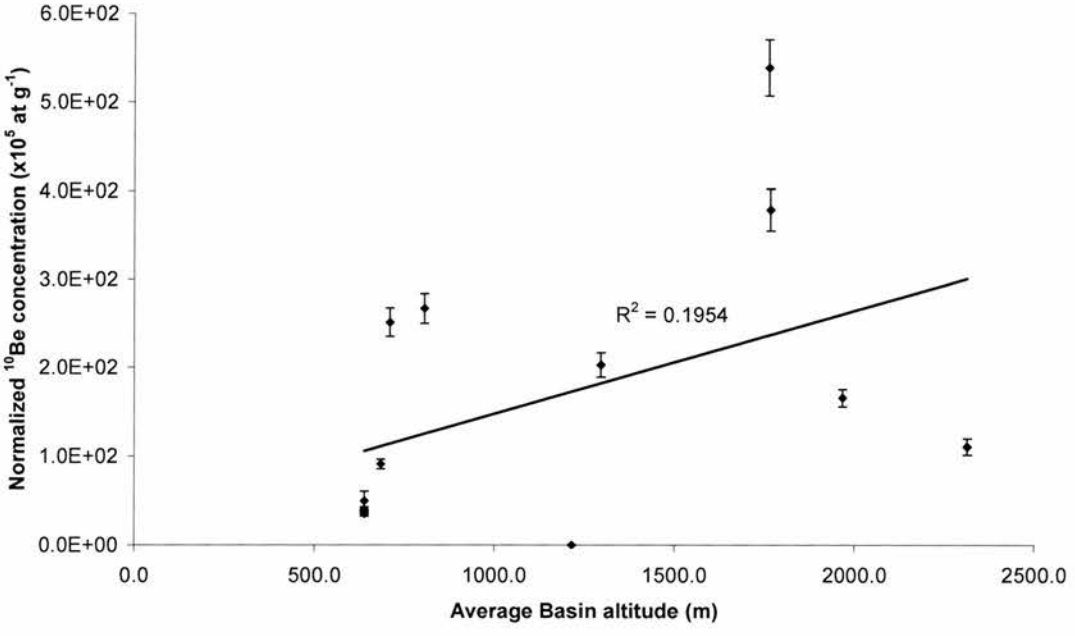

Figure A.6.14 Basin average altitude plotted against normalised ^{10}Be concentration for tributary samples.

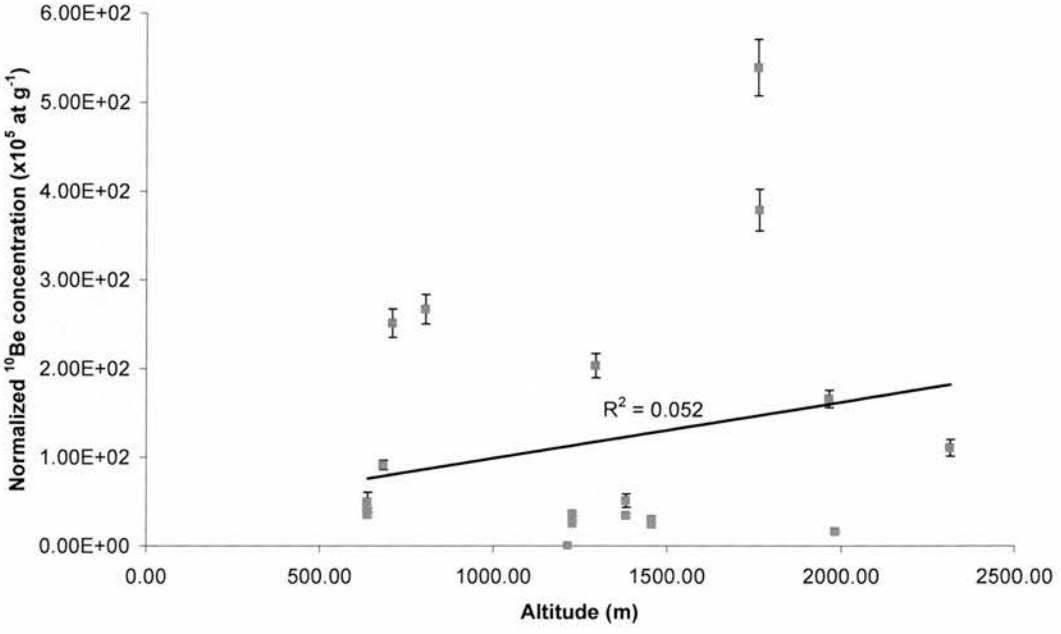

Figure A.6.15 Basin average altitude plotted against normalised ^{10}Be concentration for all fluvial samples.

A.6.6 Correlation of denudation rates with basin latitude

As described in Chapter 3 and Appendix 3, average latitude was calculated for all of the catchment averaged samples. Since the data presented here are normalized for production rate variations, latitude would not be expected to have any influence on nuclide concentration (and therefore denudation rate) and indeed, Figures A.6.16 – A.6.18 show no significant systematic variation in normalized nuclide concentration with average latitude.

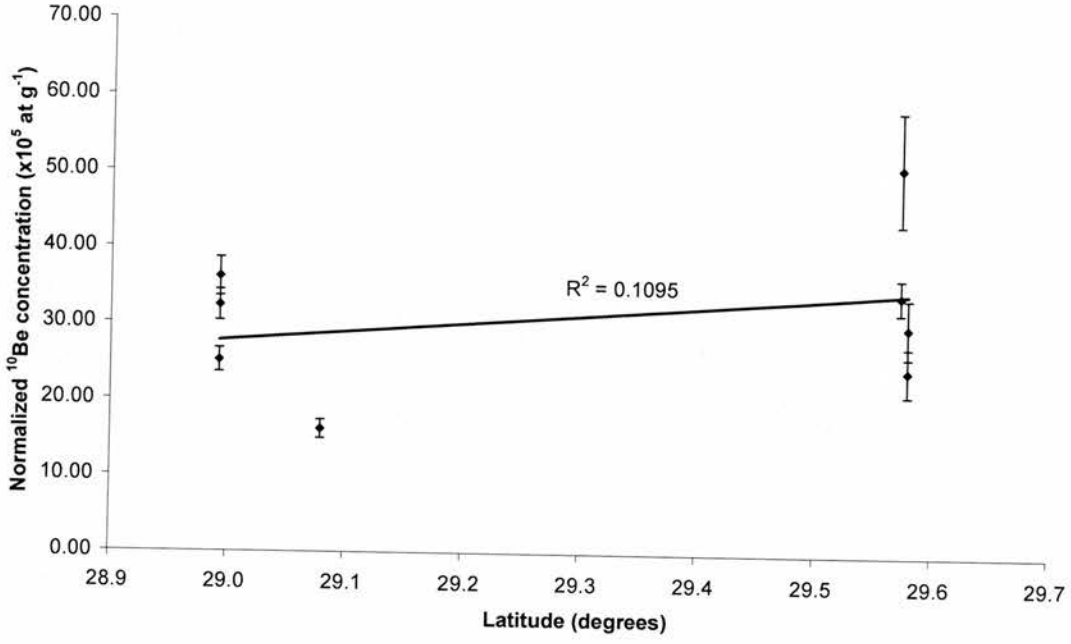

Figure A.6.16 Basin average latitude plotted against normalised ^{10}Be concentration for main channel samples.

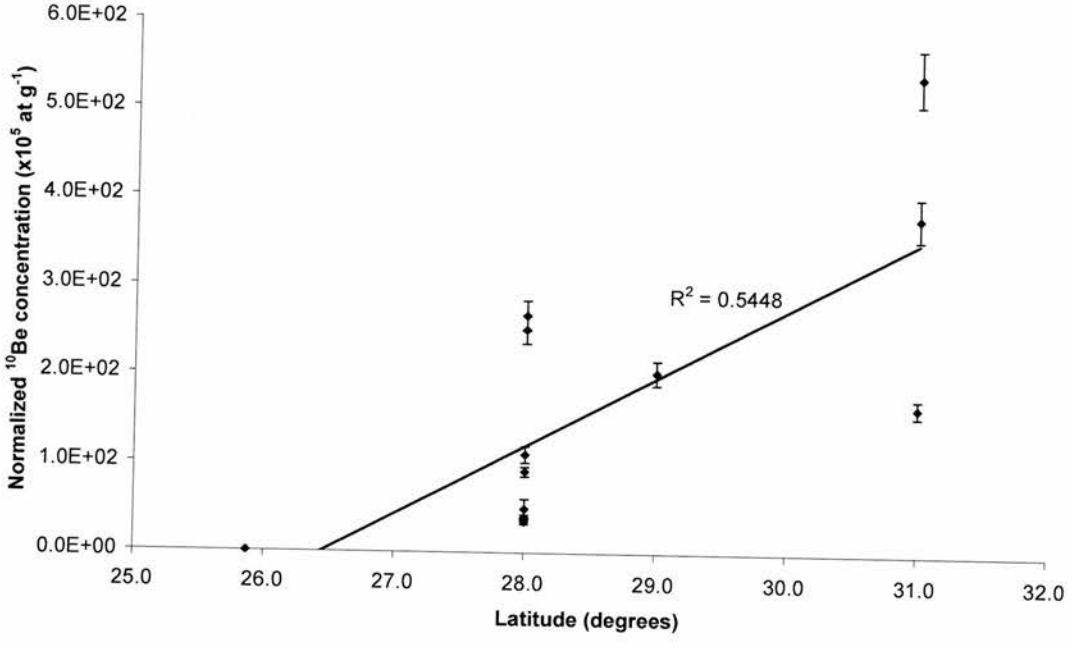

Figure A.6.17 Basin average latitude plotted against normalised ^{10}Be concentration for tributary channel samples.

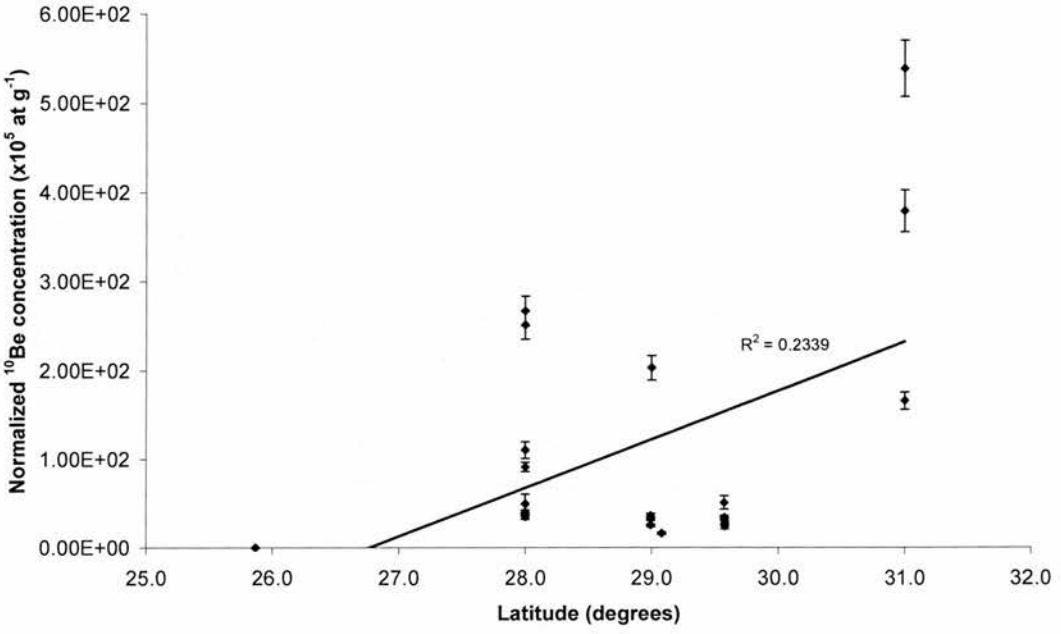

Figure A.6.18 Basin average latitude plotted against normalised ^{10}Be concentration for all fluvial samples.

A.6.7 Summary

The above discussion has compared normalized ^{10}Be concentrations (as a shorthand for production-normalised denudation rate) with gradient, relief, relief ratio, basin area, average basin altitude and average basin latitude. Climate was not compared due to the difficulty in extrapolating today's climatic conditions back over the averaging time of the samples (tens of thousands to hundreds of thousands of years). Whilst the discussion above does not show any meaningful correlation of denudation with any of the variables looked at (even the well-publicised relief-denudation relationship as described by Ahnert (1970)), it does highlight the inherent complexity in the Orange River basin. Identifying the controlling variables that influence denudation on various scales was first attempted by Schumm & Lichty (1965). A synthesis similar to theirs is impossible in this study – there are too many variables operating over different timescales and over different spatial scales, and interacting with each other to produce a meaningful hierarchy of controls on denudation in the Orange basin. With the limited number of samples in this study (and the primary focus being on establishing the first Quaternary timescale denudation rates for the Orange basin, rather than the controls on denudation) the factors controlling

denudation cannot be categorically identified. The complexity of the system makes it difficult to do so, although a more detailed study may in future elucidate the controlling factors.